Transactions of the ASME®

Technical Editor, **LEON M. KEER (1993)**

The Technological Institute
Northwestern University
Evanston, IL 60201

Transactions of the ASME, Journal of Applied Mechanics (ISSN 0021-8936) is published quarterly (Mar., June, Sept., Dec.) for $160.00 per year by The American Society of Mechanical Engineers, 345 East 47th Street, New York, NY 10017. Second class postage paid at New York, NY and additional mailing offices. POSTMASTER: Send address changes to Transactions of the ASME, Journal of Applied Mechanics, c/o THE AMERICAN SOCIETY OF MECHANICAL ENGINEERS, 22 Law Drive, Box 2300, Fairfield, NJ 07007-2300.

CHANGES OF ADDRESS must be received at Society headquarters seven weeks before they are to be effective. Please send old label and new address.

PRICES: To members, $29.00, annually: to nonmembers, $160.00. Add $20.00 for postage to countries outside the United States and Canada.

INDEXED by Applied Mechanics Reviews and Engineering Information, Inc. Canadian Goods & Services Tax Registration #126148048.

Journal of Applied Mechanics

Published Quarterly by The American Society of Mechanical Engineers

VOLUME 59 • NUMBER 2 • PART 1 • JUNE 1992

TECHNICAL PAPERS

(Contents continued on Inside Back Cover)

CONTENTS (CONTINUED)

BRIEF NOTES

BOOK REVIEWS

ANNOUNCEMENTS AND SPECIAL NOTES

W. Jiang
Asst. Professor,
Mechanical Engineering Department,
Florida International University,
Miami, FL 33199

F. A. Leckie
Professor,
Department of Mechanical and
Environmental Engineering,
University of California,
Santa Barbara, CA 93106

A Direct Method for the Shakedown Analysis of Structures Under Sustained and Cyclic Loads

This paper presents a straightforward method for the direct determination of the steady solutions in shakedown analysis. The direct method was first proposed by Zarka et al. This paper simplifies this method by showing that the modified hardening parameter field can be directly found from the yield condition and the incremental residual stress. Thus, only two elastic analyses are required to obtain the shakedown solutions without the need of performing a full-scale analysis. The two-bar structure and the tube problem are solved as examples to show the feasibility and efficiency of this approach.

1 Introduction

The response of structures subjected to cyclic loads and temperatures is often very complicated. The structure may elastically shake down, or it may incur reversed plasticity or ratchetting. Several fundamental questions can be raised; the existence of a steady state is usually of first concern. We then need to know when the shakedown will occur and what the final steady stress-strain state will be. The theoretical investigation of all the possible responses and the evaluation of the life of a comparatively complex structure can be very difficult, even if the creep effect is neglected in a first step analysis. The computer based on the finite element can help, but the numerical approach often turns out to be very expensive and cannot yield a definite and accurate answer except for a small number of cycles because of accumulated computational error. On the other hand, in practice the design is primarily based on the maximum possible stress and strain attainable under sustained and periodic loads, and thus a large amount of incremental inelastic calculations approaching the steady state is often inevitable. Note that Ainsworth (1977) has proposed a method to determine an upper bound on creep deformation based on the complete steady state, cyclic stress distributions of a similar structure that does not creep. Therefore, for practical purposes and as a way of getting out of the difficulty involved in detailed shakedown analysis for answering all shakedown questions, the transient state of the structure can be regarded as of less importance, and attention can be focused on the final steady solutions.

In 1978, Zarka et al. first proposed a direct method which permits a straightforward evaluation of the limit state of the structure on the basis of the elastic solution and the first cycle of the elastic-plastic calculation. Zarka's method takes advantage of the fact that, in the case of elastic shakedown, the plastic strain is constant. Whenever reversed plasticity occurs, however, the plastic strain varies with time and Zarka's method becomes complex. This paper presents a simple method for the direct evaluation of the steady solutions for all shakedown cases. The two-bar assembly and the tube problem are solved as examples. The feasibility and the efficiency of the approach are obvious as compared to the conventional incremental method.

This paper concerns only kinematic hardening materials, since for such materials, a steady state can always be reached.

2 Problem Formulation

The total strain ϵ is considered to be composed of three parts, the elastic strain ϵ^e, the thermal strain ϵ^T and the plastic strain ϵ^p:

$$\epsilon = \epsilon^e + \epsilon^T + \epsilon^p \tag{1}$$

The elastic strain ϵ^e relates to the current stress σ through an elastic matrix $\mathbf{D}$:

$$\epsilon^e = \mathbf{D}\sigma \tag{2}$$

while the plastic strain ϵ^p is assumed to obey the associated plastic flow law:

$$\dot{\epsilon}^p = \dot{\lambda}\, \frac{\partial f}{\partial \sigma} \tag{3}$$

where f is the yield function, and $\dot{\lambda}$ is an infinitesimal scalar factor. The creep strain is not considered here. An upper bound of the creep deformation can be estimated after the shakedown solutions are obtained using Ainsworth's method, for example.

Suppose that the material considered follows the kinematic hardening rule. The yield condition is then given by a function in the form of

Contributed by the Applied Mechanics Division of The American Society of Mechanical Engineers for presentation at the 1992 ASME Summer Mechanics and Materials Meeting, Tempe, AZ, Apr. 28–May 1, 1992.

Discussion on this paper should be addressed to the Technical Editor, Prof. Leon M. Keer, The Technological Institute, Northwestern University, Evanston, IL 60208, and will be accepted until four months after final publication of the paper itself in the Journal of Applied Mechanics. Manuscript received by the ASME Applied Mechanics Division, June 29, 1990; final revision, June 26, 1991.

Paper No. 92-APM-25.

$$f(\sigma-\alpha)=0 \tag{4}$$

where α is the back stress, also called the hardening parameter, which indicates the current center of the yield surface. Some differential relations have been proposed for the determination of the rate $\dot{\alpha}$ of the back stress. In this paper, we will use the simplest, but rather extensively used variant

$$\alpha=\mathbf{B}\epsilon^p \tag{5}$$

where B is a constant symmetric positive matrix. We can thus write

$$\epsilon^p=\mathbf{B}^{-1}\alpha. \tag{6}$$

To formulate a direct approach, Zarka et al. (1978) separated the stress and strain into two parts:

$$\begin{cases}\sigma=\sigma^{el}+\rho\\ \epsilon=\epsilon^{el}+\mathbf{e}\end{cases} \tag{7}$$

where $(\sigma^{el},\ \epsilon^{el})$ represents the purely elastic solution to the current boundary value problem, and $(\rho,\ \mathbf{e})$ represents the residual stress and strain. The residual stress should be statically admissible with zero applied forces, and the residual strain should be kinematically admissible with zero applied displacements. Generally, they all vary with time.

Zarka et al. next introduced a modified hardening parameter $\hat{\alpha}$

$$\hat{\alpha}=\alpha-\rho. \tag{8}$$

This new tensor has no physical meaning, but with it we can rewrite the yield condition, Eq. (4), as

$$f(\sigma^{el}-\hat{\alpha})=0 \tag{9}$$

and obtain a residual stress-strain relationship

$$\mathbf{e}=(\mathbf{B}^{-1}+\mathbf{D})\rho+\mathbf{B}^{-1}\hat{\alpha}. \tag{10}$$

Zarka's method is that, instead of solving a difficult plasticity problem, he tried to find an $\hat{\alpha}$ field such that at any time the yield condition is satisfied. Then the residual solution (ρ, $\mathbf{e}$) can be obtained by solving an elastic problem with homogeneous equilibrium equations and boundary conditions but with nonhomogeneous stress-strain relationships. After that, the actual solution can be found, according to Eq. (7), by superpositions. Thus, the key point of Zarka's method is how to find the $\hat{\alpha}$ field.

In the case of elastic shakedown, the $\hat{\alpha}$ field is constant, that is, it is independent of time. This fact makes Zarka's method rather simple. However, whenever reversed plasticity occurs, the $\hat{\alpha}$ field varies with time and Zarka's method loses its simplicity. Another difficulty is that many $\hat{\alpha}$ fields can be chosen that meet the requirement and there will be considerable differences in the final shakedown solution, depending on the choice of $\hat{\alpha}$ fields. To single out the correct solution, Zarka et al. calculated the first cycle and deduced, through a complex procedure, the right $\hat{\alpha}$ field.

We now present a simple and straightforward method to directly derive the $\hat{\alpha}$ field and then the shakedown solution.

It is known that under periodic loading, the stress state will always shake down due to the kinematic hardening. As a result, when shakedown is reached, the structure considered can be composed of three kinds of regions: S_1, S_2, and S_3, where S_1 is the reversed plasticity zone, S_2 yields only in the heating half cycles, and S_3 yields only in the cooling half cycles (Fig. 1). In the stress space, it means that stresses in region S_1 hit the yield surface twice in a complete cycle, whereas stresses in regions S_2 and S_3 hit the yield surface only once and remain somewhere inside the yield surface during the other half cycles (Fig. 2). In other words, the above division says that during a complete cycle when the shakedown is reached, the yield condition will be met twice in region S_1:

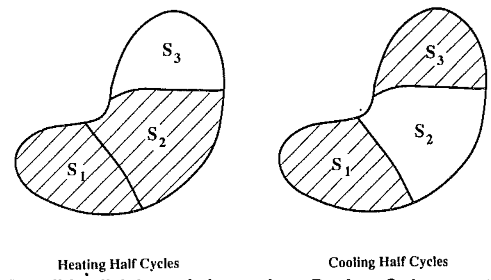

Fig. 1 Possible division of the region. Region S_1 incurs alternating plasticity; region S_2 yields only during the heating; and region S_3 yields only during the cooling.

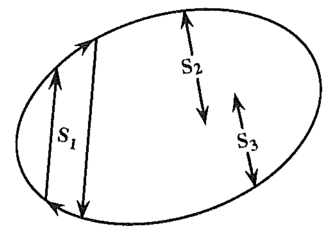

Fig. 2 Yield surface. Stresses in region S_1 hit the yield surface twice in a complete cycle. Stresses in regions S_2 and S_3 hit the yield surface only once and remain somewhere inside the yield surface during the other half cycles.

$$\begin{cases}f(\sigma_H^{el}-\hat{\alpha}_H)=0\\ f(\sigma_C^{el}-\hat{\alpha}_C)=0\end{cases} \tag{11}$$

and will be met only once in region S_2:

$$\begin{cases}f(\sigma_H^{el}-\hat{\alpha}_H)=0\\ f(\sigma_C^{el}-\hat{\alpha}_C)<0\end{cases} \tag{12}$$

and once in region S_3:

$$\begin{cases}f(\sigma_H^{el}-\hat{\alpha}_H)<0\\ f(\sigma_C^{el}-\hat{\alpha}_C)=0.\end{cases} \tag{13}$$

In Eqs. (11)–(13), the subscripts H and C are used to refer to the values for the heating and cooling half cycles, respectively.

Now suppose that the yield condition, Eq. (9), permits the solution of $\hat{\alpha}$ in terms of the stress σ^{el}. Then from Eqs. (11)–(13), $\hat{\alpha}_H$ and $\hat{\alpha}_C$ can both be found in S_1; $\hat{\alpha}_H$ can be found while $\hat{\alpha}_C$ is unknown in S_2; and $\hat{\alpha}_C$ can be found while $\hat{\alpha}_H$ is unknown in S_3. Since one of the modified hardening parameters is always known, the problem thus becomes that of finding the increment

$$\Delta\hat{\alpha}=\hat{\alpha}_C-\hat{\alpha}_H. \tag{14}$$

Once the increment $\Delta\hat{\alpha}$ is found, the $\hat{\alpha}_C$ in S_2 and $\hat{\alpha}_H$ in S_3, and consequently the entire $\hat{\alpha}$ field in the whole region, are fully determined.

From Eq. (8), we have an incremental relation:

$$\Delta\hat{\alpha}=\Delta\alpha-\Delta\rho \tag{15}$$

Since from Eq. (5) the back stress α depends uniquely on the plastic strain, whereas the regions S_2 and S_3 yield only once in a complete cycle, the plastic strain and consequently the back stress should be constant there. In other words, in these two regions, the incremental back stress $\Delta\alpha$ is zero, and the incremental modified hardening parameter $\Delta\hat{\alpha}$ equals the negative incremental residual stress $\Delta\rho$:

$$\begin{cases}\Delta\alpha=0\\ \Delta\hat{\alpha}=-\Delta\rho\end{cases}\qquad \text{in } S_2 \text{ and } S_3. \tag{16}$$

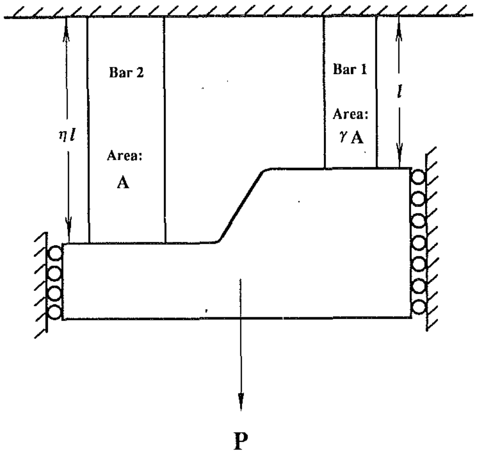

Fig. 3 Two-bar assembly. Two bars are made of the same kinematic hardening material, but of different lengths (ℓ and $\eta\ell$, respectively) and different cross-section areas (γA and A, respectively). In addition to a constant axial force P, bar 2 is subjected to a temperature change of amplitude T, while the temperature of bar 2 always stays at zero.

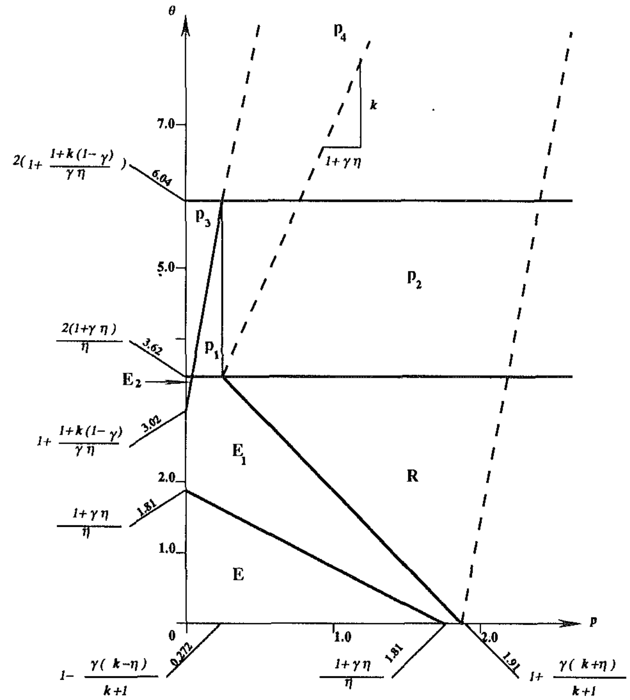

Fig. 4 Interaction diagram, two-bar assembly (k = 10, γ = 0.9, η = 1.1). Eight different kinds of behavior are possible for a two bar assembly: the purely elastic behavior E, the elastic shakedowns E_1 and E_2, the reversed plasticity responses P_1, P_2, P_3, and P_4, and the ratchetting R.

Hence, we only need to calculate the increment $\Delta\rho$ to find the increment $\Delta\hat{\alpha}$ and then the $\hat{\alpha}$ field.

It should be noted that for the reversed plasticity region, S_1, the plastic strain, and hence the back stress, vary with time so that the incremental back stress $\Delta\alpha$ does exist. However, for this region, $\hat{\alpha}_H$ and $\hat{\alpha}_C$ are both known and therefore the increment $\Delta\hat{\alpha}$ can be found directly.

From Eq. (7)

$$\Delta\rho = \Delta\sigma - \Delta\sigma^{el}. \tag{17}$$

Elastic shakedown is characterized by the fact that the incremental stress is elastic. Hence, in such a case, the residual stress ρ and, as a result, the modified hardening parameter $\hat{\alpha}$ are independent of time and thus can directly be found from the yield condition. On the other hand, whenever reversed plasticity occurs in any part of the structure, an evaluation of the incremental residual stress is necessary for the determination of the modified hardening parameter field.

In using this approach, the key point is that the yield condition should permit the solution of $\hat{\alpha}$ in terms of elastic stress σ^{el}. Also, we should know the shakedown mode, and this can be done by performing some pre-analysis. The solution procedure can best be shown by some examples.

3 Examples

Two-Bar Structure. Two-bar and three-bar structures have been studied by several authors (Zarka, et al., 1978; Megahed, 1978; Leckie and Ranaweera, 1980; etc.) to illustrate the various shakedown analysis. To begin, we will also use a two-bar structure to exemplify the direct method.

The structure considered (Fig. 3) consists of two bars made of the same kinematic hardening material, but of different lengths (ℓ and $\eta\ell$, respectively) and different cross-section areas (γA and A, respectively). The upper end of this system is fixed, and the lower end, where a constant axial force P is applied, can move only in one direction. In addition to the mechanical load, bar 2 is subjected to a temperature change of amplitude T, while the temperature of bar 1 always stays at zero.

It can be found that eight different modes of behavior are possible for such a two-bar assembly when shakedown is reached. They are the purely elastic behavior—mode E, the elastic shakedown—modes E_1 and E_2, the reversed plasticity—modes P_1, P_2, P_3, and P_4, and the ratchetting—mode R. The characteristics of these modes are shown in the following table and Fig. 4 gives the interaction diagram for a particular set of parameters. Note that if the transient states are considered, the reversed plasticity regions P_2 and P_4 and the ratchetting region R can be further divided into several subregions as shown by the dotted lines in Fig. 4. Since this paper concerns only the final shakedown solutions, we will not examine the transient behavior.

Table 1 The possible responses of the two-bar assembly

Mode			E	E1	E2	P1	P2	P3	P4	R
Bar 1	Heating	Elastic Behavior	x							
		Yield in Tension		x	x	x	x	x	x	x
		Yield in Compression								
	Cooling	Elastic Behavior	x	x	x					x
		Yield in Tension								
		Yield in Compression				x	x	x	x	
Bar 2	Heating	Elastic Behavior	x	x		x	x			x
		Yield in Tension								
		Yield in Compression			x			x	x	
	Cooling	Elastic Behavior	x	x	x	x		x		
		Yield in Tension					x		x	x
		Yield in Compression								

Now we will use the direct method to derive shakedown solutions. For convenience, the following normalized stress, strain, force, and temperature will be used in the forthcoming:

$$\begin{cases} \sigma = \dfrac{\text{stress}}{\sigma_y} \\ \epsilon = \dfrac{E \text{ strain}}{\sigma_y} \end{cases} \tag{18}$$

$$\begin{cases} p = \dfrac{P}{A\sigma_y} \\ \theta = \dfrac{E\beta T}{\sigma_y} \end{cases} \tag{19}$$

where E is Young's modulus, β is the coefficient of thermal expansion, and σ_y is the initial yield stress. They are all considered as temperature-independent material properties.

The basic relationships for the two-bar assembly are as follows.

Equilibrium equation:

$$\gamma\sigma_1 + \sigma_2 = p. \tag{20}$$

Compatibility condition:

$$\epsilon_1 = \eta\epsilon_2. \tag{21}$$

Stress-strain relationship:

$$\begin{cases} \epsilon_1 = \sigma_1 + \epsilon_1^p \\ \epsilon_2 = \sigma_2 + \theta + \epsilon_2^p. \end{cases} \tag{22}$$

Plastic strain-back stress relationship:

$$\begin{cases} \epsilon_1^p = k\alpha_1 \\ \epsilon_2^p = k\alpha_2 \end{cases} \tag{23}$$

where k is a material constant.

Yield condition:

$$\begin{cases} |\sigma_1 - \alpha_1| = 1 \\ |\sigma_2 - \alpha_2| = 1. \end{cases} \tag{24}$$

Now if the stresses and strains are expressed as the sum of two terms as shown in Eq. (7), the residual stresses and strains should satisfy the following equations.

Equilibrium equation:

$$\gamma\rho_1 + \rho_2 = 0. \tag{25}$$

Compatibility condition:

$$e_1 = \eta e_2. \tag{26}$$

Stress-strain relationship:

$$\begin{cases} e_1 = (k+1)\rho_1 + k\hat{\alpha}_1 \\ e_2 = (k+1)\rho_2 + k\hat{\alpha}_2. \end{cases} \tag{27}$$

Yield condition:

$$\begin{cases} |\sigma_1^{el} - \hat{\alpha}_1| = 1 \\ |\sigma_2^{el} - \hat{\alpha}_2| = 1. \end{cases} \tag{28}$$

Based on the above governing equations, the purely elastic solution can be found for the heating half cycles as

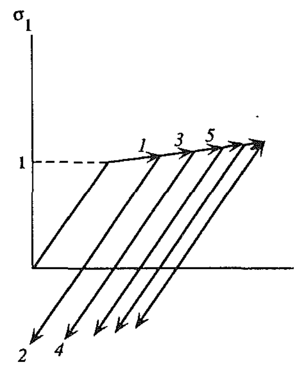

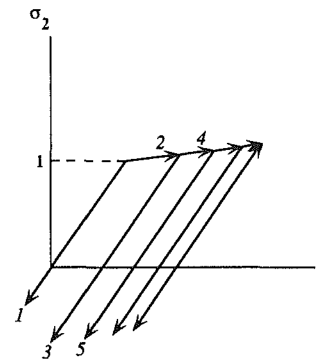

Fig. 5 Ratchetting mode *R*, two-bar assembly. Bar 1 and bar 2 yield in tension alternatively and plastic strains build-up. The kinematic hardening finally stops the ratchetting and the shakedown occurs.

$$\begin{cases} \sigma_1^{el} = \dfrac{\eta(p+\theta)}{1+\gamma\eta} \\ \sigma_2^{el} = \dfrac{p-\gamma\eta\theta}{1+\gamma\eta} \end{cases} \tag{29}$$

and for the cooling half cycles as

$$\begin{cases} \sigma_1^{el} = \dfrac{\eta p}{1+\gamma\eta} \\ \sigma_2^{el} = \dfrac{p}{1+\gamma\eta} \end{cases} \tag{30}$$

and the residual stresses can be expressed in terms of the modified hardening parameters as

$$\begin{cases} \rho_1 = \dfrac{k(\eta\hat{\alpha}_2 - \hat{\alpha}_1)}{(k+1)(1+\gamma\eta)} \\ \rho_2 = -\dfrac{k\gamma(\eta\hat{\alpha}_2 - \hat{\alpha}_1)}{(k+1)(1+\gamma\eta)}. \end{cases} \tag{31}$$

Therefore, once the modified hardening parameters are found, the residual stresses can be determined directly and the shakedown solution can be obtained by a superposition based on Eq. (7).

As an example, let us first consider the ratchetting mode R. In this case, bar 1 yields in tension during the heating and remains elastic during the cooling, while bar 2 behaves elastically during the heating, but yields, also in tension, during the cooling (Fig. 5). Since both bars yield in tension alternatively, the plastic strain will build up and ratchetting occurs. However, the kinematic hardening will finally stop the ratchetting so that the structure will incur large but still finite deformations when the steady state is reached.

According to our general description, Fig. 1, there will be only two regions S_2 and S_3 in this ratchetting mode. Since it is the case of elastic shakedown, the modified hardening parameter $\hat{\alpha}$ fields are constant and can be determined from the yield conditions, Eq. (28), directly

$$\begin{cases} \hat{\alpha}_1 = \dfrac{\eta(p+\theta)}{1+\gamma\eta} - 1 \\ \hat{\alpha}_2 = \dfrac{p}{1+\gamma\eta} - 1. \end{cases} \tag{32}$$

Now from Eq. (31) the residual stresses, which are also constant during the cycles, can be determined

$$\begin{cases} \rho_1 = -\dfrac{k[\eta\theta - (1-\eta)(1+\gamma\eta)]}{(k+1)(1+\gamma\eta)^2} \\ \rho_2 = \dfrac{k\gamma[\eta\theta - (1-\eta)(1+\gamma\eta)]}{(k+1)(1+\gamma\eta)^2} \end{cases} \tag{33}$$

and finally a superposition gives the shakedown solutions. For the heating, we have

$$\begin{cases} \sigma_1 = \dfrac{1}{(k+1)(1+\gamma\eta)^2}\{(k+1)(1+\gamma\eta)\eta p \\ \qquad + [(k+1)\gamma\eta + 1]\eta\theta + k(1-\eta)(1+\gamma\eta)\} \\ \sigma_2 = \dfrac{1}{(k+1)(1+\gamma\eta)^2}\{(k+1)(1+\gamma\eta)p \\ \qquad - [(k+1)\gamma\eta + 1]\gamma\eta\theta - k\gamma(1-\eta)(1+\gamma\eta)\} \end{cases} \tag{34}$$

and for the cooling,

$$\begin{cases} \sigma_1 = \dfrac{1}{(k+1)(1+\gamma\eta)^2}[(k+1)(1+\gamma\eta)\eta p \\ \qquad - k\eta\theta + k(1-\eta)(1+\gamma\eta)] \\ \sigma_2 = \dfrac{1}{(k+1)(1+\gamma\eta)^2}[(k+1)(1+\gamma\eta)p \\ \qquad + k\gamma\eta\theta - k\gamma(1-\eta)(1+\gamma\eta)]. \end{cases} \tag{35}$$

It is seen from the development that, in the case of elastic shakedown, the steady solution can be found using a very simple, straightforward approach. The derivation of this steady solution based on the conventional incremental calculation is considerably more complex.

We next consider the reversed plasticity mode P_2. In this case, bar 1 incurs reversed plasticity during the cycles, while bar 2 yields in tension during the cooling and remains elastic during the heating (Fig. 6). Referring to Fig. 1, we now have two regions S_1 and S_2, and therefore, an incremental solution is necessary in the present situation.

Using the yield condition, we can only find the modified hardening parameter for bar 1 during the heating:

$$\hat{\alpha}_1 = \frac{\eta(p+\theta)}{1+\gamma\eta} - 1 \tag{36}$$

while during the cooling, the modified hardening parameters for both bars are known:

$$\begin{cases} \hat{\alpha}_1 = \dfrac{\eta p}{1+\gamma\eta} + 1 \\ \hat{\alpha}_2 = \dfrac{p}{1+\gamma\eta} - 1. \end{cases} \tag{37}$$

Thus, we need to find the increment

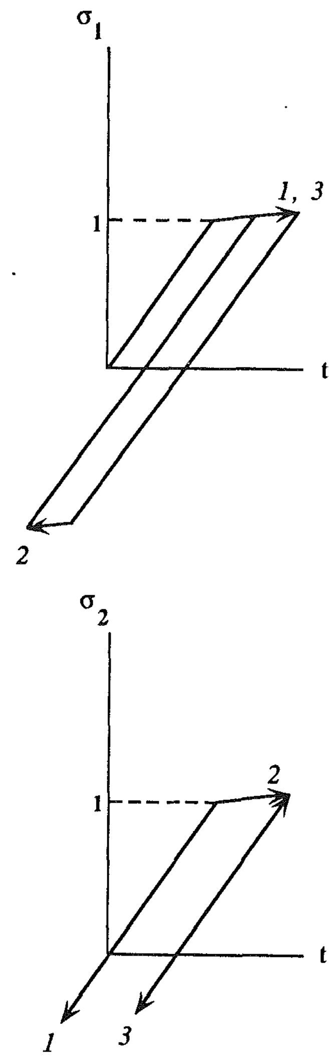

Fig. 6 Reversed plasticity mode P_2, two-bar assembly. Bar 1 incurs reversed plasticity during the cycles, while bar 2 yields in tension during the cooling and remains elastic during the heating.

$$\Delta\hat{\alpha}_2 = -\Delta\rho_2 \tag{38}$$

for bar 2.

The incremental residual stresses should satisfy the equilibrium equation

$$\gamma\Delta\rho_1 + \Delta\rho_2 = 0 \tag{39}$$

and the compatibility condition

$$\Delta e_1 = \eta\Delta e_2 \tag{40}$$

where, by Eqs. (27) and (36)–(38),

$$\begin{cases} \Delta e_1 = (k+1)\Delta\rho_1 - k\left(\dfrac{\eta\theta}{1+\gamma\eta} - 2\right) \\ \Delta e_2 = \Delta\rho_2. \end{cases} \tag{41}$$

The solution to Eqs. (39) and (40) is

$$\begin{cases} \Delta\rho_1 = \dfrac{k[\eta\theta - 2(1+\gamma\eta)]}{(k+1+\gamma\eta)(1+\gamma\eta)} \\ \Delta\rho_2 = -\dfrac{k\gamma[\eta\theta - 2(1+\gamma\eta)]}{(k+1+\gamma\eta)(1+\gamma\eta)}. \end{cases} \tag{42}$$

Then, the modified hardening parameter for bar 2 during the heating can be found:

$$\hat{\alpha}_2 = \frac{1}{(k+1+\gamma\eta)(1+\gamma\eta)} \{ (k+1+\gamma\eta)p - k\gamma\eta\theta - (1+\gamma\eta)[k(1-2\gamma)+(1+\gamma\eta)] \}, \quad (43)$$

and the residual stresses can be determined from Eq. (31). Finally, a superposition yields the shakedown solution:

For the heating half cycles,

$$\sigma_1 = \frac{1}{(k+1)(k+1+\gamma\eta)(1+\gamma\eta)} \{ (k+1)\eta[(k+1+\gamma\eta)p + (1+\gamma\eta)\theta] + k[k(1-\eta+2\gamma\eta)+(1-\eta)(1+\gamma\eta)] \}$$

$$\sigma_2 = \frac{1}{(k+1)(k+1+\gamma\eta)(1+\gamma\eta)} \{ (k+1)[(k+1+\gamma\eta)p - (1+\gamma\eta)\gamma\eta\theta] - k\gamma[k(1-\eta+2\gamma\eta)+(1-\eta)(1+\gamma\eta)] \} \quad (44)$$

and for the cooling half cycles.

$$\begin{cases} \sigma_1 = \dfrac{1}{(k+1)(1+\gamma\eta)} [(k+1)\eta p - k(1+\eta)] \\ \sigma_2 = \dfrac{1}{(k+1)(1+\gamma\eta)} [(k+1)p + k\gamma(1+\eta)]. \end{cases} \quad (45)$$

The shakedown solutions for all possible modes can be derived using the direct method. We will not give these solutions in this paper due to the space limitation.

Tube Problem. The tube problem has received great attention in the literature. The ratchetting behavior was first analyzed for nuclear reactor pressure vessels by Miller (1959) and later by Edmunds and Beer (1961), Burgreen (1968), and Bree (1967, 1968).

Bree studied the response of a cylindrical tube subjected to a sustained internal pressure and a cyclic temperature drop across its wall. Using a very simple one-dimensional model, assuming a linear temperature distribution across the tube wall and considering primarily an elastic-perfectly plastic material behavior, he studied various responses of the tube. Later, Mulcahy (1976) analyzed the same problem using a linear kinematic hardening model. Megahed (1978) adopted a bilinear temperature distribution and considered the effects due to cyclic hardening and creep. Leckie and Ranaweera (1980) reanalyzed this problem using a more realistic parabolic temperature distribution, and a bound on the creep deformation was found. All of these researches, however, were based on Bree's simplified model. As this model is very simple, it is natural to doubt whether it can model the actual situation and yield acceptable results.

Our previous research (Jiang, 1985) discarded all the assumptions and simplifications made by Bree and achieved closed-form shakedown solutions for all possible responses using the conventional incremental method. While the incremental method worked, the derivation turned out to be complex and time consuming. Now we will use the direct method to reanalyze this problem to illustrate the simplicity and efficiency of the approach suggested.

For convenience, some of the basic relationships are cited in the following. The details can be found from the previous research.

Consider a long cylindrical tube that is subjected to an internal pressure p, an external pressure q, a centrifugal force caused by the rotation of an angular velocity ω, and an arbitrarily distributed temperature field T across the tube wall (Fig. 7). All the loads and temperature can be either sustained or cyclic in the analysis.

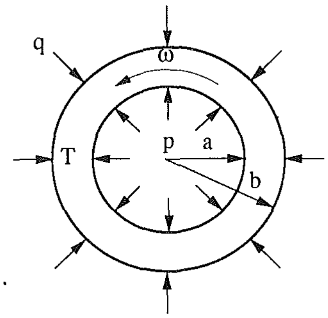

Fig. 7 Loading situation, tube problem. The tube is subjected to an internal pressure *p*, an external pressure *q*, a centrifugal force caused by the rotation of an angular velocity *ω*, and a distributed temperature field *T* across the tube wall.

Due to the symmetry, σ_r and σ_θ are the only stresses, and ϵ_r and ϵ_θ are the only strains we must deal with. For simplification, the loads, stresses, and strains are normalized as follows:

$$\begin{cases} P = \dfrac{p}{\tau_y} \\ Q = \dfrac{q}{\tau_y} \\ \theta = \dfrac{E\beta T}{2\tau_y} = t_a t(r) \\ f = \dfrac{\rho\omega^2}{\tau_y} \end{cases} \quad (46)$$

$$\begin{cases} \sigma = \dfrac{\sigma_r}{\tau_y} \\ \tau = \dfrac{\sigma_\theta - \sigma_r}{2\tau_y} \end{cases} \quad (47)$$

$$\begin{cases} e_r = \dfrac{G\epsilon_r}{\tau_y} \\ \epsilon_\theta = \dfrac{G\epsilon_\theta}{\tau_y} \end{cases} \quad (48)$$

where E is Young's modulus, G is the shear modulus, β is the thermal expansion coefficient, ρ is the mass density, t_a is the normalized temperature at the inner wall, $t(r)$ characterizes the temperature distribution, and τ_y is the yield stress in shear.

There is only one equilibrium equation, namely

$$\frac{d\sigma}{dr} - \frac{2\tau}{r} + fr = 0 \quad (49)$$

one compatibility condition, namely

$$\frac{de_\theta}{dr} + \frac{e_\theta - e_r}{r} = 0 \quad (50)$$

and two boundary conditions

$$\begin{cases} \sigma|_{r=a} = -P \\ \sigma|_{r=b} = -Q \end{cases} \quad (51)$$

that need to be satisfied. For the kinematic hardening material, the stress-strain relationships are

$$\begin{cases} e_r = \dfrac{1}{2}[(1-2\nu)\sigma - 2\nu\tau] + \theta - e_p \\ e_\theta = \dfrac{1}{2}[(1-2\nu)\sigma + 2(1-\nu)\tau] + \theta + e_p \end{cases} \quad (52)$$

where e_p is the normalized plastic strain:

$$e_p = \frac{G}{m}(\tau - \tau_s) \tag{53}$$

in which

$$\tau_s = \text{sign}(\tau) \tag{54}$$

indicates the yield direction, and m is the hardening constant.

The yield condition is given by

$$\tau - \alpha = \tau_s \tag{55}$$

where

$$\alpha = \frac{m e_p}{G} \tag{56}$$

is the back stress or the hardening parameter.

Now divide the stresses and strains into two parts according to the general procedure:

$$\begin{cases} \sigma = \sigma^{el} + \bar{\sigma} \\ \tau = \tau^{el} + \bar{\tau} \end{cases} \tag{57}$$

$$\begin{cases} e_r = e_r^{el} + \bar{e}_r \\ e_\theta = e_\theta^{el} + \bar{e}_\theta \end{cases} \tag{58}$$

where (σ^{el}, τ^{el}) and $(e_r^{el}, e_\theta^{el})$ represent the purely elastic solution, whereas $(\bar{\sigma}, \bar{\tau})$ and $(\bar{e}_r, \bar{e}_\theta)$ are the residual stresses and strains. The residual stresses should satisfy the homogeneous equilibrium equation

$$\frac{d\bar{\sigma}}{dr} - \frac{2\bar{\tau}}{r} = 0 \tag{59}$$

and the residual strains should satisfy the compatibility condition

$$\frac{d\bar{e}_\theta}{dr} + \frac{\bar{e}_\theta - \bar{e}_r}{r} = 0. \tag{60}$$

The residual stress-strain relationships can be found as

$$\begin{cases} \bar{e}_r = \dfrac{1-2\nu}{2}\bar{\sigma} - \dfrac{G+m\nu}{m}\bar{\tau} - \dfrac{G}{m}\hat{\alpha} \\ \bar{e}_\theta = \dfrac{1-2\nu}{2}\bar{\sigma} + \dfrac{G+m(1-\nu)}{m}\bar{\tau} + \dfrac{G}{m}\hat{\alpha} \end{cases} \tag{61}$$

and the yield condition, Eq. (55), becomes

$$\tau^{el} - \hat{\alpha} = \tau_s \tag{62}$$

where, in Eqs. (61) and (62), $\hat{\alpha}$ is the modified hardening parameter

$$\hat{\alpha} = \alpha - \bar{\tau}. \tag{63}$$

Based on the above basic equations, the purely elastic solution can be found as

$$\begin{aligned} \sigma^{el} &= \frac{1}{b^2-a^2}\left[Pa^2\left(1-\frac{b^2}{r^2}\right) - Qb^2\left(1-\frac{a^2}{r^2}\right)\right] \\ &\quad + \frac{f(3-2\nu)}{8(1-\nu)}\left(1-\frac{a^2}{r^2}\right)(b^2-r^2) + \frac{t_a}{1-\nu}S(a,b) \\ \tau^{el} &= \frac{(P-Q)a^2b^2}{(b^2-a^2)r^2} + \frac{f}{8(1-\nu)}\left[(1-2\nu)r^2 + (3-2\nu)\frac{a^2b^2}{r^2}\right] \\ &\quad + \frac{t_a}{1-\nu}Z(a,b) \end{aligned} \tag{64}$$

where

$$\begin{cases} S(a,b) = 2\left[\dfrac{1}{b^2-a^2}\left(1-\dfrac{a^2}{r^2}\right)\displaystyle\int_a^b trdr - \dfrac{1}{r^2}\int_a^r trdr\right] \\ Z(a,b) = -t + \dfrac{2a^2}{(b^2-a^2)r^2}\displaystyle\int_a^b trdr + \dfrac{2}{r^2}\int_a^r trdr \end{cases} \tag{65}$$

and the general residual solution can be found as

$$\begin{cases} \bar{\sigma} = -\dfrac{2G}{G+m(1-\nu)}\displaystyle\int \dfrac{\hat{\alpha}}{r}dr + C_1 - \dfrac{C_2}{r^2} \\ \bar{\tau} = -\dfrac{G}{G+m(1-\nu)}\hat{\alpha} + \dfrac{C_2}{r^2} \end{cases} \tag{66}$$

where C_1 and C_1 are constants to be determined from the boundary and continuity conditions.

It is seen that if we can find the modified hardening parameter $\hat{\alpha}$ field, the residual stresses can be found by some integrations, and the shakedown solution can be obtained through a simple superposition.

To illustrate the direct method, we consider a case, which was classified as ratchetting mode R_2 in our previous research (Jiang, 1985).

In the case of ratchetting mode R_2, the inner tube wall yields and the outer tube wall remains in elasticity during the odd half cycles, while both walls yield during the even half cycles. As a result, there exists a reversed plasticity zone near the inner tube surface, and a ratchetting zone in some middle part of the tube wall (Fig. 8(a)). During the cycles, the ratchetting zone will gradually shrink and finally tend to zero when shakedown is attained, because of the kinematic hardening. Fig. 8(b) shows the shakedown pattern of this mode, where three different kinds of regions exist: the reversed plasticity zone S_1 ($a \le r \le c$), and the elastic shakedown zones S_2 ($c \le r \le d$) and S_3 ($d \le r \le b$).

As previously mentioned, due to the occurrence of the reversed plasticity, the increment $\Delta\hat{\alpha}$ should be found in order to determine the $\hat{\alpha}$ field.

Since the stresses in region S_1 hit the yield surface twice during the cycles, the modified hardening parameter $\hat{\alpha}$ can be found from the yield condition, Eq. (62), for both the heating and cooling, the increment $\Delta\hat{\alpha}$ being known there:

$$\Delta\hat{\alpha} = \Delta\tau^{el} + 2 \qquad a \le r \le c \tag{67}$$

On the other hand, the stresses in regions S_2 and S_3 hit the yield surface only once during the cycles so that we need to find the increment $\Delta\hat{\alpha}$ in these two regions to determine the $\hat{\alpha}$ field. Due to the fact that the back stress does not vary in the elastic shakedown zones, Eq. (63) yields

$$\Delta\hat{\alpha} = -\Delta\bar{\tau} \qquad c \le r \le b \tag{68}$$

Therefore, the problem becomes that of finding the incremental residual stress $\Delta\bar{\tau}$.

The incremental residual stresses $(\Delta\bar{\sigma}, \Delta\bar{\tau})$ and the incremental residual strains $(\Delta\bar{e}_r, \Delta\bar{e}_\theta)$ should satisfy the equilibrium equation, Eq. (59), and the compatibility condition, Eq. (60). The incremental residual stress-strain relationships can be found from Eqs. (61), (67), and (68):

$$\begin{cases} \Delta\bar{e}_r = \dfrac{1-2\nu}{2}\Delta\bar{\sigma} - \dfrac{G+m\nu}{m}\Delta\bar{\tau} - \dfrac{G}{m}(\Delta\tau^{el}+2) \\ \Delta\bar{e}_\theta = \dfrac{1-2\nu}{2}\Delta\bar{\sigma} + \dfrac{G+m(1-\nu)}{m}\Delta\bar{\tau} + \dfrac{G}{m}(\Delta\tau^{el}+2) \end{cases} \quad a \le r \le c \tag{69}$$

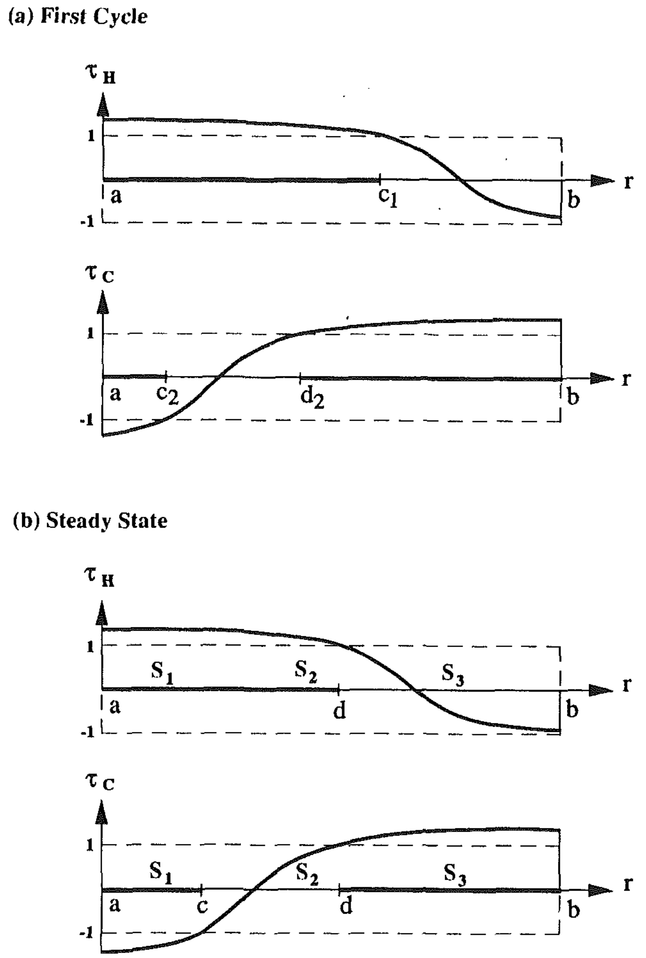

Fig. 8 Ratchetting mode R_2, tube problem. A ratchetting zone exists in some middle part of the tube wall. The ratchetting zone gradually shrinks and finally disappears when the shakedown is attained as a result of the kinematic hardening.

$$\begin{cases} \Delta\bar{e}_r = \dfrac{1-2\nu}{2}\Delta\bar{\sigma} - \nu\Delta\bar{\tau} \\ \Delta\bar{e}_\theta = \dfrac{1-2\nu}{2}\Delta\bar{\sigma} + (1-\nu)\Delta\bar{\tau} \end{cases} \qquad c\le r\le b. \tag{70}$$

Based on these equations, the incremental residual stress $\Delta\hat{\tau}$ can be determined. Assuming that the pressures are sustained loads, while the centrifugal force and the temperature are cyclic, we find

$$\Delta\bar{\tau} = \frac{Ga^2b^2}{[G+m(1-\nu)](b^2-a^2)r^2}\left[2\left(1-\frac{c^2}{a^2}+2\ln\frac{c}{a}\right) + \frac{f(1-2\nu)}{8(1-\nu)}\left(\frac{c^2-a^2}{a}\right)^2 - \frac{t_a}{1-\nu}S_d^T(a,c)\right] \qquad c\le r\le b \tag{71}$$

where

$$S_d^T(a,c) = -t_c\left(1-\frac{c^2}{a^2}\right) - \frac{2}{a^2}\int_a^c trdr. \tag{72}$$

Then, by the yield condition, Eq. (62), the elastic solution, Eq. (64), and Eqs. (68) and (71), the modified hardening parameter can be obtained as follows. For the heating half cycles:

$$\hat{\alpha} = \begin{cases} \dfrac{(P-Q)a^2b^2}{(b^2-a^2)r^2} + \dfrac{f}{8(1-\nu)}\left[(1-2\nu)r^2 + (3-2\nu)\dfrac{a^2b^2}{r^2}\right] + \dfrac{t_a}{1-\nu}Z(a,b) - 1 & a\le r\le d \\ \dfrac{(P-Q)a^2b^2}{(b^2-a^2)r^2} + \dfrac{Ga^2b^2}{[G+m(1-\nu)](b^2-a^2)r^2} \times\left[2\left(1-\dfrac{c^2}{a^2}+2\ln\dfrac{c}{a}\right) + \dfrac{f(1-2\nu)}{8(1-\nu)}\left(\dfrac{c^2-a^2}{a}\right)^2 - \dfrac{t_a}{1-\nu}S_d^T(a,c)\right] - 1 & d\le r\le b. \end{cases} \tag{73}$$

For the cooling half cycles:

$$\hat{\alpha} = \begin{cases} \dfrac{(P-Q)a^2b^2}{(b^2-a^2)r^2} + 1 & a\le r\le c \\ \dfrac{(P-Q)a^2b^2}{(b^2-a^2)r^2} + \dfrac{f}{8(1-\nu)}\left[(1-2\nu)r^2 + (3-2\nu)\dfrac{a^2b^2}{r^2}\right] + \dfrac{t_a}{1-\nu}Z(a,b) - 1 - \dfrac{Ga^2b^2}{[G+m(1-\nu)](b^2-a^2)r^2} \times\left[2\left(1-\dfrac{c^2}{a^2}+2\ln\dfrac{c}{a}\right) + \dfrac{f(1-2\nu)}{8(1-\nu)}\left(\dfrac{c^2-a^2}{a}\right)^2 - \dfrac{t_a}{1-\nu}S_d^T(a,c)\right] & c\le r\le d \\ \dfrac{(P-Q)a^2b^2}{(b^2-a^2)r^2} - 1 & d\le r\le b. \end{cases} \tag{74}$$

Now the residual stresses can be found from the general solution, Eq. (66), and a superposition with the purely elastic solution finally yields the shakedown solution: For the heating half cycles,

$$\begin{cases} \sigma = -P + \dfrac{1}{G+m(1-\nu)}\left\{2G\ln\dfrac{r}{a} + \dfrac{R}{a^2}\left(1-\dfrac{a^2}{r^2}\right) + \dfrac{f}{8}(a^2-r^2)\left[4G+m(3-2\nu) + m(1-2\nu)\dfrac{d^4}{a^2r^2}\right] + mt_aS^T(a,d)\right\} \\ \tau = \dfrac{1}{G+m(1-\nu)}\left[G + \dfrac{R}{r^2} + \dfrac{m(1-2\nu)f}{8}\left(r^2-\dfrac{d^4}{r^2}\right) + mt_aZ^T(a,d)\right] \qquad a\le r\le d \end{cases} \tag{75}$$

$$
\begin{cases}
\sigma = -Q + \dfrac{1}{G+m(1-\nu)}\left[2G\ln\dfrac{r}{b} + \dfrac{R}{b^2}\left(1-\dfrac{b^2}{r^2}\right)\right] \\
\qquad + \dfrac{f}{8(1-\nu)}(b^2-r^2)\left[(3-2\nu)+(1-2\nu)\dfrac{d^4}{b^2r^2}\right] \\
\qquad + \dfrac{t_a}{1-\nu}S^T(b,d) \\
\tau = \dfrac{1}{G+m(1-\nu)}\left(G+\dfrac{R}{r^2}\right) + \dfrac{f(1-2\nu)}{8(1-\nu)}\left(r^2-\dfrac{d^4}{r^2}\right) \\
\qquad + \dfrac{t_a}{1-\nu}Z^T(a,d) \qquad d\le r\le b.
\end{cases} \tag{76}
$$

For the cooling half cycles,

$$
\begin{cases}
\sigma = -P - \dfrac{1}{G+m(1-\nu)}\left[2G\ln\dfrac{r}{a} - \dfrac{R}{a^2}\left(1-\dfrac{a^2}{r^2}\right)\right] \\
\tau = -\dfrac{1}{G+m(1-\nu)}\left(G-\dfrac{R}{r^2}\right) \qquad a\le r\le c
\end{cases} \tag{77}
$$

$$
\begin{cases}
\sigma = -P + \dfrac{1}{G+m(1-\nu)}\left[2G\ln\dfrac{ar}{c^2} + \dfrac{R}{a^2}\left(1-\dfrac{a^2}{r^2}\right)\right. \\
\qquad \left. + \dfrac{G(1-2\nu)f}{8(1-\nu)}(c^2-r^2)\left(1-\dfrac{d^4}{c^2r^2}\right) - \dfrac{Gt_a}{1-\nu}S^T(c,d)\right] \\
\tau = \dfrac{1}{G+m(1-\nu)}\left[G+\dfrac{R}{r^2} - \dfrac{G(1-2\nu)f}{8(1-\nu)}\left(r^2-\dfrac{d^4}{r^2}\right)\right. \\
\qquad \left. - \dfrac{Gt_a}{1-\nu}Z^T(c,d)\right] \qquad c\le r\le d
\end{cases} \tag{78}
$$

$$
\begin{cases}
\sigma = -Q + \dfrac{1}{G+m(1-\nu)}\left(2G\ln\dfrac{r}{b} + \dfrac{R}{b^2}\left(1-\dfrac{b^2}{r^2}\right)\right] \\
\tau = \dfrac{1}{G+m(1-\nu)}\left(G+\dfrac{R}{r^2}\right) \qquad d\le r\le b
\end{cases} \tag{79}
$$

where

$$
R = \frac{a^2b^2}{b^2-a^2}\left\{[G+m(1-\nu)](P-Q) - 2G\ln\frac{ab}{c^2} - \frac{G(1-2\nu)f}{8(1-\nu)}\left(\frac{c^2-d^2}{c}\right)^2 + \frac{Gt_a}{1-\nu}S_d^T(c,d)\right\} \tag{80}
$$

and

$$
\begin{cases}
S^T(c,d) = \dfrac{d^2}{c^2}\left(t_d - \dfrac{2}{d^2}\displaystyle\int_c^d trdr\right) - \dfrac{d^2}{r^2}\left(t_d - \dfrac{2}{d^2}\displaystyle\int_r^d trdr\right) \\
Z^T(c,d) = -t + \dfrac{d^2}{r^2}\left(t_d - \dfrac{2}{d^2}\displaystyle\int_r^d trdr\right).
\end{cases} \tag{81}
$$

It is seen that due to the different responses in different regions, the shakedown solution consists of several local solutions. The problem remaining is how to find the boundaries c and d of the different regions. Figure 8(b) shows that the point c is the boundary where the response of the tube changes from reversed plasticity to elastic shakedown, so that the incremental normalized shear stress at this point equals just -2.

On the other hand, point d borders two elastic shakedown zones, one yielding during the heating and the other yielding during the cooling, so that the shear stress remains constant at this point. As a result, two conditions are available for the determination of these two boundaries.

$$
\begin{cases}
\Delta\tau|_{r=c} = -2 \\
\Delta\tau|_{r=d} = 0
\end{cases} \tag{82}
$$

or,

$$
\begin{cases}
2 - \dfrac{f(1-2\nu)}{8(1-\nu)}\left(c^2-\dfrac{d^4}{c^2}\right) - \dfrac{t_a}{1-\nu}Z_c^T(c,d) = 0 \\
\dfrac{4G}{G+m(1-\nu)}\ln\dfrac{a}{c} \\
\quad + \dfrac{f}{8(1-\nu)}\left\{(b^2-a^2)\left[(3-2\nu)+(1-2\nu)\dfrac{d^4}{a^2b^2}\right]\right. \\
\quad \left. - \dfrac{G(1-2\nu)}{G+m(1-\nu)}(a^2-c^2)\left(1-\dfrac{d^4}{a^2c^2}\right)\right\} \\
\quad + \dfrac{t_a}{1-\nu}\left\{S_d^T(b,d) - \dfrac{1}{G+m(1-\nu)}[GS_d^T(c,d)\right. \\
\quad \left. + m(1-\nu)S_d^T(a,d)]\right\} = 0
\end{cases} \tag{83}
$$

where

$$
Z_c^T(c,d) = -t_c + t_d\frac{d^2}{c^2} - \frac{2}{c^2}\int_c^d trdr \tag{84}
$$

The shakedown solution, Eqs. (75)–(79), is identical to the one we derived using the traditional incremental method, and agrees very well with the experiment performed by Corum et al. (Jiang, 1985), which justifies the direct method we developed.

4 Conclusions

This paper presents a simple direct method for the straightforward determination of the shakedown solutions of structures subjected to various sustained and cyclic loadings. The advantage of the direct method is that the well-established theory of elasticity can be used to solve difficult plasticity problems which traditionally have to be attacked using complex, step-by-step, and time-consuming incremental analysis. The direct method was first proposed by Zarka, et al. The most important point in their framework is the introduction and the use of the modified hardening parameter field. However, the determination of this field turned out to be very complex in their original work. This paper greatly simplifies Zarka's method by showing that the modified hardening parameter field can be directly found from the yield condition and the incremental residual stress. Thus, only two elastic analyses are required in the determination of shakedown solutions without the need of performing a full-scale elastic-plastic analysis.

It can be seen that Zarka's formulation, for example, a residual stress-strain relationship like Eq. (10), requires a unique mapping between plastic stress and back stress. Thus, Zarka's approach is limited to linear kinematic hardening. On the other hand, for high-temperature problems and nonisothermal problems, the back stress evolution is actually temperature and rate dependent, and an accurate representation of cyclic plasticity requires, in general, a nonlinear kinematic hardening rule. However, the elastic-plastic response of the structure under sustained and cyclic loadings is usually very complicated, and consequently, any complex constitutive laws would make the problem intractable. Since the purpose of this research is to find directly the steady-state solutions to avoid the time-consuming and expensive transient-state calculations, the linear kinematic hardening rule becomes an ideal one that can be dealt with and render at the same time satisfactory results. The technique developed in this paper obviously is a very useful one under such idealization.

The key point of the present method is that the yield condition should permit the solving of the modified hardening parameter in terms of the purely elastic stresses. A question may be raised as to the conditions which would make this requirement possible. We have succeeded in solving several interesting problems using the direct method. Such general conditions, however, are still under investigation. We hope we can address this problem in the near future.

Several examples have been given in this paper to illustrate the feasibility and the efficiency of the approach. It is believed that this version of the direct method is very promising.

References

Ainsworth, R. A., 1977, "Application of Bounds for Creeping Structures Subjected to Load Variations above the Shakedown Limit," *International Journal of Solids and Structures*, Vol. 13, pp. 981–993.

Bree, J., 1967, "Elastic Plastic Behavior of Thin Tubes Subjected to Internal Pressure and Intermittent High Heat Fluxes," *J. Strain Analysis*, Vol. 2, pp. 226–238.

Bree, J., 1968, "Incremental Growth Due To Creep and Plastic Yielding of Thin Tubes Subjected to Internal Pressure and Cyclic Thermal Stresses," *J. Strain Analysis*, Vol. 3, pp. 122–127.

Burgreen, D., 1968, "The Thermal Ratchet Mechanism," ASME, *J. Basic Eng.*, Vol. 90, pp. 319–324.

Burgreen, D., 1968, "Structural Growth Induced by Thermal Cycling," ASME, *J. Basic Eng.*, Vol. 90, pp. 469–475.

Corum, J. M., Young, H. C., and Grindell, A. G., 1975, "Thermal Ratchetting in Pipes Subjected to Intermittent Thermal Downshocks at Elevated Temperatures," *Pressure Vessels and Piping: Verification and Qualification of Inelastic Computer Programs*, ASME, New York, pp. 79–98.

Drabble, F., and Johnson, W., 1963–1964, "The Development of the Zones of Yielding in Thick-Walled Spherical Shells of Non-Work-Hardening Material Subjected to a Steady-State Radial Temperature Gradient and an Internal or External Pressure," *Proc. Instn. Mech. Engrs.*, Vol. 178, Pt. 3L, pp. 267–278.

Edmunds, H. G., and Beer, F. J., 1961, "Notes on Incremental Collapse in Pressure Vessels," *J. Mech. Eng. Sci.* Vol. 5, pp. 187–199.

Gatewood, B. E., 1960, "The Problem of Strain Accumulation Under Thermal Cycling," *J. Aerospace Sci.*, Vol. 27, p. 461.

Jiang, W., 1985, "The Elastic-Plastic and Shakedown Analysis of Tubes Subjected to Sustained and Cyclic Loads," Ph.D. Thesis, University of Illinois at Urbana-Champaign.

Leckie, F. A., and Ranaweera, M. P., 1980, "The Theoretical Assessment of Deformation and Damage of a High Temperature Component," Oak Ridge National Laboratory, Subcontract No. 7689.

Megahed, M. M., 1978, "On the Inelastic Deformation of Structures Subjected to Variable Loading," Ph.D. Thesis, Liecester.

Megahed, M. M., 1978, "Kinematic Hardening Analysis of the Modes of Deformation of Thin Tubes," unpublished report.

Miller, D. R., 1959, "Thermal Stress Ratchet Mechanism in Pressure Vessels," ASME, *J. Basic Eng.*, Vol. 81, pp. 190–196.

Mulcahy, T. M., 1976, "Thermal Ratchetting of a Beam Element Having an Idealized Bauschinger Effect," ASME, *J. Eng. Materials and Technology*, pp. 264–271.

Tribout, J., Inglebert, G., and Casier, J., 1983, "A Simplified Method for the Inelastic Analysis of Structures under Cyclic Loadings," ASME *Journal of Pressure Vessel Technology*, Vol. 105.

Zarka, J., 1976, "Principe des Methodes Actuelles de Resolution Numerique des Problemes Classiques en Mecanique des Solides," Cours a l' E.N.S.T.A., Paris.

Zarka, J., Arnaudeau, F. C., Casier, J., and Baylac, G., 1978, "A Practical Method to Determine Elastic or Plastic Shakedown of Structures," *Simplified Methods in Pressure Vessel Analysis*, presented at 1978 *ASME/CSME Pressure Vessel and Piping Conference*, Montreal.

A Theory of Plasticity for Porous Materials and Particle-Reinforced Composites

Y. P. Qiu
Research Engineer,
Sonoco Products Co.,
555 Science Drive, Suite B,
University of Wisconsin Research Park,
Madison, WI 53711
Assoc. Mem. ASME

G. J. Weng
Professor,
Department of Mechanical
and Aerospace Engineering,
Rutgers University,
New Brunswick, NJ 08903
Fellow ASME.

An energy criterion is introduced to define the effective stress of the ductile matrix, and with which Tandon and Weng's (1988) theory of particle-reinforced plasticity is capable of predicting the desired plastic volume expansion under a pure hydrostatic tension. This modification also makes the theory suitable for application to porous materials at high triaxiality. Despite its simplicity, it offers a reasonable range of accuracy in the fully plastic state and is also versatile enough to account for the influence of pore shape. The theory is especially accurate when the work-hardening modulus of the ductile matrix is high, consistent with the concept of a linear comparison material adopted. If the matrix is also elastically incompressible, the theory with spherical voids is found to coincide with Ponte Castaneda's (1991) lower bound for the strain potential (or upper bound in the sense of flow stress) of the Hashin-Shtrikman (1963) type, and with any other randomly oriented spheroidal voids, it provides an overall stress-strain relation which lies below this upper-bound curve. This energy approach is finally generalized to a particle-reinforced composite where the inclusions can be elastically stiffer or softer than the matrix, and it is also demonstrated that the prediction by the new theory is always softer than Tandon and Weng's original one.

1 Introduction

In a recent paper, Tandon and Weng (1988) developed a simple theory of particle-reinforced plasticity under any proportionally increasing combined stress, where elastic spherical inclusions are homogeneously embedded in the ductile matrix. The theory makes use of a linear comparison material, whose elastic moduli at every instant are chosen to coincide with the average secant moduli of the matrix to reflect its elastoplastic state. Following Eshelby's (1957) equivalent-inclusion principle and Mori-Tanaka's (1973) mean-field method, the composite is subsequently replaced by the comparison material filled with equivalent transformation strains. This approach allows one to find the average stress of the matrix in terms of the macroscopic stress, and then by appealing to the constitutive equation of the ductile phase, the overall stress-strain relation of the two-phase system can be easily determined.

The advantage of adopting a linear comparison material is that it allows one to use the results of many well-developed linear theories; although not fully nonlinear, it is analytically amenable and provides plausible approximation to the nonlinear problems which otherwise may have to be solved numerically. Such an advantage has also been recognized by Talbolt and Willis (1985, 1987), Ponte Castaneda and Willis (1988), Willis (1990, 1991), and Ponte Castaneda (1991), who have used this idea and Hill's (1956) energy principles to construct various nonlinear bounds. These bounds are perhaps the most general and rigorous ones available to date.

It is in part guided by the development of these bounds that an improved version of Tandon and Weng's (1988) theory will be presented here. While the original theory is reasonably acceptable for a particle-strengthened solid, it is less so with porous materials, especially under the high triaxiality. Under a pure hydrostatic loading the overall response of an isotropic porous material would remain linear, unable to exhibit the expected nonlinear behavior. The reason is that the effective stress of the ductile matrix was calculated directly from its mean deviatoric stress and, therefore, under a hydrostatic tension (or compression) it vanishes completely. Thus, when applied to a porous material, the original theory has to be restricted to low triaxiality. Such a restriction is not as critical to a system where the elastic moduli of inclusions are stiffer than the matrix, as in this case the overall nonlinearity under a pure hydrostatic loading is very small (see, for instance, Chu and Hashin, 1971). In any event, the inability of the original approach to predict the plastic volume expansion under an iso-

Contributed by the Applied Mechanics Division of THE AMERICAN SOCIETY OF MECHANICAL ENGINEERS for presentation at the 1992 ASME Summer Mechanics and Materials Meeting, Tempe, AZ, Apr. 28–May 1, 1992.

Discussion on this paper should be addressed to the Technical Editor, Prof. Leon M. Keer, The Technological Institute, Northwestern University, Evanston, IL 60208, and will be accepted until four months after final publication of the paper itself in the JOURNAL OF APPLIED MECHANICS. Manuscript received by the ASME Applied Mechanics Division, Dec. 12, 1990; final revision, Apr. 30, 1991.

Paper No. 92-APM-7.

tropic tension (though possible under any other kinds of loading) is a rather undesirable feature of the theory and must be removed.

Instead of calculating the effective stress of the matrix from its mean deviatoric stress, an energy approach will be proposed to define this quantity. This new theory is as simple and versatile as the original one, and yet further possesses the desired feature of plastic volume expansion under a pure hydrostatic tension. In addition, when the matrix is elastically incompressible, the new theory associated with spherical voids turns out to coincide with Ponte Castaneda's lower bound for the strain potential (or upper bound in the sense of flow stress) of the Hashin-Shtrikman (1963) type, and with any other randomly oriented spheroidal voids, the corresponding stress-strain relations always fall below this upper-bound curve. As the original theory, this new one is intended only for proportional loading under small deformation. Although in a two-phase composite the average stress of the ductile matrix is not strictly proportional, its deviation usually falls within Budiansky's (1959) limit (see, for instance, Zhao and Weng, 1990, for spherical inclusions); the deformation theory therefore will be used for simplicity.

2 Constitutive Equations

The ductile matrix will be referred to as phase 0, and the voids or elastic inclusions as phase 1. The elastic bulk and shear moduli of the rth phase will be denoted by κ_r and μ_r, respectively, with a volume fraction c_r. In the plastic state the effective stress and strain of the matrix is taken to follow the modified Ludwik equation

$$\sigma_e = \sigma_y + h \cdot (\epsilon_e^p)^n, \tag{1}$$

where σ_y, h and n ($0 \le n \le 1$) are the tensile yield stress, strength coefficient, and work-hardening exponent, in turn, and σ_e and ϵ_e^p are the usual von Mises effective stress and plastic strain, defined as

$$\sigma_e = \left(\frac{3}{2}\sigma'_{ij}\sigma'_{ij}\right)^{1/2}, \ \epsilon_e^p = \left(\frac{2}{3}\epsilon_{ij}^p\epsilon_{ij}^p\right)^{1/2}, \tag{2}$$

in terms of the deviatoric stress σ'_{ij}.

Tandon and Weng's (1988) theory takes the elastic moduli of the comparison material to be equal to the "secant" moduli of the matrix. At a given plastic state the secant Young's modulus is given by

$$E_0^s = \frac{1}{\dfrac{1}{E_0} + \dfrac{\epsilon_e^p}{\sigma_y + h \cdot (\epsilon_e^p)^n}}, \tag{3}$$

in terms of the oridinary Young's modulus E_0. The secant bulk and shear moduli and the secant Poisson ratio follow as

$$\kappa_0^s = \kappa_0 = \frac{E_0^s}{3(1-2\nu_0^s)}, \quad \mu_0^s = \frac{E_0^s}{2(1+\nu_0^s)}, \ \nu_0^s = \frac{1}{2} - \left(\frac{1}{2} - \nu_0\right)\frac{E_0^s}{E_0}, \tag{4}$$

from the isotropic relation and plastic incompressibility, ν_0 being the usual Poisson's ratio. The plastic state of the matrix is seen to be characterized by ϵ_e^p, or any of E_0^s, μ_0^s, and ν_0^s.

For a 6061 aluminum these constants are (Arsenault, 1984; Nieh and Chellman, 1984)

$$E_0 = 68.3 \text{ GPa}, \ \nu_0 = 0.33, \ \sigma_y = 250 \text{ MPa}, \quad h = 173 \text{ MPa}, \ n = 0.455; \tag{5}$$

this set of data will be used in subsequent calculations.

In passing we note that constitutive Eq. (1) can also be written in terms of the strain potential $f(\sigma_e)$,

$$\epsilon_e = \epsilon_e^e + \epsilon_e^p = \frac{\sigma_e}{3\mu_0} + \left(\frac{\sigma_e - \sigma_y}{h}\right)^{1/n} = \frac{\partial f(\sigma_e)}{\partial \sigma_e} = f'(\sigma_e), \tag{6}$$

which in turn yields

$$f(\sigma_e) = \frac{1}{6\mu_0}\sigma_e^2 + \frac{n}{n+1}\frac{1}{h^{1/n}}(\sigma_e - \sigma_y)^{\frac{n+1}{n}}, \tag{7}$$

in the plastic state. The hydrostatic part of the potential is simply $1/(2\kappa_0)\,\sigma_m^2$ in terms of the mean tension σ_m ($\sigma_m = \sigma_{kk}/3$). This description will be needed when we later discuss the connection between the present theory and Ponte Castaneda's bounds.

3 The Overall Secant Moduli of the Porous Material and the Effective Stress of the Matrix

The foundation leading from Hill's (1965) self-consistent scheme in polycrystal plasticity and Mori-Tanaka's (1973) method in composite elasticity to the development of Tandon and Weng's (1988) theory of particle-reinforced solids has been discussed in detail there and only the principal results will be cited. When both the composite and the comparison material are subjected to the same boundary traction giving rise to a uniform stress $\bar{\sigma}_{ij}$, the average hydrostatic and deviatoric stresses in the matrix are given by

$$\bar{\sigma}_{kk}^{(0)} = a_0\bar{\sigma}_{kk}, \quad a_0 = \frac{\alpha_0^s(\kappa_1 - \kappa_0) + \kappa_0}{(c_1 + c_0\alpha_0^s)(\kappa_1 - \kappa_0) + \kappa_0}, \tag{8}$$

$$\bar{\sigma}_{ij}'^{(0)} = b_0\bar{\sigma}'_{ij}, \quad b_0 = \frac{\beta_0^s(\mu_1 - \mu_0^s) + \mu_0^s}{(c_1 + c_0\beta_0^s)(\mu_1 - \mu_0^s) + \mu_0^s}, \tag{9}$$

where

$$\alpha_0^s = \frac{1}{3}\frac{1+\nu_0^s}{1-\nu_0^s}, \quad \beta_0^s = \frac{2(4-5\nu_0^s)}{15(1-\nu_0^s)}, \tag{10}$$

and κ_1 and μ_1 reduce to zero when specified for voids.

The overall secant bulk and shear moduli of the composite are

$$\frac{\kappa_s}{\kappa_0} = 1 + \frac{c_1(\kappa_1 - \kappa_0)}{c_0\alpha_0^s(\kappa_1 - \kappa_0) + \kappa_0}, \tag{11}$$

$$\frac{\mu_s}{\mu_0^s} = 1 + \frac{c_1(\mu_1 - \mu_0^s)}{c_0\beta_0^s(\mu_1 - \mu_0^s) + \mu_0^s}. \tag{12}$$

In the elastic state this pair of moduli—as originally pointed out by Weng (1984)—coincides with Hashin and Shtrikman's (1963) lower (or upper) bounds if the matrix is softer (or harder) than the inclusions. Equation (11) implies that, even though the matrix is plastically incompressible, the composite as a whole is not.

In Tandon and Weng's original approach, the effective stress of the matrix was calculated from

$$\sigma_e^{(0)} = \left(\frac{3}{2}\bar{\sigma}_{ij}'^{(0)}\bar{\sigma}_{ij}'^{(0)}\right)^{1/2}, \tag{13}$$

and this is to satisfy constitutive Eq. (1), which in turn provides an ϵ_e^p, and E_0^s, μ_0^s and ν_0^s. The overall behavior then follows from (11) and (12). Tandon and Weng (1988) have applied this theory to determine the tensile behavior of a silica/epoxy composite and found good agreement with the experimental data even up to $c_1 = 47$ percent. However, if the external loading is purely hydrostatic, $\sigma_e^{(0)}$ in (13) is zero and this approach would lead to no overall plastic response.

To alleviate this problem, we recognize that von Mises' effective stress essentially represents the elastic distortional energy of the material, and when it is nonuniformly deformed, this quantity is perhaps better derived from the energy, instead of from the mean stress (13). The energy approach can also account for the contribution of local heterogeneity to a certain extent, and is believed to be able to reflect the general plastic state of the matrix more accurately. Now keeping in mind that the comparison material possessing the equivalent transformation strain in the regions occupied by the voids is a linear solid, we may write its elastic energy of a unit volume as

$$U_s=\frac{1}{6\mu_s}\bar{\sigma}_e^2+\frac{1}{2\kappa_s}\bar{\sigma}_m^2=\frac{1}{2}\int_{V_0}\sigma_{ij}^{(0)}(\mathbf{x})\epsilon_{ij}^{(0)}(\mathbf{x})dV, \tag{14}$$

in terms of the local stress and strain fields in matrix, since the voided regions contribute no energy. The detailed $\sigma_{ij}^{(0)}(\mathbf{x})$-field in the matrix is in general not known, but it fluctuates over its mean $\bar{\sigma}_{ij}^{(0)}$ with some "perturbed" field $\sigma_{ij}^{pt}(\mathbf{x})$. Then, we may write

$$\frac{1}{2}\int_{V_0}\sigma_{ij}^{(0)}(\mathbf{x})\epsilon_{ij}^{(0)}(\mathbf{x})dV$$
$$=\frac{1}{2}\left[\frac{c_0}{2\mu_0^s}\left(\bar{\sigma}_{ij}'^{(0)}\bar{\sigma}_{ij}'^{(0)}+\frac{1}{c_0}\int_{V_0}\sigma_{ij}'^{pt(0)}(\mathbf{x})\sigma_{ij}'^{pt(0)}(\mathbf{x})dV\right)\right.$$
$$\left.+\frac{c_0}{9\kappa_0}\left(\bar{\sigma}_{kk}^{(0)2}+\frac{1}{c_0}\int_{V_0}\sigma_{kk}^{pt(0)2}(\mathbf{x})dV\right)\right]. \tag{15}$$

We now define the effective stress of the matrix $\sigma_e^{(0)}$ from its distortional energy

$$\sigma_e^{(0)2}=\frac{3}{2}\left(\bar{\sigma}_{ij}'^{(0)}\bar{\sigma}_{ij}'^{(0)}+\frac{1}{c_0}\int_{V_0}\sigma_{ij}'^{pt(0)}(\mathbf{x})\sigma_{ij}'^{pt(0)}(\mathbf{x})dV\right). \tag{16}$$

This new $\sigma_e^{(0)}$ is always greater than the original one calculated from $\bar{\sigma}_{ij}'^{(0)}$ alone, and also includes the contribution from the local perturbed field. The overall response predicted by the new theory, therefore, will always be softer. Now returning to (14), we find

$$\sigma_e^{(0)2}=\frac{6\mu_0^s}{c_0}\left(\frac{1}{6\mu_s}\bar{\sigma}_e^2+\frac{1}{2\kappa_s}\bar{\sigma}_m^2\right)-\frac{3\mu_0^s}{\kappa_0}\left(\bar{\sigma}_m^{(0)2}+<\sigma_m^{pt(0)2}(\mathbf{x})>\right), \tag{17}$$

where $<\cdot>$ is the volume average of the said quantity.

For a porous material, $\bar{\sigma}_m^{(0)}$ is simply given by $\bar{\sigma}_m^{(0)}=(1/c_0)\,\bar{\sigma}_m$, and

$$\frac{\kappa_s}{\kappa_0}=\frac{1}{1+\dfrac{c_1}{c_0}\dfrac{3\kappa_0+4\mu_0^s}{4\mu_0^s}},\quad \frac{\mu_s}{\mu_0^s}=\frac{1}{1+\dfrac{c_1}{c_0}\dfrac{5(3\kappa_0+4\mu_0^s)}{9\kappa_0+8\mu_0^s}}. \tag{18}$$

This pair of moduli, as mentioned earlier, coincides with Hashin and Shtrikman's (1963) upper bounds in the elastic case.

It is evident from (17) that, even under a purely hydrostatic loading, the effective stress of the matrix is now nonvanishing.

4 Elastically Incompressible Matrix and the Connection with Ponte Castaneda's Bound of the Hashin-Shtrikman Type

When the matrix is elastically also incompressible ($\kappa_0\to\infty$), Ponte Castaneda (1991) has provided a lower bound for the strain potential under a prescribed stress. For the convex function chosen here, this is equivalent to an upper bound for the overall stress at a given prescribed strain. The possible connection between the present theory and his bound is explored here.

According to the present theory, the effective secant bulk and shear moduli of the porous medium in this case can be further reduced to

$$\frac{\kappa_s}{\mu_0^s}=\frac{4c_0}{3c_1},\quad \frac{\mu_s}{\mu_0^s}=\frac{c_0}{1+\dfrac{2}{3}c_1}, \tag{19}$$

from (18), and the effective stress of the matrix follows from (17) as

$$\sigma_e^{(0)}=\frac{1}{c_0}\left[\left(1+\frac{2}{3}c_1\right)\bar{\sigma}_e^2+\frac{9}{4}c_1\bar{\sigma}_m^2\right]^{1/2}=s,\ \text{say}. \tag{20}$$

At this $\sigma_e^{(0)}$, we have, from (6),

$$\epsilon_e^{(0)}=f'(s)\quad\text{and}\quad \mu_0^s=\frac{s}{3f'(s)}, \tag{21}$$

and, consequently,

$$\kappa_s=\frac{4c_0}{3c_1}\cdot\frac{s}{3f'(s)},\quad \mu_s=\frac{c_0}{1+\dfrac{2}{3}c_1}\cdot\frac{s}{3f'(s)}. \tag{22}$$

On the other hand, Ponte Castaneda's theory allows one to construct a lower bound for the strain potential $\tilde{U}_-(\bar{\sigma})$ (which was referred to as stress potential in his paper) of the nonlinear solid from that of a linear composite $\tilde{U}$ possessing an identical microgeometry. The best possible linear bound of this type is the Hashin-Shtrikman (1963) bound $\tilde{U}_-^{HS}$. With this, Ponte Castaneda's lower bound is simply given in terms of the strain potential of the matrix (7),

$$\tilde{U}_-^{PC}(\bar{\sigma})=c_0f(s), \tag{23}$$

with the same s as in (20). The corresponding mean and effective strains of the composite then follow from

$$\bar{\epsilon}_m=c_0\frac{1}{3}\frac{\partial f(s)}{\partial\bar{\sigma}_m}=\frac{1}{3}c_0f'(s)\frac{\partial s}{\partial\bar{\sigma}_m}=\frac{3}{4}\frac{c_1}{c_0}\frac{\bar{\sigma}_m}{s}f'(s),$$
$$\bar{\epsilon}_e=c_0\frac{\partial f(s)}{\partial\bar{\sigma}_e}=c_0f'(s)\frac{\partial s}{\partial\bar{\sigma}_e}=\left(1+\frac{2}{3}c_1\right)\frac{1}{c_0}\frac{\bar{\sigma}_e}{s}f'(s). \tag{24}$$

Since $\kappa_s=\bar{\sigma}_m/(3\bar{\epsilon}_m)$ and $\mu_s=\bar{\sigma}_e/(3\bar{\epsilon}_e)$, the overall stress-strain relation derived from this bound is seen to coincide with (22). In retrospect, Tandon and Weng's (1988) original approach would lead to a result which coincides with that derived from Willis' (1990) type-1 bound and, as pointed out by him, is suitable only when the triaxiality is not high.

The quantitative accuracy of the theory can in part be assessed by comparing it to the exact solution when the porous material is subject to a pure hydrostatic tension $\bar{\sigma}_m$. Based on the model of composite sphere assemblage and adopting a bilinear ($n=1$) stress-strain curve for the ductile matrix, the overall stress-strain curve can be derived analytically following the approach of Hill (1950) and Chadwick (1963). With the specific constitutive equation adopted in (1), detailed study for the symmetric deformation has been carried out by Qiu (1990), and with the bilinear curve ($n=1$), analytic results are summarized in the Appendix. At $c_1=30$ percent, the results by both the present theory and the exact analysis are shown in Fig. 1 at four different E_0^p/E_0 ratios, where E_0^p is the tangent modulus of the matrix in the plastic range ($E_0^p=d\sigma/d\epsilon$). Here the material constants used are those of aluminum given in (5), except for $\nu_0=0.5$, $n=1$, and

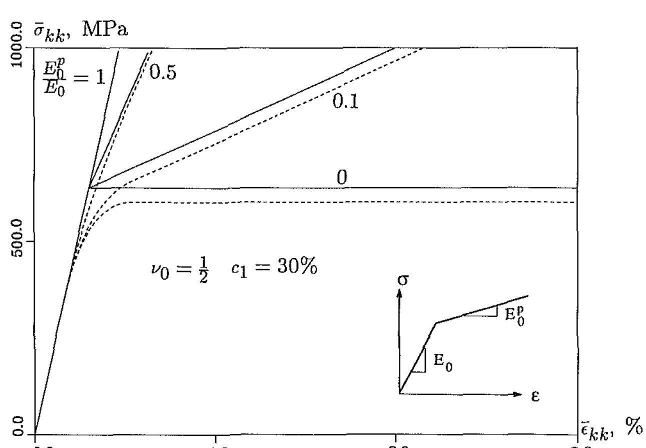

Fig. 1 Present theory versus the exact solution for a porous material under pure dilatation: elastically incompressible matrix

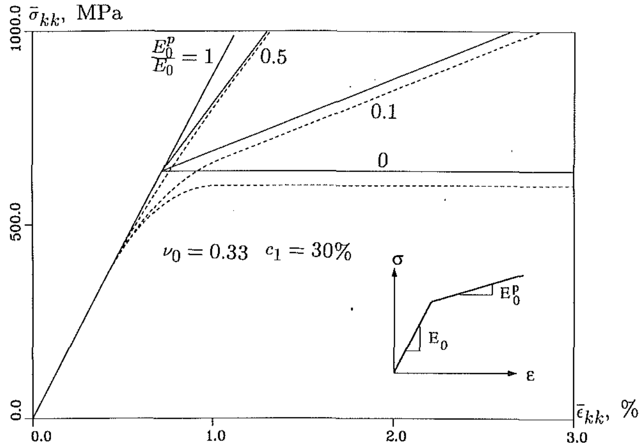

Fig. 2 Present theory versus the exact solution for a porous material under pure dilatation: elastically compressible matrix

$$h = \frac{E_0}{\dfrac{E_0}{E_0^p} - 1}. \tag{25}$$

The solid lines derived from the present theory (and the PC bound) are consistently higher than the dotted ones from the exact analysis, thereby justifying its upper-bound status. Since local yielding is not fully accounted for by this theory, the estimated initial yield point is noticeably higher than the actual one. (If such an information is desired, it can also be found from the mean-field approach by using the additional jump condition at the interface as suggested by Tandon and Weng (1986a) and the same initial yield point would have been obtained here.) But in the fully plastic range, the predictions by the present theory are seen to be generally acceptable. The greatest discrepancy occurs with an ideally plastic matrix ($E_0^p = 0$) where the error is about 7.5 percent at $\bar{\epsilon}_{kk} = 0.03$. The agreement steadily improves with an increasing work-hardening modulus, and coincides exactly when $E_0^p/E_0 = 1$ (elastic).

The fact that the present theory provides a more accurate result when E_0^p/E_0 is high is attributed to the linear comparison material adopted in the theoretical formulation. Such an approximation is apparently more justifiable with a high E_0^p/E_0 and becomes less so with an ideally plastic solid. Since most metals exhibit a certain degree of work-hardening, the theory is believed to be a sensible one for this class of materials in the fully plastic range.

5 Elastically Compressible Matrix

When the matrix is elastically compressible, the contribution to the total energy by the hydrostatic component—the last two terms in (17)—must be subtracted in order to find $\sigma_e^{(0)}$. Under a general $\bar{\sigma}_{ij}$, however, the perturbed term is usually not known (in particular, when the voids are not spherical). But under a pure $\bar{\sigma}_m$, the symmetric problem can still be solved analytically (see the Appendix) and this allows one to assess the degree of accuracy if this term is neglected in the calculation. We again used the properties of aluminum, with $\nu_0 = 0.33$, and adopted the bilinear curve ($n = 1$) as before to calculate the stress-strain curves at the same four E_0^p/E_0 ratios. The results by the present theory (after neglecting the $\sigma_m^{pt(0)}$-term) and the exact analysis are shown as solid and dashed lines, respectively, in Fig. 2. It appears that by such an approximation the theory exhibits about the same degree of accuracy as in the incompressible case (Fig. 1).

These simple calculations suggest that, as an approximation, the perturbed term in (17) may be discarded and the effective stress be taken as

$$\sigma_e^{(0)2} = \frac{6\mu_0^s}{c_0}\left(\frac{1}{6\mu_s}\bar{\sigma}_e^2 + \frac{1}{2\kappa_s}\bar{\sigma}_m^2\right) - \frac{3\mu_0^s}{\kappa_0}\bar{\sigma}_m^{(0)2}. \tag{26}$$

No other types of loading can have an exact solution. Finite element analysis, however, has been carried out for pure tension and pure shear by Hom and McMeeking (1989). They adopted the constitutive equation

$$(\sigma_e/\sigma_0)^{1/N} - \sigma_e/\sigma_0 = (3\mu_0/\sigma_0)\cdot\epsilon_e^p \tag{27}$$

instead of (1) for the matrix, with $N = 0.1$, $E_0/\sigma_0 = 200$, and $\nu_0 = 0.3$. With this set of data, we also applied (26) to calculate the overall response of the porous material at $c_1 = 6.5$ percent. The results provided by the present theory, their finite element calculations, and those of Gurson (1977) and Tvergaard (1981)—both taken from Hom and McMeeking— are depicted in Figs. 3(*a*) and (*b*) for pure tension and pure shear, respectively. Despite the simplicity of the present theory, its quantitative accuracy is seen to be satisfactory.

6 Influence of the Pore Shape on the Isotropic Response

The preceding principle can be applied to examine the influence of pore shape on the overall elastoplastic response of a porous material containing randomly oriented spheroidal pores. Let the shape of pores be represented by the aspect ratio α (length-to-diameter ratio). The overall secant moduli of the porous medium then can be deduced from the effective moduli derived by Tandon and Weng (1986b) for a two-phase composite

$$\frac{\kappa_s}{\kappa_0} = \frac{1}{1 + c_1 p}, \quad \frac{\mu_s}{\mu_0^s} = \frac{1}{1 + c_1 q}, \tag{28}$$

where

$$p = p_2/p_1, \quad q = q_2/q_1; \tag{29}$$

and after making use of the properties of the voids,

$$p_1 = q_1 = c_0,$$

$$p_2 = \frac{1 - \nu_0^s}{6(1 - 2\nu_0^s)} \times \frac{18\alpha^2 - 4(1 + \nu_0^s)(\alpha^2 - 1) - 3[2(1 - 2\nu_0^s)(\alpha^2 - 1) + 3(2\alpha^2 + 1)]g}{2\alpha^2 + [(1 - 4\alpha^2) + (1 + \nu_0^s)(\alpha^2 - 1)]g},$$

$$q_2 = -\frac{8(1 - \nu_0^s)(\alpha^2 - 1)}{5}\left[-\frac{1}{4\alpha^2 + [(1 - 2\nu_0^s)(\alpha^2 - 1) - 3(\alpha^2 + 1)]g} + \frac{1}{\alpha^2 - 4(1 - \nu_0^s)(\alpha^2 - 1) + [2(1 - 2\nu_0^s)(\alpha^2 - 1) - 3/2]g}\right]$$
$$- \frac{4(1 - \nu_0^s)(\alpha^2 - 1)}{15}\,\frac{1}{2\alpha^2 + [(1 - 4\alpha^2) + (1 + \nu_0^s)(\alpha^2 - 1)g]g}, \tag{30}$$

and for the parameter g,

$$g = \frac{\alpha}{(\alpha^2 - 1)^{3/2}}[\alpha(\alpha^2 - 1)^{1/2} - \cosh^{-1}\alpha], \quad \text{prolate shape}$$
$$= \frac{2}{3}, \quad \text{sphere}$$
$$= \frac{\alpha}{(1 - \alpha^2)^{3/2}}[\cos^{-1}\alpha - \alpha(1 - \alpha^2)^{1/2}], \quad \text{oblate shape.} \tag{31}$$

With spherical voids ($\alpha = 1$), this set of moduli reduces to the simple upper-bound form in (18).

If the matrix is elastically also incompressible ($\nu_0^s = 1/2$), further simplification can be made:

$$\frac{\kappa_s}{\mu_0^s} = \frac{2c_0}{c_1}\,\frac{2\alpha^2 - (\alpha^2 - 1)g}{2\alpha^2 + 1}, \quad \frac{\mu_s}{\mu_0^s} = \frac{1}{1 + \dfrac{c_1}{c_0}q_2}, \tag{32}$$

where

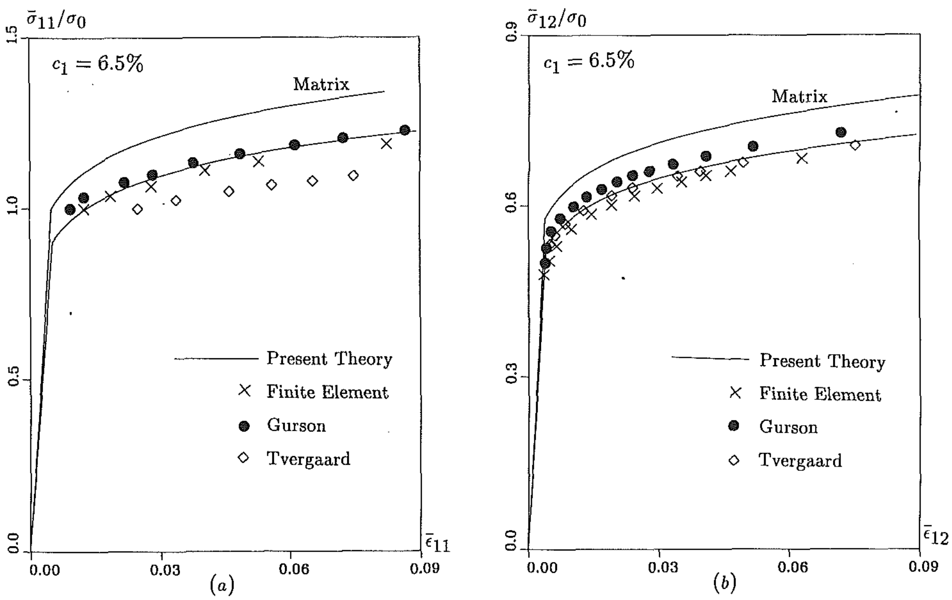

Fig. 3 Present theory versus finite element calculations and other models for a porous material under (a) pure tension and (b) pure shear

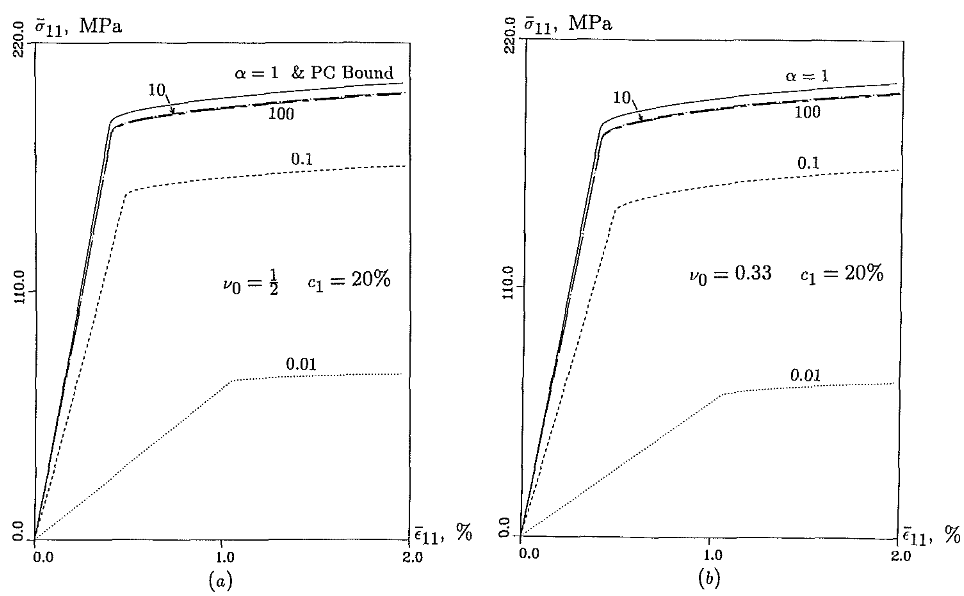

Fig. 4 Pore-shape dependence of the tensile behavior of a porous material with (a) elastically incompressible and (b) elastically compressible matrix

$$q_2 = -\frac{4(\alpha^2-1)}{5}\left\{\frac{1}{-4\alpha^2+3(\alpha^2+1)g} + \frac{2}{4-2\alpha^2-3g} + \frac{1}{3(2-3g)[2\alpha^2-(\alpha^2-1)g]}\right\}. \quad (33)$$

Using the general properties of aluminum given in (5), the tensile properties of the porous material with an elastically incompressible matrix ($\nu_0 = 0.5$) and a compressible one ($\nu_0 = 0.33$) are plotted in Figs. 4(*a*) and (*b*), respectively, at $c_1 = 20$ percent. Consistent with the known elastic behavior (see Tandon and Weng, 1986b), the disk or penny-shaped pores are seen to cause the severest weakening effect in both cases, whereas the spherical voids are the least damaging. The overall response appears to be relatively insensitive to the pore shape when it is prolate, but the sensitivity is quite pronounced when it becomes oblate. In the incompressible case, the top curve on the left also coincides with that derived from Ponte Castaneda's lower bound of strain potential (or upper bound in the sense of flow stress). Although no such upper-bound connection can be claimed for the upper right curve, any other type of pore shape all results in a softer response for the porous material.

7 Generalization to a Particle-Reinforced Isotropic Composite at Low Concentration

Under the condition of low concentration, this new definition of effective stress also permits one to examine the overall elastoplastic behavior of a particle-reinforced composite. With spherical inclusions, the effective secant moduli are already given in (11) and (12). The average stress of the matrix is given in (8) and (9), and for the inclusions,

$$\bar{\sigma}_m^{(1)} = a_1 \bar{\sigma}_m, \quad a_1 = \frac{\kappa_1}{(c_1 + c_0 \alpha_0^s)(\kappa_1 - \kappa_0) + \kappa_0},$$

$$\bar{\sigma}_{ij}'^{(1)} = b_1 \bar{\sigma}_{ij}'^{(0)}, \quad b_1 = \frac{\mu_1}{(c_1 + c_0 \beta_0^s)(\mu_1 - \mu_0^s) + \mu_0^s}. \tag{34}$$

The elastic inclusions will also contribute to the total elastic nergy U_s in (14), and the effective stress $\sigma_e^{(0)}$, originally defined in (16), now takes the form

$$\sigma_e^{(0)2} = \frac{6\mu_0^s}{c_0}\left(\frac{1}{6\mu_s}\bar{\sigma}_e^2 + \frac{1}{2\kappa_s}\bar{\sigma}_m^2\right) - \frac{3\mu_0^s}{\kappa_0}(\bar{\sigma}_m^{(0)2} + <\sigma_m^{pt(0)2}>)$$
$$-\frac{6\mu_0^s}{c_0}\bullet c_1\left[\frac{1}{6\mu_1}(\bar{\sigma}_e^{(1)2} + <\sigma_e^{pt(1)2}>) + \frac{1}{2\kappa_1}(\bar{\sigma}_m^{(1)2} + <\sigma_m^{pt(1)2}>)\right] \tag{35}$$

instead of (17). The evaluation of this quantity requires the knowledge of $<\sigma_e^{pt(1)2}>$ and $<\sigma_m^{pt(1)2}>$ as well, and these, in general, are not known. At low concentration, however, the stress field in the inclusions must be reasonably uniform, and consequently, these contributions will be dropped. Again, neglecting $<\sigma_m^{pt(0)2}>$ as before, the effective stress of the ductile matrix becomes

$$\sigma_e^{(0)2} = \frac{\mu_0^s}{c_0}\left\{\left[\frac{1}{\mu_s} - \frac{c_1 b_1^2}{\mu_1}\right]\bar{\sigma}_e^2 + 3\left[\frac{1}{\kappa_s} - \frac{c_0 a_0^2}{\kappa_0} - \frac{c_1 a_1^2}{\kappa_1}\right]\bar{\sigma}_m^2\right\}, \tag{36}$$

after making use of the relations in (9) and (34).

To assess the accuracy of this model we again compare it to the exact solutions when the composite sphere assemblage is subjected to a pure hydrostatic tension. Such an exact analysis has been carried out by Chu and Hashin (1971) using Ramberg-Osgood's constitutive equation (without a yield point), and by Qiu (1990) using (1) (see the Appendix for the end result of the bilinear case). The value of E_0, σ_y, and ν_0 here are taken as those of aluminum in (5), but with $n=1$. The present theory coincides with the exact analysis when $E_0^p/E_0 = 1$, as the dilatational field in the inclusion and the ductile matrix are both truly uniform (Hill, 1963). The most critical test lies with the ideally plastic matrix; so two types of h or E_0^p are selected: $h = E_0^p = 0$, and $E_0^p/E_0 = 0.1$. Taking $\nu_1 = \nu_0 = 0.33$ for simplicity, the results at $c_1 = 30$ percent are shown in Figs. 5(*a*) and (*b*), respectively. To investigate the influence of inclusion stiffness on the plastic volume expansion of the composite, each is investigated with five E_1/E_0 ratios: ∞, 10, 1, 0.1, and 0. Both the exact analysis (the dashed lines) and the present theory (the solid lines) indicate that, when inclusions are elastically stiffer than the matrix ($E_1 > E_0$), the overall nonlinearity or plastic volume expansion, as asserted before, is indeed small, and disappears completely when both phases possess the same elastic moduli. However, it becomes more visible when inclusions are elastically softer than the matrix, with voids giving rise to the most pronounced effect. The overall accuracy of the present theory, even at this finite concentration, is seen to be remarkable indeed. (There is, of course, no assurance that under other types of loading, or when the inclusions are not spherical, the same degree of accuracy can be achieved.)

Finally, it is instructive to compare the new theory with Tandon and Weng's (1988) original one. When the inclusions are elastically stiffer than the matrix, we choose the silicon carbide/aluminum system with $E_1 = 490$ GPa and $\nu_1 = 0.17$ for the carbides (Arsenault, 1984), and subject it to a pure tension. For a composite with elastically softer inclusions, we choose $E_1 = 6.83$ GPa (one order of magnitude softer) and $\nu_1 = 0.33$. The overall stress-strain curves of the matrix and the composite are shown in Fig. 6(*a*) when the inclusions are stiffer and in Fig. 6(*b*) when they are softer. The new theory, as expected, gives a softer estimate for the overall behavior of the composite, regardless of the relative rigidity of the inclusions.

Acknowledgment

This work was supported by the National Science Foundation, under Grants MSS-8918235 and MSS-9114745, and by the Office of Naval Research, under Grant N-00014-91-J-1937. Dr. Yapa Rajapakse is the Scientific Officer at ONR.

References

Arsenault, R. J., 1984, "The Strengthening of Aluminum Alloy 6061 by Fiber and Platelet Silicon Carbide," *Materials Science and Engineering*, Vol. 64, pp. 117–181.

Budiansky, B., 1959, "A Reassessment of Deformation Theories of Plasticity," ASME Journal of Applied Mechanics, Vol. 26, pp. 259–264.

Chadwick, P., 1963, "Compression of a Spherical Shell of Work-Hardening Materials," *International Journal of Mechanical Sciences*, Vol. 5, pp. 165–182.

Chu, T. Y., and Hashin, Z., 1971, "Plastic Behavior of Composites and Porous Media Under Isotropic Stress," *International Journal of Engineering Science*, Vol. 9, pp. 971–994.

Eshelby, J. D., 1957, "The Determination of the Elastic Field of an Ellipsoidal Inclusion and Related Problems," *Proceedings of the Royal Society, London*, Vol. A241, pp. 376–396.

Gurson, A. L., 1977, "Continuum Theory of Ductile Rupture by Void Nucleation and Growth: Part I—Yield Criteria and Flow Rules for Porous Ductile Media," *ASME Journal of Engineering Materials and Technology*, Vol. 99, pp. 1–15.

Hashin, Z., and Shtrikman, S., 1963, "A Variational Approach to the Theory of the Elastic Behavior of Multiphase Materials," *Journal of Mechanics and Physics of Solids*, Vol. 11, pp. 127–140.

Hill, R., 1950, *The Mathematical Theory of Plasticity*, Clarendon Press, Oxford, pp. 97–106.

Hill, R., 1956, "New Horizons in the Mechanics of Solids," *Journal of the Mechanics and Physics of Solids*, Vol. 5, pp. 66–74.

Hill, R., 1963, "Elastic Properties of Reinforced Solids: Some Theoretical Principles," *Journal of the Mechanics and Physics of Solids*, Vol. 11, pp. 357–372.

Hill, R., 1965, "Continuum Micromechanics of Elastoplastic Polycrystals," *Journal of the Mechanics and Physics of Solids*, Vol. 13, pp. 89–101.

Hom, C. L., and McMeeking, R. M., 1989, "Void Growth in Elastic-Plastic Materials," ASME Journal of Applied Mechanics, Vol. 56, pp. 309–317.

Mori, T., and Tanaka, K., 1973, "Average Stress in the Matrix and Average Elastic Energy of Materials with Misfitting Inclusions," *Acta Metallurgica*, Vol. 21, pp. 571–574.

Nieh, T. G., and Chellman, D. J., 1984, "Modulus Measurements in Discontinuous Reinforced Aluminum Composites," *Scripta Metallurgica*, Vol. 8, pp. 925–928.

Qiu, Y. P., 1990, "Theory of Inclusions in the Elastic and Elastic-Plastic Deformation of Composite Materials," Ph.D. Dissertation, Rutgers University.

Ponte Castaneda, P., and Willis, J. R., 1988, "On the Overall Properties of Nonlinearly Viscous Composites," *Proceedings of the Royal Society, London*, Vol. A416, pp. 217–244.

Ponte Castaneda, P., 1991, "The Effective Mechanical Properties of Nonlinear Isotropic Composites," *Journal of the Mechanics and Physics of Solids*, Vol. 39, pp. 45–71.

Talbolt, D. R. S., and Willis, J. R., 1985, "Variational Principle for Inhomogeneous Nonlinear Media," *IMA Journal of Applied Mathematics*, Vol. 35, pp. 39–54.

Talbolt, D. R. S., and Willis, J. R., 1987, "Bounds and Self-Consistent Estimates for the Overall Properties of Nonlinear Composites," *IMA Journal of Applied Mathematics*, Vol. 39, pp. 215–240.

Tandon, G. P., and Weng, G. J., 1986a, "Stress Distribution in and Around Spheroidal Inclusions and Voids at Finite Concentration," ASME Journal of Applied Mechanics, Vol. 53, pp. 511–518.

Tandon, G. P., and Weng, G. J., 1986b, "Average Stress in the Matrix and Effective Moduli of Randomly Oriented Composites," *Composite Science and Technology*, Vol. 27, pp. 111–132.

Tandon, G. P., and Weng, G. J., 1988, "A Theory of Particle-Reinforced Plasticity," ASME Journal of Applied Mechanics, Vol. 55, pp. 126–135.

Tvergaard, V., 1981, "Influence of Voids on Shear Band Instability Under Plane Strain Condition," *International Journal of Fracture*, Vol. 17, pp. 389–407.

Weng, G. J., 1984, "Some Elastic Properties of Reinforced Solids, with Special Reference to Isotropic Ones Containing Spherical Inclusions," *International Journal of Engineering Science*, Vol. 22, pp. 845–856.

Willis, J. R., 1990, "Variational Estimates for the Overall Behavior of a Nonlinear Matrix-Inclusion Composite," *Micromechanics and Inhomogeneity* (The Toshio Mura Anniversary Volume), G. J. Weng, M. Taya, and H. Abe, eds., Springer-Verlag, New York, pp. 581–597.

Willis, J. R., 1991, "On Methods for Bounding the Overall Properties of

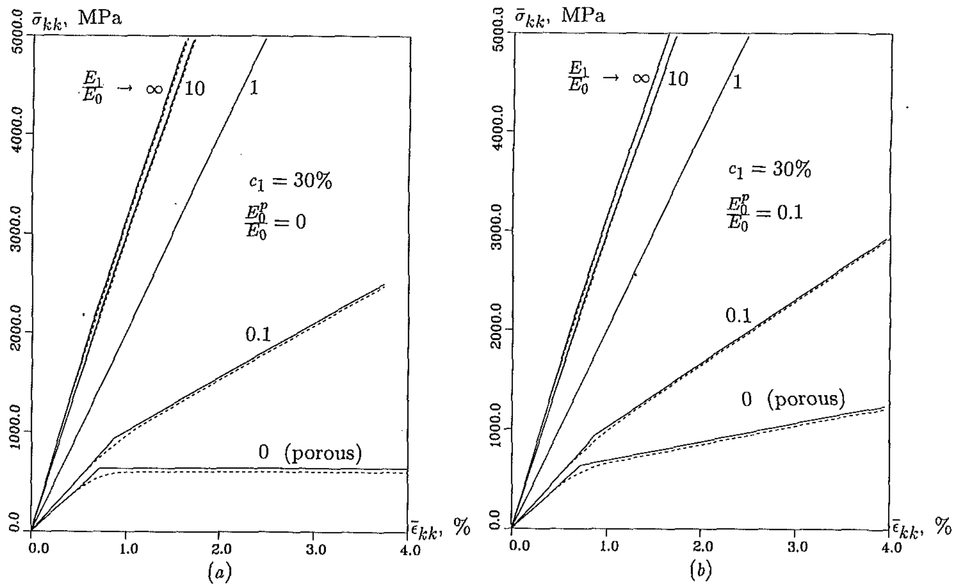

Fig. 5 Present theory versus the exact solution for a two-phase composite containing spherical inclusions under pure dilatation, and the influence of the elastic stiffness of inclusions on the overall plastic volume expansion; (*a*) ideally plastic matrix $E_0^p = 0$ and (*b*) with a work-hardening modulus $E_0^p/E_0 = 0.1$

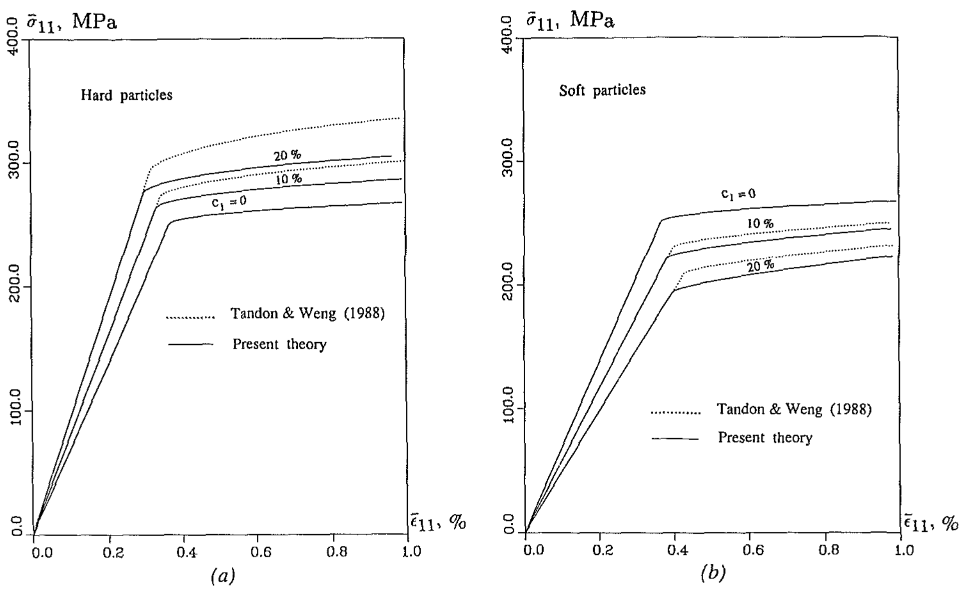

Fig. 6 Comparison between Tandon and Weng's (1988) original theory and the present one

Nonlinear Composites," *Journal of the Mechanics and Physics of Solids*, Vol. 39, pp. 73–86.

Zhao, Y. H., and Weng, G. J., 1990, "Theory of Plasticity for a Class of Inclusion and Fiber-Reinforced Composites," *Micromechanics and Inhomogeneity* (The Toshio Mura Anniversary Volume), G. J. Weng, M. Taya, and H. Abe, eds., Springer-Verlag, New York, pp. 599–622.

APPENDIX

Exact Solution for the Overall Stress-Strain Relation Under a Pure Hydrostatic Loading

Within the small-strain range (without considering the void growth or collapse) and assuming a bilinear stress-strain relation ($n=1$) for the matrix, the overall hydrostatic stress-strain curve for a particle-reinforced composite can be constructed in three steps:

(i) The onset of yielding occurs at

$$\bar{\sigma}_{kk} = \pm\left[2(1-c_1) + \frac{9\kappa_1}{1-\frac{\kappa_1}{\kappa_0}}\,\frac{1-\nu_0}{E_0}\right]\sigma_y, \tag{A1}$$

$$\bar{\epsilon}_{kk} = \pm\left[\frac{2}{3\kappa_0} + \frac{1}{2\mu_0}c_1 + \frac{3\kappa_1}{\kappa_0-\kappa_1}\,\frac{1-\nu_0}{E_0}\right]\sigma_y, \tag{A2}$$

where, and hereafter, the positive sign is chosen when $\kappa_1 < \kappa_0$, and the negative sign is selected when $\kappa_1 > \kappa_0$.

(ii) Partial yielding in the matrix, with $r=R$, denoting the elastic/plastic boundary:

$$\bar{\sigma}_{kk} = \pm \left[2\left(1 - \frac{R^3}{a_2^3}\right) + \frac{9\kappa_1}{1 - \frac{\kappa_1}{\kappa_0}} \frac{1-\nu_0}{E_0} \frac{R^3}{a_1^3} + 6H \ln \frac{R}{a_1} + \frac{4(1-\nu_0)}{E_0} HhR^3 \left(\frac{1}{a_1^3} - \frac{1}{R^3}\right)\right] \sigma_y, \quad \text{(A3)}$$

where a_1 and a_2 are the radii of the inclusion and matrix, and $H = [1 + 2(1-\nu_0)h/E_0]^{-1}$. Using R as the parameter, the $\bar{\sigma}_{kk}$ versus $\bar{\epsilon}_{kk}$ relation can be generated by increasing R from a_1 to a_2.

$$\epsilon_{rr}^p(a_2) = \frac{\pm \left[\frac{3\kappa_1}{1 - \frac{\kappa_1}{\kappa_0}} \frac{1-\nu_0}{E_0} \frac{1}{c_1} + \frac{2}{3} H \ln \frac{1}{c_1} + \frac{4(1-\nu_0)}{3E_0} Hh \left(\frac{1}{c_1} - 1\right)\right] \sigma_y - \frac{1}{3} \bar{\sigma}_{kk}}{\frac{3\kappa_1}{1 - \frac{\kappa_1}{\kappa_0}} \frac{1}{2Hc_1} + \frac{2h}{3}\left(\frac{1}{c_1} - 1\right)}, \quad \text{(A5)}$$

(iii) Fully plastic state: At a given $\bar{\sigma}_{kk}$, the radial strain at the outer boundary $r = a_2$ can be written as

$$\bar{\epsilon}_{kk} = \pm \left[\frac{3\kappa_1}{\kappa_0 - \kappa_1} \frac{1-\nu_0}{E_0} \frac{R^3}{a_1^3} + \frac{2}{3\kappa_0} + \frac{1}{2\mu_0} \frac{R^3}{a_2^3} + \frac{2}{\kappa_0} H \ln \frac{R}{a_1} + \frac{4(1-\nu_0)}{3\kappa_0 E_0} HhR^3 \left(\frac{1}{a_1^3} - \frac{1}{R^3}\right)\right] \sigma_y, \quad \text{(A4)}$$

and for the composite,

$$\bar{\epsilon}_{kk} = \frac{\bar{\sigma}_{kk}}{3\kappa_0} \pm \frac{3(1-\nu_0)}{E_0} \sigma_y - \frac{3}{2H} \epsilon_{rr}^p(a_2). \quad \text{(A6)}$$

Then by increasing $\bar{\sigma}_{kk}$, the $\bar{\sigma}_{kk}$ versus $\bar{\epsilon}_{kk}$ curve can be constructed.

These results can be applied to a porous material ($\kappa_1 = E_1 = 0$), and elastically incompressible matrix ($\nu_0 = 1/2$). Detailed derivation can be found in Qiu (1990).

Nicola Marzari
Dipartimento di Fisica,
via Valerio 2,
30100 Trieste, Italy

Mauro Ferrari
Department of Civil Engineering, and
Department of Materials Science
and Mineral Engineering,
University of California,
Berkeley, CA 94720

Textural and Micromorphological Effects on the Overall Elastic Response of Macroscopically Anisotropic Composites

The Mori-Tanaka elastic response of composites with inclusions exhibiting nontrivial orientation distributions is studied. The effect of texture is evaluated for various fiber and matrix materials, various inclusion geometries, and in the presence of anisotropic fibers. In particular, the effect of misalignment is studied. The polyphase extension of the Mori-Tanaka theory is employed to determine the effective response of aligned composites containing defects of different morphologies.

Introduction

For injection-molded short-fiberglass-reinforced composites, the orientation profile of the fibers is determined by several factors, such as the shape of the mold, the fiber concentration level, the occurrence of turbulent phenomena, and the temperature field (Chung and Cohen, 1985). In first approximation, the fibers may be assumed to be oriented along the flow lines. It is then easy to visualize that the general orientation distribution for these composites will not be random, three-dimensionally or two-dimensionally, unless particular conditions are met. This fact, which is common to most other forming techniques, prompts questions about the incidence of the orientation portrait—or texture— on the overall mechanical response of composite materials.

A second, well-known microstructural factor that influences the overall composite response is fiber geometry, that is in turn controlled by extrusion parameters (e.g., Boscolo et al., 1990).

With this background, the homogenizing approach of Mori-Tanaka (1973) is here extended and employed to evaluate the effective elastic response of textured composite with arbitrary ellipsoidal inclusion geometry. Multiphase cases are considered, and arbitrary inclusion anisotropy is a priori permitted. Numerical techniques are employed to explicitly compute the effective stiffness tensor and elicit its dependence on the compositional, distribution, and micromorphological data. The inclusions' orientation profiles are here statistically represented by orientation probability density functions, following Ferrari and Johnson (1989).

Several works on the effective medium theory based on the assumption of Mori and Tanaka have appeared in the recent literature on composite and porous materials, among which Taya (1981), Taya and Mura (1981), Takao et al. (1982), Weng (1984), Benveniste (1986, 1987), Benveniste et al. (1989), Zhao et al. (1989), and Ferrari and Johnson (1989). Favorable theoretical considerations on this method include that: (i) Its predictions lie within the known exact bounds for macroscopically isotropic (Weng, 1984; Norris, 1989) and transversely isotropic composites (Zhao et al., 1989); Norris, 1989); (ii) The Mori-Tanaka effective stiffness tensor is symmetric for random or unidirectional biphase composites, as well as for all biphase composites with spherical or isotropic inclusions (Ferrari, 1991); (iii) The model was shown to be in excellent agreement with experimental evidence for several material and distributional combinations (Weng, 1984; Boscolo et al., 1990).

The Mori-Tanaka model thus appears to be on firm ground, for use in most technologically significant applications. However, to its detriment it is noted that: (a) Property (i) does not generalize to multiphase composites (Norris, 1989), with the notable exception of those with spherical inclusions (Tandon and Weng, 1986); The Mori-Tanaka stiffness tensor associated with textured or multiphase media is generally asymmetric (Benveniste et al., 1989; Weng, 1990; Qiu and Weng, 1990; Ferrari, 1991); (c) At the unitary fiber concentration limit, the Mori-Tanaka approach is also found to exhibit a physically unacceptable behavior, unless the fibers are isotropic or perfectly aligned (Ferrari, 1991). Even for the case of isotropy, the accuracy of the method at high concentrations was challenged (Christensen, 1990).

None of the systems examined in the sequel suffers from any of the drawbacks (a)–(c), with the exception of a slight asymmetry exhibited by the effective stiffness tensor of Section 3.5. Since the present approach yields the *entire* stiffness tensor, its symmetry or lack thereof may be directly verified.

Contributed by the Applied Mechanics Division of The American Society of Mechanical Engineers for presentations at the 1992 ASME Summer Mechanics and Materials Meeting, Tempe, AZ, Apr. 28–May 1, 1992.

Discussion on this paper should be addressed to the Technical Editor, Prof. Leon M. Keer, The Technological Institute, Northwestern University, Evanston, IL 60208, and will be accepted until four months after final publication of the paper itself in the Journal of Applied Mechanics. Manuscript received by the ASME Applied Mechanics Division; Dec. 3, 1990; final revision, July 13, 1991. Associate Editor: G. J. Dvorak.

Paper No. 92-APM-32.

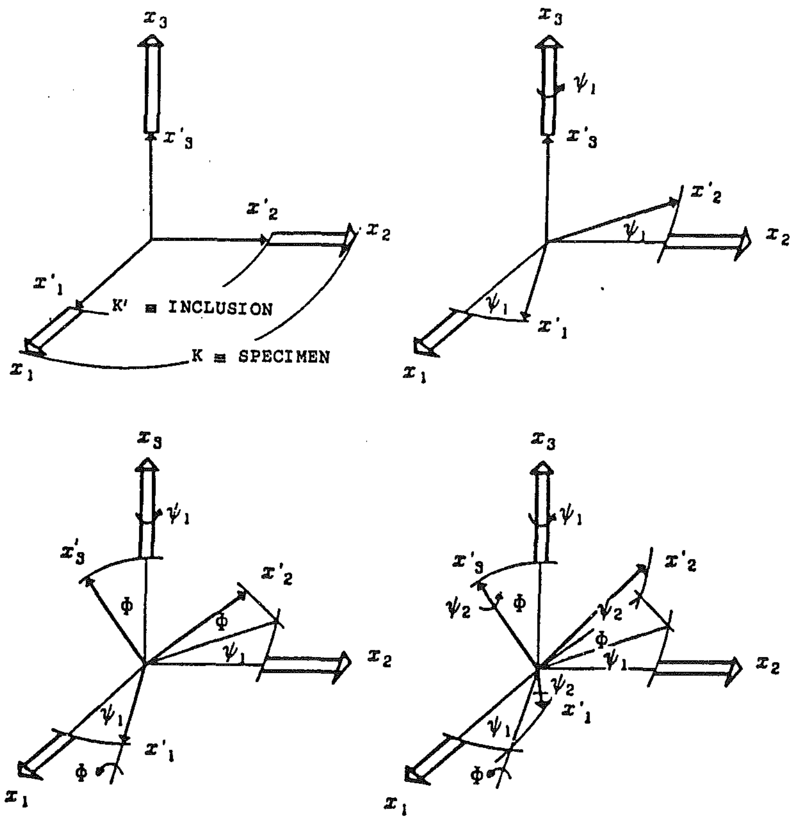

Fig. 1 Convention on Euler angles

Approaches other than the Mori-Tanaka scheme may be used for the estimation of the effective elasticities of inhomogeneous materials, but, to the best of the authors' knowledge, none has been used for materials with arbitrary inclusions morphology, texture, material symmetry, or with more than two phases.

2 The Mori-Tanaka Homogenizing Scheme for N-Phase Short Fiber Composites with Texture

By an "effective medium," which is elastically equivalent to a given inhomogeneous material, the homogeneous material is indicated, the stiffness tensor $\mathbf{C}$ of which maps an homogeneous deformation ϵ^o applied at the boundary of the real body into the average stress $\bar{\sigma}$ thus generated

$$\bar{\sigma} = \mathbf{C}\epsilon^o. \tag{1}$$

Let a representative volume element of a composite material be constituted by a matrix phase, of elastic tensor $\mathbf{C}^m$, reinforced by N-1 families of inclusions (fibers), the stiffness tensors of which are denoted by $\mathbf{C}^i$, for $i = 1,2, \ldots N-1$. The orientation distribution of the ith family of fibers, all of the members of which are taken to have the same shape and to be composed of the same material, is described by the orientation probability density function $f_i(\psi_1, \phi, \psi_2)$, also known as ODF. Its argument is a triad of Euler angles, collectively defined as g, indicating the orientation of the fiber-fixed frame K' with respect to the sample-fixed frame K, according to the convention given in Fig. 1.

The texture-weighted orientation average of any given tensorial field $\mathbf{F}^i$, defined on the ith fiber family, and expressed in a sample-fixed frame is

$$\langle \mathbf{F}^i(g) \rangle_i \equiv 1/8\pi^2 \int_0^{\pi}\int_0^{2\pi}\int_0^{2\pi} \Pi(\mathbf{F}^i) f^i(g) \sin\phi \, d\psi_1 d\psi_2 d\phi \tag{2}$$

where $\Pi(.)$ is the frame change operator. Thus, the typical element of the tensor $\Pi(\mathbf{F}^i)$ is a linear combination of R-fold products of elements of Euler matrix, R being the tensorial rank of $\mathbf{F}^i$.

The orientation-dependent strain concentration tensors $\mathbf{A}^i$, for $i = 1 \ldots N-1$, are now introduced as

$$\bar{\epsilon}^i = \mathbf{A}^i \epsilon^o \tag{3}$$

thus relating $\bar{\epsilon}^i$, the average strain in ith inclusion family, to the global average strain ϵ^o. In terms of the unknown tensors $\mathbf{A}^i$, the effective stiffness is thus deduced to be

$$\mathbf{C} = \mathbf{C}^m + \Sigma_i \alpha_i \langle (\mathbf{C}^i - \mathbf{C}^m)\mathbf{A}^i \rangle_i \tag{4}$$

where α_i is the volume fraction occupied by the ith family of fibers, and all explicit summations are on the range $i = 1, \ldots, N-1$.

The assumption of Mori-Tanaka (1973), originally intended for the isotropic biphase case only, is generalized here for N-phases:

$$\mathbf{A}^i = \mathbf{T}^i[\alpha_m \mathbf{I} + \Sigma_j \alpha_j \langle \mathbf{T}^j \rangle_j]^{-1} \tag{5}$$

where $\mathbf{I}$ is the fourth-rank tensorial identity, $\mathbf{T}^i$ is Wu's tensor

$$\mathbf{T}^i = [\mathbf{I} + \mathbf{E}^i(\mathbf{C}^m)^{-1}(\mathbf{C}^i - \mathbf{C}^m)]^1, \tag{6}$$

and $\mathbf{E}^i$ is Eshelby's tensor, which may be found in (Mura, 1982).

The effective stiffness tensor, obtained via (4) and (5), is

$$\mathbf{C}^{MT} = \mathbf{C}^m + \Sigma_i \alpha_i \langle (\mathbf{C}^i - \mathbf{C}^m)\mathbf{T}^i \rangle_i [\alpha_m \mathbf{I} + \Sigma_j \alpha_j \langle \mathbf{T}^j \rangle_j]^{-1}. \tag{7}$$

This treatment introduces a dependence of the effective response on the morphology of the embedded phases, through Eshelby's tensors $\mathbf{E}^i$, as these tensors are functions of the aspect ratios of the inclusions (assumed to be ellipsoidal). The orientation profiles of all embedded phases enter the scheme in a statistical sense, via the ODF-weighted Euler integrals of type 2. The ODFs may be deduced theoretically, through rheological

Table 1 Percentage of cylinder axes or disk normals contained within ± x rad of the direction of alignment (two-dimensional variation, in the x1-x2 plane), for various ln γ

Ln γ	$x=\pi/6$	$x=\pi/9$	$x=\pi/18$
−3	32.20	21.28	10.54
−2	31.82	20.96	10.34
−1	36.69	24.67	12.38
0	54.12	37.85	19.50
1	77.79	58.43	31.60
2	99.91	82.04	49.77
3	95.59	97.31	73.14
4	100.00	99.97	93.18
5	100.00	100.00	99.74

considerations, or experimentally—from microphotographic analysis (Boscolo et al., 1990) or otherwise. If the experimental approach is selected, or certain analytical developments are to be pursued, it is convenient to expand the ODF in a series of generalized spherical functions. The relative harmonic analysis results were originally presented by Ferrari and Johnson (1989). Their notation and methods will be used throughout this work.

3 Dependent of the Effective Moduli on the Material, Geometric, and Distributional Characteristics of Composites Exhibiting Texture

3.1 Dependence of the Effective Young's Moduli on the Fiber Orientation Distribution. A typical polyester-fiberglass composite is considered here, with an isotropic matrix of elastic moduli (λm, μm) = (4.9, 1.2) GPa, containing one family of isotropic inclusions of moduli ($\lambda 1$, $\mu 1$) = (20, 30) GPa. The fibers are taken *to occupy 1/3 of the composite, volume wise.* Three inclusion geometries are separately considered:

(i) Circular cylinder: $a1/a3 \to 0$, $a1 = a2$ and nonzero.
(ii) Disk-like shapes: $a1/a3 = 50$, $a1 = a2$.
(iii) Triaxial ellipsoidal: $(a1/a3, a2/a3) = (3, 2)$.

Here and throughout this work, ai is the semi-axis of the inclusion in the ith coordinate direction of the inclusion-fixed reference frame. For ease of visualization, we selected the $x3'$ axis of the fiber-fixed frame K' to be aligned with the cylinder axis for case (i), and with the normal to the disk for case (ii).

Two orientation probability density functions are separately studied:

$$f_1(g;\gamma)=k_\gamma G_\gamma(\psi_1-\pi)\delta(\Phi-\pi/2)\delta(\psi_2) \tag{8}$$

and

$$f_2(g;\gamma)=k_\gamma G_\gamma(\psi_1-\pi)G_\gamma(\phi-\pi/2)\ G_\gamma(\psi_2-\pi), \tag{9}$$

where

$$G_\gamma(x)=\exp(-\gamma x^2). \tag{10}$$

$\delta(x-\bar{x})$ is Dirac's delta distribution, centered at $\bar{x}$, and k_γ is a γ-dependent normalization constant. The G-functions are symmetric with respect to the central point of their range of definition, given the indicated choice of arguments.

3.1.1 Effective Moduli Under the Orientation Distribution (8). Upon varying γ from 0 to ∞ in (8), the orientation distribution is made to vary from a condition of transverse isotropy around the $x3$-axis of the lab-fixed frame to a condition of perfect alignment of the $x3'$ axes with the $x2$ direction of the lab-fixed frame. In particular, $\gamma = 0$ corresponds to the $x3'$ axes being randomly distributed in the lab-fixed $x1$–$x2$ plane. As γ approaches ∞, the orientation distribution tends to a Dirac's delta, centered at $(\psi_1, \Phi, \psi_2) = (\pi, \pi/2, 0)$. It may be noted that $\gamma = \infty$ yields transverse isotropy around the $x2$-axis, provided that the inclusions be spheroidal ($a1 = a2$). The distribution $f_1(g; \gamma)$ models in-plane fiber misalignment around the $x2$-axis, a quantitative assessment of which is given in Table 1 as a function of ln γ.

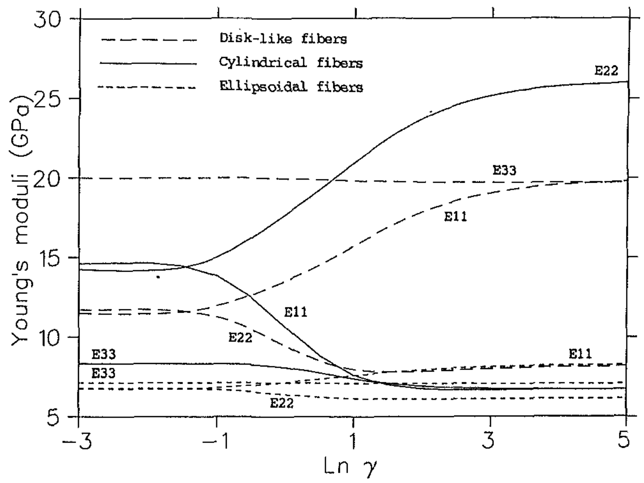

Fig. 2 Dependence of the moduli on ln γ (Section 3.1.1)

Figure 2 exhibits the dependence of the Young's moduli in the three composite coordinate directions on ln γ. For the cylindrical geometry (case (i)), $E11$ and $E22$ are seen to coalesce, as γ tends to 0. This is the expected result, considering that the vanishing of γ corresponds to the cylinders axes being contained in the $x1$-$x2$ plane, and there randomly oriented. For vanishing γ, $E11$ and $E22$ tend to a limit value, higher than $E33$. As γ grows, $E11$ decreases and coalesces with $E33$, while $E22$ asymptotically approaches the upper Hashin-Hill bound. For the sake of comparison, Young's effective modulus for the same composite, in condition of macroscopic isotropy ($f(.) = 1$), is $E = 10.8$ GPa.

With the disk-like geometry (case (ii)), the highest value for the moduli is attained by $E33$, corresponding to $\gamma = 0$. As γ increases, $E33$ tapers off, while $E11$ increases. For γ approaching ∞, these moduli reach the same asymptotic value. The isotropic modulus for this composite is $E = 13.8$ GPa. For both cases (i) and (ii), $E33$ shows a moderate decrease with the improving of the alignment.

The Young's moduli for the geometric type (iii) exhibit the expected trends, and vary minimally with γ. Their values always remain close, and considerably well below the corresponding value for the other geometric types studied. The isotropic modulus for this composite is $E = 6.8$ GPa.

3.1.2 Effective Moduli Under the Orientation Distribution (9). In conjunction with (9), the orientation parameter γ is allowed to vary in the range $(0, \infty)$. The case $\gamma = 0$ corresponds to three-dimensional isotropy. As γ approaches ∞, the orientation distribution tends to a Dirac's delta, centered at $(\psi_1, \phi, \psi_2) = (\pi, \pi/2, \pi)$. This rotation exchanges the $x2'$ and $x3'$ directions. Thus, for case (i), all of the cylinders are aligned with the $x2$ lab-fixed axis, while for case (ii), all of the disks' normals are. In this sense, $f_2(g; \gamma)$ models three-dimensional fiber misalignment about the lab-fixed $x2$ axis.

Figure 3 displays the dependence of the Young's moduli in the coordinate directions on ln γ, for the three inclusion geometries specified above. For both the cylindrical and the disk-like geometry, at large values of γ, $E11$ and $E33$ approximately coincide. The corresponding $E22$ is considerably higher, for the cylindrical inclusions, but much lower, for the disk-like ones. The effective moduli associated with (8) and (9) coincide, for large γ, for cases (i) and (ii), as expected from the limit properties of these distributions. For the spheroidal case, the $E22$ and $E33$ values are exchanged.

3.2 Dependence on the Effective Young's Moduli on the Inclusion Material, Morphology, and Concentration for Composites Exhibiting Texture. Textured biphase composites are

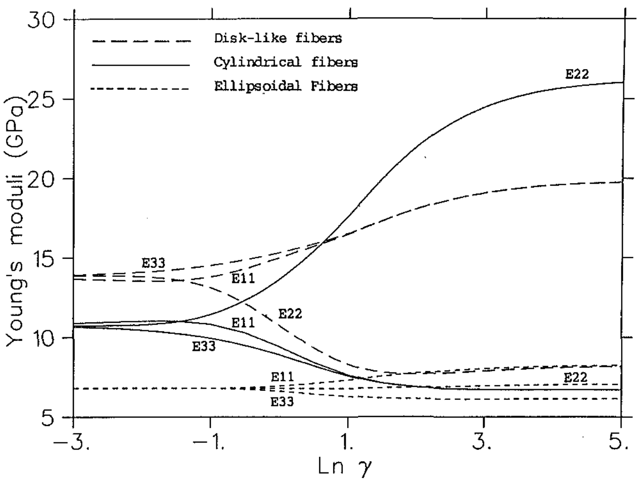

Fig. 3 Dependence of the moduli on ln γ (Section 3.1.2)

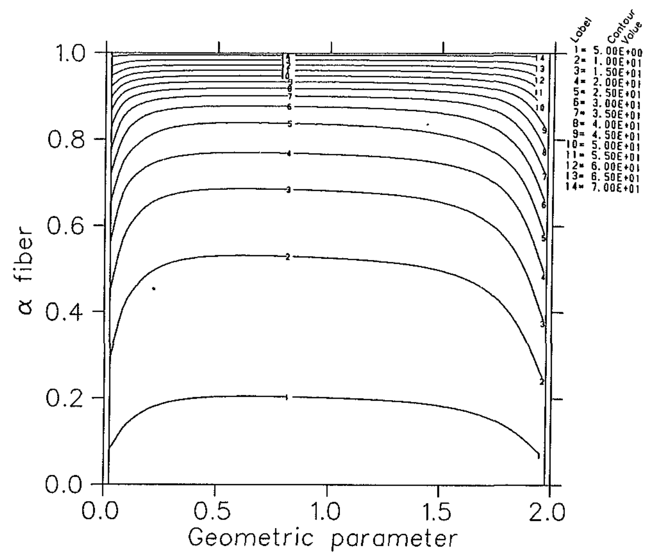

Fig. 4 Dependence of $E11 = E22$ on inclusions' geometric parameter m and concentration, texture given by (11) (Section 3.2.1)

considered here, consisting of a polyester matrix material with Lame's moduli (λm, μm) = (4.9, 1.2) GPa, and inclusions of variable constituent material, morphology, and concentration levels. The texture is given by the orientation probability density function

$$f(g) = k\delta(\Phi - \pi/2)\delta(\psi_2). \tag{11}$$

For this function all ψ_1 values are equi-probable, and (ϕ, ψ_2) are fixed at the values ($\pi/2$, 0). Thus, all the $x3'$-axes of all inclusion-fixed frames lie in the $x1$-$x2$ plane, and are randomly oriented there. This entails transverse isotropy of the elastic properties around the $x3$ axis of the sample-fixed frame.

Spheroidal inclusions are considered, with semi-axes $a1 = a2$. For the description of the effects of the inclusions' geometry on the macroscopic moduli, the geometric parameter m is introduced as

$$m = \begin{cases} a3/a1, & \text{for } m \in [0, 1] \\ 2 - a1/a3, & \text{for } m \in [1, 2] \end{cases} \tag{12}$$

Thus, as m grows from 0 to 1, it describes oblate spheroids of increasing thickness, whereas in the range [1, 2], it describes prolate spheroids—the case $m = 2$ corresponding to infinite axial length.

3.2.1 Effect of the Inclusion Geometry and Concentration for a Given Inclusion Material. An inclusion material, with Lame's constant (λf, μf) = (20, 30) GPa, is employed here. Figures 4 and 5 display the contour lines of the graph, giving $E11 = E22$ and $E33$ as functions of the inclusions' concentration level and geometric parameter m. Some interesting features are:

(i) For $m > 1$, and any concentration level, $E11$ is greater than the isotropic modulus, which in turn exceeds $E33$. For $m < 1$, this chain of inequalities is reversed. At $m = 1$, the three moduli obviously coincide: spherical inclusions of isotropic materials are incapable of texture.

(ii) At any concentration level, $E11$ and $E33$ are monotonically increasing functions of m, for $m > 1$ and $m < 1$, respectively. In the complementary ranges for m, they are not monotonic.

(iii) The highest overall modulus, at any fixed fiber concentration, corresponds to $E33$ for disk-like inclusions.

For the case of random orientations ($f(g) = 1$), it is found that any assigned value of the isotropic modulus E is realized with the minimum (maximum) amount of reinforcing material for the case of vanishing (unitary) aspect ratio corresponding to the higher (lower) Hashin-Shtrikman bound for a fixed inclusions' concentration.

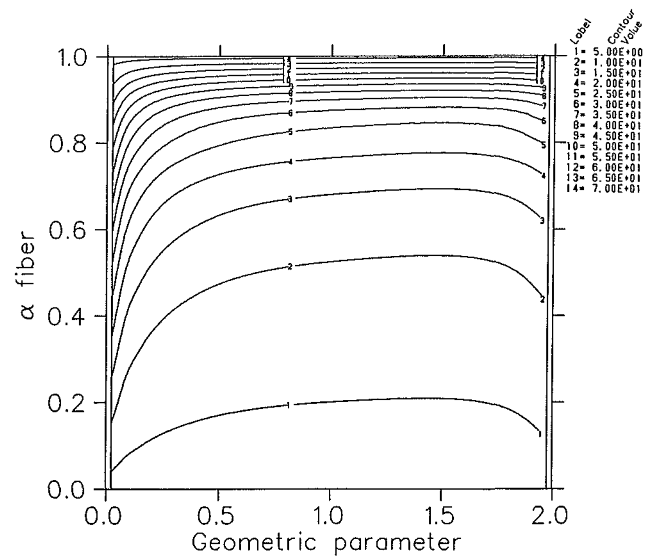

Fig. 5 Dependence of $E33$ on inclusions' geometric parameter m and concentration, texture given by (11) (Section 3.2.1)

3.2.2 Effect of the Inclusion Modulus and Geometry at a Fixed Concentration Level. The independent variables of this section are the inclusions' Young's modulus and geometric parameter m. The dependence of $E11 = E22$ and $E33$ on these variables is given in Figs. 6 and 7, where the inclusions' Poisson ratio is fixed at 0.2, and the concentration level is $\alpha = 1/3$. Smaller aspect ratios are shown to have a greater relative stiffening effect on the material, in the direction along the transverse isotropy axis $x3$, while higher ratios enhance more the in-plane modulus $E11$. It is interesting to note that equal moduli may be obtained employing fibers of slightly different aspect ratios, and considerably different moduli. In order to stress this point, that may be of technological relevance, we explicitly note that, for this composite, the value of $E33 = 8.00$ GPa is obtained for fibers of modulus $E_f = 100$ GPa and aspect ratio of 0.37, and for fibers of modulus $E_f = 300$ GPa, and aspect ratio of 0.45. For these cases, $E11 = 6.7$ and 6.9 GPa, respectively.

Figure 7 shows that the $E11$ modulus associated with the cylindrical geometry greatly exceeds the corresponding mod-

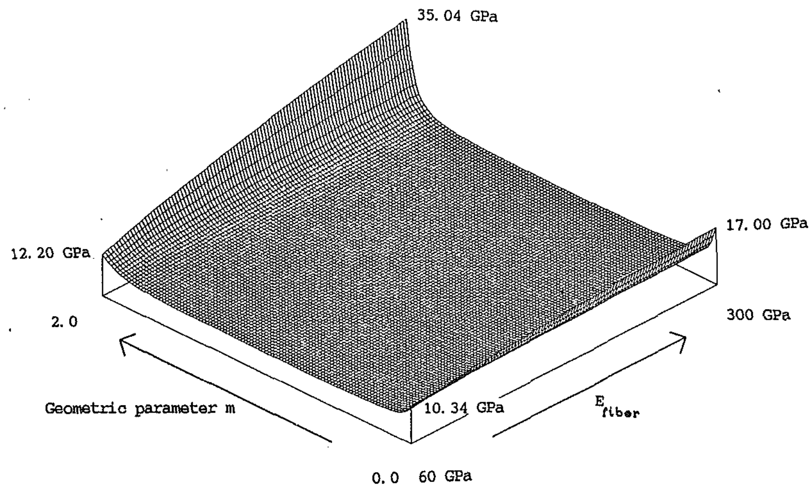

Fig. 6 Dependence of $E11 = E22$ on inclusions' geometric parameter m and Young's modulus, texture given by 11 (Section 3.2.2)

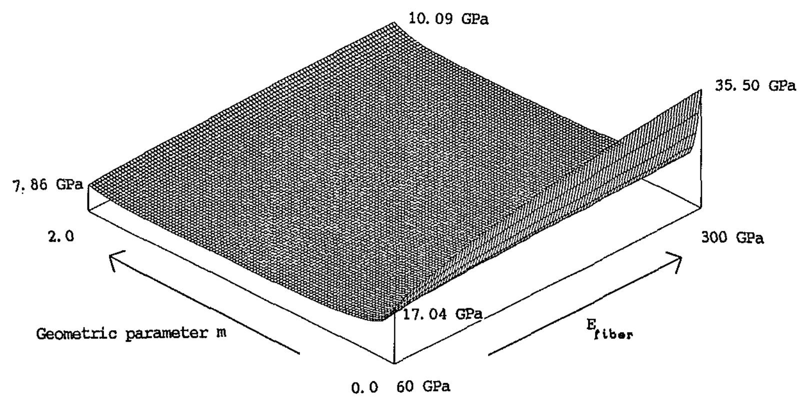

Fig. 7 Dependence of $E33$ on inclusions' geometric parameter m and concentration, texture given by (11) (Section 3.2.2)

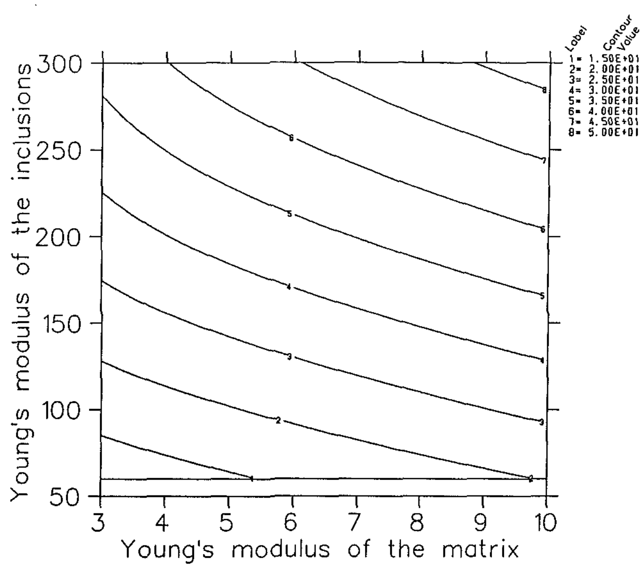

Fig. 8 Equimodular lines for $E11 = E22$, in terms of the Young's moduli of the inclusions and of the matrix, texture given by (11) (Section 3.3)

ulus, for the disk-like case, at high-fiber moduli. Thus property (iii) of Section 3.2.1 is not generally true.

Comparing Figs. 7–8, it is noted that the presence of texture depresses the modulus-reinforcing effect due to the slenderness of the fibers in the $x3$-direction, while it attenuates the in-plane reinforcing effect due to the fibers' higher stiffness for disk-like geometry.

3.3 Effect of the Constituent Materials' Moduli on the Effective Young's Moduli, for Textured Composites. Figures 8 and 9 display the equimodular lines for $E11 = E22$ and $E33$ in terms of the Young's moduli of the inclusions and of the matrix. The Poisson's ratios are fixed at $(\nu m, \nu f) = (0.39, 0.2)$. The texture is given by (11), the volume fraction is $\alpha = 1/3$, and the inclusions are prolate spheroids, with $a1/a3 = 50$, $a2 = a3$. The analysis of Fig. 9 shows that comparable $E33$-enhancement is obtained by slightly increasing the matrix modulus, while employing fibers of much lower stiffness. For instance, to both $(E_f, E_m) = (300, 5.6)$ and $(100, 7.3)$ GPa, there corresponds an effective $E33 = 16$ GPa. An analogous behavior is not exhibited by the in-plane modulus $E11$.

3.4 Poly-Inclusion Materials. Homogenization of a textured material containing more than one type of inclusion is performed here according to Eq. (7). As matrix material, the isotropic polymer of Sections 3.1 and 3.2 is selected. The first inclusion type consists of cylindrical glass fibers, with the moduli given in Section 3.1 and with $a1/a3 = 100$, $a2 = a3$. The fibers are perfectly aligned along the specimen $x1$-direction:

$$f^1(g) = k\delta(\psi_1)\delta(\Phi)\delta(\psi_2). \tag{13}$$

The inclusion families 2 and 3 are voids of disk-like and spherical geometry, respectively. The geometry of the disk-like voids, or cracks, is specified as $a1/a3 = 50$, $a1 = a2$. Taking $f^2(.) = f^1(.)$, the fibers are orthogonal to the disks' normals.

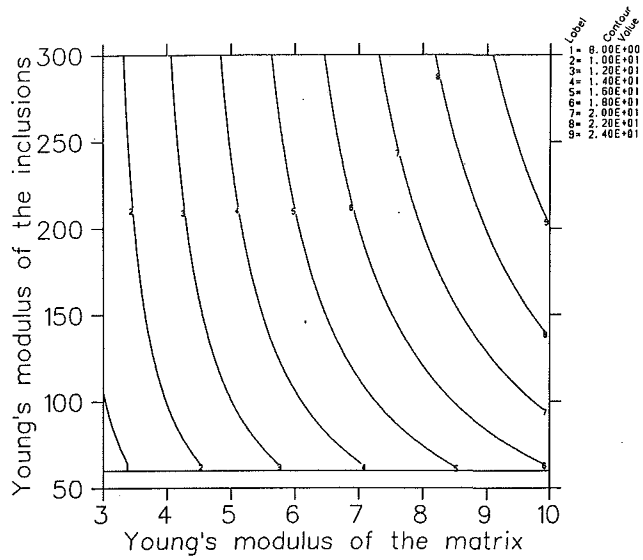

Fig. 9 Equimodular lines for $E33$ in terms of the Youngs' moduli of the inclusions and of the matrix, texture given by (11) (Section (3.3)

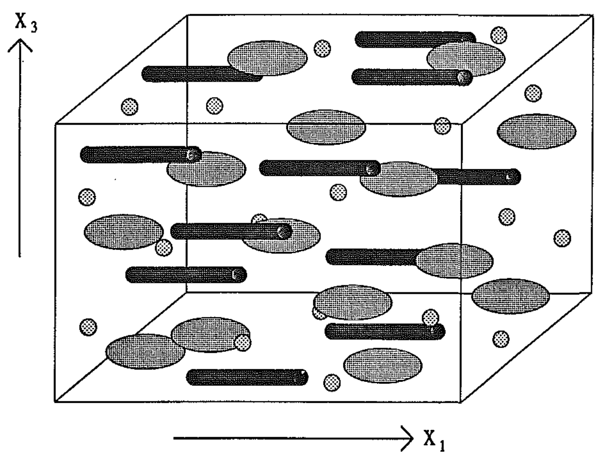

Fig. 10 Volume element of the composite of Section (3.4)

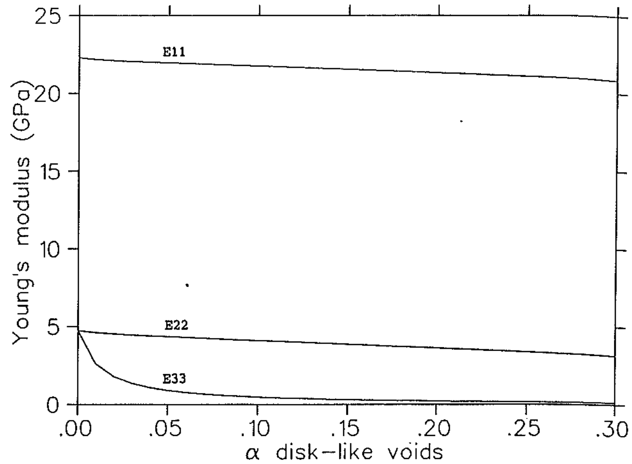

Fig. 11 Dependence of $E11$, $E22$, and $E33$ on the concentrations of disk-like voids, for (α_1, α_3) = (0.33, 0.15) (Section 3.4)

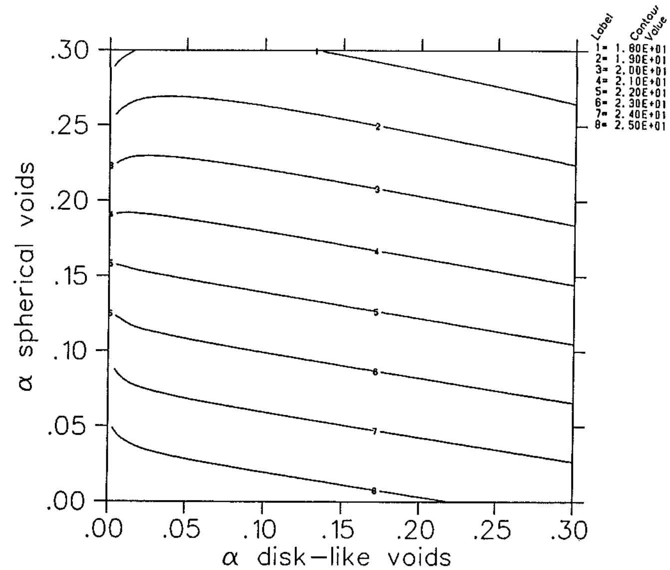

Fig. 12 Equimodular lines for $E11$, in terms of the concentration of disk-like and spherical cavities, for α_1 = 0.33 (Section 3.4)

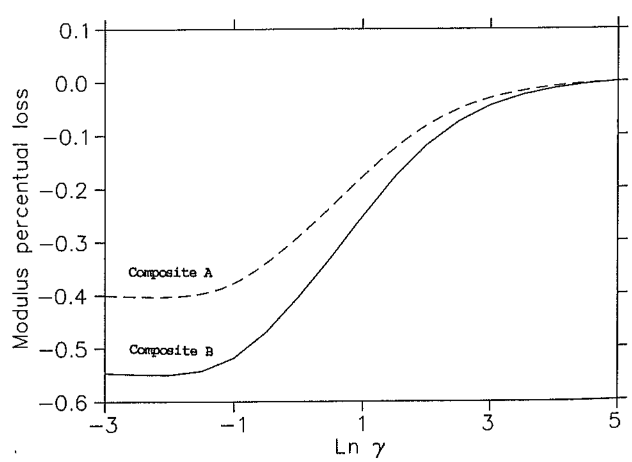

Fig. 13 Percentual loss in longitudinal modulus due to misalignment for E-glass and HM graphite fiber in polyester matrix (Section 3.5)

Figure 10 shows a representative volume element of this arrangement which models a delaminating unidirectional composite laminate containing the typical air bubbles that originate during the material processing.

Figure 11 displays the three orthogonal moduli as a function of the concentration of disk-like cavities for the fixed value of $(\alpha_1, \alpha_3) = (0.33, 0.15)$. The modulus $E33$—in the direction normal to the disks—decreases very rapidly to an almost-zero value, while $E11$ and $E22$ are respectively reduced by about 5 percent and 30 percent, for $\alpha_2 = 0.3$ only. The concentration of the spherical voids is found not to significantly affect the reduction rate $\partial E33/\partial\alpha_2$. Figure 12 displays a surprising feature of the Mori-Tanaka prediction for the modulus $E11$ of this composite: A critical value $\bar{\alpha}_3$ is seen to exist, such that for a fixed $\hat{\alpha} > \bar{\alpha}_3$, a differential increase in α_2 from zero results in a higher value for $E11$.

3.5 Effect of Texture on the Young's Moduli of Composites With Anisotropic Inclusions. Two biphase composites are considered here, both with a 1/3 volume fraction occupied by fibers of cylindrical geometry—the ratios being $(a1/a3, a2/a3) = (10, 1)$. The texture is given by (8), thus *modeling two-dimensional fiber misalignment about the* $x1$-axis. The matrix material is, for both composites, the isotropic polymer of Sections 3.1.1. The fiber materials are E-glass and high-modulus graphite, for composite A and B, respectively. The glass moduli were given in Section 3.1. The graphite fibers are transversely isotropic. Letting the material and the geometrical transverse isotropy axes coincide (along $x1'$), the independent moduli of the graphite are $(C^f_{11}, C^f_{12}, C^f_{22}, C^f_{23}, C^f_{55}) = (360, 5, 40, 30, 20)$ GPa. Figure 13 reports the percentual loss of the effective longitudinal modulus of these composites due to misalignment.

The Mori-Tanaka effective stiffness tensor corresponding to Composite B is not symmetric, but each of its elements differs from the corresponding element of its symmetric part by less than two percent.

4 Discussion/Conclusions

The Mori-Tanaka analysis of the effects of the fiber orientation distribution and morphology was performed here for biphase and multiphase composites with isotropic and anistropic fibers. Some observations on the considered cases are:

1 Relevance of the fiber geometry: At a given fiber concentration, significant reinforcement is obtained only by employing fibers of near-extremal geometries (see Sections 3.1 and 3.2.2).

2 Relevance of the fiber alignment, for unidirectional composites: About 90 percent of the longitudinal modulus, corresponding to the perfect alignment is attained for planar distributions with 90 percent of the fiber directions scattered by less than 30 degrees. This result holds for both the isotropic and the anisotropic cases considered (Sections 3.1.1 and 3.5).

3 Unidirectional distributions of isotropic disks and cylinders are dual. While cylinders provide the maximum longitudinal reinforcement, the disks provide optimal in-plane stiffening if the embedded phase is stiffer.

4 Disk-like inclusions of more compliant material cause the maximum relative modulus reduction in the direction along their normal (Section 3.4). If the disk material is stiffer, the in-plane directions are maximally reinforced.

The known relations of the Mori-Tanaka predictions to the Hashin-Shtrickman and Hashin-Hill bounds were numerically confirmed here.

Acknowledgment

This work was partially supported by the Committee on Research of the University of California at Berkeley and through the support of M.F. in the form of a Faculty Research Grant.

References

Benveniste, Y., 1986, "On the Mori-Tanaka Method in Cracked Bodies," *Mech. Res. Comm.*, Vol. 13, pp. 193–201.

Benveniste, Y., 1987, "A New Approach to the Application of Mori-Tanaka's Theory in Composite Materials," *Mechanics of Materials*, Vol. 6, pp. 147–157.

Benveniste, Y., Dvorak, G. J., and Chen, T., 1989, "Stress Fields in Composites with Coated Inclusions," *Mechanics of Materials*, Vol. 7, pp. 305–319.

Boscolo, A., Ferrari, M., Pitacco, I., and Virgolini, M. P., 1990, "Mechanical Response of Anisotropic Fiberglass-Reinforced PBT via Microstructural Data," *EuroMech 269*, A. Vautrin and H. Sol, eds., pp. 238–245.

Christensen, R. M., 1990, "A Critical Evaluation for a Class of Micro-Mechanics Models," *J. Mech. Phys. Solids*, Vol. 38, No. 3, pp. 379–404.

Chung, R., and Cohen, C., 1985, "Glass-Fiber Reinforced Thermoplastics I. Wall and Effect on the Rheological Properties," *Polym. Eng. Sci.*, Vol. 25, pp. 1001–1007.

Ferrari, M., 1991, "Asymmetry and the High Concentration Limit of the Mori-Tanaka Effective Medium Theory," *Mech. of Mat.*, Vol. 11, pp. 251–256.

Ferrari, M., and Johnson, G. C., 1989, "The Effective Elasticities of Short-Fiber Composites with Arbitrary Orientation Distribution," *Mechanics of Materials*, Vol. 8, pp. 67–73.

Mori, T., and Tanaka, K., 1973, "Average Stress in Matrix and Average Elastic Energy of Materials with Misfitting Inclusions," *Acta Metallurgica*, Vol. 21, pp. 571–574.

Mura, T., 1982, *Micromechanics of Defects in Solids*, Martinus Nijoff, The Hague.

Norris, A., 1989, "An Examination of the Mori-Tanaka Effective Medium Approximation for Multiphase Composites," ASME JOURNAL OF APPLIED MECHANICS, Vol. 56, pp. 83–88.

Qiu, Y. P., and Weng, G. J., 1990, "On the Application of the Mori-Tanaka Theory Involving Transversely Isotropic Spheroidal Inclusions," *Intl. J. Eng. Sci.*, Vol. 28, No. 11, pp. 1121–1137.

Takao, Y., Chou, T. W., and Taya, M., 1982, "Effective Longitudinal Young's Modulus of Misoriented Short-Fiber Composites," ASME JOURNAL OF APPLIED MECHANICS, Vol. 49, p. 536.

Tandon, G. P., and Weng, G. J., 1990, "Average Stress in Matrix and Effective Moduli of Randomly Oriented Composites," *Comp. Sci. Tech.*, Vol. 27, pp. 111–132.

Taya, M., 1981, "On Stiffness and Strength of an Aligned Short-Fiber Reinforced Composite Containing Penny-Shaped Cracks in the Matrix," *J. Comp. Mater.*, Vol. 15, pp. 198–210.

Taya, M., and Mura, T., 1981, "On Stiffness and Strength of an Aligned Short-Fiber Composite Containing Fiber-end Cracks Under Uniaxial Applied Stress," ASME JOURNAL OF APPLIED MECHANICS, Vol. 48, pp. 361–367.

Weng, G. J., 1984, "Some Elastic Properties of Reinforced Solids, With Special Reference to Isotropic Ones Containing Spherical Inclusions," *Int. J. Engr. Sci.*, Vol. 22, No. 7, pp. 845–856.

Weng, G. J., 1990, "The Theoretical Connection Between Mori-Tanaka Theory and the Hashin-Shtrickman-Walpole Bounds," *Intl. J. Eng. Sci.*, Vol. 28, No. 11, pp. 1111–1120.

Zhao, Y. H., Tandon, G. P., and Weng, G. J., 1989, "Elastic Moduli for a Class of Porous Materials," *Acta Mechanica*, Vol. 76, pp. 105–130.

The Plastic Buckling of Axially Compressed Square Tubes

S. Li[1]

S. R. Reid
Mem. ASME

Department of Mechanical Engineering,
UMIST,
Manchester, M60 1QD, U.K.

A plastic buckling analysis for axially compressed square tubes is described in this paper. Deformation theory is used together with the realistic edge conditions for the panels of the tube introduced in our previous paper (Li and Reid, 1990), referred to hereafter as LR. The results obtained further our understanding of a number of problems related to the plastic buckling of axially compressed square tubes and simply supported rectangular plates, which have remained unsolved hitherto and seem rather puzzling. One of these is the discrepancy between experimental results and the results of plastic buckling analysis performed using the incremental theory of plasticity and the unexpected agreement between the results of calculations based on deformation theory for plates and experimental data obtained from tests conducted on tubes. The non-negligible difference between plates and tubes obtained in the present paper suggests that new experiments should be carried out to provide a more accurate assessment of the predictions of the two theories. Discussion of the results herein also advances our understanding of the compact crushing behavior of square tubes beyond that given in LR. An important conclusion reached is that strain hardening cannot be neglected for the plastic buckling analysis of square tubes even if the degree of hardening is small since doing so leads to an unrealistic buckling mode.

1 Introduction

The elastic buckling analysis of square tubes under axial compression has been describe in LR. This treatment gave some insight into the subsequent crushing behavior of such tubes with regard to the generation of compact or noncompact crushing modes. However, when crushing is produced (for example, in using such tubes as impact energy absorbers), plastic deformation is inevitably involved (Mahmood and Paluszny, 1981).

In general, plastic deformation is initiated at one of two stages. Either buckling takes place in the elastic range and, as the deformation increases in the post-buckling phase, plastic deformation develops where the stress state reaches the yield surface of the material. For problems in this category the previous work can be used to predict the buckling behavior. In order to pursue the subsequent crushing process, post-buckling analysis in conjunction with elastoplastic analysis has to be employed which usually involves very complicated and time-consuming calculations. Alternatively, plastic deformation occurs before buckling takes place. In this case, the results of the authors' previous work are no longer applicable directly, and a plastic buckling analysis has to be performed. The present paper is concerned with this latter category of behavior.

As is well known, plastic buckling is a controversial subject. The theory for columns has been well established since the work of Shanley (1947). However, for plates, the results seem somewhat contradictory. The well-known conclusion that the deformation theory of plasticity gives better results than the incremental theory is supported by experimental results (Gerard et al., 1957). It has been shown that plastic buckling analysis, which uses incremental theory, is affected significantly by the shape of the yield surface of the material, although this was not taken into account in the early incremental analysis (Sewell, 1964). It seems that a more correct understanding of the nature of the problem might stem from introducing a proper shape for the yield surface into an incremental analysis. While this would be an interesting line to follow, it will not be pursued in the present paper. Rather, a simple analysis will be developed which utilizes deformation theory together with realistic edge conditions for the panels of the tube. This reveals some significant differences between the plastic behavior of tubes and simply supported plates similar to those shown in LR for elastic buckling. These differences challenge the commonly accepted conclusion regarding the agreement between experimental results and results from deformation theory.

2 Equations for Plastic Buckling and Their Solutions

In the plastic buckling analysis of axially compressed tubes which follows, Stowell's approach (Gerard, 1962) is utilized. This was established for simply supported plates and therefore

[1]Permanent address: Department of Aircraft Engineering, Nanjing Aeronautical Institute, Nanjing, China.

Contributed by the Applied Mechanics Division of The American Society of Mechanical Engineers for publication in the ASME Journal of Applied Mechanics.

Discussion on this paper should be addressed to the Technical Editor, Prof. Leon M. Keer, The Technological Institute, Northwestern University, Evanston, IL 60208, and will be accepted until four months after final publication of the paper itself in the Journal of Applied Mechanics. Manuscript received by the ASME Applied Mechanics Division, June 29, 1990; final revision, Jan. 14, 1991.

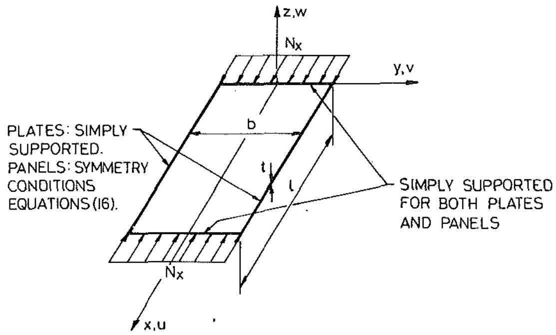

Fig. 1 A simply supported plate or a panel of a square tube under axial compression

all the assumptions made for plates are adopted here for the panels of the tube, except that the edges across the joints of the panels are no longer simply supported. For the sake of convenient reference, Stowell's plastic buckling analysis of simply supported plates by deformation theory is summarized in the Appendix. There, Stowell's classical formula for the buckling load is simplified for an elastic, linearly strain-hardening material by eliminating its implicit nature. For this case a comprehensive dimensionless parameter s is introduced which encapsulates the influence of all of the material parameters on the buckling load.

For panels of a square tube under axial compression as shown in Fig. 1, the incremental in-plane and out-of-plane buckling displacements are coupled when the realistic edge conditions described in LR are used. Therefore, solutions of the buckling equations involve all of them. With the elastic-plastic stress-strain relations (A1), the buckling equations can be expressed as

$$\left.\begin{aligned} e u_{,xx}+\frac{1}{4}u_{,yy}+\frac{3}{4}v_{,xy}=0 \\ v_{,yy}+\frac{1}{4}v_{,xx}+\frac{3}{4}u_{,xy}=0 \end{aligned}\right\} \tag{1}$$

$$e w_{,xxxx}+2w_{,xxyy}+w_{,yyyy}-N_x/D w_{,xx}=0. \tag{2}$$

All symbols here and subsequently are defined in the Nomenclature section.

In much the same way as in LR, by assuming that

$$\left.\begin{aligned} u=U(y)\cos\alpha x \\ v=V(y)\sin\alpha x \end{aligned}\right\} \tag{3}$$

$$w=W(y)\sin\alpha x, \tag{4}$$

where $\alpha=m\pi/l$, the simply supported conditions along the loaded edges are automatically satisfied. Equations (1) and (2) then reduce to

$$\left.\begin{aligned} \frac{1}{4}U''-e\alpha^2U+\frac{3}{4}\alpha V'=0 \\ V''-\frac{1}{4}\alpha^2V-\frac{3}{4}\alpha U'=0 \end{aligned}\right\} \tag{5}$$

$$W''''-2\alpha^2W''+\alpha^4(e-\lambda^2K)W=0 \tag{6}$$

where primes stand for derivatives with respect to y. Equations (5) are associated with in-plane displacements while Eq. (6) describes the out-of-plane displacement. Their solutions give the buckling mode and they are discussed separately as follows.

2.1 Solutions of Eqs. (5)—In-Plane Deformation. The solutions of Eqs. (5) are determined by the characteristic roots which are two pairs of complex conjugates

$$r=\pm p\pm iq$$

where

$$(p,\,q)=\frac{\alpha}{\sqrt{2}}\sqrt{\sqrt{e}\pm(2e-1)}. \tag{7}$$

Obviously, the values of p and q, and consequently the form of the solutions, depend on the value of e which is related to the material properties. As has been discussed in LR, symmetry about the x-axis ($y=0$) is always assumed.

For *perfectly-plastic materials*, $e=1/4$, $p=0$, and $q=\alpha/\sqrt{2}$. In this case, the solutions of Eqs. (5) can be expressed in the following form

$$\left.\begin{aligned} U=A_1\cos qy+A_2y\sin qy \\ V=B_1\sin qy+B_2y\cos qy \end{aligned}\right\} \tag{8}$$

where A_1, A_2, B_1 and B_2 are constants which are related to each other due to equations (5) by

$$\left.\begin{aligned} A_1=\sqrt{2}B_1+\frac{2}{3}\frac{1}{\alpha}B_2 \\ A_2=-\sqrt{2}B_2. \end{aligned}\right\} \tag{9}$$

For *strain-hardening materials*, $1/4<e<1$, $p>0$, and $q>0$. The solutions of Eqs. (5) are

$$\left.\begin{aligned} U=A_1\sinh py\sin qy+A_2\cosh py\cos qy \\ V=B_1\sinh py\cos qy+B_2\cosh py\sin qy \end{aligned}\right\} \tag{10}$$

the constants A_1, A_2, B_1, and B_2 being related by

$$\left.\begin{aligned} \frac{3}{4}\alpha qA_1+\frac{3}{4}\alpha PA_2-\left(p^2-q^2-\frac{1}{4}\alpha^2\right)B_1-2PqB_2=0 \\ \frac{3}{4}\alpha pA_1-\frac{3}{4}\alpha qA_2+2pqB_1-\left(p^2-q^2-\frac{1}{4}\alpha^2\right)B_2=0. \end{aligned}\right\} \tag{11}$$

For *elastic materials* $e=1$, $p=\alpha$, $q=0$. In this case, the solutions of Eqs. (5) have the form

Nomenclature

b = width of plates or panels of a square tube
e = $\frac{1}{4}+\frac{3}{4}\frac{E_t}{E_s}$
h = b/t = relative width
k = l/b = aspect ratio
l = length of plates or panels of a square tube
m = axial half-wave number
t = thickness of plates or panels of a square tube
u, v, w = incremental displacement components in directions defined in Fig. 1
$\overline{w}$ = ratio of out-of-plane deflection at edge to deflection at the center of the panel
D = $E_st^3/9$ = plastic bending rigidity
E = Young's modulus in elastic range
E_s, E_t = secant and tangent moduli
K = N_xb^2/π^2D = dimensionless buckling load
N_x = axial in-plane force per unit width (positive for compression)
s = $\frac{\pi^2}{9h^2}\frac{1}{\sigma_o/E}\frac{E_t/E}{1-(E_t/E)}$
s_p = $h^2 s$
α = $m\pi/l$
λ = k/m = dimensionless half-wavelength
θ = $\pi/2\lambda$

$$\left.\begin{aligned} U&=A_1\sinh py+A_2 y\cosh qy\\ V&=B_1\sinh py+B_2 y\cosh qy\end{aligned}\right\} \qquad (12)$$

which have been fully analysed and discussed in LR, and will therefore not be considered further in the present paper.

2.2 Solutions of Eq. (6)—Out-of-Plane Deformation. The solution of Eq. (6) could take several different forms, depending on the value of K.

$$\text{If } K<e/\lambda^2, \text{ then } W=C_1\cosh\beta y+C_2\cosh\mu y. \qquad (13)$$

$$\text{If } K=e/\lambda^2, \text{ then } W=C_1\cosh\beta y+C_2 y\sinh\beta y. \qquad (14)$$

$$\text{If } K>e/\lambda^2, \text{ then } W=C_1\cosh\beta y+C_2\cos\gamma y. \qquad (15)$$

Here,

$$\beta=\alpha\sqrt{\sqrt{K\lambda^2+1-e}+1};\ \mu=\alpha\sqrt{-\sqrt{K\lambda^2+1-e}+1}$$

$$\text{and } \gamma=\alpha\sqrt{\sqrt{K\lambda^2+1-e}-1}.$$

3 Determination of Buckling Load K and Buckling Mode

In order to determine the buckling load and the corresponding buckling mode, conditions along the edges between the panels of a tube have to be imposed. In LR, such edge conditions were obtained by continuity considerations between panels and then simplified according to the symmetry or antisymmetry about the diagonals of any cross-section of the tube. The buckling mode corresponds to antisymmetric edge conditions in most cases except for very short tubes, therefore only these edge conditions will be considered in the present paper. These are expressed as follows:

$$\left.\begin{aligned} u&=0\\ v+w&=0\\ M_y&=0\\ N_y-T_y&=0\end{aligned}\right\} \text{ along } y=b/2 \qquad (16)$$

where $T_y=Q_y+M_{xy,y}$ is the equivalent transverse shear force of thin plate theory. Edge conditions (16) are imposed at the edge $y=b/2$ while those at $y=-b/2$ are satisfied automatically by the symmetric nature of displacement fields (8), (10), and (13)–(15) about $y=0$.

In applying the above edge conditions it should be noted that there is more than one form of field both for the in-plane and out-of-plane displacements, any combination of them giving an admissible mode for buckling. Which of the admissible modes gives the buckling mode is determined by which results in the lowest value of buckling load K. Substituting any of the admissible modes into edge conditions (16), along with equations (9) or (11), leads to 6 homogeneous equations for A_1, A_2, B_1, B_2, C_1 and C_2. The buckling criterion is expressed by the nontrivial solution condition for the homogeneous equations. This results in an implicit transcendental equation for K, the implicit nature being enhanced by the fact that e depends on K for a general strain-hardening law. Therefore, a computational solution scheme has to be employed for each of the admissible modes. The results show that the form of the buckling mode is completely determined by all of the material properties. In particular, the strain-hardening properties influence the solution, which reveals the danger in using a perfectly-plastic material model in the buckling analysis of a square tube under axial compression. This is discussed as follows.

3.1 Perfectly-Plastic Material. For tubes of perfectly plastic material, the in-plane displacement components of the buckling mode are given by Eqs. (8) and the out-of-plane component is found to be in the form of Eq. (13), since this corresponds to the lowest value of K of the three forms given in Eqs. (13)–(15). Compared with simply-supported plates, the minimum value of K is much lower for the panels of a tube although it corresponds to the same dimensionless half-wavelength of $1/\sqrt{2}$.

Unfortunately, the corresponding buckling mode gives a saddled-shaped surface for the buckled panel, which contradicts experimental observations completely—as can be seen from Fig. 2, which shows the buckling mode for a typical cross-section. It seems that the panels of a tube behave in a similar way to plate columns (unloaded edges free). In fact, if the expression for N_y is derived from the buckling mode, it is found that N_y vanishes identically along the edges $y=\pm b/2$ for the axial dimensionless half-wavelength of $1/\sqrt{2}$, and therefore some kind of free edges are produced since M_y and T_y vanish at the same time. The only difference is that plate columns tend to buckle into one half-wave along the whole length while the panels of a tube would take a number of half-waves so that the half-wavelength approaches $1/\sqrt{2}$.

This unrealistic mode appears only for perfectly plastic materials. It suggests that for the plastic buckling analysis of a square tube under axial compression, neglect of the strain hardening properties of the material does not lead to physically reasonable results.

3.2 Strain-Hardening Material. For materials with strain hardening, no solution for K could be found involving the out-of-plane mode given by Eq. (13), while the mode described by Eq. (14) is related to the trivial mode, K and m both being zero. Therefore, the buckling mode is given by Eqs. (10) and (15). With this mode the nontrivial solution condition is expressed in Eq. (17)

$$\begin{vmatrix}
\sinh\psi\theta\sin\varphi\theta & \cosh\psi\theta\cos\varphi\theta & 0 & 0 & 0 & 0\\
\frac{3}{4}\varphi & \frac{3}{4}\psi & -\left(\psi^2-\varphi^2-\frac{1}{4}\right) & -2\psi\varphi & 0 & 0\\
\frac{3}{4}\psi & -\frac{3}{4}\varphi & 2\psi\varphi & -\left(\psi^2-\varphi^2-\frac{1}{4}\right) & 0 & 0\\
-\frac{1}{2}\sinh\psi\theta\sin\varphi\theta & -\frac{1}{2}\cosh\psi\theta\cos\varphi\theta & \begin{array}{c}-\varphi\sinh\psi\theta\sin\varphi\theta\\ +\psi\cosh\psi\theta\cos\varphi\theta\end{array} & \begin{array}{c}\psi\sinh\psi\theta\sin\varphi\theta\\ +\varphi\cosh\psi\theta\cos\varphi\theta\end{array} & \frac{\theta^2}{3h^2}\xi\left(\xi^2-\frac{3}{2}\right)\sinh\xi\theta & \frac{\theta^2}{3h^2}\eta\left(\eta^2+\frac{3}{2}\right)\sin\eta\theta\\
0 & 0 & \sinh\psi\theta\cos\varphi\theta & \cosh\psi\theta\sin\varphi\theta & \cosh\xi\theta & \cos\eta\theta\\
0 & 0 & 0 & 0 & \left(\xi^2-\frac{1}{2}\right)\cosh\xi\theta & -\left(\eta^2+\frac{1}{2}\right)\cos\eta\theta
\end{vmatrix}=0 \qquad (17)$$

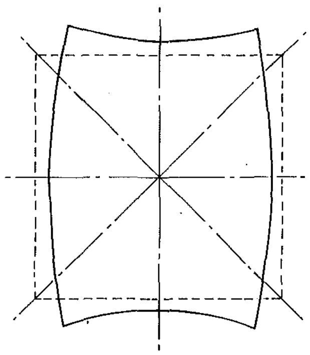

Fig. 2 A typical cross-section of the buckling mode of tubes of perfectly-plastic material

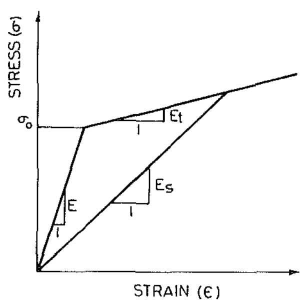

Fig. 3 The stress-strain relation of elastic, linear strain-hardening materials

where

$$\theta = \pi/2\lambda$$

$$\psi = \sqrt{\frac{1}{2}\,[\sqrt{e} + (2e-1)]}$$

$$\varphi = \sqrt{\frac{1}{2}\,[\sqrt{e} - (2e-1)]}$$

$$\xi = \sqrt{\sqrt{K\lambda^2 + 1 - e} + 1}$$

and $\eta = \sqrt{\sqrt{K\lambda^2 + 1 - e} - 1}$.

The buckling load K can then be obtained using an iteration scheme in which the value of the parameter e is adjusted to the latest value of K until convergence is reached.

The above procedure for solving plastic buckling problems for tubes is applicable for any type of strain-hardening material. In order to provide a simple example of the analysis and to aid the discussions, attention is confined to a material with linear strain-hardening, as shown in Fig. 3. For the plastic buckling of plates of this type of material, it is appropriate (see Appendix) to define

$$s = \frac{\pi^2}{9h^2} \cdot \frac{1}{\sigma_o/E} \cdot \frac{E_t/E}{1-(E_t/E)}. \tag{18}$$

This parameter encapsulates the contributions of the material properties completely. With it, e can be expressed as

$$e = 1 - \frac{3}{4}\,\frac{1}{1+sK}. \tag{19}$$

It is clear from Eq. (18) that the influence of thickness is also contained in the parameter s. However, for tubes there is another way in which thickness can affect the buckling behavior. This results from the fourth of Eqs. (16). For the purpose of some of the later discussions, it is helpful to introduce another parameter s_p, at this stage defined by

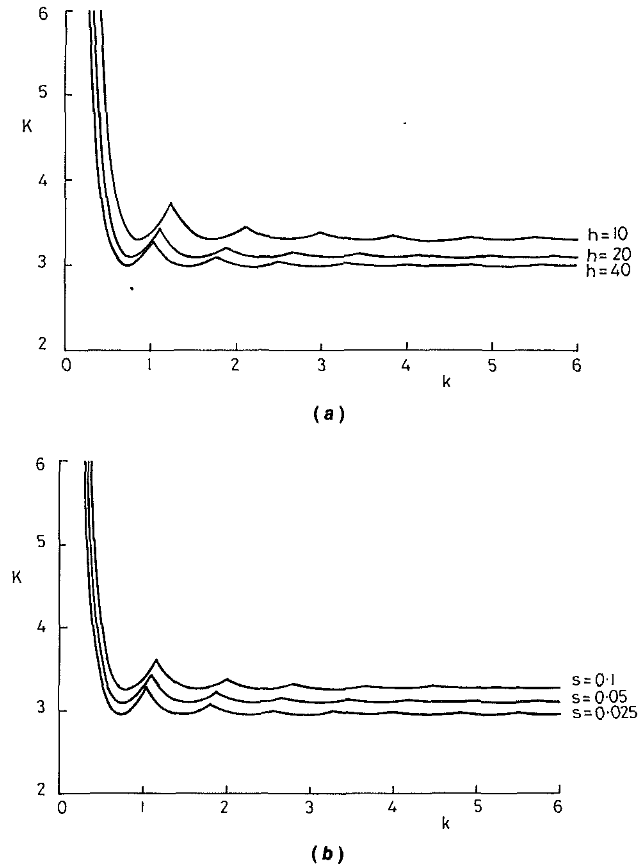

Fig. 4 Nondimensional buckling load K versus aspect ratio k; (a) variation with relative width h ($s_p = 20$), (b) variation with s ($h = 20$)

$$s_p = h^2 s = \frac{\pi}{9}\,\frac{1}{\sigma_o/E}\,\frac{E_t/E}{1-(E_t/E)}. \tag{20}$$

This allows the material and geometrical properties of the tube to be separated.

4 Results and Discussion for Linearly Strain-Hardening Material

The results for the plastic buckling of square tubes under axial compression are obtained by solving Eq. (17) for any given material properties and tube dimensions. They show a number of interesting features which are discussed in turn as follows.

4.1 Buckling Load. The nondimensional buckling load K is plotted in Figs. 4(a) and (b) against the aspect ratio k for $s_p = 20$ with a number of different relative widths, h, and for $h = 20$ with a number of different values of s. The curves given can be used for tubes of finite length. In general, K increases with s but decreases with h, which is the opposite of the influence of h on the elastic buckling load as described in LR. These tendencies are clearly seen from Fig. 5(a) and (b), respectively, where curves are presented for long tubes. In Fig. 5(a) there exists a peak for K at a certain value of h. This peak characterizes the twofold influence of h in the problem. The increase of h tends to stiffen the tube by maintaining the edges between the panels in straight lines due to the fourth of the edge conditions given in Eqs. (16). This effect has been demonstrated for the elastic case in LR. However, an increase in h or a decrease in thickness will reduce the influence of the strain-hardening of the material and therefore, soften the tube, as shown in the Appendix for plates where an increase in h corresponds to a decrease in s. In reality, the peaks in the

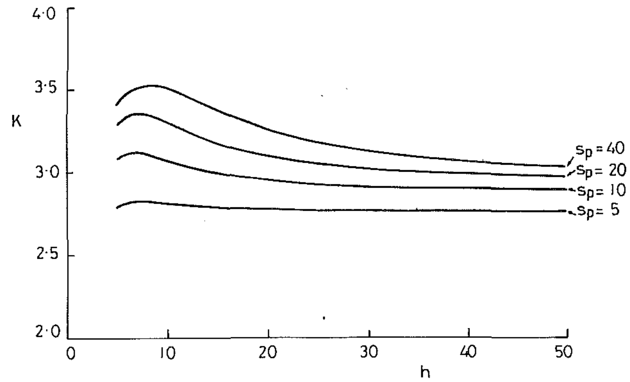

(a)

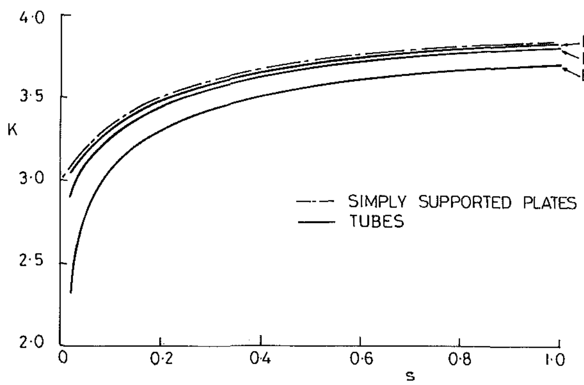

(b)

Fig. 5 Nondimensional buckling load of long tubes; (*a*) *K* versus relative width *h* for given values of s_p, (*b*) *K* versus *s* for given values of relative width *h*

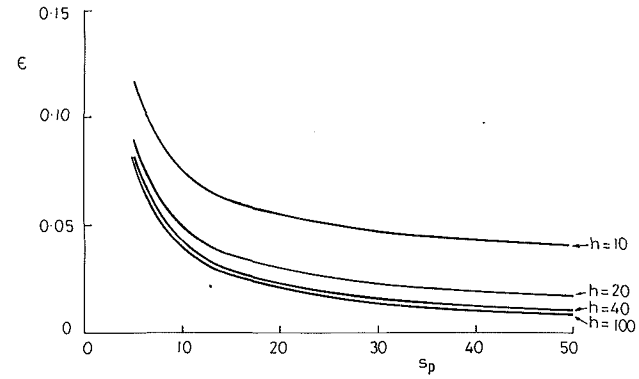

Fig. 6 Fractional difference between nondimensional buckling load for long plates and tubes, ϵ, versus s_p for given values of relative width *h*

curves would not affect the buckling behavior significantly, since tubes of relative widths which are less than or equal to the values corresponding to the peaks are seldom used. Therefore, practically, the former influence of h and K overrides the latter.

4.2 Comparison Between Tubes and Plates. In elastic buckling, the results for plates are reproduced by very thin tubes. Figure 5(*b*) also seems to suggest this tendency for plastic buckling. Unfortunately, to draw such a conclusion would be invalid. This can be verified as follows. As h tends to infinity, Eq. (17) reduces to the product of two subdeterminants.

$$\begin{vmatrix} \sinh\psi\theta\sin\varphi\theta & \cosh\psi\theta\cos\varphi\theta & 0 & 0 \\ \frac{3}{4}\varphi & \frac{3}{4}\psi & -\left(\psi^2-\varphi^2-\frac{1}{4}\right) & -2\psi\varphi \\ \frac{3}{4}\psi & -\frac{3}{4}\varphi & 2\psi\varphi & -\left(\psi^2-\varphi^2-\frac{1}{4}\right) \\ -\frac{1}{2}\sinh\psi\theta\sin\varphi\theta & -\frac{1}{2}\cosh\psi\theta\cos\varphi\theta & \begin{matrix}-\varphi\sinh\psi\theta\sin\varphi\theta \\ +\psi\cosh\psi\theta\cos\varphi\theta\end{matrix} & \begin{matrix}\psi\sinh\psi\theta\sin\varphi\theta \\ +\varphi\cosh\psi\theta\cos\varphi\theta\end{matrix} \end{vmatrix} \begin{vmatrix} \cosh\xi\theta & \cos\eta\theta \\ \left(\xi^2-\frac{1}{2}\right)\cosh\xi\theta & -\left(\eta^2+\frac{1}{2}\right)\cos\eta\theta \end{vmatrix} = 0 \quad (21)$$

The vanishing of the second determinant gives the plastic buckling condition for plates, but it does not necessarily vanish now for tubes. For a given material, s_p is a constant and as h tends to infinity, s approaches zero, so that e approaches 1/4 and ψ approaches zero. The first determinant therefore tends to vanish. Thus, theoretically, no equivalence exists between tubes and plates where plastic buckling is concerned, even for arbitrarily thin plates and tubes, regardless of the physical consideration that very thin tubes and plates would buckle in the elastic range. In general, the buckling load for tubes is lower than that for plates. The difference between them is shown in Fig. 6, where ϵ is defined as

$$\epsilon=(K_{\text{plate}}-K_{\text{tube}})/K_{\text{plate}}.$$

If the relative width of the tube is greater than 20, then the difference is hardly affected by h. However, the values of ϵ are sensitive to s_p for materials with small values of s_p.

In the light of the above discussion, the comparison made between experimental results and the theoretical results by deformation theory and incremental theory for the plastic buckling of plates should be reassessed, since the experiments reported by Gerard (1957) were conducted on tubes rather than on simply-supported plates directly. The agreement between such experimental results and the results from deformation theory could therefore have been fortuitous. If the experiments were carried out by introducing edge conditions nearer to true simple supports than those imposed within tubes, the buckling loads could be higher than those obtained in tube experiments. Thus they might deviate from the result obtained by deformation theory towards the results given by incremental theory. In order to achieve a full understanding of the plastic buckling of plates, further experimental research is suggested.

4.3 Edge Deflections. As in the elastic buckling case, the edges between the panels of a square tube deflect during buckling when buckling takes place in the plastic range. The deflection in plastic buckling is usually larger than that in elastic buckling, although the amount is affected by factors such as h and s_p as shown in Fig. 7(*a*) and (*b*), where the relative edge deflection, i.e., the ratio of the deflection along the edges to that along the center line, is plotted against h and s, respectively. Generally, speaking, the smaller the h, i.e., the thicker the tube, and the smaller the s, the larger is the edge deflection. Large rates of change are apparent for small values of h and s.

4.4 Compact Crushing Modes. Compact and noncompact crushing behavior of square tubes under axial compression

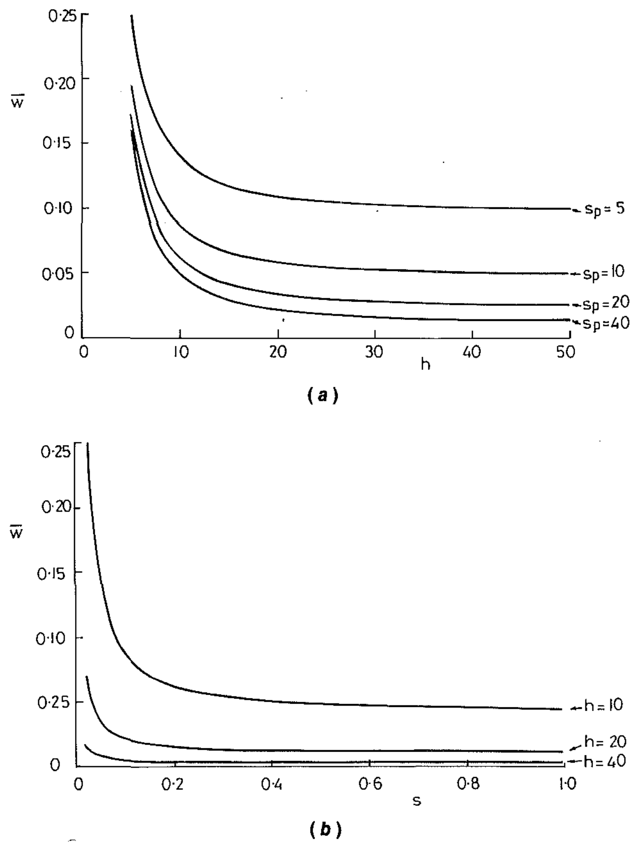

Fig. 7 Relative edge deflection of long tubes; (a) relative edge deflection $\bar{w}$ versus relative width h for given values of s_p, (b) relative edge deflection $\bar{w}$ versus s for given values of relative width h

have been discussed in LR with reference to the edge deflection. However, for most common materials, the value of h, which restricts the buckling to occur within the elastic range, would not allow sufficiently large edge deflections to lead to a subsequent compact mode. Usually a compact crushing process has plastic buckling as its first stage (Mahmood and Paluszny, 1981). Once the buckling is plastic, larger edge deflections than those predicted by elastic buckling analysis are produced as mentioned previously. This is one reason which favors the formation of a subsequent compact mode when the buckling is in the plastic range.

Another reason is the reduction in the half-wavelength of the buckling mode. From our earlier work it is known that the buckling behavior of square tubes differs from that of plates because of the different edge conditions between panels of the tube. However, such edge conditions seem hardly to affect the longitudinal half-wavelength of the buckling mode as can also be seen in the elastic case (see LR). From the calculations made in this paper, it is also true that the half-wavelength of the buckling mode of tubes is nearly the same as that of plates in the case of plastic buckling. Thus, Fig. A2 in the Appendix could be used to determine the half-wavelength for long tubes buckling plastically, if the material is linear strain hardening. For a folding mechanism in a compact crushing process, the longitudinal half-wavelength is shorter than the elastic buckling half-wavelength and smaller edge deflections are required for the same degree of folding deformation. In other words, with the same amount of edge deflection, the shorter the half-wavelength, the larger the folding deformation and, therefore, the shorter the half-wavelength, the larger the folding deformation and, therefore, the easier to develop a compact mode. From this qualitative argument, a conclusion about the reason for the development of compact crushing modes can be drawn. It is due to interaction between the edge deflection and the shorter half-wavelength in the early stages of the crushing deformation.

The reduction in longitudinal half-wavelength has another interesting aspect for designers when the tubes are used as energy absorbers. In design, if the parameter s is chosen to be as small as possible (which can be achieved by using materials with a high yield stress and low strain-hardening rate, or by reducing the relative width h, while ensuring that the buckling occurs in the plastic range and crushing is in a compact mode), more folds can be expected, and therefore higher specific energy absorption capacities obtained.

References

Gerard, G., et al., 1957, "Handbook of Structural Stability, Part I, Buckling of Flat Plates," NACA TN3781.

Gerard, G., 1962, *Introduction to Structural Stability Theory*, McGraw-Hill, New York.

Li, S., and Reid, S. R., 1990, "Relationship Between the Elastic Buckling of Square Tubes and Rectangular Plates," ASME Journal of Applied Mechanics, Vol. 57, pp. 969–973.

Mahmood, H. F., and Paluszny, A., 1981, "Design of Thin-Walled Columns for Crush Energy Management—Their Strength and Mode of Collapse," *Proc. 4th International Conference Vehicle Struct. Mech. SAE*, pp. 7–18.

Sewell, M. J., 1964, "A General Theory of Elastic and Plastic Failure, Part II," *Journal of Mech. Phys. Solids*, Vol. 12, pp. 279–297.

Shanley, F. R., 1947, "Inelastic Column Theory," *JAS*, Vol. 14, pp. 261–267.

Stowell, E. Z., 1948, "A Unified Theory of Plastic Buckling of Columns and Plates," NACA TN1556.

APPENDIX

Plastic Buckling of a Uniaxially Compressed Simply-Supported Plate of Elastic Linear Strain-Hardening Material

In Stowell's (1948) theory for the plastic buckling of uniaxially compressed simply-supported plates (described in Gerard (1962)), the following assumptions were made:

(i) In the prebuckling stage, the plate remains in a uniaxial stress state,

(ii) Buckling takes place entirely in the plastic regime and therefore Poisson's ratio is taken to be 0.5 from the incompressibility condition,

(iii) Since buckling corresponds to a bifurcation in the fundamental equilibrium path as in Shanley's column, no strain reversal takes place.

Based on these assumptions, the stress-strain relations can be obtained

$$\sigma_x = \frac{4}{3} E_s \left(e\epsilon_x + \frac{1}{2} \epsilon_y \right)$$

$$\sigma_y = \frac{4}{3} E_s \left(\frac{1}{2} \epsilon_x + \epsilon_y \right)$$

$$\tau_{xy} = \frac{1}{3} E_s \gamma_{xy} \qquad \text{(A1)}$$

where σ_x, ϵ_x, etc., are all increments of deviation from the fundamental path. $e = 1/4 + 3E_t/4E_s$ where E_s and E_t are the secant and tangent moduli of the material, respectively, and are functions of strain in general. Using the stress-strain relations, the buckling equation can be written as

$$ew,_{xxxx} + 2w,_{xxyy} + w,_{xxyy} - \frac{N_x}{D} w,_{xx} = 0. \qquad \text{(A2)}$$

From this, the dimensionless buckling load can be deduced as

$$K = \lambda^2 + 2 + \frac{e}{\lambda^2}. \qquad \text{(A3)}$$

Although Stowell's theory has attracted some criticism (Sewell, 1964), it remains the most popular theory for plates and the most common analysis for practical use due to its relative simplicity. Equation (A3) is referred to as Stowell's formula. Since E_s and E_t may not be constants but will be related to K in general, Eq. (A3) gives K implicitly.

Equation (A3) has been used extensively in this form. Each time it is used, some kind of iteration procedure has to be employed to obtain an accurate value of K, except for perfectly-plastic materials where the implicit nature of Eq. (A3) is eliminated due to the fact that $E_t = 0$.

While no attempt will be made here to improve this formula in the general case, it is possible and also helpful to simplify the procedure for those materials which are well described as being linearly strain hardening. This behavior actually covers a large category of materials in practical use.

The stress-strain relationship for a linear strain-hardening material is characterized by parameters E, E_t, and σ_o as is shown in Fig. 3. The thickness t of the plate is also involved in the relationship between K and E_s. Therefore, all of the parameters E, E_t, σ_o, and t could affect the plastic buckling behavior of such plates. In order to discuss their influence, extensive calculations are required. However, a careful re-examination reveals that it is possible to merge all these parameters into a single properly defined dimensionless parameter which makes the above discussion very straightforward for the linearly strain-hardening case.

Under the assumptions made, K can be expressed as follows in terms of the axial strain ϵ_x.

$$K = \frac{N_x b^2}{\pi^2 D_s} = \frac{9h^2}{\pi^2}\frac{\sigma_x}{E_s} = \frac{9h^2}{\pi^2}\epsilon_x \tag{A4}$$

This equation, along with the stress-strain relationship

$$\epsilon_x = \frac{\sigma_o}{E} + \frac{1}{E_t}(\sigma_x - \sigma_o), \tag{A5}$$

gives

$$E_t/E_s = 1 - \frac{1}{1+sK}, \tag{A6}$$

where

$$s = \frac{\pi^2}{9h^2}\frac{1}{\sigma_o/E}\frac{E_t/E}{1-(E_t/E)}. \tag{A7}$$

By introducing the parameter s, Eq. (A3) becomes

$$K = \lambda^2 + 2 + \left(1 - \frac{3}{4}\frac{1}{1+sK}\right)\frac{1}{\lambda^2}. \tag{A8}$$

Rearranging, we obtain an explicit expression for K

$$K = \frac{1}{2}\left[\lambda^2 + 2 + \frac{1}{\lambda^2} - \frac{1}{s} + \sqrt{\left(\lambda^2 + 2 + \frac{1}{\lambda^2} - \frac{1}{s}\right)^2 + \frac{4}{s}\left(\lambda^2 + 2 + \frac{1}{4\lambda^2}\right)}\,\right]. \tag{A9}$$

The other root is discarded since it gives a negative value of K and is therefore inadmissible. This expression only contains the half-wavelength λ and the parameter s and is clearly very convenient to use.

It is interesting to note that as s approaches infinity and zero corresponding to elastic and perfectly plastic materials, respectively, the above expression gives the correct expressions for K in these limiting cases.

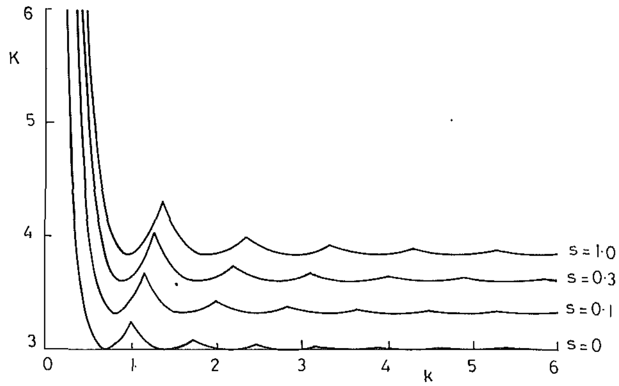

Fig. A1 Nondimensional buckling load K versus aspect ratio k for given values of s for a simply supported plate

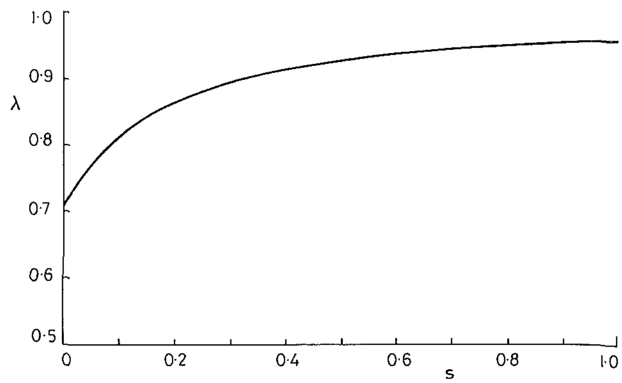

Fig. A2 Nondimensional half-wavelength λ for long, simply supported plates versus parameter s

To discuss how K changes with s, we examine the derivative of K with respect to s.

$$\frac{dK}{ds} = \frac{1}{s^2}\left[1 - \frac{\lambda^2 + 2 - \frac{1}{2\lambda^2} + \frac{1}{s}}{\sqrt{\left(\lambda^2 + 2 + \frac{1}{\lambda^2} - \frac{1}{s}\right)^2 + \frac{4}{s}\left(\lambda^2 + 2 + \frac{1}{4\lambda^2}\right)}}\right] \tag{A10}$$

For any practical value of λ satisfying $0 < \lambda < \sqrt{2}$, we have

$$dK/ds > 0.$$

Therefore, practically, K increases with s monotonically, which is clearly seen in Fig. A1. In view of this and reviewing expression (A7) for the parameter s, it can be concluded that K increases with increase in thickness and with increasing tangent modulus and decreases with increases in the yield stress.

For long plates, K takes the minimum value with respect to λ which can be found from

$$dK/d\lambda = 0.$$

The minimized K and the corresponding λ are also affected by s. These are shown in Fig. 5(b) and Fig. A2, respectively. As s varies from zero (perfectly plastic) to infinity (elastic), K takes values from 3 to 4 and λ from $1/\sqrt{2}$ to 1. Higher rates of increase of K and λ with s are found for lower values of s.

A Multiaxial Stochastic Constitutive Law for Concrete: Part I—Theoretical Development

A. Fafitis
Assoc. Professor,
Department of Civil Engineering,
Arizona State University,
Tempe, AZ 85287

Y. H. Won
Asst. Professor,
Department of Civil Engineering,
Korea Third Military Academy
Kyungbuk, Youngchun-goo 771-849,
Korea

An incremental three-dimensional constitutive relation for concrete has been developed. The linear anisotropic and path-dependent behavior is modeled by updating the stiffness matrix at each load increment. The material is assumed incrementally elastic and the six elastic moduli E_{11}, E_{12} .... E_{33} *are expressed in terms of both the tangential hydrostatic and deviatoric stiffness whereas the three tangential shear moduli are expressed in terms of the deviatoric stiffness only. The hydrostatic and deviatoric stiffness are determined from uniaxial stress-strain relationships by employing the space truss concept. The unaxial stress-strain relationships are in a sense the stress-strain relationships of the members of the truss, and they were based on a rheological stochastic model developed earlier. The predictions of the model compare favorably with experimental data reported by various investigators. Complex loading paths are reproduced with acceptable accuracy as is demonstrated in the second part of this paper.*

Introduction

If the sophisticated methods that are available today are to be employed in the analysis of concrete structures, models that capture and reproduce with accuracy the complex characteristics of concrete behavior are essential. Since the accuracy of any analytical method is limited by the accuracy of the model that is employed, the development of modeling should be parallel to the increase in sophistication of the analytical tools.

There are a number of constitutive models for concrete available in the literature. Among those, the endochronic theory (Bazant and Bhat, 1976; Bazant and Shieh, 1978; Bazant and Shieh, 1980) is perhaps one of the most comprehensive models, but the number of parameters involved is large and they are not easily determined. The total strain theory models (Ahmad and Shah, 1982; Ahmad et al., 1986; Ottosen, 1979) are restricted to path-independent loadings, while hypoelastic models (Darwin and Pecknold, 1977a; Elwi and Murray, 1979; Gerstle, 1981) can approximate path dependency. Some fracture mechanics models (Maekawa and Okamura, 1983; Van Mier, 1986) have also been proposed for concrete and geomaterials but their predictions for complex loadings are not yet satisfactory.

A number of models known as network models (Baker, 1959; Burt and Dougill, 1977; Papadopoulos, 1984; Reinius, 1965) have been proposed in the past, but their accuracy was not always satisfactory. Although a random network has the potential to duplicate heterogeneous material behavior, it is difficult to develop accurate models for brittle materials.

A stochastic model (Fafitis and Shah, 1984; Fafitis and Shah, 1986) with continuous fracturing elastoplastic elements has been developed recently, and the present work is a generalization of this model. The model is based on incrementally linear elastic (hypoelastic) behavior of the material. The constitutive equation has a small number of material constants which can be determined from uniaxial experiments.

Concrete is a material that develops microcracks at a very early age even under no externally applied stress. Because these microcracks have a random orientation, their effects to the macroscopically observed response to external load is not oriented, and the material can be considered initially isotropic. However, when it is subjected to external load, it develops cracks which do not have the random orientation of the microcracks and the material, depending on the magnitude of loading, can no longer be assumed isotropic. A better approximation at this stage is to model the concrete as orthotropic. There is a large number of constitutive relations that are characterized by an orthotropic tangential stiffness or compliance matrix (Bathe and Ramaswamy, 1979; Darwin and Pecknold, 1977b; Elwi and Murray, 1979; Isenburg and Adam, 1970; Liu et al., 1972). One of the problems associated with this modeling is the determination of shear moduli. In the past, the shear moduli have been expressed in terms of Young's moduli and Poisson's ratios. The drawback of the above approaches is that the shear moduli, being functions of Young's moduli and Poisson's ratios, are independent of shear strains

Contributed by the Applied Mechanics Division of The American Society of Mechanical Engineers for presentation at the 1992 ASME Summer Mechanics and Materials Meeting, Tempe, AZ, Apr. 28–May 1, 1992.

Discussion on this paper should be addressed to the Technical Editor, Professor Leon M. Keer, The Technological Institute, Northwestern University, Evanston, IL 60208, and will be accepted until four months after final publication of the paper itself in the Journal of Applied Mechanics. Manuscript received by the ASME Applied Mechanics Division, Aug. 25, 1988; final revision, Sept. 25, 1991.

Paper No. 92-APM-13.

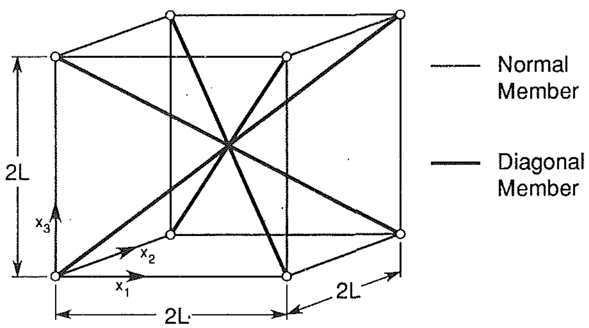

Fig. 1 Cubic space truss consisting of 12 normal and 4 diagonal members

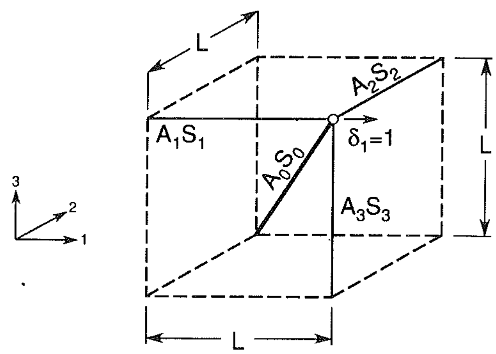

Fig. 2 One eighth of the space truss

(or shear stresses). In this investigation the shear moduli are considered as functions of shear strain. The material is assumed initially isotropic.

Tangential Elastic Moduli

The general incrementally linear stress-strain relation for an orthotropic elastic material can be written in a matrix form with, at most, nine independent elastic moduli (Chen and Saleeb, 1982) as follows:

$$\begin{bmatrix} d\sigma_1 \\ d\sigma_2 \\ d\sigma_3 \\ d\tau_{12} \\ d\tau_{23} \\ d\tau_{31} \end{bmatrix} = \begin{bmatrix} E_{11} & E_{12} & E_{13} & 0 & 0 & 0 \\ E_{12} & E_{22} & E_{23} & 0 & 0 & 0 \\ E_{13} & E_{23} & E_{33} & 0 & 0 & 0 \\ 0 & 0 & 0 & G_{12} & 0 & 0 \\ 0 & 0 & 0 & 0 & G_{23} & 0 \\ 0 & 0 & 0 & 0 & 0 & G_{31} \end{bmatrix} \begin{bmatrix} d\epsilon_1 \\ d\epsilon_2 \\ d\epsilon_3 \\ d\gamma_{12} \\ d\gamma_{23} \\ d\gamma_{31} \end{bmatrix} \tag{1}$$

where $d\sigma$ and $d\epsilon$ are normal stress and strain increments; $d\tau$ and $d\gamma$ are shear stress and strain increments; and E_{ij} and G_{ij} are tangential elastic moduli, which will be called in the sequel normal and shear moduli, respectively.

To express nonlinear stress-strain relationship as well as path dependency, the normal moduli are expressed as functions of the total normal strains

$$E_{ij}=f_{ij}(\epsilon_1,\epsilon_2,\epsilon_3)=f_{ij}(\epsilon_k). \tag{2a}$$

The strain can be decomposed into two parts: the octahedral part, ϵ_o, associated with change in volume and the deviatoric part, e_k, associated with change in shape. Thus, we can write the tangential normal moduli as

$$E_{ij}=f_{ij}(\epsilon_o,e_k) \tag{2b}$$

where $\epsilon_0 = (\epsilon_1 + \epsilon_2 + \epsilon_3)/3$, $e_k = \epsilon_k - \epsilon_o$, $k = 1, 2, 3$.

The decomposition in volumetric (octahedral) and deviatoric components can be modeled by a space truss as shown in Fig. 1. The diagonal members model the volumetric component and the normal members the deviatoric. The shear moduli G_{ij} will be expressed as functions of shear strains in the following section.

The advantage of this modeling is that, as it will be shown in the sequel, the triaxial behavior of concrete can be modeled by combination of uniaxial models and the stiffness of the members can be calculated at each strain increment from appropriate uniaxial stress-strain relationships (Ahmad et. al., 1986; Hognestad, 1951; Saenz, 1964; Sargin, 1971). There are a number of uniaxial stress-strain relations for concrete available in the literature that might be used for the uniaxial modeling of the truss members. In this investigation, a recently developed stochastic model which has the facility for strain history and unloading is employed (Fafitis and Shah, 1986).

Because of the symmetry of the model only part of the structure is shown in Fig. 2. The axial stiffness of the normal members is A_iS_i and the stiffness of the diagonal members is A_oS_o. In order that this model reproduce the experimentally observed behavior of concrete, S_i and S_o are related to deviatoric and hydrostatic (octahedral) stiffness as will be discussed later.

For a unit displacement in direction 1 at point 0, the corresponding forces in direction 1, 2, 3 are

$$f_1=\frac{A_iS_i}{l}+\frac{1}{3}\frac{A_oS_o}{l_o} \tag{3a}$$

$$f_2=f_3=\frac{1}{3}\frac{A_oS_o}{l_o} \tag{3b}$$

where $l_o = \sqrt{3}l$.

Similarly, from the unit displacement in direction 2 and 3, we can get the corresponding forces. For the stress-strain relationship we can select $l = 1$, and then displacements are equivalent to strains. For convenience we take $A_i = 1$ and $A_o = \sqrt{3}$. Then $Ai/l = Ao/l_o = 1$ and the incremental force (stress)–displacement (strain) relationship can be written in matrix form

$$\begin{bmatrix} df_1 \\ df_2 \\ df_3 \end{bmatrix} \begin{bmatrix} S_1+S_o/3, & S_o/3, & S_o/3 \\ S_o/3, & S_2+S_o/3 & S_o/3 \\ S_o/3, & S_o/3, & S_3+S_o/3 \end{bmatrix} \begin{bmatrix} d\delta_1 \\ d\delta_2 \\ d\delta_3 \end{bmatrix} \tag{4}$$

where df_i and $d\delta_i$ are incremental nodal forces and nodal displacements in the i-direction.

The required stiffness of the normal and diagonal members of the truss of Fig. 2 will be defined later. The derivation of the appropriate formulas of the stiffnesses of the truss members is based on the assumption that the normal moduli can be expressed as the sum of two functions, h and g_{ij}. The first function depends on both the volumetric and deviatoric strains whereas the second function depends on deviatoric strains only. Therefore, the normal moduli can be written as

$$E_{ij}=h(\epsilon_o,e_k)+g_{ij}(e_k). \tag{5}$$

From the first row of Eq. (1), after substituting E_{ij} from Eq. (5) we have

$$d\sigma_1=[g_{11}(e_k)+h(\epsilon_o,e_k)]d\epsilon_1+[g_{12}(e_k)+h(\epsilon_o,e_k)]d\epsilon_2 + [g_{13}(e_k)+h(\epsilon_o,e_k)]d\epsilon_3 \tag{6}$$

substituting $d\epsilon_i = d\epsilon_o + de_i$, we get

$$d\sigma_1=[g_{11}(e_k)+g_{12}(e_k)+g_{13}(e_k)]d\epsilon_o+3h(\epsilon_o,e_k)d\epsilon_o + g_{11}(e_k)de_1+g_{12}(e_k)de_2+g_{13}(e_k)de_3 + h(\epsilon_o,e_k)(de_1+de_2+de_3) \tag{7}$$

where $de_1 + de_2 + de_3$ is the summation of incremental deviatoric strain, which is zero. Letting $de_1 + de_2 + de_3 = 0$, in Eq. (7) we have

$$d\sigma_1=[g_{11}(e_k)+g_{12}(e_k)+g_{13}(e_k)]d\epsilon_o+3h(\epsilon_o,e_k)d\epsilon_o + g_{11}(e_k)de_1+g_{12}(e_k)de_2+g_{13}(e_k)de_3. \tag{8}$$

It is assumed in the following derivation that the stress increment in direction 1 ($d\sigma_1$) caused by deviatoric strain increments in direction 2 and 3 (de_2, de_3) can be ignored. Therefore, we assume

$$g_{ij}=0 \text{ for } i\neq j. \tag{9}$$

Equation (9) shows that the functions g_{ij} exist only in diagonal terms. Since $g_{ij} = 0$ for $i \neq j$, we can drop the second index for g_{ij} (e.g., $g_{11} = g_1$, etc.). Substituting Eq. (9) into Eq. (8), we get

$$d\sigma_1 = g_1(e_k)(d\epsilon_o + de_1) + 3h(\epsilon_o,e_k)d\epsilon_o. \tag{10}$$

Substituting $d\epsilon_o + de_1 = d\epsilon_1$ and $d\epsilon_o = (d\epsilon_1 + d\epsilon_2 + d\epsilon_3)/3$, we get

$$d\sigma_1 = [g_1(e_k) + h(\epsilon_o,e_k)]d\epsilon_1 + h(\epsilon_o,e_k)d\epsilon_2 + h(\epsilon_o,e_k)d\epsilon_3. \tag{11}$$

By similar reasoning from the second and third rows of Eq. (1) we can write the relations of normal stress and strain increments as follows:

$$\begin{bmatrix} d\sigma_1 \\ d\sigma_2 \\ d\sigma_3 \end{bmatrix} = \begin{bmatrix} g_1(e_k)+h(\epsilon_o,e_k), h(\epsilon_o,e_k), h(\epsilon_o,e_k) \\ h(\epsilon_o,e_k), g_2(e_k)+h(\epsilon_o,e_k), h(\epsilon_o,e_k) \\ h(\epsilon_o,e_k), h(\epsilon_o,e_k), g_3(e_k)+h(\epsilon_o,e_k) \end{bmatrix} \begin{bmatrix} d\epsilon_1 \\ d\epsilon_2 \\ d\epsilon_3 \end{bmatrix}. \tag{12}$$

Comparison of Eqs. (12) and (4) indicates that the functions g_i and h are related to the stiffness of the members of the space truss of Fig. 2. The diagonal members have stiffness $S_0A_0/l_0 = 3h$ and the normal members have stiffness $S_iA_i/l_i = g_i$.

Determination of $g_i(e_k)$ and $h(\epsilon_o,e_k)$

The tangential deviatoric and hydrostatic stiffnesses will be determined from uniaxial stress-strain relations. Considering uniaxial stress in direction 1 ($d\sigma_2 = d\sigma_3 = 0$), we have

$$d\sigma_o = \frac{1}{3}\, d\sigma_1. \tag{13}$$

Since $d\epsilon_2 = d\epsilon_3 = -\nu d\epsilon_1$, we can write

$$d\epsilon_0 = \frac{1-2\nu}{3}\, d\epsilon_1 \tag{14}$$

where ν is a function of ϵ_i. From Eq. (13) and Eq. (14) we get

$$\frac{d\sigma_o}{d\epsilon_o} = \frac{1}{1-2\nu}\,\frac{d\sigma_1}{d\epsilon_1}. \tag{15}$$

Note that all variables of Eq. (15) depend only on uniaxial strain ϵ_1. Eq. (15) can be written as

$$K_o(\epsilon_1) = \frac{1}{1-2\nu}\, E_t(\epsilon_1) \tag{16}$$

where K_o is the hydrostatic tangential stiffness ($d\sigma_o/d\epsilon_o$) and E_t is the uniaxial tangential stiffness ($d\sigma_1/d\epsilon_1$). We also have

$$ds_1 = d\sigma_1 - \frac{d\sigma_1}{3} = \frac{2}{3}\, d\sigma_1 \tag{17}$$

and

$$de_1 = \frac{2}{3}\,(1+\nu)d\epsilon_1. \tag{18}$$

From the Eqs. (17) and (18) we can get

$$\frac{ds_1}{de_1} = \frac{1}{1+\nu}\,\frac{d\sigma_1}{d\epsilon_1}, \tag{19}$$

and Eq. (19) can be written as

$$K_i(\epsilon_i) = \frac{1}{1+\nu(\epsilon_i)}\, E_t(\epsilon_i) \tag{20}$$

where K_i is the deviatoric tangential stiffness (ds_i/de_i).

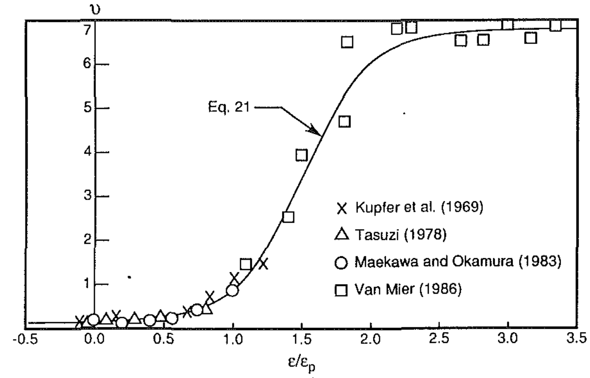

Fig. 3 Comparison of tangential Poisson's ratio with experimental data

The significance of Eqs. (16) and (20) is that the functions K_o and K_i are related to the uniaxial stress-strain relationship which can be obtained experimentally with relative easiness or approximated by one of the available uniaxial models.

The tangential Poisson's ratio can be approximated by the following polynomials to fit existing experimental data (Kupfer et al., 1969; Schickert and Winkler, 1977; Tasuji et al., 1978; Van Mier, 1985) as shown in Fig. 3.

$$\begin{aligned} &\nu(\epsilon) = 0.18 \text{ for } \epsilon/\epsilon_p \leq 0 \\ &\nu(\epsilon) = 0.82(\epsilon/\epsilon_p)^{3.4} + 0.18 \text{ for } 0 < \epsilon/\epsilon_p < 1.5 \\ &\nu(\epsilon) = -0.82(3-\epsilon/\epsilon_p)^{3.4} + 6.7 \text{ for } 1.5 < \epsilon/\epsilon_p < 3 \\ &\nu(\epsilon) = 6.7 \text{ for } \epsilon/\epsilon_p > 3 \end{aligned} \tag{21}$$

where ϵ_p is the strain at peak stress.

In order to determine $g_i(e_k)$, we consider strain increment in direction i only. Letting the strain increment in direction 1 such that $d\epsilon_i = x$, $d\epsilon_2 = d\epsilon_3 = 0$, we get from Eq. (12)

$$\begin{aligned} d\sigma_1 &= (g_1+h)x \\ d\sigma_2 &= d\sigma_3 hx. \end{aligned} \tag{22}$$

The octahedral stress increment is

$$d\sigma_o = (1/3g_1 + h)x. \tag{23}$$

The component of the deviatoric stress increment in direction 1 is

$$ds_1 = 2/3g_1x. \tag{24}$$

The octahedral strain increment is

$$de_o = 1/3x. \tag{25}$$

The component of the deviatoric strain increment in direction 1 is

$$de_1 = 2/3x. \tag{26}$$

From Eq. (24) and (26) we can write

$$K_1(e_1) = ds_1/de_1 = g_1(e_1). \tag{27}$$

Note that g_1 must be a function of e_1 only.
For directions 2 and 3 we can get similar relations. Generally,

$$g_i(e_i) = K_i(e_i). \tag{28}$$

Since $K_i(e_i) = E_t(e_i)/(1 + \nu(e_i))$, from Eq. (20) we can write

$$g_i = g(e_i) = K_i(e_i). \tag{29}$$

In order to determine $h(\epsilon_o, e_k)$ we consider hydrostatic strain increment since $h(\epsilon_o, e_k)$ corresponds to diagonal stiffness. Considering octahedral strain $d\epsilon_1 = d\epsilon_2 = d\epsilon_3 = x$, from Eq. (12) we get

$$\begin{aligned} d\sigma_1 &= (g_1+3h)x \\ d\sigma_2 &= (g_2+3h)x \\ d\sigma_3 &= (g_3+3h)x. \end{aligned} \tag{30}$$

The octahedral stress increment is

$$d\sigma_0 = 1/3\,(g_1+g_2+g_3)x + 3hx. \tag{31}$$

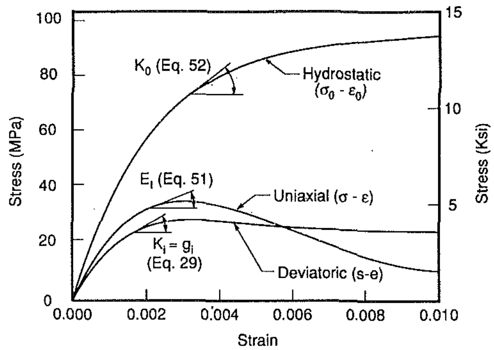

Fig. 4 Deviatoric and hydrostatic stress-strain curves

The octahedral strain increment is

$$d\epsilon_o = x. \tag{32}$$

From (31) and (32) the hydrostatic stiffness is written as

$$K_o(\epsilon_o) = 1/3(g_1+g_2+g_3)x+3h. \tag{33}$$

Substituting Eq. (33) into Eq. (27) we can write

$$h(\epsilon_o, e_k) = 1/3K_o(\epsilon_o) - 1/9(K_1+K_2+K_3). \tag{34}$$

In Eqs. (29) and (34) the values of K_1, K_2, K_3 (same as g_1, g_2, and g_3) for any given deviatoric strain e_1, e_2, and e_3 can be found if the stress-strain relationship $(s - e)$ is known and the value of K_o for any hydrostatic strain can be found if the stress-strain relationship $(\sigma_o - \epsilon_o)$ is known. Therefore, for the calculation of the tangential stiffnesses, we need only two stress-strain relationships which are one-dimension curves. In the present work these stress-strain relationships are taken from a recently developed rheological stochastic model, which will be discussed in the following section. In Fig. 4, shown schematically, are these curves ($\sigma_o - \epsilon_o$ and $s - e$), and the stiffness K_o, K_i, and E_t needed for Eqs. (16) and (20). Note that the $s - e$ curve is related to the uniaxial curve $(\sigma - \epsilon)$ through Eq. (24).

In Fig. 4 the uniaxial curve was calculated using Eq. (51), the deviatoric stress-strain curve was calculated using Eq. (20), and the hydrostatic stress-strain curve was calculated using Eq. (52).

In linear elastic problems, g_i and h are constants having the initial values of g_i and h at $\epsilon_o = 0$ and $e_i = 0$ ($g(0)$ and $h(0)$). If the functions (g and h) are constants, then the first row of the matrix in Eq. (12) can be integrated to give Hooke's law as follows.

From Eq. (12) we have

$$\sigma_1 = (g(0)+h(0))\epsilon_1 + h(0)\epsilon_2 + h(0)\epsilon_3. \tag{35}$$

Substituting Eq. (29) and (34) into Eq. (35) we have

$$\sigma_1 = K_1(0)\epsilon_1 + [(K_o(0) - (K_1(0)+K_2(0) + K_3(0))/3](\epsilon_1+\epsilon_2+\epsilon_3). \tag{36}$$

Substituting Eq. (16) and (20) into Eq. (36)

$$\sigma_1 = \frac{E}{1+\nu}\epsilon_1 + \frac{\nu E}{(1+\nu)(1-2\nu)}(\epsilon_1+\epsilon_2+\epsilon_3). \tag{37}$$

Note that in linear elasticity, $E_t(\epsilon_i)$ is constant E, and ν is also constant. Similarly, from the second and third row of Eq. (12) we can get

$$\begin{bmatrix}\sigma_1\\ \sigma_2\\ \sigma_3\end{bmatrix} = \frac{E}{(1+\nu)(1-2\nu)}\begin{bmatrix}1-\nu & \nu & \nu\\ \nu & 1-\nu & \nu\\ \nu & \nu & 1-\nu\end{bmatrix}\begin{bmatrix}\epsilon_1\\ \epsilon_2\\ \epsilon_3\end{bmatrix}. \tag{38}$$

Equation (38) is the well-known three-dimensional linear elastic constitutive equation in the principal coordinate system. Therefore, the nonlinear model developed in the preceding sections yields the generalized Hook's law in principal axes (Eq. (38)) as a special case in which g and h are constant, independent of the current strain, as it is assumed in the linear theory of elasticity.

Tangential Shear Moduli

The shear modulus of a transversely isotropic material in the ij-plane can be written (Saada, 1974)

$$G_{ij} = \frac{1}{2}(E_{ij} - E_{ij}) \tag{39}$$

(the summation convention in E_{ij} is not applicable). Equation (39) can be used to determine the upper and lower limit of the shear moduli of an orthotropic material. Since G_{12} should be equal to G_{21}, from Eq. (39) we have

$$G_{12} = \frac{1}{2}(E_{11} - E_{12}) \text{ or } G_{12} = \frac{1}{2}(E_{22} - E_{21}) \tag{40}$$

where $E_{11} = E_{22}$ and $E_{12} = E_{21}$ for transversely isotropic material, while $E_{11} \neq E_{22}$ for orthotropic material. We have (from Eq. (12))

$$E_{11} = g_1 + h \tag{41}$$

$$E_{22} = g_2 + h \tag{42}$$

$$E_{12} = E_{21} = h. \tag{43}$$

Let $g_1 > g_2$. If $E_{11} = E_{22} = g_1 + h$, we can get an upper limit of G_{12} equal to $g_1/2$, whereas if $E_{11} = E_{22} = g_2 + h$, we can get a lower limit of G_{12} equal to $g_2/2$. We can therefore assume

$$\frac{1}{2}g_2 \le G_{12} \le \frac{1}{2}g_1 \tag{44}$$

that is, G_{ij} is a function of deviatoric stiffness and has a value between $g_1/2$ and $g_2/2$. From Eqs. (20) and (29) we can get the upper limit G^U_{12} and lower limit G^L_{12} of the shear modulus G_{12}:

$$G^U_{12} = \frac{1}{2}g_1 = \frac{E_t(e_1)}{2(1+\nu(e_1))} \tag{45}$$

$$G^L_{12} = \frac{1}{2}g_2 = \frac{E_t(e_2)}{2(1+\nu(e_2))}. \tag{46}$$

Based on Eqs. (45) and (46), one can use a value between G^U_{ij} and G^L_{ij} for shear moduli, and this has been done in the past (Bathe and Ramaswamy, 1979; Darwin and Pecknold, 1977a; Elwi and Murray, 1979; Isenberg and Adam, 1970; Lin et al., 1972). However, as it is shown below, in some cases the shear modulus defined in this way cannot express the nonlinear behavior of the material. In Fig. 5(*a*) is shown a square concrete panel subjected to normal stress σ_o and in Fig. 5(*b*) the square section ABCD subjected to equivalent shear stress $\tau_o = \sigma_o$. If the material was linearly elastic, the deformations $\delta_1 = \delta_2$ can be calculated theoretically as shown in Fig. 5(*c*). If Eqs. (45) and (46) are used, a finite element analysis of section ABDC (Fig. 5(*b*)) gives the deformation $\delta_1 = \delta_2$ as shown in Fig. 5(*c*). Note that although Eqs. (45) and (46) are not linear, the deformations are very close to linear (Fig. 5(*c*)). The reason is that in the loading case of Fig. 5(*b*), $ei = 0$ hence Eqs. (45) and (46) do not capture the material nonlinearity.

In this investigation the shear moduli are assumed

$$G_{ij} = \frac{1}{2}g(\epsilon_{ij}). \tag{47}$$

The deformation of the panel of Fig. 5(*a*) were calculated by the finite element method using Eq. (12) modified for biaxial stress. These deformations are plotted in Fig. 5(*c*). It is clear that the nonlinearity is captured by Eq. (12) and the deformations δ_1 and δ_2 are not equal. Using finite element analysis and Eq. (47), the deformations of section ABCD of Fig. 5(*b*)

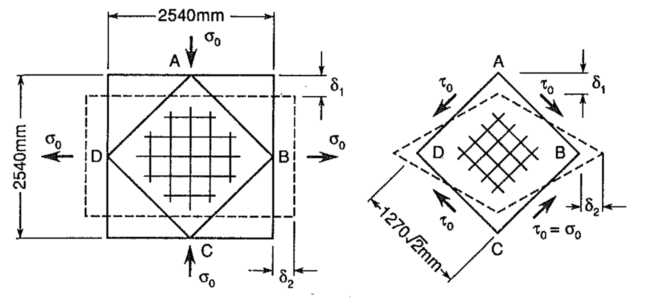

(a) Square concrete panel under principal stresses σ_0 (mesh of 100 elements)

(b) Inside section ABCD under pure shear stresses τ_0 (mesh of 49 elements)

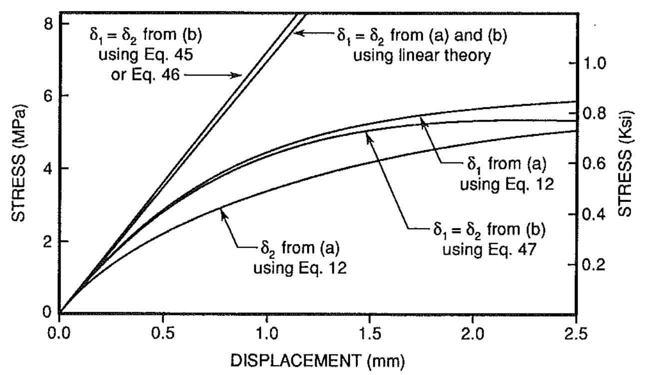

(c) Stress – displacement curves

Fig. 5 Finite element analysis of two panels under equivalent stress

were calculated and plotted in Fig. 5(*c*). It is seen that the deformation is now nonlinear and lies between the deformations from Eq. (12) as it was expected.

With Eqs. (41) through (43) and Eq. (47), the tangential stiffness matrix can be written as follows:

$$\begin{bmatrix} d\sigma_1 \\ d\sigma_2 \\ d\sigma_3 \\ d\tau_{12} \\ d\tau_{23} \\ d\tau_{31} \end{bmatrix} = \begin{bmatrix} g_1+h & h & h & 0 & 0 & 0 \\ h & g_2+h & h & 0 & 0 & 0 \\ h & h & g_3+h & 0 & 0 & 0 \\ 0 & 0 & 0 & g_{12}/2 & 0 & 0 \\ 0 & 0 & 0 & 0 & g_{23}/2 & 0 \\ 0 & 0 & 0 & 0 & 0 & g_{31}/2 \end{bmatrix} \begin{bmatrix} d\epsilon_1 \\ d\epsilon_2 \\ d\epsilon_3 \\ d\gamma_{12} \\ d\gamma_{23} \\ d\gamma_{31} \end{bmatrix} \tag{48}$$

where $g_{ij} = g(\epsilon_{ij})$. Note that the values of g_i and g_{ij} are calculated from the same function g for different strains. The physical meaning of g and h can be interpreted as the stiffness of the truss members of Fig. 1. Since all normal stiffnesses are initially equal (i.e., equal to the initial value of g) and all diagonal stiffnesses are also equal (i.e., equal to the initial value of h), the behavior is initially isotropic. However, depending on the stress history, the members are strained differently and the elements of the matrix of Eq. (48) take on values depending on the load. Thus, the material behaves as a path-dependent material with stress-induced anisotropy.

Conjunction With Stochastic Model

The stress-strain relationships of the stochastic model (Fafitis and Shah, 1986), which has been selected to simulate the uniaxial and hydrostatic stress-strain relationships, are

$$\sigma = E\epsilon\left(1+\frac{b\epsilon}{2}\right)\exp(-b\epsilon) \tag{49}$$

Table 1 λ values

λi, λo		Compressive Strain	Tensile Strain
Normal Moduli	compressive stress	-1, -1	1, 1
	tensile stress	-10, -10	10, 25
	zero stress (plane stress)	-5.6	1.8
	zero stress (uniaxial)	-3.2	3.2
Shear Moduli		-4.0	4.0

$$\sigma_o = \frac{E\epsilon}{b_o}\,[(1-\exp(-b_o\epsilon_o)]. \tag{50}$$

The formulas for the uniaxial and hydrostatic stress-strain relationships given by Eqs. (49) and (50) are based on a model consisting of an infinite number of elastoplastic elements connected in parallel. The initial stiffness of all elements is constant, but the yielding strain of each one is random with exponential distribution. Each element has a limited life depending on the total strain that it undergoes. When the total strains (in tension or compression) reaches this limit, which is also random with exponential distribution, the element fractures. Thus for any loading history, the elements fracture continuously, and as a result, the model exhibits peak and strain softening under monotonic loading and also hysteric loops and path-dependent response under nonmonotonic (e.g., cyclic) loading. The constants b and b_o in Eqs. (49) and (50) are the constants of the exponential distribution (Fafitis and Shah, 1984). The tangential stiffnesses are the derivatives of Eqs. (49) and (50):

$$E_t(\epsilon_i) = \alpha\left[1-\frac{(\lambda_i b\epsilon_i)^2}{2}\right]\exp(-\lambda_i b\epsilon_i) \tag{51}$$

$$K_o(\epsilon_o) = \beta\exp(-\lambda_o b_o \epsilon_o) \tag{52}$$

in which α and β are material constants to be defined in the next paragraphs and λ_i and λ_o are introduced to account for compressive, tensile, and zero stress, and compressive and tensile strain as shown in Table 1.

All parameters (α, β, b, b_o) can be determined from unaxial stress-strain relationships as follows: The initial Poisson's ratio of uniaxial stress ($\sigma_2 = \sigma_3 = 0$) is defined as $\nu_{in} = -d\epsilon_2/d\epsilon_1 = -d\epsilon_3/d\epsilon_1$ when ϵ_i tend to zero. From the second row of Eq. (12) one can write

$$\nu_{in} = \frac{h_{in}}{g_{in}+2h_{in}}. \tag{53}$$

Note that g_{in} is the same in the three principal directions because the material is assumed initially isotropic.

The initial elastic modulus for uniaxial stress ($\sigma_2 = \sigma_3 = 0$) is defined as $E_{in} = d\sigma_1/d\epsilon_1$ when ϵ_i tend to zero. From the first row of Eq. (12)

$$E_{in} = g_{in} + h_{in}(1-2\nu_{in}). \tag{54}$$

Solving for g_{in} and h_{in} Eqs. (53) and (54) give

$$g_{in} = \frac{E_{in}}{1+\nu_{in}} \tag{55}$$

$$h_{in} = \frac{\nu_{in}E_{in}}{(1-2\nu_{in})(1+\nu_{in})}. \tag{56}$$

From Eqs. (51) and (55), one can write

$$\alpha = E_t(0) = E_{in}. \tag{57}$$

E_{in} for concrete may be taken as $E_{in} = 4730\sqrt{f'c}$ MPa where $f'c$ is the concrete compressive strength in MPa (ACI Committee 318). Substituting Eq. (55) into Eq. (34) and from Eqs. (52) and (56), we can write

$$\beta = K_o(0) = E_{in}/(1-2\nu_{in}). \tag{58}$$

Equations (57) and (58) agree with Eqs. (16) and (20) at the onset of loading, as should be expected.

We can calculate b as follows: Since the tangent of Eq. (49) is equal to zero at peak we can get, from Eq. (51),

$$\epsilon_p = \frac{\sqrt{2}}{\lambda_i b} \tag{59}$$

where ϵ_p is the corresponding strain at peak stress.

Substituting Eq. (59) into Eq. (49) with $E = E_{in}$ and $\lambda_i = -1$, we can get

$$b = -0.5869\,\frac{E_{in}}{\sigma_p} \tag{60}$$

where σ_p is the peak stress which can be taken as the concrete strength.

In order to determine b_o we need the initial stiffness, which is equal to β (Eq. (58)), and another hydrostatic stiffness at any strain. Because $E_t/(1-2\nu)$ becomes undetermined near peak stress, 0.5 ϵ_p is used to determine b_o. From the uniaxial compressive stress-strain curve (Eq. (52)) and with $\lambda_o = -1$, we get

$$K_o(0.5\epsilon_p) = \beta\,\exp(0.5\epsilon_p b_o). \tag{61}$$

Substituting Eq. (58) into Eq. (61), we get

$$b_o = \frac{1}{0.5\epsilon_p}\left[\ln\frac{E_t(0.5\epsilon_p)}{1-2\nu(0.5\epsilon_p)} - \ln\frac{E_{in}}{1-2\nu_{in}}\right] \tag{62}$$

where E_t $(0.5\epsilon_p)$ is given by Eq. (51) at $\epsilon = 0.5\epsilon_p$, $\nu(0.5\epsilon_p)$ is given by Eq. (21) at $\epsilon = 0.5\epsilon p$ (that is $\nu = 0.26$), and ν_{in} is given by Eq. (21) at $\epsilon = 0$ (that is $v_{in} = 0.18$). The value of ϵ_p in Eq. (62) is calculated using Eq. (59).

Conclusions

A tangential stiffness matrix to predict multiaxial stress-strain curves of concrete is proposed. The model is based on a space truss where the diagonal members represent hydrostatic stiffness and the normal members represent deviatoric stiffness. Hydrostatic stiffness and deviatoric stiffness could be determined by only three parameters which can be determined from a uniaxial compressive stress-strain curve. Those parameters were peak stress, initial elastic modulus, and tangential Poisson's ratio. The peak stress is assumed equal to concrete strength, the initial elastic modulus is measured experimentally or calculated by available empirical formulas, and the Poisson's ratio is calculated by a proposed empirical formula. The incremental formulation is quite general and proportional as well as nonproportional loading with quite complex load path can be handled. The predictions of the model compared favorably with the experimental results by various investigators (Kupfer et al., 1969; Schickert and Winkler, 1977; Van Mier, 1986) as it is demonstrated in Part II of this paper.

References

ACI Committee 318, 1989, "Building Code Requirements for Reinforced Concrete (ACI 318-71)," ACI, Detroit.

Ahmad, S. H., and Shah, S. P., 1982, "Complete Triaxial Stress-Strain Curves for Concrete," *Journal of Structural Engineering*, ASCE, Vol. 108, No. ST4, Apr., pp. 728–742.

Ahmad, S. H., Shah, S. P., and Khaloo, A. R., 1986, "Orthotropic Model of Concrete for Triaxial Stresses," *Journal of Structural Engineering*, ASCE, Vol. 112, No. 1, Jan., pp. 165–181.

Baker, A. L. L., 1959, "An Analysis of Deformation and Failure Characteristics of Concrete," *Magazine of Concrete Research*, Vol. 11, No. 33, Nov., pp. 119–128.

Bathe, K. J., and Ramaswamy, S., 1979, "On Three-Dimensional Nonlinear Analysis of Concrete Structures," *Nuclear Engineering and Design*, Vol. 52, No. 3, May, pp. 385–409.

Bazant, Z. P., and Bhat, P., 1976, "Endochronic Theory of Inelasticity and Failure of Concrete," *Journal of Engineering Mechanics*, ASCE, Vol. 102, No. EM4, Aug., pp. 701–722.

Bazant, Z. P., and Shieh, C. L., 1978, "Endochronic Model for Nonlinear Triaxial Behavior of Concrete," *Nuclear Engineering and Design*, Vol. 47, pp. 305–315.

Bazant, Z. P., and Shieh, C. L., 1980, "Hysteretic Fracturing Endochronic Theory for Concrete," *Journal of Engineering Mechanics*, ASCE, Vol. 106, No. EM5, Oct., pp. 929–950.

Burt, N. J., and Dougill, J. W., 1977, "Progressive Failure in a Model Heterogeneous Medium," *Journal of Engineering Mechanics*, ASCE, Vol. 103, No. EM3, June, pp. 449–464.

Chen, W. F., and Saleeb, A. T., 1982, "Constitutive Equations for Engineering Materials," *Elasticity and Modelling*, Vol. 1, John Wiley and Sons, New York.

Darwin, D., and Pecknold, D. A., 1977a, "Analysis of Cyclic Loading of Plane R/C Structures," *Computers and Structures*, Vol. 7, pp. 137–147.

Darwin, D., and Pecknold, D. A., 1977b, "Nonlinear Biaxial Law for Concrete," *Journal of Engineering Mechanics*, ASCE, Vol. 103, No. EM2, April, pp. 229–241.

Elwi, A. A., and Murray, D. W., 1979, "A 3D Hypoelastic Concrete Constitutive Relationship," *Journal of Engineering Mechanics*, ASCE, Vol. 105, No. EM4, Aug., pp. 623–641.

Fafitis, A., and Shah, S. P., 1984, "Rheological Model for Cyclic Loading of Concrete," *Journal of Structural Engineering*, ASCE, Vol. 110, No. 9, Sept., pp. 2085–2102.

Fafitis, A., and Shah, S. P., 1986, "Constitutive Model for Biaxial Cyclic Loading of Concrete," *Journal of Engineering Mechanics*, ASCE, Vol. 112, No. 8, Aug., pp. 760–775.

Gerstle, K. H., 1981, "Simple Formulation of Triaxial Concrete Behavior," *Journal of ACI*, Vol. 78, No. 5, Sept.-Oct., pp. 382–387.

Hognestad, E., 1951, "A Study of Combined Bending and Axial Load in Reinforced Concrete Members," *University of Illinois Engineering Experimental Station*, Bulletin Series No. 399, Nov., pp. 128.

Isenburg, J., and Adam, S., 1970, "Analysis of Orthotropic Reinforced Concrete Structures," *Journal of the Structural Engineering Division*, ASCE, Vol. 96, No. ST12, Dec., pp. 2607–2624.

Kupfer, H., Hisdorf, H. K., and Rush, H., 1969, "Behavior of Concrete Under Biaxial Stress," *Journal of ACI*, Aug., pp. 656–666.

Liu, T. C. Y., Nilson, A. H., and Slate, F. O., 1972, "Biaxial Stress-Strain Relations for Concrete," *Journal of the Structural Engineering Division*, ASCE, Vol. 98, No. ST5, May, pp. 1025–1034.

Maekawa, K., and Okamura, H., 1983, "The Deformational Behavior and Constitutive Model," *Journal of the Faculty of Engineering*, The University of Tokyo, Vol. 37, No. 2.

Moarenzadeh, F., and Kuguel, R., 1969, "Fracture of Concrete," *Journal of Materials*, Vol. 4, No. 3, pp. 497–519.

Ottosen, N. S., 1979, "Constitutive Model for Short-Time Loading of Concrete," *Journal of Engineering Mechanics*, ASCE, Vol. 105, No. EM1, Feb., pp. 127–141.

Papadopoulos, P. G., 1984, "Biaxial Network Constitutive Model," *Journal of Engineering Mechanics*, ASCE, Vol. 110, No. 3, March, pp. 449–464.

Reinius, E., 1965, "A Theory of the Deformation and the Failure of Concrete," *Magazine of Concrete Research*, Nov., 1965, pp. 157–160, (summary of Professor Reinius' paper published in Betong, No. 1, pp. 15–43).

Saada, A.S., 1974, *Elasticity: Theory and Applications*, Pergamon Press, New York, pp. 643.

Saenz, I. P., 1964, discussion of "Equation for Stress-Strain Curve of Concrete," by P. Desayi and S. Krishman, *Journal of ACI*, Vol. 61, No. 9, Sept. pp. 1229–1235.

Sargin, M., 1971, "Stress-Strain Relationships for Concrete and the Analysis of Structural Sections," *Study No. 4*, Solid Mechanics Division, University of Waterloo, Waterloo, Ontario, Canada.

Schickert, G., and Winkler, H., 1977, "Results of Tests Concerning Strength and Strain of Concrete Subjected to Multiaxial Compressive Stresses," Bundesanstalt fur Materialprufing (BAM), Bericht Nr. 46, Berlin, Germany, May, pp. 124.

Tasjui, M. E., Slate, F. O., and Nilson, A. H., 1978, "Stress-Strain Response and Fracture of Concrete in Biaxial Loading," *Journal of ACI*, Vol. 75, No. 7, July, pp. 306–312.

Van Mier, J. G. M., 1986, "Fracture of Concrete Under Complex Stress," *HERON*, Vol. 31, No. 3.

Van Mier, J. G. M., 1985, "Strain-Softening of the Concrete Under Multiaxial Loading Conditions," Ph.D. Dissertation, Eindhoven University of Technology, Eindhoven, The Netherlands.

Y. H. Won
Asst. Professor,
Department of Civil Engineering,
Korea Third Military Academy,
Kyungbuk, Youngehun-goo, 771-849,
Korea

A. Fafitis
Assoc. Professor,
Department of Civil Engineering,
Arizona State University,
Tempe, AZ 85287

A Multiaxial Stochastic Constitutive Law for Concrete With Dilatancy: Part II—Comparison With Experimental Data

The salient features and concepts of a model developed in Part I of this paper are reviewed. The model is extended to include dilatancy and shear compaction which are determined from uniaxial stress-strain relationships. The parameters of the model are the peak stress, initial elastic modulus, and tangential Poisson's ratio. The peak stress is assumed equal to the compressive strength of the concrete specimen, the initial elastic modulus and the Poisson's ratio is calculated by proposed empirical formulas. Predictions of the model compare favorably with experimental data reported by various investigators. Responses of concrete specimens subjected to prescribed triaxial proportional stresses, triaxial proportional strains and stresses, hydrostatic plus stress combinations with loading paths on the deviatoric stress plane, biaxial compressive, biaxial tensile, and uniaxial tensile loadings are predicted and compared with test data. All predictions are satisfactory.

Introduction

A three-dimensional constitutive model based on incrementally linear elastic (hypoelastic) behavior was formulated previously. The material is assumed initially isotropic, but it becomes anisotropic at later stages of loading (stress induced anisotropy). In order to express a nonlinear stress-strain relationship as well as path-dependency, the elastic moduli should be functions of the total strain history. The strain can be decomposed into two parts, the octahedral part, associated with change in volume, and the deviatoric part, associated with change in shape. The motivation for the decomposition in volumetric (octahedral) and deviatoric components comes from a space truss concept explained earlier. The advantage of this modeling is that the triaxial behavior of concrete can be modeled by a combination of uniaxial models and the stiffness of the members can be calculated at each strain increment from appropriate uniaxial stress-strain relationships. The stiffnesses of the truss members are equivalent to the hydrostatic and deviatoric stiffness of the material. The member stiffnesses are obtained from the tangential values of the deviatoric stress-strain curve and the hydrostatic stress-strain curve which can be determined from uniaxial stress-strain relationships.

The salient features of the model will be reviewed briefly in the following section, and then the model will be used to predict some experimental data available in the literature. The dilatancy of brittle materials, like concrete, is modeled by some empirical equations calibrated to fit a large number of existing experimental data.

Review of the Model

In this investigation, for the uniaxial stress-strain relationship, we used a recently developed rheological stochastic model which has the facility for strain history and unloading (Fafitis and Shah, 1984; Fafitis and Shah, 1986). The model is characterized by three parameters: the peak stress, the strain corresponding to peak stress, and the tangential Poisson's ratio. In matrix form the proposed constitutive law is given as follows:

$$\begin{bmatrix} d\sigma_1 \\ d\sigma_2 \\ d\sigma_3 \\ d\tau_{12} \\ d\tau_{23} \\ d\tau_{31} \end{bmatrix} = \begin{bmatrix} g_1+h & h & h & 0 & 0 & 0 \\ h & g_2+h & h & 0 & 0 & 0 \\ h & h & g_3+h & 0 & 0 & 0 \\ 0 & 0 & 0 & g_{12}/2 & 0 & 0 \\ 0 & 0 & 0 & 0 & g_{23}/2 & 0 \\ 0 & 0 & 0 & 0 & 0 & g_{31}/2 \end{bmatrix} \begin{bmatrix} d\epsilon_1 \\ d\epsilon_2 \\ d\epsilon_3 \\ d\gamma_{12} \\ d\gamma_{23} \\ d\gamma_{31} \end{bmatrix} - \begin{bmatrix} d\bar{\sigma} \\ d\bar{\sigma} \\ d\bar{\sigma} \\ 0 \\ 0 \\ 0 \end{bmatrix} \tag{1}$$

Contributed by the Applied Mechanics Division of The American Society of Mechanical Engineers for presentation at the 1992 ASME Summer Mechanics and Materials Meeting, Tempe, AZ, Apr. 28–May 1, 1992.

Discussion on this paper should be addressed to the Technical Editor, Prof. Leon M. Keer, The Technological Institute, Northwestern University, Evanston, IL 60208, and will be accepted until four months after final publication of the paper itself in the Journal of Applied Mechanics. Manuscript received by the ASME Applied Mechanics Division, Aug. 25, 1988; final revision, Sept. 25, 1991.

Paper No. 92-APM-14.

where $d\sigma_i$, $d\tau_{ij}$, $d\epsilon_i$, and $d\gamma_{ij}$, are the incremental normal and shear stress and strains. The additional incremental stress vector $\{d\bar{\sigma}\}$ in the right side of Eq. (1) is the dilatancy which will be discussed in the following section, and g_i, g_{ij}, and h are the abbreviations of $g(e_i)$, $g(\epsilon_{ij})$, and $h(\epsilon_o, e_k)$, respectively, which are defined as

$$g(e_i) = K_i(e_i) = \frac{1}{1+\nu} E_t \tag{2}$$

$$h(\epsilon_o, e_k) = \frac{1}{3} K_o(\epsilon_o) - \frac{1}{9}(K_1 + K_2 + K_3) \tag{3}$$

where K_i and K_o are deviatoric stiffness and hydrostatic stiffness, respectively. E_t is a uniaxial stiffness which is equal to the tangential value of the uniaxial stress-strain curve.

From the uniaxial model we have

$$E_t(\epsilon_i) = E_{in}\left[1 - \frac{(\lambda_i b \epsilon_i)^2}{2}\right]\exp(\lambda_i b \epsilon_i) \tag{4}$$

$$K_o(\epsilon_o) = \frac{E_{in}}{1 - 2\nu_{in}} \exp(-\lambda_o b_o \epsilon_o) \tag{5}$$

where E_{in} is the initial elastic modulus and ν_{in} is the initial Poisson's ratio. E_{in} may be taken as $E_{in} = 4730\sqrt{f'c}$ MPa where $f'c$ is the compressive strength of concrete in MPa (ACI Committee 318, 1989). For compressive stress, λ_i and λ_o are equal to ± 1, for the tensile stress, λ_i is equal to ± 10, while λ_o is equal to 25. For positive (tensile) strain, λ_i and λ_o are positive, for the negative (compressive) strain, λ_i and λ_o are negative.

In Eqs. (4) and (5), b and b_o are probability distribution parameters and they are given by the following formulas

$$b = -0.5869 \frac{E_{in}}{\sigma_p} \tag{6}$$

$$b_o = \frac{1}{0.5\,\epsilon_p}\left[\ln - \frac{E_t(0.5\,\epsilon_p)}{1 - 2\nu(0.5\,\epsilon_p)} - \ln\frac{E_{in}}{1 - 2\nu_{in}}\right] \tag{7}$$

where σ_p is peak stress, which can be taken equal to the compressive strength $f'c$, and ϵ_p is the corresponding strain at peak stress which is

$$\epsilon_p = \frac{\sqrt{2}}{\lambda_i b}. \tag{8}$$

The Poisson's ratio is given by the following empirical equations:

$$\begin{aligned} \nu(\epsilon) &= 0.18 \text{ for } \epsilon/\epsilon_p < 0 \\ \nu(\epsilon) &= 0.82\,(\epsilon/\epsilon_p)^{3.4} + 0.18 \text{ for } 0 < \epsilon/\epsilon_p < 1.5 \\ \nu(\epsilon) &= -0.82\,(3 - \epsilon/\epsilon_p)^{3.4} + 6.7 \text{ for } \epsilon/\epsilon_p < 0 \\ \nu(\epsilon) &= 6.7 \text{ for } \epsilon/\epsilon_p > 3. \end{aligned} \tag{9}$$

The linear elastic constitutive relations (generalized Hooke's Law) is a special case of the model proposed here. The incremental formulation is quite general and proportional as well as nonproportional loading with any load path can be handled.

Dilatancy

From experimental observations it has been found that brittle materials, like concrete, exhibit dilatancy, which is volumetric change under deviatoric stress. Dilatancy, in this investigation, is accounted for by adding an extra term in the compliance matrix as follows:

$$\{d\epsilon\} = [F]\{d\sigma\} + \{d\bar{\epsilon}\} \tag{10}$$

where $\{d\epsilon\}$ is dilatancy component. The stiffness matrix can be written as

$$\{d\bar{\sigma}\} = [S]\{d\epsilon\} - [S]\{d\bar{\sigma}\} \tag{11}$$

where $[S] = [F]^{-1}$. We can write Eq. (11) as

$$\{d\sigma\} = [S]\{d\epsilon\} - \{d\bar{\sigma}\} \tag{12}$$

where $\{d\bar{\sigma}\} = [S]\{d\bar{\epsilon}\}$. Note that in Eq. (1) we consider dilatancy due to diagonal components of the stress tensor. Letting $d\sigma^*$ indicate uniaxial dilatancy and if $d\sigma_2 = d\sigma_3 = 0$, Eq. (1) will give

$$d\sigma_2 = hd\epsilon_1 + (g_2 + h)d\epsilon_2 + hd\epsilon_3 - d\bar{\sigma}^* = 0.$$

Substituting

$$\nu = -d\epsilon_2/d\epsilon_1 = -d\epsilon_3/d\epsilon_1$$

we get

$$d\bar{\sigma}^* = (h - 2\nu h - \nu g_2)d\epsilon_1. \tag{13}$$

If Eq. (13) is plotted for different concrete strengths it can be seen from Fig. 1 that the effect of $f'c$ on Eq. (13) is not appreciable, therefore for numerical convenience, we express uniaxial dilatancy independent of $f'c$ as follows:

$$\frac{d\bar{\sigma}^*}{d\epsilon_1^*} = \left[A\left(\left|\frac{\epsilon}{\epsilon_p} - 0.39\right|\right)^3 + B\right] \tag{14}$$

where $A = 10^7$; $B = 5.5 \times 10^5$.

In multiaxial stress we define a relative constant between a reference strain increment from the uniaxial stress and an actual strain increment as

$$\psi = \frac{|de_1| + |de_2| + |de_3|}{|de_1^*| + |de_2^*| + |de_3^*|} \tag{15}$$

where the asterisk indicates uniaxial values. We assume that the dilatancy increment on the right side of Eq.(1) can be calculated by

$$\frac{\overline{d\sigma}(\epsilon_1)}{d\epsilon_1} = \psi \frac{\overline{d\sigma}^*(\epsilon_1^*)}{d\epsilon_1^*} \tag{16}$$

where $\epsilon_1^* = \int \psi d\epsilon_1^*$ and $d\epsilon_1^*$ is the most compressive longitudinal strain increment. Figure 2 shows schematically the relation between uniaxial and multiaxial dilatancy. In the following section of the effect of dilatancy is shown in Figs. 4, 7, 9, and 11 where the model is compared with experimental data.

Comparison with Tests Subjected to Proportional Loading

To determine the stress-strain curves of concrete subjected to any arbitrary loading using the model proposed here, one needs to know the uniaxial peak stress σ_p and the Poisson's ratio $\nu(\epsilon)$. In the present investigation the Poisson's ratio is calculated from Eq. (1). The predicted stress-strain curves are compared with experimental data obtained by various investigators in the sequel. In the following figures, negative values

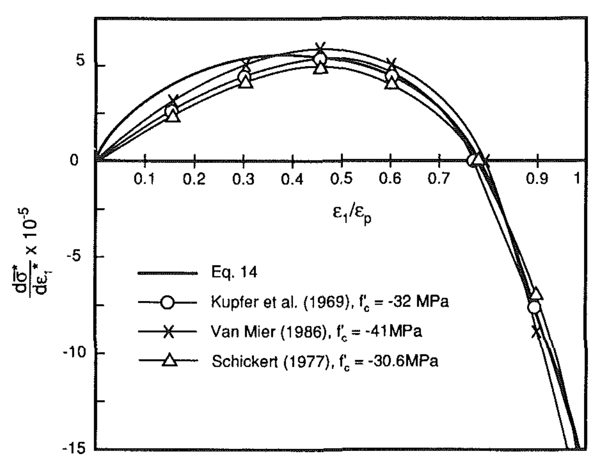

Fig. 1 Dilatancy and shear compaction of uniaxial compressive stress

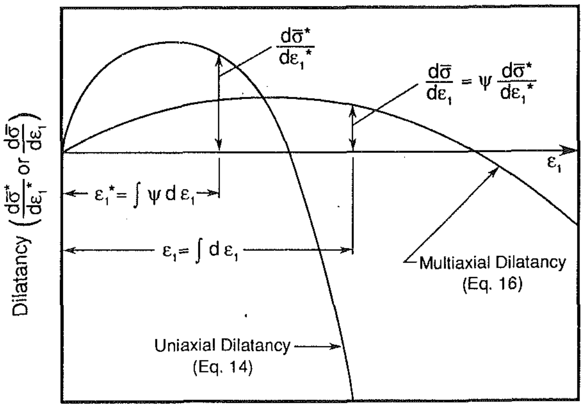

Fig. 2 Relationship between uniaxial and multiaxial dilatancy

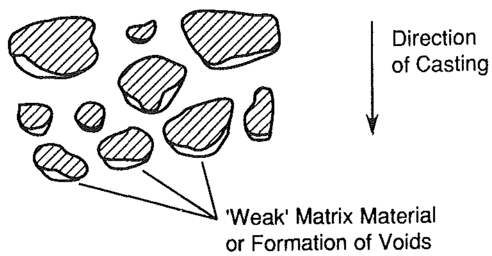

Fig. 3 Accumulation of weak planes under large aggregate particles

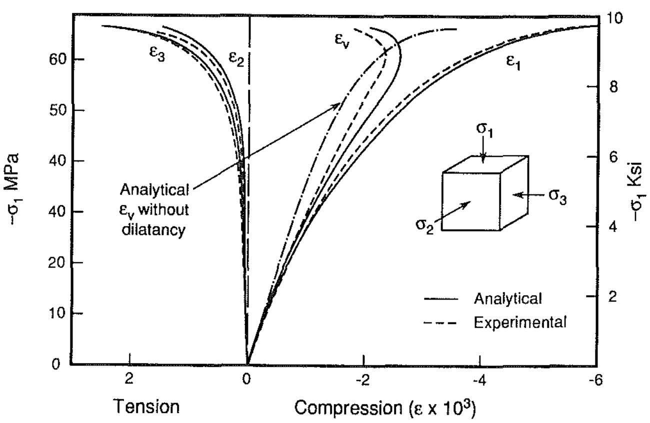

Fig. 4 Comparison of analytical with experimental results of proportional triaxial loading ($\sigma_2/\sigma_1 = 0.1$, $\sigma_3/\sigma_1 = 0.05$, parallel)

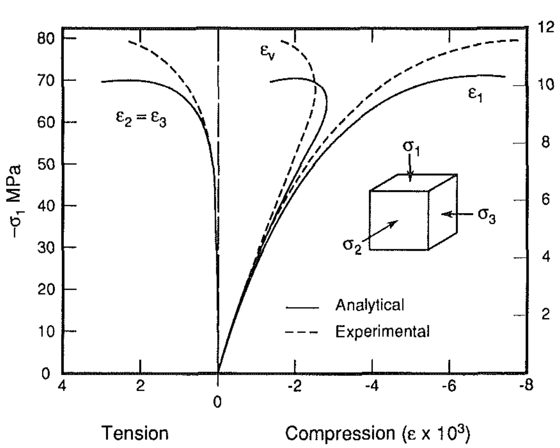

Fig. 5 Comparison of analytical with experimental results of proportional triaxial loading ($\sigma_2/\sigma_1 = 0.1$, $\sigma_3/\sigma_1 = 0.1$, perpendicular)

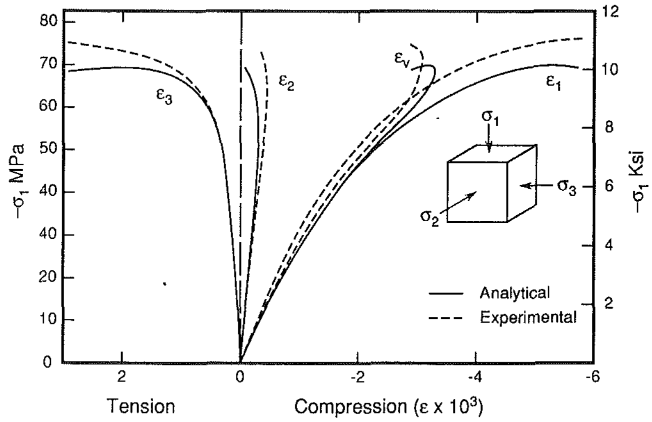

Fig. 6 Comparison of analytical with experimental results of proportional triaxial loading ($\sigma_2/\sigma_1 = 0.33$, $\sigma_3/\sigma_1 = 0.05$, perpendicular)

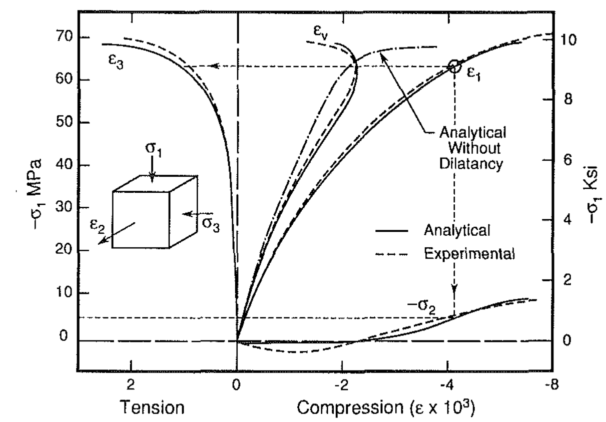

Fig. 7 Comparison of analytical with experimental results of proportional strain and stress ($\epsilon_2/\epsilon_1 = -0.2$, $\sigma_3/\sigma_1 = 0.05$, perpendicular)

indicate compressive stresses or strains, while positive values indicate tensile stresses or strains and ϵ_v indicate volumetric strain ($\epsilon_v = \epsilon_1 + \epsilon_2 + \epsilon_3$).

Van Mier (1986) tested 100 mm cube concrete specimens under monotonically increasing loading. The loading was proportional; that is, the ratios σ_2/σ_1 and σ_3/σ_1 were kept constant. These experiments were conducted under displacement control in the major loaded direction (σ_1), and load control in the other two directions. In concrete, weaker planes are developed under the larger aggregate particles as shown in Fig. 3.

These weak planes are the result of bleeding, shrinkage, and temperature difference during the hardening process of the concrete and they are parallel to the bottom of the specimens (perpendicular to the casting direction). In the experiments conducted by Van Mier the loading is distinguished in parallel and perpendicular to the direction of casting. The response predicted by the model is compared with the experimental results reported by Van Mier in Figs. 4 through 9. In Fig. 4 the loading was $\sigma_2/\sigma_1 = 0.1$ and $\sigma_3/\sigma_1 = 0.05$, and was compressive parallel to the direction of casting. The volumetric strain curve without dilatancy is shown in this figure for comparison. In Fig. 5 the loading was $\sigma_2/\sigma_1 = 0.1$ and $\sigma_3/\sigma_1 = 0.1$, and σ_1 was perpendicular compression. In Fig. 6 the loading was $\sigma_2/\sigma_1 = 0.33$ and $\sigma_3/\sigma_1 = 0.05$, and σ_1 was perpendicular compression.

In the uniaxial compressive tests of 100 mm cube, the peak stress, σ_p, was -41 MPa for parallel loading and -42 MPa for perpendicular loading with regard to the direction of cast-

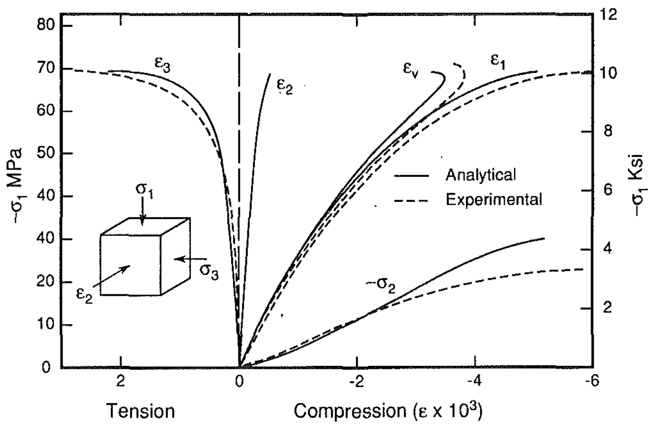

Fig. 8 Comparison of analytical with experimental results of proportional strain and stress ($\epsilon_2/\epsilon_1 = 0.1$, $\sigma_3/\sigma_1 = 0.05$, perpendicular)

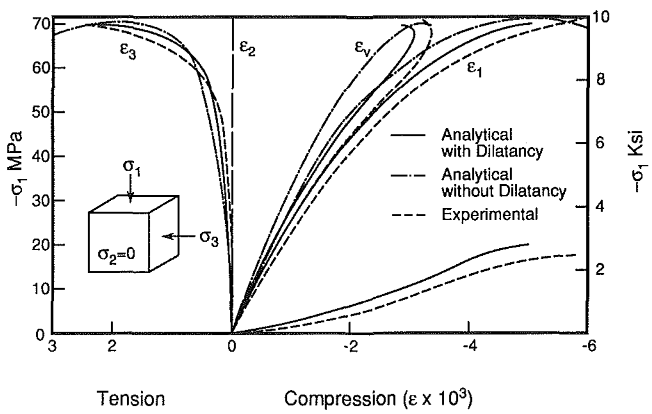

Fig. 9 Comparison of analytical with experimental results of proportional strain and stress ($\epsilon_2/\epsilon_1 = 0$, $\sigma_3/\sigma_1 = 0.05$, perpendicular)

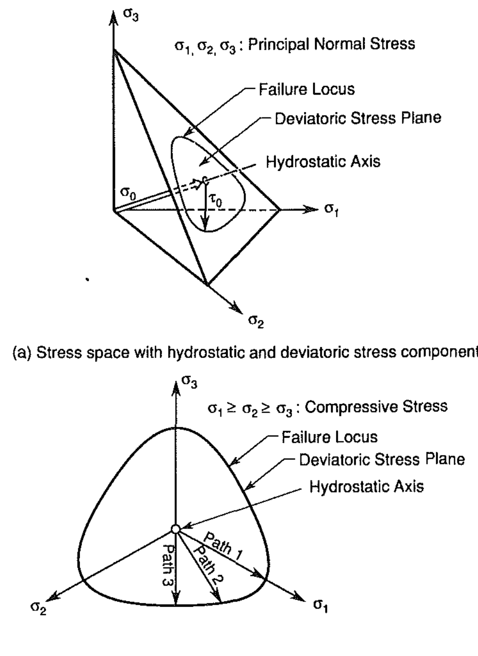

Fig. 10 Stress paths

ing. The initial elastic modulus, E_{in} was approximately 30,000 MPa. The parameters of the model were calculated as follows: For parallel loading, $b = 434$, $b_o = 440$; and for perpendicular loading, $b = 429$, $b_o = 434$.

Another set of tests performed by Van Mier using 100 mm cube concrete specimens is the following: The strain in direction 2 was proportional of the strain of direction 1 and the stress of direction 3 was proportional to the stress in direction 1. Therefore, the ratios ϵ_2/ϵ_1 and σ_3/σ_1 were kept constant.

In Figs. 7, 8, and 9, we plot ϵ_1, ϵ_2, and ϵ_3 versus σ_1, and also σ_2 versus ϵ_1. For example, in Fig. 7 at $\sigma_1 = -62.7$ MPa (-9101 psi), ϵ_1 is -0.00415 and σ_2 is -6.4 MPa (-925 psi). In Fig. 7 the loading was $\epsilon_2/\epsilon_1 = -0.2$ and $\sigma_3/\sigma_1 = 0.05$ while σ_1 was perpendicular compression. In Fig. 8 the loading was $\epsilon_2/\epsilon_1 = 0.1$ and $\sigma_3/\sigma_1 = 0.05$ while σ_1 was perpendicular compression. In Fig. 9 the loading was $\epsilon_2/\epsilon_1 = 0$ and $\sigma_3/\sigma_1 = 0.05$ while σ_1 was parallel compression.

Comparison with Tests Subjected to Nonproportional Loading

Schickert and Winkler (1977) performed multiaxial tests in several laboratories using 100 mm cube specimens which were cast in one place. The purpose of testing at different laboratories with different equipment was to eliminate the influence of the testing machines. Triaxial loading was performed by first subjecting the cube to a specified hydrostatic stress and

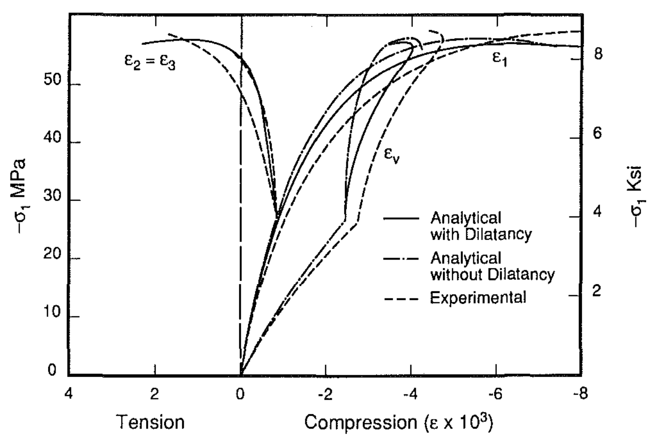

Fig. 11 Comparison of analytical with experimental results of nonproportional triaxial loading (hydrostatic stress = −25.5 MPa, $\sigma_2/\sigma_1 = 0.33$, $\sigma_3/\sigma_1 = 0.05$, perpendicular)

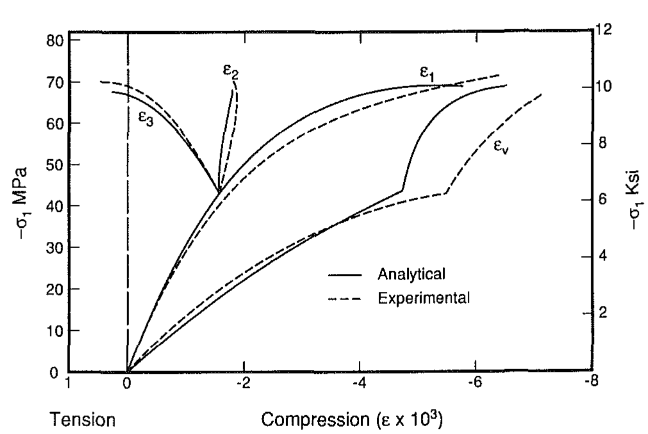

Fig. 12 Comparison of analytical with experimental results of nonproportional triaxial loading (hydrostatic stress = −42.5 MPa, $\sigma_2/\sigma_1 = 0$, $\sigma_3/\sigma_1 = -1$)

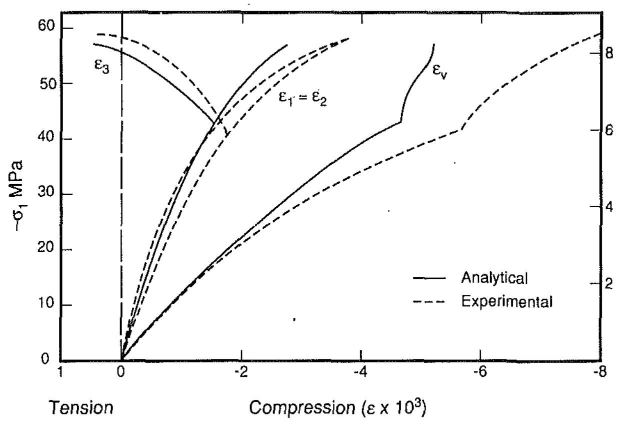

Fig. 13 Comparison of analytical with experimental results of nonproportional triaxial loading (hydrostatic stress = -42.5 MPa, $\sigma_2/\sigma_1 = 1$, $\sigma_3/\sigma_1 = -2$)

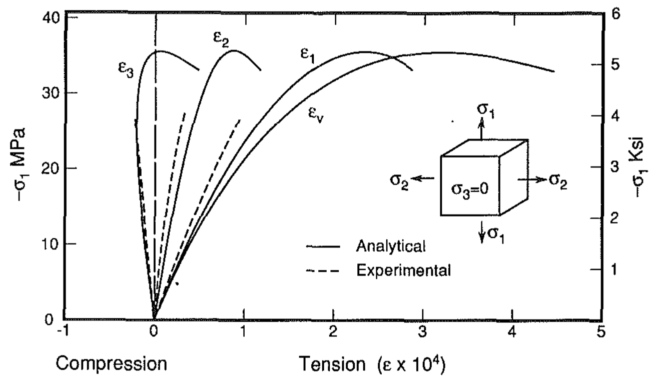

Fig. 15 Comparison of analytical with experimental results of biaxial tensile loading ($\sigma_2/\sigma_1 = 0.55$)

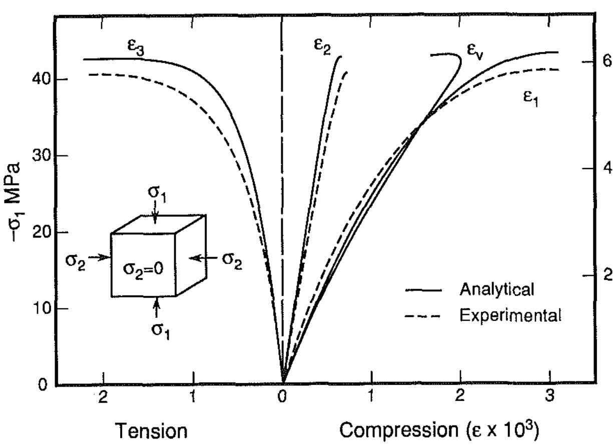

Fig. 14 Comparison of analytical with experimental results of biaxial compressive loading ($\sigma_2/\sigma_1 = 0.52$)

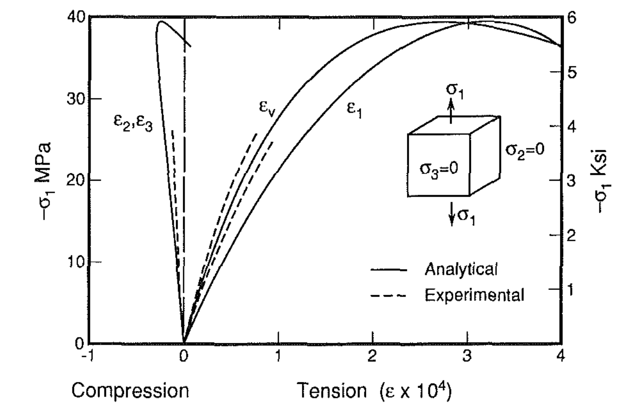

Fig. 16 Comparison of analytical with experimental results of uniaxial tensile loading

then to stress combinations which followed one of the three stress paths shown in Fig. 10. (Those loading paths are on the deviatoric stress plane at specified hydrostatic stress.)

Figure 11 shows the comparison of tests on path 1 (Fig. 10*b*), with hydrostatic stress -25.5 MPa (-3698 psi) and $\sigma_2/\sigma_1 = \sigma_3/\sigma_1 = -0.5$ (σ_1 compressive). The analytical curves, without dilatancy, are also shown in this figure for comparison. In Fig. 12, the tests are on path 2 with hydrostatic stress -42.5 MPa (-6162 psi) and $\sigma_2/\sigma_1 = 0$, $\sigma_3/\sigma_1 = -1$ (σ_1 compressive). In Fig. 13 are shown tests on path 3 in which the hydrostatic stress is -42.5 MPa (-6162 psi) and $\sigma_2/\sigma_1 = 1$, $\sigma_3/\sigma_1 = -2$, while σ_1 is compressive. For the uniaxial compressive tests of the 100 mm cube peak stress, σ_p was equal to -30.6 MPa (-4438 psi). The initial elastic modulus was calculated 24840 MPa (3602 ksi). The parameters of the stochastic model were calculated as follows: $b = 476$, $b_o = 483$. The analytical curves exhibit a somewhat ductile trend than do the experimental curves. However, the overall response is satisfactory.

Comparison with Tests Subjected to Tensile Loading

The three-dimensional model previously presented can simulate biaxial loading behavior with the following adjustment of λ values: If octahedral stress is compressive, $\lambda = \pm 1.8$; if octahedral stress is tensile, $\lambda = \pm 5.6$. Uniaxial loading behavior can be simulated with $\lambda = \pm 3.2$.

In Figs. 14, 15, and 16 the results are shown of the biaxial and uniaxial tests conducted by Kupfer et al. (1969). These results are compared with the predicted values of the triaxial model developed here. The specimens were $200 \times 200 \times 50$ mm concrete prisms subjected to biaxial stress combinations with "brush bearing platens." For the tensile tests, the filaments were glued to the concrete.

In Fig. 14 a proportional compressive loading $\sigma_2/\sigma_1 = 0.52$ was applied. The value of $\lambda_3 = 1.8$ was used for zero stress in direction 3. In Fig. 15, the proportional tensile loading was $\sigma_2/\sigma_1 = 0.55$. The value of $\lambda_3 = 5.6$ was used for zero stress in direction 3. In Fig. 16, a uniaxial tensile stress σ_1 was applied, and $\lambda_2 = \lambda_3 = 3.2$ was used for the stress directions 2 and 3.

From the uniaxial compressive test of the prism, the peak stress σ_p was 32 MPa (-4650 psi). The initial elastic modulus was calculated 26800 MPa (3886 ksi). The parameters of the stochastic model were calculated as follows: $b = 490$, $b_o = 497$.

Conclusions

Although in some cases the analytical curves exhibit a somewhat less ductile trend, overall predictions of the model compared favorably with experimental results. The comparisons show that the developed model can handle multiaxial compressive and tensile behavior under loadings of proportional stress, proportional strain and stress, and nonproportional stress. Dilatancy and shear compaction could be determined from uniaxial stress-strain relationship and then generalized to multiaxial behavior. The only input parameter was the compressive strength of the concrete. Then the initial elastic modulus was calculated by the formula adopted by the American Concrete Institute using the concrete strength only, and the Poisson's ratio was determined by a proposed empirical formula.

References

ACI Committee 318, 1989, "Building Code Requirements for Reinforced Concrete (ACI 318-71)," ACI, Detroit.

Fafitis, A., and Shah, S. P., 1984, "Rheological Model for Cyclic Loading of Concrete," *Journal of Structural Engineering*, ASCE, Vol. 110, No. 9, Sept., pp. 2085–2102.

Fafitis, A., and Shah, S. P., 1986, "Constitutive Model for Biaxial Cyclic Loading of Concrete," *Journal of Engineering Mechanics*, ASCE, Vol. 112, No. 8, Aug., pp. 760–775.

Kupfer, H., Hisdorf, H. K., and Rush, H., 1969, "Behavior of Concrete under Biaxial Stress," *Journal of ACI*, Aug., pp. 656–666.

Schickert, G., and Winkler, H., 1977, "Results of Tests Concerning Strength and Strain of Concrete Subjected to Multiaxial Compressive Stresses," *Bundesanstalt fur Materialprufing* (*BAM*), Bericht Nr. 46, Berlin, Germany, May, p. 124.

Van Mier, J. G. M., 1986, "Fracture of Concrete under Complex Stress," *HERON*, Vol. 31, No. 3.

Van Mier, J. G. M., 1985, "Strain-Softening of the Concrete under Multiaxial Loading Conditions," Ph.D. Dissertation, Eindhoven University of Technology, Eindhoven, The Netherlands.

K. M. Liechti
Assoc. Professor,
Mem. ASME.

Y. S. Chai
Graduate Research Assistant.

Department of Aerospace Engineering
and Engineering Mechanics,
The University of Texas at Austin,
Austin, TX 78712

Asymmetric Shielding in Interfacial Fracture Under In-Plane Shear

The toughness of a glass/epoxy interface was measured over a wide range of mode mixes. A toughening effect was associated with increasing positive and negative in-plane shear components. Optical interference measurements of normal crack opening displacements near the crack front and complementary finite element analyses were used to examine near-front behavior during crack initiation. Estimates of the toughening based on plastic dissipation, bulk viscoelastic dissipation, and interface asperity shielding did not fully account for the measured values. The results suggest that the inelastic behavior of the epoxy, frictional, and, perhaps, three-dimensional effects should be considered.

1 Introduction

Interfacial crack growth occurs in a number of applications of technological importance. Because of the fact that the fracture path is constrained irrespective of the orientation of the globally applied loads and also because of the mismatch of material properties across the interface, crack growth is inherently mixed mode. Critical and subcritical crack growth must then be governed by some combination of mode I, II, and III fracture parameters. The simplest approach, using one parameter, seeks to determine an effective parameter that can account for all mode mixes in a unifying manner. This is particularly useful for subcritical crack growth where correlations of crack growth rates fall on one curve for all mode mixes when the proper parameter is found. An alternative is to consider a two-parameter approach where one parameter represents the mode mix or direction and the other a magnitude. For critical crack growth, the magnitude will generally be a function of mode mix. The form the function is usually determined experimentally but may, as mechanisms are better understood, even be predicted.

The most common approach for examining interfacial crack initiation has been to consider the interfacial fracture toughness, G_c, as a function of the fracture mode mix. The various methods that have been used over the years to obtain various degrees of mode mix were summarized in a previous paper (Liechti and Chai, 1991). In the first study of interfacial toughness as a function of mode mix, Malyshev and Salganik (1965) found that the toughness of a plexiglass/epoxy interface was independent of mode mix. The only other example of a bimaterial combination with a constant toughness was provided by Takashi et al. (1978). The first evidence of a toughening effect as the relative amount of shear mode was increased came from some experiments with adhesively bonded scarf joints (aluminum/epoxy) that failed adhesively (Trantina, 1972). Similar trends were observed by Anderson et al. (1974a) using cone, blister, and peel specimens. They suggested (1974b) that the noted increase in toughness with increasing shear was due to microbranching of the crack into the weaker medium because SEM micrographs revealed a concomittant increase in fracture surface roughness. Plastic and viscoleastic dissipation effects were also cited as possible contributors. Large-scale yielding was in fact noted in some experiments conducted by Mulville et al. (1978) who made use of a single aluminum/epoxy specimen subjected to multiaxial loads. Liechti and Hanson (1988) detected an increase in the degree of small-scale yielding and toughness with increasing mode II component in glass/epoxy blister specimens by measuring normal crack opening displacements (NCOD) using crack opening interferometry (Liechti and Knauss, 1982a). Although the increase in toughness was not linked quantitatively to the increase in plastic dissipation, some recent work by Argon et al. (1989) and Gupta et al. (1989) suggests that plastic dissipation, even in mode I, can be a substantial component of the interfacial toughness.

A more recent use of the multi-specimen approach for fracture toughness measurements was summarized by Cao and Evans (1989). An increasing toughness with shear component was again detected. It was linked to an asperity shielding effect (Evans and Hutchinson, 1989) due to the initial roughness of the interface. Mulville and Mast (1975) found that rougher interfaces linearly increased toughness for one mode mix in crack growth that replicated the interfacial roughness. Interestingly, it was found that a 500 Angstrom layer of epoxy remained on the aluminum substrate. Rosenfeld et al. (1990) have recently added a micro-indentation technique to the array of mixed-mode interfacial fracture property specimens that have been developed. The results were consistent with those obtained from other experiments they conducted using glass/epoxy cantilever beam and four-point flexure (Charalambides et al., 1989) specimens. Another recent development has been

Contributed by the Applied Mechanics Division of The American Society of Mechanical Engineers for publication in the ASME Journal of Applied Mechanics.

Discussion on this paper should be addressed to the Technical Editor, Professor Leon M. Keer, The Technological Institute, Northwestern University, Evanston, IL 60208, and will be accepted until four months after final publication of the paper itself in the Journal of Applied Mechanics. Manuscript received by the ASME Applied Mechanics Division, Mar. 12, 1990; final revision, Mar. 15, 1991.

made by Wang and Suo (1990) who used a single specimen, the brazil nut sandwich, loaded at various orientations to investigate the toughness of various interfaces. Finally, the concept of using the shapes of delamination fronts to examine mode III toughening effects has recently been exploited by Jensen et al. (1990), using the straight cut test. Further exploitation of this concept may be facilitated by making use of a simplified analysis for extracting three-dimensional mode mixes from curved delamination fronts that has been recently proposed by Chai (1990).

There has been relatively little examination of the effect of mode mix on subcritical crack growth. Gent and Kinloch (1971) used a number of different test pieces, with an elastomer on mylar, to examine time-dependent crack growth. The dependence of the adhesive fracture energy on an effective crack propagation velocity that accounted for viscoelastic effects was the same for all test pieces. The mode mix was not explicitly extracted and may not have differed to the degree that was expected. However, mode-mix independence was established for an elastomer/glass specimen under biaxial loads when a vectorial crack opening displacement parameter, that accounted for measured finite deformations, was used to correlate crack velocities (Liechti and Knauss, 1982b). Near-tip crack opening displacements were also used (Chan and Davidson, 1989) to extract local stress intensity factor changes, ΔK, under cyclic fiber matrix debonding (alumina/magnesium alloy). An effective ΔK parameter, based on the total energy release rate or J-integral, accounted for mode-mix effects. However, the J-integral did not serve as an effective mixed-mode fracture parameter in some recent experiments with environmentally assisted crack growth in rubber to metal bonds (Hamadeh et al., 1989; Lin, 1989 and Adamjee, 1989). It was found (Adamjee, 1989) that crack growth velocities for a given J-value were strongly dependent on crack opening angle to the extent that no propagation occurred under globally applied shear loads.

The purpose of the work presented here was to examine interfacial crack initiation over a wide range of mode mixes. The analysis and development of a suitable specimen and biaxial loading device have already been described (Liechti and Chai, 1990). This paper will present the results and analysis of a series of experiments that were conducted with various combinations of tensile and positive or negative shear loads. Indications are that the toughening effect is dependent on the sign of the shear component.

2 Analysis of Individual Experiments

The specimen that was used for the crack initiation experiments was the edge-cracked bi-material strip made of glass and epoxy (Fig. 1). The epoxy, a modified bisphenol (Araldite 502) that had been mixed with an amido-amine hardener (Araldite 955), was cast directly to the glass and cured at room temperature for at least a week. The initial crack was produced by inserting a razor at the interface and wedging it open to a length of approximately $6h$. When the specimen was viewed under crossed polars, there was no evidence of residual stresses, presumably due to the long, room-temperature cure. The specimen was placed in a specially developed bi-axial loading device that applied displacements along the clamped boundaries, $x_2 = \pm h$. Bond-normal displacements, v_0, were applied along $x_2 = h$, whereas bond-tangential displacements, u_0, were applied to the glass along $x_2 = -h$. The actuators consisted of microstepping stepper motors and preloaded ball screws that were controlled by a personal computer so that complex applied displacement histories could be prescribed. The reactions normal and tangential to the interface were also acquired and recorded by the computer. The NCOD along the crack front were also measured by introducing monochromatic light through the glass and resolving with a microscope the interference fringes produced by the beams reflected from the crack faces. The interference fringes were recorded on a video system for subsequent data reduction using digital image analysis procedures.

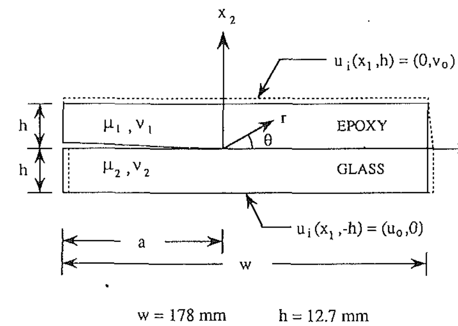

Fig. 1 The edge-cracked bi-material strip specimen

Under bond-normal applied displacements, Atkinson (1977) showed that the energy release rate, G, for the bi-material strip was given by

$$G=\frac{v_0^2}{h}\left[\frac{(1-2\nu_1)}{\mu_1(1-\nu_1)}+\frac{(1-2\nu_2)}{\mu_2(1-\nu_2)}\right]^{-1} \tag{1}$$

where the elastic properties are defined in Fig. 1.

Simple energy arguments, for sufficiently long cracks, yield

$$G=\frac{u_0^2}{h}\left[\frac{1}{\mu_1}+\frac{1}{\mu_2}\right]^{-1} \tag{2}$$

for bond-tangential loadings.

The mode mix or mixity, ψ, was defined in terms of the complex stress intensity factor, K, and the glass and epoxy heights, h, as

$$\psi=\tan^{-1}\left\{\frac{\mathrm{Im}[Kh^{i\epsilon}]}{\mathrm{Re}[Kh^{i\epsilon}]}\right\}. \tag{3}$$

The bimaterial constant, ϵ, is given by

$$\epsilon=\frac{1}{2\pi}\ln\left[\frac{\kappa_1\mu_2+\mu_1}{\kappa_2\mu_1+\mu_2}\right] \tag{4}$$

under plane strain

$$\kappa_\alpha=3-4\nu_\alpha, \quad \alpha=1,2. \tag{5}$$

The real and imaginary parts K_1 and K_2 of the complex stress intensity factor were extracted from finite element solutions and a conservation integral approach (Yau and Wang, 1984). For positive v_0, the mode-mix ranges from -60 deg $< \psi <$ 90 deg under positive and negative bond tangential displacements (Liechti and Chai, 1991).

The uniaxial tensile behavior of the epoxy was determined under ramp and step loadings. Epoxy coupons were cut from the remains of fractured crack initiation specimens. The ramp tests were conducted under displacement control at 0.0125 mm/s. The Young's modulus and Poisson's ratio were determined from load and strain gage measurements whereas an extensometer was used to obtain the overall response (Fig. 2(a)). In specimens that did not fracture prematurely due to bubbles, the maximum stress marked the onset of shear banding. The large strain response following the drop from the ultimate strength was idealized in subsequent analyses as the dashed line shown in Fig. 2(a). In order to later investigate asymptotic fields, a Ramberg-Osgood fit

$$\epsilon=\frac{\sigma}{E}+\frac{3}{7}\left(\frac{\sigma}{\sigma_0}\right)^{n-1} \tag{6}$$

was made of the data up three percent strain. The values of the parameters are listed in Table 1.

Relaxation tests were conducted at temperatures of 21°C

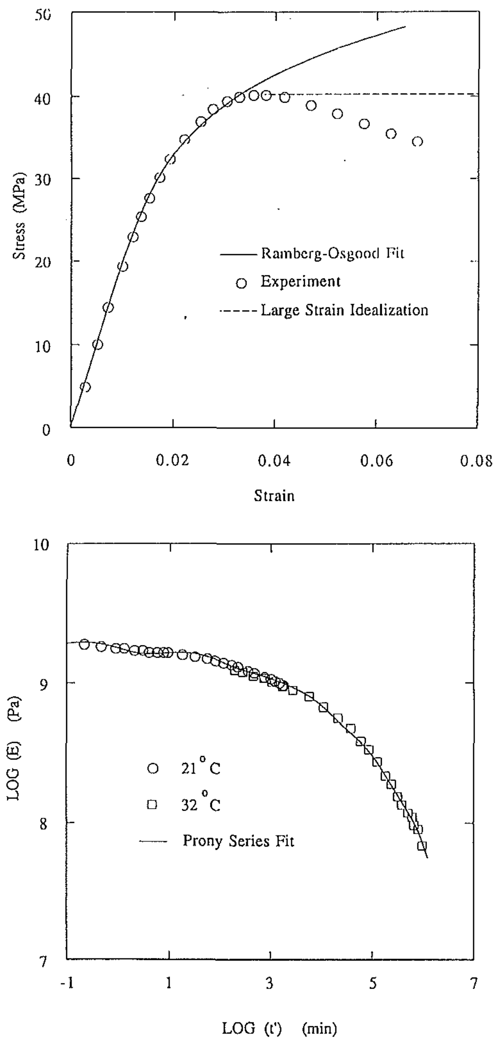

Fig. 2 Tensile response of the epoxy under ramp and step loads

and 32°C to obtain a limited master curve (Fig. 2(*b*)). The line is an eight-term Prony Series representation of the measurements and was used with a constant Poisson ratio assumption in viscoelastic analyses of typical load histories in the crack initiation tests (Chai, 1990). The analyses confirmed experimental observations that the NCOD did not exhibit any viscoelastic effects under bond-normal and bond-tangential displacements. However, there was some relaxation in the reactions, particularly under bond-tangential displacements, and sufficient recovery time was therefore provided between experiments.

A series of crack initiation tests was conducted by applying load histories that consisted of various amounts of bond-tangential applied displacements, u_{0_s}, followed by bond-normal applied displacements, v_{0_c}, until crack initiation occurred. A detailed analysis of three loading cases is now provided in order to provide some insight to later results. Each loading case was analyzed using the ABAQUS finite element code, first considering small strains and the epoxy response to be linearly elastic. A second, nonlinear analysis was based on finite deformations and an incremental plasticity model using J_2-flow theory and isotropic hardening following the measured stress-strain behavior and the dashed line idealization for large strains (Fig. 2(*a*)). In both cases, any tendency for the crack faces to make contact was accommodated by special gap elements, so that crack-face interpenetration could not occur. A more detailed elastoplastic analysis of an interface crack with contact has recently been given by Aravas and Sharma (1991).

Table 1 Material properties

Material	Young's Modulus E (GPa)	Poisson's Ratio ν	σ_0 (MPa)	Hardening Exponent (n)
Epoxy	2.03	0.37	40.4	6
Glass	68.95	0.20	—	—

glass-epoxy Dundurs' parameter $\alpha = -0.9366$
$\beta = -0.1879$
Bimaterial constant $\epsilon = 0.0605$

Bond-Normal Loading. Bond-normal loading refers to the case where $u_{0_s} = 0$ and bond-normal displacements were applied until steady crack propagation occurred. The measured and predicted NCOD are compared in Fig. 3(*a*). There was always some initial opening due to a slight preload applied to the specimen in order to properly align the optics. The same preload was applied in the finite element analysis to ensure agreement at $\bar{u}_0 = \bar{v}_0 = 0$ where $\bar{u}_0 = u_0/u_{0_s}$ and $\bar{v}_0 = v_0/v_{0_c}$. It can be seen that close agreement was also obtained at crack initiation ($\bar{u}_0 = 0$, $\bar{v}_0 = 1$) and that a linear analysis was sufficient. The asymptotic behavior of the NCOD near the crack front was examined in double logarithmic form (Fig. 3(*b*)). The measured NCOD resulted in linear profiles having slopes of 0.51 and 0.52 at $\bar{v}_0 = 0$ and 1, respectively. The nonlinear and linear analyses agreed down to the 1 μm level indicating that the degree of adhesion in this case was such that very little plastic deformation was excited in the epoxy before debonding occurred. Previous bond-normal loading experiments (Liechti and Chai, 1991) had given rise to larger scale yielding due to a higher degree of adhesion. The yielding had been readily apparent in the bilinear form that the logarithmic plots took.

Because of the degree of magnification that was used to observe the crack front region, the process of crack initiation was a gradual one, even though the fracture toughness levels were relatively low. It was therefore possible to record an increase in energy release rate, G_R, as stable crack extension occurred (Fig. 3(*c*)). The energy release rates were derived from finite element solutions whose NCOD matched the measured values. The first data point ($da/a = 0$) reflects the initial preload that was applied. After the second data point, the time interval between the subsequent levels of crack extension was 0.5*s* which indicates that the initial slow growth was followed by a sharp transition to a higher but steady velocity, which was characterized by an essentially constant energy release rate or NCOD profile. The critical value of energy release rate, G_c, and associated applied displacement, v_{0_c}, were taken at the instant of the transition to faster, steady propagation.

Sequential Loading With Positive Bond-Tangential Displacements. The example of this loading class that is considered now involved the highest level of positive bond-tangential applied displacements that was applied in the crack initiation studies. The initial NCOD profile (Fig. 4(*a*), $\bar{u}_0 = \bar{v}_0 = 0$) was matched by an initial bond-normal preload. The application of positive bond-tangential applied displacements resulted in a decrease in NCOD that lead to the crack-face contact shown at $\bar{u}_0 = 1$, $\bar{v}_0 = 0$. The extent of contact was well predicted but there was some difference between the linear and nonlinear solutions with the former being closer to the measured NCOD. Bond-normal applied displacements were then applied until crack initiation ($\bar{u}_0 = \bar{v}_0 = 1$). The nonlinear solution for NCOD displayed some blunting when compared to the linear case but it was insufficient to fully capture the measured blunting. However, further removed from the crack front, the agreement between predictions and measurements was reasonable.

The corresponding crack-front asymptotics for this sequential loading are shown in Fig. 4(*b*). The measured NCOD under the slight preload ($\overline{u}_0 = \overline{v}_0 = 0$) followed a linear profile with a slope of $m_E = 0.55$. By the time crack initiation occurred, the measured profile had taken on a bilinear profile reflecting elastic response in the far field ($m_E = 0.60$) and inelastic response in the near field where the slope was $m_P = 0.45$. The predicted NCOD at initiation had far-field slopes $m_E = 0.65$ and 0.7 for the linear and nonlinear analyses, respectively. Interestingly enough, the NCOD profile corresponding to the linear solution became steeper as the crack front was approached instead of maintaining its far-field value. The higher slope suggests a weaker strain singularity and the possibility that, when the NCOD are examined very close to the crack front under bond-tangential applied displacements, the crack appears as a notch (Shih, 1990). Note that this was not the case for the tangential crack opening displacements (TCOD) obtained from the linear solution whose profile had a slope of 0.48.

The near-front slope, $m_P = 0.45$, of the measured NCOD did not correspond to the value expected from the power-law hardening model of the epoxy stress-strain behavior ($n = 6$) and HRR singular fields where $m_P = 1/(n+1) = 0.14$. The same was true of the near front slopes of the NCOD and TCOD solutions obtained from the nonlinear analysis at $\overline{u}_0 = \overline{v}_0 = 1$. For $r < 10$ μm, the slopes were, respectively, $m_P = 0.23$ and 0.36. These results suggest that the inelastic behavior of the epoxy under multiaxial stress states needs to be more closely examined.

The resistance curve for this sequential loading is shown in Fig. 4(*c*). It can be seen that some crack extension occurred during the tangential loading phase ($\overline{v}_0 = 0$) even though the crack faces were in contact in the near-front region. As a result of the contact, the extent of crack growth up to $\overline{u}_0 = 1$, $\overline{v}_0 = 0$ could only be determined once bond-normal displacements had been applied, at which time the crack faces opened to the crack length developed under tangential loading and slow crack extension progressed until the crack velocity suddenly increased to a steady value. The energy release rate value associated with the transition was taken to be G_c. The numbers associated with the crack extension values that were obtained at 2.0-second intervals correspond to the slopes of the bilinear logarithmic NCOD profiles. The numbers above the resistance curve are the slopes, m_E, in the elastic or far-field region. The numbers below the resistance curves are the corresponding near front slopes, m_P. It can be seen that, once the faster, steady crack

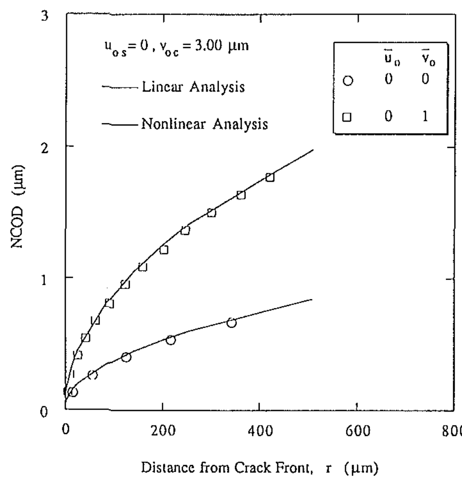

a) NCOD Profiles

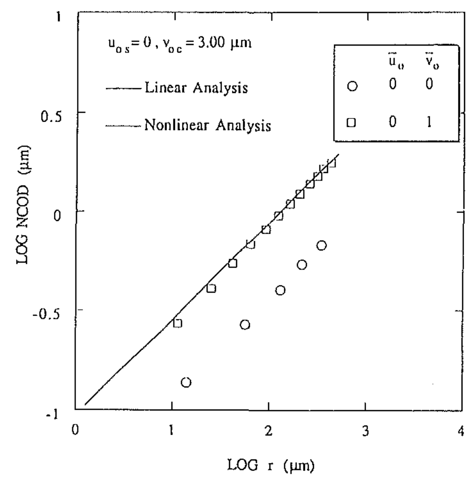

b) COD Asymptotics

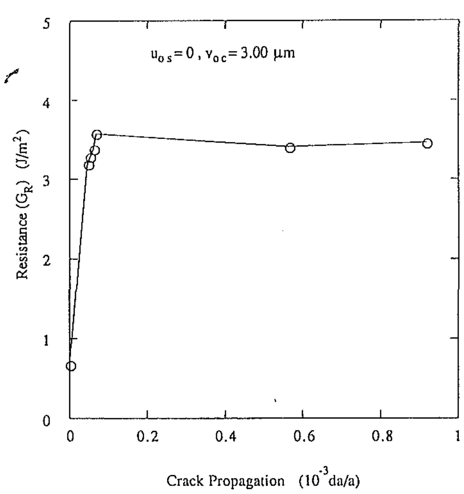

c) Resistance Curve

Fig. 3 Crack initiation characteristics under bond-normal applied displacements

propagation occurred, the bilinear profile was essentially lost. The plastic zone size behind the crack front, r_p, was taken to be the point of discontinuity in the bilinear profiles. The plastic zone size increased under the slow crack extension and then dropped noticeably just before the crack velocity increased suddenly, after which there was no detectable plastic zone, presumably due to rate effects (Needleman, 1990). The maximum plastic zone size was 141 μm, much larger than the value associated with a purely bond-normal loading, but still small scale in nature. The finite element prediction for the value of r_p at $\bar{u}_0 = \bar{v}_0 = 1$ was 164 μm. The fracture toughness for this degree of mixity ($\psi = -58$) was 36 J/m^2, also much higher than the value under purely bond-normal loading. The more obvious degree of blunting and stable crack growth is also brought out in the degree of stable crack extension under the two load cases which increased to $da/a = 0.8 \times 10^{-3}$ from $da/a = 0.1 \times 10^{-3}$.

Sequential Loading with Negative Bond-Tangential Displacements. In the sequential loading described here, negative bond-tangential applied displacements were followed by bond-normal displacements until steady crack propagation occurred. The measured and predicted NCOD are first compared in Fig. 5(*a*) where the measured initial state was matched by applying a suitable level of bond-normal applied displacement. The application of negative bond-tangential applied displacements further increased the NCOD in the near-front region. The comparison made at $\bar{u}_0 = 1$, $\bar{v}_0 = 0$ reveals that there was very little difference in the linear and nonlinear analyses which overpredicted the NCOD very close to the crack front. The same was essentially true at initiation, $\bar{u}_0 = \bar{v}_0 = 1$.

The associated double logarithmic NCOD profiles are shown in Fig. 5(*b*). The initial state profile was linear with a slope $m_E = 0.55$. At initiation, the measured elastic slope had decreased to $m_E = 0.45$ while there was a hint of inelastic response giving $m_P = 0.42$. The corresponding slopes from the analyses were $m_E = 0.33$ and $m_P = 0.37$. The TCOD had slopes $m_E = 0.49$ and $m_P = 0.40$. Again, neither the measured nor the predicted slopes in regions of inelastic response showed any sign of HRR singular behavior in the crack opening displacements. Furthermore, it can again be seen that the far-field elastic NCOD did not follow the expected square root behavior whereas the TCOD did, suggesting that the notch effect discussed earlier was again apparent.

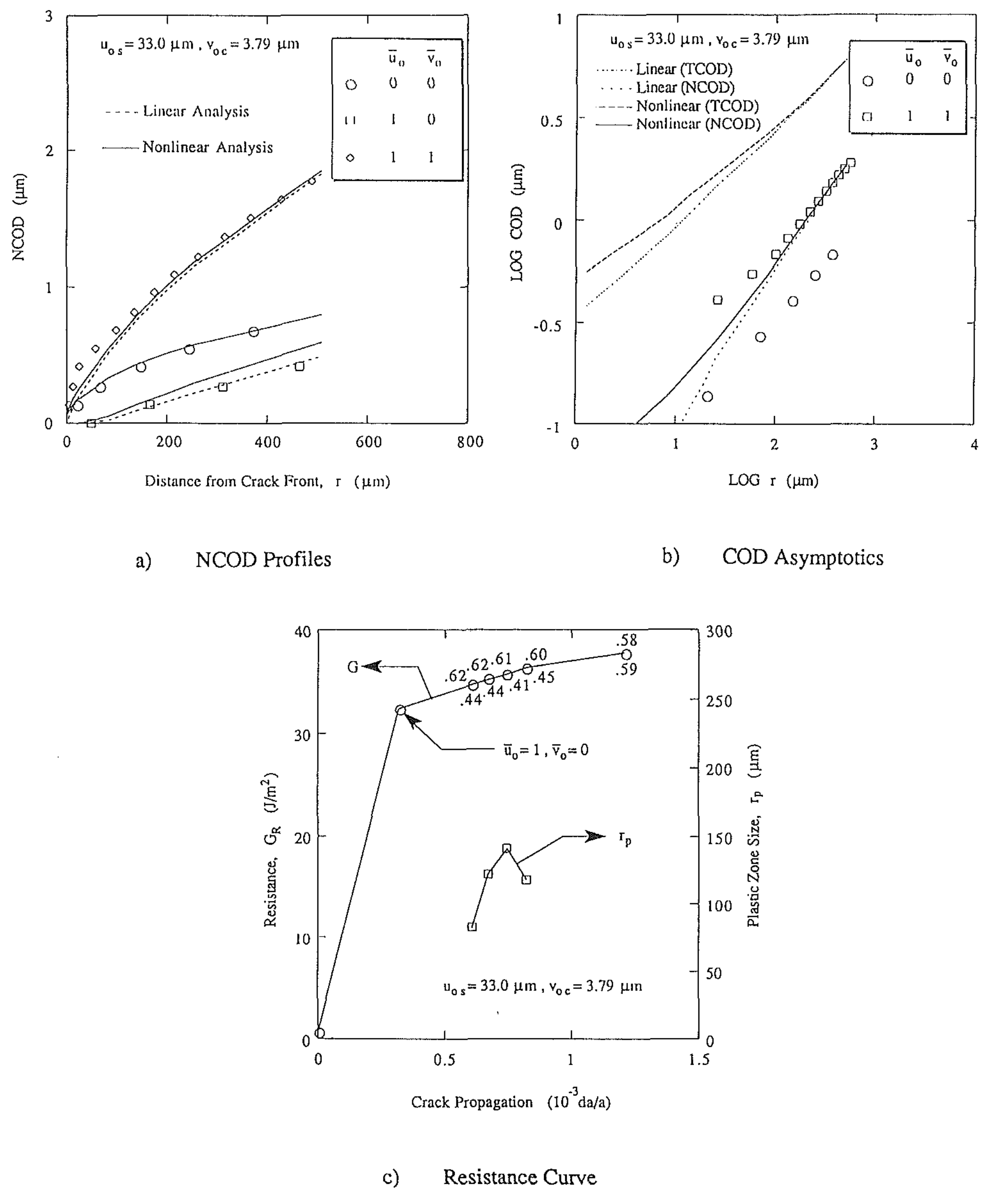

Fig. 4 Crack initiation characteristics under sequential loading with positive bond-tangential applied displacements

The resistance curve for this loading was obtained by matching the measured NCOD in the region of elastic response and extracting the energy release rate and mixity from the finite element solution. There was a smaller amount of stable crack extension under negative u_0 than had been noted for a similar amount of positive u_0. Crack initiation, as previously defined, occurred shortly after the application of bond-normal applied displacements and it was again associated with a drop in plastic zone size. The maximum extent of the plastic zone behind the crack front was approximately 100 μm, about two-thirds of the value notched for the positive bond-tangential load. The predicted plastic zone size, 180 μm, was considerably higher than the measured value, in keeping with the overprediction of NCOD. There was no measurable plastic zone associated with steady crack propagation.

3 Interfacial Toughness

The experiments that were analyzed in the previous section were part of a series that was conducted over a range of mode mixes by applying various amounts of positive or negative bond-tangential applied displacements and then adding bond-normal applied displacements until steady propagation occurred. The mode mix thus obtained ranged from -60 deg $< \psi <$ 90 deg, limited essentially by crack branching effects. Resistance curves of the types shown in Figs. 3(*c*), 4(*c*), and 5(*c*) were obtained for each experiment and G_c, the critical value associated with the sudden jump in crack velocity, was extracted. The G_c values, or interfacial toughness, were plotted as a function of mode mix (Fig. 6).

The results were obtained from four specimens that had the same degree of adhesion, as can be seen by the consistency of toughness values where mode mixes overlapped. For 0 deg $< \psi <$ 45 deg, the toughness was relatively independent of mode mix and thus a mixed-mode fracture criterion for initiation that required a constant value of G_c to be attained seems reasonable. However, for -60 deg $< \psi <$ 0 deg and 45 deg $< \psi <$ 90 deg, the interfacial toughness was highly dependent on mode mix, with the maximum toughness being approximately ten times the minimum value. As a result, the immediate recommendation for design purposes is that the toughness of any particular interfacial crack configuration should be evaluated at the appropriate degree of mode mix.

Another way to view the results shown in Fig. 6 is to plot

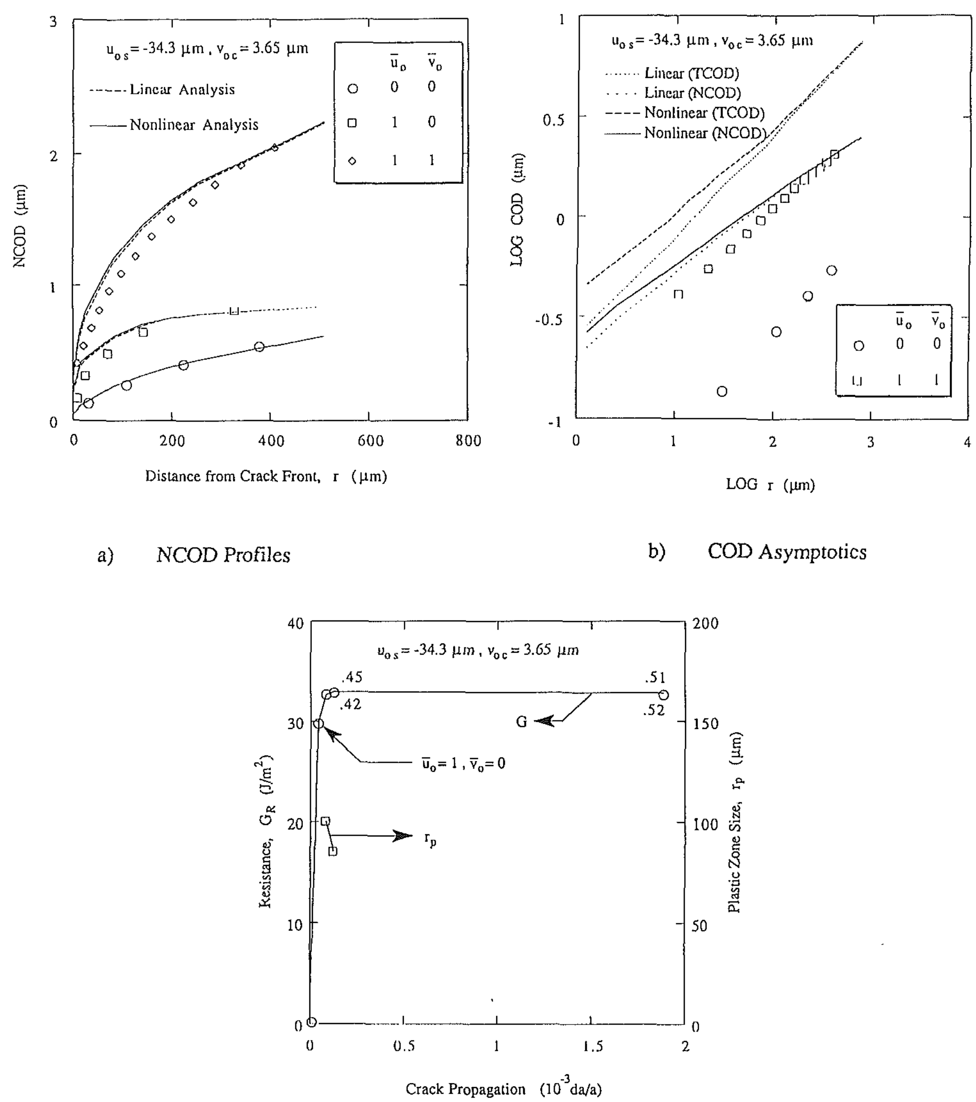

a) NCOD Profiles

b) COD Asymptotics

c) Resistance Curve

Fig. 5 Crack initiation characteristics under sequential loading with negative bond-tangential applied displacements

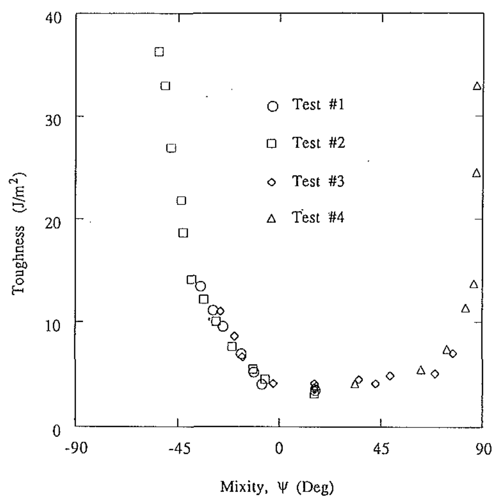

Fig. 6 Interfacial toughness

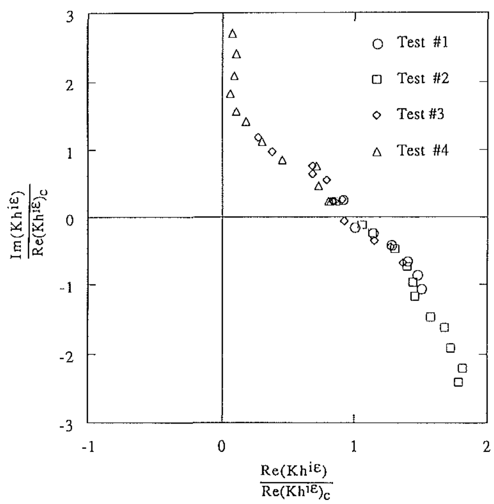

Fig. 7 Interfacial crack initiation envelope

the interaction diagram depicted in Fig. 7. The fracture initiation envelope represents the combinations of the real and imaginary parts of the complex K combination $Kh^{i\epsilon}$ that were required in order for crack extension to occur. The envelope in the first quadrant was almost closed except for small values of $\mathrm{Re}[Kh^{i\epsilon}]$. The sharp increase in toughness there is reasonable if one considers what would happen for zero or slightly negative values of $\mathrm{Re}[Kh^{i\epsilon}]$. Under such conditions, although there will always be some opening near the crack front (Comninou and Schmeuser, 1979; Liechti and Knauss, 1982b; Liechti and Chai, 1991), the degree of crack-face contact further away would be greater, possibly making it more difficult for a crack to propagate due to far-field frictional effects. In the fourth quadrant, the envelope showed no signs of returning to zero $\mathrm{Re}(Kh^{i\epsilon})$ for the range of mixities that were considered. It is conceivable that the envelope in this region would never close because of near-front closing (compressive) tendencies acting in conjunction with frictional effects.

Toughening Effects. For a smooth, frictionless interface with an intrinsic adhesive energy, γ_a, so low that any yielding in the constituent materials under any loading would be confined to submicron dimensions, one could expect that the interfacial toughness, G_c, would be the same as γ_a for all mode mixes. Higher values of γ_a would excite inelastic deformations in one or both constituents and the associated dissipation would make G_c greater than γ_a. The possibility of mode-mix effects then arises because increased shear tends to facilitate inelastic deformation. Fracture surface roughness may also have a toughening effect due to microbranching, asperity locking, and frictional effects. The purpose of the following discussion is to examine a number of potential toughening mechanisms that might account for the increases in toughness shown in Fig. 6.

The contributions to the overall interfacial toughness, G_c, that were considered here were the intrinsic adhesive energy, γ_a, the rate of plastic dissipation near the crack front, $\dot{W}_p$, the rate of bulk viscoelastic dissipation, $\dot{W}_v$, in the specimen, and shielding due to the initial roughness of the interface, ΔG_c. Thus, in effect, we expect that

$$G_c = \gamma_a + \dot{W}_p + \dot{W}_v + \Delta G_c. \tag{7}$$

where $(\dot{\ }) \equiv d(\ )/da$. The possibility of microbranching, cited as a cause of toughening in the work of Anderson et al. (1974b), was not included because SEM micrographs of the epoxy fracture surface did not reveal any features. If any existed they must therefore have been smaller than 0.01 μm. Although friction may have an effect on toughness, it was beyond the scope of this study.

Previous work (Liechti and Hanson, 1988) had suggested that the toughening effect was associated with increases in plastic dissipation because plastic zone sizes increased with increasing shear component. This possibility was considered here by first examining the plastic zone shapes and sizes associated with various degrees of mode mix. The plastic zone shapes that developed at initiation under the three loadings already considered in detail in Section 2 are shown in Figs. 8(a)–8(c). The mode mixes represented there are $\psi = 16$ deg, -54 deg and 88 deg and the plastic zone boundary in the epoxy was taken from the nonlinear solutions at an equivalent stress level of 20 MPa, the yield strength under uniaxial tension. The shapes are qualitatively the same as those shown by Shih and Asaro (1991). The plastically deformed region under bond-normal loading was extremely small in comparison to the plastic zones that developed under the sequential loadings with positive and negative u_0. The extent of the plastic zone ahead of the crack front was taken to be representative of trends in plastic zone volume and was obtained for all the other experiments that were conducted (Fig. 8(d)). The plastic zone sizes, thus defined, followed the same trends that the toughness exhibited with mode mix. Although all yielding was small scale in nature, there were large increases in size as the shear component increased.

The next step that was taken was to estimate the rate of plastic dissipation associated with points that enter the plastic zones discussed above and then leave them as the crack initiates. Each point in this plastic zone is loaded to some maximum stress and is then unloaded to zero stress as it is left behind. The plastic energy dissipated by all points undergoing some loading/unloading cycle within plastic zone occupying a volume V_p is given by

$$W_p = \int_{V_p} \int_0^{\epsilon_{ij}^0} \sigma_{ij} d\epsilon_{ij} dV - W_e \tag{8}$$

where W_e is the elastic strain energy and ϵ_{ij}^0 is the current state of strain. W_p was extracted for any mixity and critical load level using a post processing option in ABAQUS. Since fracture parameters are independent of crack length in the strip specimen, Eq. (8) represents the energy dissipated by a series of points along $x_1 = c$ (a constant) that enter and leave the plastic zone as the crack front passes by. The rate change of W_p per unit crack extension over the specimen thickness, b, is then

$$\dot{W}_p = \frac{W_p}{b\Delta a}. \tag{9}$$

For the purposes of this approximation, the plastic zone shape

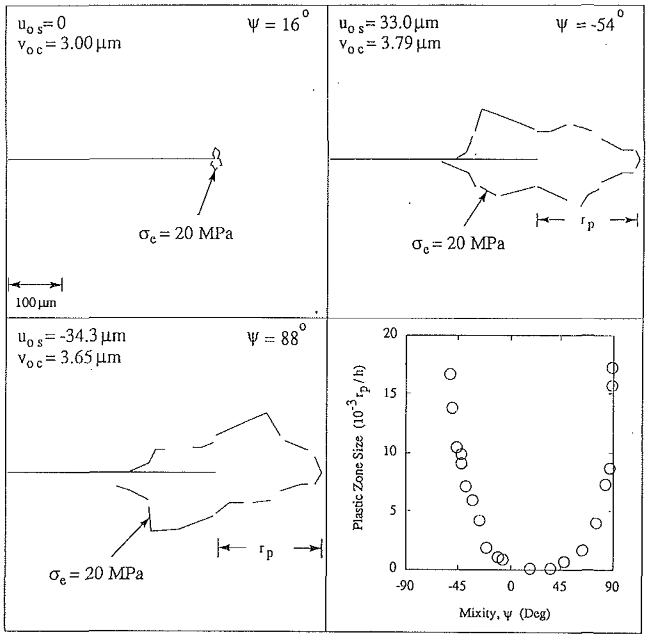

Fig. 8 Plastic zone shapes and sizes at initiation

was taken to be rectangular (Chai, 1990), so that the crack growth increment, Δa, was

$$\Delta a = 2r_p \tag{10}$$

for all points entering and leaving the plastic zone. A more rigorous calculation of $\dot{W}_p$ was conducted by Shivakumar and Crews (1987) for cracks in tough, homogeneous materials. A finite element analysis of a growing crack was used that was beyond the scope of this study. The effect of residual strain energy locked in the wake, which was not considered here, was found to be small.. The values of $\dot{W}_p$ calculated from (9) (Fig. 9(*a*)) were distributed in much the same way was as the toughness values. However, the maximum value of $\dot{W}_p$ was 2.5 J/m^2, more than an order of magnitude less than the maximum G_c value of 36 J/m^2, perhaps indicating the need for a more rigorous dissipation analysis that includes better modeling of the inelastic behavior of the epoxy.

The second potential contribution to the overall interfacial toughness that was considered was the possibility of viscoelastic dissipation in the bulk of the epoxy ahead of the crack since some relaxation had been observed, particularly under shear (Chai, 1990, Fig. 15). It was determined by considering the history of a strip of stressed material of length, Δa, that was originally ahead of the crack front and then unloaded with the passage of the crack front. The viscoelastic dissipation due to a loading/unloading cycle is

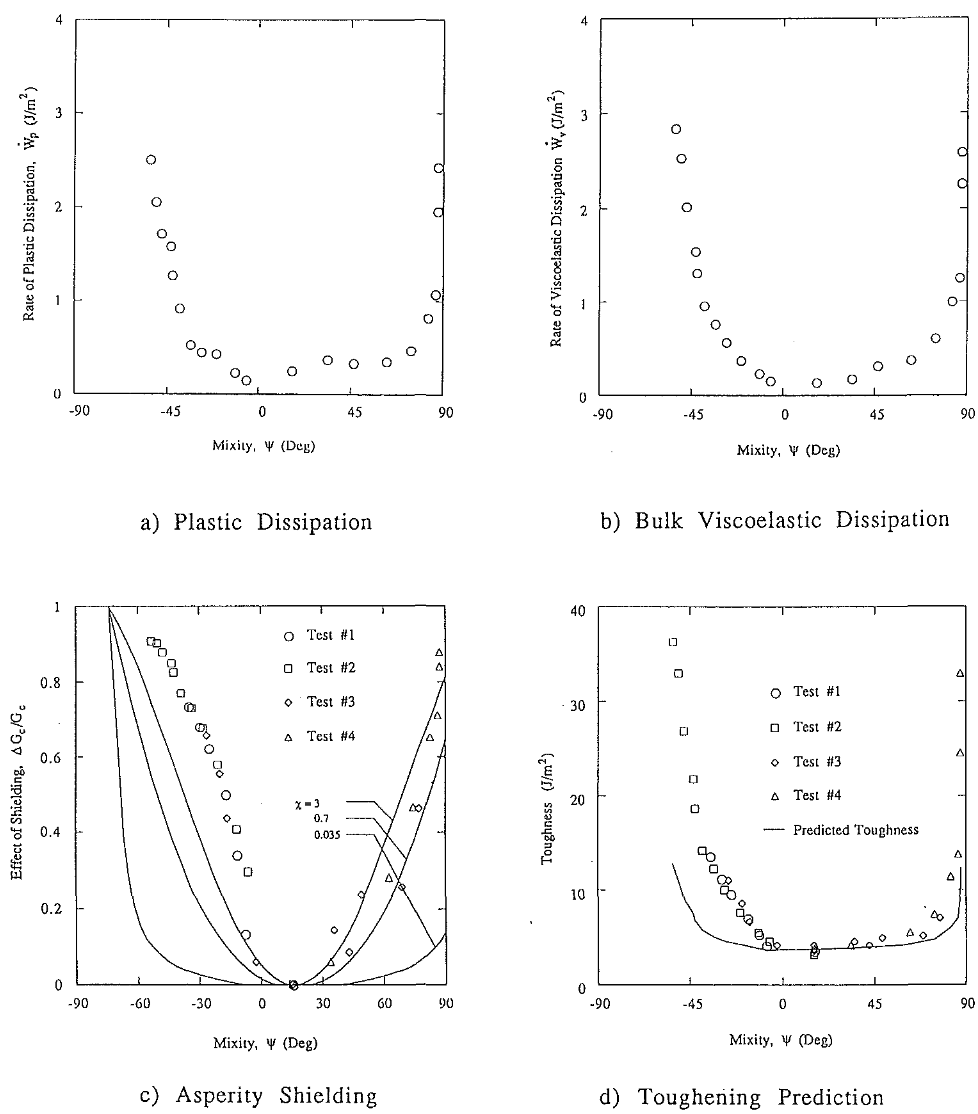

a) Plastic Dissipation

b) Bulk Viscoelastic Dissipation

c) Asperity Shielding

d) Toughening Prediction

Fig. 9 Possible toughening effects

$$W_v = \int_V \int_0^{t_0} \sigma_{ij} \dot{\epsilon}_{ij} dt \, dV. \tag{11}$$

The viscoelastic dissipation in the strip was therefore

$$\Delta W_v = hb\Delta a \int_0^{t_0} \sigma_{ij} \dot{\epsilon}_{ij} dt. \tag{12}$$

The rate of change of dissipation with respect to crack extension was then

$$\dot{W}_v = \frac{\Delta W_v}{b\Delta a} = h \int_0^{t_0} \sigma_{ij} \dot{\epsilon}_{ij} dt \tag{13}$$

The calculation was repeated for each degree of mixity and the results are shown in Fig. 9(*b*)). Under bond-normal loading, $\dot{W}_v$ was almost zero but as the degree of shear was increased, there was the same dramatic increase for large $|\psi|$ values. However, although the distribution of $\dot{W}_v$ was much the same as that of G_c, the values were again considerably lower. The maximum value of $\dot{W}_v$ was 3 J/m^2 which was an order of magnitude lower than the maximum G_c of 36 J/m^2.

Thus it is clear that, although both the plastic and viscoelastic dissipation rates considered here did not increase with increasing shear component, they did not account for the noted increase in interfacial toughness. In fact, since fracture surface roughness does not provide any shielding under bond-normal loading (ψ = 16 deg), the intrinsic adhesive energy γ_a can be found from

$$\gamma_a = [G_c - \dot{W}_p - \dot{W}_v]_{\psi=16} = 4 \ J/m^2. \tag{14}$$

Previous work by Anderson et al. (1974b) using a scanning electron microscope and analyses by Evans and Hutchinson (1989) suggest that the roughness of the fracture surface contributed to the increase in overall toughness that was noted in associated fracture toughness experiments. In Anderson et al. (1974b), the roughness of the fracture surface was considered to have been formed by microbranching of the main crack into the more brittle medium, increasing the effective area of the crack faces. Scanning electron micrographs revealed an increase in the degree of microbranching and hence crack-face area. It was then postulated that, if the increase crack surface area were incorporated in the critical energy release rate calculation, the variation of G_c with mode mix might disappear. In our work, scanning electron micrographs were made of the epoxy fracture surfaces that were obtained for various degrees of mixity. Within the resolution of the SEM (0.01 ~ 0.015 μm), there was no indication whatsoever of any surface features on the epoxy fracture surface, making it unlikely that microbranching could have occurred.

The surface roughness effect considered by Evans and Hutchinson (1989) was that due to the interlocking of crack face asperities that resulted from crack growth along an initially rough interface. The basic idea was that, under bond normal loading, the asperities would not touch and there would be no increase in G_c above γ_a, all other dissipative effects being zero. It was then argued that, as increasing amounts of shear were added, the asperities would contact and thus provide a shielding or toughening effect. The model has several simplifications including an idealized interface morphology, homogeneous elastic properties, and no friction. The increase in overall interfacial toughness ΔG_c due to the shielding effect was taken to be

$$\Delta G_c = G_c - \gamma_a.$$

The governing material parameter χ is given by

$$\chi = \frac{EH^2}{\gamma_a L} \tag{16}$$

where H is the amplitude of the interfacial roughness, L is the wavelength of the roughness, and E is Young's modulus.

The effects of shielding, represented by $\Delta G_c/G_c$, with mode mix (ψ) for various values of the nondimensional material parameter, χ, are plotted in Fig. 9(*c*). The solid lines are model predictions and the discrete points are a replot of the experimental results in Fig. 6. Most of experimental data in the range 16 deg < ψ < 90 deg fall between χ = 0.7 and 3. In the current work, the epoxy was cast directly to a glass adherend whose surface had been polished to a flatness of $\lambda/4$ per inch. The rms amplitude (H) and wavelength (L) of the interfacial roughness were approximately 0.002 μm and 2 μm, respectively. By substituting the modulus of the glass (E = 70 GPa) and the intrinsic adhesive energy (γ_a = 4 J/m^2), current experimental conditions gave rise to a value of χ = 0.035 which produced a toughening effect that was much lower than was measured.

Since the minimum value of G_s occurred at ψ = 16 deg, it was taken as the zero shielding value of ψ in the asperity shielding model. Since the model did not account for friction, the predicted shielding was symmetric about $\psi|_{\Delta G_c=0}$ as shown in Fig. 9(*c*). When the toughness data is considered with respect to ψ = 16 deg and χ values between 3 and 0.7, it can be seen that there was a much stronger shielding effect for ψ < 16 deg than for ψ > 16 deg. Although some of this asymmetry was provided by plasticity and viscoelasticity effects (Figs. 9(*a*), 9(*b*)) most of it must be due to friction which has not yet been considered as a shielding mechanism.

The location of the minimum value of G_c is arbitrary, depending on the choice of the length scale in ψ (Eq. (3)). In this work the chosen length scale was h, a choice based on geometry. Other suggestions (Rice, 1988) have included 1 μm or some characteristic length of the material such as a damage zone, crosslink length, K-dominant zone, etc. Changing the length scale to 1 μm shifts ψ to the left by about 35 deg so that the minimum value of G_c would occur at ψ = −17 deg. For the results presented here, the length scale that shifts ΔG_c = 0 to ψ = 0 is about 140 μm, somewhat smaller than the largest values of plastic zone size that developed.

The sum of the contributions to the toughening effect that have been considered to date are summarized in Fig. 9(*d*) as the predicted toughness. It can be seen that they fall short of the measured values. Although we do expect a synergism between surface roughness and viscoplastic effects, it is unlikely to contribute substantially to the simple addition given here. The comparisons of predicted and measured NCOD particularly under bond-tangential loading (Fig. 4) suggest that one source of improvement could come from better modeling of the inelastic response of the epoxy under multiaxial stress conditions. Another possibility may be frictional contact of crack faces. However, in this context, it must be remembered that all G_c values were obtained under some degree of bond-normal applied displacements which means that, at initiation, the crack faces could only have been in contact over very small regions (less than 1 μm). During the bond-tangential phase of the sequential loadings, the degree of crack face contact was larger, but less than 100 μm. Another factor which may have to be considered in more detail is the variation the crack front shape with mode mix. During the crack initiation experiments, the level of magnification that was used to resolve rear-front fringes was such that the entire crack front could not be monitored. Although it did appear, over the limited field of view, that self-similar growth occurred for all mode mixes, it is possible that edge effects (Chai, 1990) could have produced variations in crack-front geometry, but not to the extent observed by Liechti and Knauss (1982b).

4 Conclusions

A single specimen under biaxial loads was used to determine the interfacial fracture toughness of a glass/epoxy combination over a wide range of mode mixes (−60 deg < ψ < 90 deg).

The toughness increased with increasing positive and negative in-plane shear components. Optical interference measurements of NCOD that were made near the crack front revealed large variations in plastic zone size with mode mix. In the plastic zone, the singularities expected from a power-law hardening representation of the epoxy stress-strain behavior did not arise. Even when the measured stress-strain behavior was considered, the measured NCOD under positive bond-tangential applied displacements revealed a greater degree of blunting than was predicted by finite element analyses that incorporated finite deformation and incremental plasticity. This and the fact that the estimated plastic dissipation, bulk viscoelastic dissipation and interfacial asperity shielding did not account for the noted toughening with shear suggest that the inelastic deformation of the epoxy should be given further consideration. The toughening effect was notably higher for negative mode mixes, suggesting that frictional effects may play a role.

Acknowledgment

The authors would like to acknowledge the support of the National Science Foundation through Grant Number MSM-8813822. The digital image analysis system and some of the loading device components were provided under the University Research Instrumentation Program through the Office of Naval Research (Grant Number N00014-84-G-0175). We would also like to thank Jan Shrode for her timely preparation of the manuscript.

References

Adamjee, W., 1989, "Mixed-Mode Fracture Analysis of Cathodic Delamination in Rubber to Metal Bonds," Engineering Mechanics Research Laboratory Report #EMRL 89/8, M.S. Thesis, Dec. 1989, The University of Texas at Austin.

Anderson, G. P., DeVries, K. L., and Williams, M. L., 1974a, "Mixed Mode Stress Field Effect in Adhesive Fracture," *International Journal of Fracture*, Vol. 10, pp. 565–583.

Anderson, G. P., DeVries, K. L., and Williams, M. L., 1974b, "The Influence of Loading Direction Upon the Character of Adhesive Bonding," *J. Colloid and Int. Sci.*, Vol. 47, pp. 600–609.

Aravas, N., and Sharma, S. M., 1991, "An Elastoplastic Analysis of the Interface Crack with Contact Zones," *Journal of the Mechanics and Physics of Solids*, Vol. 39, pp. 311–344.

Argon, S. A., Gupta, V., Landis, H. S., and Cornie, J. A., 1989, "Intrinsic Toughness of Interfaces Between *SiC* Coatings and Substrates of *Si* or *C* Fiber," *Journal of Materials Science*, Vol. 24, pp. 1406–1412.

Atkinson, C., 1977, "On Quasistatic Problems of Cracks in a Non-Homogeneous Elastic Layer," *Acta Mechanica*, Vol. 26, pp. 103–113.

Cao, H. C., and Evans, A. G., 1989, "An Experimental Study of the Fracture Resistance of Bimaterial Interfaces," *Mechanics of Materials*, Vol. 7, pp. 295–304.

Chai, H., 1990, "Three-Dimensional Fracture Analysis of Thin Film Debonding," *International Journal of Fracture*, Vol. 46, pp. 237–256.

Chai, Y.-S., 1990, "Interfacial Toughness under Biaxial Loading," Engineering Mechanics Research Laboratory Report #EMRL 90/1, Ph.D. Dissertation, The University of Texas at Austin.

Chan, K. S., and Davidson, D. L., 1989, "Driving Forces for Composite Interface Fatigue Cracks," *Engineering Fracture Mechanics*, Vol. 33, pp. 451–466.

Charalambides, P. G., Lund, J., Evans, A. G., and McMeeking, R. M., 1989, "A Test Specimen for Determining the Fracture Resistance of Bimaterial Interfaces," ASME Journal of Applied Mechanics, Vol. 56, pp. 77–82.

Comninou, M., and Schmueser, D., 1979, "The Interface Crack in a Combined Tension-Compression and Shear Field," ASME Journal of Applied Mechanics, Vol. 46, pp. 345–348.

Evans, A. G., and Hutchinson, J. W., 1989, "Effects of Non-Planarity on the Mixed-Mode Fracture Resistance of Bimaterial Interfaces," *Acta Metallurgica*, Vol. 37, pp. 909–916.

Gupta, V., Argon, A. S., and Cornie, J. A., 1989, "Interfaces with Controlled Toughness as Mechanical Fuses to Isolate Fibers from Damage," *Journal of Materials Science*, Vol. 24, pp. 1207–1218.

Hamadeh, R. F., Dillard, D. A., and Davis, M. E., 1989, "Durability of Elastomer/Metal Adhesive Bonds: Stress Effects on Delamination," *Journal of Adhesion Science*, in review.

Jensen, H. M., Hutchinson, J. W., and Kim, K.-S., 1990, "Decohesion of a Cut Prestressed Film on a Substrate," *International Journal of Solids and Structures*, Vol. 26, pp. 1099–1114.

Liechti, K. M., and Knauss, W. G., 1982, "Crack Propagation at Material Interfaces: I. Experimental Technique to Determine Crack Profiles," *Experimental Mechanics*, Vol. 22, pp. 262–269.

Liechti, K. M., and Knauss, W. G., 1982b, "Crack Propagation at Material Interfaces: II. Experiments on Mode Interaction," *Experimental Mechanics*, Vol. 22, pp. 383–391.

Liechti, K. M., and Hanson, E. C., 1988, "Nonlinear Effects in Mixed-Mode Interfacial Delaminations," *International Journal of Fracture*, Vol. 36, pp. 199–217.

Liechti, K. M., and Chai, Y.-S., 1991, "Biaxial Loading Experiments for Determining Interfacial Toughness," ASME Journal of Applied Mechanics, Vol. 58, pp. 680–687.

Lin, C., 1989, "Fracture Analysis of Cathodic Delamination in Rubber to Metal Bonds," Engineering Mechanics Research Laboratory Report #EMRL 89/7, Ph.D. Dissertation, The University of Texas at Austin.

Malyshev, B. M., and Salganik, R. L., 1965, "The Strength of Adhesive Joints Using the Theory of Cracks," *International Journal of Fracture*, Vol. 1, pp. 114–128.

Mulville, D. R., and Vaishnav, R. N., 1975, "Interfacial Crack Propagation," *Journal of Adhesion*, Vol. 7, pp. 215–233.

Mulville, D. R., Hunston, D. L., and Mast, P. W., 1978, "Developing Failure Criteria for Adhesive Joints under Complex Loading," *J. Eng. Mat. Tech.*, Vol. 100, pp. 25–31.

Needleman, A., 1990, "An Analysis of Tensile Decohesion Along an Interface," *Journal of the Mechanics and Physics of Solids*, Vol. 38, pp. 289–324.

Rosenfeld, L. G., Ritter, J. E., Lardner, T. J., and Lin, M. R., 1990, "Use of the Microindentation Technique for Determining Interfacial Fracture Energy," *Journal of Applied Physics*, Vol. 67, pp. 3391–3396.

Shih, C. F., Asaro, R. J., and O'Dowd, N. P., 1991, "Elastic-Plastic Analysis of Cracks on Bimaterial Interfaces: Part II—Structure of Small Scale Yielding Fields," ASME Journal of Applied Mechanics, Vol. 58, pp. 450–463.

Shih, C. F., 1990, private communication.

Shivakumar, K. N., and Crews, J. H., Jr., 1987, "Energy Dissipation Associated with Crack Extension in an Elastic-Plastic Material," *Engineering Fracture Mechanics*, Vol. 28, pp. 319–330.

Takashi, N., Yamazaki, K., Natsume, T., and Takebe, T., 1978, "Debonding of an Al-Epoxy System by Blister Method," *21st Japan Congress on Materials Research—Non-Metallic Materials*, pp. 260–264.

Trantina, G. C., 1972, "Combined Mode Crack Extension in Adhesive Joints," *Journal of Composite Materials*, Vol. 6, pp. 271–385.

Wang, J.-S., and Suo, Z., 1990, "Experimental Determination of Interfacial Toughness Curves Using Brazil-Nut Sandwiches," *Acta. Metall. Mater.*, Vol. 38, pp. 1279–1290.

Yau, J. F., and Wang, S. S., 1984, "An Analysis of Interface Cracks Between Dissimilar Isotropic Materials Using Conservation Integrals in Elasticity," *Engineering Fracture Mechanics*, Vol. 20, pp. 423–432.

S. N. Chang

D.-T. Chung

Agency for Defence Development,
Materials Research and Development Center
Taejon 300-600, South Korea

Y.-F. Li

S. Nemat-Nasser
Fellow ASME.

Center of Excellence for Advanced Materials,
Department of Applied Mechanics and
Engineering Science,
University of California, San Diego,
La Jolla, Ca 92093

Target Configurations for Plate-Impact Recovery Experiments

Normal plate impact recovery experiments have been perfomed on thin plates of ceramics, with and without a back momentum trap, in a one-stage gas gun. The free-surface velocity of the momentum trap was measured, using a normal velocity (or displacement) interferometer. In all recovered samples, cross-shaped cracks were seen to have been formed during the impact, at impact velocities as low as 27 m/s, even though star-shaped flyer plates were used. These cracks appear to be due to in-plane tensile stresses which develop in the sample as a result of the size mismatch between the flyer plate and the specimen (the impacting area of the flyer being smaller than the impacted area of the target) and because of the free-edge effects. Finite element computations, using PRONTO-2D and DYNA-3D, based on linear elasticity, confirm this observation. Based on numerical computations, a simple configuration for plate impact experiments is proposed, which minimizes the in-plane tensile stresses allowing recovery experiments at much higher velocities than possible by the star-shaped flyer plate configuration. This is confirmed by normal plate impact recovery experiments which produced no tensile cracks at velocities in a range where the star-shaped flyer invariably introduces cross-shaped cracks in the sample. The new configuration includes lateral as well as longitudinal momentum traps.

Introduction

Flyer-plate impact experiments with momentum traps and displacement and velocity interferometry provide a powerful technique for recovery studies of deformation and failure modes of materials. With a suitable design of flyer, specimen, and momentum trap configuration, it is possible to subject the specimen to predetermined stress pulses of varied durations and amplitudes, and to directly monitor these pulses by interferometric measurement of the particle displacements and velocities at the back face of the momentum trap.

In the plate-impact study of ceramics and ceramic composites, it is of importance to avoid the generation of undesirable tensile stresses in the specimen. Such stresses can emerge through wave reflection from the boundaries of the flyer, specimen, and momentum traps, as well as through size mismatch between the flyer and the specimen, i.e., when the impacting area of the flyer is smaller than the impacted area of the target.

To avoid tensile stresses reflecting from the free boundaries, a star-shaped flyer plate has been proposed by Kumar and Clifton (1977) and extensively used; (see, e.g., Yaziv, (1985). Notwithstanding this, tensile cracks are commonly observed to form normal to the free edges of brittle samples, in the middle of each edge. These cracks are longer on the back face, which is in contact with the momentum trap, than on the front impact face, suggesting that they are formed at the free edges of the sample on the back face, and then extend through the thickness normal to the edge.

To understand the origin of such cracking, two and three-dimensional finite element simulations are performed, using PRONTO-2D (Taylor and Flanagan, 1987) and DYNA-3D (Hallquist and Benson, 1986) and assuming a linearly elastic response. Preliminary results of this effort were reported by Chang et al. (1989). Here we examine this problem in some detail both numerically and experimentally.

Calculations confirm that in-plane tensile stresses are generated in the back face of the sample. These in-plane tensile stresses are essentially due to the fact that the impacting area of the flyer is smaller than the total area of the sample. They occur whenever the sample area is larger than the area of the flyer plate, whatever the shape of the flyer plate (e.g., star-shaped) or the sample (e.g., star-shaped). Their intensity increases with an increase in the linear momentum transmitted and an increase in the mismatch in the flyer and the target areas. They can produce tensile cracks on the back face, possibly from existing microcracks. A simple estimate based on linear fracture mechanics shows that, to produce a crack in this material by a 0.5 GPa tensile stress, a preexisting flaw of 200–300 mm is required at an interior point, but a flaw of only half this size at an edge. Since the sample is cut at the edges, the cracking invariably starts there, where there tend to be more and larger pre-existing flaws. In addition to tensile stresses due to the impact area mismatch, waves reflecting off the free

Contributed by the Applied Mechanics Division of The American Society of Mechanical Engineers for presentation at the 1992 ASME Summer Mechanics and Materials Meeting, Tempe, AZ, Apr. 28–May 1, 1992.

Discussion on this paper should be addressed to the Technical Editor, Prof. Leon M. Keer, The Technological Institute, Northwestern University, Evanston, IL 50208, and will be accepted until four months after final publication of the paper itself in the Journal of Applied Mechanics. Manuscript received by the ASME Applied Mechanics Division, Dec. 4, 1990; final revision, May 2, 1991. Paper No. 92-APM-18.

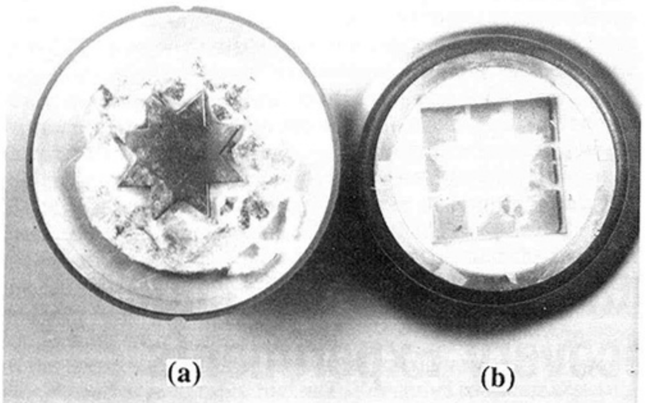

Fig. 1 (*a*) Star-shaped flyer plate with projectile after test; (*b*) the star-shaped trace on impacted face of square aluminum-coated Mg-PSZ specimen

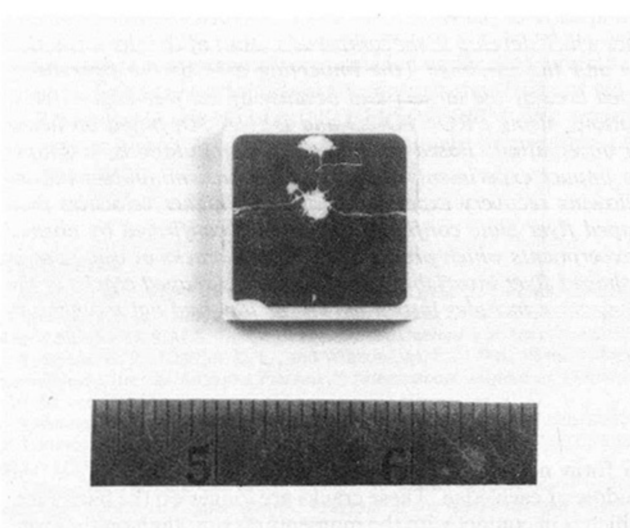

Fig. 2(*a*)

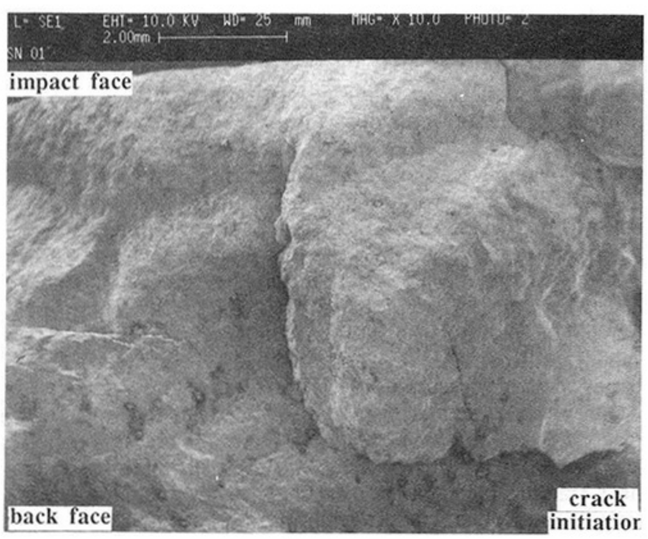

Fig. 2(*b*)

Fig. 2 (*a*) Back face of Mg-PSZ specimen impacted at 47 m/s showing cracks emanating from the middle of four edges; (*b*) fracture surface normal to the impact direction showing crack initiation and growth toward the impact face

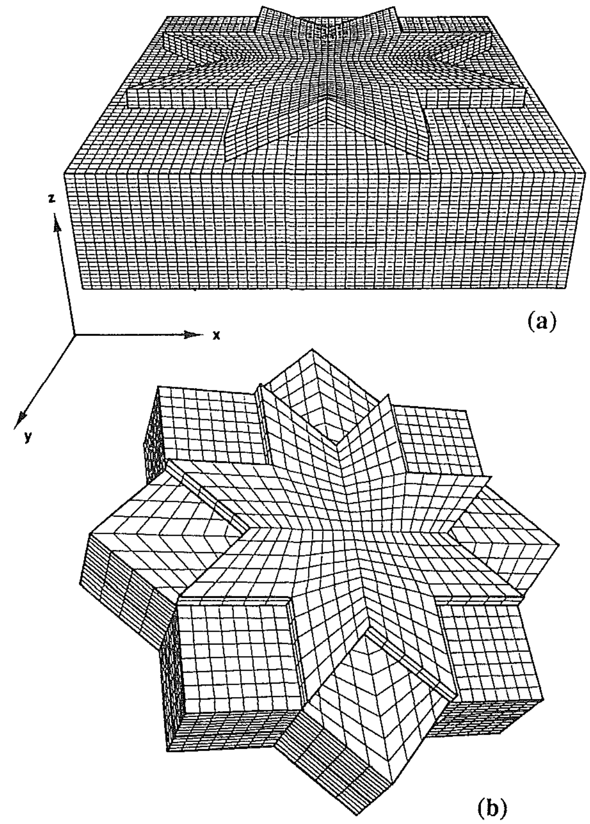

Fig. 3 Plate impact configurations for DYNA-3D computation; (*a*) star-shaped flyer plate and square target plate and momentum trap; (*b*) star-shaped flyer, target, and momentum trap

edges do produce in-plane tensile stresses which can cause cracking. Hence, both the size effect (i.e., mismatch in impact areas) and the effect of free edges must be carefully considered for a proper recovery design.

Based on numerical computations a simple construction is proposed, which should alleviate some of the problems of cracking, especially those associated with the flyer-sample impact area mismatch. All the parts entering this construction, including the flyer plate, are rectangular. The relative dimensions are estimated from the finite element computations, to minimize the possibility of cracking. The effectiveness of this construction is established experimentally.

In the sequel, we first report our experimental results, and then discuss our numerical study.

Experimental Procedures

The specimens used in this experimental work are 25.4-mm square 8-mm thick Mg-PSZ plates. Compression plane waves are generated in these plates by the impact of a star-shaped flyer in a 59.3-mm diameter gas gun. The specimen, flyer plate, and momentum trap are lapped to be optically flat. The experimental setup is carefully aligned to ensure a plane longitudinal wave at the center of the specimen. The targets are subjected to normal compression ranging from 0.5 to 2.5 GPa and pulse duration of about 1 μs. After the first impact, the projectile is stopped by an anvil which prevents subsequent additional impacts. The rear surface velocity of the momentum trap is measured by normal displacement interferometry (NDI; Baker, 1968) and normal velocity interferometry (NVI; Baker and Hollenbach, 1965). Since the momentum trap remains elastic, this measurement yields the normal stress transmitted by the sample to the momentum trap. The recovered specimens are cut normal to the impact face, polished, and analyzed by optical and scanning electron microscopy and X-ray diffractometry.

Experimental Results and Discussion

Cracks in Recovered Specimens. Figures 1(*a*) and (*b*) show the star-shaped flyer plate with projectile, and the trace of the star-shaped flyer on the impact face of the sample. With the star-shaped flyer plate, cracks are observed to have formed at the middle of each free edge of the sample, extending toward the center. These cracks are longer on the back face than on the front face of the sample. Figure 2(*a*) shows the back face of the cracked specimen, and Fig. 2(*b*) displays the fracture surface normal to the impact direction (from one of the four pieces shown in Fig. 2(*a*)). The cracks initiate at the center of the edge of the specimen and propagate toward the impact face. The cracks are short when the impact velocity is low (or the flyer plate is thin). They are always longer on the back face than on the impact face.

Numerical Simulation of Plate Impact Experiment. Since we are concerned with brittle materials such as ceramics and their composites, a great deal can be learned from analysis based on linear elasticity. Therefore, two and three-dimensional finite element computations are performed, assuming linear elasticity, to understand wave interaction in various plate impact configurations. Figures 3(*a*) and (*b*) show three-dimensional meshes consisting of hexahedron elements to simulate the normal plate impact test with star-shaped flyers, targets, and momentum traps. All the dimensions and materials used in the computations are similar to those used in the experiments. The computations show that in-plane (*i.e., in the* x, y*-plane*) *tensile stresses are developed in the sample when the impact area of the flyer plate is smaller than the area of the target, essentially independently of the shapes of the flyer plate and the sample.* These in-plane tensile stresses can then initiate tensile cracks on the back face of the sample. For a star-shaped flyer plate and a rectangular sample, typical contours of constant σ_{xx} are shown in the first quadrant of the x, y-plane, a short distance (i.e., one element) from the back face of the specimen, at a fixed instant; see Fig. 4 ($a-d$). As is seen, at the upper left corner and at the lower right corner which are the centers of two edges of the sample, the generated in-plane tensile stresses are maximum. Later, the tensile stresses are also generated at the center of the plate, as is seen in Figs. 4(*c*) and (*d*). It is noted that the contour lines of σ_{yy} and σ_{xx} are symmetric with respect to the diagonal line from the upper right to the lower left in the quadrant. The stress state of Fig. 4($a-d$) can clearly explain the fracturing of the PSZ square target plate, impacted at a velocity of 47 m/s. In this test, four

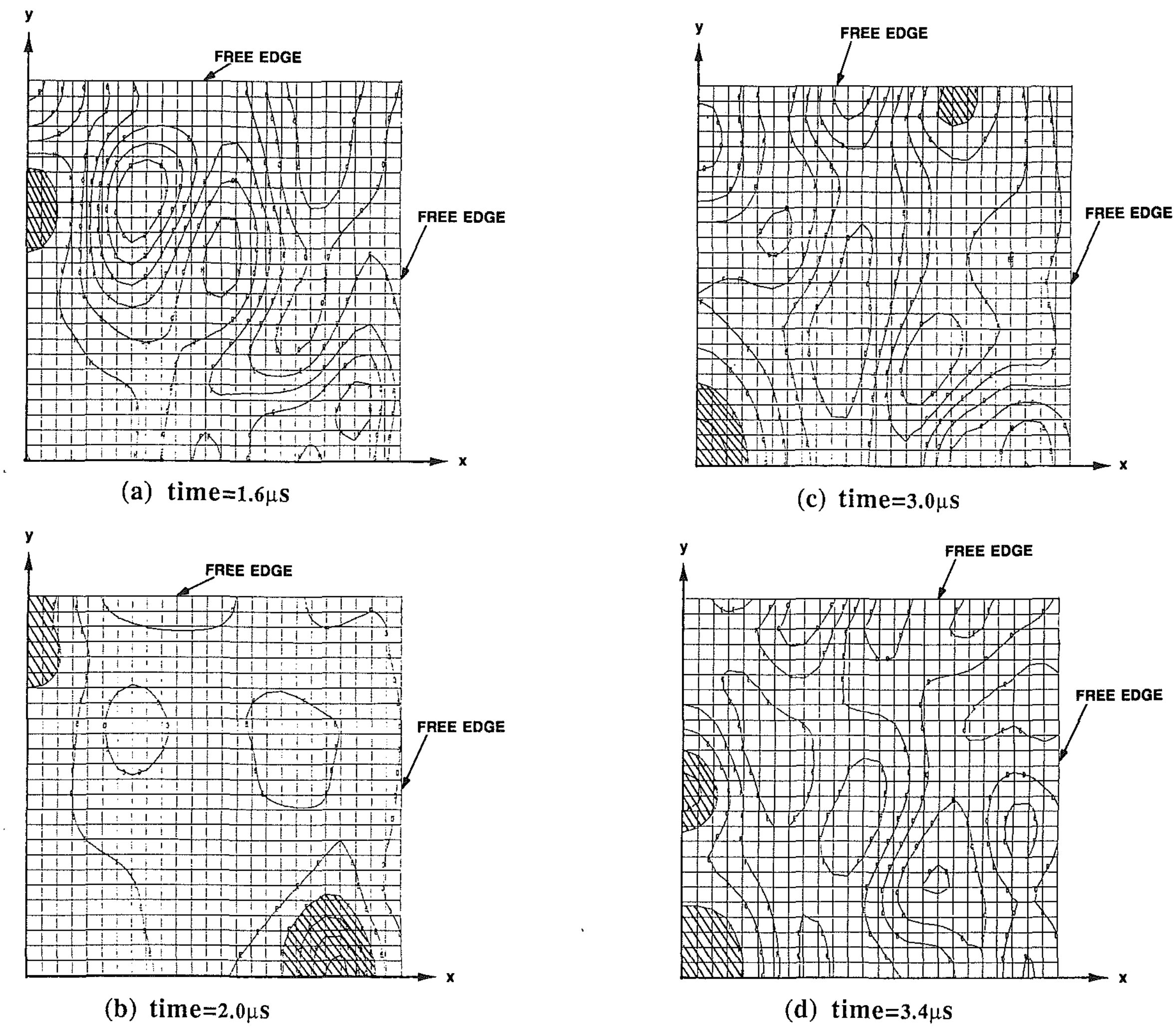

Fig. 4 Contour plots of σ_{xx} in the first quadrant of the x, y-plane parallel to the impact face, a short distance from the back face of the specimen at indicated instances after impact for Fig. 3(*a*) configuration (impact velocity is 60 m/s); in-plane tensile stresses in hatched area are greater than 400 MPa: three-dimensional elasticity calculation

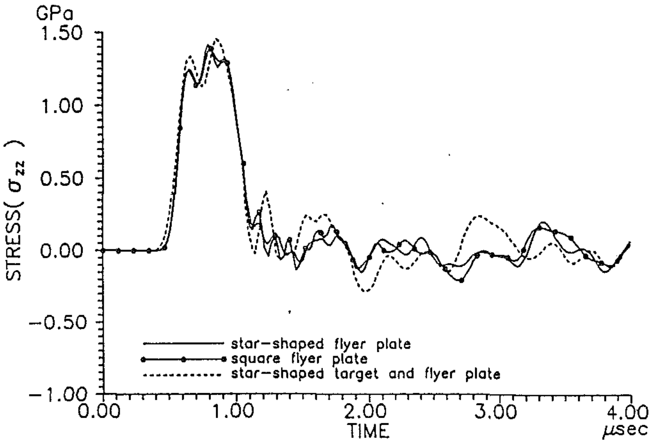

(a)

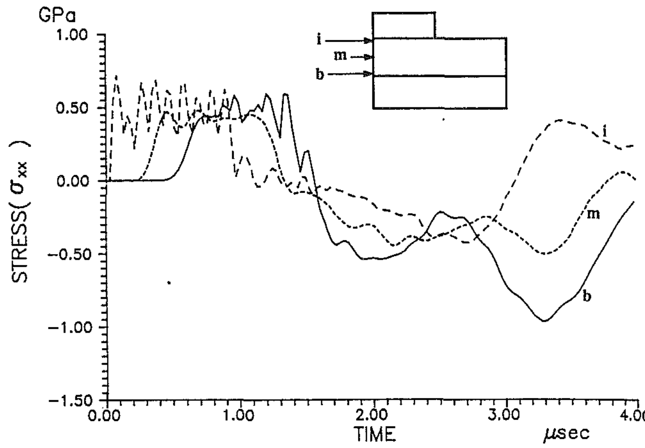

(a)

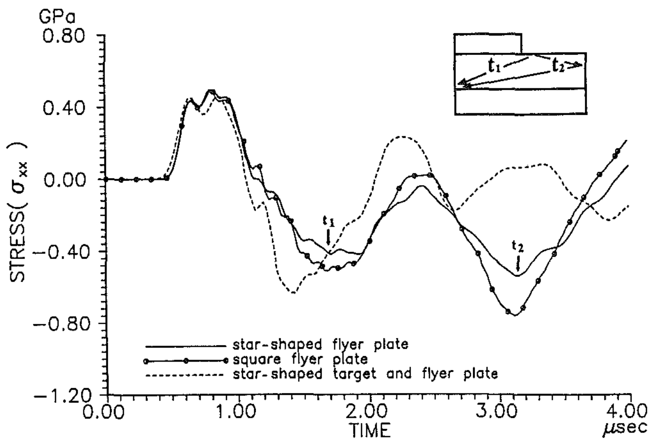

(b)

Fig. 5 Time history plots of (*a*) σ_{zz} and (*b*) σ_{xx} at the center near the back face of the specimen in different configurations: a three-dimensional elasticity calculation; impact velocity is 60 m/s; *z* is the impact direction (compression is positive)

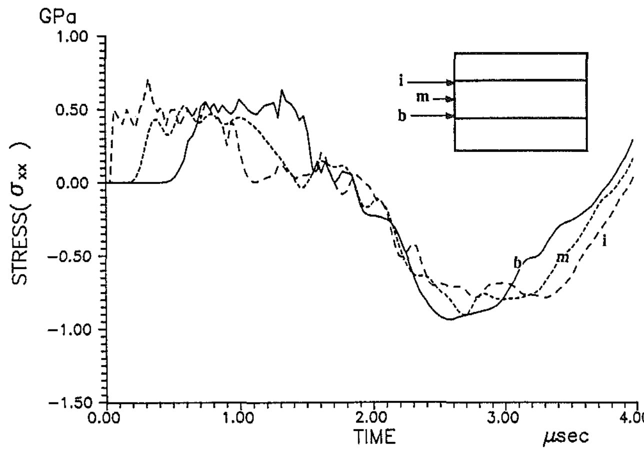

(b)

Fig. 6 (*a*) σ_{xx} at different locations along the central axis of the specimen in star-shaped flyer configuration and (*b*) σ_{xx} at different locations along the central axis of the specimen for square flyer configuration: a three-dimensional elasticity calculation; impact velocity is 60 m/s; *z* is the impact direction (compression is positive)

fracture pieces were recovered. In our experience, fractures of this kind at such low velocities have occurred as a rule with essentially no exception.

We have also performed similar three-dimensional computations for a configuration involving *a star-shaped flyer* and *a star-shaped sample*, which has been used by Longy and Cagnoux (1989) as shown in Fig. 3(*b*). Here again, since the target has greater area (its impacted face is larger) than the flyer, large in-plane tensile stresses are produced at the back face of the sample. A typical example is seen in Figs. 5(*a*) and (*b*). In these figures, we have plotted the σ_{zz}-stress (Fig. 5(*a*)) and the in-plane σ_{xx}-stress (Fig. 5(*b*)) at the center near the back face of the target (an element from the back momentum trap), for the following configurations:

(1) star-shaped flyer, square target and back momentum trap;
(2) square flyer (with the same impact area as the star-shaped flyer plate in (1)), square target and back momentum trap;
(3) star-shaped flyer, target, and momentum trap.

The σ_{zz}-stress profiles are shown in Fig. 5(*a*) and the corresponding σ_{xx}-stress profiles in Fig. 5(*b*); these are for a fixed point on the back of the sample. As is seen, large tensile stresses are produced for all three flyer-target configurations. There are two peak tensile stresses which follow the main compressive pulse, although in the case of configuration (3), the second tensile pulse is reduced. The first appears to be due to the size (area) mismatch, and the second is generated from the lateral boundary of the target after the separation of the momentum trap. The time, t_1 in Fig. 5(*b*), when the first tensile pulse is maximum, corresponds to the travelling time of the elastic wave from the traction-free part of the impact face of the specimen. The time t_1 denotes the travelling time from the edge of the flyer plate to the lateral boundary of the target and then to the point of calculation. Figure 6(*a*) shows σ_{xx}-time plots predicted at three different locations for configuration (1). These are: near the impact face(*i*); in the middle(*m*); and near the back face(*b*); all three are along the central axis of the square target. The first tensile peak appears only at the back face. In-plane tensile stresses, originating from the target-flyer area mismatch, increase in magnitude as the calculation point approaches the back face. After three microseconds, the tensile stress along the central axis is larger near the back face than in the middle, while the compression stress is built up near the impact face. This may be due to the fact that the impact face of the flyer is smaller than that of the target. For the case of configuration (2) we do not observe this phenomenon, as is seen in Fig. 6(*b*). Figure 7 shows the effect of flyer plate thickness, at a constant impact velocity, on the tensile stresses calculated for configuration (1). The magnitude of the tensile stresses increases with increasing thickness of the flyer plate.

It thus appears that, if the flyer plate is smaller (has smaller

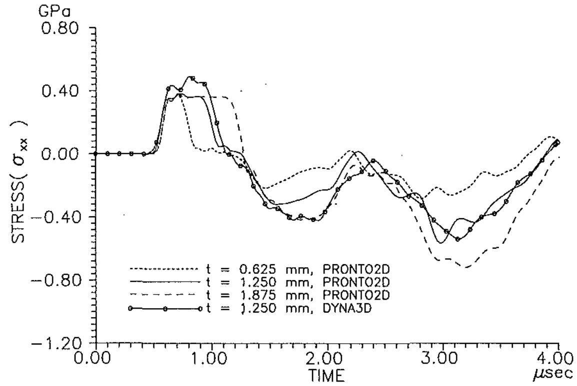

Fig. 7 Time history plots of σ_{xx} at the center near the back face of the specimen showing the effect of flyer plate thickness for an impact velocity of 60 m/s; results from the three-dimensional calculation are also shown for comparison with those from PRONTO-2D (compression is positive)

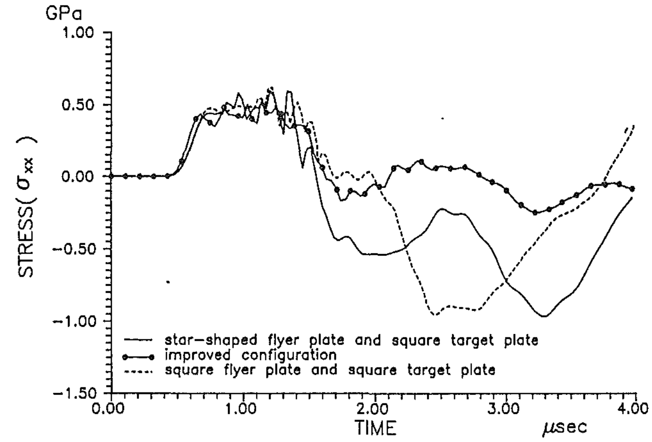

Fig. 9 Time history plots of σ_{xx} at the center near the back face of the specimen for different configurations: impact velocity is 60 m/s (compression is positive)

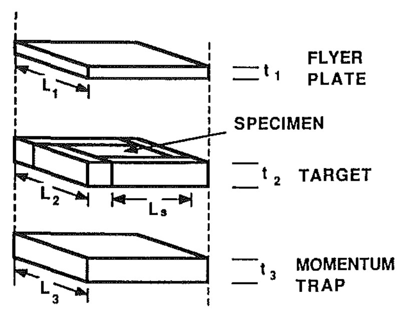

Fig. 8 Schematic drawing of improved configuration for the normal plate-impact recovery test

impacting area) than the target and if it imparts sufficient momentum to the target, then tension cracks can be generated on the back face of the target, normal to the free edges for a rectangular brittle target. These cracks may propagate through the thickness, toward the front face of the target. This confirms our experimental results shown in Fig. 2(*b*). While cracks can form at interior flaws in regions of high tensile stresses, there are two obvious reasons why edge cracks are more likely to be formed than cracks away from the edges for the kind of experiments with rectangular targets discussed in the previous section. They are: (1) the cutting process produces pre-existing flaws at the sample edges; and (2) the same in-plane tensile driving stress activates an edge flaw of roughly half the size of an interior flaw. Our experiments clearly show that cracks are invariably initiated at the back face of the sample, from its edges. The star-shaped flyer plate does *not* prevent this kind of cracking.

Improved Flyer-Target Configuration. To minimize fracturing of the sample in normal plate-impact experiments, it is necessary to reduce or eliminate the unwanted in-plane tensile stresses. To this end, computational simulations are used to obtain wave profiles due to the plate impact for various geometries of flyer plate and target. Linear elasticity theory is employed and both PRONTO-2D and DYNA-3D computer codes are used. The results show that with a flyer plate larger than the target and with lateral momentum traps attached to the sample, the tensile stresses can be eliminated in a range of impact velocities, and minimized, in general. The dimensions of the flyer plate must be related to those of the target in order to obtain an optimal result. Figure 8 shows a square configuration designed to reduce the tensile stresses. The dimensions in this construction must be constrained as follows:

$$L_1 \geq L_2 \geq L_3 \geq L_s, \quad L_2 - L_s \geq 4t_1, \quad L_2 - L_s \geq 4t_2, \quad t_3 \geq t_1.$$

The symbols are defined in Fig. 8. It is noted that the width of a lateral momentum trap, $(L_2 L_s)/2$, should be larger than twice the thickness of the flyer and the target. Figure 9 shows the σ_{xx}-time diagram for the following configurations:

(*a*) star-shaped flyer, square target and back momentum trap;
(*b*) the proposed configuration which includes lateral and back momentum traps;
(*c*) square flyer that matches the impact size, square target and back momentum trap without lateral momentum trap.

Numerical simulations show that, for the same linear momentum, the magnitude of the first tensile pulse decreases with decreasing size mismatch between the flyer and the target. Thus, in the case of configuration (*c*), there is only one in-plane tensile stress peak, generated from the lateral free surfaces of the target.

Experimental Verification of Proposed Configuration

Normal plate-impact recovery tests of the proposed configuration, configuration (*b*), have been performed. The sample and the lateral momentum traps are made of Mg-PSZ. The flyer plate and the back momentum trap are maraging steel; see Fig. 10(*a*). Four copper wires attached to the target are to monitor the tilt at the time of the impact. The target assembly is placed in a carefully designed holder in order that the projectile is stopped by an anvil after the first impact, which is shown in Fig. 10(*b*). This recovery experiment produces no tensile cracks in the PSZ sample impacted at 66 m/s. The cracks occur in the Mg-PSZ lateral momentum traps, as schematically illustrated in Fig. 10(*c*).

The impedance of various constituents in the impact assembly must be carefully matched, in order to reduce complex wave interactions, and hence in-plane tensile stresses; see Fig. 11. However, computations show that, even when the entire target assembly consists of the same material (e.g., Mg-PSZ), an in-plane tensile stress of about 400 MPa is generated by an impact velocity of 120 m/s, right after the compressive stress pulse passes the center of the specimen.

To check this computational prediction, an impact test of the proposed configuration with Mg-PSZ flyer plate, specimen, and momentum traps has been performed. Figure 12(*a*) shows a recovered Mg-PSZ target assembly impacted at 122 m/s (longitudinal compressive stress is 2.5 GPa). The sample was fractured into four pieces by the in-plane tensile stresses, possibly generated from the interface of the specimen and the lateral momentum traps. No damage was observed in the specimen due to the uniaxial compressive stresses. Figures 12(*b*)

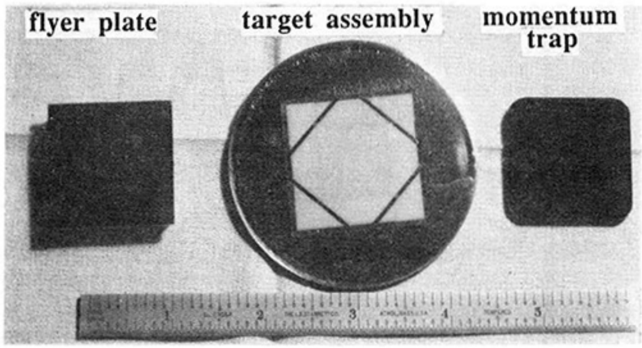

Fig. 10(*a*)

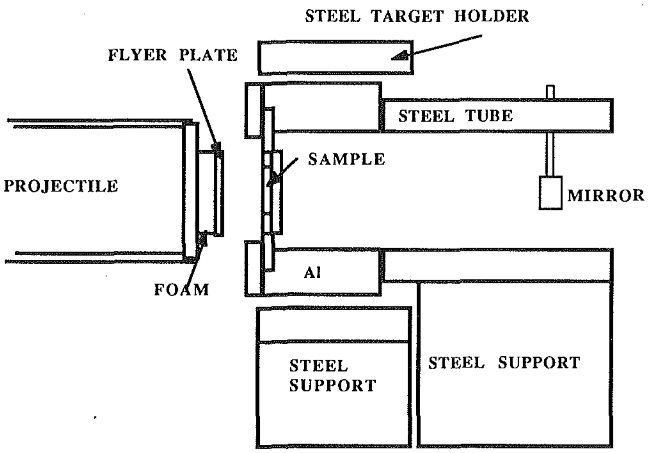

Fig. 10(*b*)

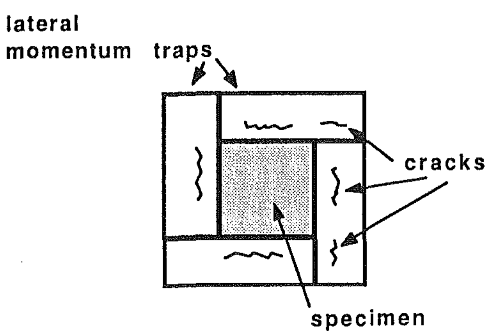

Fig. 10(*c*)

Fig. 10 (*a*) Photographs of flyer plate, target assembly, and momentum trap; the target consists of a Mg-PSZ sample and four lateral momentum traps, copper wire tilt pins, and aluminum ring; dimensions of the maraging steel flyer plate are 34.3mm × 34.3mm with 2.54mm thickness, specimen is 19.1mm × 19.1mm × 3.8mm, and the lateral momentum trap is 7.6mm × 26.7mm × 3.8mm; (*b*) plate-impact arrangement to study the effect of uniaxial compressive strain on material response; (*c*) schematic drawing of cracks in lateral momentum traps produced in a 66 m/s impact experiment

and (*c*) show a recovered Mg-PSZ momentum trap which originally was a rectangular plate. Spalling has occurred on a single plane at mid-thickness of the momentum trap, splitting it into two half-plates. These half-plates are then fractured by the in-plane tensile stresses. Figure 12(*b*) shows the fractured half-plate next to the back face of the specimen, and Fig. 12(*c*) shows the other half-plate. X-ray diffraction analysis shows evidence of tetragonal to monoclinic ($t \rightarrow m$) phase transformation on the spalled surfaces. However, it was not possible to detect any such transformation at the interior of the im-

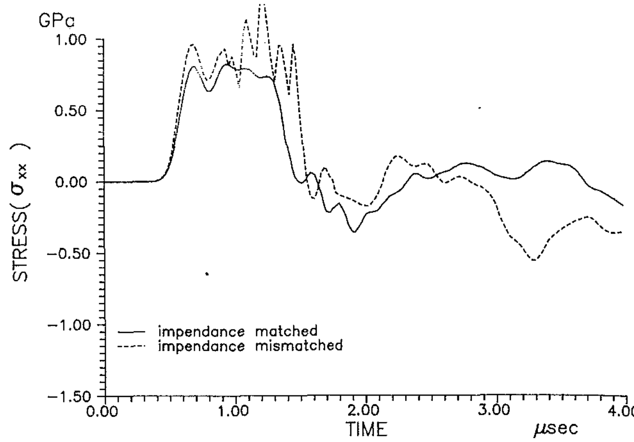

Fig. 11 Time history plots of σ_{xx} at the center near the back face of the specimen showing the effect of impedance difference on generating in-plane tensile stresses; for the same improved square configuration the generated tensile stress is higher in the Mg-PSZ target when impacted by a maraging steel flyer than when impacted by an Mg-PSZ flyer; impact velocity is 120 m/s (compression is positive)

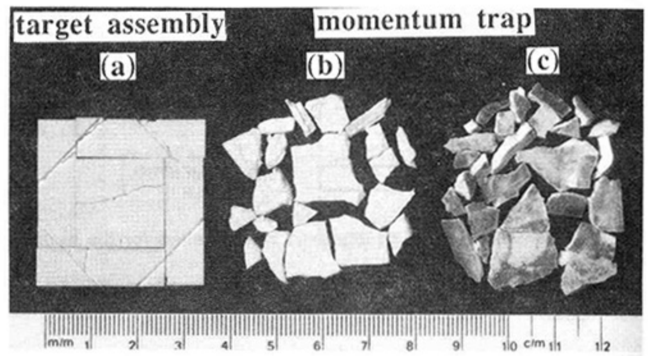

Fig. 12 Photographs of recovered Mg-PSZ target assembly after impacted at 122 m/s by Mg-PSZ flyer plate, showing the specimen fractured into four pieces (*a*) and the back momentum trap spalled into two plates ((*b*) and (*c*)); a part of the back momentum trap next to the back face of the target assembly (*b*) and a free-surface part of the back momentum trap sputter-coated gold-platinum to reflect the laser beam (*c*)

pacted specimen which was not subjected to any axial tensile stresses.

Conclusions

In plate-impact recovery experiments with star-shaped flyer plates, cracks have been observed at the middle of each free edge of ceramic samples, even at impact velocities as low as 27 m/s. Two and three-dimensional finite element simulations show that tensile stresses in the specimen are generated through wave reflection from the boundaries of the flyer, specimen, and the momentum traps, as well as through size (area) mismatch between the flyer and the target. When the impact face of the flyer is smaller than that of the target specimen, in-plane tensile stresses are generated in the specimen. An improved configuration for soft-recovery impact experiments is suggested, based on numerical computations using linear elasticity and two and three-dimensional finite element codes. All parts in this configuration are rectangular. The predictions of these numerical simulations have been verified experimentally. No cracks are observed in the recovered samples which were impacted at less than 66 m/s. However, at an impact velocity of 122 m/s, the sample was broken into four pieces, even though the same material (Mg-PSZ) was used for the entire assembly. The three-dimensional computations suggest that in-plane tensile stress pulses originate from the interface between the specimen and the lateral momentum traps. These tensile stresses can therefore be reduced, using a large specimen with lateral momentum traps. Our carefully coordinated experimental and computational study suggests that a better understanding of wave interaction, which leads to the generation of tensile stresses in plate-impact recovery experiments, is necessary in order to be able to study the dynamic behavior of brittle materials at high and ultrahigh strain rates.

Acknowledgment

The authors acknowledge valuable discussions with Dr. D. J. Benson regarding the use of DYNA-3D code. The computations reported here were carried out on a CRAY-XMP at San Diego Supercomputer Center, access to which was made possible by a National Science Foundation program. This work was supported by the U.S. Army Research Office under Contract Nos. DAAL-03-86-K-0169 and DAAL-03-88-K-0118 to the University of California, San Diego.

References

Barker, L. M., 1968, "Fine Structure of Compressive and Release Wave Shapes in Aluminum Measured by the Velocity Interferometer Technique," *Behavior of Dense Media Under High Dynamic Pressures*, Gordon and Breach, New York, pp. 483–504.

Barker, L. M., and Hollenbach, R. E., 1965, "Interferometer Technique for Measuring the Dynamic Mechanical Properties of Materials," *Review of Scientific Instruments*, Vol. 36, pp. 1617–1620.

Chang, S. N., Chung, D.-T., Ravichandran, G., and Nemat-Nasser, S., 1990, "Plate Impact Experiments on Mg-PSZ and Improved Target Configuration," *Shock Compression of Condensed Matter-1989*, Proc. APS Topical Conference, Albuquerque, NM, Aug.14–17, 1989, pp. 389–392.

Hallquist, J. O., and Benson, D. J., 1986, "DYNA-3D User's Manual," Lawrence Livermore National Laboratory, Report No. UCID 19592, Rev. 2.

Kumar, P., and Clifton, R. J., 1977, "A Star-Shaped Flyer for Plate-Impact Recovery Experiments," *Journal of Applied Physics*, Vol. 48, p. 4850–4852.

Longy, F., and Cagnoux, J., 1989, "Plasticity and Microcracking in Shock-Loaded Alumina," *Journal of American Ceramic Society*, Vol. 76, pp. 971–979.

Taylor, L. M., and Flanagan, D. P., 1987, "PRONT0-2D, A Two-Dimensional Transient Solid Dynamic Program," SAND86-0594, Sandia National Laboratory, Albuquerque, NM.

Yaziv, D., 1985, "Shock Fracture and Recompaction of Ceramics," Ph.D. Thesis, University of Dayton Research Institute, Dayton, OH.

Hisao Hasegawa
Professor,
Department of Mechanical Engineering,
Maiji University,
Tama-ku, Kawasaki 214, Japan

Ven-Gen Lee
Graduate Student.

Toshio Mura
Professor,
Fellow ASME.

Department of Civil Engineering,
Northwestern University,
Evanston, IL 60208

Green's Functions for Axisymmetric Problems of Dissimilar Elastic Solids

Green's functions are obtained for axisymmetric body force problems of dissimilar elastic solids. The Green's functions are defined as a solution to the problem of a dissimilar elastic solid subjected to axisymmetric body forces acting along a circle in a radial, a torsional, and an axial direction. As a special case of the present results, Green's functions are obtained for problems of an elastic half-space with the free surface or rigidly fixed surface and of a homogeneous isotropic elastic solid. An application of the Green's functions is investigated for an eigenstrain problem.

1 Introduction

The aim of this paper is to show a fundamental solution for axisymmetric problems of dissimilar elastic solids. The fundamental solution may be called the Green's functions for axisymmetric body force problems of dissimilar elastic solids.

Various numerical methods of solution were recently developed for engineering problems. In most of these methods of solution, such as boundary element methods, charge simulation methods, eigenstrain methods (Mura, 1987), body force methods (Nisitani, 1967) and so on, fundamental solutions are used to formulate integral equations for a problem. In order to efficiently obtain more accurate results, Green's functions are used by Yuuki et al. (1987), Kisu et al. (1986), Hasegawa (1981, 1982, 1984a, 1984b, 1988, 1990), Lee and Keer (1986), Lee et al. (1987), Lee et al. (1988), and others, because the Green's functions completely satisfy part of the boundary conditions of the problem. They apply the Green's functions, such as Mindlin's solutions (Mindlin, 1936), for a point force in an elastic half-space, Rongved (1955) or Dundurs-Hetenyi's solutions (Dundurs and Hetenyi, 1961, 1965; Hetenyi and Dundurs, 1962) for a point force in an dissimilar elastic solid and other solutions instead of Kelvin's solution (Kelvin and Tait, 1985) for a point force in an infinite solid.

The Green's functions shown here are defined as a solution to the problem of a dissimilar elastic solid subjected to axisymmetric body forces which act as a radial, a torsional, and an axial force distributed along a circle. As a special case of the Green's functions by taking the parameter ξ equal to zero, Green's functions are obtained for an elastic half-space with a free surface; $\xi\rightarrow\infty$ for an elastic half-space with a rigidly fixed surface, and $\xi=1$ for a homogeneous isotropic elastic solid. Here, ξ represents the ratio of elastic constants. To obtain the Green's functions we use stress functions (Hasegawa, 1975, 1976) for axisymmetric body force problems and for axisymmetric surface force problems of elasticity.

An application of the Greens's functions, shown in this paper, is investigated for an eigenstrain problem (Mura, 1987) in the theory of micromechanics of materials.

2 Definition of Green's Functions

In this paper we use cylindrical coordinates and denote them by (r, θ, z) or $(i=1, 2, 3)$. Figure 1 shows a dissimilar elastic solid with Lamé elastic constants λ_k and μ_k $(k=1, 2)$. The half-space $(0\leq r \angle \infty, z\geq 0)$ will be referred to as region $k=1$ and the half-space $(0\leq r\angle \infty, z\leq 0)$ as region $k=2$.

The Green's functions shown are defined as a solution to the problem of the dissimilar elastic solid, as shown in Fig. 1, subjected to axisymmetric body forces

$$F_i=\frac{1}{2\pi r}\,\delta(r-a)\delta(z-h)\ (i=1, 2, 3) \tag{1}$$

distributed uniformly along a circle $(r=a, z=h)$ in the interior of the solid where $\delta(\ )$ is a Dirac delta function. The body forces F_i $(i=1, 2, 3)$, are illustrated in Fig. 2 for a radial force F_1 acting in the r-direction, in Fig. 3 for a torsional force F_2 acting in the θ-direction, and in Fig. 4 for an axial force F_3 acting in the z-direction, respectively.

We assume that the two half-spaces are perfectly bonded to each other at the interface $(z=0)$. The boundary conditions at the interface $(z=0)$ are

$$z=0,\ 0\leq r\leq\infty;\ u_i^1=u_i^2,\ \sigma_z^1=\sigma_z^2,\ \tau_{zr}^1=\tau_{zr}^2,\ \tau_{z\theta}^1=\tau_{z\theta}^2 \tag{2}$$

where superscripts 1 and 2 refer to the quantity corresponding to the region $k=1$ and 2, respectively.

Contributed by the Applied Mechanics Division of The American Society of Mechanical Engineers for presentation at the 1992 ASME Summer Mechanics and Materials Meeting, Tempe, AZ, Apr. 28–May 1, 1992.

Discussion on this paper should be addressed to the Technical Editor, Prof. Leon M. Keer, The Technological Institute, Northwestern University, Evanston, IL 60208, and will be accepted until four months after final publication of the paper itself in the Journal of Applied Mechanics. Manuscript received by the ASME Applied Mechanics Division, Nov. 7, 1990; final revision, Apr. 17, 1991. Paper No. 92-APM-26.

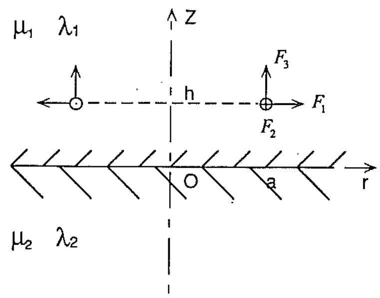

Fig. 1 A dissimilar elastic solid with elastic constants λ_k and μ_k

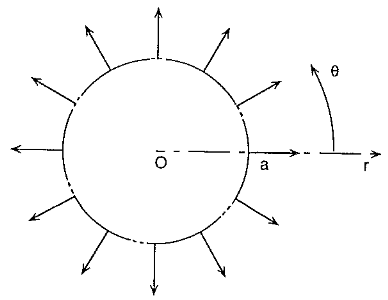

Fig. 2 A radial force acting along a circle

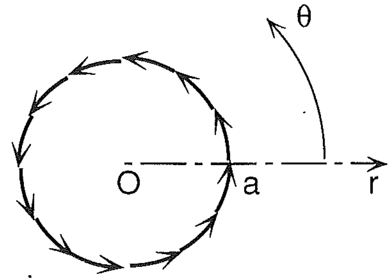

Fig. 3 A torsional force acting along a circle

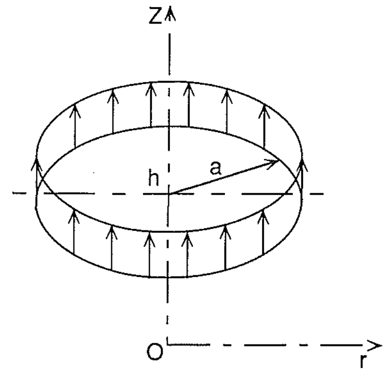

Fig. 4 An axial force acting along a circle

3 Basic Equations

3.1 Fundamental Equations. We consider axisymmetric deformations of an elastic solid. That is, the displacements and stresses treated here are independent of angle θ in cylindrical coordinates. It is well known that the displacement components u_i, $(i=1, 2, 3)$, satisfy the fundamental equations

$$\mu\left(\nabla^2-\frac{1}{r^2}\right)u_i+\mu\delta_{3i}\frac{u_i}{r^2}+(\lambda+\mu)\text{grad}_i\text{div } U+F_i=0 \qquad (3)$$

where U is a vector with the components u_i; λ and μ are the Lame's constants; F_i are body forces; and δ_{3i} is a Kronecker's delta. The solution u_i for (3) can be obtained (Hasegawa, 1975) by

$$2\mu\ u_i=2(1-\nu)\left(\nabla^2-\frac{1}{r^2}+\delta_{3i}\frac{1}{r^2}\right)\phi_i-\text{grad}_i\text{div}\phi \qquad (4)$$

where ϕ is a vector with the components ϕ_i, $(i=1, 2, 3)$, which are stress functions satisfying the equations

$$\left(\nabla^2-\frac{1}{r^2}+\delta_{3i}\frac{1}{r^2}\right)^2\phi_i=\frac{-1}{1-\nu}F_i \qquad (5)$$

and ν is Poisson's ratio of materials.

The stresses (Hasegawa, 1976) in terms of stress functions ϕ_i can be obtained from (4) by using Hooke's law.

3.2 Stress Functions for Body Force Problems. It was shown in a previous paper (Hasegawa, 1976) that the displacements u_i due to the body forces F_i acting in a semi-infinite region $(0\le r\angle\infty, z\ge 0)$ can be obtained by the stress functions

$$\phi_i=\frac{-2}{\pi(1-\nu)}\int_0^\infty\int_0^\infty\overline{F}_i\frac{\alpha J_n(\alpha r)}{(\alpha^2+\beta^2)^2}\cos\beta z d\alpha d\beta \qquad (6)$$

where

$$\overline{F}_i=\int_0^\infty\int_0^\infty F_i r J_n(\alpha r)\cos\beta z drdz \qquad (7)$$

and $J_n(\alpha r)$ is a Bessel function of the first kind of order n. We must take $n=1$ for $i=1, 2$, and $n=0$ for $i=3$.

In this paper, we assume that the body forces F_i of Eq. (1) act in the region $k=1$ $(z\ge 0)$. From (1) and (7) we have

$$\overline{F}_i=\frac{1}{2\pi}J_n(\alpha a)\cos\beta h \qquad (8)$$

for the present problem. From (4), (6) and Hooke's law, we can obtain:

(i) For the radial force F_1 as shown in Fig. 2;

$$2\mu_1\mu_1=\frac{2}{\pi(1-\nu_1)}\int_0^\infty\int_0^\infty\alpha\overline{F}_1\left\{\frac{2(1-\nu_1)}{\alpha^2+\beta^2}-\frac{\alpha^2}{(\alpha^2+\beta^2)^2}\right\}\times J_1(\alpha r)\cos\beta z d\alpha d\beta,$$

$$u_2=0,$$

$$2\mu_1\mu_3=\frac{-2}{\pi(1-\nu_1)}\int_0^\infty\int_0^\infty\overline{F}_1\frac{\alpha^2\beta}{(\alpha^2+\beta^2)^2}J_0(\alpha r)\sin\beta z d\alpha d\beta,$$

$$\sigma_z=\frac{-2}{\pi(1-\nu_1)}\int_0^\infty\int_0^\infty\alpha^2\overline{F}_1\left\{\frac{1-\nu_1}{\alpha^2+\beta^2}-\frac{\alpha^2}{(\alpha^2+\beta^2)^2}\right\}\times J_0(\alpha r)\cos\beta z d\alpha d\beta,$$

$$\tau_{zr}=\frac{2}{\pi(1-\nu_1)}\int_0^\infty\int_0^\infty\alpha\beta\overline{F}_1\left\{\frac{\alpha^2}{(\alpha^2+\beta^2)^2}-\frac{1-\nu_1}{\alpha^2+\beta^2}\right\}\times J_1(\alpha r)\sin\beta z d\alpha d\beta,$$

$$\tau_{z\theta}=0. \qquad (9)$$

(ii) For the torsional force F_2 as shown in Fig. 3,

$$u_1=u_3=0,$$

$$\mu_1 u_2=\frac{2}{\pi}\int_0^\infty\int_0^\infty\overline{F}_2\frac{\alpha J_1(\alpha r)}{\alpha^2+\beta^2}\cos\beta z d\alpha d\beta,$$

$$\tau_{z\theta}=\frac{-2}{\pi}\int_0^\infty\int_0^\infty\overline{F}_2\frac{\alpha\beta J_1(\alpha r)}{\alpha^2+\beta^2}\sin\beta z d\alpha d\beta,$$

$$\sigma_z=\tau_{zr}=0. \qquad (10)$$

(iii) For the axial force F_3 as shown in Fig. 4,

$$2\mu_1 u_1 = \frac{2}{\pi(1-\nu_1)} \int_0^\infty \int_0^\infty \overline{F}_3 \frac{\alpha^2\beta}{(\alpha^2+\beta^2)^2} J_1(\alpha r) \sin \beta z d\alpha d\beta,$$

$$u_2 = 0,$$

$$2\mu_1 u_3 = \frac{2}{\pi(1-\nu_1)} \int_0^\infty \int_0^\infty \alpha \overline{F}_3 \left\{ \frac{2(1-\nu_1)}{\alpha^2+\beta^2} - \frac{\beta^2}{(\alpha^2+\beta^2)^2} \right\} \times J_0(\alpha r) \cos \beta z d\alpha d\beta,$$

$$\sigma_z = \frac{-2}{\pi(1-\nu_1)} \int_0^\infty \int_0^\infty \alpha\beta \overline{F}_3 \left\{ \frac{1-\nu_1}{\alpha^2+\beta^2} + \frac{\alpha^2}{(\alpha^2+\beta^2)^2} \right\} \times J_0(\alpha r) \sin \beta z d\alpha d\beta,$$

$$\tau_{zr} = \frac{-2}{\pi(1-\nu_1)} \int_0^\infty \int_0^\infty \alpha^2 \overline{F}_3 \left\{ \frac{1-\nu_1}{\alpha^2+\beta^2} - \frac{\beta^2}{(\alpha^2+\beta^2)^2} \right\} \times J_1(\alpha r) \cos \beta z d\alpha d\beta,$$

$$\tau_{z\theta} = 0. \tag{11}$$

where ν_k ($k=1, 2$), are Poisson's ratios of the region k. The expressions of stresses were presented only for the components necessary to determine the constants in the stress functions (12) for surface force problems shown in the next section. It is easily seen that (9), (10) and (11) do not usually satisfy the boundary conditions (2) on the plane $z=0$. That is, the plane $z=0$ is a symmetry plane for the body forces F_1 and F_2 while $z=0$ is an antisymmetric plane for the body force F_3.

3.3 Stress Functions for Surface Force Problems of a Half Space. In order to obtain the solutions satisfying the boundary conditions (2), we shall use the stress functions (Hasegawa, 1975, 1984a, 1984b)

$$\phi_3^k = \int_0^\infty \frac{1}{\alpha^2} J_0(\alpha r)(A_k + \alpha z B_k) \exp \{(-1)^k \alpha z\} d\alpha,$$

$$\phi_2^k = \int_0^\infty \frac{1}{2(1-\nu_1)\alpha} C_k r J_2(\alpha r) \exp \{(-1)^k \alpha z\} d\alpha, \tag{12}$$

for surface force problems of a half-space where A_k, B_k, and C_k, ($k=1, 2$), are arbitrary constants which are determined by the boundary conditions (2), and k is taken as 1 for the region ($z \geq 0$) and as 2 for the region ($z \leq 0$).

From (4) and (12), we can obtain, for the region $k=1$ ($z \geq 0$),

$$2\mu_1 u_1 = -\int_0^\infty \{A_1 - (1-\alpha z)B_1\} J_1(\alpha r) e^{-\alpha z} d\alpha,$$

$$\mu_1 u_2 = \int_0^\infty C_1 J_1(\alpha r) e^{-\alpha z} d\alpha,$$

$$2\mu_1 u_3 = -\int_0^\infty [A_1 + \{2(1-2\nu_1) + \alpha z\} B_1] J_0(\alpha r) e^{-\alpha z} d\alpha,$$

$$\sigma_z = \int_0^\infty \alpha \{A_1 + (1-2\nu_1+\alpha z)B_1\} J_0(\alpha r) e^{-\alpha z} d\alpha,$$

$$\tau_{zr} = \int_0^\infty \alpha \{A_1 + (\alpha z - 2\nu_1)B_1\} J_1(\alpha r) e^{-\alpha z} d\alpha,$$

$$\tau_{z\theta} = -\int_0^\infty \alpha C_1 J_1(\alpha r) e^{-\alpha z} d\alpha. \tag{13}$$

Similarly, for the region $k=2$ ($z \leq 0$), we have

$$2\mu_2 u_1 = -\int_0^\infty \{A_2 + (1+\alpha z)B_2\} J_1(\alpha r) e^{\alpha z} d\alpha,$$

$$\mu_2 u_2 = \int_0^\infty \alpha C_2 J_1(\alpha r) e^{\alpha z} d\alpha,$$

$$2\mu_2 u_3 = -\int_0^\infty [A_2 + \{\alpha z - 2(1-2\nu_2)\} B_2] J_0(\alpha r) e^{\alpha z} d\alpha,$$

$$\sigma_z = -\int_0^\infty \alpha \{A_2 - (1-2\nu_2-\alpha z)B_2\} J_0(\alpha r) e^{\alpha z} dz,$$

$$\tau_{zr} = \int_0^\infty \alpha \{A_2 + (\alpha z + 2\nu_2)B_2\} J_1(\alpha r) e^{\alpha z} d\alpha,$$

$$\tau_{z\theta} = -\int_0^\infty \alpha C_2 J_1(\alpha r) e^{\alpha z} d\alpha. \tag{14}$$

4 Green's Functions

Here we shall obtain the Green's functions defined in Section 2. We assume that the body forces F_i of (1) act separately for each component $i=1, 2$ and 3 in the region $k=1$ ($z \geq 0$). Simple superposition of the Green's functions yields the ones for the case where the three components of the body forces act at the same time.

4.1 A Radial Body Force F_1. For the region $k=1$ ($z \geq 0$), we shall express the displacements u_i and stresses σ_{ij} by using (9) and (13) as follows:

$$\begin{Bmatrix} u_i \\ \sigma_{ij} \end{Bmatrix} = \begin{Bmatrix} u_i \\ \sigma_{ij} \end{Bmatrix} \text{ of Eq. (9)} + \begin{Bmatrix} u_i \\ \sigma_{ij} \end{Bmatrix} \text{ of Eq. (13)}. \tag{15}$$

In the region $k=2$ ($z \leq 0$), there are no body forces. Therefore, we can express the displacements and stresses in the region $k=2$ by only (14) for surface problems. That is

$$\begin{Bmatrix} u_i \\ \sigma_{ij} \end{Bmatrix} = \begin{Bmatrix} u_i \\ \sigma_{ij} \end{Bmatrix} \text{ of Eq. (14)}. \tag{16}$$

By application of the boundry conditions (2) to (15) and (16), the constants A_k, B_k, and C_k can be determined as follows:

$$A_1 = \frac{1}{2\xi_2} \xi(X+Y) + \frac{1}{2\xi_1} [(1-4\nu_1)\xi X - \{4\nu_1 + (3-4\nu_1)\xi\} Y],$$

$$B_1 = \frac{-1}{\xi_1} (\xi X + Y),$$

$$A_2 = \frac{1}{2\xi_2} \xi(1-4\nu_2)(X+Y) + \frac{1}{2\xi_1} \xi \{X - (3-4\nu_1)Y\},$$

$$B_2 = \frac{1}{\xi_2} \xi(X+Y) \tag{17}$$

where

$$\xi = \frac{\mu_2}{\mu_1},\ \xi_1 = 1 + (3-4\nu_1)\xi,\ \xi_2 = \xi + 3 - 4\nu_2 \tag{18}$$

and X and Y are

$$X = \frac{2}{\pi(1-\nu_1)} \int_0^\infty \alpha \overline{F}_1 \left\{ \frac{2(1-\nu_1)}{\alpha^2+\beta^2} - \frac{\alpha^2}{(\alpha^2+\beta^2)^2} \right\} d\beta,$$

$$Y = \frac{2}{\pi(1-\nu_1)} \int_0^\infty \alpha \overline{F}_1 \left\{ \frac{\alpha^2}{(\alpha^2+\beta^2)} - \frac{1-\nu_1}{(\alpha^2+\beta^2)} \right\} d\beta. \tag{19}$$

Now, we shall obtain the Green's functions for the radial body force F_1 as shown in Fig. 2. From (8) and (19), we have

$$X = \frac{1}{4\pi(1-\nu_1)} (3-4\nu_1-\alpha h) J_1(\alpha a) e^{-\alpha h},$$

$$Y = \frac{-1}{4\pi(1-\nu_1)} (1-2\nu_1-\alpha h)\ J_1\ (\alpha a) e^{-\alpha h}. \tag{20}$$

By substituting (20) into (15) and (16) through (13), (14), and (17), we finally obtain the following results. Here use was made of the integral formulae developed by Erdelyi (1954) and Eason et al. (1955).

(i) For the region $k=1$ $(z\geq 0)$,

$$2\mu_1 u_{11}=\frac{1}{D}\left[\sum_{i=1}^{2}\left\{(3-4\nu_1)Q_{1/2}(x_i)+\frac{z_i^2}{2ar}\frac{G_1(x_i)}{x_i^2-1}\right\}\right.$$
$$-2\left\{3-4\nu_1-(1-\nu_1)\left(\frac{3-4\nu_1}{\xi_1}+\frac{3-4\nu_2}{\xi_2}\right)\right\}Q_{1/2}(x_2)$$
$$\left.+\left\{\frac{2(1-\nu_1)}{\xi_1}-1\right\}\frac{z_2^2G_1(x_2)}{ar(x_2^2-1)}+\frac{1-\xi}{\xi_1}\frac{zh}{ar}\frac{q_4(x_2)}{x_2^2-1}\right]$$

$u_{21}=0$

$$2\mu_1 u_{31}=\frac{1}{rD}\left[\sum_{i=1}^{2}\frac{-z_i}{2}\left\{Q_{1/2}(x_i)-\frac{x_i-r/a}{x_i^2-1}G_1(x_i)\right\}\right.$$
$$-(1-\nu_1)\left(\frac{3-4\nu_1}{\xi_1}-\frac{3-4\nu_2}{\xi_2}\right)rq_3(x_2)+\frac{1-\xi}{\xi_1}\frac{zhz_2}{2ar}\frac{q_5(x_2)}{x_2^2-1}$$
$$\left.+\left\{z-\frac{2(1-\nu_1)z_1}{\xi_1}\right\}\left\{Q_{1/2}(x_2)-\frac{x_2-r/a}{x_2^2-1}G_1(x_2)\right\}\right].\qquad(21)$$

(ii) For the region $k=2$ $(z\leq 0)$,

$$2\mu_2 u_{11}=\frac{2(1-\nu_1)}{D}\left[\left(\frac{3-4\nu_1}{\xi_1}+\frac{3-4\nu_2}{\xi_2}\right)Q_{1/2}(x_1)\right.$$
$$\left.-\left(\frac{h}{\xi_1}-\frac{z}{\xi_2}\right)\frac{z_1}{ar}\frac{G_1(x_1)}{x_2^2-1}\right],$$

$u_{21}=0,$

$$2\mu_2 u_{31}=\frac{1-\nu_1}{rD}\left[2\left(\frac{h}{\xi_1}-\frac{z}{\xi_2}\right)\left\{Q_{1/2}(x_1)-\frac{x_1-r/a}{x_1^3-1}G_1(x_1)\right\}\right.$$
$$\left.-\left(\frac{3-4\nu_1}{\xi_1}-\frac{3-4\nu_2}{\xi_2}\right)rq_3\,(x_1)\right]\qquad(22)$$

where $Q_n(x)$ is a Legendre function of the second kind of the order n, and

$$z_1=z-h,\ z_2=z+h,$$
$$x_i=\frac{r^2+a^2+z_i^2}{2ar},$$
$$G_1(x)=xQ_{1/2}(x)-Q_{-1/2}(x),$$
$$G_2(x)=xQ_{-1/2}(x)-Q_{1/2}(x).\qquad(23)$$

Also, D and $q_n(x_i)$ are expressed in (50) and (51) of Section 6. In the aforementioned expressions, the notation u_{ij} represents the displacement component in the i-direction at point (r, z) when a unit ring force in the j-direction at point (a, h) corresponds to the Green's functions G_{ij} in the theory of micromechanics (Mura, 1987).

4.2 A Torsional Body Force F_2. Green's functions for torsional body force F_2, as shown in Fig. 3, were obtained in a previous paper (Hasegawa, 1988) by using (10) and the stress functions ϕ_2 in (12), and are expressed as follows:

(i) For the region $k=1$ $(z\geq 0)$,

$$2\mu_1 u_{22}=\frac{1}{2\pi^2\sqrt{ar}}\left\{\sum_{i=1}^{2}Q_{1/2}(x_i)-\frac{2\xi}{1+\xi}Q_{1/2}(x_2)\right\},$$
$$u_{12}=u_{32}=0.\qquad(24)$$

(ii) For the region $k=2$ $(z\leq 0)$,

$$2\mu_2 u_{22}=\frac{1}{\pi^2\sqrt{ar}}Q_{1/2}(x_1),$$
$$u_{12}=u_{32}=0.\qquad(25)$$

4.3 An Axial Body Force F_3. For the region $k=1$ $(z\geq 0)$, we can express the displacements and stresses as follows:

$$\begin{Bmatrix}u_i\\ \sigma_{ij}\end{Bmatrix}=\begin{Bmatrix}u_i\\ \sigma_{ij}\end{Bmatrix}\text{ of Eq. (11)}+\begin{Bmatrix}u_i\\ \sigma_{ij}\end{Bmatrix}\text{ of Eq. (13).}\qquad(26)$$

In the region $k=2$ $(z\leq 0)$ there are no body forces. Therefore, we can use (14) for the region. That is,

$$\begin{Bmatrix}u_i\\ \sigma_{ij}\end{Bmatrix}=\begin{Bmatrix}u_i\\ \sigma_{ij}\end{Bmatrix}\text{ of Eq. (14).}\qquad(27)$$

From (26), (27) and the boundary condition (2), we can obtain

$$A_1=\frac{\xi X}{2}\left(\frac{1}{\xi_2}-\frac{1-4\nu_1}{\xi_1}\right)+\frac{Y}{2}\left(\frac{1-4\nu_1}{\xi_1}+\frac{3-4\nu_2}{\xi_2}\right),$$
$$B_1=\frac{\xi X-Y}{\xi_1},$$
$$A_2=\frac{\xi X}{2}\left(\frac{1-4\nu_1}{\xi_2}-\frac{1}{\xi_1}\right)-\frac{\xi Y}{2}\left(\frac{3-4\nu_1}{\xi_1}+\frac{1-4\nu_2}{\xi_2}\right),$$
$$B_2=\frac{\xi(X-Y)}{\xi_2}\qquad(28)$$

where X and Y are

$$X=\frac{2}{\pi(1-\nu_1)}\int_0^\infty\alpha\overline{F}_3\left\{\frac{2(1-\nu_1)}{\alpha^2+\beta^2}-\frac{\beta^2}{(\alpha^2+\beta^2)^2}\right\}d\beta,$$
$$Y=\frac{2}{\pi(1-\nu_1)}\int_0^\infty\alpha\overline{F}_3\left\{\frac{1-\nu_1}{\alpha^2+\beta^2}-\frac{\beta^2}{(\alpha^2+\beta^2)^2}\right\}d\beta.\qquad(29)$$

Now, we shall obtain the Green's functions for body forces F_3 as shown in Fig. 4. From (8) and (29) we have

$$X=\frac{3-4\nu_1+\alpha h}{4\pi(1-\nu_1)}J_0(\alpha a)e^{-\alpha h},$$
$$Y=\frac{1-2\nu_1+\alpha h}{4\pi(1-\nu_1)}J_0(\alpha a)e^{-\alpha h}.\qquad(30)$$

By substituting (30) into (26) and (27) through (13), (14), and (28), we can obtain:

(i) For the region $k=1$ $(z\geq 0)$,

$$2\mu_1 u_{13}=\frac{1}{aD}\left[\sum_{i=1}^{2}\frac{z_i}{2}\left\{Q_{1/2}(x_i)-\frac{x_i-a/r}{x_i^2-1}G_1(x_i)\right\}\right.$$
$$-(1-\nu_1)\left(\frac{3-4\nu_1}{\xi_1}-\frac{3-4\nu_2}{\xi_2}\right)aq_3'(x_2)+\frac{1-\xi}{\xi_1}\frac{zhz_2}{2ar}\frac{1}{x_2^2-1}q_5'(x_2)$$
$$\left.-\left\{z-\frac{2(1-\nu_1)z_1}{\xi_1}\right\}\left\{Q_{1/2}(x_2)-\frac{x_2-a/r}{x_2^2-1}G_1(x_2)\right\}\right],$$

$u_{23}=0,$

$$2\mu_1 u_{33}=\frac{1}{D}\left[\sum_{i=1}^{2}\left\{(3-4\nu_1)Q_{-1/2}(x_i)+\frac{z_i^2}{2ar}\frac{1}{x_i^2-1}G_2(x_i)\right\}\right.$$
$$-2\left\{3-4\nu_1-(1-\nu_1)\left(\frac{3-4\nu_1}{\xi_1}+\frac{3-4\nu_2}{\xi_2}\right)\right\}Q_{-1/2}(x_2)$$

$$-\frac{1}{ar}\frac{1}{x_2^2-1}\left\{\left[1-\frac{2(1-\nu_1)}{\xi_1}\right]\right.$$
$$\left.\times z_2^2 G_2(x_2)+\frac{1-\xi}{\xi_1}zhq_1(x_2)\right\}. \quad (31)$$

(ii) For the region $k=2$ $(z\le 0)$,

$$2\mu_2 u_{13}=\frac{\xi}{D'}\left[\left(\frac{3-4\nu_2}{\xi_2}-\frac{3-4\nu_1}{\xi_1}\right)q_3'(x_1)\right.$$
$$\left.+\frac{2}{a}\left(\frac{z}{\xi_2}-\frac{h}{\xi_1}\right)\left\{Q_{1/2}(x_1)-\frac{x_1-a/r}{x_1^2-1}G_1(x_1)\right\}\right],$$

$$u_{23}=0,$$

$$2\mu_2 u_{33}=\frac{2\xi}{D'}\left\{\left(\frac{3-4\nu_1}{\xi_1}+\frac{3-4\nu_2}{\xi_2}\right)Q_{-1/2}(x_1)\right.$$
$$\left.+\left(\frac{z}{\xi_2}-\frac{h}{\xi_1}\right)\frac{z_1}{ar}\frac{1}{x_1^2-1}G_2(x_1)\right\}. \quad (32)$$

5 Special Cases

Here we shall consider special cases of the Green's functions for a dissimilar elastic solid obtained in the previous section. These are the cases whereby $\xi=\mu_2/\mu_1=0$, ∞ and 1.

5.1 Green's Functions for an Elastic Half-Space With a Free Surface.

Taking the parameter $\xi=0$ in (21), (24), and (31), we obtain:

(i) For a radial force as shown in Fig. 2,

$$2\mu_1 u_{11}=\frac{1}{D}\left[\sum_{i=1}^{2}\left\{(3-4\nu_1)Q_{1/2}(x_i)+\frac{z_i^2}{2ar}\frac{G_1(x_i)}{x_i^2-1}\right\}\right.$$
$$\left.+2(1-2\nu_1)^2 Q_{1/2}(x_2)+\frac{(1-2\nu_1)z_2^2G_1(x_2)+zhq_4(x_2)}{ar(x_2^2-1)}\right],$$

$$u_{21}=0,$$

$$2\mu_1 u_{31}=\frac{-1}{D}\left[\sum_{i=1}^{2}\frac{z_i}{2r}\left\{Q_{1/2}(x_i)-\frac{x_i-r/a}{x_i^2-1}G_1(x_i)\right\}\right.$$
$$+2(1-\nu_1)(1-2\nu_1)q_3(x_2)-\frac{zhz_2}{2ar^2}\frac{q_5(x_2)}{x_2^2-1}$$
$$\left.+\frac{2(1-\nu_1)-z}{r}\left\{Q_{1/2}(x_2)-\frac{x_2-r/a}{x_2^2-1}G_1(x_2)\right\}\right]. \quad (33)$$

(ii) For a torsional force as shown in Fig. 3,

$$2\mu_1 u_{22}=\frac{1}{2\pi^2\sqrt{ar}}\sum_{i=1}^{2}Q_{1/2}(x_i),$$
$$u_{12}=u_{32}=0. \quad (34)$$

(iii) For an axial force as shown in Fig. 4,

$$2\mu_1 u_{13}=\frac{1}{2aD}\left[\sum_{i=1}^{2}z_i\left\{Q_{1/2}(x_i)-\frac{x_i-a/r}{x_i^2-1}G_1(x_i)\right\}\right.$$
$$-4(1-\nu_1)(1-2\nu_1)aq_3'(x_2)+\frac{zhz_2}{ar}$$
$$\left.\times\frac{q_5'(x_2)}{x_2^2-1}+2\{2(1-2\nu_1)z_1-z\}\left\{Q_{1/2}(x_2)-\frac{x_2-a/r}{x_2^2-1}G_1(x_2)\right\}\right],$$

$$u_{23}=0$$

$$2\mu_1 u_{33}=\frac{1}{D}\left[\sum_{i=1}^{2}\left\{(3-4\nu_1)Q_{-1/2}(x_i)+\frac{z_i^2}{2ar}\frac{G_2(x_i)}{x_i^2-1}\right\}\right.$$
$$\left.+2(1-2\nu_1)^2Q_{-1/2}(x_2)+\frac{(1-2\nu_1)z_2^2G_2(x_2)-zhq_1(x_2)}{ar(x_2^2-1)}\right]. \quad (35)$$

These expressions coincide with the results (Hasegawa, 1976, 1984a) for Green's functions of axisymmetric body force problems of a single elastic half-space $(0\le r<\infty,\ z\ge 0)$ satisfying the traction-free boundary condition

$$z=0,\ 0\le r<\infty;\ \sigma_z=\tau_{zr}=\tau_{z\theta}=0. \quad (36)$$

5.2 Green's Functions for an Elastic Half-Space with a Rigidly Fixed Surface.

Taking the parameter $\xi\to\infty$ in (21), (24), and (31), we obtain:

(i) For a radial force as shown in Fig. 2,

$$2\mu_1 u_{11}=\frac{-1}{D}\left[\sum_{i=1}^{2}(-1)^i\left\{(3-4\nu_1)Q_{1/2}(x_i)\right.\right.$$
$$\left.\left.+\frac{z_i^2}{2ar}\frac{G_1(x_i)}{x_i^2-1}\right\}+\frac{zh}{(3-4\nu_1)ar}\frac{q_4(x_2)}{x_2^2-1}\right],$$

$$u_{21}=0,$$

$$2\mu_1 u_{31}=\frac{1}{2rD}\left[\sum_{i=1}^{2}(-1)^i z_1\left\{Q_{1/2}(x_i)-\frac{x_i-r/a}{x_i^2-1}G_1(x_i)\right\}\right.$$
$$\left.-\frac{zhz_2}{(3-4\nu_1)ar}\frac{q_5(x_2)}{x_2^2-1}\right]. \quad (37)$$

(ii) For a torsional force as shown in Fig. 3,

$$2\mu_1 u_{22}=\frac{1}{2\pi^2\sqrt{ar}}\sum_{i=1}^{2}(-1)^{i+1}Q_{1/2}(x_i),$$
$$u_{12}=u_{32}=0. \quad (38)$$

(iii) For an axial force as shown in Fig. 4,

$$2\mu_1 u_{13}=\frac{1}{2aD}\left[\sum_{i=1}^{2}(-1)^{i+1}z_1\left\{Q_{1/2}(x_i)-\frac{x_i-a/r}{x_i^2-1}G_1(x_i)\right\}\right.$$
$$\left.-\frac{zhz_2}{(3-4\nu_1)ar}\frac{q_5'(x_2)}{x_2^2-1}\right],$$

$$u_{23}=0,$$

$$2\mu_1 u_{33}=\frac{1}{D}\left[\sum_{i=1}^{2}(-1)^{i+1}\left\{(3-4\nu_1)Q_{-1/2}(x_i)+\frac{z_i^2}{2ar}\frac{G_2(x_i)}{x_i^2-1}\right\}\right.$$
$$\left.+\frac{zh}{(3-4\nu_1)ar}\frac{q_1(x_2)}{x_2^2-1}\right]. \quad (39)$$

These expressions may be called the Green's functions for axisymmetric body force problems of a single elastic half-space $(0\le r<\infty,\ z\ge 0)$ with the rigidly fixed boundary. That is, these expressions satisfy the boundary condition

$$z=0,\ 0\le r<\infty;\ u_i=0. \quad (40)$$

5.3 Fundamental Solutions for Axisymmetric Problems of Elasticity.

Assumption $\xi=1$ in (21), (24), and (31), or (22), (25), and (32) yields:

(i) For a radial force as shown in Fig. 2,

$$2\mu u_{11}=\frac{1}{D}\left[(3-4\nu)Q_{1/2}(x_1)+\frac{z_1^2}{2ar}\frac{G_1(x_1)}{x_1^2-1}\right\},$$

$$u_{21}=0,$$

$$2\mu u_{31}=\frac{-z_1}{2rD}\left\{Q_{1/2}(x_1)-\frac{x_1-r/a}{x_1^2-1}G_1(x_1)\right\}. \quad (41)$$

(ii) For a torsional force as shown in Fig. 3,

$$2\mu u_{22}=\frac{1}{2\pi^2\sqrt{ar}}Q_{1/2}(x_1),$$
$$u_{12}=u_{32}=0. \quad (42)$$

(iii) For an axial force as shown in Fig. 4,

$$2\mu u_{13}=\frac{z_1}{2aD}\left\{Q_{1/2}(x_1)-\frac{x_1-a/r}{x_1^2-1}G_1(x_1)\right\},$$

$$u_{23}=0,$$

$$2\mu u_{33}=\frac{1}{D}\left\{(3-4\mu)Q_{-1/2}(x_1)+\frac{z_1^2}{2ar}\frac{G_2(x_1)}{x_1^2-1}\right\}. \tag{43}$$

These expressions coincide with the results (Hasegawa, 1975, 1981, 1984a; Kermanidis, 1975) for fundamental solutions for axisymmetric problems of the homogeneous elastic whole space ($0\le r<\infty,\ -\infty<z\le\infty$).

6 Expressions for Stresses

In a practical application of Green's functions, it is necessary to use expressions for stresses. Here we shall present stress components derived from the displacement Green's functions. By using Hooke's law, together with the displacements for a dissimilar solid obtained in the Section 4, we obtain

(i) Stress Green's functions for a radial force as shown in Fig. 2;

(*a*) For the region $k=1$ ($z\ge 0$),

$$\begin{aligned}\sigma_r=\frac{1}{rD}\Bigg[&\sum_{i=1}^{2}\left\{\frac{3-2\nu_1}{2}\left[Q_{1/2}(x_i)-\frac{x_i-r/a}{x_i^2}G_1(x_i)\right]\right.\\&\left.-(3-4\nu_1)Q_{1/2}(x_i)-\frac{z_i^2}{4ar}\frac{q_5(x_i)+2G_1(x_i)}{x_i^2-1}\right\}\\&+\left\{(1-\nu_1)\left(\frac{3}{\xi_1}-\frac{\xi}{\xi_2}-1\right)-1\right\}\left\{Q_{1/2}(x_2)-\frac{x_2-r/a}{x_2^2-1}G_1(x_2)\right\}\\&+\left\{\frac{z_2}{2}+\frac{\nu_1(z+\xi h)-z_2}{\xi_1}\right\}\frac{z_2}{ar}\frac{q_5(x_2)}{x_2^2-1}\\&+\left\{1-\frac{2(1-\nu_1)}{\xi_1}\right\}\frac{z_2^2}{ar}\frac{G_1(x_2)}{x_2^2-1}\\&-2\left\{1+(1-\nu_1)\left(\frac{3-4\nu_1}{\xi_1}+\frac{3-4\nu_2}{\xi_2}-4\right)\right\}Q_{1/2}(x_2)\\&-\frac{1-\xi}{\xi_1}\frac{zh}{2ar}\frac{q_6(x_2)+2q_4(x_2)}{x_2^2-1}\Bigg],\end{aligned}$$

$$\begin{aligned}\sigma_\theta=\frac{1}{rD}\Bigg[&\sum_{i=1}^{2}\left\{(3-4\nu_1)Q_{1/2}(x_i)+\frac{z_i^2}{2ar}\frac{G_1(x_i)}{x_i^2-1}\right.\\&\left.+\nu_1\left[Q_{1/2}(x_i)-\frac{x_i-r/a}{x_i^2-1}G_1(x_i)\right]\right\}\\&+2\left\{(1-\nu_1)\left(\frac{3-4\nu_1}{\xi_1}+\frac{3-4\nu_2}{\xi_2}-4\right)+1\right\}Q_{1/2}(x_2)\\&+\frac{1}{ar}\frac{1}{x_2^2-1}\left\{\left[\frac{2(1-\nu_1)}{\xi_1}-1\right]z_2^2G_1(x_2)\right.\\&\left.+\frac{(1-\xi)[zhq_4(x_2)-\nu_1hz_2q_5(x_2)]}{\xi_1}\right\}\\&+2\nu_1\left\{\frac{2(1-\nu_1)}{\xi_1}-1\right\}\left\{Q_{1/2}(x_2)-\frac{x_2-r/a}{x_2^2-1}G_1(x_2)\right\}\Bigg],\end{aligned}$$

$$\begin{aligned}\sigma_z=\frac{1}{rD}\Bigg[&\sum_{i=1}^{2}\left\{\frac{z_i^2}{4ar}\frac{q_5(x_i)}{x_i^2-1}\right.\\&\left.-\frac{1-2\nu_1}{2}\left[Q_{1/2}(x_i)-\frac{x_i-r/a}{x_i^2-1}G_1(x_i)\right]\right\}\\&+\left\{(1-\nu_i)\left(\frac{1}{\xi_1}+\frac{\xi}{\xi_2}+1\right)-1\right\}\left\{Q_{1/2}(x_2)-\frac{x_2-r/a}{x_2^2-1}G_1(x_2)\right\}\\&+\left\{\frac{2(1-\nu_1)(z+\xi h)}{\xi_1}-z_2\right\}\frac{z_2}{2ar}\frac{q_5(x_2)}{x_2^2-1}+\frac{1-\xi}{\xi_1}\frac{zh}{2ar}q_6(x_2)\Bigg],\end{aligned}$$

$$\begin{aligned}\tau_{rz}=\frac{1}{arD}\Bigg[&\sum_{i=1}^{2}\frac{z_i}{x_i^2-1}\left\{\frac{q_4(x_i)}{2}+(1-\nu_1)G_1(x_i)\right\}\\&+(1-\nu_i)\left(\frac{1}{\xi_1}-\frac{\xi}{\xi_2}-1\right)\frac{z_2}{x_2^2-1}G_1(x_2)\\&+\left\{\frac{2(1-\nu_1)(z-\xi h)}{\xi_1}-z\right\}\frac{q_4(x_2)}{x_2^2-1}\\&-\frac{1-\xi}{\xi_1}\frac{zhz_2}{ar}\frac{1}{x_2^2-1}\left\{\frac{Q_{1/2}(x_2)}{2}-\frac{2x_2}{x_2^2-1}q_4(x_2)\right.\\&+\frac{1}{x_2^2-1}\left[\frac{z_i^2}{ar}Q_{-1/2}(x_2)+4\left(1-\frac{x_2}{x_2^2-1}\frac{z_2^2}{ar}\right)G_2(x_2)\right.\\&\left.\left.-\frac{z_2^2}{4ar}G_1(x_2)\right]\right\}\Bigg],\end{aligned}\tag{44}$$

$$\tau_{z\theta}=\tau_{r\theta}=0.$$

(*b*) For the region $k=2$ ($z\le 0$),

$$\begin{aligned}\sigma_r=\frac{\xi}{rD'}\Bigg[&\left(\frac{3-4\nu_1}{\xi_1}+\frac{3}{\xi_2}\right)\left\{Q_{1/2}(x_1)-\frac{x_1-r/a}{x_1^2-1}G_1(x_1)\right\}\\&+\left(\frac{h}{\xi_1}-\frac{z}{\xi_2}\right)\frac{z_1}{ar}\frac{q_5(x_1)+2G_1(x_1)}{x_1^2-1}\\&+2\left(\frac{3-4\nu_1}{\xi_1}+\frac{3-4\nu_2}{\xi_2}\right)Q_{1/2}(x_1)\Bigg],\end{aligned}$$

$$\begin{aligned}\sigma_\theta=\frac{2\xi}{rD'}\Bigg[&\frac{2\nu_2}{\xi_2}\left\{Q_{1/2}(x_1)-\frac{x_1-r/a}{x_1^2-1}G_1(x_1)\right\}\\&+\left(\frac{3-4\nu_1}{\xi_1}+\frac{3-4\nu_2}{\xi_2}\right)Q_{1/2}(x_1)-\left(\frac{h}{\xi_1}-\frac{z}{\xi_2}\right)\frac{z_1}{2ar}\frac{G_1(x_1)}{x_1^2-1}\Bigg],\end{aligned}$$

$$\begin{aligned}\sigma_z=\frac{\xi}{rD'}\Bigg[&\left(\frac{1}{\xi_2}-\frac{3-4\nu_1}{\xi_1}\right)\left\{Q_{1/2}(x_2)-\frac{x_1-r/a}{x_1^2-1}G_1(x_1)\right\}\\&-\left(\frac{h}{\xi_1}-\frac{z}{\xi_2}\right)\frac{z_1}{ar}\frac{q_5(x_1)}{x_1^2-1}\Bigg],\end{aligned}$$

$$\tau_{rz}=\frac{-\xi}{arD'}\frac{1}{x_1^2-1}\left[\left(\frac{3-4\nu_1}{\xi_1}+\frac{1}{\xi_2}\right)z_1G_1(x_1)+2\left(\frac{h}{\xi_1}-\frac{z}{\xi_2}\right)q_4(x_1)\right],$$

$$\tau_{z\theta}=\tau_{r\theta}=0. \tag{45}$$

(ii) Stress Green's functions for a torsional force as shown in Fig. 3:

(*a*) For the region $k=1$ $(z \geq 0)$,

$$\tau_{z\theta}=\frac{1}{8\pi^2\sqrt{arar}}\left\{\sum_{i=1}^{2}\frac{z_i}{x_i^2-1}G_1(x_i)-\frac{2\xi}{1+\xi}\frac{z_2}{x_2^2-1}G_1(x_2)\right\},$$

$$\tau_{r\theta}=\frac{-1}{8\pi^2 r\sqrt{ar}}\left[\sum_{i=1}^{2}\left\{3Q_{1/2}(x_i)+\frac{x_i-r/a}{x_i^2-1}G_1(x_i)\right\}-\frac{2\xi}{1+\xi}\left\{3Q_{1/2}(x_2)+\frac{x_2-r/a}{x_2^2-1}G_1(x_2)\right\}\right],$$

$$\sigma_r=\sigma_\theta=\sigma_z=\tau_{rz}=0.$$

(*b*) For the region $k=2$ $(z\leq 0)$,

$$\tau_{z\theta}=\frac{\xi z_1}{4\pi^2 ar\sqrt{ar}(1+\xi)}\frac{G_1(x_1)}{x_1^2-1},$$

$$\tau_{r\theta}=\frac{-\xi}{4\pi^2 r\sqrt{ar}(1+\xi)}\left\{3Q_{1/2}(x_1)+\frac{x_1-r/a}{x_1^2-1}G_1(x_1)\right\},$$

$$\sigma_r=\sigma_\theta=\sigma_z=\tau_{rz}=0. \tag{47}$$

(iii) Stress Green's functions for an axial force as shown in Fig. 4:

(*a*) For the region $k=1$ $(z \geq 0)$,

$$\sigma_r=\frac{-1}{arD}\left[\sum_{i=1}^{2}\frac{z_i}{2}\left\{Q_{1/2}(x_i)+\frac{1}{x_i^2-1}[q_1(x_i)+2\nu_1 G_2(x_i)-(x_i-a/r)G_1(x_i)]\right\}\right.$$
$$+\left\{(1-\nu_1)\left(\frac{3}{\xi_1}+\frac{\xi}{\xi_2}+1\right)-2\right\}\frac{z_2}{x_2^2-1}G_2(x_2)$$
$$+\left\{\frac{2(1-\nu_1)(z+\xi h)-(1-\xi)h}{\xi_1}-z_2\right\}\frac{q_1(x_2)}{x_2^2-1}$$
$$-(1-\nu_1)\left(\frac{3-4\nu_1}{\xi_1}-\frac{3-4\nu_2}{\xi_2}\right)aq_3'(x_2)$$
$$-\left\{z-\frac{2(1-\nu_1)z_1}{\xi_1}\right\}\left\{Q_{1/2}(x_2)-\frac{x_2-a/r}{x_2^2-1}G_1(x_2)\right\}$$
$$\left.+\frac{(1-\xi)(zhz_2)(2q_2(x_2)+q_5'(x_2))}{\xi_1\quad 2ar\quad x_2^2-1}\right],$$

$$\sigma_\theta=\frac{1}{arD}\left[\sum_{i=1}^{2}\frac{z_i}{2}\left\{Q_{1/2}(x_i)-\frac{1}{x_i^2-1}[(x_i-a/r)G_1(x_i)+2\nu_1 G_2(x_i)]\right\}+2\nu_1\left\{1-\frac{2(1-\nu_1)}{\xi_1}\right\}\frac{z_2}{x_2^2-1}G_2(x_2)\right.$$
$$+\frac{1-\xi}{\xi_1}\frac{h}{x_2^2-1}\left\{2\nu_1 q_1(x_2)+\frac{zz_2}{2ar}q_5'(x_2)\right\}$$
$$-(1-\nu_1)\left(\frac{3-4\nu_1}{\xi_1}-\frac{3-4\nu_2}{\xi_2}\right)aq_3'(x_2)$$
$$\left.-\left\{z-\frac{2(1-\nu_1)z_1}{\xi_1}\right\}\left\{Q_{1/2}(x_2)-\frac{x_2^2-a/r}{x_2^2-1}G_1(x_2)\right\}\right],$$

$$\sigma_z=\frac{1}{arD}\left[\sum_{i=1}^{2}\frac{z_i}{x_i^2-1}\left\{\frac{q_1(x_i)}{2}-(1-\nu_1)G_2(x_i)\right\}\right.$$
$$+\frac{1}{x_2^2-1}\left\{(1-\nu_1)\xi\left(\frac{3-4\nu_1}{\xi_1}+\frac{1}{\xi_2}\right)z_2 G_2(x_2)\right.$$
$$\left.\left.-\left[z-\frac{2(1-\nu_1)(z-\xi h)}{\xi_1}\right]q_1(x_2)+\frac{(1-\xi)zhz_2}{\xi_1\quad ar}q_2(x_2)\right\}\right],$$

$$\tau_{rz}=\frac{-1}{aD}\left[\sum_{i=1}^{2}\frac{1}{2}\left\{(1-2\nu_1)Q_{1/2}(x_i)-\frac{x_i-a/r}{x_i^2-1}G_1(x_i)\right]\right.$$
$$+\left.\frac{z_i^2\,q_5'(x_i)}{2ar\,x_i^2-1}\right\}+\left\{1-(1-\nu_1)\left(\frac{1}{\xi_1}+\frac{\xi}{\xi_2}+1\right)\right\}$$
$$\times\left\{Q_{1/2}(x_2)-\frac{x_2-a/r}{x_2^2-1}G_1(x_1)\right\}$$
$$-\left\{z_2-\frac{2(1-\nu_1)(z+\xi h)}{\xi_1}\right\}\frac{z_2\,q_5'(x_2)}{2ar\,x_2^2-1}$$
$$\left.+\frac{(1-\xi)\,zh}{\xi_1\quad 2ar}\frac{q_6'(x_2)}{x_2^2-1}\right],$$

$$\tau_{z\theta}=\tau_{r\theta}=0. \tag{48}$$

(*b*) For the region $k=2$ $(z\leq 0)$;

$$\sigma_r=\frac{\xi}{arD'}\left[\left(\frac{3-4\nu_1}{\xi_1}-\frac{3}{\xi_2}\right)\frac{z_1}{x_1^2-1}G_2(x_1)\right.$$
$$+\left(\frac{3-4\nu_1}{\xi_1}-\frac{3-4\nu_2}{\xi_2}\right)aq_3'x_1(x_1)+2\left(\frac{h}{\xi_1}-\frac{z}{\xi_2}\right)\left\{Q_{1/2}(x_1)\right.$$
$$\left.\left.+\frac{1}{x_1^2-1}\left[q_1(x_1)-\left(x_1-\frac{a}{r}\right)G_1(x_1)\right]\right\}\right],$$

$$\sigma_\theta=\frac{-\xi}{arD'}\left[2\left(\frac{h}{\xi_1}-\frac{z}{\xi_2}\right)\left\{Q_{1/2}(x_1)-\frac{x_1-a/r}{x_1^2-1}G_1(x_1)\right\}\right.$$
$$\left.+\left(\frac{3-4\nu_1}{\xi_1}-\frac{3-4\nu_2}{\xi_2}\right)aq_3'(x_1)+\frac{4\nu_2}{\xi_2}\frac{z_1}{x_1^2-1}G_2(x_1)\right],$$

$$\sigma_z=\frac{-\xi}{arD'}\frac{1}{x_1^2-1}\left\{\left(\frac{3-4\nu_1}{\xi_1}+\frac{1}{\xi_2}\right)z_1 G_2(x_1)+2\left(\frac{h}{\xi_1}-\frac{z}{\xi_2}\right)q_1(x_1)\right\},$$

$$\tau_{rz}=\frac{-\xi}{aD}\left[\left(\frac{3-4\nu_1}{\xi_1}-\frac{1}{\xi_2}\right)\left\{Q_{1/2}(x_1)-\frac{x_1-a/r}{x_1^2-1}G_1(x_1)\right\}\right.$$
$$\left.-\left(\frac{h}{\xi_1}-\frac{z}{\xi_2}\right)\frac{z_1\,q_5'}{arx_1^2-1}\right],$$

$$\tau_{z\theta}=\tau_{r\theta}=0 \tag{49}$$

where D and D' are

$$D=8\pi^2\sqrt{ar}(1-\nu_1),\ D'=8\pi^2\sqrt{ar} \tag{50}$$

and $q_n(x_i)$, $(n=1\sim 6)$ represent

$$q_1=\left\{1-\frac{2x_i}{x_i^2-1}\frac{z_i^2}{ar}\right\}G_2(x_i)+\frac{z_i^2}{2ar}Q_{-1/2}(x_i),$$

$$q_2=\left\{\frac{2x_i}{x_i^2-1}q_1(x_i)-\left(\frac{3}{2}-\frac{x_i}{(x_i^2-1)}\frac{z_i^2}{ar}\right)Q_{-1/2}(x_i)\right.$$
$$\left.+\frac{G_2(x_i)}{x_i^2-1}\left\{4x_i^2-\frac{z_i^2}{ar}\left(\frac{7}{4}+\frac{4}{x_i^2-1}\right)\right\}\right\},$$

$$q_3=\frac{\pi\sqrt{ar}}{a}\{1+\mathrm{SGN}(a-r)\}-\frac{z_2}{a}\left\{Q_{-1/2}(x_i)+\frac{a-r}{a+r}k\Pi(p,k)\right\},$$
$$(a\neq r)$$

$$= \pi - \frac{z_i}{a} Q_{-1/2}(x_i), \qquad (a = r)$$

$$a_4 = G_1(x_i) - \frac{z_i^2}{2ar} Q_{1/2}(x_i) + \frac{2}{x_i^2 - 1} \frac{z_i^2}{ar} G_2(x_i),$$

$$a_5 = 3Q_{-1/2}(x_i) + \frac{r}{a} Q_{1/2}(x_i) - \frac{4}{x_i^2 - 1} \left\{ G_1(x_i) + \frac{r}{a} G_2(x_i) \right\},$$

$$q_6 = \left(1 - \frac{2x_i \ z_i^2}{x_i^2 - 1ar}\right) q_5(x_i) + \frac{1}{(x_i^2 - 1)2ar} \frac{z_i^2}{} \left\{ \left(\frac{r}{a} + \frac{16x_i^2}{x_i^2 - 1}\right) G_1(x_i) - \left(3 - \left(\frac{r}{a}\right) \frac{16x_i}{x_i^2 - 1}\right) G_2(x_i) - 12Q_{1/2}(x_i) - \frac{4r}{a} Q_{-1/2}(x_i) \right\},$$

$$q_i' = q_i(a \leftrightarrow r) \tag{51}$$

where SGN (a-r) takes $+1$, 0 or -1 when the sign of the value $(a-r)$ is positive, zero, or negative, respectively. Also, $q_n(a \leftrightarrow r)$ means the exchange of a for r and r for a in the expression $q_n(x_i)$, and $\Pi(p, k')$ is a complete elliptic integral of the third kind. Here p and k' are

$$p = \frac{4ar}{(a+r)^2}, \ k'^2 = \frac{4ar}{(a+r)^2 + z_2^2}. \tag{52}$$

7 A Simple Application

As an example of application of Green's functions we consider eigenstrain problems. It is well known (Mura, 1987) that the displacements u_i due to axisymmetric eigenstrains

$$\epsilon_r^* = \epsilon_r^*(r, z), \ \epsilon_\theta^* = \epsilon_\theta^*(r, z), \ \epsilon_z^* = \epsilon_z^*(r, z),$$
$$\gamma_{rz}^* = \gamma_{rz}^*(r, z), \ \gamma_{r\theta}^* = \gamma_{r\theta}^*(r, z), \ \gamma_{z\theta}^* = \gamma_{z\theta}^*(r, z), \tag{53}$$

satisfy (3) if we put $-F_i$ instead of F_i in (3). Here we used the engineering strains, and F_i is given by

$$F_1 = \frac{2\mu}{r} \frac{\partial}{\partial r} \{ r(\epsilon_r^* - \epsilon_\theta^*) \} + \lambda \frac{\partial}{\partial r} (\epsilon_r^* + \epsilon_z^*) + (\lambda + 2\mu) \frac{\partial}{\partial r} \epsilon_\theta^* + \mu \frac{\partial}{\partial z} \gamma_{rz}^*,$$

$$F_2 = \mu \left(\frac{\partial}{\partial r} \gamma_{r\theta}^* + \frac{\partial}{\partial z} \gamma_{z\theta}^* + \frac{2}{r} \gamma_{r\theta}^* \right),$$

$$F_3 = \lambda \frac{\partial}{\partial z} (\epsilon_r^* + \epsilon_\theta^*) + (\lambda + 2\mu) \frac{\partial}{\partial z} \epsilon_z^* + \frac{\mu}{r} \frac{\partial}{\partial r} (r \gamma_{rz}^*). \tag{54}$$

From the foregoing results, we see that solutions for axisymmetric eigenstrain problems can be obtained by the expression

$$u_i^k = -\int_\Omega F_j(a,h) u_{ij}^k(r,z,a,h) d\Omega \tag{55}$$

where Ω is a domain of distribution of eigenstrains and $u_{ij}^k(r, z, a, h)$, $(i, j = 1, 2, 3)$ are Green's functions for the region k.

By applying the above results, exact solutions in closed forms will be obtained for the axisymmetric stress and displacement fields caused by a solid cylindrical inclusion with uniform axial eigenstrain

$$\epsilon_z^* = \epsilon_0 \{ S(z+b) - S(z-b) \} \{ 1 - S(r-c) \},$$
$$\epsilon_r^* = \epsilon_\theta^* = \gamma_{rz}^* = \gamma_{r\theta}^* = \gamma_{z\theta}^* = 0 \tag{56}$$

in a future paper (Hasegawa et al., 1991). Here, $S(\ )$ is a Heaviside step function, ϵ_0 is the magnitude of eigenstrain, and C and $2b$ are radius and length of the inclusion.

8 Concluding Remarks

The principle results of this paper are summarized as follows:

1 Green's functions for axisymmetric body force problems of dissimilar elastic solids were derived by applying stress functions for body force and surface force problems of elasticity.

2 As a special case, Green's functions are also obtained for problems of (i) an elastic half-space with the traction-free boundary, (ii) an elastic half-space with the rigidly fixed boundary, and (iii) a homogeneous isotropic elastic solid.

3 An application of the Green's functions was described for eigenstrain problems.

Acknowledgment

The authors wish to thank to Mr. T. Koya, Mr. W. Yeih and Dr. K.-U. King in Northwestern University for the typing of the manuscript. This research was supported by the U.S. Army ARO DAAL 03-89-K-0019, and also by Shin Nippon Seitetsu Co.

References

Dundurs, J., and Hetenyi, M., 1961, "The Elastic Plane With a Circular Insert Loaded by a Radial Force," ASME JOURNAL OF APPLIED MECHANICS, Vol. 28, pp. 103–111.

Dundurs, J., and Hetenyi, M., 1965, "Transmission of Force Between Two Semi-infinite Solids," ASME JOURNAL OF APPLIED MECHANICS, Vol. 32, pp. 671–674.

Eason, G., Noble, B., and Sneddon, I. N., 1955, "On Certain Integrals of Lipschitz-Hankel Type Involving Products of Bessel Functions," *Philosophical Transaction Royal Society, London*, Vol. A247, pp. 529–551.

Erdelyi, A., ed., 1954, *Tables of Integral Transforms*, Vol. 2, McGraw-Hill, New York.

Hasegawa, H., 1975, "An Extension of Love's Solution for Axisymmetric Problems of Elasticity," *Bulletin of the JSME*, Vol. 18, pp. 484–492.

Hasegawa, H., 1976, "Axisymmetric Body Force Problems of an Elastic Half Space," *Bulletin of the JSME*, Vol. 19, pp. 1262–1269.

Hasegawa, H., 1981, "On the Stress Concentration Problem of a Circular Shaft With a Semicircular Groove Under Tension (An Application of Green's Functions for Body Force Problems of a Soliod Cylinder)," *Bulletin of the JSME*, Vol. 24, pp. 520–527.

Hasegawa, H., 1982, "Green's Functions for Torsional Body Force Problems of an Elastic Thick Plate and their Application," *Bulletin of the JSME*, Vol. 25, pp. 9–15.

Hasegawa, H., 1984a, "Green's Functions for Axisymmetric Body Force Problems of an Elastic Half Space and their Application," *Bulletin of the JSME*, Vol. 27, pp. 1829–1835.

Hasegawa, H., 1984b, "Green's Functions for Axisymmetric Surface Force Problems of an Elastic Half Space and their Application," *Theoretical and Applied Mechanics*, Vol. 32, pp. 291–300.

Hasegawa, H., 1988, "A Fundamental Solution and Boundary Element Method for Torsion Problems of a Bonded Dissimilar Elastic Solid," *Boundary Element Method in Applied Mechanics*, M. Tanaka and T. A. Cruse, eds., Pergamon Press, pp. 139–145.

Hasegawa, H., 1990, "Green's Functions for Torsional Body Force Problems of an Elastic Layer on an Elastic Half Space," *JSME International Journal*, Series I, Vol. 33, pp. 468–473.

Hasegawa, H., Lee, V. G., and Mura, T., 1991, "The Stress Fields Caused by a Circular Cylinder Inclusion," submitted to ASME JOURNAL OF APPLIED MECHANICS.

Hetenyi, M., and Dundurs, J., 1962, "The Elastic Plane With a Circular Insert, Loaded by Tangentially Directed Force," ASME JOURNAL OF APPLIED MECHANICS, Vol. 29, pp. 362–368.

Kelvin, L., and Tait, P. G., 1895, *Natural Philosophy*, Part II, Cambridge University Press, p. 279.

Kermanidis, T., 1975, "A Numerical Solution for Axially Symmetric Elasticity Problems," *International Journal of Solids and Structures*, Vol. 11, pp. 493–500.

Kisu, H., Yuuki, R., and Ura, A., 1986, "On the Usefulness of Mindlin's Solution in Three-Dimensional Boundary Element Analysis," *Transaction of Japan Society of Mechanical Engineers*, Vol. 52, pp. 1864–1872.

Lee, J. C., Farris, T. N., and Keer, L. M., 1987, "Stress Intensity Factors for Cracks of Arbitrary Shape Near a Interfacial Boundary," *Engineering Fracture Mechanics*, Vol. 27, pp. 27–41.

Lee, J. C., and Keer, L. M., 1986, "Study of a Three-Dimensional Crack Terminating at an Interface," ASME JOURNAL OF APPLIED MECHANICS, Vol. 53, pp. 311–316.

Lee, T. S., Advani, S. H., and Lee, L. K., 1988, "Three-Dimensional Analysis of an Arbitrary Shaped Pressurized Crack Transversing a Bi-material Interface," *Engineering Fracture Mechanics*, Vol. 30, pp. 191–209.

Mindlin, R. D., 1936, "Force at a Point in the Interior of a Semi-infinite Solid," *Physics*, Vol. 17, pp. 195–202.

Mura, T., 1987, *Micromechanics of Defects in Solids*, Martinus Nijihoff, p. 11.

Nisitani, H., 1967, "On the Study of Two-Dimensional Stress Analysis by Using Digital Computer," *Journal of Japan Society Mechanical Engineers*, Vol. 70, pp. 627–635.

Rongved, L., 1955, "Force Interior to One of Two Joined Semi-infinite Solids," *Proceedings of the Second Midwestern Conference on Solid Mechanics*, pp. 1–13.

Yuuki, R., Cho, S.-B., Matsumoto, T., and Kisu, H., 1987, "Efficient Boundary Element Elastostatic Analysis Using Hetenyi's Fundamental Solution," *Transaction of Japan Society of Mechanical Engineers*, Series A, Vol. 53, pp. 1581–1589.

APPENDIX

The following integral formulas are used to evaluate the integrals that appear in this paper.

$$\int_0^\infty J_0(\alpha a)J_0(\alpha r)e^{-\alpha z}d\alpha = \frac{1}{\pi\sqrt{ar}}Q_{-1/2}(x),$$

$$\int_0^\infty J_1(\alpha a)J_0(\alpha r)e^{-\alpha z}d\alpha = \frac{1}{2\sqrt{ar}}\left\{\sqrt{\frac{r}{a}}[1+\mathrm{SGN}(a-r)] - \frac{z}{\pi a}[Q_{-1/2}(x) + \frac{a-r}{a+r}k\Pi(p,k)\right\},$$

$$\int_0^\infty \alpha J_1(\alpha a)J_0(\alpha r)e^{-\alpha z}d\alpha = \frac{1}{2\pi\sqrt{ar}}\left\{Q_{1/2}(x) - \frac{x-r/a}{x^2-1}G_1(x)\right\},$$

$$\int_0^\infty J_1(\alpha a)J_1(\alpha r)e^{-\alpha z}d\alpha = \frac{1}{\pi\sqrt{ar}}Q_{1/2}(x),$$

$$\int_0^\infty \alpha J_1(\alpha a)J_1(\alpha r)e^{-\alpha z}d\alpha = -\frac{1}{2\pi\sqrt{ar}}\frac{z}{ar}\frac{1}{x^2-1}G_1(x),$$

$$\int_0^\infty J_1(\alpha a)J_1(\alpha r)e^{-\alpha z}d\alpha = \frac{1}{4\pi ar\sqrt{ar}}[\pi\sqrt{ar}\{r^2 + a^2 + (r^2-a^2)\mathrm{SGN}(a-r) + z(a-r)^2k\Pi(p,k) - 2arz\,Q_{1/2}(x) - z(a^2+r^2)Q_{-1/2}(x)],$$

$$\int_0^\infty \frac{1}{\alpha}J_1(\alpha a)J_0(\alpha r)e^{-\alpha z}d\alpha = \frac{r}{2\pi\sqrt{ar}}\left[2G_2(x) + \left(\frac{a-r}{a+r}\right)\left(\frac{z^2}{ar}\right)k\Pi(p,k) - \frac{\pi z}{\sqrt{ar}}\{1+\mathrm{SGN}(a-r)\}\right]$$

We can also use the following relations:

$$Q_{1/2}(x) = xkF(k) - \sqrt{2(x+1)}E(k),$$

$$Q_{-1/2}(x) = kF(k)$$

where $F(k)$ and $E(k)$ are elliptic integrals of the first and second kinds, respectively.

J. L. Carvalho

J. H. Curran
Mem. ASME

Department of Civil Engineering,
University of Toronto,
Toronto M5S 1A4, Canada

Two-Dimensional Green's Functions for Elastic Bi-materials

Two-dimensional plane-strain fundamental solutions for elastic bi-materials are developed using the nuclei of strain method. The method is a reduction of the three-dimensional approach previously derived by Vijayakumar and Cormack. The structure of the three-dimensional solution is preserved and the two-dimensional nuclei of strain and their corresponding vector functions are reported in this paper. Application of these solutions to the boundary element method is demonstrated via a hydraulic fracturing example.

Introduction

Considering that two-dimensional analyses are often justified and less expensive than three-dimensional ones, and considering that most research ventures start by addressing problems in their two-dimensional (simplified) form, the authors were led to seek the two-dimensional fundamental solutions for elastic bi-materials. Using the three-dimensional solutions as the starting point, the two-dimensional solutions are obtained by integration of the former with respect to one of the axes contained by the interface and letting the limits of integration approach infinity (plane strain). These solutions are the basis of boundary element numerical techniques and were derived with this particular application in mind. More specifically, the authors are interested in the propagation of fractures through bonded layered media. Vertical containment and direction of propagation of hydraulic fractures is of primary interest to the oil industry and one of the factors which control their behavior is the material property contrast. The importance of these solutions lies in the fact that the interface is implicitly contained in them, thus eliminating the need of discretization which may cause numerical instabilities and costly analyses (both in time and memory requirements).

Galerkin Vectors

Before presenting the solutions in elastic bi-materials, a brief introduction to Galerkin vectors will follow. A Galerkin vector is a vector function that satisfies a fourth-order equation and has as its components Galerkin stress functions (Mindlin, 1936). Taking as the starting point the equilibrium equation in terms of the displacements, **u**, for a homogeneous, isotropic, linear elastic material, we write in vector form

$$\mu\left(\nabla^2+\frac{1}{1-2\nu}\nabla\operatorname{div}\right)\mathbf{u}+\mathbf{K}=0, \tag{1}$$

where **K** is the body force vector and μ and ν are the shear modulus and Poisson's ratio, respectively.

In the Galerkin vector approach, operators of order two on vector functions are used rather than taking the classical approach of representing the displacement as the product of a constant and the gradient of a scalar function ϕ (Westergaard, 1952). There are two such operators in the equilibrium Eq. (1), namely, the Laplace operator ∇^2 and the operator $\nabla\operatorname{div}$. Both these operators may be applied to a vector function. The equilibrium equation is satisfied if (Westergaard, 1952)

$$2\mu\mathbf{u}=[2(1-\nu)\nabla^2-\nabla\operatorname{div}]\mathbf{F}, \tag{2}$$

provided that

$$\nabla^4\mathbf{F}=\frac{\mathbf{K}}{1-\nu}. \tag{3}$$

The following expressions are obtained directly from Eq. (2) and the constitutive laws for a homogeneous, isotropic, linear elastic material:

$$2\mu u=2(1-\nu)\nabla^2X-\frac{\partial}{\partial x}\operatorname{div}\mathbf{F}$$

$$2\mu v=2(1-\nu)\nabla^2Y-\frac{\partial}{\partial y}\operatorname{div}\mathbf{F}$$

$$2\mu w=2(1-\nu)\nabla^2Z-\frac{\partial}{\partial z}\operatorname{div}\mathbf{F}$$

$$\sigma_{xx}=2(1-\nu)\frac{\partial\nabla^2X}{\partial x}+\left(\nu\nabla^2-\frac{\partial^2}{\partial x^2}\right)\operatorname{div}\mathbf{F}$$

$$\sigma_{yy}=2(1-\nu)\frac{\partial\nabla^2Y}{\partial y}+\left(\nu\nabla^2-\frac{\partial^2}{\partial y^2}\right)\operatorname{div}\mathbf{F}$$

$$\sigma_{zz}=2(1-\nu)\frac{\partial\nabla^2Z}{\partial z}+\left(\nu\nabla^2-\frac{\partial^2}{\partial z^2}\right)\operatorname{div}\mathbf{F}$$

$$\sigma_{kk}=\sigma_{xx}+\sigma_{yy}+\sigma_{zz}=(1+\nu)\nabla^2\operatorname{div}\mathbf{F}$$

$$\sigma_{xy}=(1-\nu)\left(\frac{\partial\nabla^2X}{\partial y}+\frac{\partial\nabla^2Y}{\partial x}\right)-\frac{\partial^2}{\partial x\partial y}\operatorname{div}\mathbf{F}$$

Contributed by the Applied Mechanics Division of THE AMERICAN SOCIETY OF MECHANICAL ENGINEERS for publication in the ASME JOURNAL OF APPLIED MECHANICS.

Discussion on this paper should be addressed to the Technical Editor, Prof. Leon M. Keer, The Technological Institute, Northwestern University, Evanston, IL 60208, and will be accepted until four months after final publication of the paper itself in the JOURNAL OF APPLIED MECHANICS. Manuscript received by the ASME Applied Mechanics Division Aug. 15, 1990; final revision Feb. 12, 1991.

$$\sigma_{yz} = (1-\nu)\left(\frac{\partial \nabla^2 Y}{\partial z} + \frac{\partial \nabla^2 Z}{\partial y}\right) - \frac{\partial^2}{\partial y \partial z}\,\mathrm{div}\mathbf{F}$$
$$\sigma_{zx} = (1-\nu)\left(\frac{\partial \nabla^2 X}{\partial z} + \frac{\partial \nabla^2 Z}{\partial x}\right) - \frac{\partial^2}{\partial x \partial z}\,\mathrm{div}\mathbf{F}$$

where X, Y, and Z are the components of the vector $\mathbf{F}$ in the i, j, and k directions, respectively, and are part of a group of solutions known as *nuclei of strain*.

Method of Images

The method of images is a technique that uses superposition of known solutions to solve new problems. The method earned its name from the fact that combinations of known solutions are applied at points which are equi-distant from global axes. These points are referred to as *object* and *image* points.

One of the well-known solutions obtained by this method is Mindlin's solution (1936) for a point force in the interior of an elastic half-space. Mindlin's solution is a particular case of the more general solution for bi-materials, where the second material has zero modulus (nonexistent). Several authors have derived solutions for point forces in the interior of one of two semi-infinite solids joined by a bonded interface (Rongved, 1955), or a sliding interface (Dundurs and Hetényi, 1965). The case of a bonded interface where the second material is rigid, i.e., an elastic half-space with a fixed boundary, has also been solved (Phan-Thien, 1983). Only the latter has made use of the nuclei of strain in conjunction with the method of images. All of the above solutions were obtained for point forces. However, some approaches to the fracture propagation problem (e.g., displacement discontinuity) require solutions for other nuclei of strain.

Vijayakumar and Cormack (1987a) have derived a general approach to obtain solutions to the bi-material problem. They have defined classes of nuclei of strain from which any one nucleus may be chosen as the singular nucleus applied at the object point. Each of these classes of nuclei defines a *closed* set, in the sense that when any nucleus is selected to be applied at the object point, the nuclei contained in the class are sufficient to obtain a solution, i.e., create any specified condition at the interface. Not only have these authors derived the solution for all the nuclei of strain (see Fig. A1), but they have also structured the method to obtain them. A brief presentation of the method follows.

Consider two independent infinite spaces with different elastic properties, paying particular attention to the plane $z=0$ (Fig. 1(*a*) and 1(*b*)).

We apply the nucleus of strain of interest (e.g., Point force) at the object point of material 1 and a linear combination of all the nuclei of strain from the same class at the image point of material 1.

Independently, using the same class as for material 1, we apply a different linear combination of all the nuclei of strain at the object point of material 2. Coefficients for these two linear combinations can be found such that specified quantities (displacements and stresses) are identical at the plane $z=0$ of both spaces.

Therefore, the positive half-space of material 1 contains the singular nucleus of interest, the negative half-space of material 2 has no singularity at all since there were no nuclei applied within it, and the planes $z=0$ of both materials exhibit the same behavior, as far as selected matched quantities are concerned. This means that the two mentioned half-spaces can be juxtaposed (Fig. 1(*c*)), creating the solution for a bi-material with specified properties at the interface (e.g., bonded or frictionless).

The solution vector, $\mathbf{s}$, obtained by the application of nuclei of strain at each point can be decomposed into three entities (Vijayakumar and Cormack, 1987a): vectors containing all the

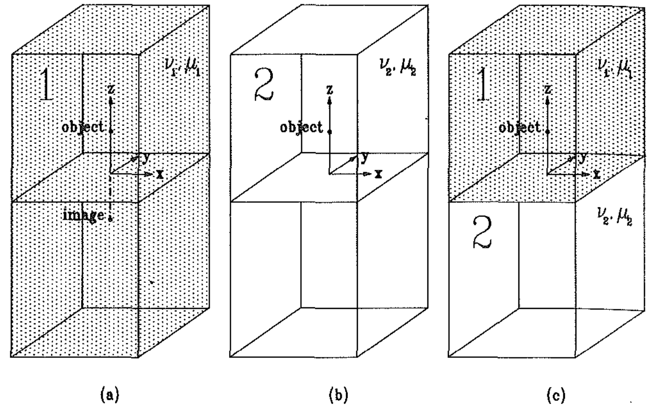

Fig. 1 Representation of bi-material

nuclei of strain in the class of the singular nucleus ($\mathbf{F}_A$, $\overline{\mathbf{F}}_A$), matrices of material properties ($\mathbf{C}_A$) solely dependent on the elastic constants μ and ν, and a vector containing the intensities of the nuclei of strain applied at the considered points. In the case of the object point in material 1 (singular point), the only nonzero entry in the vector of intensities of the nuclei of strain ($\mathbf{a}$) is the one corresponding to the singular nucleus. In the case of the image point of material 1 and the object point of material 2, the vectors of intensities of the nuclei of strain ($\bar{\mathbf{a}}$ and $\bar{\bar{\mathbf{a}}}$, respectively) will depend on the vector $\mathbf{a}$ and the properties of the interface; they can be represented as follows:

$$\begin{aligned}\bar{\mathbf{a}} &= [\mathbf{R}_A]\mathbf{a} \\ \bar{\bar{\mathbf{a}}} &= [\mathbf{T}_A]\mathbf{a}\end{aligned} \tag{5}$$

where $[\mathbf{R}_A]$ and $[\mathbf{T}_A]$ are called the "reflection" and the "transmission" matrices due to the analogy between the bimaterial problem and the light transmission problem in optics (Vijayakumar and Cormack, 1987a). The matrices $[\mathbf{R}_A]$ and $[\mathbf{T}_A]$ depend on the material properties of both materials and the conditions set at the interface.

Defining the solution vector as

$$\mathbf{s}^T = [u, v, w, \sigma_{xx}, \sigma_{yy}, \sigma_{zz}, \tau_{xz}, \tau_{yz}, \tau_{xy}], \tag{6}$$

we have, in material 1,

$$\mathbf{s} = \mathbf{F}_A \mathbf{C}_A(\mu_1, \nu_1)\mathbf{a} + \overline{\mathbf{F}}_A \mathbf{C}_A(\mu_1, \nu_1)\bar{\mathbf{a}} \tag{7}$$

and, in material 2,

$$\mathbf{s} = \mathbf{F}_A \mathbf{C}_A(\mu_2, \nu_2)\bar{\bar{\mathbf{a}}} \tag{8}$$

where

$$\mathbf{F}_A = \begin{bmatrix} \mathbf{f}_{Au}^T & & 0 \\ & \mathbf{f}_{Av}^T & \\ & & \ddots \\ 0 & & \mathbf{f}_{Axy}^T \end{bmatrix};$$

$$\overline{\mathbf{F}}_A = \begin{bmatrix} \bar{\mathbf{f}}_{Au}^T & & 0 \\ & \bar{\mathbf{f}}_{Av}^T & \\ & & \ddots \\ 0 & & \bar{\mathbf{f}}_{Axy}^T \end{bmatrix};$$

$$\mathbf{C}_A = \begin{bmatrix} \mathbf{C}_{Au}^T \\ \mathbf{C}_{Av}^T \\ \vdots \\ \mathbf{C}_{Axy}^T \end{bmatrix}; \tag{9}$$

$\mathbf{f}_{Au}$, $\mathbf{f}_{Av}$, ..., $\mathbf{f}_{Axy}$ are the vectors of nuclei of strain applied at the object point; $\bar{\mathbf{f}}_{Au}$, $\bar{\mathbf{f}}_{Av}$, ..., $\bar{\mathbf{f}}_{Axy}$ are the vectors of nuclei of strain applied at the image point; $\mathbf{C}_{Au}$, $\mathbf{C}_{Av}$, ..., $\mathbf{C}_{Axy}$ are the matrices of material properties; and $\mathbf{a}$, $\bar{\mathbf{a}}$, and $\bar{\bar{\mathbf{a}}}$ are the vectors of intensities of the nuclei of strain.

Previous Solutions (Three-Dimensional)

There are two major types of classes of nuclei of strain. The first creates a stress field which is axisymmetric about the normal to the interface. Only one class (class A) exhibits this property. It contains 6 nuclei of strain, among which are the point force and the double force, both normal to the interface.

The second type of classes of nuclei create an asymmetrical stress state. These classes contain 8 nuclei of strain. Class B has the point force in the x-direction (parallel to the interface) as its basic nucleus and class C has the point force in the y-direction (parallel to the interface) as its basic nucleus. Class C can be obtained from class B by a simple interchange of the x and y variables and the $\mathbf{i}$ and $\mathbf{j}$ unit vectors. All of these nuclei of strain have to be scaled (see Tables 1 and 2) to enable the decomposition of the solution as shown in the previous section.

Because these classes do not contain all the necessary nuclei to form the "Displacement Discontinuity" solutions, four more classes were introduced (Vijayakumar and Cormack, 1987a). They were obtained by differentiation of the nuclei of strain in classes B and C. They have as their basic nuclei the double force in the x-direction (class D) and the y-direction (class E), the double force in the x-direction with moment about the z-axis (class F) and the double force in the y-direction with moment about the z-axis (class G). As before, nuclei in classes E and G can be obtained from the nuclei in classes D and F, respectively, by interchanging x and y variables $\mathbf{i}$ and $\mathbf{j}$ unit vectors.

Although there are seven classes of nuclei of strain, there are only two sets of reflection and transmission matrices. One set is associated with class A and a second set associated with classes B through G. The reason for this is that class C is identical (except for axes) to class B and classes D, E, F and G were obtained from classes B and C. The same is true for the material property matrices. Reflection and transmission matrices exist for two different conditions at the interface. The first is a bonded interface, i.e., the displacements, the normal stress across the interface and the shear stresses are the same on both sides of the interface (Vijayakumar and Cormack, 1987a). The second is a frictionless interface, i.e., the displacement normal to the interface and the normal stress across the interface are conserved; the shear stresses are equal to zero (Vijayakumar and Cormack, 1987b).

Two-Dimensional Solutions (Plane Strain)

The structure of the two-dimensional solutions is the same as that of the three-dimensional ones. The material property matrices and the reflection and transmission matrices do not change. This shows the advantage of using Vijayakumar and Cormack's structuring method for obtaining the solutions.

Therefore, for the two-dimensional plane-strain case, only the nuclei of strain need to be derived. Rather than trying to find the different nuclei of strain by solving the bi-harmonic equation, we can use the three-dimensional nuclei as a starting point. By integrating the three-dimensional nuclei of strain with respect to an axis parallel to the interface, from $-\infty$ to $+\infty$, we generate a continuous line of nuclei in that direction, thus a plane-strain condition on the plane whose normal is the axis of integration. Therefore, choosing the y-axis as the axis of integration, we obtain

$$\mathbf{F}_{2D} = \lim_{a\to\infty} \int_{-a}^{a} \mathbf{F}_{3D}\, dy \tag{10}$$

where

$\mathbf{F}_{3D}$ is any three-dimensional nucleus, and

$\mathbf{F}_{2D}$ is the two-dimensional nucleus corresponding to $\mathbf{F}_{3D}$.

Note that because of the plane-strain condition the point force in the y-direction, the double force in the y-direction and the double forces with moment about the z-axis cease to have any meaning. This is reflected in the integration of the corresponding three-dimensional nuclei, as they either yield null two-dimensional nuclei or are oriented in the y-direction. Therefore, the classes of nuclei C, E, F, and G are not required in two dimensions. Also, as a result of the plane-strain hypothesis, the displacement in the y-direction and the stresses on the y-plane for all solutions are

$$\begin{aligned} v &= 0 \\ \sigma_{xy} &= \sigma_{zy} = 0 \\ \sigma_{yy} &= \nu(\sigma_{xx} + \sigma_{zz}). \end{aligned} \tag{11}$$

The nuclei of strain for classes A'(unscaled), A, B, and D

Table 1 Nuclei in class A′ (unscaled), two-dimensional

Type	Functional form at object point $z = c$	Functional form at image point $z = -c$	Physical significance
$A'1$	$-\mathbf{k}\, r^2 \log r$	$-\mathbf{k}\, \bar{r}^2 \log \bar{r}$*	Single force in z-direction
$A'2$	$-\mathbf{k}\, 2(z-c) \log r$	$-\mathbf{k}\, 2(z+c) \log \bar{r}$	Double force in the z-direction
$A'3$	$-\mathbf{k}\left\{2x \arctan\left(\frac{x}{r-z+c}\right) + (z-c)(\log r - 1)\right\}$	$\mathbf{k}\left\{2x \arctan\left(\frac{x}{\bar{r}+z+c}\right) - (z+c)(\log \bar{r} - 1)\right\}$	Centre of dilation
$A'4$	$-\mathbf{k}\left\{2x(z-c) \arctan\left(\frac{x}{r-z+c}\right) - (z-c)^2 - x^2 \log r\right\}$	$\mathbf{k}\left\{2x(z+c) \arctan\left(\frac{x}{\bar{r}+z+c}\right) + (z+c)^2 + x^2 \log \bar{r}\right\}$	Line of centres of dilation†
$A'5$	$-\mathbf{k}\, 2 \log r$	$-\mathbf{k}\, 2 \log \bar{r}$	Doublet with axis parallel to z-axis
$A'6$	$\mathbf{k}\, \frac{2z(z-c)}{r^2}$	$\mathbf{k}\, \frac{2z(z+c)}{\bar{r}^2}$	Multiplet

* $\bar{r} = (x^2 + (z+c)^2)^{\frac{1}{2}}$

† In this case, the line extends from $z = c$ to $z = +\infty$ for nucleus at object and from $z = -c$ to $z = -\infty$ for nucleus at image point.

Table 2 Nuclei in class A (scaled), two-dimensional

Type	Functional form at object point $z = c$	Functional form at image point $z = -c$	Multiplication factor
$A1$	$-\mathbf{k}\, r^2 \log r$	$-\mathbf{k}\, \bar{r}^2 \log \bar{r}$	1
$A2$	$-\mathbf{k}\, 2c(z-c) \log r$	$-\mathbf{k}\, 2c(z+c) \log \bar{r}$	c
$A3$	$-\mathbf{k}c\left\{2x \arctan\left(\frac{x}{r-z+c}\right) + (z-c)(\log r - 1)\right\}$	$\mathbf{k}c\left\{2x \arctan\left(\frac{x}{\bar{r}+z+c}\right) - (z+c)(\log \bar{r} - 1)\right\}$	c
$A4$	$-\mathbf{k}\left\{2x(z-c) \arctan\left(\frac{x}{r-z+c}\right) - (z-c)^2 - x^2 \log r\right\}$	$\mathbf{k}\left\{2x(z+c) \arctan\left(\frac{x}{\bar{r}+z+c}\right) + (z+c)^2 + x^2 \log \bar{r}\right\}$	1
$A5$	$-\mathbf{k}\, 2c^2 \log r$	$-\mathbf{k}\, 2c^2 \log \bar{r}$	c^2
$A6$	$\mathbf{k}\,\frac{2c^2 z(z-c)}{r^2}$	$\mathbf{k}\,\frac{2c^2 z(z+c)}{\bar{r}^2}$	c^2

Table 3 Nuclei in class B (scaled), two-dimensional

Type	Functional form at object point $z = c$	Functional form at image point $z = -c$	Physical significance
$B1$	$-\mathbf{i}\, r^2 \log r$	$-\mathbf{i}\, \bar{r}^2 \log \bar{r}$	Single force in x-direction
$B2$	$-\mathbf{k}\, 2cx \log r$	$-\mathbf{k}\, 2cx \log \bar{r}$	Double force in the z-direction with moment about y-axis
$B3$	$-\mathbf{i}\, 2c(z-c) \log r$	$-\mathbf{i}\, 2c(z+c) \log \bar{r}$	Double force in the x-direction with moment about y-axis
$B4$	$-\mathbf{i}c\left\{2x \arctan\left(\frac{x}{r-z+c}\right) + (z-c)(\log r - 1)\right\}$	$\mathbf{i}c\left\{2x \arctan\left(\frac{x}{\bar{r}+z+c}\right) - (z+c)(\log \bar{r} - 1)\right\}$	—
$B5$	$-\mathbf{i}\left\{2x(z-c) \arctan\left(\frac{x}{r-z+c}\right) - (z-c)^2 - x^2 \log r\right\}$	$\mathbf{i}\left\{2x(z+c) \arctan\left(\frac{x}{\bar{r}+z+c}\right) + (z+c)^2 + x^2 \log \bar{r}\right\}$	Linearly varying line of doublets parallel to x-axis along z-axis *
$B6$	$-\mathbf{k}x\left\{2x \arctan\left(\frac{x}{r-z+c}\right) + (z-c)(\log r - 1)\right\}$	$\mathbf{k}x\left\{2x \arctan\left(\frac{x}{\bar{r}+z+c}\right) - (z+c)(\log \bar{r} - 1)\right\}$	Line of double forces in z-direction with moment about y-axis placed along z-axis *
$B7$	$-\mathbf{i}\, 2c^2 \log r$	$-\mathbf{i}\, 2c^2 \log \bar{r}$	Doublet with axis parallel to x-axis
$B8$	$\mathbf{k}\,\frac{2c^2 z(z-c)}{r^2}$	$\mathbf{k}\,\frac{2c^2 z(z+c)}{\bar{r}^2}$	Multiplet

* In these cases, the line extends from $z = c$ to $z = +\infty$ for nucleus at object and from $z = -c$ to $z = -\infty$ for nucleus at image point.

are shown on Tables 1, 2, 3, and 4, respectively, and their pictorial representations are shown in Fig. A1. The two-dimensional $\mathbf{f}$ and $\bar{\mathbf{f}}$ vectors for classes A and B required for the structured solution method (see Eqs. (6)–(8)) are reported in the Appendix. The $\mathbf{f}$ and $\bar{\mathbf{f}}$ vectors for class D can be obtained from class B by differentiation with respect to x.

Application

In the petroleum industry, one of the most widely used methods for enhancing production is the hydraulic fracturing process. The method involves packing off a section of a borehole in the "pay zone" (layer containing the hydrocarbon) and hydraulically pressurizing it until the formation fractures. The fracture is then propagated by keeping the borehole pressurized, typically by controlling the flow rate at the surface. During the extension phase of the fracturing process, a proppant (e.g., sand) is mixed with the fracturing fluid to prevent the closing of the fracture once the well is depressurized.

In modeling the fracturing process, there are a number of complex mechanics aspects that need to be considered. These include: response of the formation to the creation, pressurization and extension of the fracture, flow of fluid in the fracture, mechanics of fracturing at the fracture tip, diffusion of the fracturing fluid into the formation, influence of different concentrations of proppant on the properties of the fracturing fluid, etc.

In order to simplify the design process, the geometry of the hydraulically created fracture is often assumed a priori. For instance, in the case of layered media, perfect containment is often assumed, which implies a rectangular-shaped fracture, aligned with the major in situ principal stress. Also, the influence of the contrast in elastic stiffness between the pay zone and bounding layers is usually ignored. By using the solutions

Table 4 Nuclei in class D (scaled), two-dimensional

Type	Functional form at object point $z=c$	Functional form at image point $z=-c$	Physical significance
$D1$	$-\mathbf{i}\,2x\log r$	$-\mathbf{i}\,2x\log\bar{r}$	Double force in x-direction
$D2$	$-\mathbf{k}c\left\{2\log r+\dfrac{2x^2}{r^2}\right\}$	$-\mathbf{k}c\left\{2\log\bar{r}+\dfrac{2x^2}{\bar{r}^2}\right\}$	—
$D3$	$-\mathbf{i}\,\dfrac{2cx(z-c)}{r^2}$	$-\mathbf{i}\,\dfrac{2cx(z+c)}{\bar{r}^2}$	—
$D4$	$-\mathbf{i}\,4c\arctan\left(\dfrac{x}{r-z+c}\right)$	$-\mathbf{i}\,4c\arctan\left(\dfrac{x}{\bar{r}+z+c}\right)$	—
$D5$	$-\mathbf{i}\left\{4(z-c)\arctan\left(\dfrac{x}{r-z+c}\right)-2\log r\right\}$	$\mathbf{i}\left\{4(z+c)\arctan\left(\dfrac{x}{\bar{r}+z+c}\right)+2\log\bar{r}\right\}$	—
$D6$	$-\mathbf{k}\left\{6x\arctan\left(\dfrac{x}{r-z+c}\right)+(z-c)(\log r-1)\right\}$	$\mathbf{k}\left\{6x\arctan\left(\dfrac{x}{\bar{r}+z+c}\right)-(z+c)(\log\bar{r}-1)\right\}$	—
$D7$	$\mathbf{i}\,\dfrac{2c^2x}{r^2}$	$-\mathbf{i}\,\dfrac{2c^2x}{\bar{r}^2}$	—
$D8$	$\mathbf{k}c^2\left\{\dfrac{2z}{r^2}-\dfrac{4x^2z}{r^4}\right\}$	$\mathbf{k}c^2\left\{\dfrac{2z}{\bar{r}^2}-\dfrac{4x^2z}{\bar{r}^4}\right\}$	—

presented in this paper, it becomes much more practical to solve for the geometry of the fracture, as the computational effort in carrying out a stress analysis of elastic bi-materials is greatly reduced.

A numerical model based on the displacement discontinuity method has been developed to investigate the influence of bonded interfaces on fracture propagation. The method uses for Green's functions the singular displacement discontinuity solutions for bonded bi-materials. These are obtained by linear combinations of the solutions presented in the previous section. A boundary element, weighted residuals approach is employed in the numerical scheme for the stress analysis and a finite element, parallel plate model is used for the fluid flow in the fracture. The effect of a material of different stiffness at a given distance from a fracture parallel to the interface was investigated for a range of stiffness ratios and distances from the interface (see Fig. 2). Of interest are the effects on both the propagation path and the propagation pressure. Only the former is presented in this paper.

Three ratios of 'distance to interface' to fracture half-length, $2\delta/L$, were analyzed for material contrasts (E_1^*/E_2^*, where $E^*=E/(1-\nu^2)$) of 0.1, 0.5, and 2 when the fracture lies in material 1.

The presence of a stiffer material 2 drives the fracture away from the interface in search of a more compliant zone. Ultimately, the fracture appears to have a preferred angle of propagation for each E_1^*/E_2^* ratio, which is independent of its initial distance from the interface (Figs. 3 through 5). When the angle "arctan($2\delta/L$)" is smaller than the preferred angle of propagation, i.e., the fracture is close to the interface, it feels the second material in a much stronger way and the initial propagation angle is steeper than the asymptotic value. When the angle arctan($2\delta/L$) is greater than the preferred angle of propagation, the initial propagation angle is shallower than the asymptotic value. This behavior is analogous to the behavior of parallel fractures (Jeffrey et al., 1987), i.e., the fractures have a tendency to drive each other apart at a constant angle which depends on the original distance between them.

Conversely, when the second material is softer than the one containing the fracture, it attracts the fracture towards the interface in the same manner the stiffer material drove it away,

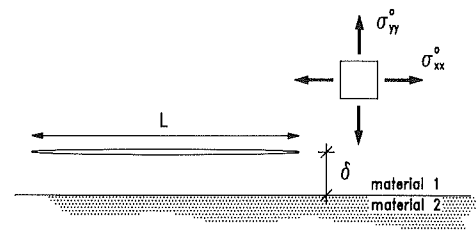

Fig. 2 Fracture parallel to interface

i.e., the fractures closer to the interface will start propagating at a steeper angle than the fractures further away from the interface. The asymptotic propagation path for fractures growing towards a softer material is right along the interface, without crossing it.

Conclusion

Two-dimensional Green's functions for elastic bi-materials have been derived by reducing the three-dimensional nuclei of strain through an integral procedure. The availability of these fundamental solutions is crucial for boundary element techniques.

In the case of bi-materials, the conventional method of solution, using the boundary element method, is to discretize the interface with a double layer of elements (geometrically coincident), one for each material. The desired interface behavior is then imposed on the interface elements. This results in very large systems of equations due to the need to extend the discretization well away from the zone of interest. However, the most serious deficiency of the discretization method is that numerical instabilities develop as the fracture gets closer to the interface, requiring smaller elements and resulting in loss of accuracy.

The solution presented in this paper overcomes the time and storage requirements for the large systems of equations generated by the discretized method of solution as well as the numerical instabilities and loss of accuracy which are present in these conventional methods.

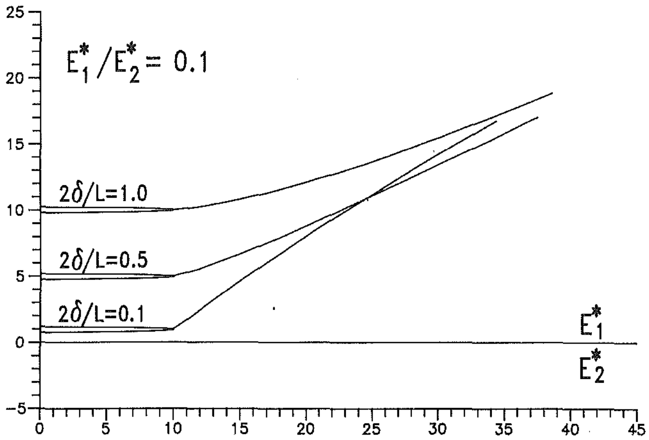

Fig. 3 Propagation path ($E_1^*/E_2^* = 0.1$)

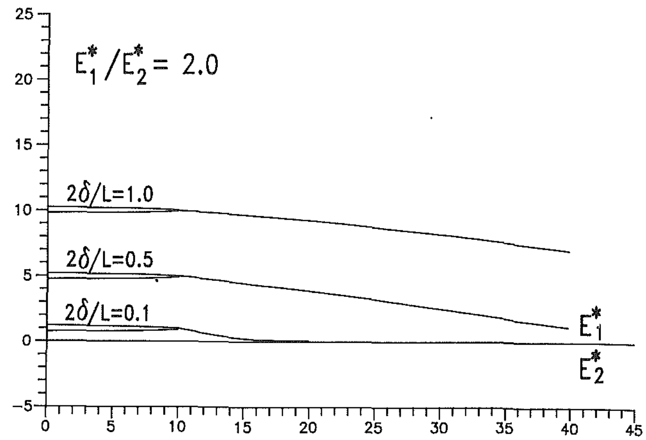

Fig. 5 Propagation path ($E_1^*/E_2^* = 2.0$)

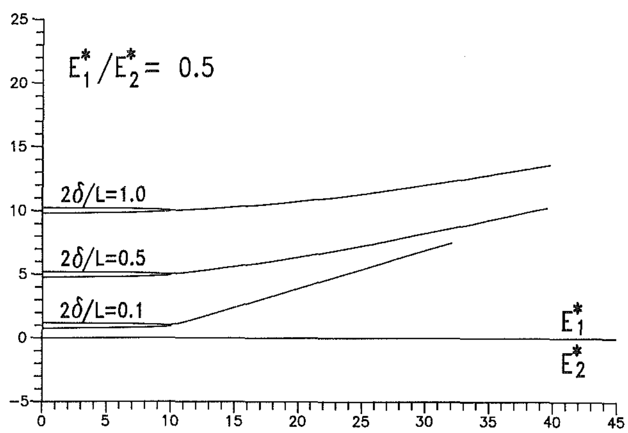

Fig. 4 Propagation path ($E_1^*/E_2^* = 0.5$)

Acknowledgment

The work which led to this paper was sponsored by the Natural Sciences and Engineering Research Council of Canada (NSERC) through an operating grant to J. H. Curran. This financial support is greatly appreciated.

References

Dundurs, J., and Hetényi, M., 1965, "Transmission of Force Between Two Semi-infinite Solids," ASME JOURNAL OF APPLIED MECHANICS, Vol. 32, pp. 671–674.

Jeffrey, R. G., Vandamme, L., and Roegiers, J.-C., 1987, "Mechanical Interactions in Branched or Subparallel Hydraulic Fractures," Paper SPE/DOE 16422 presented at the SPE/DOE Low Permeability Reservoirs Symposium, Denver, Colo., May 18–19.

Mindlin, R. D., 1936, "Force at a Point in the Interior of a Semi-Infinite Solid," *Physics*, Vol. 7, No. 4, pp. 195–202.

Phan-Thien, N., 1983, "On the Image System for the Kelvin-State," *Journal of Elasticity*, No. 13, pp. 231–235.

Rongved, L., 1955, "Force Interior to One of Two Joined Semi-Infinite Solids," *Proc. of the Second Midwestern Conference on Solid Mechanics*, pp. 1–13.

Vijayakumar, S., and Cormack, D. E., 1987a, "Green's Functions for the Biharmonic Equation: Bonded Elastic Media," *SIAM Journal of Applied Mathematics*, Vol. 47, No. 5, pp. 982–997.

Vijayakumar, S., and Cormack, D. E., 1987b, "Nuclei of Strain for Bimaterial Elastic Media with Sliding Interface," *Journal of Elasticity*, No. 17, pp. 285–290.

Westergaard, H. M., 1952, *Theory of Elastic and Plasticity*, Harvard University Press, Cambridge, MA.

APPENDIX

The vector components of the matrices $\mathbf{F}_A$ and $\overline{\mathbf{F}}_A$ are given below in compact form. The appropriate expressions for the vectors of the matrix $\mathbf{F}_A$ are obtained by replacing $\hat{\mathbf{f}}_A$'s by $\mathbf{f}_A$'s and $\hat{r}$ by r and assuming the lower sign wherever the dual sign, i.e., ($\pm$) or ($\mp$), appears. The vector components of matrix $\overline{\mathbf{F}}_A$ are obtained by replacing $\hat{\mathbf{f}}_A$'s by $\overline{\mathbf{f}}_A$'s and $\hat{r}$ by $\bar{r}$ and assuming the upper sign wherever the dual sign appears.

$$r = (x^2 + (z-c)^2)^{1/2} \qquad \text{(A1)}$$
$$\bar{r} = (x^2 + (z+c)^2)^{1/2}$$

$$\hat{\mathbf{f}}_{Au}^T = \left[\pm 2\arctan\left(\frac{x}{\hat{r} \pm z + c}\right), \frac{x(z\pm c)}{\hat{r}^2}, \frac{xc}{\hat{r}^2}, \frac{2x(z\pm c)^2 c}{\hat{r}^4}, \frac{2x(z\pm c)c^2}{\hat{r}^4}, \frac{\pm 2xc^3}{\hat{r}^4}, \frac{8xz(z\pm c)^2c^2}{\hat{r}^6} \right]$$

$$\hat{\mathbf{f}}_{Av}^T = [0, 0, 0, 0, 0, 0, 0]$$

$$\hat{\mathbf{f}}_{Aw}^T = \left[-\ln\hat{r}, \frac{(z\pm c)^2}{\hat{r}^2}, \frac{(z\pm c)c}{\hat{r}^2}, \frac{c^2}{\hat{r}^2}, \frac{2(z\pm c)^3 c}{\hat{r}^4}, \frac{2(z\pm c)^2c^2}{\hat{r}^4}, \frac{2(z\pm c)c^3}{\hat{r}^4}, \frac{8z(z\pm c)^3c^2}{\hat{r}^6} \right]$$

$$\hat{\mathbf{f}}_{Axx}^T = \left[\frac{(z\pm c)}{\hat{r}^2}, \frac{c}{\hat{r}^2}, \frac{2x^2(z\pm c)}{\hat{r}^4}, \frac{2x^2c}{\hat{r}^4}, \frac{2(z\pm c)^2c}{\hat{r}^4}, \frac{2(z\pm c)c^2}{\hat{r}^4}, \frac{\pm 2c^3}{\hat{r}^4}, \frac{8x^2(z\pm c)^2c}{\hat{r}^6}, \frac{8x^2(z\pm c)c^2}{\hat{r}^6}, \frac{\pm 8x^2c^3}{\hat{r}^6}, \frac{8(z\pm c)^3c^2}{\hat{r}^6}, \frac{\pm 8(z\pm c)^2c^3}{\hat{r}^6}, \frac{2}{x}\arctan\left(\frac{x}{\hat{r}\pm z + c}\right), \frac{\mp(z\pm c)}{\hat{r}^2} + \frac{2}{x}\arctan\left(\frac{x}{\hat{r}\pm z + c}\right), \frac{48x^2z(z\pm c)^2c^2}{\hat{r}^8} \right]$$

$$\hat{\mathbf{f}}_{Ayy}^T = \left[\frac{(z\pm c)}{\hat{r}^2}, \frac{c}{\hat{r}^2}, \frac{(z\pm c)}{\hat{r}^2}, \frac{c}{\hat{r}^2}, \frac{2(z\pm c)^2c}{\hat{r}^4}, \frac{2(z\pm c)c^2}{\hat{r}^4}, \frac{\pm 2c^3}{\hat{r}^4}, \frac{2(z\pm c)^2c}{\hat{r}^4}, \frac{2(z\pm c)c^2}{\hat{r}^4}, \frac{\pm 2c^3}{\hat{r}^4}, \frac{8(z\pm c)^3c^2}{\hat{r}^6}, \frac{\pm 8(z\pm c)^2c^3}{\hat{r}^6}, \frac{2}{x}\arctan\left(\frac{x}{\hat{r}\pm z + c}\right), \frac{2}{x}\arctan\left(\frac{x}{\hat{r}\pm z + c}\right), \frac{8z(z\pm c)^2c^2}{\hat{r}^6} \right]$$

$$\hat{\mathbf{f}}_{Azz}^T = \left[\frac{(z\pm c)}{\hat{r}^2}, \frac{c}{\hat{r}^2}, \frac{2(z\pm c)^3}{\hat{r}^4}, \frac{2(z\pm c)^2c}{\hat{r}^4}, \frac{2(z\pm c)c^2}{\hat{r}^4}, \frac{\pm 2c^3}{\hat{r}^4}, \frac{8(z\pm c)^4c}{\hat{r}^6}, \frac{8(z\pm c)^3c^2}{\hat{r}^6}, \frac{\pm 8(z\pm c)^2c^3}{\hat{r}^6}, \frac{48z(z\pm c)^4c^2}{\hat{r}^8} \right]$$

$$\hat{\mathbf{f}}^T_{Axz}=\left[\frac{x}{\hat{r}^2},\frac{2x(z\pm c)^2}{\hat{r}^4},\frac{2x(z\pm c)c}{\hat{r}^4},\frac{2xc^2}{\hat{r}^4},\frac{8x(z\pm c)^3c}{\hat{r}^6},\right.$$
$$\left.\frac{8x(z\pm c)^2c^2}{\hat{r}^6},\frac{\pm 8x(z\pm c)c^3}{\hat{r}^6},\frac{48xz(z\pm c)^3c^2}{\hat{r}^8}\right]$$

$$\hat{\mathbf{f}}^T_{Ayz}=[0,\ 0,\ 0,\ 0,\ 0,\ 0,\ 0,\ 0]$$
$$\hat{\mathbf{f}}^T_{Axy}=[0,\ 0,\ 0,\ 0,\ 0,\ 0,\ 0].$$

The appropriate expressions for the vectors of the matrix $\mathbf{F}_B$ are obtained by replacing $\hat{\mathbf{f}}_B$'s by $\mathbf{f}_B$'s and $\hat{r}$ by r and assuming the lower sign wherever the dual sign appears. The vector components of matrix $\overline{\mathbf{F}}_B$ are obtained by replacing $\hat{\mathbf{f}}_A$'s by $\overline{\mathbf{f}}_B$'s and $\hat{r}$ by $\bar{r}$ and assuming the upper sign wherever the dual sign appears.

$$\hat{\mathbf{f}}^T_{Bu}=\left[-\ln\hat{r},\frac{-c}{(z\pm c)}\ln\hat{r},\frac{x^2}{\hat{r}},\frac{x^2c}{(z\pm c)\hat{r}^2},\frac{(z\pm c)c}{\hat{r}^2},\right.$$
$$\frac{c^2}{\hat{r}^2},\frac{2x^2(z\pm c)c}{\hat{r}^4},\frac{2x^2c^2}{\hat{r}^4},\frac{2z(z\pm c)c^2}{\hat{r}^4},$$
$$\left.-(1+\ln\hat{r}),\frac{-c}{(z+c)}(1+\ln\hat{r}),\frac{8x^2z(z\pm c)c^2}{\hat{r}^6}\right]$$

$$\hat{\mathbf{f}}^T_{Bv}=[0,\ 0,\ 0,\ 0,\ 0,\ 0,\ 0]$$

$$\hat{\mathbf{f}}^T_{Bw}=\left[\frac{x(z\pm c)}{\hat{r}^2},\frac{xc}{\hat{r}^2},\frac{2x(z\pm c)^2c}{\hat{r}^4},\frac{2x(z\pm c)c^2}{\hat{r}^4},\right.$$
$$\left.\frac{\mp 2xc^3}{\hat{r}^4},\ \mp 2\arctan\left(\frac{x}{\hat{r}\pm z+c}\right),\frac{8xz(z\pm c)^2c^2}{\hat{r}^6}\right]$$

$$\hat{\mathbf{f}}^T_{Bxx}=\left[\frac{x}{\hat{r}^2},\frac{2x^3}{\hat{r}^4},\frac{2x(z\pm c)c}{\hat{r}^4},\frac{2xc^2}{\hat{r}^4},\frac{8x^3(z\pm c)c}{\hat{r}^6},\right.$$
$$\frac{8x^3c^2}{\hat{r}^6},\frac{8xz(z\pm c)c^2}{\hat{r}^6},\frac{8x(z\pm c)^2c^2}{\hat{r}^6},$$
$$\left.\frac{x}{\hat{r}^2},\frac{2xc(z\pm c)}{\hat{r}^4},\frac{48x^3z(z\pm c)c^2}{\hat{r}^8}\right]$$

$$\hat{\mathbf{f}}^T_{Byy}=\left[\frac{x}{\hat{r}^2},\frac{x}{\hat{r}^2},\frac{2x(z\pm c)c}{\hat{r}^4},\frac{2xc^2}{\hat{r}^4},\frac{2x(z\pm c)c}{\hat{r}^6},\frac{2xc^2}{\hat{r}^4},\right.$$
$$\left.\frac{8xz(z\pm c)c^2}{\hat{r}^6},\frac{8x(z\pm c)^2c^2}{\hat{r}^6},0,\ 0,\ \frac{8xz(z\pm c)c^2}{\hat{r}^6}\right]$$

$$\hat{\mathbf{f}}^T_{Bzz}=\left[\frac{x}{\hat{r}^2},\frac{2x(z\pm c)^2}{\hat{r}^4},\frac{2x(z\pm c)c}{\hat{r}^4},\frac{2xc^2}{\hat{r}^4},\frac{8x(z\pm c)^3c}{\hat{r}^6},\right.$$
$$\left.\frac{8x(z\pm c)^2c^2}{\hat{r}^6},\frac{8xz(z\pm c)c^2}{\hat{r}^6},\frac{48xz(z\pm c)^3c^2}{\hat{r}^8}\right]$$

$$\hat{\mathbf{f}}^T_{Bxz}=\left[\frac{(z\pm c)}{\hat{r}^2},\frac{c}{\hat{r}^2},\frac{2x^2(z\pm c)}{\hat{r}^4},\frac{2x^2c}{\hat{r}^4},\frac{2(z\pm c)^2c}{\hat{r}^4},\right.$$
$$\frac{2(z\pm c)c^2}{\hat{r}^4},\frac{2zc^2}{\hat{r}^4},\frac{8x^2(z\pm c)^2c}{\hat{r}^6},\frac{8x^2(z\pm c)c^2}{\hat{r}^6},$$
$$\left.\frac{8x^2zc^2}{\hat{r}^6},\frac{8z(z\pm c)^2c^2}{\hat{r}^6},\frac{-(z\pm c)}{\hat{r}^2},\frac{48x^2z(z\pm c)^2c^2}{\hat{r}^8}\right]$$

$$\hat{\mathbf{f}}^T_{Byz}=[0,\ 0,\ 0,\ 0,\ 0,\ 0,\ 0]$$
$$\hat{\mathbf{f}}^T_{Bxy}=[0,\ 0,\ 0,\ 0,\ 0,\ 0,\ 0,\ 0,\ 0,\ 0].$$

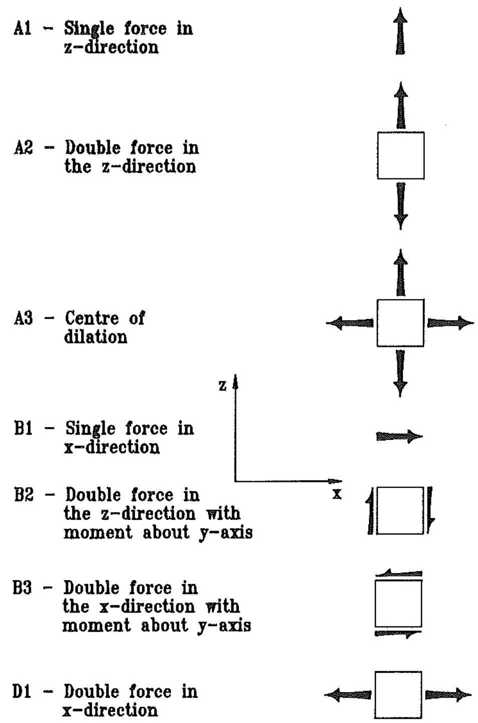

Fig. A1 Pictorial representation of nuclei of strain

On the Role of Elastic Constants in Multiphase Contact Problems

J. M. Neumeister
Division of Solid Mechanics,
Chalmers University of Technology,
S-412 96, Göteborg, Sweden

For a plane composite body consisting of an arbitrary number of different linearly elastic constituents under conditions of plane deformation or plane stress, the minimum number of required elastic constants describing the stress field is determined. For conditions in accordance with the assumptions of Michell and Dundurs, i.e., for prescribed surface tractions and no net forces on internal boundaries, the state of stress in a body involving N *different phases is found to be determined by only* 2N-2 *combinations of the elastic constants. This result holds for conditions of complete adhesion and frictionless slip at the interfaces of the materials.*

1 Introduction

Recent progress in materials science, the development of new sophisticated application-designed materials, and especially the unique qualities of composite materials, have given a renewed interest in the problems arising when several different material phases interact with each other. Examples are load transmitting joints, stress concentrations, interface cracks, multiwedge problems, inclusions, contact problems, etc. While studying multimaterial problems, one aspect of particular interest is the influence of the constituents' material properties on the state of stress due to external loading.

Many problems are accurately described with conditions of plane strain or plane stress. Linear plane elasticity is conveniently formulated through complex variables (Muskhelishvili, 1953). For an isotropic plane linearly elastic body loaded with surface tractions, the state of stress is independent of its elastic parameters under circumstances given by Michell (1899): viz., in the absence of body forces and if the resultant force, but not necessarily the couple, vanishes over each boundary separately. With unbalanced forces on holes, the solution contains terms involving Poisson's ratio (c.f., Muskhelishvili, 1953).

An interesting and very useful result concerning composite bodies consisting of two linearly elastic isotropic phases was found by Dundurs (1967). Under the same conditions as stated in Michell's paper, the state of stress in such an aggregate depends on only two variables: viz., two combinations of the four elastic parameters involved. In an illuminating discussion it was shown how these combinations can be used for classifying material combinations with regard to stress singularities (Dundurs, 1969).

Contributed by the Applied Mechanics Division of The American Society of Mechanical Engineers for presentation at the 1992 ASME Summer Mechanics and Materials Meeting, Tempe, AZ, Apr. 28–May 1, 1992.

Discussion on this paper should be addressed to the Technical Editor, Prof. Leon M. Keer, The Technological Institute, Northwestern University, Evanston, IL 60208, and will be accepted until four months after final publication of the paper itself in the Journal of Applied Mechanics. Manuscript received by the ASME Applied Mechanics Division, Mar. 30, 1990; final revision, Nov. 18, 1991.

Paper No. 92-APM-29.

Plane conditions can be achieved only in plane deformation or generalized plane deformation when two or more dissimilar materials are involved. With a global state of plane stress, generally a three-dimensional state of stress would appear in the vicinity of a material interface. But by means of Saint-Venant's principle, the effects of a disturbance at a contact zone decay with increasing distance. A comprehensive investigation concerning Saint-Venants principle was given by Horgan and Knowles (1983) and, furthermore, updated by Horgan (1989).

In the present paper, heterogeneous systems are considered which could be regarded as being in states of either generalized plane strain or generalized plane stress. The thickness of the systems considered is thus assumed to be constant and either very large or very small in comparison with all other dimensions, which includes the radii of curvature of interface boundary contours. All participating materials are supposed to be isotropic and linearly elastic. The heterogenous systems, the aggregates of different material phases, can here be arbitrary in shape and in diversification of the constituents involved and complete adhesion as well as frictionless slip between them is accounted for. The study is focused on conditions similar to the ones stipulated by Michell (1899) and Dundurs (1967), i.e., loading by prescribed surface tractions with resultant forces vanishing over each boundary.

The analysis in the following sections adopts the notation of Dundurs (1967, 1969). Some minor additions of sub and superscripts have been made to distinguish between different systems of reference such as material phases, domains, and coordinates. In fact, Section 2 is merely a recapitulation of the proof performed by Dundurs (1967), where some steps important to the succeeding analysis have been stressed.

The results found in this paper form a general theorem concerning plane multiphase problems regarding the minimum number of independent variables necessary to describe the state of stress. Under the preconditions mentioned above, the state of stress in a composite with N different phases is determined by only $2N$-2 combinations of the elastic parameters. The results of Michell and Dundurs are contained within this formula; they refer to $N=1$ and $N=2$, respectively.

2 Continuity Conditions Between Two Phases in Contact

It is well known that in a plane problem, the state of stress can be expressed in terms of the Airy stress function Φ involving two analytic functions $\phi(z)$ and $\chi(z)$. Any stress function is expressible in the form

$$\Phi = \mathrm{Re}[\bar{z}\phi(z) + \chi(z)]. \quad (1)$$

Here, Re denotes the real part. With the notation

$$\psi(z) = \frac{\mathrm{d}\chi(z)}{\mathrm{d}z}, \quad (2)$$

the components of the displacements are given by

$$2\mu(u_x + \mathrm{i}u_y) = \kappa\phi(z) - z\overline{\phi'(z)} - \overline{\psi(z)}, \quad (3)$$

whereas the stress components are determined by the equations

$$\sigma_x + \sigma_y = 2[\phi'(z) + \overline{\phi'(z)}], \quad (4)$$

$$\sigma_y - \sigma_x + 2\mathrm{i}\tau_{xy} = 2[\bar{z}\phi''(z) + \psi'(z)]. \quad (5)$$

The elastic constants here are the shear modulus μ and $\kappa = 3 - 4\nu$ for the plane deformation and $\kappa = (3-\nu)/(1+\nu)$ for plane stress, with ν denoting Poisson's ratio.

If the displacements are prescribed along an arc s of the boundary, the boundary condition on the complex potentials is

$$\kappa\phi(z) - z\overline{\phi'(z)} - \overline{\psi(z)} = 2\mu[u_x(s) + \mathrm{i}u_y(s)]. \quad (6)$$

When tractions T_x and T_y are specified at the boundary, the proper conditions on the complex potentials at the boundary are expressed in terms of the tractions acting on the boundary integrated along the arc s, i.e., resultant forces along the arc. These integrated take the form

$$\phi(z) + z\overline{\phi'(z)} + \overline{\psi(z)} + A = \mathrm{i}\int_0^s [T_x(s) + \mathrm{i}T_y(s)]\mathrm{d}s. \quad (7)$$

The arc coordinate s in Eqs. (7), (8) must be chosen so that the material is on the left when moving in its positive direction. The potentials describing the state of stress are not unique. When integrated along s as in Eq. (8), the lower integration limit, viz., the origin of s, yields the constant A. This constant depends on the choice of potentials and the location of the origin of s.

In a plane problem with two different phases in contact, the continuity conditions at the interfaces depend on whether there is complete adhesion between the phases or not. The present analysis requires that the zones of contact are known, and hence separation or load-dependent slip is excluded.

For a bonded interface the requirements are that the displacements and the tractions are continuous at the interface. With subscripts 1 and 2 referring to the two phases, this is expressed as

$$(u_x + \mathrm{i}u_y)_1 = (u_x + \mathrm{i}u_y)_2, \quad (8)$$

$$(T_x + \mathrm{i}T_y)_1 = -(T_x + \mathrm{i}T_y)_2, \quad (9)$$

at all common boundaries. Using the same arc coordinate s for both materials Eqs. (8) and (9), the continuity conditions reduce to the following conditions on the complex potentials, c.f., Eqs. (6), (7)

$$\frac{\mu_2}{\mu_1}[\kappa_1\phi_1(z) - z\overline{\phi_1'(z)} - \overline{\psi_1(z)}] = \kappa_2\phi_2(z) - z\overline{\phi_2'(z)} - \overline{\psi_2(z)}, \quad (10)$$

$$\phi_1(z) + z\overline{\phi_1'(z)} + \overline{\psi_1(z)} + A_1 = \phi_2(z) + z\overline{\phi_2'(z)} + \overline{\psi_2(z)} + A_2 \quad (11)$$

where the sign of the right-hand member in the latter equation is shifted due to the fact that the definition of s is reversed for one of the phases.

In general, the constants A_1 and A_2 are determined by the choice of potentials and origins of the arc coordinate s. It is, however, possible to add terms to the complex potentials of the form

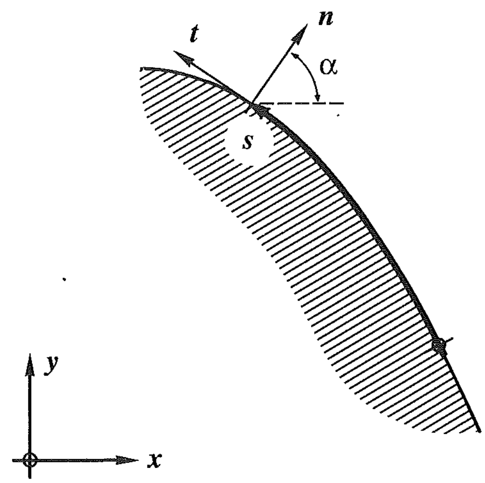

Fig. 1 The conditions at one boundary of a plane body

$$\phi(z) = \gamma, \quad \psi(z) = \kappa\bar{\gamma}, \quad (12)$$

where γ is an arbitrary complex constant without changing the displacement and stress fields in order to change the constants A_1 and A_2. It is hence possible to make the two constants A_1 and A_2 cancel in Eq. (11).

A multiply connected region of a phase has several contours and boundary and continuity conditions need to be formulated at every one of these. The constant A in Eq. (7) can be adjusted at will, as shown above, for only one of the boundaries, for all other contours it is settled by the choice of the origin of s.

If the resultant vectors of tractions vanish on every hole in the composite body, the integral

$$\oint_S (T_x + \mathrm{i}T_y)\mathrm{d}s \quad (13)$$

vanishes on every closed contour S within the body. The value of the line integral between two coordinates z^0 and z^1

$$\int_{z^0}^{z^1} (T_x + \mathrm{i}T_y)\mathrm{d}s \quad (14)$$

is thus path independent. For a particular choice of origins of the arc coordinates s, viz. z^0 (at the outer boundary) and z^1 at another (internal) boundary, the corresponding constant A^1 is given by

$$A^1 - A^0 = -[\phi_1 + z\overline{\phi_1'(z)} + \overline{\psi_1(z)}] = -\mathrm{i}\int_{z^0}^{z^1}(T_x + \mathrm{i}T_y)\mathrm{d}s. \quad (15)$$

It is independent of the path L from z^0 to z^1 but depends on the locations of z^0 and z^1, see also Fig. 2. For the formulation of boundary conditions at the inner boundary, it is always possible to modify the potentials for the inclusion phase in the manner of Eqs. (12) in order to make A_1 equal to A_2. This process can always be repeated to account for inclusions inside inclusions, for intrusions, holes, etc.

With the notations $\theta_i = z\overline{\phi_i'(z)} + \overline{\psi_i(z)}$ and $\Gamma_{21} = \mu_2/\mu_1$, Eqs. (10) and (11) may be written as

$$\begin{bmatrix} \Gamma_{21}\kappa_1 & -\Gamma_{21} \\ 1 & 1 \end{bmatrix}\begin{bmatrix} \phi_1 \\ \theta_1 \end{bmatrix} = \begin{bmatrix} \kappa_2 & -1 \\ 1 & 1 \end{bmatrix}\begin{bmatrix} \phi_2 \\ \theta_2 \end{bmatrix}. \quad (16)$$

After solving ϕ_1 and θ_1, the relations between the two sets of complex functions can be written as

$$\begin{bmatrix} \phi_1 \\ \theta_1 \end{bmatrix} = \begin{bmatrix} a_{12} & b_{12} \\ c_{12} & d_{12} \end{bmatrix}\begin{bmatrix} \phi_2 \\ \theta_2 \end{bmatrix}, \quad (17)$$

where

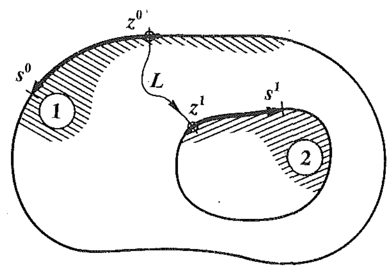

Fig. 2 Arc coordinates s^i, origins z^i and integral path L for a body with inclusion

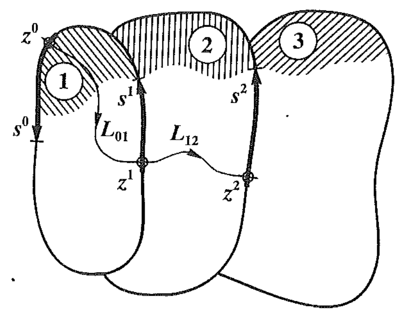

Fig. 3 Three phases in contact of which two are completely separated by the third intermediate phase

$$a_{12}=\frac{\Gamma_{21}+\kappa_2}{\Gamma_{21}(\kappa_1+1)},\ b_{12}=\frac{\Gamma_{21}-1}{\Gamma_{21}(\kappa_1+1)},$$

$$c_{12}=\frac{\Gamma_{21}\kappa_1-\kappa_2}{\Gamma_{21}(\kappa_1+1)},\ d_{12}=\frac{\Gamma_{21}\kappa_1+1}{\Gamma_{21}(\kappa_1+1)}. \quad (18)$$

Obviously, these four combinations of elastic constants cannot be chosen arbitrarily since

$$c_{12}=1-a_{12}, \quad d_{12}=1-b_{12}. \quad (19)$$

For each isolated domain k of a phase, the state of stress is defined by a new set of complex potentials $\phi^k(z)$ and $\psi^k(z)$. The conditions of continuity between every one of these domains and the other surrounding phase can thus be formulated in the same manner as stated in Eq. (16).

The implication is that if no net forces appear on internal boundaries, the state of stress in a plane problem, with two different materials, depends on only two combinations of elastic constants.

For a perfectly smooth interface, i.e., if there is no friction between the two phases, the normal components of tractions and displacements are continuous, and the tangential component of traction vanishes while tangential displacements may be discontinuous over an interface provided no separation occurs. Appropriate formulas for the displacement and stress components are given by

$$2\mu(u_n+\mathrm{i}u_t)=\mathrm{e}^{-\mathrm{i}\alpha}[\kappa\phi(z)-z\overline{\phi'(z)}-\overline{\psi(z)}], \quad (20)$$

and

$$T_n-\mathrm{i}T_t=\phi'(z)+\overline{\phi'(z)}-\mathrm{e}^{2\mathrm{i}\alpha}[\bar{z}\phi''(z)+\psi'(z)]. \quad (21)$$

Here, subscripts n and t refer to normal and tangential directions, respectively, and the angle α is taken as defined in Fig. 1. Proceeding in the same manner as for the bonded interface but omitting the details, one finds, again, that all boundary conditions can be expressed using only two combinations of elastic parameters. It has also been shown that for slip between the phases, with a law of friction relating tangential to normal tractions at interfaces, no elastic constants appear when expressing this condition in terms of the complex potentials (Dundurs, 1967). However, the extent of such slip zones may depend on the level of loading, and hence these kinds of considerations have to be treated separately since the problem becomes nonlinear.

The results so far are well known and are often used in various kinds of applications. They were first revealed by Dundurs (1967) who proposed two convenient combinations η, δ of constitutive parameters defined as

$$\eta_{12}=\frac{\Gamma_{12}\kappa_1+1}{\kappa_2+1}, \quad \delta_{12}=\frac{\Gamma_{21}+\kappa_2}{\kappa_2+1}. \quad (22)$$

In a subsequent publication he introduced new combinations α, β often referred to as Dundur's constants (Dundurs, 1969) here with $\Gamma_{21}=\mu_2/\mu_1$,

$$\alpha_{12}=\frac{\Gamma_{21}(\kappa_1+1)-(\kappa_2+1)}{\Gamma_{21}(\kappa_1+1)+(\kappa_2+1)}, \quad \beta_{12}=\frac{\Gamma_{21}(\kappa_1-1)-(\kappa_2-1)}{\Gamma_{21}(\kappa_1+1)+(\kappa_2+1)}, \quad (23)$$

which have the advantage of changing sign but preserving the magnitude when the labeling of phases is shifted.

3 Relations for Three Phases

While dealing with contact problem involving more than two phases, the question arises whether it is possible to reduce the required number of elastic constants in a similar way.

Introducing three different phases denoted by subscripts 1, 2 and 3, the state of stress in every isolated domain can be expressed in terms of two complex potentials. Three materials provide three contact possibilities. At each interface the potentials for the two phases are related by conditions of continuity of displacements and resulting tractions (for complete adhesion); they are stated by Eqs. (24), (25) with $i, j=1, 2, 3$.

$$\frac{\mu_j}{\mu_i}[\kappa_i\phi_i(z)-z\overline{\phi_i'(z)}-\overline{\psi_i(z)}]=\kappa_j\phi_j(z)-z\overline{\phi_j'(z)}-\overline{\psi_j(z)}, \quad (24)$$

$$\phi_i(z)+z\overline{\phi_i'(z)}+\overline{\psi_i(z)}+A_i=\phi_j(z)+z\overline{\phi_j'(z)}+\overline{\psi_j(z)}+A_j. \quad (25)$$

It needs to be shown that it is possible to adjust the potentials in order to make the complex terms A_i and A_j equal in each of Eqs. (25) for particular choices of origins of the interface arc coordinates s.

If the potentials for a phase at the outer boundary C^0, arbitrarily labeled as 1, are adjusted to give

$$\phi_1(z^0)+z^0\overline{\phi_1'(z^0)}+\overline{\psi_1(z^0)}=0 \quad (26)$$

for a point z_0 at the boundary taken as origin of an arc coordinate s^0 (that is, the complex constant A_1^0 is zero), then the constant A_1^1 for another point z^1 at any other boundary C^1 is given by Eq. (15). Suppose that the boundary C^1 is an interface between phase 1 and phase 2 or phase 3. It is always possible to make the constants terms A_2^1 or A_3^1 equal to A_1^1 for a coordinate z^1 at the interface by adding terms of the type given in Eqs. (12) to the potentials $\phi_2(z)$, $\psi_2(z)$ or $\phi_3(z)$, $\psi_3(z)$. This is chosen as origin for the arc coordinate S^1 when formulating the continuity conditions.

For a configuration with tree phases, of which two are separated completely by the third intermediate phase, i.e., if there is no contact between, say, phases 1 and 3, Dundurs' formulation would apply directly. Only two sets of contact conditions are needed and thus, in all, four constants would be sufficient to determine the stress field, c.f. Fig. 3. Also, for a composite body with each boundary of every domain of a phase in contact with only one other phase, it is sufficient to adjust the potentials once, since conditions of continuity can be expressed with the same arc coordinate s around the whole closed boundary loop.

Consider now a configuration with all three phases in mutual contact and where at least one point z^1 exists, which is common to all three phases in Fig. 4. If the potentials $\phi_2(z)$, $\psi_2(z)$ and $\phi_3(z)$, $\psi_3(z)$ are adjusted to make A_2^1 and A_3^1 equal to A_1^1 at that particular point z^1, it is obvious that the constant term also

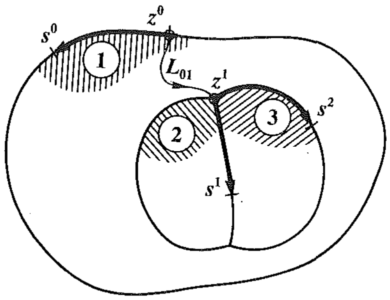

Fig. 4 Three phases in mutual contact and with a point z^l common to all domains

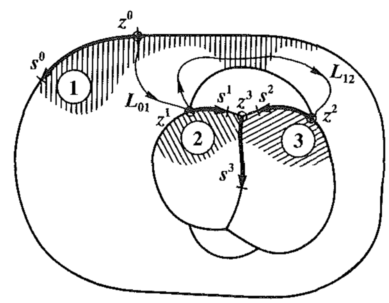

Fig. 5 Three phases in mutual contact but without any common point

vanishes in Eq. (25) when formulating continuity conditions between phases 2 and 3 when z^1 is taken as origin for s^3.

With the three phases in mutual contact but without a common point—that is, if there are holes in the body—one origin is not sufficient to formulate the problem. A possible configuration is shown in Fig. 5. Assume that $\phi_2(z)$, $\psi_2(z)$ are adjusted for an origin z^1 common for phases 1 and 2 while $\phi_3(z)$, $\psi_3(z)$ are adjusted accordingly for z^2 on the interface between phases 1 and 3. The constants A_2^1 and A_3^2 are given by Eq. (15). These two differ, provided there are surface tractions on the hole boundary. This follows by taking the (arbitrary) integral path from z^0 to z^2 through z^1.

$$A_2^1 = -\mathrm{i}\int_{z^0}^{z^1}(T_x+\mathrm{i}T_y)\mathrm{d}s - \mathrm{i}\int_{z^1}^{z^2}(T_x+\mathrm{i}T_y)\mathrm{d}s$$
$$= A_3^2 - \mathrm{i}\int_{z^1}^{z^2}(T_x+\mathrm{i}T_y)\mathrm{d}s. \quad (27)$$

A new arc coordinate s^3 with origin z^3 is needed to formulate continuity conditions between phases 2 and 3. The traction resultants acting on phases 2 and 3 along an arc s^3 can be expressed taking z^1 and z^2 as starting points instead (and using s^1 and s^2). The resultants of tractions T_x and T_y acting on phase 2 involve the integral

$$\mathrm{i}\int_0^{s^3}(T_x+\mathrm{i}T_y)_2\mathrm{d}s^3 = -\Bigg[\phi_2(z)+z\overline{\phi_2'(z)}$$
$$+\overline{\psi_2(z)}+A_2^1-\mathrm{i}\int_{z^1}^{z^3}(T_x+\mathrm{i}T_y)_3\mathrm{d}s^2\Bigg]. \quad (28)$$

Acting on phase 3 we have

$$\mathrm{i}\int_0^{s^3}(T_x+\mathrm{i}T_y)_3\mathrm{d}s^3 = \phi_3(z)+z\overline{\phi_3'(z)}$$
$$+\overline{\psi_3(z)}+A_3^2-\mathrm{i}\int_{z^2}^{z^3}(T_x+\mathrm{i}T_y)_3\mathrm{d}s^2. \quad (29)$$

Expressed in terms of the complex potentials, continuous tractions along s^3 require (c.f. Eq. (9))

$$\phi_2(z)+z\overline{\phi_2'(z)}+\overline{\psi_2(z)}+A_2^1-\mathrm{i}\int_{z^1}^{z^3}(T_x+\mathrm{i}T_y)_2\mathrm{d}s^1$$
$$=\phi_3(z)+z\overline{\phi_3'(z)}+\overline{\psi_3(z)}+A_3^2-\mathrm{i}\int_{z^2}^{z^3}(T_x+\mathrm{i}T_y)_3\mathrm{d}s^2. \quad (30)$$

With Eqs. (15), (27) there follows that all constants in Eq. (35) above cancel if

$$\mathrm{i}\int_{z^1}^{z^3}(T_x+\mathrm{i}T_y)_2\mathrm{d}s+\mathrm{i}\int_{z^3}^{z^2}(T_x+\mathrm{i}T_y)_3\mathrm{d}s+\mathrm{i}\int_{z^2}^{z^1}(T_x+\mathrm{i}T_y)_1\mathrm{d}s=0. \quad (31)$$

This is true if the resultant of the tractions acting along the closed curve $z^1 \to z^3 \to z^2 \to z^1$ vanishes, i.e., if no net forces appear on the hole boundary.

In the same manner as above, it can be shown that if the potentials are adjusted to make the constant term in Eq. (25) vanish at one point and at one interface, they automatically have the same feature for any other choice of interface arc coordinate and origin.

Proceeding in the same manner as in the preceding section, the continuity conditions at an interface produce, for each set of possible material contact combinations, two relations among these potentials involving four constant of which two are mutually independent.

For contact between materials i and j, the two constants could be defined according to Eqs. (17), (18) with $\Gamma_{ji}=\mu_j/\mu_i$ and $i, j = 1$, 2 or 3

$$a_{ij}=\frac{\Gamma_{ji}+\kappa_j}{\Gamma_{ji}(\kappa_i+1)},\ b_{ij}=\frac{\Gamma_{ji}-1}{\Gamma_{ji}(\kappa_i+1)}. \quad (32)$$

Three materials provide three contact possibilities, and consequently three sets of constants given in Eqs. (32) involving in all six constitutive parameters, namely a_{12}, b_{12}, a_{13}, b_{13}, and a_{23}, b_{23}. Of interest in this context is whether these can be chosen independently, or if there are any relations among them. (They depend on five different constitutive parameters since only the stiffness ratios are relevant.)

One finds that only four constants are sufficient to express the continuity conditions since two independent relations exist among the original six constants. A possible set of correlations would be

$$a_{23}(a_{12}-b_{12})-(a_{13}-b_{12})=0, \quad (33)$$

$$b_{23}(a_{12}-b_{12})-(b_{13}-b_{12})=0. \quad (34)$$

When, in a similar manner, extending Dundurs' constants to refer to contact between phases i and j

$$\alpha_{ij}=\frac{\Gamma_{ji}(\kappa_i+1)-(\kappa_j+1)}{\Gamma_{ji}(\kappa_i+1)+(\kappa_j+1)},\ \beta_{ij}=\frac{\Gamma_{ji}(\kappa_i-1)-(\kappa_j-1)}{\Gamma_{ji}(\kappa_i+1)+(\kappa_j+1)}, \quad (35)$$

three other sets of combinations α_{12}, β_{12}; α_{13}, β_{13}; and α_{23}, β_{23} arise. These are related to the original constants a_{ij}, b_{ij} in Eqs. (32) as follows:

$$a_{ij}=\frac{1-\beta_{ij}}{1+\alpha_{ij}},\quad b_{ij}=\frac{\alpha_{ij}-\beta_{ij}}{1+\alpha_{ij}}. \quad (36)$$

Two independent relations among the extended set of Dundurs constants can now be determined by, e.g., substituting Eqs. (36) into Eqs. (33), (34). After some rearrangement, they could be expressed as

$$\alpha_{12}\alpha_{13}\alpha_{23}-\alpha_{12}+\alpha_{13}-\alpha_{23}=0, \quad (37)$$

$$(\alpha_{13}-\alpha_{12})\beta_{23}-(\beta_{13}-\beta_{12}+\alpha_{12}\beta_{13}-\alpha_{13}\beta_{12})\alpha_{23}=0. \quad (38)$$

The relations among the Dundurs' constants Eqs. (37), (38) can be expressed in different ways. Noting that $\alpha_{13}=-\alpha_{31}$, Eq. (37) reverts back to itself upon relabeling of the phases while Eq. (38) does not. However, it is possible to find other relations with this self-preserving feature as linear combinations of Eqs. (37), (38).

Again, if there are no net forces on internal boundaries, it is possible to make the constant terms in Eq. (7) A_1, A_2, and A_3 cancel for the three phases. The relations among the complex potentials due to continuity conditions, and thus the state of stress in the whole three-phase composite body, depends on only four combinations of elastic parameters.

4 The General Case With an Arbitrary Number of Phases

For a composite body consisting of N elastic materials, there are at most $(N^2-N)/2$ different combinations of phases in contact with each other. At every interface, four conditions of continuity have to be fulfilled. These conditions depend on only $2N$ elastic constants. The state of stress in such a body with prescribed surface tractions could be expressed using $2N$-1 combinations of the elastic constants. If, however, no net forces are present on internal boundaries in the body, the state of stress is determined by only $2N$-2 combinations. To show this we proceed in the following manner:

In every isolated domain of a phase the state of stress is governed by a set of complex potentials. At every contour of such a domain, which it shares with another domain, conditions of continuity have to be established. Expressed in terms of the potentials, these are an equality for every z along an arc s coinciding with the common contour (c.f. Eqs. (10, 11)). The conclusions in Sections 2 and 3 rely on the possibility of letting the constants A_i cancel out in the equations relating stresses across an interface, viz. Eqs. (11), (25). In Section 2 it was shown that with two different phases it is always possible to achieve this by adjusting the complex potentials in one of the phases. In Section 3 it was proved that once this is done for two domains in contact, the constant terms vanish automatically also at the boundaries, which these two share with a region of a third phase.

The difference between the constant terms in Eq. (7) for different choices of origins s is solely dependent of the integral of tractions acting along any contour between these coordinates (see Eq. (15)). By successively adjusting the potentials for a particular arc coordinate at the interface in order to make the constants equal, the potentials in every single region are adjusted. Generally while doing so, domains may have to be accounted for which border an already adjusted region. Then the constants for each of the phases at that particular border are already determined. But, evidently, the difference between them is zero, since they have been determined following a closed loop inside the composite body; and due to the preconditions, tractions vanish when integrated along a closed loop.

It then follows that the potentials at every boundary common to two regions can be related in the manner of Eq. (17). Returning to the constants given in Eqs. (32), relating the two sets of complex potentials for the materials i and j in contact with each other along a boundary, the relations among the six of them for a three-phase problem, given by Eqs. (33), (34), could be written as

$$\begin{bmatrix} a_{23} \\ b_{23} \end{bmatrix} = \frac{1}{a_{12}-b_{12}} \begin{bmatrix} (a_{13}-b_{12}) \\ (b_{13}-b_{12}) \end{bmatrix}. \tag{39}$$

If, for a problem involving N different phases the N-1 possible contact combinations between a material arbitrarily chosen as no. 1 and all other materials k, the $2N$-2 constants a_{1k} and b_{1k} are established, all other possibilities of contact between two phases i and j can be expressed with these constants by the use of Eq. (39) by just replacing 2 and 3 by i and j, respectively,

$$\begin{bmatrix} a_{ij} \\ b_{ij} \end{bmatrix} = \frac{1}{a_{1i}-b_{1i}} \begin{bmatrix} (a_{1j}-b_{1i}) \\ (b_{1j}-b_{1i}) \end{bmatrix}. \tag{40}$$

Table 1 Pressures and radial coordinates at surfaces and interfaces

$r=$	a_1	$\sqrt{\lambda_1}a_1$	$\sqrt{\lambda_1\lambda_2}a_1$	$\sqrt{\lambda_1\lambda_2\lambda_3}a_1$	$\sqrt{\lambda_1\lambda_2\lambda_3\lambda_4}a_1$
$\sigma_r=$	0	$-q_{12}$	$-q_{23}$	$-q_{31}$	$-q_0$

Thus, all constants relating stress functions, in regions of different phases, to each other can be expressed with only $2N$-2 combinations of elastic constants.

5 Illustrative Example

A simple example is provided in the following. A circular disk with a concentrical hole, inner radius a, outer radius b, loaded axisymmetrically by internal pressure p, and external pressure q under conditions of plane stress is considered. The radial displacement u_r is given by

$$u_r(r) = \frac{r}{E}(\sigma_\phi - \nu\sigma_r) = \frac{r}{E}\frac{(1+\nu)(b/r)^2(p-q)+(1-\nu)(p-(b/a)^2q)}{(b/a)^2-1}, \tag{41}$$

where E is Young's modulus. Four such rings of three different materials, fitting perfectly into each other when unloaded, are now put together. The materials are, from inside outwards, denoted as 1, 2, 3 and 1, respectively. In this way every phase is in contact with the two others. For the innermost ring the ratio of radii is given by $(b_1/a_1)^2=\lambda_1$, the square of ratios of radii for the remaining rings being given in the same manner by λ_2, λ_3, and λ_4. Basic unknowns are the interface pressures q_{12}, q_{23}, and q_{31}, whereas loading is pressure q_0 at the outer surface. The inner boundary of the four-ring aggregate is supposed to be unloaded (see also Table 1).

Continuity of radial displacements and stresses at all interfaces requires that

$$\begin{bmatrix} C_{11} & C_{12} & C_{13} \\ C_{21} & C_{22} & C_{23} \\ C_{31} & C_{32} & C_{33} \end{bmatrix} \begin{bmatrix} q_{12} \\ q_{23} \\ q_{31} \end{bmatrix} = \begin{bmatrix} 0 \\ 0 \\ Q \end{bmatrix}, \tag{42}$$

where

$$C_{11} = -\frac{1}{E_1}\left(\frac{\lambda_1+1}{\lambda_1-1}-\nu_1\right) - \frac{1}{E_2}\left(\frac{\lambda_2+1}{\lambda_2-1}+\nu_2\right),$$

$$C_{12} = \frac{1}{E_2}\frac{2\lambda_2}{\lambda_2-1},$$

$$C_{13} = 0,$$

$$C_{21} = \frac{1}{E_2}\frac{2}{\lambda_2-1},$$

$$C_{22} = -\frac{1}{E_2}\left(\frac{\lambda_2+1}{\lambda_2-1}-\nu_2\right) - \frac{1}{E_3}\left(\frac{\lambda_3+1}{\lambda_3-1}+\nu_3\right),$$

$$C_{23} = \frac{1}{E_3}\frac{2\lambda_3}{\lambda_3-1},$$

$$C_{31} = 0,$$

$$C_{32} = \frac{1}{E_3}\frac{2}{\lambda_3-1},$$

$$C_{33} = -\frac{1}{E_3}\left(\frac{\lambda_3+1}{\lambda_3-1}-\nu_3\right) - \frac{1}{E_1}\left(\frac{\lambda_4+1}{\lambda_4-1}+\nu_1\right),$$

$$Q = -\frac{1}{E_1}\frac{2\lambda_4}{\lambda_4-1}q_0.$$

It needs to be shown that the set of equations can be expressed in terms of only four constants, e.g., a_{12}, b_{12} and α_{13}, b_{13} given by Eqs. (32). With the substitutions

$$\Gamma_{ji}\frac{1+\nu_j}{1+\nu_i}=\frac{E_j}{E_i}, \quad \nu_i=\frac{3-\kappa_i}{1+\kappa_i} \tag{43}$$

(where $i, j=1, 2$ or 3), the set of Eqs. (42) can be rewritten with the new elements

$$C'_{11}=-\frac{\lambda_1+1}{\lambda_1-1}-\frac{\lambda_2+1}{\lambda_2-1}(a_{12}-b_{12})+3b_{12}+a_{12}-1,$$

$$C'_{12}=\frac{2\lambda_2}{\lambda_2-1}(a_{12}-b_{12}),$$

$$C'_{13}=0,$$

$$C'_{21}=\frac{2}{\lambda_2-1}(a_{12}-b_{12}),$$

$$C'_{22}=-\frac{\lambda_2+1}{\lambda_2-1}(a_{12}-b_{12})-\frac{\lambda_3+1}{\lambda_3-1}(a_{13}-b_{13})-3(b_{12}-b_{13})-(a_{12}-a_{13}),$$

$$C'_{23}=\frac{2\lambda_3}{\lambda_3-1}(a_{13}-b_{13}),$$

$$C'_{31}=0,$$

$$C'_{32}=\frac{2}{\lambda_3-1}(a_{13}-b_{13}),$$

$$C'_{33}=-\frac{\lambda_3+1}{\lambda_3-1}(a_{12}-b_{12})-\frac{\lambda_4+1}{\lambda_4-1}(a_{13}-b_{13})-3b_{13}-a_{13}+1,$$

$$Q'=-\frac{2\lambda_4}{\lambda_4-1}q_0.$$

It is seen that only four combinations of elastic parameters are sufficient to formulate the equations determining the interface pressures. It follows that the state of stress in the whole composite body depends on only four constants.

6 Discussion

The results presented in this paper concerning the minimum number of elastic constants required to describe the state of stress in a composite can be of use in a wide range of engineering problems. They can be summed up in the following statement: The state of stress in a composite body consisting of N different constituents, due to boundary tractions with resultant forces vanishing over each boundary, remains unchanged for any set of materials which preserves $2N$-2 certain constants.

The choice of these constants is obviously not unique; any combination which can be constructed with, e.g., the original set defined by Eq. (32) will do. The best choice may depend on the type of problem considered.

The author believes that one particular application, where the results can be useful, is the modeling of contact problems involving anisotropic materials. The compression of a semi-infinite strip against a half plane, as studied by Adams and Bogy (1976), could be modeled with the presented reduction of constitutive parameters if one (or both) of the elastic components were orthotropic. Another problem where the results are applicable is the order of singularity at a multiwedge corner (Theocaris, 1974).

The results found in this study could intuitively be realized taking the Dundurs theorem (1967) as a starting point. If a material phase is in contact with only one other phase, the continuity conditions along the interface can be formulated using only two combinations of constitutive parameters. Assume that a composite body consisting of N different phases is loaded by surface tractions. Generally, every phase could

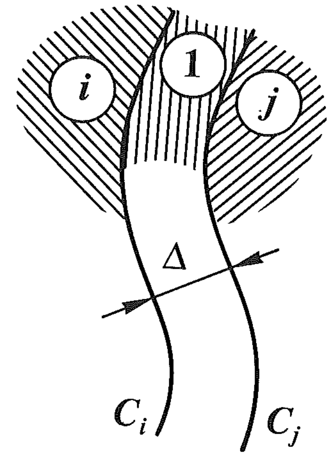

Fig. 6 Thin intermediate layer of material 1 between all domains of other phases i and j

be in contact with every other phase and every domain could be in contact with several phases simultaneously. Now carry out the imaginary operation of inserting a thin layer of one material, arbitrarily labeled as no. 1, between the two dissimilar materials at every interface in the body. Then every material would be in contact with only phase 1, and due to Dundurs' theorem, the N-1 contact combinations can be modeled separately using, in all, only $2N$-2 constants. If these intermediate layers are sufficiently thin, neither the stresses nor the displacements in the original material domains would differ notably. And, naturally, when the thickness approaches zero, one would regain the state of stress in the original problem.

Expressed in terms of the equations given previously the relations between the complex potentials, determining the stresses in the adjacent phases i and j are given by, c.f. Eqs. (17, 19, 32),

$$\begin{bmatrix}\phi_i\\ \theta_i\end{bmatrix}=\begin{bmatrix}a_{ij} & b_{ij}\\ 1-a_{ij} & 1-b_{ij}\end{bmatrix}\begin{bmatrix}\phi_j\\ \theta_j\end{bmatrix}. \tag{44}$$

Suppose there exists an intermediate layer of material 1 (thickness Δ) between them (see Fig. 6). This layer borders to phase i along the contour C_i and to phase j at C_j. In that layer the state of stress is given by the potentials ϕ_1 and θ_1. These are related to the potentials in phases i and j as

$$\begin{bmatrix}\phi_1\\ \theta_1\end{bmatrix}=\begin{bmatrix}a_{1i} & b_{1i}\\ 1-a_{1i} & 1-b_{1i}\end{bmatrix}\begin{bmatrix}\phi_i\\ \theta_i\end{bmatrix} \tag{45}$$

at C_i, and as

$$\begin{bmatrix}\phi_1\\ \theta_1\end{bmatrix}=\begin{bmatrix}a_{1j} & b_{1j}\\ 1-a_{1j} & 1-b_{1j}\end{bmatrix}\begin{bmatrix}\phi_j\\ \theta_j\end{bmatrix} \tag{46}$$

at C_j.

Letting the thickness Δ approach zero, the boundary contours C_i and C_j would finally coincide, the relations above would be valid along the same contour $C_i=C_j$ and could be set equal. Eliminating ϕ_1 and θ_1 in Eqs. (45), (46) and solving these for ϕ_i and θ_i yields relations for potentials between phases i and j.

$$\begin{bmatrix}\phi_i\\ \theta_i\end{bmatrix}=\frac{1}{a_{1i}-b_{1i}}\begin{bmatrix}(1-b_{1i}) & -b_{1i}\\ -(1-a_{1i}) & a_{1i}\end{bmatrix}\begin{bmatrix}a_{1j} & b_{1j}\\ 1-a_{1j} & 1-b_{1j}\end{bmatrix}\begin{bmatrix}\phi_j\\ \theta_j\end{bmatrix} \tag{47}$$

Insertion of expressions for the constants a_{1i}, b_{1i} and a_{1j}, b_{1j} gives the expected result, namely Eq. (44). As a matter of fact, the two matrix relations (45), (46) provide an alternative way for deducing the two relations (33), (34) (the two independent relations among the constants a_{1i}, b_{1i}; a_{1j}, b_{1j} and a_{ij}, b_{ij}) by identification of matrix elements in Eq. (47).

This also suggests a method to eliminate two combinations of constitutive parameters already while formulating the problem. Contact conditions between two phases are expressed through a chosen "dummy material," one of the material phases involved.

Acknowledgment

The results in this paper derive from a project partly financed by the Volvo Truck Corporation and the Swedish National Board for Technical Development (STU). Valuable discussions with Prof. J. Hult are gratefully acknowledged.

References

Adams, G. G., and Bogy, D. B., 1976, "The Plane Solution for the Elastic Contact Problem of a Semi-infinite Strip and Half Plane," ASME Journal of Applied Mechanics, Vol. 43, pp. 603–607.

Dundurs, J., 1967, "Effect of Elastic Constants in a Composite Under Plane Deformation," *Journal of Composite Materials*, Vol. 1, pp. 310–322.

Dundurs, J., 1969, discussion, ASME Journal of Applied Mechanics, Vol. 36, pp. 650–652.

Horgan, C. O., and Knowles, J. K., 1983, "Recent Developments Concerning Saint-Venant's Principle," *Advances in Applied Mechanics*, Vol. 23, T. Y. Wu and J. W., Hutchinson, eds., Academic Press, New York, pp. 179–269.

Horgan, C. O., 1989, "Recent Developments Concerning Saint-Venant's Principle—An Update," *Applied Mechanics Reviews*, Vol. 42, pp. 295–303.

Michell, J. H., 1899, "On the Direct Determination of Stress in an Elastic Solid With Application to the Theory of Plates," *Proceedings of the London Mathematical Society*, Vol. 31, pp. 100–124.

Muskhelishvili, N. I., 1953, *Some Basic Problems of the Mathematical Theory of Elasticity*, translated by J. R. M. Radok, P. Noordhoff, Groningen.

Theocaris, P. S., 1974, "The Order of Singularity at a Multi-Wedge Corner of a Composite Plate," *Int. Journal of Engineering Science*, Vol. 12, pp. 107–120.

Three-Dimensional Slightly Nonplanar Cracks

Huajian Gao
Division of Applied Mechanics,
Stanford University,
Stanford, CA 94305
Mem. ASME

Three-dimensional slightly nonplanar cracks are studied via a perturbation method valid to the first-order accuracy in the deviation of the crack shape from a perfectly planar reference crack. The Bueckner-Rice crack-face weight functions are used in the perturbation analysis to establish a relationship, within first-order accuracy, between the apparent and local stress intensity factors for the nonplanar crack. Perturbation solutions for a cosine wavy crack with arbitrary wavelengths are used to examine the effects of three T*-stress components,* T_{xx}, T_{xz}, T_{zz}, *on the stability of a mode 1 planar crack in the* x-z *plane with front lying along the* z*-axis. A condition for the mode 1 crack to be stable against three-dimensional wavy perturbations of wavelengths* λ_x *and* λ_z *is determined as* $T_{xx}+T_{zz}g<0$ *where* g *is negative, with a very small magnitude, for* $0<\lambda_x/\lambda_z<1/\sqrt{3}$ *and positive for* $1/\sqrt{3}<\lambda_x/\lambda_z<\infty$*; this suggests that when* $T_{xx}=0$*, a compressive stress* T_{zz} *may cause crack deflection with large wavelengths parallel to the crack front and a tensile stress* T_{zz} *may cause deflection with small wavelengths parallel to the front. For comparable* T*-stress values, it is shown that a negative* T_{xx} *always enhances the stability of a mode 1 planar crack and a negative* T_{zz} *ensures the stability of a mode 1 crack against perturbations parallel to the crack front. The shear component* T_{xz}*, while not affecting the mode 1 path stability, induces a mode 3 stress intensity factor once crack deflection occurs, and thus promotes the formation of en echelon-type cracking patterns.*

Introduction

In this paper we pose the following three-dimensional crack problem. That is, suppose a quasi-statically propagating crack in a homogeneous and isotropic linear elastic body; when the crack surfaces are assumed to be perfectly planar, the applied stress field can be characterized by some apparent stress intensity factors. However, due to loading asymmetry or material inhomogeneities, curved or branched crack extension may occur so that the actual crack profile follows a slightly nonplanar surface. The question is how the crack surface morphology affects the local stress intensities near the crack tip, i.e., what is the relationship between the apparent and local stress intensity values for the slightly nonplanar crack? This problem will be examined via a perturbation approach in which the nonplanar crack is viewed as being perturbed from a perfectly planar reference crack occupying the projection region of the actual crack on a chosen reference plane.

Under certain loading and geometry conditions, it is conceivable that portions of the crack surfaces may be forced into contact during nonplanar three-dimensional crack growth. However, for simplicity, we shall only consider those cases in which sufficient crack opening ensures that no crack face contacts will occur. The perturbation algorithm we use, which is valid to the first-order accuracy in the deviation of the actual crack shape from a planar reference crack, can be carried out for any crack geometry as soon as one knows the stress intensity factory solutions due to arbitrary point forces acting on the surfaces of the reference crack. Such point force solutions correspond to the concept of crack-face weight functions (Bueckner, 1970, 1973; Rice, 1972) in elastic crack analysis. Previous applications of the three-dimensional weight function method include in-plane configurational perturbations of a planar crack (e.g., Rice, 1985a, 1989; Gao and Rice, 1987a,b), crack interaction with transformation strains and dislocations (e.g., Rice, 1985b; Gao, 1989a; Gao and Rice, 1989a), crack trapping by obstacles (e.g., Gao and Rice, 1989b), cracks in a weakly nonhomogeneous solid (Gao, 1991), etc. The weight function solutions have been analytically determined for internal and external circular cracks (Bueckner, 1987; Gao, 1989b), with semi-infinite half-plane cracks as a special case. Finite element schemes (e.g., Parks and Kamenetzky, 1979; Sham, 1987) also exist for determining the weight functions numerically for arbitrary two or three-dimensional geometries. The present paper may be viewed as a new application of the weight function technique to slightly nonplanar crack problems in three-dimensional regime.

The two-dimensional problem of a slightly nonplanar crack has been studied by a different perturbation technique based on Muskhelishvili's complex variable representations (e.g.,

Contributed by the Applied Mechanics Division of The American Society of Mechanical Engineers for presentation at the 1992 ASME Summer Mechanics and Materials Meeting, Tempe, AZ, Apr. 28–May 1, 1992.

Discussion on this paper should be addressed to the Technical Editor, Prof. Leon M. Keer, The Technological Institute, Northwestern University, Evanston, IL 60208, and will be accepted until four months after final publication of the paper itself in the Journal of Applied Mechanics. Manuscript received by the ASME Applied Mechanics Division, Mar. 7, 199; final revision, Nov. 18, 1991. Paper No. 92-APM-30.

Banichuk, 1970; Goldstein and Salganik, 1970, 1974; Cotterell and Rice, 1980; Karihaloo et al., 1981). In those studies, the perturbation solutions, which satisfy the boundary conditions approximately along the crack surfaces, have been used to explain phenonmena such as curved or branched crack extensions during quasi-static crack propagation. Cotterell and Rice (1980) used stress intensity factor solutions of first-order accuracy to examine the stability of the fracture path of a quasi-statically growing two-dimensional crack under mode I conditions; they found that the path stability is controlled by the nonsingular stress term T_{xx}, acting in parallel to the crack growth direction, in the Irwin-Williams expansion of the crack-tip field, namely, the mode I path is stable if $T_{xx}<0$ and unstable if $T_{xx}>0$. This stability criterion has since been widely used in explaining or predicting two-dimensional crack growth under various loading and material conditions. Most recently, Gao and Chiu (1992) used complex variable representations in the two-dimensional anisotropic elasticity theory and presented a second-order perturbation analysis for slightly curved cracks in materials with arbitrary anisotropy. The solutions derived in (Gao and Chiu, 1992) have been used to examine the roles of anisotropy in curved or branched crack growth. Along the above line of progress, this paper extends the existing work by studying the three-dimensional effects of a nonplanar crack. In the three-dimensional case, there are three T-stress components acting in parallel to the crack, rather than only one component in the two-dimensional case, which may affect the growth of a nonplanar crack.

The perturbation method we develop here applies to any crack geometries as long as the crack-face weight function solutions are known for the corresponding reference crack. For simplicity, we use a half-plane crack model to study the effects of nonplanar crack perturbations on a much smaller scale than global dimensions, such as a crack size. In such analysis, the reference crack is taken as a semi-infinite planar crack for which the crack-face weight function solutions are fully available in the literature. First-order perturbation formulae are given for the stress intensity factors along the front of a slightly nonplanar crack with arbitrary surface profile. The perturbation formulae provide an approximate relationship between the apparent and local stress intensity values for the perturbed crack. The three-dimensional perturbation solutions reduce to the corresponding two-dimensional solutions existing in the literature when the half-plane crack is perturbed only in the direction of the crack growth. We use the solution to a cosine wavy perturbation along an originally planar crack to examine the stability of a planar crack under pure mode 1 loading against nonlinear perturbations. The mode 1 planar crack is said to be stable if the induced mode 2 stress intensity factor due to an imposed infinitesimal perturbation is positive at a wave peak along the crack front; this ensures that the subsequent crack growth will suppress the perturbation by branching toward the original planar position. The effects of the T-stress components on the mode 1 crack stability are studied in detail using the perturbation results. It is concluded that while T_{xx} controls the stability of the crack against perturbations parallel to the growth direction, the components T_{zz}, acting in parallel to the crack front, is mainly responsible for the crack stability against perturbations parallel to the crack front. The shear component T_{xz}, while not affecting the mode 1 stability, generates a mode 3 stress intensity factor once nonplanar crack perturbation occurs, and thus may contribute to the formation of *en echelon* cracking pattern (under mixed mode 1 and 3).

Perturbation Approach to Slightly Nonplanar Cracks

Consider a three-dimensional crack along a nonplanar curved surface $\tilde{c}$ with $\tilde{c}^+$ denoting the upper crack face and $\tilde{c}^-$ the lower crack face. When $\tilde{c}$ is only slightly different from its

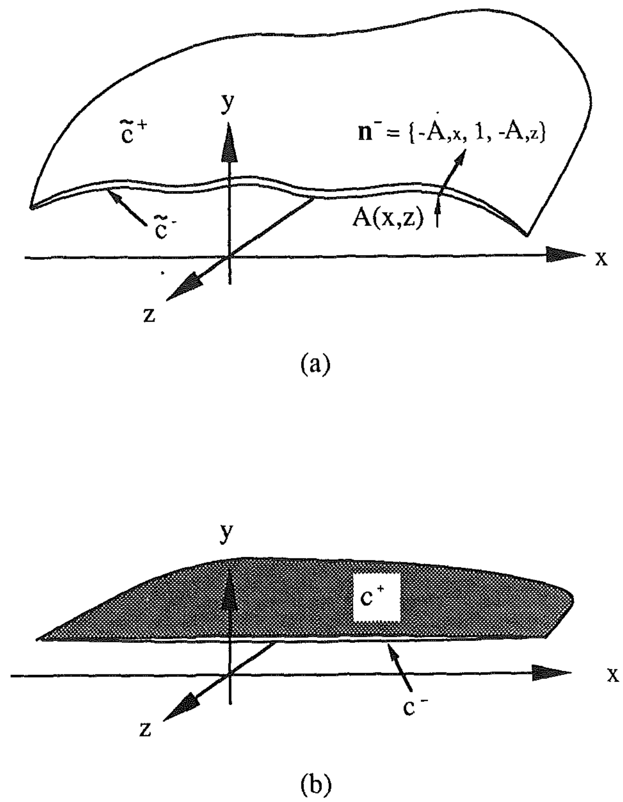

Fig. 1 (*a*) **A slightly nonplanar crack with surfaces $\tilde{c}^\pm$; (*b*) the reference crack occupying region *c*, the planar projection of $\tilde{c}$**

planar projection c on a chosen reference plane, say the x-z plane, one may devise a perturbation procedure to calculate solutions for the curved crack based on the solutions for a reference planar crack occupying the projection region c (Figs. 1). Let the curved surface $\tilde{c}$ be described by

$$y=A(x,z) \tag{1}$$

where $A(x,z)$ represents a small perturbation of the crack surface from its reference planar position on c (in the x-z plane) to the actual position on $\tilde{c}$. The solution to the curved crack can be written in the perturbation form

$$\sigma_{ij}=\sigma_{ij}^0+\tilde{\sigma}_{ij} \tag{2}$$

where σ_{ij}^0 represents the solution for the reference crack and the "disturbance" term $\tilde{\sigma}_{ij}$ will be retained only to the first-order accuracy in $A(x,z)$. As a crack face point along $\tilde{c}^+$ or $\tilde{c}^-$ is perturbed to the corresponding reference position along the reference crack, the stress field is perturbed as

$$\sigma_{ij}(x,A,z)=\sigma_{ij}^0(x,0,z)+A(x,z)\sigma_{ij,y}^0(x,0,z) + \tilde{\sigma}_{ij}(x,0,z)+0(A^2) \tag{3}$$

where $(\ )_{,y}$ means differentiation with respect to the variable y.

Assuming that the crack is subject to traction t_i^+ on the upper crack surface and t_i^- on the lower surface, the boundary condition may be written as

$$(\sigma_{ij}n_j)^\pm = t_i^\pm \text{ on } \tilde{c}^\pm \tag{4}$$

where the summation convention over repeated indices is implied and the outward normals $\mathbf{n}^\pm$ have components

$$n_x^\pm = \pm A_{,x}(x,z), \quad n_y^\pm = \mp 1, \quad n_y^\pm = \pm A_{,z}(x,z) \tag{5}$$

within first-order accuracy. Substituting Eqs. (3) and (5) into (4) and neglecting higher-order terms lead to

$$(\sigma_{yy}^0+\tilde{\sigma}_{yy}+A\sigma_{yy,y}^0-A_{,q}\sigma_{yq}^0)^\pm = \mp t_y^\pm$$

$$(\sigma_{yp}^0+\tilde{\sigma}_{yp}+A\sigma_{yp,y}^0-A_{,q}\sigma_{qp}^0)^\pm = \mp t_p^\pm \text{ on } c^\pm \tag{6}$$

where A stands for $A(x,z)$ and the subscripts p,q range over x and z only. Letting the reference planar crack be subject to the same surface tractions as the actual nonplanar crack, the zeroth-order equations are obtained as

$$(\sigma_{yy}^0)^\pm = \mp t_y^\pm,\ (\sigma_{yp}^0)^\pm = \mp t_p^\pm \quad \text{on } c^\pm. \tag{7}$$

Now, collecting the remaining first-order terms in Eqs. (6) and using the equilibrium equations, $\sigma_{yj,y}+\sigma_{qj,q}=0$, we obtain two first-order equations

$$(\tilde{\sigma}_{yy})^\pm = (A\sigma_{yq}^0)_{,q}^\pm = \mp (At_q^\pm)_{,q},\quad (\tilde{\sigma}_{yp})^\pm = (A\sigma_{qp}^0)_{,q}^\pm \quad \text{on } c^\pm. \tag{8}$$

Equations (8) mean that the first-order stress terms can be treated as being induced by some "effective" traction along the reference crack surfaces. Thus, the original nonplanar crack problem has been converted, within first-order accuracy, into one of a planar crack subject to the crack-face tractions

$$(t_y^{\text{eff}})^\pm = t_y^\pm + (At_q^\pm)_{,q},\quad (t_p^{\text{eff}})^\pm = t_p^\pm \mp (A\sigma_{qp}^0)_{,q}^\pm \quad \text{on } c^\pm. \tag{9}$$

The weighted average of the crack face weight functions, corresponding to the solutions for the stress intensity factors due to point forces, with the effective tractions in (9) then gives the solution to a slightly nonplanar crack. If the crack faces are free of traction, i.e., $t_j=0$, the effective forces in (9) reduce to

$$(t_y^{\text{eff}})^\pm = 0,\quad (t_p^{\text{eff}})^\pm = \mp (A\sigma_{qp}^0)_{,q}^\pm \quad \text{on } c^\pm. \tag{10}$$

In this case, the effective traction contains only shear forces distributed along the reference crack surfaces. The type of tractions in Eqs. (9), (10) generally do not have the same magnitude on the upper and lower crack faces because the hoop stress components σ_{qp}^0 may have different values on each crack face.

A Semi-Infinite Planar Crack

Apparent Versus Local Stress Intensity Factors. For simplicity, in this paper we only consider nonplanar crack perturbations on a much smaller scale than global dimensions such as a crack size. To study those problems, we use a half-plane crack model in which the reference crack is taken as a semi-infinite half-plane crack shown in Figs. 2. Before perturbation, the half-plane crack (Fig. 2(*a*)) is subject to an applied "K-field" with stress intensity factors K_α^∞, where $\alpha=1,2,3$ denotes the crack modes, so that the reference stress field is given by

$$\sigma_{ij}^0 = \sum_{\alpha=1}^{3} \frac{K_\alpha^\infty}{\sqrt{2\pi r}} f_{ij}^\alpha(\theta) + T_{ij}. \tag{11}$$

Here, r, θ are the polar coordinates at the crack tip (Fig. 2(*b*)), T_{ij} represents the nonsingular T-stresses and the $f_{ij}^\alpha(\theta)$ are the well-known angular functions for the crack-tip field (see, e.g., Kanninen and Popelar, 1985). There are three nonsingular T-stress components, T_{xx}, T_{xz}, and T_{zz}, which play an important role in the three-dimensional nonplanar crack perturbation. Along the crack faces ($x<0$), the traction components σ_{yj}^0 vanish and the tangential stresses are

$$(\sigma_{xx}^0)^\pm = T_{xx} \mp \frac{2K_2^\infty}{\sqrt{-2\pi x}},\quad (\sigma_{xz}^0)^\pm = T_{xz} \mp \frac{K_3^\infty}{\sqrt{-2\pi x}},$$

$$(\sigma_{zz}^0)^\pm = T_{zz} \mp \nu \frac{2K_2^\infty}{\sqrt{-2\pi x}}. \tag{12}$$

A fundamental problem can be posed as follows. The applied stress intensities K_α^∞, which cause the singular stress field (11) when the crack is assumed to be perfectly planar, may be viewed as the "apparent" stress intensity factors for the cracked body. However, due to loading asymmetry or local material inhomogeneities, curved or branched crack extension may occur so that the actual crack surfaces are not perfectly planar. Rather, they may exhibit some nonplanar surface morphology, and

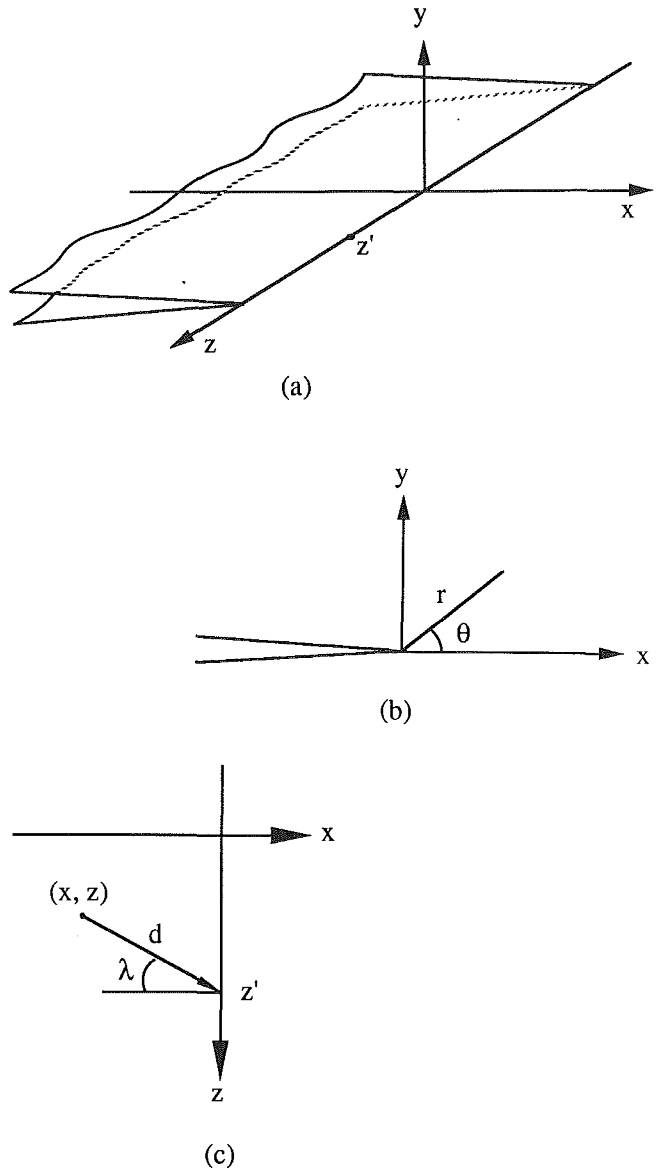

Fig. 2 (*a*) A half-plane crack in cartesian coordinates x, y, z; (*b*) the polar coordinates r, θ at the crack tip; (*c*) the geometrical parameters d and λ

the "real" stress intensity factors K_α^{tip} at the crack tip will differ from their apparent values K_α^∞. The questions are how to determine K_α^{tip} from K_α^∞, and how the three-dimensional crack surface morphology affects the crack growth which is governed by the local stress intensities K_α^{tip}, rather than K_α^∞. The perturbation approach can be used to provide an approximate description and understanding on these issues.

Three-Dimensional Crack-Face Weight Functions for a Half-Plane Crack. Equations (7)–(10) indicate that the problem of a slightly nonplanar crack can be treated as a planar crack subject to prescribed crack-face tractions. The solutions to such problems may be obtained by linear superposition on the point force solutions for the stress intensity factors, corresponding to the crack-face weight functions. For the half-plane crack geometry, the crack-face weight function $h_{\alpha j}^+(z';x,z)$ (or $h_{\alpha j}^-$) is defined as the mode α stress intensity factor at an observation point z' along the crack front due to a unit point force in j direction acting at the crack-face position $x,0^+,z$ (or $x,0^-,z$). Knowledge of $h_{\alpha j}^\pm(z';x,z)$ allows one to construct the solution due to arbitrary crack-face tractions by linear superposition. For example, if the crack-face tractions are given as $t_j^\pm(x,z)$, the crack-tip stress intensity factors $K_\alpha^{\text{tip}}(z')$ are

$$K_\alpha^{\text{tip}}(z') = \int_{-\infty}^{\infty}\int_{-\infty}^{0} [t_j^+(x,z) h_{\alpha j}^+(z';x,z) + t_j^-(x,z) h_{\alpha j}^-(z';x,z)]dxdz. \quad (13)$$

The weight functions $h_{\alpha j}^{\pm}(z';x,z)$ for half-plane cracks have been given in explicit forms by Bueckner (1987) as

$$h_{1x}^{\pm} = \frac{(1-2\nu)}{8(1-\nu)\sqrt{\pi}} d^{-3/2}\cos\frac{3\lambda}{2}, \quad h_{1y}^{\pm} = \pm\sqrt{\frac{-x}{2\pi^3}}d^{-2}$$

$$h_{1z}^{\pm} = \frac{(1-2\nu)}{8(1-\nu)\sqrt{\pi}} d^{-3/2}\sin\frac{3\lambda}{2} \quad (14)$$

$$h_{2x}^{\pm} = \pm\sqrt{\frac{-x}{2\pi^3}}d^{-2}\left(1+\frac{2\nu}{2-\nu}\cos 2\lambda\right),$$

$$h_{2y}^{\pm} = -\frac{(1-2\nu)}{4(2-\nu)\sqrt{\pi}} d^{-3/2}\cos\frac{3\lambda}{2}$$

$$h_{2z}^{\pm} = \pm\frac{2\nu}{2-\nu}\sqrt{\frac{-x}{2\pi^3}}\, d^{-2}\sin 2\lambda \quad (15)$$

$$h_{3x}^{\pm} = \pm\frac{2\nu}{2-\nu}\sqrt{\frac{-x}{2\pi^3}}\, d^{-2}\sin 2\lambda,$$

$$h_{3y}^{\pm} = -\frac{(1-2\nu)}{2(2-\nu)\sqrt{\pi}} d^{-3/2}\sin\frac{3\lambda}{2}$$

$$h_{3z}^{\pm} = \pm\sqrt{\frac{-x}{2\pi^3}}d^{-2}\left(1-\frac{2\nu}{2-\nu}\cos 2\lambda\right) \quad (16)$$

where

$$d^2 = x^2 + (z-z')^2, \quad \lambda = \tan^{-1}\frac{z-z'}{x} \quad (17)$$

are geometrical parameters shown in Fig. 2(*c*). The weight function solutions for internal and external circular cracks can be found in (Bueckner, 1987; Gao, 1989b), and numerical solutions can be calculated for two or three-dimensional weight functions associated with arbitrary crack geometries by finite element schemes (Parks and Kamenetzky, 1979; Sham, 1987).

Perturbation Analysis of Slightly Nonplanar Cracks

Apparent K_α^∞ Versus Local K_α^{tip}. The crack-face weight functions given in Eqs. (14)–(17) allow one to calculate the stress intensity factors due to arbitrary crack-face tractions. Since the problem of a slightly nonplanar crack can be treated as a planar crack with effective crack-face tractions given in Eqs. (9), one may use the weight function solutions to calculate the local stress intensity factors at the crack tip.

A nonplanar crack perturbation may influence the local stress intensity factors in two ways. First, change in the crack surface profile, from a planar surface to a nonplanar one, may result in changes in the stress distribution ahead the crack tip. Second, the crack tip may locally change its orientation during the perturbation; since the stress intensity factors are defined as measuring the strength of the normal and shear stresses along the prolongation of the local tangent plane at the crack tip, a slight kink or branch in the crack-tip orientation may also cause a variation in the stress intensity factors. Within first-order accuracy, one may write

$$K_\alpha^{\text{tip}} = K_\alpha^\infty + \tilde{K}_\alpha^s + \tilde{K}_\alpha^t \quad (18)$$

where $\tilde{K}_\alpha^s$ represents the effect of the crack surface morphology and $\tilde{K}_\alpha^t$ represents the effect of the crack-tip orientation. In writing Eq. (18) we have neglected higher-order terms such as the coupling between $\tilde{K}_\alpha^s$ and $\tilde{K}_\alpha^t$.

Since the coupling effects between $\tilde{K}_\alpha^s$ and $\tilde{K}_\alpha^t$ are of higher order, in calculating $\tilde{K}_\alpha^s$, one may ignore changes in the crack-tip orientation and, similarly, in calculating $\tilde{K}_\alpha^t$, one may ignore changes in the crack surface morphology. To obtain $\tilde{K}_\alpha^s$ for the half-plane crack geometry, temporarily assume that the crack front remains perfectly straight such that the crack tip has the same orientation as the reference crack tip, i.e.,

$$A(0,z) = A_{,x}(0,z) = 0. \quad (19)$$

In this case, $\tilde{K}_\alpha^t$ vanishes and the crack-tip stress intensity factors are defined such that ahead of the crack tip at $x>0$,

$$\{\sigma_{yx}, \sigma_{yy}, \sigma_{yz}\} = \frac{\{K_2^\infty + \tilde{K}_2^s, K_1^\infty + \tilde{K}_1^s, K_3^\infty + \tilde{K}_3^s\}}{\sqrt{2\pi x}}. \quad (20)$$

For a half-plane crack subject to apparent stress intensity factors K_α^∞, the crack faces are assumed to be free of traction. Substituting the tangential stress components in Eqs. (12) into the effective force expressions in (10) and then using Eq. (13), one fluids that the mode 1 result can be written as

$$\tilde{K}_1^s(z') = K_2^\infty B_2(z') + K_3^\infty B_3(z') \quad (21)$$

where

$$B_2(z') = -4\int_{-\infty}^{\infty}\int_{-\infty}^{0} \times \frac{A(x,z)h_{1x,x}^+(z';x,z) - \nu A_{,z}(x,z)h_{1z}^+(z';x,z)}{\sqrt{-2\pi x}}\, dxdz$$

$$B_3(z') = +2\int_{-\infty}^{\infty}\int_{-\infty}^{0} \times \frac{A_{,z}(x,z)h_{1x}^+(z';x,z) - A(x,z)h_{1z,x}^+(z';x,z)}{\sqrt{-2\pi x}}\, dxdz. \quad (22)$$

Similarly, the shear mode results are

$$\tilde{K}_2^s(z') = T_{xx}C_{2xx}(z') + T_{xz}C_{2xz}(z') + T_{zz}C_{2zz}(z')$$
$$\tilde{K}_3^s(z') = T_{xx}C_{3xx}(z') + T_{xz}C_{3xz}(z') + T_{zz}C_{3zz}(z') \quad (23)$$

where

$$C_{2xx}(z') = -2\int_{-\infty}^{\infty}\int_{-\infty}^{0} A_{,x}(x,z)h_{2x}^+(z';x,z)dxdz$$

$$C_{2xz}(z') = -2\int_{-\infty}^{\infty}\int_{-\infty}^{0} [A_{,z}(x,z)h_{2x}^+(z';x,z) + A_{,x}(x,z)h_{2z}^+(z';x,z)]dxdz$$

$$C_{2zz}(z') = -2\int_{-\infty}^{\infty}\int_{-\infty}^{0} A_{,z}(x,z)h_{2z}^+(z';x,z)dxdz \quad (24)$$

and

$$C_{3xx}(z') = -2\int_{-\infty}^{\infty}\int_{-\infty}^{0} A_{,x}(x,z)h_{3x}^+(z';x,z)dxdz$$

$$C_{3xz}(z') = -2\int_{-\infty}^{\infty}\int_{-\infty}^{0} [A_{,z}(x,z)h_{3x}^+(z';x,z) + A_{,x}(x,z)h_{3z}^+(z';x,z)]dxdz$$

$$C_{3zz}(z') = -2\int_{-\infty}^{\infty}\int_{-\infty}^{0} A_{,z}(x,z)h_{3z}^+(z';x,z)dxdz \quad (25)$$

represents the effects of the T-stresses on the nonplanar crack perturbation. In deriving the mode I equations in (22), we have made an integration by parts for terms involving $(A/\sqrt{-2\pi x})_{,x}$, which appear in the original expressions of the effective tractions. This manipulation is crucial for the integrals in (22) to remain convergent for an arbitrary crack profile $A(x,z)$, even when the condition (19) is violated. Thus, the part of the stress intensity variation, $\tilde{K}_\alpha^s$, due to crack surface morphology change is completely determined from Eqs. (21)–(25) as soon as the crack profile function $A(x,z)$ is given.

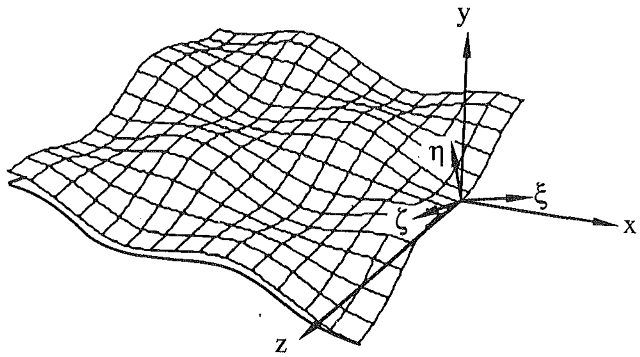

Fig. 3 A wavy nonplanar crack; local crack-tip coordinates ξ, η, ζ and global coordinates x, y, z

In general cases, the quantities $K_\alpha^\infty + \tilde{K}_\alpha^s$ still measure the first-order variation in strength of the stress components σ_{yj} near the crack tip in $y=0$ plane, as in Eq. (20), but they do not correspond to the true stress intensity factors because the crack tip may have been slightly tilted due to the local out-of-plane perturbations along the crack front. By definition, $K_\alpha^{\rm tip}$ should measure the strength of the normal and shear stresses along the prolongation of the local tangent plane at the crack tip, i.e., in the local coordinates ξ, η, ζ (Fig. 3),

$$\{\sigma_{\eta\xi},\ \sigma_{\eta\eta},\ \sigma_{\eta\zeta}\} = \frac{\{K_2^{\rm tip},\ K_1^{\rm tip},\ K_3^{\rm tip}\}}{\sqrt{2\pi\xi}}. \qquad (26)$$

Geometrical relations can be used to calculate the true stress intensity factors $K_\alpha^{\rm tip}$ from the crack-tip orientation angles and the values of K_α^∞ and $\tilde{K}_\alpha^s$. For the half-plane crack geometry, the unit vectors in ξ, η, ζ directions at an observation point z' along the crack front can be expressed to first order as

$$\mathbf{e}_\xi = \{1,\omega,0\},\quad \mathbf{e}_\eta = \{-\omega,1,-\gamma\},\quad \mathbf{e}_\zeta = \{0,\gamma,1\} \qquad (27)$$

where the angles $\omega = A_{,x}(0,z')$ and $\gamma = A_{,z}(0,z')$ give the orientation of the crack tip relative to the cartesian coordinates x, y, z. Equations (27) indicate that the crack-tip coordinates ξ, η, ζ are related to x, y, z by two consecutive rotations, one about the z axis by ω and then another about the x axis by γ. The stress field in the local tangent plane $\eta=0$ can be obtained from the stresses σ_{yj} in the $y=0$ plane by utilizing the well-known crack-tip field in Eq. (11). Then the components of stresses in the local ξ, η, ζ directions are calculated by a coordinate transformation. When this is done, using Eq. (26) and ignoring higher-order terms lead to

$$K_1^{\rm tip} = K_1^\infty - (3\omega/2)K_2^\infty - 2\gamma K_3^\infty + \tilde{K}_1^s$$
$$K_2^{\rm tip} = K_2^\infty + (\omega/2)K_1^\infty + \tilde{K}_2^s$$
$$K_3^{\rm tip} = K_3^\infty + (1-2\nu)\gamma K_1^\infty + \tilde{K}_3^s \qquad (28)$$

where one may identify

$$\tilde{K}_1^t = -(3\omega/2)K_2^\infty - 2\gamma K_3^\infty,\quad \tilde{K}_2^t = (\omega/2)K_1^\infty,$$
$$\tilde{K}_3^t = (1-2\nu)\gamma K_1^\infty \qquad (29)$$

as the variations in the stress intensity factors due to change in the crack-tip orientation. Equations (28) and (21)–(25) provide an approximate relationship between the apparent stress intensity factors K_α^∞ and the local crack-tip values $K_\alpha^{\rm tip}$. With proper modifications, these perturbation formulae can be applied to other crack geometries such as internal or external circular cracks.

It is worth pointing out that the three-dimensional crack perturbation formulae derived above are consistent with the corresponding two-dimensional perturbation formulae in the literature (e.g., Cotterell and Rice, 1980). In the two-dimensional case, the crack profile is independent of the variable z such that $A(x,z) = A(x)$. Carrying out the integrations in (21)–(25) with respect to z and inserting the results into Eq. (28) lead to

$$K_1^{\rm tip} = K_1^\infty - \frac{3\omega}{2}K_2^\infty$$
$$K_2^{\rm tip} = K_2^\infty + \frac{\omega}{2}K_1^\infty - T_{xx}\sqrt{\frac{2}{\pi}}\int_{-\infty}^{0}\frac{A'(x)dx}{\sqrt{-x}}$$
$$K_3^{\rm tip} = K_3^\infty - T_{xz}\sqrt{\frac{2}{\pi}}\int_{-\infty}^{0}\frac{A'(x)dx}{\sqrt{-x}}. \qquad (30)$$

Cotterell and Rice (1980) used the equations for in-plane crack modes 1 and 2 to show that a pure mode I crack path is stable if $T_{xx}<0$ and unstable if $T_{xx}>0$.

The perturbation analysis and formulae given in Eqs. (21)–(28) indicate that, within first-order accuracy, the T-stresses do not affect the mode 1 stress intensity factors. However, the shear mode intensity factors are influenced by all three T-stress components, T_{xx}, T_{xz}, and T_{zz}. By controlling the local shear stress intensities associated with a nonplanar perturbation, the T-stresses play an important role in determining the stability of a mode 1 planar crack during growth. We shall examine this issue in detail shortly.

Cosine Wave Crack Perturbations Versus the Stability of a Mode 1 Planar Crack During Quasi-static Growth

The Effect of Mode Mixity. Consider a cosine wave crack profile

$$A(x,z) = A_0\cos k_x(x-x_0)\cos k_z z \qquad (31)$$

where A_0 is the wave amplitude and k_x, k_z are "wave numbers" which may be related to perturbation wavelengths λ_x, λ_z (in the x and z directions) as

$$k_x = 2\pi/\lambda_x,\quad k_z = 2\pi/\lambda_z. \qquad (32)$$

Since the crack occupies the region $x<0$, the parameter x_0 is chosen to locate the relative position of the crack front along the wavy surface. The aspect ratios $A_0k_x = 2\pi A_0/\lambda_x$ and $A_0k_z = 2\pi A_0/\lambda_z$ characterize the "roughness" of the crack surfaces in the x (crack growth) and z (crack front) directions. Substituting (31) into (22) and using the integral formulae in the Appendix yield

$$B_2(z') = -\frac{1-2\nu}{\sqrt{2}}A_0k_z\sqrt{\sin\phi_k}\cos\left(k_xx_0 - \frac{\phi_k}{2} + \frac{\pi}{4}\right)\cos k_z z'$$
$$B_3(z') = -\frac{1-2\nu}{\sqrt{2}(1-\nu)}A_0k_z\sqrt{\sin\phi_k}\cos\left(k_xx_0 - \frac{\phi_k}{2} + \frac{\pi}{4}\right)\sin k_z z' \qquad (33)$$

where $\phi_k = \tan^{-1}k_z/k_x = \tan^{-1}\lambda_x/\lambda_z$. Using Eqs. (29) to calculate the K-variation due to crack-tip orientation change, the final result for $K_1^{\rm tip}$ for the cosine wavy crack is

$$K_1^{\rm tip} = K_1^\infty - K_2^\infty A_0\cos k_z z'\left[\frac{1-2\nu}{\sqrt{2}}k_z\sqrt{\sin\phi_k}\cos\left(k_xx_0 - \frac{\phi_k}{2} + \frac{\pi}{4}\right) + \frac{3k_x\sin k_xx_0}{2}\right] - K_3^\infty A_0k_z\sin k_z z'\left[\frac{1-2\nu}{\sqrt{2}(1-\nu)}\sqrt{\sin\phi_k}\times\cos\left(k_xx_0 - \frac{\phi_k}{2} + \frac{\pi}{4}\right) - 2\cos k_xx_0\right]. \qquad (34)$$

Observe that the effect of K_2^∞ on $K_1^{\rm tip}(z')$ varies in phase with the crack-front profile, while the effect of K_3^∞ suffers a 90-deg phase lag. With a given mode mixity, the out-of-plane crack perturbation can increase or decrease the mode I stress intensity factor.

To further examine the effects of mode mixity, temporarily ignore the T-stress effects in the shear mode stress intensity factors. First, consider two-dimensional perturbations, in which case $A(x,z)=A(x)$ and

$$K_1^{\text{tip}}=K_1^\infty-\frac{3\omega}{2}K_2^\infty,\quad K_2^{\text{tip}}=K_2^\infty+\frac{\omega}{2}K_1^\infty,\quad K_3^{\text{tip}}=K_3^\infty. \tag{35}$$

This suggests that K_1^{tip} is increased while K_2^∞ is decreased with a negative ω (downward branching). If the crack tends to grow with local mode 1 condition, a kink will occur at an initial angle (Cotterell and Rice, 1980)

$$\omega=-2K_2^\infty/K_1^\infty. \tag{36}$$

This analysis of local crack branching has important implications. Suppose a planar crack growing quasi-statically under pure mode 1 loading. The crack will tend to remain in the planar configuration, or stable against out-of-plane perturbations, if the mode 2 stress intensity factor induced by a small perturbation causes the crack to branch back toward the planar position. Oppositely, if the subsequent branching tends to deflect the crack further away from the original planar position, an infinitesimal perturbation would be enlarged into a macroscopic instability. This principle will be used shortly to study the stability of a mode 1 planar crack.

In the special case when the wavy perturbation is parallel to the crack front, $A(x,z)=A(z)$ and

$$K_1^{\text{tip}}=K_1^\infty-\frac{1-2\nu}{\sqrt{2}}K_2^\infty A_0k_z\cos k_zz' + K_3^\infty A_0k_z\sin k_zz'\left[-\frac{1-2\nu}{\sqrt{2}(1-\nu)}+2\right]. \tag{37}$$

The above response to cosine wave crack-front perturbations can be used to construct solutions for an arbitrary crack-front profile $A(z)$ via standard Fourier cosine transform. Applying this procedure to Eq. (37) and combining the results with the shear mode solutions, one obtains

$$\begin{aligned}
K_1^{\text{tip}}(z')&=K_1^\infty-K_3^\infty\gamma\left[-\frac{1-2\nu}{\sqrt{2}(1-\nu)}+2\right]\\
&\quad+\frac{1-2\nu}{\pi\sqrt{2}}K_2^\infty PV\int_{-\infty}^{\infty}\frac{A(z)-A(z')}{(z-z')^2}\,dz\\
K_2^{\text{tip}}(z')&=K_2^\infty\\
K_3^{\text{tip}}(z')&=K_3^\infty+(1-2\nu)\gamma K_1^\infty
\end{aligned} \tag{38}$$

for arbitrary $A(z)$ which deviates slightly from constancy. Here, $\gamma=dA(z')/dz'$ and "PV" means principal value in the Cauchy sense. Thus, assuming $|K_3^\infty|\ll K_1^\infty$, a local mode 1 crack growth requires a slope,

$$\gamma=-K_3^\infty/(1-2\nu)K_1^\infty \tag{39}$$

along the crack front. In practice, this is observed in the form of *en echelon* crack segmentation patterns in growth of a crack under mixed-mode 1 and 3 loading conditions (e.g., Palaniswamy and Knauss, 1978). Segmented mixed-mode cracking patterns are also observed in brittle fracture of rock in the Earth's crust (e.g., see the review article by Pollard and Aydin, 1988). It will be shown shortly that a positive T-stress parallel to the crack front (i.e., $T_{zz}>0$) helps to destabilize a mode 1 planar crack via nonplanar crack perturbations parallel to the crack front.

The Effects of *T*-Stress on the Stability of a Mode 1 Planar Crack During Quasi-static Growth. The T-stresses change the shear mode stress intensity factors at the tip of a slightly nonplanar crack according to Eqs. (23)–(25). For the cosine wavy cracks, substituting (31) into (24), (25) and using the integral results provided in the Appendix, it can be shown that

$$\begin{aligned}
C_{2xx}&=-\sqrt{\frac{2}{k}}A_0k_x\cos k_zz'\left[\sin\left(k_xx_0-\frac{\phi_k}{2}+\frac{\pi}{4}\right)-\frac{\nu}{2-\nu}\sin\phi_k\sin\left(k_xx_0-\frac{3\phi_k}{2}-\frac{\pi}{4}\right)\right]\\
C_{2xz}&=\sqrt{\frac{2}{k}}A_0k_z\sin k_zz'\left[\cos\left(k_xx_0-\frac{\phi_k}{2}+\frac{\pi}{4}\right)+\frac{\nu}{2-\nu}\sin\left(k_xx_0-\frac{5\phi_k}{2}-\frac{\pi}{4}\right)\right]\\
C_{2zz}&=\frac{\nu}{2-\nu}\sqrt{\frac{2}{k}}A_0k_z\sin\phi_k\cos\left(k_xx_0-\frac{3\phi_k}{2}-\frac{\pi}{4}\right)\cos k_zz'
\end{aligned} \tag{40}$$

for mode 2 and

$$\begin{aligned}
C_{3xx}&=\frac{\nu}{2-\nu}\sqrt{\frac{2}{k}}A_0k_z\cos\phi_k\sin\left(k_xx_0-\frac{3\phi_k}{2}-\frac{\pi}{4}\right)\sin k_zz'\\
C_{3xz}&=-\sqrt{\frac{2}{k}}A_0\cos k_zz'\left[k_x\sin\left(k_xx_0-\frac{\phi_k}{2}+\frac{\pi}{4}\right)+\frac{\nu}{2-\nu}k_z\sin\left(k_xx_0-\frac{5\phi_k}{2}-\frac{\pi}{4}\right)\right]\\
C_{3zz}&=\sqrt{\frac{2}{k}}A_0k_z\left[\cos\left(k_xx_0-\frac{\phi_k}{2}+\frac{\pi}{4}\right)+\frac{\nu}{2-\nu}\sin\phi_k\cos\left(k_xx_0-\frac{3\phi_k}{2}-\frac{\pi}{4}\right)\right]\sin k_zz'
\end{aligned} \tag{41}$$

for mode 3. For all cases, the effects of T-stresses increase with $A_0\sqrt{k}\sim A_0/\sqrt{\lambda}$, a parameter similar to the surface roughness.

The above cosine wave crack solutions can be used to study the stability of a mode 1 planar crack during growth. To see this, first consider the special case of a two-dimensional wavy crack. Setting $k_z=0$ and $\phi_k=0$, then using Eqs. (23), (28), (40), and (41), one finds that

$$\begin{aligned}
K_2^{\text{tip}}&=K_2^\infty+K_1^\infty A_0k_x\sin k_xx_0/2-T_{xx}\sqrt{2k_x}A_0\sin(k_xx_0+\pi/4)\\
K_3^{\text{tip}}&=K_3^\infty-T_{xz}\sqrt{2k_x}A_0\sin(k_xx_0+\pi/4).
\end{aligned} \tag{42}$$

Under pure mode 1 loading, i.e., $K_2^\infty=K_3^\infty=0$, it is possible to have a perfectly planar crack growth. To test the stability of a mode 1 planar crack against nonplanar perturbations, let the crack surface be subject to an infinitesimal wavy disturbance (or, equivalently, assume that an infinitesimal fluctuation in crack surface morphology is inevitable due to imperfections). The mode 1 paths is said to be stable if during subsequent growth the crack tends to propagate back toward the original planar position, and unstable if the subsequent growth tends to deflect the crack further away from the planar path. The kinking tendency in Eq. (36) at a nonzero K_2 suggests that the stability can be interpreted as requiring that K_2^{tip} have a positive value at a wave peak such as the location $x_0=0$ (so that in subsequent crack growth $\omega<0$). When $K_2^\infty=K_3^\infty=0$ and $x_0=0$, Eqs. (42) reduce to

$$K_2^{\text{tip}}=-T_{xx}\sqrt{k_x}A_0,\quad K_3^{\text{tip}}=-T_{xz}\sqrt{k_x}A_0. \tag{43}$$

Applying the wave-peak stability condition $K_2^{\text{tip}}>0$ immediately leads to the conclusion of Cotterell and Rice (1980) that a pure mode 1 fracture path is stable if $T_{xx}<0$ and unstable if $T_{xx}>0$. The shear stress T_{xz} causes a mode III stress intensity and may contribute to the subsequent formation of *en echelon* cracking patterns once the out-of-plane crack perturbations occur.

The above wavy crack approach to the mode 1 path stability

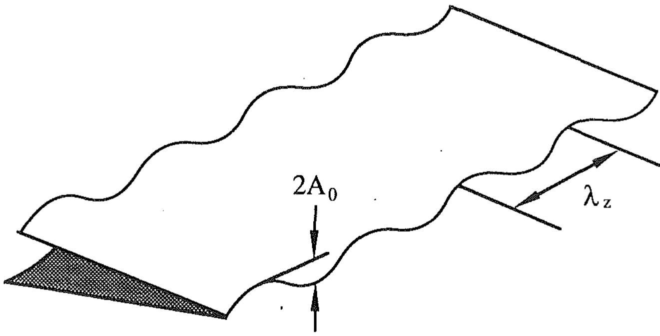

Fig. 4 A cosine wave nonplanar crack undulating parallel to the crack front

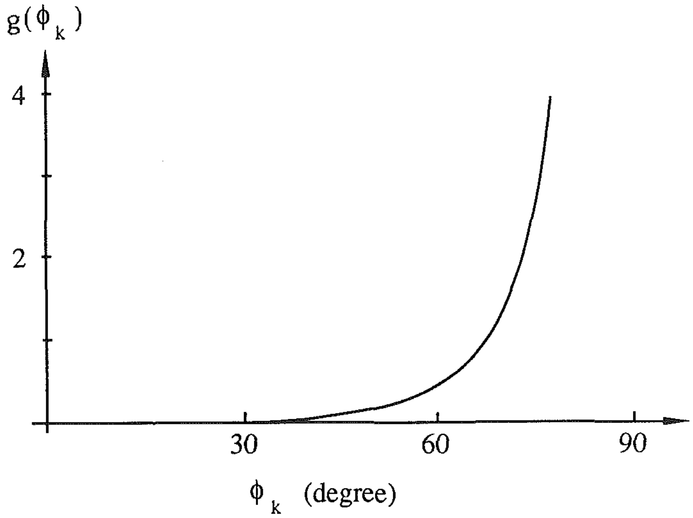

Fig. 5 Function $g(\phi_k)$ in the stability condition in Eq. (50)

is different from that of Cotterell and Rice (1980). Cotterell and Rice considered a small initial crack branching due to local imperfections and showed that the crack will grow back toward the original mode 1 path if $T_{xx}<0$ and will deflect further away from the original path if $T_{xx}>0$. The analysis of Cotterell and Rice involves the solution to an integral equation, which can not be easily extended to the three-dimensional regime. Our approach, while leading to the same conclusion as that of Cotterell and Rice in the two-dimensional cases, requires only the perturbation solution to a cosine wavy crack and may be directly extended to the three-dimensional analysis using the general cosine wavy crack solutions given in Eqs. (40), (41).

To understand the stability issue in three dimension, let us first examine the stability of a mode 1 planar crack against nonplanar perturbations parallel to the crack front. Figure 4 shows a nonplanar crack with crack face undulating parallel to the crack front. For such a crack configuration, substituting $A(x,z)=A(z)$, $k_x=0$ and $\phi_k=\pi/2$ into (40), (41) gives the formulae

$$K_2^{\rm tip}=K_2^\infty+\frac{2}{2-\nu}\,T_{xz}A_0\sqrt{2k_z}\sin k_z z'-\frac{\nu}{2-\nu}\,T_{zz}A_0\sqrt{2k_z}\cos k_z z'$$

$$K_3^{\rm tip}=K_3^\infty-(1-2\nu)K_1^\infty A_0k_z\sin k_z z'-\frac{\nu}{2-\nu}\,T_{xz}A_0\sqrt{2k_z}\cos k_z z'$$
$$-\frac{2(1-\nu)}{2-\nu}\,T_{zz}A_0\sqrt{2k_z}\sin k_z z' \quad (44)$$

to calculate the shear stress intensity factors for a wavy crack undulating in the z direction under arbitrary mode mixity and T-stesses. When $K_2^\infty=K_3^\infty=0$, the shear stress intensities at a wave peak position (e.g., $z'=0$) are

$$K_2^{\rm tip}=-\frac{\nu}{2-\nu}\,T_{zz}A_0\sqrt{2k_z},\quad K_3^{\rm tip}=-\frac{\nu}{2-\nu}\,T_{xz}A_0\sqrt{2k_z}. \quad (45)$$

Again, a positive $K_2^{\rm tip}$ signals stability of a planar crack against the wavy perturbation because, when a small disturbance occurs, subsequent crack growth tends to suppress the perturbation if $K_2^{\rm tip}>0$ at a wave peak. Therefore, a mode 1 planar crack is stable against nonplanar perturbations parallel to the crack front if $T_{zz}<0$ and unstable if $T_{zz}>0$. In latter case, the instability may eventually lead to the formation of *en echelon* segmentation along the crack front. However, the lack of a solution for the entire nonplanar three-dimensional crack growth path renders any further discussions merely speculative.

In a complete three-dimensional stability analysis, one should consider general wavy perturbations with arbitrary wavenumbers k_x and k_z. Analogous to the discussions leading to Eqs. (43), (45), it is sufficiently insightful to examine the T-stress effects at a wave peak (e.g., $x_0=z'=0$) where

$$C_{2xx}=-\sqrt{\frac{2}{k}}\,A_0k_x\left[\sin\left(\frac{\pi}{4}-\frac{\phi_k}{2}\right)+\frac{\nu}{2-\nu}\sin\phi_k\sin\left(\frac{3\phi_k}{2}+\frac{\pi}{4}\right)\right]$$
$$C_{2xz}=0$$
$$C_{2zz}=\frac{\nu}{2-\nu}\sqrt{\frac{2}{k}}\,A_0k_z\sin\phi_k\cos\left(\frac{3\phi_k}{2}+\frac{\pi}{4}\right) \quad (46)$$

and

$$C_{3xx}=0$$
$$C_{3xz}=-\sqrt{\frac{2}{k}}\,A_0\left[k_x\sin\left(\frac{\pi}{4}-\frac{\phi_k}{2}\right)-\frac{\nu}{2-\nu}\,k_z\sin\left(\frac{5\phi_k}{2}+\frac{\pi}{4}\right)\right]$$
$$C_{3zz}=0. \quad (47)$$

The stress intensity factors $K_2^{\rm tip}$ and $K_3^{\rm tip}$ at the peak position are given in terms of these coefficients by Eqs. (23). It is helpful to express $K_2^{\rm tip}$ as

$$K_2^{\rm tip}=C_{2xx}[T_{xx}+T_{zz}g(\phi_k)] \quad (48)$$

where

$$g(\phi_k)=-\frac{\nu}{2-\nu}\times\frac{\sin^2\phi_k\cos(3\phi_k/2+\pi/4)}{\cos\phi_k[\sin(\pi/4-\phi_k/2)+\nu\sin\phi_k\sin(3\phi_k/2+\pi/4)/(2-\nu)]}. \quad (49)$$

The phase angle $\phi_k=\tan^{-1}k_z/k_x=\tan^{-1}\lambda_x/\lambda_z$ varies between 0 and 90 deg so that C_{2xx} is always negative. Thus, the condition for a mode 1 planar crack to be stable against a wavy perturbation with k_x and k_z is ($K_2^{\rm tip}$(peak)>0)

$$T_{xx}+T_{zz}g(\phi_k)<0. \quad (50)$$

The function $g(\phi_k)$ is negative for $0<\phi_k<30$ deg ($0<\lambda_x/\lambda_z<1/\sqrt{3}$) and positive for 30 deg $<\phi_k<90$ deg ($1/\sqrt{3}<\lambda_x/\lambda_z<\infty$). Figure 5 plots the variation of $g(\phi_k)$ when the Poisson ratio ν is taken as 0.25. It is seen that $g(\phi_k)$ is very small for a wide range of ϕ_k. For example, $g(\phi_k)<0.1$ for $0<\phi_k<40$ deg. In this range, for comparable values of T_{xx} and T_{zz}, the stability condition (50) is practically dominated by T_{xx}. However, when $T_{xx}=0$, a large compressive stress T_{zz} may cause crack deflection with a large wavelength parallel to the crack front. When the perturbation wavelength in the z direction becomes sufficiently short, the stability becomes dominated by T_{zz}. In the extreme case when $A(x,z)=A(z)$, the stability is completely controlled by T_{zz}.

Therefore, the tension stress T_{zz} acting in parallel to the crack front has the following peculiar effects. If the crack surface morphology is lacking of short wavelength fluctuations parallel to the front, a positive T_{zz} enhances the stability of a mode 1 planar crack. Once the wavelength ratio λ_x/λ_z exceeds $1/\sqrt{3}=0.577$, the role of T_{zz} on the mode 1 crack stability is reversed, i.e., a positive T_{zz} cause the crack to deflect away from the planar position and a negative T_{zz} suppresses the deflection. Once the instability occurs, a mode 3 stress intensity factor, either pre-existing or generated by a nonzero T_{xz}, may lead to the formation of *en echelon* cracks.

Summary

We have developed a perturbation approach to three-dimensional slightly nonplanar cracks based on the concept of Bueckner-Rice crack-face weight functions. A slightly nonplanar crack is treated as being perturbed from a perfectly planar reference crack. Using a half-plane crack model, perturbation formulae are derived for determining the local stress intensity factors along the front of a nonplanar crack with perturbation wavelengths much smaller than the global dimensions such as a crack size. Using the weight function solutions available in the literature, it is possible to extend the perturbation analysis to internal or external circular cracks in an infinite solid.

The present work is also motivated by a previous study of Cotterell and Rice (1980) on the stability of a two-dimensional crack under pure mode 1 loading. In the two-dimensional case, Cotterell and Rice has shown that the mode 1 fracture path is stable if the nonsingular T-stress parallel to the crack growth, T_{xx}, is negative and unstable if T_{xx} is positive. This criterion has since been widely used in understanding the crack growth pattern in brittle solids. However, a complete stability analysis should also include the perturbations parallel to the crack front. One example is the *en echelon* crack pattern frequently occurring in both engineering and geological observations. To facilitate the three-dimensional analysis, we have approached the mode 1 stability issue from a slightly different perspective, namely, a mode 1 planar crack is said to be stable against nonplanar perturbations if the mode 2 stress intensity factor induced by an infinitesimal wave perturbation has a positive value at the wave peaks; this ensures that during subsequent growth the crack will branch back toward the planar position. Solutions have been given for cosine wavy cracks with arbitrary wavelengths in directions normal and parallel to the crack front. The cosine wavy crack solutions are used to examine the effects of three T-stress components, T_{xx}, T_{xz}, T_{zz}, on the stability of a mode 1 planar crack. It is concluded that (i) a negative T_{xx} always enhances the stability of a mode 1 planar crack against perturbations parallel the crack growth direction; (ii) a negative T_{zz} enhances the stability of a mode 1 crack against perturbations parallel to the crack front, such as the formation of *en echelon* crack patterns; (iii) a nonzero T_{xz} generates a mode 3 stress intensity factor along the front of a slightly nonplanar crack and thus may contributes to the formation of *en echelon* cracks. A complete stability condition for the mode 1 planar crack against general three-dimensional wavy perturbations of wavelengths λ_x and λ_z is given in Eq. (50) as $T_{xx}+T_{zz}g<0$ where g is negative, with a very small magnitude, for $0<\lambda_x/\lambda_z<1/\sqrt{3}$ and positive for $1/\sqrt{3}<\lambda_x/\lambda_z<\infty$; this suggests that when $T_{xx}=0$, a compressive stress T_{zz} may cause crack deflection with a large perturbation wavelength parallel to the crack front and a tensile stress T_{zz} may cause deflection with a small wavelength parallel to the front. When the T-stresses are of comparable values, g is very small for small λ_x/λ_z and very large for large λ_x/λ_z so that T_{xx} controls the perturbation in the x direction and T_{zz} controls the perturbation in the z direction. The lack of a solution for the entire nonplanar three-dimensional crack growth path makes any further discussions merely speculative. Further investigation is left to the future work.

Acknowledgment

The work reported was supported by NSF under the Research Initiation Grant No. MSS9008521 and by the NSF-MRL program through the Center for Material Research at Stanford University. The weight function formulation for slightly nonplanar cracks presented in this paper is partially based on an unpublished research note by Prof. J. R. Rice, to whom the author is also indebted for numerous helpful discussions on the subject. The author is also grateful to two anonymous reviewers for useful review comments.

References

Banichuk, N. V., 1970, "Determination of the Form of Curvilinear Crack by Small Parameter Technique," *Izv. An SSR, MTT 7*, Vol. 2, pp. 130–137 (in Russian).

Bueckner, H. F., 1987, "Weight Functions and Fundamental Fields for the Penny-Shaped and the Half-Plane Crack in Three Space," *International Journal of Solids and Structures*, Vol. 23, pp. 57–93.

Bueckner, H. F., 1973, "Field Singularities and Related Integral Representations," *Mechanics of Fracture 1: Methods of Analysis and Solution of Crack Problems*, G. C. Sih, ed., Noordhoff, Leyden, pp. 239–314.

Bueckner, H. F., 1970, "A Novel Principle for the Computation of Stress Intensity Factors," *Zeitschrift fuer angewandte Mathematik und Mechanik*, Vol. 50, pp. 529–546.

Cotterell, B., and Rice, J. R., 1980, "Slightly Curved or Kinked Cracks," *International Journal of Fracture*, Vol. 16, pp. 155–169.

Gao, H., 1991, "Fracture Analysis of Nonhomogeneous Materials Via a Moduli-Perturbation Approach," *International Journal of Solids and Structures*, Vol. 27, pp. 1663–1682.

Gao, H., 1989a, "Application of 3-D Weight Functions—I. Formulations of Problems of Crack Interaction with Transformation Strains and Dislocations," *Journal of the Mechanics and Physics of Solids*, Vol. 37, pp. 133–153.

Gao, H., 1989b, "Weight Functions for External Circular Cracks," *International Journal of Solids and Structures*, Vol. 25, pp. 107–127.

Gao, H., and Chiu, C., 1992, "Slightly Curved or Kinked Cracks in Anisotropic Elastic Solids," *International Journal of Solids and Structures*, Vol. 29, pp. 947–972.

Gao, H., and Rice, J. R., 1989a, "Application of 3-D Weight Functions—II. The Stress Field and Energy of a Shear Dislocation Loop at a Crack Tip," *Journal of the Mechanics and Physics of Solids*, Vol. 37, pp. 155–174.

Gao, H., and Rice, J. R., 1989b, "A First Order Perturbation Analysis on Crack Trapping by Arrays of Obstacles," ASME Journal of Applied Mechanics, Vol. 56, pp. 828–836.

Gao, H., and Rice, J. R., 1987a, "Somewhat Circular Tensile Cracks," *International Journal of Fracture*, Vol. 33, pp. 155–174.

Gao, H., and Rice, J. R., 1987b, "Nearly Circular Connections of Elastic Half Spaces," ASME Journal of Applied Mechanics, Vol. 54, pp. 627–634.

Goldstein, R. V., and Salganik, R. L., 1970, "Plane Problems of Curvilinear Cracks in an Elastic Solid," *Izv. An SSR, MTT 7*, Vol. 3, pp. 69–82 (in Russian).

Goldstein, R. V., and Salganik, R. L., 1974, "Brittle Fracture of Solids with Arbitrary Cracks," *International Journal of Fracture*, Vol. 10, pp. 507–523.

Kanninen, M. F., and Popelar, C. H., 1985, *Advanced Fracture Mechanics*, Oxford University Press, New York.

Karihaloo, B. L., Keer, L. M., Nemat-Nasser, S., and Oranratnachai, A., 1981, "Approximate Description of Crack Kinking and Curving," ASME Journal of Applied Mechanics, Vol. 48, pp. 515–519.

Palaniswamy, K., and Knauss, W. G., 1978, "On the Problem of Cracks Extension in Brittle Solids Under General Loading," *Mechanics Today*, Vol. 4, S. Nemat-Nasser, ed., Pergamon Press, New York, pp. 87–148.

Parks, D. M., and Kamenetzky, E. A., 1979, "Weight Functions from Virtual Crack Extensions," *International Journal of Numerical Methods in Engineering*, Vol. 14, pp. 1693–1706.

Pollard, D. D., and Aydin, A., 1988, "Progress in Understanding Jointing Over the Past Century," *Geological Society of America Bulletin*, Vol. 100, pp. 1181–1204.

Rice, J. R., 1989, "Weight Function Theory for Three-Dimensional Elastic Crack Analysis," *Fracture Mechanics: Perspectives and Directions* (Twentieth Symposium), ASTM-STP-1020, R. P. Wei and R. P. Gangloff, eds.,American Society for Testing and Materials, Philadelphia, pp. 29–57.

Rice, J. R., 1985a, "First Order Variations in Elastic Fields Due to Variation in Location of a Planar Crack Front," ASME Journal of Applied Mechanics, Vol. 52, pp. 571–579.

Rice, J. R., 1985b, "Three Dimensional Elastic Crack Tip Interactions with Transformation Strains and Dislocations," *International Journal of Solids and Structures*, Vol. 21, pp. 781–791.

Rice, J. R., 1972, "Some Remarks on Elastic Crack Tip Stress Fields," *International Journal of Solids and Structures*, Vol. 8, pp. 751–758.

Sham, T. L., 1987, "A Unified Finite Element Method for Determining Weight Functions in Two and Three Dimensions," *International Journal of Solids and Structures*, Vol. 23, pp. 1357–1372.

APPENDIX

Some Integral Results

For the convenience of the reader, here we present some of the integral formulae used in the text to derive perturbation solutions for cosine wave nonplanar cracks. For $x<0$, $d=\sqrt{x^2+(z-z')^2}$, $\lambda=\tan^{-1}[(z-z')/x]$, $k=\sqrt{k_x^2+k_z^2}$ and $\phi_k=\tan^{-1}k_z/k_x$, it may be verified that

$$\int_{-\infty}^{\infty} d^{-3/2}\cos\frac{3\lambda}{2}\cos k_z z dz = 2\sqrt{\pi k_z}e^{k_z x}\cos k_z z' \tag{A1}$$

$$\int_{-\infty}^{\infty} d^{-3/2}\cos\frac{3\lambda}{2}\sin k_z z dz = 2\sqrt{\pi k_z}e^{k_z x}\sin k_z z' \tag{A2}$$

$$\int_{-\infty}^{\infty} d^{-3/2}\sin\frac{3\lambda}{2}\cos k_z z dz = 2\sqrt{\pi k_z}e^{k_z x}\sin k_z z' \tag{A3}$$

$$\int_{-\infty}^{\infty} d^{-3/2}\sin\frac{3\lambda}{2}\sin k_z z dz = -2\sqrt{\pi k_z}e^{k_z x}\cos k_z z' \tag{A4}$$

$$\int_{-\infty}^{\infty} d^{-2}\cos k_z z dz = -\frac{\pi}{x}e^{k_z x}\cos k_z z' \tag{A5}$$

$$\int_{-\infty}^{\infty} d^{-2}\sin k_z z dz = -\frac{\pi}{x}e^{k_z x}\sin k_z z' \tag{A6}$$

$$\int_{-\infty}^{\infty} d^{-2}\cos 2\lambda\cos k_z z dz = \pi k_z e^{k_z x}\cos k_z z' \tag{A7}$$

$$\int_{-\infty}^{\infty} d^{-2}\cos 2\lambda\sin k_z z dz = \pi k_z e^{k_z x}\sin k_z z' \tag{A8}$$

$$\int_{-\infty}^{\infty} d^{-2}\sin 2\lambda\cos k_z z dz = \pi k_z e^{k_z x}\sin k_z z' \tag{A9}$$

$$\int_{-\infty}^{\infty} d^{-2}\sin 2\lambda\sin k_z z dz = -\pi k_z e^{k_z x}\cos k_z z' \tag{A10}$$

$$\int_{-\infty}^{0}\frac{1}{\sqrt{-x}}e^{k_z x}\cos k_x(x-x_0)dx = \sqrt{\frac{\pi}{k}}\cos\left(k_x x_0-\frac{\phi_k}{2}+\frac{\pi}{4}\right) \tag{A11}$$

$$\int_{-\infty}^{0}\frac{1}{\sqrt{-x}}e^{k_z x}\sin k_x(x-x_0)dx = -\sqrt{\frac{\pi}{k}}\sin\left(k_x x_0-\frac{\phi_k}{2}+\frac{\pi}{4}\right) \tag{A12}$$

$$\int_{-\infty}^{0}\sqrt{-x}\,e^{k_z x}\cos k_x(x-x_0)dx = -\frac{\sqrt{\pi}}{2k^{3/2}}\cos\left(k_x x_0-\frac{3\phi_k}{2}-\frac{\pi}{4}\right) \tag{A13}$$

$$\int_{-\infty}^{0}\sqrt{-x}\,e^{k_z x}\sin k_x(x-x_0)dx = \frac{\sqrt{\pi}}{2k^{3/2}}\sin\left(k_x x_0-\frac{3\phi_k}{2}-\frac{\pi}{4}\right) \tag{A14}$$

Kuang-Chong Wu
Professor.

Yu-Tsung Chiu
Graduate Student.

Zhong-Her Hwu
Graduate Student.

Institute of Applied Mechanics,
National Taiwan University,
Taipei 10764, Taiwan

A New Boundary Integral Equation Formulation for Linear Elastic Solids

A new boundary integral equation formulation is presented for two-dimensional linear elasticity problems for isotropic as well as anisotropic solids. The formulation is based on distributions of line forces and dislocations over a simply connected or multiply connected closed contour in an infinite body. Two types of boundary integral equations are derived. Both types of equations contain boundary tangential displacement gradients and tractions as unknowns. A general expression for the tangential stresses along the boundary in terms of the boundary tangential displacement gradients and tractions is given. The formulation is applied to obtain analytic solutions for half-plane problems. The formulation is also applied numerically to a test problem to demonstrate the accuracy of the formulation.

1 Introduction

The conventional boundary element method first developed by Rizzo (1967) for two-dimensional linear elasticity problems is based on Betti's reciprocal work theorem in conjunction with the fundamental solution of a body force. The primary unknowns used in the conventional boundary element method are the displacements and tractions. The stress field is computed from strain field using Hooke's law. As the strain field is computed by numerically differentiating the displacement field, this procedure leads to hypersingular integrals at boundary points so that special treatment is required to accurately calculate boundary strains and hence stresses. Ghosh at al. (1986) proposed an alternative boundary element formulation for isotropic bodies by partly integrating the integral associated with the boundary displacement in the conventional boundary element method. The resulting formulation is of lower order singularity and has tangential displacement gradients along the boundary as unknowns. The tangential displacement gradients and tractions together with Hooke's law can then be used to compute the tangential stresses. In this formulation the kernel associated with the tangential displacement gradients is multiple valued and proper branch cut must be introduced. Because of the presence of the multiple-valued kernel, for multiply connected regions, the formulation involves the displacements in addition to the tangential displacement gradients and tractions at the boundary. In that case, additional constraint between the displacements and the tangential displacement gradients must be imposed. Similar formulation for potential problems has been given by Choi and Kwak (1989). Another formulation was proposed by Okada et al. (1988). In their formulation, boundary integral equations are expressed in terms of the displacement gradients and the tractions and the kernels are single valued. As in Ghosh et al. (1986), the tangential stresses at the boundary can be computed directly from the displacement gradients through Hooke's law. In Okada et al. (1988), however, the unknowns are twice as many as those in the convention boundary element method fòr two-dimensional problems.

In this paper, a new formulation is presented that contains displacement tangential gradients as unknowns for two-dimensional linear elastic solids. Both isotropic and anisotropic materials are considered. The derivation of the formulation is based on the concept suggested by Altiero and Gavazza (1980) that the mechanical state in a loaded finite body can also be regarded as the state in a finite region of the same shape in an infinite body with suitable dislocations and body forces distributed over the boundary of the region. It will be shown that the densities of such dislocations and body forces are the negative of the tangential displacement gradients and the normal tractions, respectively, at the boundary of the finite body. With the solutions for a dislocation and body force in an infinite body, one can immediately obtain integral representations for the displacement gradients and tractions along an arbitrary contour in a finite body in terms of tangential displacements gradients and tractions at the boundary. The limiting representations for the displacement gradients and tractions at the points approaching the boundary then provide two types of boundary integral equations. In the present formulation, the number of unknowns is the same as that in the conventional boundary element method. The formulation is presented in complex-variable form using either Stroh formalism (1958) for anistropic elasticity or Muskhelishivilli

Contributed by the Applied Mechanics Division of The American Society of Mechanical Engineers for presentation at the 1992 ASME Summer Mechanics and Materials Meeting, Tempe, AZ, Apr. 28–May 1, 1992.

Discussion on this paper should be addressed to the Technical Editor, Prof. Leon M. Keer, The Technological Institute, Northwestern University, Evanston, IL 60208, and will be accepted until four months after final publication of the paper itself in the Journal of Applied Mechanics. Manuscript received by the ASME Applied Mechanics Division, Nov. 30, 1990; final revision, Dec. 11, 1991. Associate Editor: C. F. Shih.

Paper No. 92-APM-31.

method (1963) for isotropic elasticity. An advantage of using the complex-variable form is that in numerical implementation the boundary integrals can be analytically integrated more easily along each boundary element. Similar formulation for anisotropic composite bodies with interface cracks under antiplane shear deformation has been given by Wu and Chiu (1991).

2 Fundamental Solution

Consider a line force **F** and dislocation of Burgers vector **b** with the line direction parallel to the x_3-axis and intersecting the plane $x_3 = 0$ at $x_1 = \xi_1$, $x_2 = \xi_2$ in an infinite body. The solution due to the line force and dislocation in an anisotropic medium in terms of the displacement and stress function is given by (Stroh, 1958)

$$\mathbf{u}(z) = \mathbf{U}(z,\zeta)\mathbf{F} + \mathbf{W}(z,\zeta)\mathbf{b}, \tag{1}$$

$$\mathbf{\Phi}(z) = \mathbf{W}(z,\zeta)^T\mathbf{F} + \mathbf{V}(z,\zeta)\mathbf{b}, \tag{2}$$

where $z = x_1 + ix_2$, $i = \sqrt{-1}$, is used to denote the field point and $\zeta = \xi_1 + i\xi_2$ the source point

$$\mathbf{U}(z,\ \zeta) = \Re[\mathbf{A}\mathbf{G}(z,\zeta)\mathbf{A}^T], \tag{3}$$

$$\mathbf{W}(z,\zeta) = \Re[\mathbf{A}\mathbf{G}(z,\zeta)\mathbf{B}^T], \tag{4}$$

$$\mathbf{V}(z,\zeta) = \Re[\mathbf{B}\mathbf{G}(z,\zeta)\mathbf{B}^T], \tag{5}$$

and $\Re$ stands for the real part. Note that both **U** and **V** are symmetric. The stress function $\mathbf{\Phi}$ is defined such that

$$\mathbf{t} = -\frac{\partial \mathbf{\Phi}}{\partial s}, \tag{6}$$

with **t** as the traction on a contour s. In (3), (4), and (5), $\mathbf{A} = [\mathbf{a}_1, \mathbf{a}_2, \mathbf{a}_3]$ with $\mathbf{a}_k$ as the eigenvectors corresponding to the three eigenvalue p_k with positive imaginary part of the following equation (Stroh, 1958):

$$[\mathbf{Q} + (\mathbf{R} + \mathbf{R}^T)p_k + \mathbf{T}p_k^2]\mathbf{a}_k = 0, \tag{7}$$

where

$$Q_{ik} = C_{i1k1},$$

$$R_{ik} = C_{i1k2},$$

$$T_{ik} = C_{i2k2},$$

and **C** is the elasticity tensor. The matrix **B** is related to **A** by

$$\mathbf{B} = \mathbf{R}^T\mathbf{A} + \mathbf{T}\mathbf{A}\mathbf{P}, \tag{8}$$

where $\mathbf{P} = \mathrm{diag}\ [p_1, p_2, p_3]$. The matrix function $\mathbf{G}(z,\ \zeta)$ is given by

$$\mathbf{G}(z,\zeta) = \frac{1}{\pi i}\,\mathrm{diag}[\log(z_1 - \zeta_1),\ \log(z_2 - \zeta_2),\ \log(z_3 - \zeta_3)], \tag{9}$$

where $z_k = x_1 + p_k x_2$ and $\zeta_k = \xi_1 + p_k\xi_2$. The matrices **A** and **B** are normalized to have the following properties: (Ting, 1986)

$$\mathbf{A}\mathbf{A}^T = -\frac{i}{2}\mathbf{H}, \tag{10}$$

$$\mathbf{B}\mathbf{B}^T = \frac{i}{2}\mathbf{L}, \tag{11}$$

$$\mathbf{A}\mathbf{B}^T = \frac{1}{2}(\mathbf{I} - i\mathbf{S}), \tag{12}$$

where **H**, **L**, and **S** are real matrices and **I** is the unity matrix.

For future reference, the displacement field due to a dislocation dipole and the traction field due to a body force are given here. From (1), the displacement field due to a dislocation dipole created by placing a dislocation of Burgers **b** at (ξ_1, ξ_2) and the other dislocation $-$ **b** at $(\xi_1 + d\xi_1, \xi_2 + d\xi_2)$ is given by

$$\mathbf{u}(z) = -\frac{\partial \mathbf{W}(z,\zeta)}{\partial \sigma}\,\mathbf{b}\,d\sigma, \tag{13}$$

where $d\sigma = \sqrt{d\xi_1^2 + d\xi_2^2}$. From (6) and (2), the tractions at ζ on a contour s due to a body force at z is given by

$$\mathbf{t}(\zeta) = -\frac{\partial \mathbf{W}^T(\zeta,z)}{\partial \sigma}\,\mathbf{F}. \tag{14}$$

Equations (3), (4), and (5) are not applicable to isotropic media under plane-strain condition in which case the eigenvalue $p = i$ is a repeated root of (7). For isotropic materials, Muskhelishivilli method (1963) can be used to derive those matrices. The resulting expressions are

$$\mathbf{U}(z,\zeta) = -\frac{1}{2\pi\mu(\kappa+1)}\Re\left[\kappa\log(z-\zeta)\mathbf{I} - \frac{x_2-\xi_2}{z-\zeta}\begin{pmatrix} -i & 1 \\ 1 & i \end{pmatrix}\right], \tag{15}$$

$$\mathbf{W}(z,\zeta) = \frac{1}{2\pi(\kappa+1)}\Re\left[-\log(z-\zeta)\begin{pmatrix} i(\kappa+1) & 1-\kappa \\ \kappa-1 & i(\kappa+1) \end{pmatrix} + 2\frac{x_2-\xi_2}{z-\zeta}\begin{pmatrix} 1 & i \\ i & -1 \end{pmatrix}\right], \tag{16}$$

$$\mathbf{V}(z,\zeta) = -\frac{2\mu}{\pi(\kappa+1)}\Re\left[\log(z-\zeta)\mathbf{I} - \frac{x_2-\xi_2}{z-\zeta}\begin{pmatrix} -i & 1 \\ 1 & i \end{pmatrix}\right], \tag{17}$$

where μ is the shear modulus, $\kappa = 3 - 4\nu$ with ν as Poisson's ratio. Note that the matrices **U** and **V** for isotropic materials are also symmetric.

3 Formulation

Consider now a multiply connected region D^+ in an infinite space. The region D^+ is bounded internally by a set of contours $C_1, C_2, \ldots, C_n$ and externally by C_0 as shown in Fig. 1 for the case $n = 2$. The region exterior to D^+ and the bounding contours is denoted by D^-. The unit normal vector pointing from D^+ to D^- is denoted by **n** and the tangential unit vector **m** is defined by rotating **n** 90 degrees counterclockwise as shown in Fig. 1. For a finite body with boundary coinciding with $C = \cup_{k=0}^{n} C_k$, the conventional boundary element method is obtained by applying the Betti's reciprocal work theorem with the fundamental solution given by (1) with $\mathbf{b} = \mathbf{0}$ and (14) of a body force at the point z. The resulting equation is given by

$$\beta\mathbf{u}(z) = \int_C \left(\mathbf{U}(\zeta,z)\mathbf{t}_n(\zeta) + \frac{\partial \mathbf{W}(\zeta,z)}{\partial m}(\zeta,z)\mathbf{u}(\zeta)\right)d\sigma, \tag{18}$$

where $\mathbf{t}_n$ is the normal traction on the boundary, $\frac{\partial}{\partial m}$ denotes tangential derivative, $\beta = 1$ in D^+, and $\beta = 1/2$ at smooth boundary point. Since

$$\mathbf{U}(\zeta,z) = \mathbf{U}(z,\zeta), \tag{19}$$

$$\mathbf{W}(\zeta,z) = \mathbf{W}(z,\zeta) \pm \frac{1}{2}\mathbf{I}, \tag{20}$$

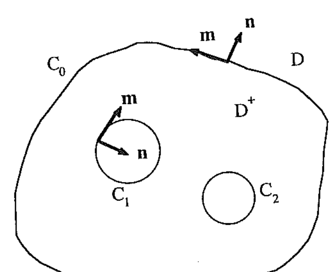

Fig. 1 A multiply connected region with external boundary C_0 and internal boundary C_i, $i = 1, \ldots, n$

(18) can also be written as

$$\beta \mathbf{u}(z) = \int_C \left(\mathbf{U}(z,\zeta)\mathbf{t}_n(\zeta) + \frac{\partial \mathbf{W}}{\partial m}(z,\zeta)\mathbf{u}(\zeta) \right) d\sigma. \tag{21}$$

Comparison of (21) with (1) and (13) reveals that displacement field in the finite body can also be regarded as that in D^+ due to the dislocation dipole $-\mathbf{u}d\sigma$ and body force density $\mathbf{f} = \mathbf{t}_n$ at C in an *infinite* space. The displacement field due to the dislocation dipoles and body forces vanishes in D^-. The formulation in (Gosh et al., 1986) is obtained by partly integrating the second integral of (18) for z in D^+ as

$$\mathbf{u}(z) = \int_C (\mathbf{U}(\zeta,z)\mathbf{t}_n(\zeta) - \mathbf{W}(\zeta,z)\mathbf{d}_m(\zeta))d\sigma + \sum_{k=1}^{m} (-1)^{k+1}\hat{\mathbf{u}}^{(k)}, \tag{22}$$

where $\mathbf{d}_m = \dfrac{\partial \mathbf{u}}{\partial m}$ is the tangential displacement gradient. In (22), the presence of $\hat{\mathbf{u}}^{(k)}$ is due to the multiple-valuedness of the matrix $\mathbf{W}$. If the branch cut for the logarithmic functions in $\mathbf{W}$ is taken to extend from z to infinity and the branch cut intersects the boundary at m points, $\hat{\mathbf{u}}^{(k)}$ is the displacement at the kth intersection point. The intersection points are arranged in increasing distance from the branch point (i.e., the first intersection point is the nearest from the branch point). Although (22) is one order less singular than the conventional boundary element method it may not be convenient for numerical implementation for multiply connected regions as bookkeeping of the intersection points is required and the compatibillity condition between the displacements and displacement gradients must be incorporated. Equation (22) is essentially the displacement field due to a distribution of body forces with the density $\mathbf{t}_n$ and a distribution of dislocations with the density $-\mathbf{d}_m$ at C. An alternative formulation can be obtained by considering the displacement gradients and tractions at a point z along an arbitrary contour s due to the dislocations and body forces. The result is

$$\beta \frac{\partial \mathbf{u}}{\partial s}(z) = \int_C \left[\frac{\partial \mathbf{U}}{\partial s}(z,\zeta)\mathbf{t}_n(\zeta) - \frac{\partial \mathbf{W}}{\partial s}(z,\zeta)\mathbf{d}_m(\zeta) \right] d\sigma, \tag{23}$$

$$\beta \mathbf{t}(z) = -\int_C \left[\frac{\partial \mathbf{W}^T}{\partial s}(z,\zeta)\mathbf{t}_n(\zeta) - \frac{\partial \mathbf{V}}{\partial s}(z,\zeta)\mathbf{d}_m(\zeta) \right] d\sigma, \tag{24}$$

where (6) has been used. Equations (23) and (24) with $\beta = 1/2$ provide a pair of boundary integral equations for the tangential displacement gradients and tractions if the contour s is chosen to coincide with the boundary. Unlike (22), the kernels in (23) and (24) are single valued and no additional conditions need be imposed between the displacements and the displacement gradients. Equation (23) is similar to that given in (Okada et al., 1988). In (Okada et al., 1988), however, all displacement gradients $u_{i,j}$ at boundary appear as variables so that the number of variables doubles. Either (23) or (24) can be solved to obtain the unknown tangential displacement gradients or tractions. Once the unknown boundary data are determined, the displacement gradients and traction in D and on the boundary C in any direction can be computed from (23) and (24). In particular, the normal displacement gradients, $\mathbf{d}_n$ $= \dfrac{\partial \mathbf{u}}{\partial n}$, and tangential tractions, $\mathbf{t}_m$ calculated according to $\mathbf{m}$ on C for anisotropic materials are given by

$$\mathbf{d}_n = -2\Re[\mathbf{A}\mathbf{J}(\omega)\mathbf{A}^T]\mathbf{t}_n + 2\Re[\mathbf{A}\mathbf{J}(\omega)\mathbf{B}^T]\mathbf{d}_m, \tag{25}$$

$$\mathbf{t}_m = -2\Re[\mathbf{B}\mathbf{J}(\omega)\mathbf{A}^T]\mathbf{t}_n + 2\Re[\mathbf{B}\mathbf{J}(\omega)\mathbf{B}^T]\mathbf{d}_m, \tag{26}$$

where

$$\mathbf{J}(\omega) = \mathrm{diag}\left[\frac{\cos\omega + p_1 \sin\omega}{-\sin\omega + p_1\cos\omega}, \frac{\cos\omega + p_2 \sin\omega}{-\sin\omega + p_2\cos\omega}, \frac{\cos\omega + p_3 \sin\omega}{-\sin\omega + p_3\cos\omega} \right] \tag{27}$$

in which ω is the angle of the normal measured counterclockwise from the x_1-axis. $\mathbf{d}_n$ and $\mathbf{t}_m$ can also be computed directly from Hooke's law by

$$\mathbf{d}_n = (\mathbf{nn})^{-1}[\mathbf{t}_n - (\mathbf{nm})\mathbf{d}_m], \tag{28}$$

$$\mathbf{t}_m = (\mathbf{mn})(\mathbf{nn})^{-1}\mathbf{t}_n + [(\mathbf{mm}) - (\mathbf{mn})(\mathbf{nn})^{-1}(\mathbf{nm})]\mathbf{d}_m, \tag{29}$$

where

$$(\mathbf{ab})_{ik} \equiv \sum_{j=1}^{3}\sum_{\ell=1}^{3} C_{ijk\ell}a_j b_\ell. \tag{30}$$

For isotropic materials, (28) and (29) become

$$\mathbf{d}_n = \frac{1}{4\mu(1-\nu)}\begin{pmatrix} (3-4\nu) - \cos 2\omega & -\sin 2\omega \\ -\sin 2\omega & (3-4\nu) + \cos 2\omega \end{pmatrix}\mathbf{t}_n - \frac{1}{2(1-\nu)}\begin{pmatrix} -\sin 2\omega & -(1-2\nu) + \cos 2\omega \\ (1-2\nu) + \cos 2\omega & \sin 2\omega \end{pmatrix}\mathbf{d}_m, \tag{31}$$

$$\mathbf{t}_m = \frac{1}{2(1-\nu)}\begin{pmatrix} -\sin 2\omega & (1-2\nu) + \cos 2\omega \\ -(1-2\nu) + \cos 2\omega & \sin 2\omega \end{pmatrix}\mathbf{t}_n + \frac{\mu}{1-\nu}\begin{pmatrix} 1-\cos 2\omega & -\sin 2\omega \\ -\sin 2\omega & 1+\cos 2\omega \end{pmatrix}\mathbf{d}_m. \tag{32}$$

The normal strain ϵ_{nn} and the antiplane shear strain ϵ_{n3} are given by

$$\epsilon_{nn} = \mathbf{n}^T\mathbf{d}_n, \ \epsilon_{n3} = \frac{1}{2}\mathbf{e}_3^T\mathbf{d}_n \tag{33}$$

where $\mathbf{e}_3$ is the unit vector in the x_3-direction. The tangential normal stress σ_{mm} and antiplane shear stress σ_{m3} are given by

$$\sigma_{mm} = \mathbf{m}^T\mathbf{t}_m, \ \sigma_{m3} = \mathbf{e}_3^T\mathbf{t}_m. \tag{34}$$

4 Analytic Solutions to Half-Plane Problems

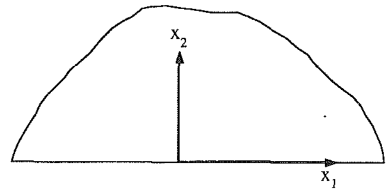

Fig. 2 A half plane subjected to surface traction or displacement

Consider a half-plane $x_2 \geq 0$, $-\infty < x_1 < \infty$ subjected to surface tractions or displacements at $x_2 = 0$ as shown in Fig. 2. For the half-plane problems, (23) and (24) become

$$\frac{\partial \mathbf{u}}{\partial x_1} = \frac{1}{\pi}\int_{-\infty}^{\infty} \frac{1}{\xi_1 - x_1}\left(\mathbf{H}\mathbf{t}_n - \mathbf{S}\frac{\partial \mathbf{u}}{\partial \xi_1} \right) d\xi_1, \tag{35}$$

$$\mathbf{t}_n = -\frac{1}{\pi}\int_{-\infty}^{\infty} \frac{1}{\xi_1 - x_1}\left(\mathbf{S}^T\mathbf{t}_n + \mathbf{L}\frac{\partial \mathbf{u}}{\partial \xi_1} \right) d\xi_1. \tag{36}$$

In deriving (35) and (36), (10), (11), and (12) have been used. Equations (35) and (36) are valid for anisotropic as well as isotropic materials. For isotropic materials, the expressions of **H**, **L**, and **S** can be found in (Ting, 1986). With the following identities (Ting, 1986):

$$\mathbf{H}\mathbf{S}^T+\mathbf{S}\mathbf{H}=\mathbf{0},$$
$$\mathbf{L}\mathbf{S}^T+\mathbf{S}\mathbf{L}=\mathbf{0},$$
$$\mathbf{H}\mathbf{L}-\mathbf{S}\mathbf{S}=\mathbf{I},$$

(35) and (36) can be inverted to give

$$\mathbf{t}_n=-\frac{1}{\pi}\int_{-\infty}^{\infty}\frac{1}{\xi_1-x_1}\mathbf{H}^{-1}\frac{\partial\mathbf{u}}{\partial\xi_1}\,d\xi_1+\mathbf{H}^{-1}\mathbf{S}\frac{\partial\mathbf{u}}{\partial x_1} \tag{37}$$

$$\frac{\partial\mathbf{u}}{\partial x_1}=\frac{1}{\pi}\int_{-\infty}^{\infty}\frac{1}{\xi_1-x_1}\mathbf{L}^{-1}\mathbf{t}_n d\xi_1-\mathbf{L}^{-1}\mathbf{S}^T\mathbf{t}_n. \tag{38}$$

If surface displacements are prescribed, (37) yields the solution for the resulting surface tractions. Similarly, if surface tractions are prescribed, (38) gives the solution for the resulting surface displacements. Equation (38) specialized for a line force agrees with the previous result by Barnett and Lothe (1975).

5 Numerical Implementation

Equations (23) and (24) can be solved numerically in the same manner as in the conventional boundary element method. For simplicity, let the boundary C be approximated by N line segments over which the normal tractions and tangential displacement gradients are assumed to be constant. The resulting discretized equations of (23) and (24) with the midpoints of the line segments chosen as the collocation points are

$$\sum_{k=1}^{N}\mathbf{W}^*_{jk}(\mathbf{d}_m)_k=\sum_{k=1}^{N}\mathbf{U}^*_{jk}(\mathbf{t}_n)_k,\ j=1,2,\ldots,N, \tag{39}$$

$$\sum_{k=1}^{N}(\mathbf{W}^*)^T_{jk}(\mathbf{t}_n)_k=\sum_{k=1}^{N}\mathbf{V}^*_{jk}(\mathbf{d}_m)_k,\ j=1,2,\ldots,N, \tag{40}$$

where $(\mathbf{d}_m)_j$ and $(\mathbf{t}_n)_j$ are the tangential displacement gradients and normal tractions at the jth element and the elements are numbered consecutively along the direction of **m**. The matrices $\mathbf{U}^*$, $\mathbf{W}^*$, and $\mathbf{V}^*$ for $j\neq k$ for anisotropic materials are given by the following analytical expressions:

$$\mathbf{U}^*_{jk}=\Re[\mathbf{A}\mathbf{G}^*_{jk}\mathbf{A}^T], \tag{41}$$

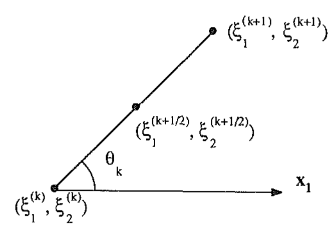

Fig. 3 Notation for the kth boundary element

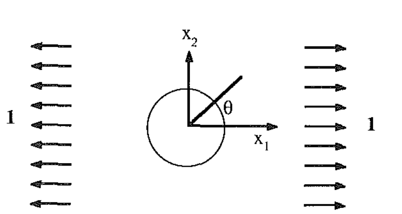

Fig. 4 An infinite body with a circular hole subjected to uniaxial tension

$$\mathbf{W}^*_{jk}=\Re[\mathbf{A}\mathbf{G}^*_{jk}\mathbf{B}^T], \tag{42}$$
$$\mathbf{V}^*_{jk}=\Re[\mathbf{B}\mathbf{G}^*_{jk}\mathbf{B}^T], \tag{43}$$

where

$$\mathbf{G}^*_{jk}=-\frac{1}{\pi i}\,\mathrm{diag}\left[\frac{\hat\zeta_1^{(j)}}{\hat\zeta_1^{(k)}}\log\left(\frac{\zeta_1^{(j+1/2)}-\zeta_1^{(k+1)}}{\zeta_1^{(j+1/2)}-\zeta_1^{(k)}}\right),\ \frac{\hat\zeta_2^{(j)}}{\hat\zeta_2^{(k)}}\log\left(\frac{\zeta_2^{(j+1/2)}-\zeta_2^{(k+1)}}{\zeta_2^{(j+1/2)}-\zeta_2^{(k)}}\right),\ \frac{\hat\zeta_3^{(j)}}{\hat\zeta_3^{(k)}}\log\left(\frac{\zeta_3^{(j+1/2)}-\zeta_3^{(k+1)}}{\zeta_3^{(j+1/2)}-\zeta_3^{(k)}}\right)\right]. \tag{44}$$

In (44), $\hat\zeta_\alpha^{(j)}=\cos\theta_j+p_\alpha\sin\theta_j$ with θ_j being the angle between the jth element and the x_1-axis, $\zeta_\alpha^{(k)}=\xi_1^{(k)}+p_\alpha\xi_2^{(k)}$ with $(\xi_1^{(k)},\ \xi_2^{(k)})$ and $(\xi_1^{(k+1)},\ \xi_2^{(k+1)})$ as the end points of the kth element, $\zeta_\alpha^{(j+1/2)}=\xi_1^{(j+1/2)}+p_\alpha\xi_2^{(j+1/2)}$ and $(\xi_1^{(j+1/2)},\ \xi_2^{(j+1/2)})$ is the midpoint of the jth element. (See Fig. 3 for the notation.) For $j\neq k$ for isotropic materials, $\mathbf{U}^*$, $\mathbf{W}^*$, and $\mathbf{V}^*$ are given by

$$\mathbf{U}^*_{jk}=-\Re[e^{i(\theta_j-\theta_k)}(\mathbf{U}(\zeta^{(j+1/2)},\ \zeta^{(k+1)})-\mathbf{U}(\zeta^{(j+1/2)},\ \zeta^{(k)}))], \tag{45}$$

$$\mathbf{W}^*_{jk}=-\Re[e^{i(\theta_j-\theta_k)}(\mathbf{W}(\zeta^{(j+1/2)},\ \zeta^{(k+1)})-\mathbf{W}(\zeta^{(j+1/2)},\ \zeta^{(k)}))], \tag{46}$$

$$\mathbf{V}_{jk}=-\Re[e^{i(\theta_j-\theta_k)}(\mathbf{V}(\zeta^{(j+1/2)},\ \zeta^{(k+1)})-\mathbf{V}(\zeta^{(j+1/2)},\ \zeta^{(k)}))]. \tag{47}$$

For $j=k$ for both anisotropic and isotropic materials,

$$\mathbf{U}^*_{jj}=\mathbf{V}^*_{jj}=\mathbf{0},\mathbf{W}^*_{jj}=\frac{1}{2}\,\mathbf{I}. \tag{48}$$

Either (39) or (40), which are referred to as type 1 and type 2 equation, respectively, can be used to solve unknown boundary variables numerically. As an example, both equations were applied to solve the problem of an infinite body containing a circular hole subjected to uniaxial tension as shown in Fig. 4.

Table 1 Hoop stress around circular hole under uniaxial tension for isotropic material

θ	type 1	type 2	exact
0	-0.960	-1.059	-1.000
10	-0.844	-0.934	-0.879
20	-0.512	-0.573	-0.532
30	-0.002	-0.020	0.000
40	0.622	0.658	0.653
50	1.287	1.380	1.347
60	1.912	2.058	2.000
70	2.421	2.612	2.532
80	2.753	2.972	2.879
90	2.869	3.098	3.000

Table 2 Hoop stress around circular hole under uniaxial tension for the composite material

θ	type 1	type 2	exact
0	-0.249	-0.280	-0.280
10	-0.227	-0.260	-0.260
20	-0.164	-0.200	-0.200
30	-0.006	-0.100	-0.100
40	0.104	-0.005	-0.005
50	0.355	0.292	0.292
60	0.791	0.728	0.728
70	1.665	1.657	1.659
80	3.519	3.836	3.841
90	5.362	6.290	6.270

The materials considered were isotropic material and a graphite-epoxy composite with the elastic constants given by

$$E_1 = 138\text{GPa},\ E_2 = 10\text{GPa},\ G_{12} = 6.5\text{GPa},\ \nu_{12} = 0.21.$$

In the numerical computations, 72 line elements were used to approximate the circular hole. The numerical results of the hoop stress along the circular hole are presented in Table 1 for isotropic material and Table 2 for the composite material. Also shown in the tables are the exact values given by Muskhelishvili (1963) for isotropic material and Lekhnitskii (1963) for the composite material. In general, the numerical results agree well with the exact values. The maximum error occurs in the case of the composite material with type 1 equation.

6 Acknowledgments

The research was supported by National Science Council of the Republic of China under grant NSC-79-0401-E002-22.

References

Altiero, N. J., and Gavazza, S. D., 1980, "On a unified boundary-integral equation method," *Journal of Elasticity*, Vol. 10, pp. 1-9.

Barnett, D. M., and Lothe, J., 1975, "Line force loadings on anisotropic half space and wedges," *Physica Norvegica*, Vol. 8, No. 1, pp. 13-22.

Choi, J. H., and Kwak, B. M., 1989, "A boundary integral equation formulation in derivative unknowns for two-dimensional potential problems," ASME Journal of Applied Mechanics, Vol. 56, pp. 617-623.

Ghosh, N., Rajiyah, H., Ghosh, S., and Mukherjee, S., 1986, "A new boundary element method formulation for linear elasticity," ASME Journal of Applied Mechanics, Vol. 53, pp. 67-76.

Lekhnitskii, S. G., 1963, *Theory of Elasticity of an Anisotropic Body*, Holden-Day, San Francisco.

Muskhelishvili, I. N., 1963, *Some Basic Problems of the Mathematical Theory of Elasticity*, (J. R. M. Radok, trans.,) Noordhoff Groningen, The Netherlands.

Okada, H., Rajiyah, H., and Atluri, S. N., 1988, "A novel displacement gradient boundary element method for elastic stress analysis with high accuracy," ASME Journal of Applied Mechanics, Vol. 55, pp. 786-794.

Rizzo, R., 1967, "An integral equation approach to boundary value problems in classical elastostatics," *Quarterly Journal of Applied Mathematics*, Vol.25, pp. 83-95.

Stroh, A. N., 1958, "Dislocations and cracks in anisotropic elasticity," *Philosophical Magazine*, Vol. 7, pp. 625-646.

Ting, T. C. T., 1986, "Explicit solution and invariance of the singularities at an interface crack in anisotropic composite," *International J. of Solids and Structures*, Vol. 22, No. 9, pp. 965-983.

Wu, K.-C., and Chiu, Y.-T., 1991, "Antiplane shear interface cracks in anisotropic bimaterials," ASME Journal of Applied Mechanics, Vol. 58, pp. 399-403.

Reflection and Transmission of Obliquely Incident Surface Waves by an Edge of a Quarter Space: Theory and Experiment

Z. L. Li
Research Associate.

J. D. Achenbach
Fellow ASME.

I. Komsky
Research Engineer.

Y. C. Lee
Graduate Student.

Center for Quality Engineering and Failure Prevention, Northwestern University, Evanston, IL 60208

The reflection and transmission of a plane time-harmonic surface wave which is obliquely incident on the edge of a quarter space is investigated theoretically, numerically, and experimentally. The theoretical formulation of the problem, which takes advantage of the translational invariance along the edge of the quarter space, is reduced to a system of singular integral equations along axes normal to the edge, for the defracted displacement components on the faces of the quarter space axes normal to the edge. The truncation of these equations leads to the definition of reflection and transmission coefficients, R *and* T. *The equations are solved for* R, T, *and the diffracted displacements by the use of the boundary element method. A self-calibrated experimental technique is proposed which deploys four surface wave transducers, and which removes the effects of variable coupling between the transducers and the faces of the quarter space as the positions of the transducers are varied. The technique is particularly suited for the measurement of* |R/T| *as a function of the angle of incidence. Excellent agreement is observed between numerically and experimentally obtained values.*

1 Introduction

The incidence of a Rayleigh surface wave on the edge of a quarter space, whose faces are free of tractions, gives rise to a complicated system of diffracted waves. At some distance from the edge the diffracted wave fields are dominated by a reflected surface wave on the face of the incident wave and a transmitted surface wave on the other face. The determination of the reflection and transmission coefficients presents a challenging problem of elastodynamic wave mechanics. Normal incidence of a surface wave on the edge has been studied analytically, numerically, and experimentally by a number of investigators. Studies published prior to 1969 have been reviewed by Knopoff (1969). In more recent work the formulation of the problem has been reduced to a system of integral equations which has then been solved numerically (see Momoi (1980) and Gautesen (1985, 1986)). Recent experimental studies are those of Bond (1979) and Kinra and Vu (1983). For oblique incidence solutions to this problem, see Gautesen (1986).

In the present paper, oblique incidence of a plane time-harmonic surface wave, under an angle θ with the normal to the edge, is considered. Since the geometrical configuration is independent of the coordinate direction along the edge (say, x_3) and since the incident wave is a plane wave, the wave system will be translationally invariant with respect to x_3. Hence, all wavefields will have the terms $\exp(ik_R x_3 \sin\theta)$ in common. By taking advantage of the translational invariance and by the use of an appropriate elastodynamic Green's function, the formulation of the problem has been reduced to a system of singular integral equations along the x_1 and x_2 axes. This system has been solved numerically by the boundary element method to yield the desired reflection and transmission coefficients, R and T, as functions of the angle of incidence.

The analytical and numerical work has been supplemented by an experimental investigation which deploys four surface wave transducers placed on two faces of an aluminum block at equal angles with the normals to the edge. The angles are increased in small steps. A new self-calibrating experimental technique is presented which removes the effects of variable coupling between the transducers and the faces of the specimen, as the angles of reflection and transmission are varied. This technique allows the measurement of $|R|/|T|$ in a simple manner. Theoretical and experimental results show excellent agreement.

For normal incidence, it has been shown in earlier studies (see, e.g., Achenbach et al. (1980)) that the reflection and transmission coefficients at the edge of a quarter space can be used as a building block to construct the reflection and trans-

Contributed by the Applied Mechanics Division of The American Society of Mechanical Engineers for presentation at the 1992 ASME Summer Mechanics and Materials Meeting, Tempe, AZ, Apr. 28–May 1, 1992.

Discussion on this paper should be addressed to the Technical Editor, Prof. Leon M. Keer, The Technological Institute, Northwestern University, Evanston, IL 60208, and will be accepted until four months after final publication of the paper itself in the Journal of Applied Mechanics. Manuscript received by the ASME Applied Mechanics Division, Mar. 20, 1991; final revision, Nov. 12, 1991.

Paper No. 92-APM-28.

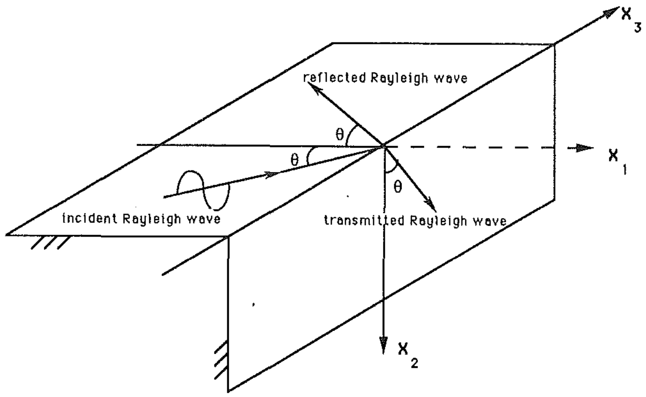

Fig. 1 Rayleigh surface wave incident on the edge of a quarter space

mission coefficients for a surface-breaking crack. For oblique incidence, reflection and transmission by a surface-breaking crack has been investigated by a singular integral equation method by Angel and Achenbach (1984).

2 Rayleigh Surface Wave Incident on the Edge of a Quarter Space

Figure 1 shows a homogeneous, isotropic, linearly elastic quarter space defined by $x_1 \leq 0, x_2 \geq 0, -\infty < x_3 < \infty$. A time-harmonic Rayleigh surface wave travelling along the free surface $x_2 = 0$, is incident on the edge of the quarter space. The angle of incidence, θ, is measured from the positive x_1-axis. The displacement components of the incident wave may be written as

$$\mathbf{u}^{in}(\mathbf{x}) = u_o \left\{ \frac{1}{k_L} \begin{pmatrix} k_R \cos\theta \\ i\Gamma_L \\ a \end{pmatrix} e^{-\Gamma_L x_2} + \frac{2k_R\Gamma_L}{(k_T^2 - 2k_R^2)k_L} \begin{pmatrix} \Gamma_T \cos\theta \\ ik_R \\ \Gamma_T \sin\theta \end{pmatrix} e^{-\Gamma_T x_2} \right\} e^{ik_R\cos\theta x_1 + iax_3} \qquad (1)$$

where

$$(k_L,\ k_T,\ k_R) = \omega/(c_L,\ c_T,\ c_R). \qquad (2a,\ b,\ c)$$

Here, ω is the angular frequency, c_L and c_T are the velocities of longitudinal and transverse waves

$$c_L^2 = (\lambda + 2\mu)/\rho, \quad c_T^2 = \mu/\rho, \qquad (3a,\ b)$$

and c_R is the velocity of Rayleigh waves. Also, λ and μ are the Lamé constants, ρ is the mass density, and

$$\Gamma_L = (k_R^2 - k_L^2)^{1/2}, \qquad (4)$$

$$\Gamma_T = (k_R^2 - k_T^2)^{1/2}, \qquad (5)$$

$$a = k_R \sin\theta. \qquad (6)$$

The interaction of the incident wave with the edge of the quarter space gives rise to an intricate system of waves. We write

$$\mathbf{u}(\mathbf{x}) = \mathbf{u}^{in}(\mathbf{x}) + \mathbf{u}^d(\mathbf{x}). \qquad (7)$$

Since the geometrical configuration is independent of the x_3-coordinate and the incident wave is a plane wave, the system of waves will be translationally invariant with respect to the x_3 coordinate. This means that $\mathbf{u}(\mathbf{x})$, $\mathbf{u}^{in}(\mathbf{x})$, and $\mathbf{u}^d(\mathbf{x})$ will depend on x_3 only through the common term exp (iax_3), where a is defined by Eq. (6). It is intuitively clear, and can be shown rigorously, that at some distance from the edge $\mathbf{u}^d(\mathbf{x})$ separates into conical diffracted longitudinal and transverse waves connected by head waves, and plane reflected and transmitted Rayleigh surface waves. The reflected and transmitted surface waves are indicated in Fig. 1. The angles of reflection and transmission are equal to the angle of incidence. Since the conical waves show geometrical attenuation, and the surface waves do not, we may write

$$u_i^d(\mathbf{x}) \approx R u_i^{RR}(\mathbf{x}), \quad \text{for fixed } x_2 > 0,\ x_1 \to -\infty, \qquad (8)$$

$$u_i^d(\mathbf{x}) \approx T u_i^{TR}(\mathbf{x}), \quad \text{for fixed } x_1 < 0,\ x_2 \to +\infty, \qquad (9)$$

where R and T are reflection and transmission coefficients, and u_i^{RR} and u_i^{TR} denote Rayleigh surface waves propagating in the negative x_1 and positive x_2 directions, respectively:

$$\mathbf{u}^{RR}(\mathbf{x}) = u_o \left\{ \frac{1}{k_L} \begin{pmatrix} -k_R \cos\theta \\ i\Gamma_L \\ a \end{pmatrix} e^{-\Gamma_L x_2} + \frac{2k_R\Gamma_L}{(k_T^2 - 2k_R^2)k_L} \begin{pmatrix} \Gamma_T \cos\theta \\ ik_R \\ \Gamma_T \sin\theta \end{pmatrix} e^{-\Gamma_T x_2} \right\} e^{-ik_R\cos\theta x_1 + iax_3}, \qquad (10)$$

$$\mathbf{u}^{TR}(\mathbf{x}) = u_o \left\{ \frac{1}{k_L} \begin{pmatrix} -i\Gamma_L \\ k_R \cos\theta \\ a \end{pmatrix} e^{\Gamma_L x_1} + \frac{2k_R\Gamma_L}{(k_T^2 - 2k_R^2)k_L} \begin{pmatrix} -ik_R \\ \Gamma_T \cos\theta \\ \Gamma_T \sin\theta \end{pmatrix} e^{\Gamma_T x_1} \right\} e^{ik_R\cos\theta x_2 + iax_3}. \qquad (11)$$

The purpose of the present paper is to determine the reflection and transmission coefficients, R and T, as functions of the angle of incidence.

Full-Space Green's Function due to a Spatially Harmonic Line Load

The solution to the diffraction problem formulated in the previous section will be obtained numerically by solving a system of boundary integral equations by the use of the boundary element method. The formulation of the system of boundary element equations is based on an elastodynamic Green's function which will be derived in this section.

The governing equations for time-harmonic elastodynamic motion are given by (see, for example, Achenbach (1973))

$$\sigma_{ij,j} + \rho\omega^2 u_i = -\rho f_i, \qquad (12)$$

where σ_{ij}, u_i, and f_i are the components of the stress tensor, the displacement vector, and the density of the body forces, respectively. In Eq. (12) and in the sequel, Latin subscripts take the values 1, 2 and 3, the summation convention is implied, and $(\ )_{,j} = \partial(\ )/\partial x_j$. The relation between stresses and displacement gradients is expressed by Hooke's law:

$$\sigma_{ij} = \lambda u_{k,k}\delta_{ij} + \mu(u_{i,j} + u_{j,i}), \qquad (13)$$

where δ_{ij} is the Kronecker delta. For convenience, we will use a two-dimensional position vector, $\mathbf{X}$, in the x_1x_2 plane.

$$\mathbf{X} = (x_1,\ x_2)$$

Now, consider the following problem

$$\sigma_{ijk,j}^G(\mathbf{x};\mathbf{Y}) + \rho\omega^2 u_{ik}^G(\mathbf{x};\mathbf{Y}) = -\rho f_{ik}^G(\mathbf{x};\mathbf{Y}) \qquad (14)$$

where

$$\rho f_{ik}^G(\mathbf{x};\mathbf{Y}) = \delta_{ik}\delta(x_1-y_1)\delta(x_2-y_2)e^{-iax_3}$$
$$= \int_{-\infty}^{\infty} \delta_{ik}\delta(x_1-y_1)\delta(x_2-y_2)\delta(x_3-y_3)e^{-iay_3}dy_3. \quad (15)$$

Here, ρf_{ik}^G defines a line load pointed in the k-direction applied at $x_1=y_1$, $x_2=y_2$, with the harmonic intensity $\exp(-iax_3)$. The solutions to (14), u_{ik}^G and σ_{ijk}^G, will be termed the displacement Green's function and the stress Green's function, due to a spatially harmonic line load. Let U_{ik} **(x;y)** denote the full-space displacement Green's function due to a point load, i.e., the displacement at **x** in the i-direction due to a unit load at **y** applied in the k-direction. The displacement Green's function u_{ik}^G can be obtained by the use of superposition as

$$u_{ik}^G(\mathbf{x};\mathbf{Y}) = \int_{-\infty}^{\infty} U_{ik}(\mathbf{x};\mathbf{y})e^{-iay_3}dy_3 = \overline{u}_{ik}^G(\mathbf{X};\mathbf{Y})e^{-iax_3}, \quad (16)$$

where

$$\overline{u}_{ik}^G = \frac{1}{4\mu}\left\{H_o^{(1)}(\overline{k}_T R)\delta_{ik} + L_{ik}[H_o^{(1)}(\overline{k}_T R) - H_o^{(1)}(\overline{k}_L R)\right\}. \quad (17)$$

Here, $H_o^{(1)}(\ )$ is the Hankel function of the zeroth order of the first kind, and L_{ik} is the following operator:

$$L_{ik} = \frac{1}{k_T^2}\left[\delta_{\alpha k}\delta_{\beta i}\frac{\partial^2}{\partial x_\alpha \partial x_\beta} - ia(\delta_{3k}\delta_{\alpha i} + \delta_{3i}\delta_{\alpha k})\frac{\partial}{\partial x_\alpha} - a^2\delta_{3k}\delta_{3i}\right]. \quad (18)$$

In (18) and in the sequel, the summation convention is also implied for Greek subscripts which, however, only take the values 1 and 2. Other relevant quantities in (17) and (18) are

$$R = [(x_1-y_1)^2 + (x_2-y_2)^2]^{1/2}, \quad (19)$$

and

$$\overline{k}_T = (k_T^2 - a^2)^{1/2}, \quad \overline{k}_L = (k_L^2 - a^2)^{1/2}, \quad (20a,b)$$

where k_T and k_L are the transverse and longitudinal wave numbers, defined by $(2a,b)$, respectively.

An explicit expression for U_{ik} **(x;y)** and the details of the derivation of Eq. (16) and (17) are given in the Appendix. Substituting (16) into (13), we obtain the stress Green's functions due to a spatially harmonic line load

$$\sigma_{ijk}^G(\mathbf{x};\mathbf{Y}) = \overline{\sigma}_{ijk}^G(\mathbf{X};\mathbf{Y})e^{-iax_3}, \quad (21)$$

where

$$\overline{\sigma}_{ijk}^G(\mathbf{X};\mathbf{Y}) = \lambda(\overline{u}_{\gamma k,\gamma}^G - ia\overline{u}_{3k}^G)\delta_{ij} + \mu[\overline{u}_{ik,\gamma}^G\delta_{\gamma j} + \overline{u}_{jk,\gamma}^G\delta_{\gamma i} - ia(\overline{u}_{ik}^G\delta_{3j} + \overline{u}_{jk}^G\delta_{3i})]. \quad (22)$$

4 Integral Representation for the Edge-Diffracted Field

The diffracted fields satisfy

$$\sigma_{ij,j}^d + \rho\omega^2 u_i^d = 0. \quad (23)$$

As was mentioned in Section 2, all field variables have the common factor $\exp(iax_3)$. We write

$$u_i^d(\mathbf{x}) = \overline{u}_i^d(\mathbf{X})e^{iax_3}, \ \sigma_{ij}^d(\mathbf{x}) = \overline{\sigma}_{ij}^d(\mathbf{X})e^{iax_3}. \quad (24)$$

Substitution of (24) into (23) yields

$$\overline{\sigma}_{i\beta,\beta}^d(\mathbf{X}) + ia\overline{\sigma}_{i3}^d(\mathbf{X}) + \rho\omega^2\overline{u}_i^d(\mathbf{X}) = 0. \quad (25)$$

Note that the Green's functions corresponding to a spatially harmonic line load satisfy the following equations:

$$\overline{\sigma}_{i\beta k,\beta}^G(\mathbf{X}) - ia\overline{\sigma}_{i3k}^G(\mathbf{X}) + \rho\omega^2\overline{u}_{ik}^G(\mathbf{X}) = -\delta_{ik}\delta(x_1-y_1)\delta(x_2-y_2). \quad (26)$$

Now, we define a tensor $W_{\beta k}(\mathbf{X})$ as

$$W_{\beta k} = \overline{\sigma}_{i\beta}^d\overline{u}_{ik}^G - \overline{u}_i^d\overline{\sigma}_{i\beta k}^G. \quad (27)$$

Differentiating (27) with respect to x_β, we obtain

$$W_{\beta k,\beta} = \delta(x_1-y_1)\delta(x_2-y_2)\overline{u}_k^d + \overline{\sigma}_{i\beta}^d\overline{u}_{ik,\beta}^G - ia\overline{\sigma}_{i3}^d\overline{u}_{ik}^G) - (\overline{\sigma}_{i\beta k}^G\overline{u}_{i,\beta}^d + ia\overline{\sigma}_{i3k}^G\overline{u}_i^d), \quad (28)$$

where equations (25) and (26) have also been used.

We also have

$$\sigma_{ij}^d u_{ik,j}^G = \overline{\sigma}_{ij}^d e^{iax_3}(\overline{u}_{ik,\beta}^G\delta_{j\beta} - ia\overline{u}_{ik}^G\delta_{3j})e^{-iax_3} = \overline{\sigma}_{i\beta}^d\overline{u}_{ik,\beta}^G - ia\overline{\sigma}_{i3}^d\overline{u}_{ik}^G, \quad (29)$$

$$\sigma_{ijk}^G u_{i,j}^d = \overline{\sigma}_{ijk}^G e^{-iax_3}(\overline{u}_{i,\beta}^d\delta_{j\beta} + ia\overline{u}_i^d\delta_{3j})e^{iax_3} = \overline{\sigma}_{i\beta k}^G\overline{u}_{i,\beta}^d + ia\overline{\sigma}_{i3k}^G\overline{u}_i^d. \quad (30)$$

By the use of Hooke's law, Eq. (13), it follows that

$$\sigma_{ij}^d u_{ik,j}^G = \sigma_{ijk}^G u_{i,j}^d. \quad (31)$$

Equation (28) can be simplified by using (29)–(31) to the form

$$W_{\beta k,\beta} = \delta(x_1-y_1)\delta(x_2-y_2)\overline{u}_k^d. \quad (32)$$

Consider a two-dimensional domain D in the x_1x_2-plane. Let ∂D denote the boundary of D. Integrating Eq. (32) over D and using Stokes theorem yields

$$\epsilon(\mathbf{Y})\overline{u}_k^d(\mathbf{Y}) = \int_D W_{\beta k,\beta}ds(\mathbf{X}) = \int_{\partial D} W_{\beta k}n_\beta d\ell(\mathbf{X})$$
$$= \int_{\partial D} [\overline{u}_{ik}^G(\overline{\sigma}_{i\beta}^d n_\beta) - (\overline{\sigma}_{i\beta k}^G n_\beta)\overline{u}_i^d]d\ell(\mathbf{X}), \quad (33)$$

where n_β is the outward normal to the ∂D and

$$\epsilon(\mathbf{Y}) = \begin{cases} 1, & \mathbf{Y} \in D \\ 0, & \mathbf{Y} \notin D. \end{cases} \quad (34)$$

Equation (33) is the integral representation for the diffracted field.

5 Boundary Integral Equation for the Edge-Diffracted Field

In the limit $\mathbf{Y} \to \partial D$, $\mathbf{Y} \notin D$, (33) becomes

$$\int_{\partial D} (\overline{u}_{ik}^G\overline{\sigma}_{i\beta}^d - \overline{\sigma}_{i\beta k}^G\overline{u}_i^d)n_\beta d\ell = 0, \quad (35)$$

which is the boundary integral equation for the diffracted fields. For the waves diffracted by the edge of a quarter space, Eq. (35) can be written as

$$\int_{-\infty}^0 (-\overline{u}_{ik}^G\overline{\sigma}_{i2}^d + \overline{\sigma}_{i2k}^G u_i^d)dx_1 + \int_0^\infty (\overline{u}_{ik}^G\overline{\sigma}_{i1}^d - \overline{\sigma}_{i1k}^G\overline{u}_i^d)dx_2 = 0,$$
$$\text{for } y_1<0,\ y_2=0^- \text{ and } y_1=0^+,\ y_2>0. \quad (36)$$

By the use of the traction-free conditions,

$$(\sigma_\beta^{in} + \sigma_{i\beta}^d)n_\beta = 0, \text{ for } y_1<0,\ y_2=0 \text{ and } y_2>0,\ y_1=0$$

and

$$\sigma_{i2}^{in} = 0, \text{ for } y_1<0,\ y_2=0.$$

Equation (36) reduces to

$$\int_{-\infty}^0 \overline{\sigma}_{i2k}^G\overline{u}_i^d dx_1 - \int_0^\infty \sigma_{i1k}^G\overline{u}_i^d dx_2 = \int_0^\infty \overline{u}_{ik}^G\overline{\sigma}_{i1}^{in}dx_2$$
$$\text{for } y_1<0,\ y_2=0^- \text{ and } y_1=0^+,\ y_2>0. \quad (37)$$

Equation (37) is the integral equation for the edge-diffracted displacement fields $\overline{u}_i^d$ on the free surfaces of the quarter space. In (37), the integral paths extend, however, to infinity, which is not suitable for a numerical procedure. These integral paths can be reduced to finite length by the use of Eqs. (8)–(9). If $|x_{1A}|$ ($x_{1A}<0$) and x_{2A} are large enough so that for $x_2=0$, $x_1<x_{1A}$ the displacement fields $\overline{u}_i^d(\mathbf{x})$ can be expressed approximately by (8), and for $x_1=0$, $x_2>x_{2A}$ by (9), we can rewrite Eq. (37) as

$$\int_{x_{1A}}^{0} \bar{\sigma}^{G}_{i2k}\bar{u}^{d}_{i}dx_1 - \int_{o}^{x_{2A}} \bar{\sigma}^{G}_{i1k}\bar{u}^{d}_{i}dx_2 + R\int_{-\infty}^{x_{1A}} \bar{\sigma}^{G}_{i2k}\bar{u}^{RR}_{i}dx_1$$

$$- T\int_{x_{2A}}^{\infty} \bar{\sigma}^{G}_{i1k}\bar{u}^{TR}_{i}dx_2 = \int_{0}^{\infty} \bar{u}^{G}_{ik}\bar{\sigma}^{in}_{i1}dx_2$$

$$\text{for } y_1<0,\ y_2=0^{-} \text{ and } y_1=0^{+},\ y_2>0. \quad (38)$$

If σ^{RR}_{ij} denote the stresses corresponding to u^{RR}_{i}, we can write

$$\int_{-\infty}^{x_{1A}} \bar{\sigma}^{G}_{i2k}\bar{u}^{RR}_{i}dx_1 = - \int_{x_{1A}}^{0} \bar{\sigma}^{G}_{i2k}\bar{u}^{RR}_{i}dx_1$$

$$- \int_{0}^{\infty} (\bar{u}^{G}_{ik}\bar{\sigma}^{RR}_{i1}dx_2 - \bar{\sigma}^{G}_{i1k}\bar{u}^{RR}_{i})dx_2, \quad (39)$$

where $\bar{\sigma}^{RR}_{i2} = 0$ on $x_2 = 0$, $x_1 < 0$ has also been used. Using a similar approach, we can also obtain:

$$\int_{x_{2A}}^{\infty} \bar{\sigma}^{G}_{i1k}\bar{u}^{TR}_{i}dx_2 = - \int_{0}^{x_{2A}} \bar{\sigma}^{G}_{i1k}\bar{u}^{TR}_{i}dx_2 - \int_{-\infty}^{0} (\bar{u}^{G}_{ik}\bar{\sigma}^{TR}_{i2}$$

$$- \bar{\sigma}^{G}_{i2k}\bar{u}^{TR}_{i})dx_1. \quad (40)$$

Since σ^{in}_{i1}, σ^{RR}_{i1}, and $\bar{u}^{RR}_{i}$ decay exponentially as x_2 increases, the upper limit of integration in the integral on the right-hand side of (39) may be truncated at, for example, $x_2 = x_{2A}$, without loss of accuracy. Also, since σ^{TR}_{i2} and u^{TR}_{i} decay exponentially as $|x_1|$ increases, the lower limit of integration in the integral on the right-hand side of (40) may be truncated at $x_1 = x_{1A}$. Substitution of (39) and (40) into (38) then yields:

$$\int_{x_{1A}}^{0} \bar{\sigma}^{G}_{i2k}\bar{u}^{d}_{i}dx_1 - \int_{o}^{x_{2A}} \bar{\sigma}^{G}_{i1k}\bar{u}^{d}_{i}dx_2$$

$$-R\left[\int_{x_{1A}}^{o} \bar{\sigma}^{G}_{i2k}\bar{u}^{RR}_{i}dx_1 - \int_{o}^{x_{2A}} (\bar{u}^{G}_{ik}\bar{\sigma}^{RR}_{i1} - \bar{\sigma}^{G}_{i1k}\bar{u}^{RR}_{i})dx_2\right]$$

$$+T\left[\int_{o}^{x_{2A}} \bar{\sigma}^{G}_{i1k}\bar{u}^{TR}_{i}dx_2 + \int_{x_{1A}}^{o} (\bar{u}^{G}_{ik}\bar{\sigma}^{RR}_{i2} - \bar{\sigma}^{G}_{i2k}\bar{u}^{TR}_{i})dx_1\right]$$

$$= \int_{o}^{x_{2A}} \bar{u}^{G}_{ik}\bar{\sigma}^{in}_{i1}dx_2. \quad (41)$$

Equation (41) defines the system of boundary integral equations which can be solved in the usual manner by the boundary element method. Note that the unknowns in (41) are $\bar{u}^{d}_{i}$, R, and T.

6 Numerical Results

In the numerical calculations, the wavelength of transverse waves, $\lambda_T = 2\pi/k_T$, is used as the normalization factor for lengths. The lengths of the elements vary with distance from the edge. If x_{1c} is the x_1-coordinate of the center of an element on $x_2 = 0$, $x_1 < 0$, the size of the element, say h, increases as $|x_{1c}|$ increases until $h = h_c$ (here, h_c is a constant, for example, when $\theta = 0$, $h_c = 0.1\ \lambda_T$). As $|x_{1c}|$ increases further, the elements remain constant in length, namely h_c. An analogous variation of element lengths was implemented on the boundary $x_1 = 0$, $x_2 > 0$. Also, as θ increases, the value of h_c required for the desired accuracy decreases. In addition, appropriate values of $|x_{1A}|$ and x_{2B} have to be selected. The larger the values of $|x_{1A}|$ and x_{2B}, the larger the number of elements in the solution of the system of boundary integral equations. For different numbers of elements, the calculated absolute values of the displacement components in the x_2 direction, $|u^{d}_{2}|$, are shown in Fig. 2(a) for $\theta = 0$ deg, in Fig. 2(b) for $\theta = 45$ deg and in Fig. 2(c) for $\theta = 70$ deg. It was found that 150 elements on each side of the edge yield results of acceptable accuracy.

As a check on the accuracy of this computation for the case $\theta = 0$, the values of the reflection and transmission coefficients

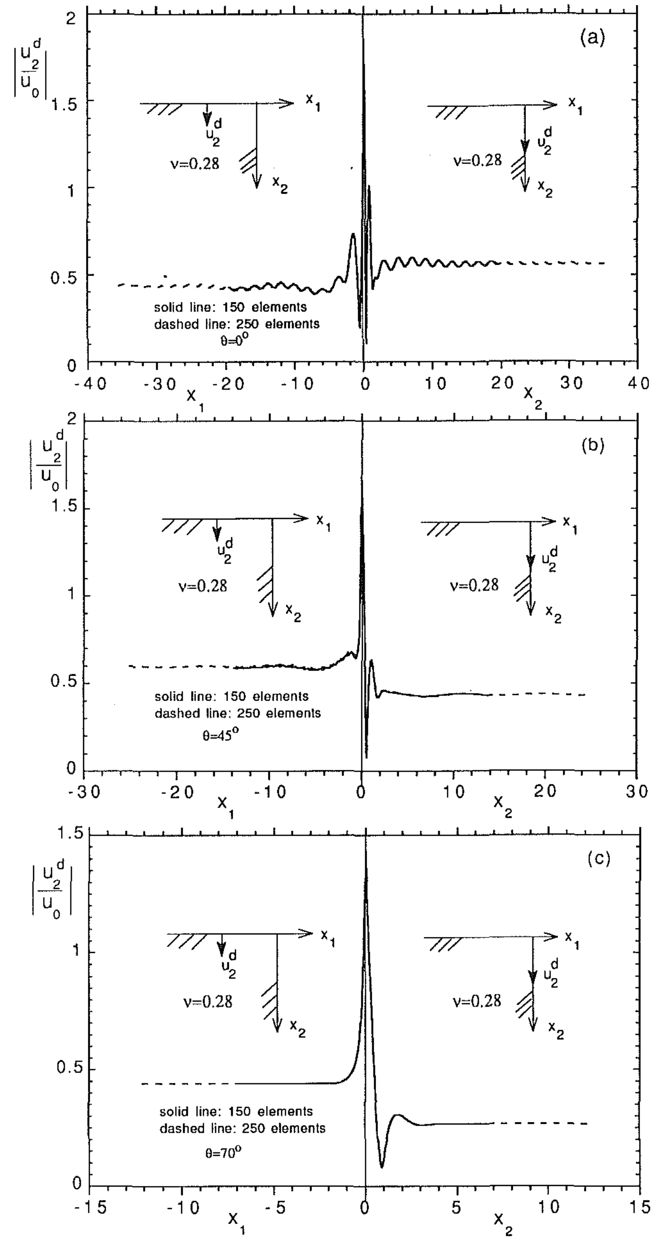

Fig. 2 Absolute values of the components in the x_2-direction of the diffracted displacement fields. Poisson's ratio $\nu = .28$. (a) $\theta = 0$ deg, (b) $\theta = 45$ deg, (c) $\theta = 70$ deg

obtained in this work are compared in Table 1 with those obtained by Gautesen (1985). The agreement is very good. Figure 3 shows the amplitudes of the reflection and transmission coefficients versus the angle of incidence θ for $\nu = 1/3$. It is noted that the surface wave is completely transmitted at $\theta \sim 75.5$ deg.

When the angle of incidence exceeds a critical angle, namely, when

$$\theta \geq \sin^{-1}\left(\frac{k_T}{k_R}\right) = \theta_c, \quad (42)$$

no diffracted body waves exists. Consequently, all incident energy must be carried away by the reflected and transmitted Rayleigh surface waves. Hence, we will have the following energy balance

$$|R|^2 + |T|^2 = 1 \text{ for } \theta > \theta_c. \quad (43)$$

For Poisson's ratio $\nu = 1/3$, Eq. (42) yields $\theta_c = 68.74$ deg. For all values of $\theta > \theta_c$, the numerically calculated values of

Table 1 Absolute Values and Phases of the Reflection and Transmission Coefficients for Normal Incidence

	Poisson's ratio	$\lvert R \rvert$	$\lvert T \rvert$	ϕ_R	ϕ_T
Gautesen	0.17	0.27	0.68	50 deg–55 deg	~ -80 deg
This work	0.17	0.26	0.68	53 deg	-80 deg
Gautesen	0.25	0.32	0.68	39 deg ~ 45 deg	~ -81 deg
This work	0.25	0.32	0.68	38 deg	-80 deg
Gautesen	0.33	0.39	0.67	29 deg ~ 32 deg	~ -82 deg
This work	0.33	0.40	0.67	38 deg	-82 deg

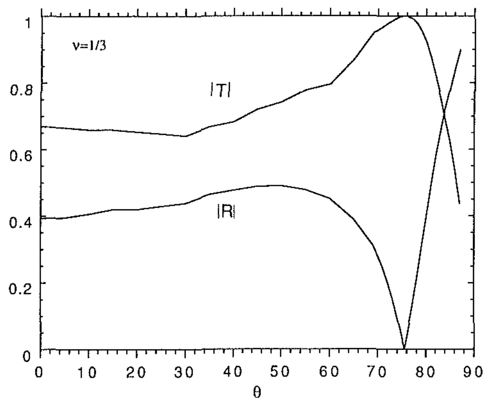

Fig. 3 Absolute values for the reflection and transmission coefficients versus the angle of incidence, θ. Poisson's ratio $\nu = 1/3$.

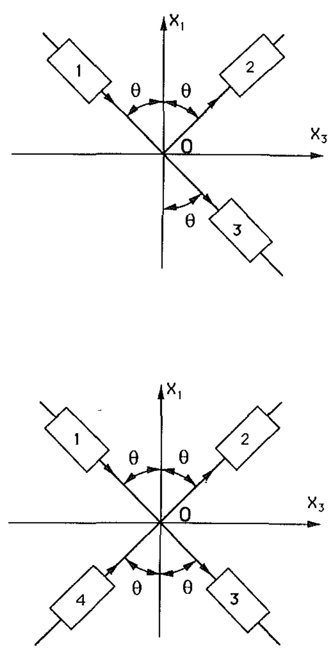

(a)

(b)

Fig. 4 Folded out depictions of transducer placements

$\lvert R \rvert$ and $\lvert T \rvert$ satisfy $\lvert R \rvert^2 + \lvert T \rvert^2 = 1$ to seven significant digits, which provides a check on the accuracy of the numerical calculations.

7 Experimental Work

Experimental results were obtained by the use of surface wave transducers, which were placed on two perpendicularly intersecting faces of a polished aluminum block. The transducers were coupled to the aluminum by the application of a thin layer of oil couplant. In principle, it would seem to be a rather simple experiment to measure the reflection and transmission coefficients for comparison with the theoretical results. A transducer placed at a desired angle of incidence, θ, produces the signal. A second transducer, placed on he same face under the angle of reflection θ, receives the reflected signal, while a third transducer, placed on the intersecting face of the block, again under the angle θ, received the transmitted signal. A folded-out depiction of this configuration is shown in Fig. 4(*a*). Unfortunately, this is not an effective way of measuring the reflection and transmission coefficients, primarily because the coupling between the transducers and the specimen is unpredictable and very difficult to reproduce when the transducers are moved from one angle of incidence to another. Hence, there is no guarantee that the incident wave is the same for each angle of incidence, nor that, due to variation in the coupling, the reflected and transmitted waves would be measured with the same response functions by the receiving transducers. Since it is not possible to calibrate the complete set-up for every angle of incidence, this paper proposes a configuration of transducers suitable for a self-calibrating measurement technique. This is feasible in a simple manner for the measurement of $\lvert R \rvert / \lvert T \rvert$, rather than $\lvert R \rvert$ and $\lvert T \rvert$ separately. For comparison of theoretical and experimental results, the quantity $\lvert R \rvert / \lvert T \rvert$ provides almost equally useful information.

A configuration of transmitting and receiving transducers for a self-calibrating technique is shown in Fig. 4(*b*). Four transducers are used. A special holder was designed to move and align these four transducers over incremental values of the angle θ. The coupling must be of good quality, but by virtue of the self-calibrating features of the technique it does not have to be the same as the angle of incidence is varied. In the experiment both transducers 1 and 4 are fired in sequence, and for both cases, the reflections and transmissions are measured.

Suppose transducer 1 is fired first. In the frequency domain the amplitude of the voltage at transducer 3 may be expressed in terms of response functions. We may write for the voltage 3:

$$V_{13} = A_1 \cdot D_{10} \cdot T \cdot D_{03} \cdot S_3. \tag{44}$$

Here the response function, A_1, includes the signal strength of transducers 1 and the signal transmission from transducer 1 to the specimen. D_{10} is the response function for transmission along the distance from 1 to 0 including attenuation and diffraction, T is the transmission coefficient of the edge, D_{03} is the response function for transmission along the distance from 0 to 3, and S_3 is the response function of transducer 3, including transmission from the specimen to the transducer. Similarly, we have for the reflected signal

$$V_{12} = A_1 \cdot D_{10} \cdot R \cdot D_{02} \cdot S_2. \tag{45}$$

Similar expressions are obtained when transducer 4 is fired. We have

$$V_{42} = A_4 \cdot D_{40} \cdot T \cdot D_{02} \cdot S_2 \tag{46}$$

$$V_{43} = A_4 \cdot D_{40} \cdot R \cdot D_{03} \cdot S_3 \tag{47}$$

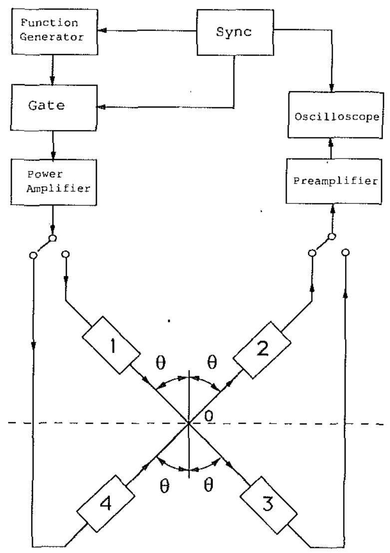

Fig. 5 Schematic of the set-up of the experiment for oblique incidence

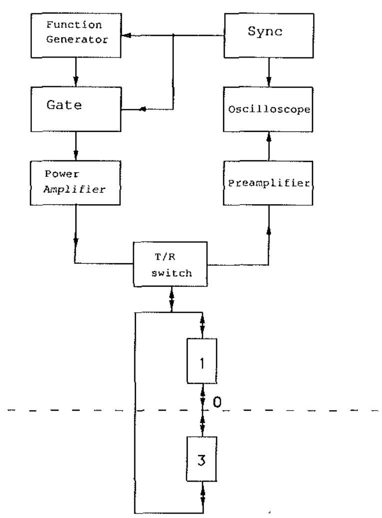

Fig. 6 Schematic of the set-up of the experiment for normal incidence

Next, we consider the ratio $V_{12}\cdot V_{43}/V_{13}\cdot V_{42}$. It then easily follows that

$$\left|\frac{R}{T}\right| = \left|\frac{V_{12}\cdot V_{43}}{V_{13}\cdot V_{42}}\right|^{1/2}. \tag{48}$$

It is of great importance that by the present technique the ratio $|R|/|T|$ can be measured independently of the distance and the surface conditions between each transducer and the edge, and independently of the coupling between the transducers and the surface of the specimen. When moving the transducers from one angle of incidence to another, it is virtually impossible to maintain these conditions the same for a sequence of tests.

As shown in Fig. 4(*b*), four transducers (two transmitters and two receivers) are used for measurements at all angles of incidence, except $\theta = 0$. A schematic of the set-up for the experiment is shown in Fig. 5. For $\theta = 0$, two transducers are used. For this case a schematic is shown in Fig. 6. Equation (48) is now replaced by

$$\left|\frac{R}{T}\right| = \left|\frac{V_{11}\cdot V_{33}}{V_{13}\cdot V_{31}}\right|^{1/2}. \tag{49}$$

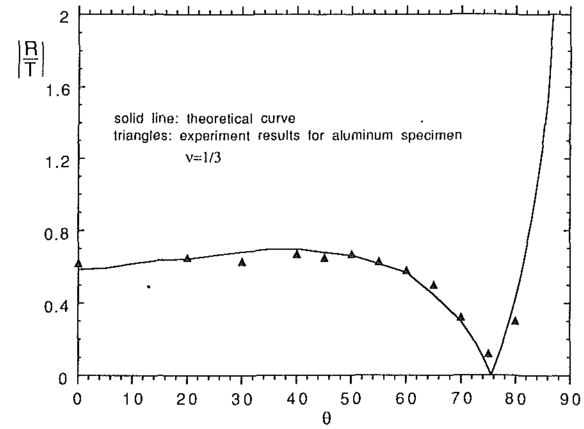

Fig. 7 Comparison of theoretical and experimental values of $|R/T|$

To maintain exactly the same conditions of electrical signal generation and amplification, the two transducers are connected in parallel. Since the measured voltage amplitudes for the transmitted signals, V_{13} and V_{31}, are overlapping, the signals used in Eq. (49) are taken as half the total measured amplitude. To prevent overlap of the signals V_{11} and V_{33} the transducers should be installed at different distance from the edge.

Figure 7 shows a comparison of the theoretical and experimental values of $|R|/|T|$. The agreement is excellent.

Acknowledgment

This work was carried out in the course of research for Contract DEFG02-86-ER13484 with the Department of Energy, Office of Basic Energy Sciences, Engineering Research Program.

References

Achenbach, J. D., 1973, *Wave Propagation in Elastic Solids*, North-Holland, Amsterdam.

Achenbach, J. D., Gautesen, A. K., and Mendelsohn, D. A., 1980, "Ray Analysis of Surface-Wave Interaction with an Edge Crack," *IEEE Transaction of Sonics and Ultrasonics*, Vol. SU-27, pp. 124–129.

Angel, Y. C., and Achenbach, J. D., 1984, "Reflection and Transmission of Obliquely Incident Rayleigh Waves by a Surface-Breaking Crack," *J. Acoust. Soc. Am.*, Vol. 75, No. 2, pp. 313–319.

Bond, L. J., 1979, "A Computer Model of the Interaction of Acoustic Surface Waves with Discontinuities," *Ulrasonics*, Vol. 17, pp. 71–77.

Gautesen, A. K., 1985, "Scattering of Rayleigh Wave by an Elastic Quarter Space," ASME Journal of Applied Mechanics, Vol. 52, pp. 664–668.

Gautesen, A. K., 1986, "Scattering of an Obliquely Incident Rayleigh Wave in an Elastic Quarter Space," *Wave Motion*, Vol. 8, pp. 27–41.

Kinra, V. K., and Vu, B. Q., 1983, "Diffraction of Rayleigh Waves in a Quarter Space," *Mech. Res. Com.*, Vol. 10, pp. 193–198.

Knopoff, L., 1969, "Elastic Wave Propagation in a Wedge," *Wave Propagation in Solids*, J. Miklowtz, ed., ASME, New York, pp. 3–42.

Kobayashi, S., 1987, "Elastodynamics," *Boundary Element Methods in Mechanics*, D. E. Beskos, ed., North-Holland, pp. 191–225.

Momoi, T., 1980, "Scattering of Rayleigh Waves in an Elastic Quarter Space," *J. Phys. Earth*, Vol. 28, pp. 385–413.

APPENDIX

Displacements Due to a Spatially Harmonic Line Load

The displacement in the x_i direction at position **x** due to a time-harmonic point load applied in the x_k direction at position **y** may be written as

$$U_{ik}(\mathbf{x};\mathbf{y}) = \frac{1}{4\pi\mu}\left[U_1(r)\,\delta_{ik} - U_2(r)\,\frac{\partial r}{\partial x_i}\frac{\partial r}{\partial x_k}\right], \tag{A1}$$

where $r = [(x_1-y_1)^2+(x_2-y_2)^2+(x_3-y_3)^2]^{1/2}$, and

$$U_1=\left[1+\frac{i}{k_T r}-\frac{1}{(k_T r)^2}\right]\frac{e^{ik_T r}}{r}-\left(\frac{k_L}{k_T}\right)^2\left[\frac{i}{k_L r}-\frac{1}{(k_L r)^2}\right]\frac{e^{ik_L r}}{r}, \quad \text{(A2)}$$

$$U_2=\left[1+\frac{3_i}{k_T r}-\frac{3}{(k_T r)^2}\right]\frac{e^{ik_T r}}{r}-\left(\frac{k_L}{k_T}\right)^2\left[1+\frac{3i}{k_L r}-\frac{3}{(k_L r)^2}\right]\frac{e^{ik_L r}}{r}. \quad \text{(A3)}$$

In these expressions, k_L and k_T are the longitudinal and transverse wave numbers defined by $(2a,b)$.

Consider the integral

$$I=\int_{-\infty}^{\infty} e^{ik_\xi r - iay_3}\,dy_3 = e^{-iax_3}\int_{-\infty}^{\infty}\frac{1}{r}\int_{-\infty}^{\infty}\frac{1}{r}\,e^{ik}\,e^{ik_\xi r+ia(x_3-y_3)}dy_3 \quad \text{(A4)}$$

where $k_\xi = k_L$ or k_T.

Let $R=[(x_1-y_1)^2+(x_2-y_2)^2]^{1/2}$, and

$$y_3-x_3=R\sinh(\eta). \quad \text{(A5)}$$

We have

$$r=[R^2+(y_3-x_3)^2]^{1/2}=R\cosh(\eta). \quad \text{(A6)}$$

Substitution of (A5) and (A6) into the right-hand side of (A4) yields

$$I=e^{-iax_3}\int_{-\infty}^{\infty} e^{iR[k_\xi\cosh(\eta)-a\ \sinh(\eta)]}d\eta. \quad \text{(A7)}$$

Let $s=\sinh^{-1}[a/(k_\xi^2-a^2)^{1/2}]$, then (A7) becomes

$$I=e^{-i\alpha x_3}\int_{-\infty}^{\infty} e^{iR(k_\xi^2-a^2)^{1/2}\cosh(\eta-s)}d\eta=e^{-iax_3}\pi i\,H_o^{(1)}(\bar{k}_\xi R), \quad \text{(A8)}$$

where $\bar{k}_\xi = (k_\xi^2-a^2)^{1/2}$, $Re(\bar{k}_\xi)\geq 0$. In the last step of (A8) the integral representation of the Hankel function of the zeroth order of the first kind has been used.

Substituting (A1)–(A3) into the integral of Eq. (16) and using (A8), we obtain Eqs. (16) and (17).

Stress Wave Radiation From a Crack Tip During Dynamic Initiation

V. Prakash

L. B. Freund
Mem. ASME

R. J. Clifton
Fellow ASME

Division of Engineering,
Brown University,
Providence, RI 02912

Plate impact experiments are conducted to study the dynamic fracture processes which occur on submicrosecond time scales. These experiments involve the plane strain loading of a plane crack by a square tensile pulse with a duration of approximately one microsecond. The crack-tip loading rates achieved are $\dot{K}_I \sim 10^8$ MPa$\sqrt{m}$ s^{-1}, which are approximately two orders of magnitude higher than those obtained in other dynamic fracture configurations. Motion of the rear surface caused by waves diffracted from the stationary crack and by waves emitted by the running crack is monitored at four points ahead of the crack tip using a laser interferometer system. The measured normal velocity of the rear surface of the specimen agrees very well with the scattered fields computed using an assumed elastic viscoplastic model, except for the appearance of a sharp spike with a duration of less than 80 nanoseconds. This spike, which is not predicted by the inverse square root singular stress fields of linear elastic fracture mechanics, is understood to be related to the onset of crack growth and coincides with the abrupt and unstable ductile growth of a microstructural void to coalescence with the main crack. The crack initiation process is modeled as the sudden formation of a very small hole at the crack tip. This admits the possibility of dynamic crack-tip stress fields with crack-tip singularities stronger ($\sim r^{-3/2}$) than the inverse square root singular fields of fracture mechanics. The elastodynamic radiation resulting from the formation of a traction free hole at the crack tip is applied first to the case of antiplane shear deformation and then to the corresponding plane strain problem. The radiated fields predicted by the strongly singular solutions are found to be in good agreement with the spikes observed in the experiments. The radius of the hole, which appears as a parameter in the solution for the radiated field, agrees reasonably well with the interparticle spacing.

1 Introduction

A central issue in the dynamic fracture of materials is the initiation of fracture from a pre-existing crack in a deformable body due to stress wave loading. The effects of material inertia and strain rate sensitivity are called into play under high rate loading conditions, and fracture may evolve differently under these circumstances than under quasi-static loading. The interpretation of experiments involving dynamic fracture under stress wave loading has been a difficult task, in part because the laboratory specimen configurations commonly used in dynamic fracture testing cannot be analyzed by existing mathematical methods, even for linear elastic material response.

A particular configuration for which it is possible to obtain an exact solution for the elastodynamic stress and deformation fields from a boundary value problem which models the interaction of a transient stress pulse with a crack is the plane strain configuration of a half plane crack, in an otherwise unbounded body, subjected to plane-wave step loading. This is the first transient plane strain elastodynamic crack problem involving wave scattering that was successfully analyzed (deHoop, 1958). In the course of obtaining the solution by integral transform methods, deHoop presented the modern version of the technique now known as the Cagniard-deHoop method of double transform inversion. The problem and its solution procedure are discussed in detail by Freund (1990).

Ravichandran and Clifton (1989) developed an experimental technique which, for all practical purposes involves loading a half plane crack by a plane tensile pulse. In this experiment, the specimen is a metal disk 6.25 cm in diameter and 0.8 cm thick. The disk is prepared with a planar crack on its midplane, with the crack edge coinciding with a diameter of the disk. The disk specimen is loaded in a plate impact apparatus by projecting a second disk against the cracked disk at high speed. The impact results in a *compressive wave* in the cracked disk.

Contributed by the Applied Mechanics Division of The American Society of Mechanical Engineers for presentation at the 1992 Applied Mechanics and Materials Meeting, Apr. 28–May 1, 1992.

Discussion on this paper should be addressed to the Technical Editor, Professor Leon M. Keer, The Technological Institute, Northwestern University, Evanston, IL 60208, and will be accepted until four months after final publication of the paper itself in the Journal of Applied Mechanics. Manuscript received by the ASME Applied Mechanics Division, Apr. 3, 1991; final revision, Dec. 11, 1991. Associate Editor: S. K. Datta.

Paper No. 92-APM-33.

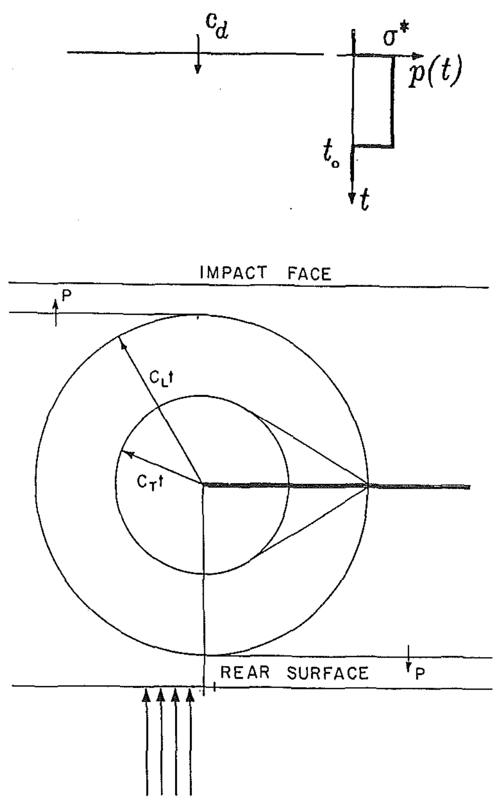

Fig. 1 Schematic of the experimental configuration

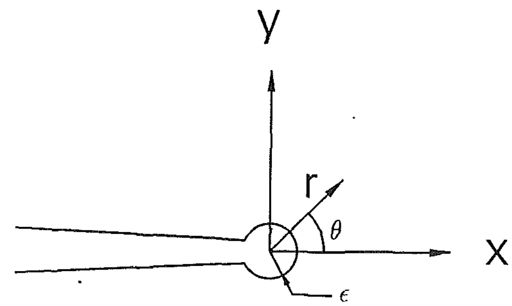

Fig. 2 Coordinate system placed at center of a very small hole introduced at the crack tip

The magnitude of this wave is determined by the impact velocity and the properties of the two materials; the duration is determined by the thickness of the impacting disk. The compressive wave travels through the specimen, passing the initially closed crack plane with little effect. The wave reflects from the traction-free back surface of the specimen as a *tensile pulse*, and it is this pulse which travels back to load the crack. The interaction of the plane pulse with the crack preserves the conditions of plane pulse loading of a half plane crack in the middle part of the specimen until scattered waves reflect back from the boundaries to the crack edge, or until unloading waves from the periphery of the disk reach the middle portion of the specimen. The scattered wave field produced by the interaction of the crack with the stress pulse is monitored on the back face of the disk specimen by means of a laser interferometer system. Recently, Prakash and Clifton (1992) used an experimental procedure similar to the one developed by Ravichandaran and Clifton (1989) to study fracture initiation in AISI 4340 VAR steel, at crack-tip loading rates of approximately 10^8 MPa$\sqrt{m}s^{-1}$ (see Fig. 1). They monitored the motion of the rear surface at four different points simultaneously during the experiment by means of a multiple beam laser interferometer system designed for this purpose. The present study was motivated by a particular feature of the recorded scattered wave field that could not be explained on the basis of standard approaches to the problem.

The measured normal velocity of the rear surface of the specimen at a typical monitoring point, shown in the schematic diagram of Fig. 1, agrees very well with computed scattered fields, using an elastic viscoplastic constitutive model, except for the appearance of a sharp spike of very short duration. Based on observations with the multiple beam interferometer, the arrival times of the spike at different measurement points is consistent with wave emission from a source at the crack edge. The suggestion arises immediately that the spike is related to the onset of crack growth. Unfortunately, no known wave solutions for dynamic fracture initiation include such a spike in particle velocity in the radiated field. Based on scattering theory, the back surface signal must be relatively insensitive to a small initial crack-tip root radius or a plastic zone associated with introduction of the initial crack. Furthermore, elastodynamic solutions for crack growth accelerating from zero initial speed show no sharp signal. Even the abrupt onset of crack propagation at a high speed can result in propagating jumps in stress and particle velocity at the wavefronts, but not in a spike of the kind observed.

A suggestion of an approach to be considered comes from the elastodynamic solution for a center of expansion with a step-function time dependence. In this case the jump in particle velocity at the wavefront is infinite, which is suggestive of a spike-like velocity-time profile when finite risetimes are considered. While the center of expansion solution is not applicable directly to the case of dynamic fracture, because it does not satisfy the boundary conditions on the crack face, the features of the solution suggest the promise of considering crack-tip fields which are more strongly singular than $r^{-1/2}$ where r is the radial distance from the crack tip. Use of such highly singular fields is allowed only if these fields are understood to apply outside a small hole centered at the crack tip. Thus, in this analysis the elastodynamic stress wave radiation resulting from the sudden formation of a traction-free hole at the tip of a loaded crack is studied. The sudden formation of a hole at the crack tip, no matter how small, admits the possibility of dynamic stress fields with singularities *stronger* than $r^{-1/2}$. For example, if the point $r = 0$ is within a small hole, the local stress field can vary as $r^{-3/2}$.

The study is reported in the following way. Section 2 includes an analysis of a problem of antiplane shear deformation. A cracked elastic solid is loaded so that a certain level of stress intensity factor is achieved. Then, a hole is suddenly introduced at the crack tip by requiring the traction to be suddenly reduced to zero on a circle of very small radius centered at the crack tip. The complete field for this problem can be obtained in a relatively straightforward manner. From the result, it is seen that the solution corresponds to a particular field in elastodynamic crack analysis called the influence function or weight function for the configuration. The plane strain problem of interest is then analyzed in Section 3 within this influence function framework, following an approach developed by Freund (1990). In the final section, quantitative results for the radiated fields predicted by the strongly singular solutions are compared to the magnitudes of the spikes observed in the experiments.

2 Preliminary Analysis for Antiplane Shear

Consider a half plane crack with traction-free faces in an elastic body under conditions of antiplane shear deformation. Initially, the body is subjected to equilibrium loading, or relatively slowly applied remote loading, so that an equilibrium

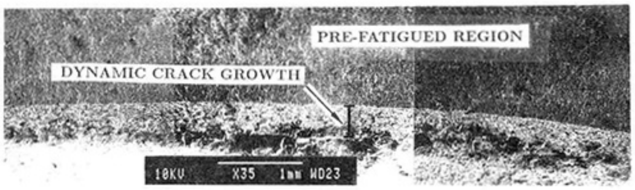

Fig. 3 Dynamic crack advance in the central region of the specimen: Shot 9005

stress intensity factor field is established in the vicinity of the crack tip. With respect to the cylindrical coordinates introduced in Fig. 3, the traction on a small circle of radius ϵ centered at the crack tip is given by

$$\tau_{rz} \approx \frac{k_0}{\sqrt{2\pi\epsilon}} \sin\frac{1}{2}\theta \tag{1}$$

where k_0 is the initial value of the stress intensity factor.

Suppose that at a certain instant of time, say $t = 0$, a traction-free hole with radius ϵ and centered at the crack tip suddenly appears. As a result of the appearance of this hole, a stress wave is radiated away from the edge of the crack, and it is the purpose of this section to examine the main features of this stress wave. The wave field is determined from the solution of a particular boundary value problem. In cylindrical coordinates, the particle displacement in the z-direction $w(r, \theta, t)$ is governed by the scalar wave equation

$$\frac{\partial^2 w}{\partial r^2} + \frac{1}{r}\frac{\partial w}{\partial r} + \frac{1}{r^2}\frac{\partial^2 w}{\partial \theta^2} = \frac{1}{c^2}\frac{\partial^2 w}{\partial t^2} \tag{2}$$

where c is the shear wave speed in the material. The solution is subject to the initial conditions

$$w(r, \theta, 0) = w_t(r, \theta, 0) = 0 \tag{3}$$

throughout $r > \epsilon$, the boundary conditions

$$\tau_{\theta z}(r, \pm\pi, t) = 0 \tag{4}$$

for $r > \epsilon$, and the boundary condition

$$\tau_{rz}(\epsilon, \theta, t) = -h(t)\frac{k_0}{\sqrt{2\pi\epsilon}} \sin\frac{1}{2}\theta \tag{5}$$

where $h(t)$ is the unit step function. The last condition ensures that the surface of the small hole is indeed traction free for $t > 0$.

To solve this boundary value problem, the Laplace transform on time, defined by

$$\hat{w}(r,\theta,s) = \int_0^\infty e^{-st} w(r,\theta,t)\,dt, \tag{6}$$

is first applied to the governing equations and boundary conditions. The resulting time-independent Helmholtz partial differential equation admits a separable solution of the form

$$\hat{w}(r,\theta,s) = \sum_{n=1}^{\infty} B_n K_{\lambda_n}\left(\frac{rs}{c}\right)\sin(\lambda_n\theta) \tag{7}$$

where B_n are constants to be determined from the boundary condition at $r = \epsilon$, K_{λ_n} is the modified Bessel function of the second kind of order λ_n, and

$$\lambda_n = -\left(\frac{2n-1}{2}\right) \quad n = 1, 2, \ldots, \infty. \tag{8}$$

If the complete traction distribution on $r = \epsilon$ by the initial equilibrium field is to be negated by the dynamic field, then all of the coefficients B_n are nonzero and they can be determined explicitly. However, if ϵ is very small compared to any other physical dimensions in the configuration, then the traction on $r = \epsilon$ is dominated by the stress intensity factor term (1). In this case, $B_n = 0$ for $n \geq 2$, and B_1 is determined from the boundary conditions (5). From Hooke's law,

$$\hat{\tau}_{rz}(r,\theta,s) = \mu\frac{\partial \hat{w}}{\partial r}(r,\theta,s) \tag{9}$$

where μ is the elastic shear modulus. If this equation is to be enforced on $r = \epsilon$, $-\pi < \theta < \pi$, then the left side is given by (5) and the right side is given by the derivative of (7) with respect to r. This provides an equation for B_1, yielding

$$B_1 = \frac{c}{s^2\mu}\frac{k_0}{\sqrt{2\pi\epsilon}}\frac{1}{K'_{1/2}(\epsilon s/c)} \tag{10}$$

where the prime denotes the derivative of the modified Bessel function with respect to its argument. The complete solution to the radiation problem is then

$$\hat{w}(r,\theta,s) = -\frac{c}{s^2\mu}\frac{k_0}{\sqrt{2\pi\epsilon}}\frac{K_{1/2}(rs/c)}{K'_{1/2}(\epsilon s/c)}\sin\frac{1}{2}\theta. \tag{11}$$

The modified Bessel function can be eliminated from (11) by means of the identity $\sqrt{\pi/2z}K_{1/2}(z) = (\pi/2z)e^{-z}$ (Abramowitz and Stegun, 1970). Formal Laplace transform inversion then yields

$$w(r,\theta,t) = \sqrt{\frac{2}{\pi r}}\frac{\epsilon k_0}{\mu}\left(1 - \exp\left[-\frac{c}{2\epsilon}\left(t - \frac{r-\epsilon}{c}\right)\right]\right) \times \sin\frac{1}{2}\theta h[t - (r-\epsilon)/c]. \tag{12}$$

This is the desired elastodynamic field, representing the radiation produced by the sudden introduction of a small stress-free hole at the crack tip.

The features of this field are evident from the solution (12). First, the displacement field is square root singular in r as $r \to 0$, so that the corresponding stress components are singular as $r^{-3/2}$ at the crack tip. Solutions having this property are customarily rejected in elastic fracture mechanics on the physical grounds that the displacement is unbounded at the crack tip and the mechanical energy density of the deformation field is unbounded. With the introduction of the small hole at the crack tip, however, both the displacement singularity and the energy density singularity are eliminated from the field, no matter how small the hole may be. With this proviso, the solution (12) is acceptable for any $\epsilon > 0$.

The solution also shows that the particle displacement distribution is continuous at the wavefront for any nonzero value of ϵ. During the early time period (i.e., just behind the wavefront) the particle displacement increases linearly in time and then grows very rapidly to the long-time limiting value of the solution (12). Thus, the increment in displacement Δw in the immediate vicinity of the wavefront is

$$\Delta w = \sqrt{\frac{2}{\pi r}}\frac{\epsilon k_0}{\mu}\sin\frac{1}{2}\theta. \tag{13}$$

This increment in displacement Δw can also be obtained directly from Eq. (11) in the limit when ϵ becomes vanishingly small. By replacing the factor $K'_{1/2}(\epsilon s/c)$ in (11) by its asymptotic form as $\epsilon s/c \to 0$ (Abramowitz and Stegun, 1970), the formal inversion yields

$$w(r,\theta,t) \sim \sqrt{\frac{2}{\pi r}}\frac{\epsilon k_0}{\mu}\sin\frac{1}{2}\theta h\left(t - \frac{r}{c}\right), \tag{14}$$

which yields (13), when evaluated at the wavefront—that is in the limit $t \to r/c$. This rapid growth in displacement at the wavefront can be understood to arise from the fact that the traction (5) on $r = \epsilon$ is reduced to zero abruptly. If instead, the traction on the small hole is reduced to zero continuously, but in a very short time, the displacement at the wavefront given by (12) still provides a good approximation. Associated with the particle displacement is the particle velocity given by

$$\dot{w}=\frac{c}{\mu}\frac{k_0}{\sqrt{2\pi r}}\exp\left[-\frac{c}{2\epsilon}\left(t-\frac{r-\epsilon}{c}\right)\right]\sin\frac{1}{2}\theta \text{ for } t\geq\frac{r-\epsilon}{c}. \quad (15)$$

This solution represents a jump or a discontinuity in the particle velocity traveling with the wavefront. At times just after the passage of the wavefront, the particle velocity decays rapidly towards zero for small ϵ. This sudden jump and then a very rapid decay in the particle velocity represents a spike in the velocity time profile. This is precisely the type of feature observed in the experimental records in the study by Prakash and Clifton (1992). Consequently, the corresponding plane strain problem is analyzed in order to determine whether or not the displacement increment for the spike, given by (13) provides a reasonably accurate estimate of the magnitude of the observed spike for numerical values of the parameters which are consisted with the experiments.

The corresponding plane strain elastodynamic crack problem cannot be handled in the same way as the case of antiplane shear deformation analyzed above. The governing equations are far more complex and the Laplace transformed partial differential equations for particle displacement components do not admit separable solutions, in general. Consequently, another approach must be followed. The solution (13) has the general features of the so-called transient weight function of dynamic fracture mechanics introduced by Freund and Rice (1974). That is, even though the solution was obtained by solving a particular boundary value problem for the sudden appearance of a very small traction-free hole at the tip of a stressed crack, its features suggest that it could be derived for the cracked body without the need to introduce the hole, provided only that singularities in stress and displacement as $r \to 0$ are admitted which are stronger than those customarily viewed as being of relevance in dynamic fracture mechanics. In effect, what is sought is an elastodynamic field which represents radiation from a crack tip even though the crack faces are traction free and the body is initially stress free and at rest. If the strength of singularity is restricted to that in traditional fracture mechanics models, then the uniqueness theorem of elastodynamics leads immediately to the conclusion that there are no nontrivial solutions to the problem. However, if fields with stronger singularities are admitted, then the boundary value problem falls outside the domain of the uniqueness theorem and nontrivial solutions can be found. A general procedure for finding such solutions was outlined by Freund (1990) and the steps for the problem at hand are outlined in the next section.

3 Radiation for Plane Strain Deformation

Guided by the results of the preceding section, the task here is to obtain a solution of the equations of elastodynamics representing outgoing radiation in a body with a traction-free half plane crack under plane strain conditions. A right-handed rectangular xyz-coordinate system is introduced in the body, oriented so that the crack occupies the half plane $y = 0, x < 0$ and the crack edge coincides with the z-axis. The material is initially at rest and stress free over $-\infty < x < \infty$, $-\infty < y < \infty$, and the crack faces $y = \pm 0, x < 0$ are free of traction for all time $-\infty < t < \infty$. A solution is sought having the symmetry of a mode I crack-tip deformation field, so that only the half plane $y > 0$ must be considered.

The mathematical problem which leads to a solution with the properties outlined is now stated. The Helmholtz representation of the displacement vector in terms of the scalar dilatational potential ϕ and the vector shear potential ψ is adopted. For plane strain deformation that is independent of z, the vector potential ψ has only one nonzero component; this component is in the z-direction and it is denoted by ψ. Thus, two functions $\phi(x, y, t)$ and $\psi(x, y, t)$ are sought that satisfy the wave equations in two space dimensions and time

$$\frac{\partial^2\phi}{\partial x^2}+\frac{\partial^2\phi}{\partial y^2}-\frac{1}{c_d^2}\frac{\partial^2\phi}{\partial t^2}=0,\ \frac{\partial^2\psi}{\partial x^2}+\frac{\partial^2\psi}{\partial y^2}-\frac{1}{c_s^2}\frac{\partial^2\psi}{\partial t^2}=0 \quad (16)$$

in the half plane $-\infty < x < \infty$, $0 < y < \infty$ for time in the range $0 < t < \infty$. The characteristic wave speeds in (16) are the dilatational wave speed $c_d = a^{-1}$ and the shear wave speed $c_s = b^{-1}$. The wave functions satisfying (16) are subject to the boundary conditions that

$$\begin{aligned}\sigma_{yy}(x,0,t)&=0, \quad -\infty<x<0,\\ \sigma_{xy}(x,0,t)&=0, \quad -\infty<x<\infty,\\ u_y(x,0,t)&=0, \quad 0<x<\infty,\end{aligned} \quad (17)$$

for all time, where stress and displacement components are interpreted in terms of their representations in terms of displacement potentials ϕ and ψ. The initial conditions that

$$\phi(x,y,0)=\frac{\partial\phi}{\partial t}(x,y,0)=\psi(x,y,0)=\frac{\partial\psi}{\partial t}(x,y,0)=0 \quad (18)$$

for all points in the half plane ensure that the body is stress free and at rest until the crack face pressure is applied.

If only solutions that result in stress components which vary inversely with the square root of distance r from the crack tip are admitted, then the uniqueness theorem of elastodynamics implies immediately that there are no nontrivial solutions. In the present instance, however, a very small hole of radius $r = \epsilon$ is imagined to be introduced at the crack tip. Under these circumstances, stresses that have singularities stronger than inverse square root, which are normally rejected on physical grounds, can be admitted as representing the radiation field resulting from introduction of the hole. The spatial structure of the strongly singular field is dictated by the highest order spatial derivatives in the governing differential equations, so that this field is identical to that for a stationary crack under equilibrium conditions. If the tensile stress on the crack plane directly ahead of the crack tip has the form

$$\sigma_{yy}\sim\frac{q(t)}{r^{3/2}} \quad (19)$$

for arbitrarily small r and some function of time $q(t)$, then the angular variations of the stress and displacement components near the crack tip are[1]

$$\begin{pmatrix}\sigma_{xx}\\ \sigma_{xy}\\ \sigma_{yy}\end{pmatrix}\sim\frac{q(t)}{4r^{3/2}}\begin{pmatrix}\cos\frac{3}{2}\theta+3\cos\frac{7}{2}\theta\\ 3\sin\frac{7}{2}\theta-3\sin\frac{3}{2}\theta\\ 7\cos\frac{3}{2}\theta-3\cos\frac{7}{2}\theta\end{pmatrix},$$

$$\begin{pmatrix}u_x\\ u_y\end{pmatrix}\sim\frac{q(t)}{4\mu r^{1/2}}\begin{pmatrix}(8\nu-3)\cos\frac{1}{2}\theta-\cos\frac{5}{2}\theta\\ (9-8\nu)\sin\frac{1}{2}\theta-\sin\frac{5}{2}\theta\end{pmatrix}. \quad (20)$$

The boundary value problem must be solved in order to determine the radiation fields corresponding to this singular asymptotic result.

Solution of the problem proceeds by application of a one-sided Laplace transform on time defined in (6), and then a two-sided Laplace transform on x, to the governing differential equations and boundary conditions. It is noted that the boundary conditions (17) are defined only on half of the range of x.

[1]The expression $(20)_2$ differs in a numerical coefficient from the original result as given in Freund (1990) due to a misprint in that source.

Consequently, the two-sided Laplace transform cannot be applied to these boundary conditions as they stand. To remedy the situation, the boundary conditions must be extended to apply on the full range of x. To this end, two unknown functions $u_-(x, t)$ and $\sigma_+(x, t)$ are introduced. The function u_- is defined to be the displacement of the crack face $y = 0^+$ in the y-direction for $-\infty < x < 0$, $0 < t < \infty$, and to be identically zero for $0 < x < \infty$, $0 < t < \infty$. Likewise, σ_+ is defined to be the tensile stress in the y-direction on the plane $y = 0$ for $0 < x < \infty$, $0 < t < \infty$. With these definitions, the boundary conditions can be rewritten as

$$\begin{aligned} \sigma_{yy}(x,0^+,t) &= \sigma_+(x,t), \\ \sigma_{xy}(x,0^+,t) &= 0, \\ u_y(x,0^+,t) &= u_-(x,t) \end{aligned} \tag{21}$$

for the full range $-\infty < x < \infty$, $0 < t < \infty$. Obviously, the subscripts + and − are used at this point to indicate on which half of the x-axis a subscripted function is nonzero. The notation is carried over into the transformed domain, where it is found that the same subscript symbols are useful for designating a particular half plane of analyticity.

Next, the one-sided Laplace transform (6) is applied to the wave equations (16), in light of the initial conditions (18), and to the boundary conditions (21). Then, the two-sided Laplace transform defined by

$$W(\zeta,y,s) = \int_{-\infty}^{\infty} \hat{w}(x,y,s)e^{-s\zeta x}dx \tag{22}$$

is applied. The notation in (22), whereby an upper case symbol is used to denote the double transform of the function represented by the corresponding lower case symbol, is adopted as a convention. In view of the wave propagation character of the anticipated solution, the two-sided transform is expected to converge in the strip $-a < \mathrm{Re}(\zeta) < a$ of the complex ζ-plane.

Application of the Laplace transforms (6) and (22) to the differential equations in (16) yields linear second-order differential equations in y for $\Phi(\zeta, y, s)$ and $\Psi(\zeta, y, s)$, involving ζ and s as parameters. For values of ζ in the common strip of analyticity, each equation has two independent solutions, one growing exponentially and one decaying exponentially as $y \to \infty$. The wave propagation nature of the fields precludes the possibility of exponential growth as y becomes large with $-a < \mathrm{Re}(\zeta) < 0$. Consequently, only the solutions decaying as $y \to \infty$ are admitted, so that

$$\Phi(\zeta,y,s) = \frac{1}{s^{1+\gamma}}P(\zeta)e^{-s\alpha y}, \quad \Psi(\zeta,y,s) = \frac{1}{s^{1+\gamma}}Q(\zeta)e^{-s\beta y}, \tag{23}$$

where

$$\alpha = \alpha(\zeta) = (a^2 - \zeta^2)^{1/2}, \quad \beta = \beta(\zeta) = (b^2 - \zeta^2)^{1/2}. \tag{24}$$

The special form selected for the undetermined coefficients in (23) is based on the expectation that a value of γ can be found so that P and Q will not depend on s. The functions α and β in (24) are multiple valued functions of ζ in the complex ζ-plane with branch points at $\zeta = \pm a$ and $\zeta = \pm b$, respectively. The branch of the square root in α is chosen as the one yielding values of α with a positive real part at each interior point of the common strip. For future reference, the definition of α is extended to the entire ζ-plane. Branch cuts are introduced along $a \le |\mathrm{Re}(\zeta)| < \infty$, $\mathrm{Im}(\zeta) = 0$ and the branch of α which is chosen is the one which has a positive real part everywhere in the cut plane except on the branch cuts. Likewise, β is defined for the entire ζ-plane cut along $b \le |\mathrm{Re}(\zeta)| < \infty$, $\mathrm{Im}(\zeta) = 0$ and the branch with nonnegative real part is understood in (24).

The Laplace transforms must also be applied to the boundary conditions (21). If the left side of each boundary condition is expressed in terms of the displacement potentials, then the transformed boundary conditions are

$$\begin{aligned} \mu[(b^2-2\zeta^2)P(\zeta) + 2\zeta\beta Q(\zeta)] &= \Sigma_+(\zeta), \\ \mu[-2\alpha\zeta P(\zeta) + (b^2-2\zeta^2)Q(\zeta)] &= 0, \\ [-\alpha P(\zeta) - \zeta Q(\zeta)] &= U_-(\zeta) \end{aligned} \tag{25}$$

where

$$U_-(\zeta) = s^{\gamma}\int_{-\infty}^{0} \hat{u}_y(x,0^+,s)e^{-s\zeta x}dx \tag{26}$$

and

$$\zeta^{-1}\Sigma_+(\zeta) = -s^{\gamma}\int_0^{\infty}\int_x^{\infty} \hat{\sigma}_{yy}(x',0,s)dx'e^{-s\zeta x}dx. \tag{27}$$

The special form of the last expression (27) is dictated by the presence of a nonintegrable singularity in $\hat{\sigma}_{yy}$ at $x = 0$.

Application of the Wiener-Hopf technique hinges on knowledge of the asymptotic behavior of $U_-(\zeta)$ or $\Sigma_+(\zeta)$ as ζ becomes large. In the present instance, the behavior of $U_-(\zeta)$ can be found from a knowledge of the behavior of $u_y(x, 0, t)$ near $x = 0$. In order to find a solution that corresponds to the asymptotic solution (20) and that represents the sudden appearance of a hole at the crack tip, this displacement component must have the asymptotic form

$$u_y(x,0,t) \sim \frac{Ah(t)}{(-x)^{1/2}} \tag{28}$$

as $x \to 0^-$ where A is a constant to be evaluated later. From (28) it follows that the Laplace transform of u_y must have the asymptotic behavior

$$\hat{u}_y(x,0,s) \sim \frac{A}{s(-x)^{1/2}}. \tag{29}$$

The Abelian theorem on asymptotic properties of Laplace transforms then requires that

$$\lim_{x\to 0^-}(-\pi x)^{1/2}\hat{u}_y(x,0,s) = \lim_{\zeta\to-\infty}(-s\zeta)^{1/2}s^{-\gamma}U_-(\zeta). \tag{30}$$

This relation requires that $\gamma = 3/2$ and that

$$U_-(\xi) \sim \frac{A\sqrt{\pi}}{(-\zeta)^{1/2}} \text{ as } \zeta \to -\infty. \tag{31}$$

The result of substituting the transformed potentials (23) into the transformed boundary conditions is a system of three linear algebraic Eqs. (25) for the four unknown functions $P(\zeta)$, $Q(\zeta)$, $\Sigma_+(\zeta)$, and $U_-(\zeta)$. The system of equations is valid for all values of ζ in the common strip. As was anticipated, the system of equations does not involve the parameter s. If two of the equations are used to eliminate P and Q in favor of Σ_+ and U_-, then the remaining equation is

$$\Sigma_+(\zeta) = -\frac{\mu}{b^2}\frac{R(\zeta)}{\alpha(\zeta)}U_-(\zeta), \tag{32}$$

which is valid in the common strip of analyticity $-a < \mathrm{Re}(\zeta) < 0$, where

$$R(\zeta) = 4\zeta^2\alpha(\zeta)\beta(\zeta) + (b^2 - 2\zeta^2)^2. \tag{33}$$

The function R is analytic everywhere in the complex plane except at the branch points $\zeta = \pm a$ and $\zeta = \pm b$. For the branches of α and β that were selected above, R is single valued in the ζ-plane cut along $a \le |\mathrm{Re}(\zeta)| \le b$, $\mathrm{Im}(\zeta) = 0$. The function R is usually called the Rayleigh wave function because the two real roots of $R = 0$, say $\zeta = \pm c$, are the inverse wave speeds of free-surface Rayleigh waves traveling in opposite directions, each with absolute speed $c_R = 1/c$. In terms of Poisson's ratio ν, the ratio of c to b is given approximately by

$$\frac{c}{b} = \frac{1+\nu}{0.862 + 1.14\nu}. \tag{34}$$

By following the factorization procedure of the Wiener-Hopf technique (Freund, 1990), the functional Eq. (32) can be rewritten as

$$F_+(\zeta)\Sigma_+(\zeta) = -2\mu\left(1-\frac{a^2}{b^2}\right)\frac{U_-(\zeta)}{F_-(\zeta)} \tag{35}$$

where

$$F_\pm(\zeta) = \frac{\alpha_\pm(\zeta)}{(c\pm\zeta)S_\pm(\zeta)} \tag{36}$$

and

$$S_\pm(\zeta) = \exp\left\{-\frac{1}{\pi}\int_a^b \tan^{-1}\left[\frac{4\eta^2\sqrt{(\eta^2-a^2)(b^2-\eta^2)}}{(b^2-2\eta^2)^2}\right]\frac{d\eta}{\eta\pm\zeta}\right\}. \tag{37}$$

Each side of (35) is the analytic continuation of the other into its complementary half plane, so each side equals one and the same entire function. In view of (31), the entire function is the constant $-2\mu(1 - a^2/b^2)\sqrt{\pi}A$, according to Liouville's theorem. The value of this constant must ultimately be identified with the size ϵ of the hole introduced at the crack tip and the level of stress intensity acting at the instant the hole is introduced. This identification will be made after the particle velocity spike of fundamental interest is extracted from the solution.

Once $\Sigma_+(\zeta)$ and $U_-(\zeta)$ are found by means of the Wiener-Hopf procedure, the coefficients $P(\zeta)$ and $Q(\zeta)$ in (23) are readily obtained by means of (25). Of primary interest here is the first of these functions, which corresponds to the first wave arrival at any field point. This function is found to be

$$P(\zeta) = -\frac{\sqrt{\pi}A}{b^2}\frac{(b^2-2\zeta^2)}{\alpha_+(\zeta)(c-\zeta)S_-(\zeta)}. \tag{38}$$

With this coefficient in hand, the Laplace transform inversion integral for $\hat{\phi}$ can be written. The physical quantity of primary interest in the loading is the y-component of displacement $\partial\phi(x, y, t)/\partial y$. The displacement component can be determined from

$$\frac{\partial\hat{\phi}}{\partial y}(x,y,s) = \frac{1}{2\pi i}\int_{\mathcal{L}}\frac{\sqrt{\pi}A}{\sqrt{s}b^2}\frac{(b^2-2\zeta^2)\alpha_-(\zeta)}{(c-\zeta)S_-(\zeta)}e^{s\zeta x - s\alpha y}d\zeta \tag{39}$$

where $\mathcal{L}$ is the integration path within the strip of convergence. Making use of the Cagniard-de Hoop method one finds the desired path of integration in the complex ζ-plane to be defined by

$$\zeta_\pm(r,\theta,t) = -\frac{t}{r}\cos\theta \pm i\left(\frac{t^2}{r^2}-a^2\right)^{1/2}\sin\theta \tag{40}$$

where the positive root is taken. In Eq. (40)

$$r^2 = x^2+y^2 \text{ and } \tan\theta = \frac{y}{x}$$

where $0 \le \theta \le \pi$.

Inversion of the Laplace transform on time yields

$$\frac{\partial\phi}{\partial y}(r,\theta,t) = \frac{1}{2\pi i}\frac{A}{b^2}\int_{ar}^{t}\left\{\frac{(b^2-2\zeta_+^2)\alpha_-(\zeta_+)}{(c-\zeta_+)S_-(\zeta_+)}\frac{\partial\zeta_+}{\partial t} - \frac{(b^2-2\zeta_-^2)\alpha_-(\zeta_-)}{(c-\zeta_-)S_-(\zeta_-)}\frac{\partial\zeta_-}{\partial t}\right\}_{t=\tau}\frac{d\tau}{\sqrt{t-\tau}}. \tag{41}$$

This integral can be evaluated as a function of t in the range $ar < t < \infty$. Of particular interest is the behavior in the immediate vicinity of the wavefront $r = at = t/c_d$. To investigate this question, the integral is considered in the limit as $t/r \to a^+$. Consequently, the integral can be replaced by

$$\frac{\partial\phi}{\partial y}(r,\theta,t) = A\frac{\sqrt{a}\sin\theta}{\pi b^2}\frac{(b^2-2a^2\cos^2\theta)}{(c+a\cos\theta)} \times\frac{(1+\cos\theta)^{1/2}}{S_-(-a\cos\theta)}\int_{ar}^{t}\frac{\tau}{r\sqrt{\tau^2-a^2r^2}}\frac{d\tau}{\sqrt{t-\tau}} \tag{42}$$

without affecting the value of the limit as $t/r \to a^+$. Then, a change of variable in the remaining integral from τ to $\eta = \tau/r$ leads immediately to the conclusion that the limiting value of the integral is $\pi\sqrt{a/2r}$, so that the displacement increment, at any location (r, θ), resulting from the instantaneous formation of a cylindrical cavity at the crack tip is

$$\Delta u_y(r,\theta) = A\frac{a\sin\theta}{\sqrt{2r}b^2}\frac{(b^2-2a^2\cos^2\theta)}{(c+a\cos\theta)}\frac{(1+\cos\theta)^{1/2}}{S_-(-a\cos\theta)}. \tag{43}$$

The remaining task is to determine A, the strength of the strongly singular crack-tip field, in terms of the stress intensity factor of the crack-tip field generated by the plane wave loading. Three different approaches that have been used to estimate A are discussed as follows.

Estimate 1. For the experiment described in the Introduction, the loading was in the form of a plane step pulse normally incident on the crack plane. If σ^* is the tensile stress magnitude carried by the incident wave, and if the time elapsed since this wave arrived at the crack plane is t, then the stress intensity factor at the crack tip is

$$K_I(t) = 2\sigma^*\frac{\sqrt{c_d t(1-2\nu)/\pi}}{(1-\nu)}. \tag{44}$$

The loading generates an inverse square root singular crack-tip field, growing in strength as the square root of time. At a certain instant of time, say t^*, the crack initiates. The crack initiation event is understood to be associated with the abrupt formation of a very small hole of radius $r = \epsilon$ centered at the crack tip, giving rise to a field with a singularity stronger than the inverse square-root singular field. The strength of this strongly singular field can be estimated by viewing the superposition of stress fields required to create a traction-free surface at radius $r = \epsilon$. However, unlike the case of antiplane strain, the distribution of the traction around the surface $r = \epsilon$ is not the same for the $r^{-1/2}$ and $r^{-3/2}$ fields. Therefore, it is not possible to remove the tractions everywhere by superposition with a particular choice of A. The value for the strength A can be estimated by equating the stress component σ_{yy}^*, corresponding to the inverse square-root singular field, at a distance $r = \epsilon$ along $\theta = \pm\pi/2$

$$\sigma_{yy}^* \sim \frac{3}{4}\frac{K_I^*}{\sqrt{\pi\epsilon}} \tag{45}$$

to that of the same stress component in the strongly singular solution at the same point, which in view of (20) is

$$\sigma_{yy} \sim \frac{5}{4\sqrt{2}}\frac{A}{(1-\nu)}\frac{\mu}{\epsilon^{3/2}}h(t). \tag{46}$$

Then, for $t > 0$, the value of A is found to be

$$A = \frac{6}{5}(1-\nu)\frac{K_I^*}{\sqrt{2\pi}}\frac{\epsilon}{\mu} \tag{47}$$

Estimate 2. Consider again the normal, step wave loading of the crack plane resulting in an inverse square-root singular crack-tip field growing as the square root of time. The corresponding elastic strain energy $\Phi(t)$, stored in a cylindrical region centered at the crack tip and occupying a volume V, can be evaluated using

$$\Phi(t) = \frac{1}{2}\int_V \sigma_{ij}\epsilon_{ij}dV \tag{48}$$

where σ_{ij} and ϵ_{ij} are the stress and strain tensors, respectively. For the loading described, the integral (48) yields

$$\Phi^*(t) = \epsilon \frac{(1+\nu)(5-8\nu)}{8E} K_I^2(t) \qquad (49)$$

where ϵ is the radius of the cylindrical region. Now, consider that at time t^* the stress intensity factor reaches a critical level K_I^* and the crack initiates, resulting in an abrupt formation of a cylindrical cavity of radius ϵ, centered at the crack tip. The processes occurring within the region of radius ϵ involve the dynamic coalescence of voids into a cavity. The major effect is to reduce the load carrying capacity of the material in the region. An energetic approach to relating this process to the waves that emanate from the tip is to assume that the elastic strain energy released from the square-root singular field as the cavity forms is equal to the energy input to the $r^{-3/2}$ field that radiates from the crack tip. The elastic strain energy contained within the cylindrical volume is assumed to be relieved instantaneously and the input to the radiated field is assumed to be a step radial pressure acting on the boundary of the cylindrical cavity. By equating this released elastic strain energy to the work done by the radial pressure on the cylindrical boundary, the strength of the strongly singular solution can be estimated. The work done by the radial pressure is obtained by evaluating the integral

$$W = \int_{t^{*-}}^{t^{*+}} \int_{\Sigma} \sigma_{rr} v_r d\Sigma dt \qquad (50)$$

where σ_{rr} is the radial pressure and v_r is the radial particle velocity corresponding to the strongly singular crack-tip field. The times t^{*-} and t^{*+} represent the instants just before and just after the crack initiation time, t^*. The symbol Σ represents the surface area of the cylindrical cavity over which the integral is evaluated. In view of (20) the integral (50) yields

$$W = \frac{\mu A^2}{64\epsilon} \left[\frac{\pi(29-28\nu)}{(1-\nu)^2} \right] \qquad (51)$$

where μ is the shear modulus of the material. Then, the value of A is found to be

$$A = 2(1-\nu) \frac{K_I^*}{\sqrt{2\pi}} \frac{\epsilon}{\mu} \sqrt{\frac{2(5-8\nu)}{29-28\nu}}. \qquad (52)$$

Estimate 3. In the third approach to estimate A, attention is again focused on a cylindrical region of radius ϵ centered at the crack tip. The crack-tip stress field characterized by the dynamic stress intensity factor $K_I(t)$ results in large elastic deformations in the region near the crack tip. The resulting expansion ΔV of the cylindrical region of volume V is

$$\Delta V(t) = \int_V \epsilon_{kk} dV \qquad (53)$$

where ϵ_{kk} is the sum of the principal strains. The integral (53), when evaluated for the inverse square-root singular field, yields

$$\Delta V^*(t) = \frac{16}{3} \frac{(1+\nu)(1-2\nu)}{E} \frac{K_I(t)}{\sqrt{2\pi}} \epsilon^{3/2}. \qquad (54)$$

Now, consider that at the instant of crack initiation ($t = t^*$), the inverse square-root singular field transforms abruptly into a crack-tip field having a stronger singularity as described by (20). Since the more singular field is associated with the sudden loss of strength to form a very small hole at the crack tip, the unloading of the material enclosed in the cylindrical region of radius ϵ results in a sudden contraction in volume. In view of (20), the integral (53) yields

$$\Delta V(t) = -\frac{8}{3} \frac{(1+\nu)(1-2\nu)}{E(1-\nu)} \mu A \epsilon^{1/2}. \qquad (55)$$

By requiring that the contraction in volume for the strongly singular crack-tip solution (55) to be the same as the expansion obtained for the inverse square-root singular field over the same cylindrical region (54), the strength of the strongly singular crack-tip field can be obtained. For time $t > 0$, the value of A is found to be

$$A = 2(1-\nu) \frac{K_I^*}{\sqrt{2\pi}} \frac{\epsilon}{\mu}. \qquad (56)$$

The three estimates for A given by (47), (52), and (56), (henceafter denoted by A_1, A_2, and A_3, respectively) are very similar. The values A_1, A_2, and A_3 satisfy

$$A_2 : A_1 : A_3 = \sqrt{\frac{2(5-8\nu)}{(29-28\nu)}} : \frac{3}{5} : 1$$

and the inequality $A_2 < A_1 < A_3$. For $\nu = 0.3$, the estimate A_2 is 0.509. In view of the closeness of the estimates, any one of the three could be used. For the comparisons in the next section the estimate A_2 is used because of the slight preference for the energy argument which leads to this estimate.

With the constant A determined, the magnitude of the displacement increment Δu_y, can be obtained from (43) in terms of the parameters of the plane wave loading.

4 Experimental Results and Discussion

A detailed description of the experiment, the experimental procedure and the results have been presented by Prakash and Clifton (1992). In this section, typical experiments for which good experimental records were obtained are summarized and the magnitude of the observed spikes in the surface velocity versus time profiles are correlated with those predicted for the plane strain deformation case.

The material used for the study was AISI 4340 VAR steel. The material is heat treated by normalizing at 900° C for two hours, austenitizing at 850° C for two hours and then rapidly quenching in an ice-brine solution. The resulting Rockwell hardness R_c varied between 56.5 to 55.0 from the center of the disk to its circumference at a 200° C temper. The composition and various properties of this 4340 VAR steel are shown in Table 2. All experiments were conducted at room temperature (22° C). Table 3 gives the impact velocity V_0, the applied pressure σ^*, the duration of the pulse t_0 and the crack initiation time t^* for the experiments discussed in this paper. The maximum normal stress reached in the experiments corresponds to approximately 98 percent of the Hugoniot elastic limit. Figure 3 shows a typical scanning electron microscope picture of the fracture surface taken from the central region of the specimen after it was forced open in liquid nitrogen. Three distinct regions can be identified: (a) the prefatigued region, (b) the dynamic crack growth region, and (c) the region corresponding to the fracture surfaces created when the specimen was forced open after the experiment. The arrow points to the region between the position of crack initiation and the crack arrest for the stress wave induced fracture. The crack growth is very uniform along the crack front. This supports the claim that fracture occurs under fully plane strain conditions in the central part of the specimen during the times of interest in the experiment.

Figure 4 shows a typical fractograph of a region near the front of the prefatigued crack. Three different regions can be identified: (a) the prefatigued region, (b) the stretched zone, and (c) the crack growth region. The prefatigued region is easily identified as the appearance of the fracture surface in this region is very different from that of the surface formed by the high rate loading. Early crack growth is fully ductile, suggesting that the primary micromechanical mechanisms operative during the early growth process are void nucleation, growth, and subsequent coalescence. Between the prefatigued

Table 1 Physical properties of AISI 4340 VAR steel

Chemical Composition of 4340 VAR Steel

Republic Steel : Heat No. 3841687

(Weight %)

C	Mn	Ni	Cr	Mo	Cu	Si	Al	P	S	N	O	H ppm
.42	.46	1.74	.89	.21	.28	.19	.031	.009	.001	.005	.001	1.0

Heat Treatment:
- Normalize at 900° C for two hrs.
- Austentize at 850° C for two hrs.
- *followed by rapid quenching in ice brine solution*
- Temper at 200° C for two hrs, air cool.

Hardness: 55-56 R_C

Mass Density: $\rho = 7600$ Kgm^{-3}

Poisson's ratio: $\nu = 0.3$

Longitudinal wave speed: $C_L = 5.983$ mm/μs

Shear wave speed: $C_S = 3.124$ mm/μs

Rayleigh wave speed: $C_R = 2.987$ mm/μs

Table 2 Summary of experiments on AISI 4340 VAR steel

SHOT #	V_o (mm/μsec)	σ^* MPa	t_o (μsec)	t^* (nsec)
8907	0.0854	1941	0.969	190.5
9004	0.1184	2690	1.029	575.0
9005	0.1200	2727	1.029	554.5

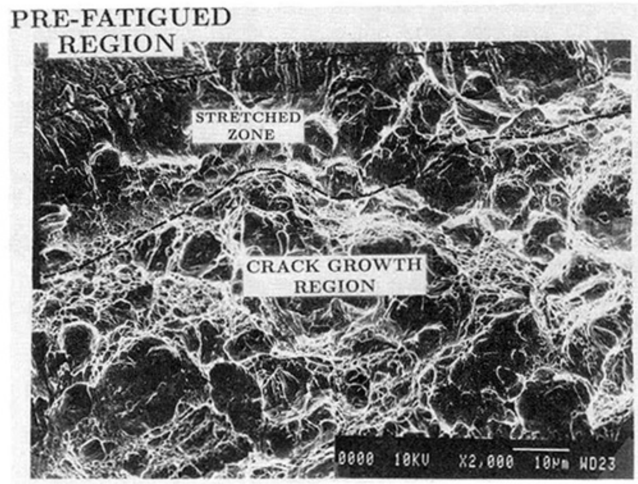

Fig. 4 Fractograph of ductile crack initiation along the crack front: Shot 9005

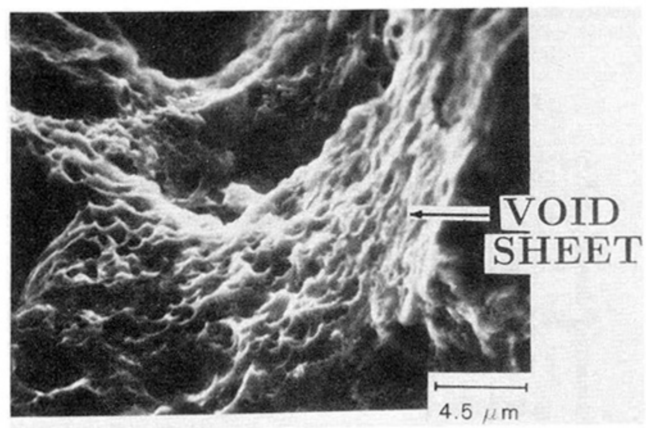

Fig. 5 Fractograph of a large void along with the void sheet: Shot 9005

region and the crack growth region lies a relatively featureless zone. This zone, designated as the plastic stretch zone has been reported by many investigators (Spitzig 1968, 1969; Griffis and Spretnak, 1970). This zone consists of coarse slip steps showing the process of fatigue crack blunting by a slip mechanism. As the plastic strain in the crack-tip region increases, the void which was initiated at the inclusion nearest the crack tip, expands under the combined influence of the local strain field and the hydrostatic tension. Initiation is understood to occur when the blunting crack tip first coalesces with the expanding void. These mechanisms suggest that the onset of crack initiation is not smooth, but corresponds to a sudden failure of the ligaments, connecting the blunted crack tip to the growing void. This leads to an abrupt formation of a small hole at the crack tip. The radiated energy accompanying the abrupt formation of the hole is understood to be responsible for the observed spike in the velocity-time profiles. Figure 5 shows a magnified picture of a typical large void which was nucleated at a large inclusion. This large void is surrounded by ligaments which have undergone intense deformation. These ligaments contain numerous small voids, commonly known as void sheets, which nucleated at submicron carbide particles.

Figure 6 shows the velocity-time profiles of the rear surface motion at the four monitoring points ahead of the crack tip for shot 8907. The data shown corresponds to the time interval of primary interest, i.e., after the first arrival of the diffracted waves at the closest monitoring point, and before any unloading waves arrive from the boundary. The time scale has been normalized by C/H where C is the longitudinal wave speed and H is one half thickness of the specimen. The velocity scale has been normalized by the impact velocity which is 85.4 m/s for this experiment. The closest monitoring point is placed at 0.68 mm ahead of the crack tip. The remaining three points are spread at 0.48 mm intervals. The solid curves correspond to the recorded velocity-time profiles at the four monitoring points. The curves with the lowest (curve A) and the highest (curve D) velocity time profiles correspond to the farthest (point A) and the closest (point D) monitoring points, respectively. The delay times between the traces correspond closely to the difference in the arrival times of the waves diffracted from the crack tip. The dashed curves correspond to the numerical simulation of the experiment using an elastic-visco-plastic model for the material, and assuming that the crack remains stationary (Prakash and Clifton, 1992). Agreement between the computed and experimentally obtained velocity-time profile is excellent up to a certain time. Thereafter, the experimental and computed profiles separate. The separation point is followed immediately by a jump in particle velocity in all four traces. This separation point is understood to correspond to the instant of crack initiation which coincides with the time of rapid formation of a small hole at the crack tip. After this time the separation between the experimental and computed traces grows. This part of the record corresponds to the crack propagation phase of the experiment.

Figures 7 and 8 show the velocity-time profiles of the rear surface at two monitoring points for shot 9004 and shot 9005, respectively. Unlike shot 8907, the velocity-time profile was monitored at only two points ahead of the prefatigued crack front. For shot 9004, the first and the second points were located 2.68 mm and 4.44 mm, respectively. For shot 9005, the first and the second points were located at 5.88 mm and 6.84 mm, respectively. As before, the solid curves correspond to the experimentally obtained profiles while the dashed curves correspond to the computed profiles. Again, the experimental and the computed curves agree well until the crack initiation

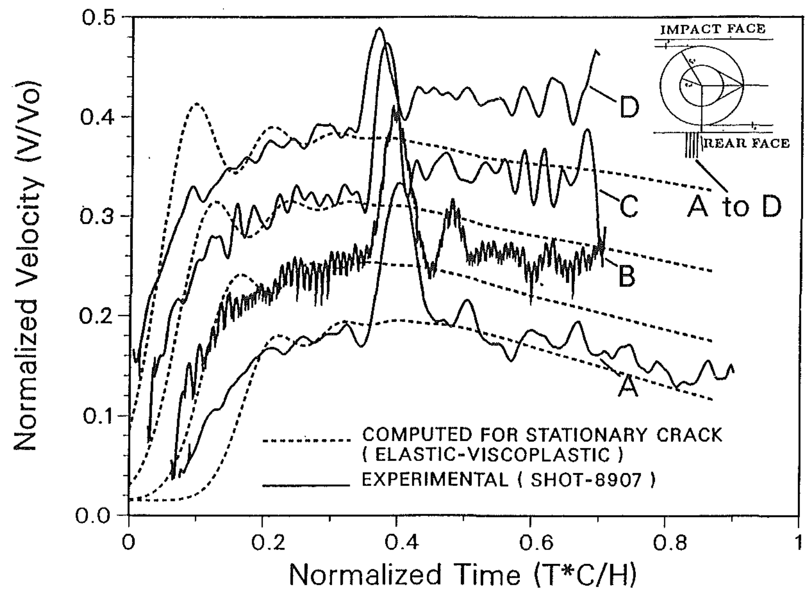

Fig. 6 Experimental and predicted (stationary crack) velocity time profiles at the four monitoring points: Shot 8907

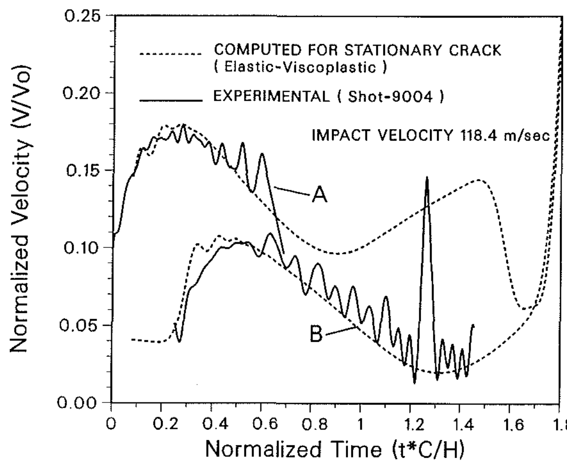

Fig. 7 Experimental and predicted (stationary crack) velocity time profiles at the monitoring points: Shot 9004

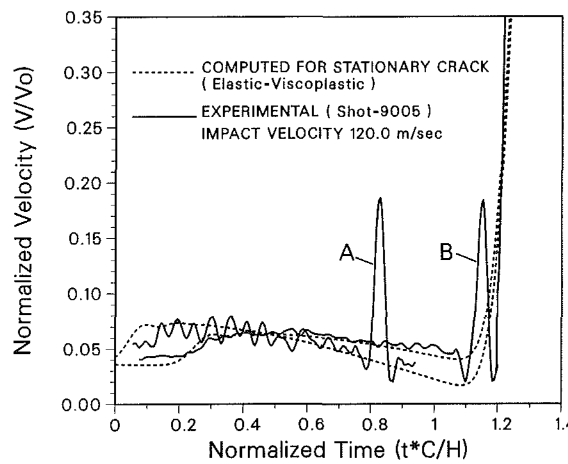

Fig. 8 Experimental and predicted (stationary crack) velocity time profiles at the monitoring points: Shot 9005

time, after which the experimental profiles show a spike which is interpreted as corresponding to the abrupt formation of a hole. At Point A, for shot 9004, the experimental data was lost after the first 400 nanoseconds due to poor fringe contrast.

Quantitative results for the radiated fields predicted by the strongly singular solution (43) can be compared with the magnitude of the spikes observed in the velocity-time profiles. The magnitude of the spike, and hence the displacement increment at a particular point on the specimen surface, is obtained by evaluating the area enclosed by the spike. The strength of the strongly singular solution, used in obtaining the quantitative displacement increment is taken to be given by Eq. (52), which is the result obtained from Estimate 2. Note that the quantitative results for the displacement increment, at any location (r, θ), are based on an analysis carried out for a step tensile pulse loading of a semi-infinite crack in an infinite medium. On the other hand, the experimental results were obtained by measuring the particle velocity on the free surface of the specimen. Hence, the predicted magnitude of the displacement increment has to be multiplied by a factor of two to have a proper comparison between the analytical and the experimental results. The parameter ϵ, which has been associated with the

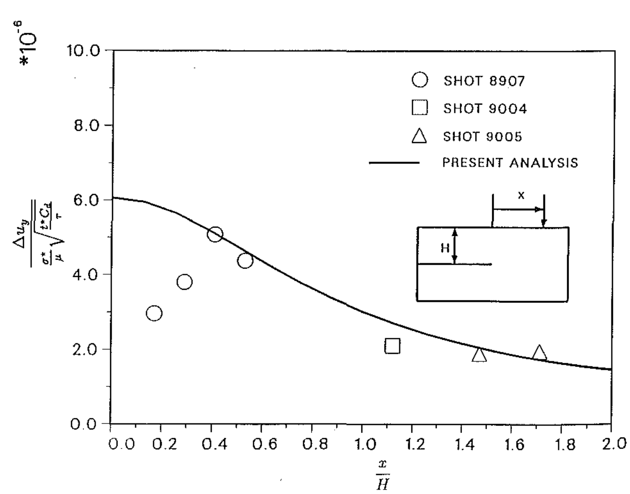

Fig. 9 Experimental and quantitatively predicted magnitudes of the displacement increment in the spikes of the velocity time profiles. The quantitatively predicted magnitudes are based on the estimation of the strength of the strongly singular solution obtained by Estimate 2.

radius of the very small hole formed at the crack tip, and hence characterizes the strength of the strongly singular solution, is taken to be 30 μm. This distance is equal to one half the interparticle spacing of the large inclusions characteristic of the present material. Figure 9 compares the predicted magnitude of the displacement increment with that obtained experimentally. The magnitude of the displacement increment, at any point x on the surface of the specimen, is normalized with respect to the factor $\sigma^*/\mu \sqrt{t^* c_d/r}$ where σ^*, t^*, μ, c_d are the same as defined before and r is the radial distance from the crack tip to the monitoring point on the surface of the specimen. The abscissa, which represents the distance on the specimen surface from the point $x = 0$, is normalized with respect to the half thickness of the specimen, H. The predicted and experimentally obtained magnitudes of the displacement increment are in quite good agreement for shot 9004 and shot 9005. For the case of shot 8907, the experimental values at the monitoring points C and D are lower than those predicted theoretically by the present analysis, but still are of the same order of magnitude.

Acknowledgment

The authors would like to express their thanks to Prof. J. D. Achenbach for suggesting the exact inversion of Eq. (11). This research was supported by the Army Research Office.

References

Abramowitz, M., and Stegun, I. A., 1970, *Handbook of Mathematical Functions*, Dover Publications, New York.

de Hoop, A. T., 1958, "*Representation Theorems for the Displacement in an Elastic Solid and their Applications to Elastodynamic Diffraction Theory*," Doctoral Disseration, Technical University of Delft.

Freund, L. B., and Rice, J., 1974, "On the determination of elastodynamic crack tip stress fields," *International Journal of Solids and Structures*, Vol. 10, pp. 411–417.

Freund, L. B., 1990, *Dynamic Fracture Mechanics*, Cambridge University Press.

Griffis, G. A., and Spretnak, J. W., 1970, "A Suggestions on the Nature of Plastic Stretch Zone," *Metallurgical Transactions*, Vol. 1, pp. 550–551.

Prakash, V., and Clifton, R. J., 1992, "Experimental and Analytical Investigation of Dynamic Fracture Under Conditions of Plane Strain," *Fracture Mechanics: 22nd Symposium*, Vol. I, H. A. Ernst, A. Sakena, and D. L. McDowell, eds., ASTM STP1131, ASTM, Philadelphia, PA, pp. 412–444.

Ravichandaran, G., and Clifton, R. J., 1989, "Dynamic Fracture Under Plane Wave Loading," *International Journal of Fracture*, Vol. 40, pp. 189–200.

Spitzig, W. A., 1968, "A Fractographic Feature of Plane Strain Fracture in 0.45C-Ni-Cr-Mo Steel," *ASM Trans. Quarterly*, Vol. 61, pp. 344–349.

Spitzig, W. A., 1969, "Correlations between Fractographic Feature and Plane Strain Fracture Toughness in an Ultra-Strength Steel," *Electron Microfractography, ASTM, STP 453, American Society of Testing Materials*, pp. 90–110.

Elastodynamic Analysis of a Periodic Array of Mode III Cracks in Transversely Isotropic Solids

Ch. Zhang
Professor,
Department of Engineering Mechanics,
Tongji University,
Shanghai 200092, China

Time-harmonic elastodynamic analysis is presented for a periodic array of collinear mode III cracks in an infinite transversely isotropic solid. The scattering problem by a single antiplane crack is first formulated, and the scattered displacement field is expressed as Fourier integrals containing the crack opening displacement. By using this representation formula and by considering the periodicity conditions in the crack spacing, a boundary integral equation is obtained for the crack opening displacement of a reference crack. The boundary integral equation is solved numerically by expanding the crack opening displacement into a series of Chebyshev polynomials. Numerical results are given to show the effects of the crack spacing, the wave frequency, the angle of incidence, and the anisotropy parameter on the elastodynamic stress intensity factors.

1 Introduction

The dynamic behavior of fiber-reinforced and laminated composites can be significantly affected by the presence of cracks. Thus, elastodynamic analysis of cracks in such materials is a subject of considerable interest. Since fiber-reinforced and laminated composites generally have a macroscopic transverse isotropy, a cracked composite material can be approximated by a cracked homogeneous, transversely isotropic, and linearly elastic solid under certain restrictions. This approach is a promising method, and it can substantially simplify the corresponding crack analysis. Time-harmonic elastodynamic analysis of an isolated crack in an infinite transversely isotropic medium has been performed by Ohyoshi (1973) for incident SH waves and by Dhawan (1982, 1983) for incident P and SV waves. A penny-shaped crack subjected to a time-harmonic longitudinal and transverse wave loading has been investigated by Tsai (1988, 1989). Diffraction of time-harmonic SH waves by an oblique crack in an orthotropic half-space has been considered by Lobanov and Novichkov (1981), while the diffraction of time-harmonic longitudinal and transverse waves by a semi-infinite crack in a transversly isotropic material has been studied by Norris and Achenbach (1984). Transient elastodynamic analysis of an isolated mode I and mode II crack has been presented by Kassir and Bandyopadhyay (1988) for an infinite orthotropic solid, by Shindo et al. (1986), and by Ang (1987) for a transversely isotropic strip. The mode I dynamic stress intensity factor for a crack in a transversely istropic layered material under the action of impact loading has been given by Ang (1988). The problem of a steadily moving crack in an orthotropic medium has been solved by Kassir and Tse (1983) and Piva (1986, 1987) for a state of plane strain, and by Danyluk and Singh (1984) for a state of antiplane strain.

In this paper, the scattering of plane time-harmonic SH waves by a periodic array of Mode III cracks in an infinite, homogeneous, transversely isotropic, and linearly elastic solid is investigated. The scattering problem by a single Mode III crack is first formulated, and the scattered displacement field is expressed as Fourier integrals containing the crack opening displacement. By using this representation formula for the scattered displacement and by considering the periodicity conditions in the crack spacing, a boundary integral equation is obtained for the crack opening displacement of a reference crack. Expanding the crack opening displacement into a series of Chebyshev polynomials, the boundary integral equation is converted to an infinite system of linear algebraic equations for the expansion coefficients which are related to the elastodynamic stress intensity factors by a simple relation. Numerical results for the elastodynamic stress intensity factors are presented as functions of the crack spacing, the dimensionless wave number, and the angle of incidence of the incident wave, as well as the anisotropy parameter.

Previous studies similar to this paper, but for a periodic array of cracks in isotropic materials, have been presented by Angel and Achenbach (1985a, b) and Mikata and Achenbach (1989) for incident P and SV waves, and by Achenbach and Li (1986) for incident SH waves.

2 Scattering by a Single Crack

Consider first a homogeneous, transversely isotropic and linearly elastic solid containing a single crack as shown in Fig. 1. The length of the crack is $2a$, and the crack is subjected to an antiplane loading produced by an incident plane, time-

Contributed by the Applied Mechanics Division of THE AMERICAN SOCIETY OF MECHANICAL ENGINEERS for publication in the ASME JOURNAL OF APPLIED MECHANICS.

Discussion on this paper should be addressed to the Technical Editor, Prof. Leon M. Keer, The Technological Institute, Northwestern University, Evanston, IL 60208 and will be accepted until four months after final publication of the paper itself in the JOURNAL OF APPLIED MECHANICS. Manuscript received by the ASME Applied Mechanics Division, Feb. 28, 1990; final revision, Nov. 12, 1990.

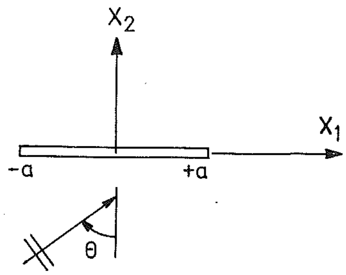

Fig. 1 An isolated crack

harmonic SH wave. Thus, the only remaining displacement component is in the x_3-direction, which satisfies the following reduced wave equation

$$C_{55}w_{,11}+C_{44}w_{,22}+\rho\omega^2 w=0, \tag{1}$$

where C_{44} and C_{55} are the elastic constants, ρ is the mass density, and ω is the angular frequency. In Eq. (1) and in what follows, a comma after a quantity stands for partial derivatives with respect to spatial variables, the time factor $\exp(-i\omega t)$ is suppressed, and the conventional summation rule over double indices is applied. The stress components are defined by

$$\sigma_{31}=C_{55}w_{,1}, \tag{2}$$

$$\sigma_{32}=C_{44}w_{,2}. \tag{3}$$

On the crack line ($x_2=0$), the continuity conditions are

$$\sigma_{32}(x_1,0^+)=\sigma_{32}(x_1,0^-), \tag{4}$$

$$w(x_1,0^+)=w(x_1,0^-),\quad |x_1|>a. \tag{5}$$

The interaction of an incident wave with the crack generates scattered waves. Thus, the total wave field can be written as a sum of the incident field and the scattered field

$$w=w^{in}+w^{sc},\quad \sigma_{3\alpha}=\sigma_{3\alpha}^{in}+\sigma_{3\alpha}^{sc}, \tag{6}$$

where w^{in} and $\sigma_{3\alpha}^{in}$ represent the incident wave field in the absence of the crack, while w^{sc} and $\sigma_{3\alpha}^{sc}$ represent the scattered wave field induced by the interaction of the incident wave with the crack. For a given incident wave field, the scattered field has to be determined so that the equation of motion (1), the continuity conditions (4) and (5), and the radiation conditions at infinity are satisfied. The scattered displacement field can be expressed as the following Fourier integrals

$$w^{sc}(\mathbf{x})=\begin{cases}\displaystyle\int_{-\infty}^{\infty} f_1(\xi)\exp(i\xi x_1-\gamma x_2)d\xi, & x_2>0,\\ \displaystyle\int_{-\infty}^{\infty} f_2(\xi)\exp(i\xi x_1+\gamma x_2)d\xi, & x_2<0,\end{cases} \tag{7}$$

in which f_1 and f_2 are yet unknown functions, and

$$\gamma=\begin{cases}[C_{44}^{-1}C_{55}(\xi^2-k_1^2)]^{1/2}, & \xi^2\geq k_1^2,\\ -i[C_{44}^{-1}C_{55}(k_1^2-\xi^2)]^{1/2}, & \xi^2<k_1^2,\end{cases} \tag{8}$$

where

$$k_1=(\rho/C_{55})^{1/2}\omega. \tag{9}$$

The radiation conditions for the scattered field are ensured by the condition (8). In terms of the scattered field, the continuity conditions (4) and (5) can be rewritten as

$$\sigma_{32}^{sc}(x_1,0^+)=\sigma_{32}^{sc}(x_1,0^-), \tag{10}$$

$$w^{sc}(x_1,0^+)=w^{sc}(x_1,0^-),\quad |x_1|>a. \tag{11}$$

The traction-free condition on the crack results in

$$\sigma_{32}^{sc}=-\sigma_{32}^{in},\quad x_2=0,\quad |x_1|<a. \tag{12}$$

Substitution of Eq. (7) into Eq. (3) and subsequent use of the continuity condition (10) yield

$$f_2=-f_1. \tag{13}$$

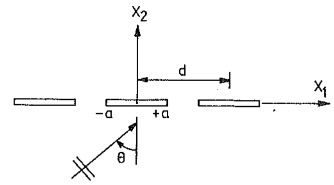

Fig. 2 A periodic array of collinear cracks

Using Eq. (13), Eqs. (7) and (11) will lead to

$$2\int_{-\infty}^{\infty} f_1(\xi)\exp(i\xi x_1)d\xi=\begin{cases}0, & |x_1|>a,\\ \Delta w(x_1), & |x_1|<a,\end{cases} \tag{14}$$

where Δw denotes the crack opening displacement defined by

$$\Delta w(x_1)=w^{sc}(x_1,0^+)-w^{sc}(x_1,0^-). \tag{15}$$

Inversion of the integral (14) yields the following expression for $f_1(\xi)$

$$f_1(\xi)=\frac{1}{4\pi}\int_{-a}^{a}\exp(-i\xi x_1)\Delta w(x_1)dx_1. \tag{16}$$

By using Eq. (13), the function $f_2(\xi)$ can be expressed as

$$f_2(\xi)=-\frac{1}{4\pi}\int_{-a}^{a}\exp(-i\xi x_1)\Delta w(x_1)dx_1. \tag{17}$$

Thus, the scattered displacement field can be written as

$$w^{sc}(\mathbf{x}')=\begin{cases}\displaystyle\frac{1}{4\pi}\int_{-a}^{a}\int_{-\infty}^{\infty}\exp[i\xi(x_1'-x_1)\\ \quad -\gamma x_2']\Delta w(x_1)d\xi dx_1, & x_2'>0,\\ \displaystyle-\frac{1}{4\pi}\int_{-a}^{a}\int_{-\infty}^{\infty}\exp[i\xi(x_1'-x_1)\\ \quad +\gamma x_2']\Delta w(x_1)d\xi dx_1, & x_2'<0,\end{cases} \tag{18}$$

where $\mathbf{x}'$ denotes the position vector of the observation point and $\mathbf{x}$ denotes the position vector of the source point.

The representation formula (18) for the scattered displacement field by a single crack will be used in the next section to analyze a periodic array of cracks.

3 Boundary Integral Equation for Periodic Collinear Mode III Cracks

Consider now a periodic array of collinear mode III cracks as shown in Fig. 2. It is assumed here that all cracks have the same length $2a$, and the distance between the centers of the two neighboring cracks is d. In this case, the scattered displacement field can be written in the following forms

$$w^{sc}(\mathbf{x}')=\begin{cases}\displaystyle\frac{1}{4\pi}\sum_{j=-\infty}^{\infty}\int_{-a}^{a}\int_{-\infty}^{\infty}\exp[i\xi(x_1'-\bar{x}_1-jd)\\ \quad -\gamma x_2']\Delta w^j(\bar{x}_1)d\xi d\bar{x}_1, & x_2'>0,\\ \displaystyle-\frac{1}{4\pi}\sum_{j=-\infty}^{\infty}\int_{-a}^{a}\int_{-\infty}^{\infty}\exp[i\xi(x_1'-\bar{x}_1-jd)\\ \quad +\gamma x_2']\Delta w^j(\bar{x}_1)d\xi d\bar{x}_1, & x_2'<0,\end{cases} \tag{19}$$

where $\Delta\overline{w}^j(x_1)$ is the crack opening displacement of the jth crack, and $\bar{\mathbf{x}}$ denotes the local coordinate system of the jth crack which is related to the global coordinate system by

$$\begin{Bmatrix}x_1\\x_2\end{Bmatrix}=\begin{Bmatrix}\bar{x}_1\\\bar{x}_2\end{Bmatrix}+\begin{Bmatrix}jd\\0\end{Bmatrix},\quad |\bar{x}_1|\leq a. \tag{20}$$

For a plane time-harmonic elastic SH wave incident under an angle θ, the displacement field has the form

$$w^{in}(x_1, x_2) = A\exp[ik(\sin\theta x_1 + \cos\theta x_2)], \tag{21}$$

where A is the amplitude of the incident wave, and k is defined by

$$k = k_1/(\sin^2\theta + C_{44}C_{55}^{-1}\cos^2\theta)^{1/2}. \tag{22}$$

By substituting Eq. (21) into Eq. (3) and by using the relation (20), the incident stress field on the cracks can be written as

$$\sigma_{32}^{in}(x_1, 0) = \bar{\sigma}_{32}^{in}\exp(ik\sin\theta jd), \tag{23}$$

where $\bar{\sigma}_{32}^{in}$ is the incident stress component on the reference crack ($|\bar{x}_1| < a$, $x_2 = 0$)

$$\bar{\sigma}_{32}^{in}(\bar{x}_1) = iAC_{44}k\cos\theta\exp(ik\sin\theta\bar{x}_1). \tag{24}$$

Since the spacing of the cracks is periodic in the x_1-direction and based on the Bloch (1928) theory for wave propagation in a periodic media, a Bloch-type ansatz is used for the crack opening displacement

$$\Delta w^j(\bar{x}_1) = \Delta w(\bar{x}_1)\exp(ik\sin\theta jd), \tag{25}$$

in which $\Delta w(\bar{x}_1)$ is the crack opening displacement of the reference crack ($|\bar{x}_1| < a, x_2 = 0$). Substituting Eq. (25) into Eq. (19) and using the relation

$$\sum_{j=-\infty}^{\infty}\exp[i(k\sin\theta - \xi)jd] = \sum_{j=-\infty}^{\infty}\delta[d(k\sin\theta - \xi)/(2\pi) - j], \tag{26}$$

the following expression is obtained

$$w^{sc}(\mathbf{x}') = \begin{cases} \dfrac{1}{4\pi}\displaystyle\int_{-a}^{a}\left\{\sum_{j=-\infty}^{\infty}\int_{-\infty}^{\infty}\exp[i\xi(x_1' - \bar{x}_1 - jd) - \gamma x_2'] \times \right. \\ \qquad \left. \delta[d(k\sin\theta - \xi)/(2\pi) - j]d\xi\right\}\Delta w(\bar{x}_1)d\bar{x}_1, \quad x_2' > 0, \\ -\dfrac{1}{4\pi}\displaystyle\int_{-a}^{a}\left\{\sum_{j=-\infty}^{\infty}\int_{-\infty}^{\infty}\exp[i\xi(x_1' - \bar{x}_1 - jd) + \gamma x_2'] \times \right. \\ \qquad \left. \delta[d(k\sin\theta - \xi)/(2\pi) - j]d\xi\right\}\Delta w(\bar{x}_1)d\bar{x}_1, \quad x_2' < 0, \end{cases} \tag{27}$$

where $\delta[\bullet]$ is the delta function. By using the sifting property of the delta function, Eq. (27) can be simplified to

$$w^{sc}(\mathbf{x}') = \begin{cases} \dfrac{1}{2d}\displaystyle\int_{-a}^{a}\sum_{j=-\infty}^{\infty}\exp[i\alpha_j(x_1' - \bar{x}_1 - jd) \\ \qquad - \gamma_j x_2']\Delta w(\bar{x}_1)d\bar{x}_1, \quad x_2' > 0, \\ -\dfrac{1}{2d}\displaystyle\int_{-a}^{a}\sum_{j=-\infty}^{\infty}\exp[i\alpha_j(x_1' - \bar{x}_1 - jd) \\ \qquad + \gamma_j x_2']\Delta w(\bar{x}_1)d\bar{x}_1, \quad x_2' < 0, \end{cases} \tag{28}$$

in which

$$\alpha_j = k\sin\theta + 2\pi j/d, \tag{29}$$

$$\gamma_j = \begin{cases} [C_{44}^{-1}C_{55}(\alpha_j^2 - k_1^2)]^{1/2}, & \alpha_j^2 \ge k_1^2 \\ -i[C_{44}^{-1}C_{55}(k_1^2 - \alpha_j^2)]^{1/2}, & \alpha_j^2 < k_1^2. \end{cases} \tag{30}$$

Equation (28) implies that the scattered field can be expressed in terms of the crack opening displacement Δw of the reference crack. Hence, Δw can serve as a fundamental unknown quantity. By substituting Eq. (28) into Eq. (3), by letting the observation point $\mathbf{x}'$ approaching the faces of the reference crack and by considering the boundary condition (12), the following boundary integral equation is obtained for the crack opening displacement Δw

$$\frac{C_{44}}{2d}\int_{-a}^{a}\sum_{j=-\infty}^{\infty}\gamma_j\exp[i\alpha_j(x_1' - \bar{x}_1)]\Delta w(\bar{x}_1)d\bar{x}_1 = \bar{\sigma}_{32}^{in}(x_1') \tag{31}$$

where $\bar{\sigma}_{32}^{in}$ is given by Eq. (24).

4 Numerical Solution of the Boundary Integral Equation

To solve the boundary integral equation (31), the unknown function Δw is expanded into a series of the form

$$\Delta w(\bar{x}_1) = (a^2 - \bar{x}_1^2)^{1/2}\sum_{m=1}^{\infty}C_m U_{m-1}(\bar{x}_1/a), \tag{32}$$

where C_m are the unknown complex expansion coefficients and U_{m-1} are the Chebyshev polynomials of the second kind. The proper behavior of $\Delta w(\bar{x}_1)$ at crack tips is considered in Eq. (32) by including the term $(a^2 - \bar{x}_1^2)^{1/2}$.

Substituting Eq. (32) into Eq. (31) using the relation

$$\int_{-1}^{1}(1 - x^2)^{1/2}U_{m-1}(x)\exp(i\alpha x)dx = \frac{m\pi}{\alpha}J_m(\alpha)\exp\left(i\frac{m-1}{2}\pi\right) \tag{33}$$

and performing the integration over $[-a, a]$ with respect to $\bar{x}_1$, multiplying both sides by $(a^2 - x_1^2)^{1/2}U_{n-1}(x_1/a)$, and integrating again over $[-a, a]$ with respect to x_1, an infinite system of linear algebraic equations for C_m is obtained as

$$\sum_{m=1}^{\infty}A_{mn}C_m = B_n, \tag{34}$$

where the matrix coefficients A_{mn} and the right-hand side B_n are given by

$$A_{mn} = mn\sum_{j=-\infty}^{\infty}\frac{\gamma_j}{\alpha_j^2}J_m(\alpha_j a)J_n(\alpha_j a)\exp[3i(m+n)\pi/2], \tag{35}$$

$$B_n = 2(-1)^n\sigma_{32}^0\frac{nd}{\pi C_{44}ka\sin\theta}J_n(ka\sin\theta)\exp[i(n-1)\pi/2], \tag{36}$$

in which

$$\sigma_{32}^0 = iAC_{44}k\cos\theta. \tag{37}$$

In Eqs. (33), (35), and (38), $J_m(\alpha)$ is the Bessel function of mth order.

5 Dynamic Stress Intensity Factors

The mode III dynamic stress intensity factors are related to the crack opening displacement by

$$K_{III}^{\pm} = \frac{(2\pi)^{1/2}}{4}(C_{44}\,C_{55})^{1/2}\lim_{\bar{x}_1 \to \pm a}\frac{1}{(a \mp \bar{x}_1)^{1/2}}\Delta w(\bar{x}_1), \tag{38}$$

where "$\pm$" indicates the crack tips at $\bar{x}_1 = a$ and $\bar{x}_1 = -a$. Substituting Eq. (32) into Eq. (38) and using the identity

$$U_{m-1}(\pm 1) = m(\pm 1)^{m-1}, \tag{39}$$

a simple relation between the dynamic stress intensity factors and the expansion coefficients is obtained as

$$K_{III}^{\pm} = \frac{(\pi a)^{1/2}}{2}(C_{44}\,C_{55})^{1/2}\sum_{m=1}^{\infty}C_m m(\pm 1)^{m-1}. \tag{40}$$

Once the coefficients C_m have been computed from Eq. (34), the mode III dynamic stress intensity factors can be calculated by using Eq. (40).

6 Discussion of Numerical Results

The geometrical and the material parameters to be specified for the numerical calculations are: the normalized crack distance d/a, the dimensionless wave number $k_1 a$, the angle of

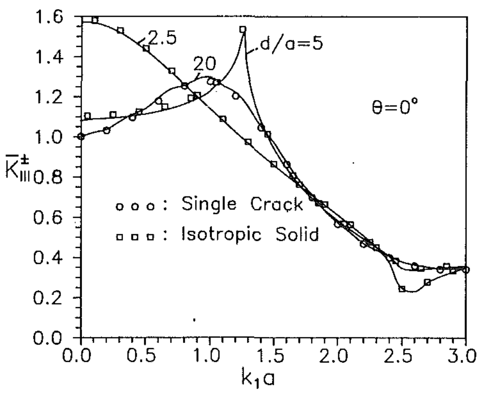

Fig. 3 Normalized dynamic stress intensity factors versus k_1a

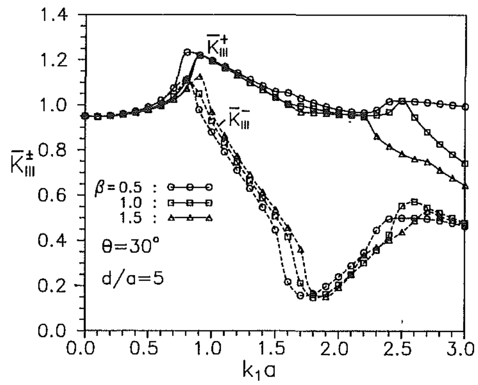

Fig. 4 Normalized dynamic stress intensity factors versus k_1a

incidence θ, and the anisotropy parameter (ratio of the elastic constants) $\beta = C_{44}/C_{55}$. For convenience, the normalized dynamic stress intensity factors

$$\overline{K}^{\pm}_{III} = |K^{\pm}_{III}|/|K^{0}_{III}| \tag{41}$$

are introduced, where

$$K^{0}_{III} = iAC_{44}k(\pi a)^{1/2}. \tag{42}$$

To compute the matrix coefficients A_{mn} and the dynamic stress intensity factors, the infinite series (35) and (40) have to be truncated. Generally, the truncations needed depend on the crack spacing, the wave frequency, the angle of incidence, and the anisotropy parameter. By using the asymptotics of the Bessel function, it can be easily shown that the series (35) behaves as $1/(\alpha_j a)^2$ for $(\alpha_j a) \to \infty$. Considering Eq. (29) it is seen that the number of terms to be summed in (35) depends mainly on the crack spacing parameter d/a. Numerical tests show that for ensuring the accuracy of A_{mn} it is enough to take $j_{max} = -j_{min} = 300$ for $2.0 < d/a < 5.0$ and $j_{max} = -j_{min} = 1000$ for $d/a = 20$. To keep the error in the dynamic stress intensity factors smaller than three percent, it is sufficient to take m_{max} in Eq. (40) slightly larger than twice the dimensionless wave number k_1a.

For normally incident plane time-harmonic SH-waves (θ = 0 deg), the normalized dynamic stress intensity factors are shown in Fig. 3 as functions of the dimensionless wave number k_1a. In this case, both crack tips possess the same stress intensity factors, i.e., $\overline{K}^{+}_{III} = \overline{K}^{-}_{III}$, due to symmetry of the problem. Figure 3 indicates that for large values of the crack distance $d/a = 5$ and $d/a = 20$, the maximum dynamic stress intensity factors exceed their corresponding static values at $k_1a = 0$. In both cases, the dynamic stress intensity factors increase first with increasing k_1a, and after reaching their maximum they then decrease with further increasing k_1a. For a small value of $d/a = 2.5$, the dynamic stress intensity factors decrease monotonically with increasing dimensionless wave number k_1a, at least in the frequency range that is considered. It is noteworthy that for $d/a = 5$, a sharp peak in the stress intensity factors is noted. In the case of $d/a = 20$, the crack spacing is sufficiently large for neglecting the interactions between individual cracks, and the corresponding dynamic stress intensity factors approach that for a single crack (Ohyoshi, 1973, Zhang and Gross, 1992) as shown in Fig. 3. This provides us with a check on the accuracy of the numerical method presented here. It is interesting to note that for normal incidence of plane, time-harmonic SH-waves, the dependence of $\overline{K}^{\pm}_{III}$ on k_1a is valid for arbitrary anisotropy parameter β. This allows us to make another comparison of the numerical results of this paper with those obtained by Zhang (1990) for a periodic array of cracks in an isotropic solid, i.e., $\beta = 1$. As can be seen from Fig. 3, an excellent agreement between both results has been obtained. It should be noted here that the method is not limited to low to moderate frequencies, and it also works well for

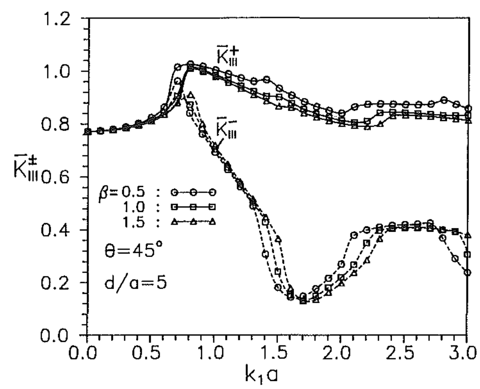

Fig. 5 Normalized dynamic stress intensity factors versus k_1a

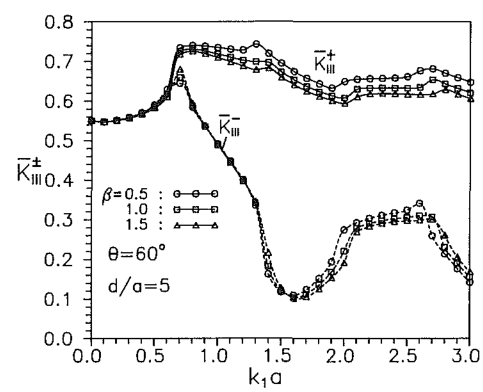

Fig. 6 Normalized dynamic stress intensity factors versus k_1a

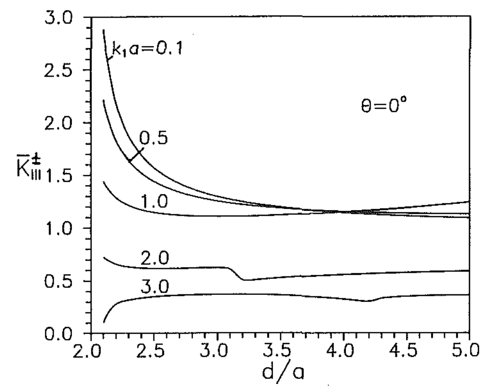

Fig. 7 Normalized dynamic stress intensity factors versus d/a

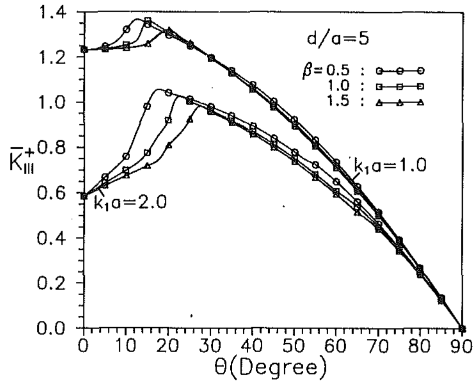

Fig. 8 Normalized dynamic stress intensity factors versus θ

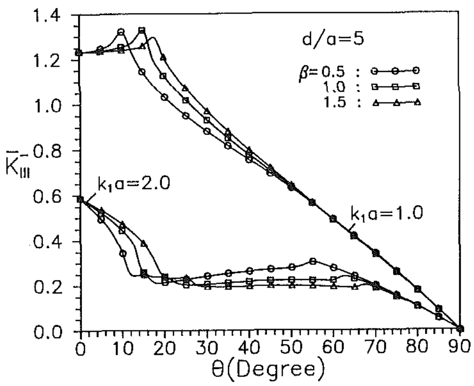

Fig. 9 Normalized dynamic stress intensity factors versus θ

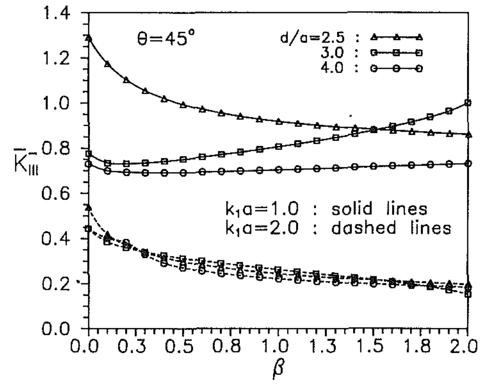

Fig. 10 Normalized dynamic stress intensity factors versus β

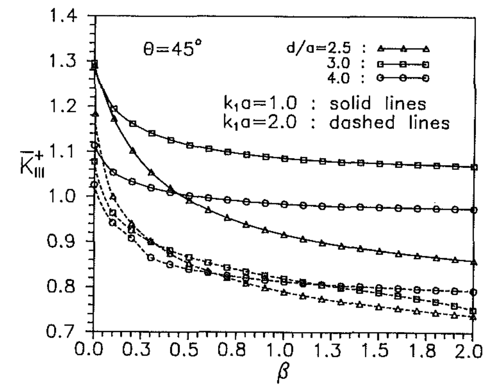

Fig. 11 Normalized dynamic stress intensity factors versus β

relatively high frequencies. Of course, the number of terms to be summed in Eq. (40) has to be increased in the latter case, but this brings no difficulties.

For plane time-harmonic SH-waves incident obliquely under $\theta = 30$ deg, 45 deg, and 60 deg, and for three anisotropy parameters $\beta = 0.5$, 1.0 and 1.5, the corresponding dynamic stress intensity factors are presented in Figs. 4–6 versus k_1a. Here, the dimensionless crack distance d/a is chosen as $d/a = 5$. In all three cases, the variation of the dynamic stress intensity factors with the dimensionless wave number k_1a is very similar. Both the $\overline{K}_{III}^{+}$-factor and the $\overline{K}_{III}^{-}$-factor have the same values at low frequencies, and they separate at high frequencies whereby $\overline{K}_{III}^{+} > \overline{K}_{III}^{-}$. This indicates that for the case considered, the right crack tips are more dangerous than the left crack tips. Also here, the maximum dynamic stress intensity factors exceed their corresponding static values. Furthermore, an oscillatory behavior in the dynamic stress intensity factors is noted at high frequencies. The effect of the material anisotropy on the dynamic stress intensity factors is negligible at low frequencies while it becomes distinct at high frequencies.

Figure 7 shows the dependence of the normalized dynamic stress intensity factors on the normalized crack distance d/a, for normally incident ($\theta = 0$ deg) plane time-harmonic SH-waves, and for several dimensionless wave numbers k_1a. Also here, the results are valid for arbitrary anisotropy parameter β. In the low frequency range, for instance for $k_1a = 0.1$ and $k_1a = 0.5$, the dynamic stress intensity factors are considerably large when the distance between neighboring cracks is small, and they decrease monotonically with increasing crack distance d/a. This means that the smaller the separation between neighboring cracks, the larger are the stress concentrations near the crack tips. The amplification in the stress intensities is reduced when the frequency of the incident wave is high, and the dependence of the dynamic stress intensity factors on the crack distance d/a becomes much more complicated. The dynamic stress intensity factors for $k_1a = 1$, 2, and 3 could be for example smaller at smaller values of d/a than that at larger values of d/a. These results show that dynamic effects can significantly alter the dependence of the dynamic stress intensity factors on the crack distance d/a. Only in the low frequency range, this dependence agrees qualitatively with that of the static analysis. For intermediate and high frequencies, this dependence could be, however, opposite to that in the static case.

Figures 8 and 9 show the dependence of the normalized dynamic stress intensity factors on the angle of incidence θ, for $d/a = 5$, $k_1a = 1.0$ and 2.0, and for $\beta = 0.5$, 1.0, and 1.5. In the case of $k_1a = 1.0$ the normalized dynamic stress intensity factors $\overline{K}_{III}^{\pm}$ first increase slightly with increasing θ, and after reaching their maximum they then decrease with further increasing θ. The influence of β on $\overline{K}_{III}^{\pm}$ in this case is small for large θ. The variation of $\overline{K}_{III}^{\pm}$ with θ becomes intricate for $k_1a = 2.0$. The special case $\theta = 0$ deg corresponds to normal incidence which has been discussed before in detail. In another special case of $\theta = 90$ deg, the incident wave produces no loadings on the faces of the cracks, and the dynamic stress intensity factors $\overline{K}_{III}^{\pm}$ are therefore identical zero.

Finally, the normalized dynamic stress intensity factors are presented in Figs. 10 and 11 versus the anisotropy parameter β, for a plane time-harmonic SH-wave incident under $\theta = 45$ deg, for $d/a = 2.5$, 3.0, and 4.0, and for $k_1a = 1.0$ and 2.0. The normalized dynamic stress intensity factors $\overline{K}_{III}^{\pm}$ decrease with increasing β, except in the case of $d/a = 3.0$ and $k_1a = 1.0$ in which $\overline{K}_{III}^{-}$ increases as β increases. The dynamic stress intensity factors for $k_1a = 1.0$ are generally larger than that for $k_1a = 2.0$. Figures 10 and 11 show that both the crack spacing and the wave frequency have strong influences on the

$\overline{K}^{\pm}_{III} - \beta$ curves. Depending on the crack spacing and on the wave frequency, the material anisotropy can either increase the dynamic stress intensity factors or decrease them.

Acknowledgments

The work reported here is supported by a grant from the Committee of Science and Technology of Shanghai and by a grant from Tongji University.

References

Achenbach, J. D., and Li, Z. L., 1986, "Reflection and Transmission of Scalar Waves by a Periodic Array of Screens," *Wave Motion*, Vol. 8, pp. 225-234.

Ang, W. T., 1987, "Transient Response of a Crack in an Anisotropic Strip," *Acta Mechanica*, Vol. 70, pp. 97-109.

Ang, W. T., 1988, "A Crack in an Anisotropic Layered Material Under the Action of Impact Loading," ASME Journal of Applied Mechanics, Vol. 55, pp. 120-125.

Angel, Y. C., and Achenbach, J. D., 1985a, "Reflection and Transmission of Elastic Waves by a Periodic Array of Cracks," ASME Journal of Applied Mechanics, Vol. 52, pp. 33-41.

Angel, Y. C., and Achenbach, J. D., 1985b, "Reflection and Transmission of Elastic Waves by a Periodic Array of Cracks: Oblique Incidence," *Wave Motion*, Vol. 7, pp. 375-397.

Bloch, F., 1928, "Über die Quantenmechanik der Elektronen," *Z. Phys.*, Vol. 52, pp. 555-600.

Danyluk, H. T., and Singh, B. M., 1984, "Closed Form Solutions for a Finite Length Crack Moving in an Orthotropic Layer of Finite Thickness," *Letters Appl. Engrg. Sci.*, Vol. 22, pp. 637-644.

Dhawan, G. K., 1982, "Interaction of Elastic Waves by a Griffith Crack in an Infinite Transversely-Isotropic Medium," *International Journal of Fracture*, Vol. 19, pp. 29-37.

Dhawan, G. K., 1983, "Interaction of SV-Waves by a Griffith Crack in an Infinite Transversely-Isotropic Medium," *International Journal of Fracture*, Vol. 20, pp. 103-110.

Kassir, M. K., and Bandyopadhyay, K. K., 1983, "Impact Response of a Cracked Orthotropic Medium," ASME Journal of Applied Mechanics, Vol. 50, pp. 630-636.

Kassir, M. K., and Tse, S,. 1983, "Moving Griffith Crack in an Orthotropic Material," *Int. J. Engrg. Sci.*, Vol. 21, pp. 315-325.

Lobanov, E. V., and Novichkov, Y. N., 1981, "Diffraction of SH-Waves by an Oblique Crack in an Orthotropic Half-Space," *Soviet Applied Mechanics*, Vol. 17, pp. 610-615.

Mikata, Y., and Achenbach, J. D., 1989, "Scattering by a Periodic Array of Collinear Cracks," *Review of Progress in Quantitative Nondestructive Evaluation*, Vol. 8A, D. O. Thompson, and D. E. Chimenti, eds., Plenum Press, pp. 87-94.

Norris, A. N., and Achenbach, J. D., 1984, "Elastic Wave Diffraction by a Semi-Infinite Crack in a Transversely Isotropic Material," *Quart. J. Mech. Appl. Math.*, Vol. 37, pp. 565-580.

Ohyoshi, T., 1973, "Effect of Orthotropy on Singular Stresses Produced Near a Crack Tip by Incident SH-Waves," *ZAMM*, Vol. 53, pp. 409-411.

Piva, A., 1986, "Elastodynamic Crack Problems in an Anisotropic Medium Through a Complex Variable Approach," *Quart. Appl. Math.*, Vol. 44, pp. 441-445.

Piva, A., 1987, "An Alternative Approach to Elastodynamic Crack Problems in an Orthotropic Medium," *Quart. Appl. Math.*, Vol. 45, pp. 97-104.

Shindo, Y., Nozaki, H., and Higaki, H., 1986, "Impact Response of a Finite Crack in an Orthotropic Strip," *Acta Mechanica*, Vol. 62, pp. 87-104.

Tsai, Y. M., 1988, "Dynamic Penny-Shaped Crack in a Transversely Isotropic Material," *Engineering Fracture Mechanics*, Vol. 31, pp. 977-984.

Tsai, Y. M., 1989, "Torsional Vibration of a Penny-Shaped Crack in a Transversely Isotropic Material," *Advances in Fracture Research ICF 7*, Vol. 3, K. Salama, et al. eds., Pergamon Press, pp. 2363-2368.

Zhang, Ch., 1990, "Dynamic Stress Intensity Factors of Periodic Collinear Antiplane Cracks," (in Chinese), *J. of Tongji University*, Vol. 18, pp. 445-451.

Zhang, Ch., and Gross, D., 1992, "Interation of Antiplane Cracks With Elastic Waves in Transversely Isotropic Materials," submitted for publication.

Shear Constitutive Relations for Laminated Anisotropic Shells and Plates: Part I—Methodology

S. B. Dong
Mem. ASME.

C. K. Chun[1]

Civil Engineering Department,
University of California,
Los Angeles, CA 90024

Shear constitutive relations of a first-order shear deformation theory for laminated anisotropic shells and plates are formulated following Mindlin's procedure for homogeneous isotropic plates. Because thickness-shear motions for laminated anisotropic thickness profiles may not be polarized in planes normal to the reference surface, the concept of generalized principal shear planes is needed. These planes are established by least-squares minimization of the out-of-plane motions of infinitely long thickness-shear waves based on an elasticity analysis of the profile. Typical shear rigidities for a variety of laminated composite and sandwich profiles are given. In a companion paper, the efficacy of this form of shear constitutive relations in predicting the response of a class of laminated composite and sandwich cylindrical shells is demonstrated.

Introduction

Classical (Kirchhoff-Love) plate and shell theory rests on the propriety of neglecting transverse shear deformation. The low shear moduli in typical laminated composite plates and shells enhance their susceptibility to shear. As a result, the range of validity of classical theory for a composite plate or shell suffers in comparison with that for a similarly shaped, homogeneous isotropic structure. For applications immediately beyond this range, a refined theory incorporating shear deformation must be used.

Many state-of-the-art surveys on shear deformation theories and applications of laminated composite plates and shells have appeared, the most recent ones are due to Noor and Burton (1989) and Kapania and Raciti (1989a, 1989b). Others include those by Bert (1979, 1984, 1985), Leissa (1981, 1987), and Reddy (1981, 1982, 1985). These reviews document the different levels of approximation used in the assortment of laminated composite plate and shell theories. Even with this considerable attention, a need remains for a first-order shear deformation theory valid for an arbitrary stacking sequence and orientation of fiber directions, i.e., for laminated *anisotropic* plates and shells. Moreover, the accuracy of any proposed constitutive relation in a refined theory must be demonstrated.

Herein, our literature review is restricted to first-order shear deformation theories with attention on the shear correction factors in the transverse shear constitutive relations. These factors are the means by which to properly assess the shear rigidities in the structural range of application. Two methods are used to determine them: (1) by assumed stress distribution and applying complementary energy principle and (2) matching cutoff frequencies of thickness-shear motions with infinitely long wavelengths. Reissner (1945, 1947) and Mindlin (1951), respectively, are synonymous with these approaches for homogeneous isotropic plates. Recall that their values of shear correction factor k^2 in shear rigidity k^2 GH (G = shear modulus, H = thickness) were 5/6 and $\pi^2/12$, respectively.

One of the first shear deformation laminated composite plate theories is due to Yang, Norris, and Stavsky (1966). They obtained their governing equations by integrating the three-dimensional elastodynamic equations over the plate thickness and introduced correction factors in an ad hoc manner. Whitney and Pagano (1970) presented a refined laminated anisotropic plate theory, but left open the issue of proper values for the shear correction factors. Later, Whitney (1972) gave correction factors for some laminated and sandwich plates using statical considerations. Reissner (1972, 1979) has also treated transverse shear effects in laminated anisotropic plates by extending his earlier approach for isotropic plates. Dong and Tso (1972) presented constitutive equations for laminated orthotropic shells with the correction factors based on the fundamental thickness-shear cutoff frequencies in the two orthogonal directions. Shear correction factors for other cross-ply plates were given by Dong (1972). Chatterjee and Kulkarni (1979) offered a method for shear correction factors for laminated anisotropic plates with particular attention to the cross-coupling shear term $k_{12}^2 A_{45}$. However, they did not fully explained nor justified their method.

[1]Current address: Daewoo Motor Company, Ltd., Advanced Engineering Department, Inchon, South Korea.

Contributed by the Applied Mechanics Division of The American Society of Mechanical Engineers for the presentation at the 1992 ASME Summer Mechanics and Material Meeting, Tempe, AZ, Apr. 28–May 1, 1992.

Discussion on this paper should be addressed to the Technical Editor, Prof. Leon M. Keer, The Technological Institute, Northwestern University, Evanston, IL 60208, and will be accepted until four months after final publication of the paper itself in the Journal of Applied Mechanics. Manuscript received by the ASME Applied Mechanics Division, Dec. 12, 1990; final revision, May 20, 1991.

Paper No. 92-APM-10.

This paper is concerned with a methodology for constructing rational transverse shear constitutive relations for a first-order shear deformation theory for laminated anisotropic plate and shell theory suitable for an arbitrary stacking sequence and orientation of materials. The approach is an extension of that used by Dong and Tso (1972) for laminated orthotropic (general cross-ply) shells. For cross-ply constructions, two mutually orthogonal planes of polarized motions exist naturally, permitting a straightforward matching of the cutoff frequencies to deduce the shear correction factors. The difficulty with a completely arbitrary laminated thickness profile is that polarized thickness-shear motions generally will not occur in any plane normal to the reference surface. Herein, the concept of generalized polarized motions on two mutually orthogonal planes is introduced, and transverse shear constitutive relations are established in these principal directions. Numerical values of the shear correction factors for a variety of laminated composite and sandwich profiles are given to provide some insight. In a companion paper, the accuracy of these shear constitutive relations for predicting structural response of a class of laminated composite and sandwich cylindrical shells will be addressed.

Preliminaries

Let (ξ_1, ξ_2, z) be orthogonal curvilinear coordinates with (ξ_1, ξ_2) as the shell's reference surface coordinates and z as the transverse coordinate and let t denote time. According to the fundamental kinematic hypothesis in a first-order shear deformation-theory, the shell displacements (U_1, U_2, W) in the coordinate directions can be expressed in terms of three reference surface displacements, (u_1, u_2, w) and two bending rotations (β_1, β_2) as

$$(U_i(\xi_1, \xi_2, z, t) = u_i(\xi_1, \xi_2, t) + z\beta_1(\xi_1, \xi_2, t), \quad (i=1, 2);$$
$$W(\xi_1, \xi_2, z, t) = w(\xi_1, \xi_2, t). \tag{1}$$

These five kinematic variables enter into strain-displacement relations defining eight deformation measures, which are grouped into three arrays, i.e., $\{\epsilon\}^T = [\epsilon_{11}, \epsilon_{22}, \gamma_{12},]$, $\{\kappa\}^T = [\kappa_{11}, \kappa_{22}, \kappa_{12}]$, and $\{\gamma\}^T = [\gamma_{1z}, \gamma_{2z}]$. Their corresponding force and moment resultants are denoted by the arrays $\{N\}^T = [N_{11}, N_{22}, N_{12}]$, $\{M\}^T = [M_{11}, M_{22}, M_{12}]$, $\{Q\}^T = [Q_1, Q_2]$, which are defined by integrals of the in-plane $(\sigma_{11}, \sigma_{22}, \sigma_{12})$ and transverse shear $(\sigma_{1z}, \sigma_{2z})$ stresses over the thickness profile, i.e.,

$$(N_{ij}, Q_i) = \int_h (\sigma_{ij}, \sigma_{iz})dz \quad ; \quad M_{ij} = \int_h \sigma_{ij} z\, dz; \; (i, j=1, 2). \tag{2}$$

The constitutive relations are conveniently cast in two parts. One part relates $(\{N\}, \{M\})$ to $(\{\epsilon\}, \{\kappa\})$, i.e., the relation that shows the inherent extensional-flexural coupling in laminated composite profiles:

$$\begin{bmatrix} N \\ M \end{bmatrix} = \begin{bmatrix} A & B \\ B & D \end{bmatrix} \begin{bmatrix} \epsilon \\ \kappa \end{bmatrix} \tag{3}$$

where the extensional, coupling, and flexural rigidities (A_{ij}, B_{ij}, D_{ij}) in matrices $[A]$, $[B]$, and $[D]$ are given by the integrals:

$$(A_{ij}, B_{ij}, D_{ij}) = \int_h Q_{ij}^{(k)}(1, z, z^2)dz \tag{4}$$

with $Q_{ij}^{(k)}$'s as the reduced stiffnesses kth layer. The second part pertains to the shear constitutive relations, which is the focus of our attention.

Shear Constitutive Relations

The shear constitutive relation in a first-order shear deformation theory for laminated anisotropic shells or plates is of the form

$$\begin{bmatrix} Q_1 \\ Q_2 \end{bmatrix} = \begin{bmatrix} \Gamma_{55} & \Gamma_{45} \\ \Gamma_{45} & \Gamma_{44} \end{bmatrix} \begin{bmatrix} \gamma_{1z} \\ \gamma_{2z} \end{bmatrix} \tag{5}$$

where $(\Gamma_{55}, \Gamma_{44}, \Gamma_{45})$ are the transverse shear rigidities. In a first-order shear deformation theory, the shear angles γ_{iz}'s are generalized coordinates representing weighted average shear strains over the entire profile. Note the absence of shear correction factors in Eq. (5) as they are implicitly taken to be part of the Γ_{ij}'s coefficients.

Dong and Tso (1972) established shear constitutive relations for a laminated orthotropic shell (i.e., cross-ply constructions) by adaptation of Mindlin's approach. These relations were of the form:

$$\begin{bmatrix} Q_1 \\ Q_2 \end{bmatrix} = \begin{bmatrix} \Gamma_{55} & \cdot \\ \cdot & \Gamma_{44} \end{bmatrix} \begin{bmatrix} \gamma_{1z} \\ \gamma_{2z} \end{bmatrix} = \begin{bmatrix} k_{11}^2 A_{55} & \cdot \\ \cdot & k_{22}^2 A_{44} \end{bmatrix} \begin{bmatrix} \gamma_{1z} \\ \gamma_{2z} \end{bmatrix} \tag{6}$$ [1]

where

$$(A_{55}, A_{44}) = \int_h (Q_{55}^{(k)}, Q_{44}^{(k)})dz \tag{7}$$

and (k_{11}^2, k_{22}^2) are shear correction factors. Observed that $\Gamma_{45} = k_{12}^2 A_{45} = 0$ because A_{45} is indentically zero in this case. It was convenient to use the shear correction factors here, however, the crucial issue concerns the estimation of Γ_{55} and Γ_{44}. Each shear rigidity Γ_{ii} was found by equating the first-order shear deformation theory formula for the squared natural frequency of infinitely long thickness-shear waves in a plate with that determined by linear elasticity. The matchings in each of the two coordinate directions lead to the following equations where ω_1^2, ω_2^2 are understood to be frequency data from linear elasticity.

$$\Gamma_{55} = \frac{\rho_1\rho_3 - \rho_2^2}{\rho_1}\omega_2^2 \quad ; \quad \Gamma_{44} = \frac{\rho_1\rho_3 - \rho_2^2}{\rho_1}\omega_1^2 \tag{8}$$

where ρ_1, ρ_2, ρ_3 are plate or shell inertias defined by:

$$(\rho_1, \rho_2, \rho_3) = \int_h \rho^{(k)}(1, z, z^2)dz. \tag{9}$$

There are no conceptual difficulties here as the thickness-shear motions are naturally polarized in two mutually orthogonal planes as illustrated in Fig. 1(*a*) for a cross-ply plate rotated by 45 deg.

For general laminated anisotropic profiles, inconsistencies arise. On one hand, elasticity results show that polarized motions in two mutually orthogonal planes are not possible as seen by examples of a three-layer and an eleven-layer profile in Figs. 1(*b*) and 1(*c*). Yet, Eq. (5) admits a transformation to principal directions (i.e., rotation to two mutually orthogonal directions that eliminates Γ_{45}). To generalize Mindlin's approach in this case, assume the existence of two mutually orthogonal planes called *generalized principal shear planes* which act as the principal directions in a first-order shear deformation theory. Let $\overline{\Gamma}_{55}$, $\overline{\Gamma}_{44}$ be the two principal shear rigidities in the principal directions. Equation (8) holds in the principal directions upon replacing Γ_{ii}'s by the barred values, i.e.,

$$\overline{\Gamma}_{55} = \frac{\rho_1\rho_3 - \rho_2^2}{\rho_1}\omega_2^2 \quad ; \quad \overline{\Gamma}_{44} = \frac{\rho_1\rho_3 - \rho_2^2}{\rho_1}\omega_1^2. \tag{10}$$

The two generalized principal planes are defined by a least-

[1]The subscripts 55, 44 are reversed from those in Dong and Tso (1972). Here, they adhere to contracted notation convention where shear subscripts 1, 3 and 2, 3 are denoted by 5 and 4, respectively.

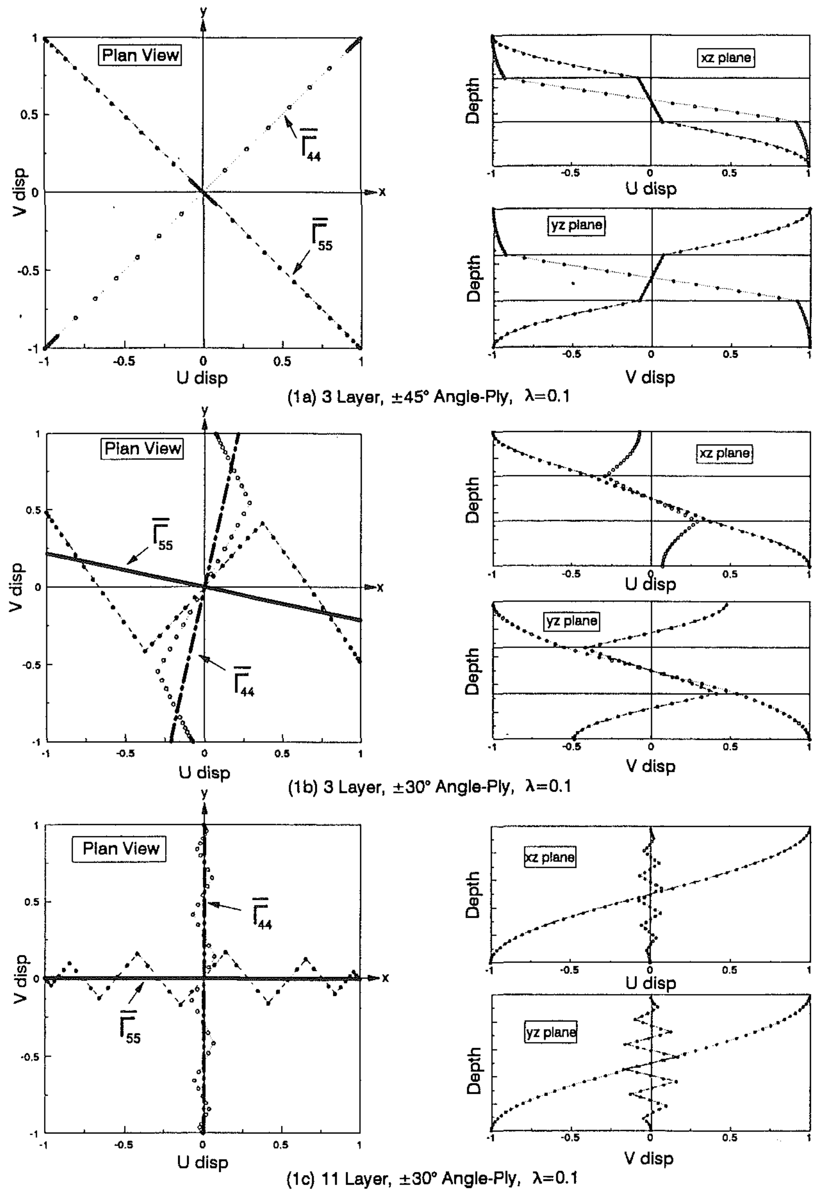

Fig. 1 Infinitely long, thickness-shear motions and generalized principal planes

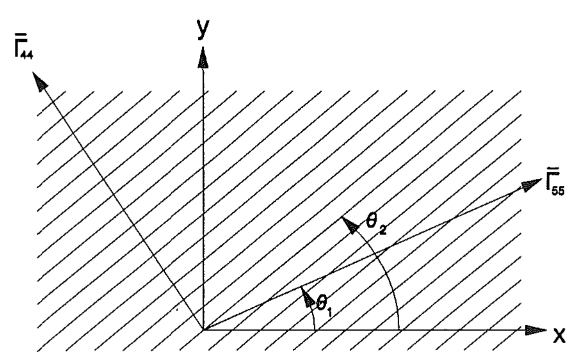

θ_1 -angle between x-axis and $\bar{\Gamma}_{55}$ generalized principal plane.
θ_2 -angle between x-axis and fiber direction.

Fig. 2 Orientation of ply-angle and generalized principal planes

squares minimization of the out-of-plane displacements of the two fundamental natural motions of infinitely long thickness-shear waves. This procedure is described in a subsequent section. Once $\bar{\Gamma}_{55}$ and $\bar{\Gamma}_{44}$ and the principal directions are known, then Γ_{55}, Γ_{44}, Γ_{45} in the coordinate directions may be obtained by a two-dimensional transformation, i.e.,

$$\begin{bmatrix} \Gamma_{55} \\ \Gamma_{44} \\ \Gamma_{45} \end{bmatrix} = \begin{bmatrix} \cos^2\theta & \sin^2\theta \\ \sin^2\theta & \cos^2\theta \\ \cos\theta\sin\theta & -\cos\theta\sin\theta \end{bmatrix} \begin{bmatrix} \bar{\Gamma}_{55} \\ \bar{\Gamma}_{44} \end{bmatrix}. \tag{11}$$

In Eqs. (10) and (11), adopt the convention that $\bar{\Gamma}_{44} \le \bar{\Gamma}_{55}$ and $\omega_1^2 \le \omega_2^2$ and let θ be the angle from the x-axis to the direction of $\bar{\Gamma}_{55}$ as illustrated by θ_1 in Fig. 2. Observe that significant values of Γ_{45} can only occur when $\bar{\Gamma}_{55}$ is quite distinct from $\bar{\Gamma}_{44}$.

Elastodynamic Analysis of Infinitely Long Thickness-Shear Motions

The frequencies for infinitely long thickness-shear waves in a plate based on linear elastodynamics are determined by finite element analysis. The governing equations are predicated on Hamilton's principle in the form:

Table 1 Regular symmetric (±45 deg) angle-ply profile

λ	plies	$\bar{\Gamma}_{44}$	$\bar{\Gamma}_{55}$	Pr. Angle	$\bar{A}_{44}$	$\bar{A}_{55}$	$\bar{k}^2_{22}$	$\bar{k}^2_{11}$
	3	0.12201	0.16758	-45.00	0.70000	0.40000	0.174	0.419
	5	0.14245	0.14953	-45.00	0.64000	0.46000	0.223	0.325
	7	0.14654	0.14900	-45.00	0.61429	0.48571	0.239	0.307
	9	0.14792	0.14906	-45.00	0.60000	0.50000	0.247	0.298
0.1	11	0.14854	0.14915	-45.00	0.59091	0.50909	0.251	0.293
	13	0.14886	0.14923	-45.00	0.58462	0.51538	0.255	0.290
	15	0.14905	0.14929	-45.00	0.58000	0.52000	0.257	0.287
	.	.	.	.	.	.	.	.
	51	0.14950	0.14951	-45.00	0.55882	0.54118	0.268	0.276
	3	0.42416	0.50813	-45.00	0.80000	0.60000	0.530	0.847
	5	0.46066	0.47297	-45.00	0.76000	0.64000	0.606	0.739
	7	0.46635	0.47051	-45.00	0.74286	0.65714	0.628	0.716
0.4	9	0.46812	0.47002	-45.00	0.73333	0.66667	0.638	0.705
	11	0.46886	0.46989	-45.00	0.72727	0.67273	0.645	0.698
	13	0.46924	0.46986	-45.00	0.72308	0.67692	0.649	0.694
	.	.	.	.	.	.	.	.
	51	0.46995	0.46996	-45.00	0.70588	0.69412	0.666	0.677
	3	0.77015	0.78802	-45.00	0.96667	0.93333	0.797	0.844
	5	0.77782	0.78038	-45.00	0.96000	0.94000	0.810	0.830
	7	0.77871	0.77957	-45.00	0.95714	0.94286	0.814	0.827
0.9	9	0.77896	0.77935	-45.00	0.95556	0.94444	0.815	0.825
	11	0.77906	0.77927	-45.00	0.95455	0.94545	0.816	0.824
	13	0.77911	0.77923	-45.00	0.95385	0.94615	0.817	0.824
	.	.	.	.	.	.	.	.
	51	0.77918	0.77918	-45.00	0.95098	0.94902	0.819	0.821

The $\bar{A}_{45}$'s are identically zero in all cases.

Table 2 Regular antisymmetric (±45 deg) angle-ply profile

λ	plies	$\bar{\Gamma}_{55}=\bar{\Gamma}_{44}$	$\bar{A}_{55}=\bar{A}_{44}$	$\bar{k}^2_{11}=\bar{k}^2_{22}$
	2	0.13100	0.550	0.238
	4	0.14329	0.550	0.261
	6	0.14706	0.550	0.267
0.1	8	0.14819	0.550	0.269
	10	0.14869	0.550	0.270
	12	0.14896	0.550	0.271
	.	.	.	.
	50	0.14951	0.550	0.272
	2	0.45040	0.700	0.643
	4	0.46424	0.700	0.663
	6	0.46779	0.700	0.668
0.4	8	0.46881	0.700	0.670
	10	0.46924	0.700	0.670
	12	0.46948	0.700	0.671
	.	.	. .	.
	50	0.46995	0.700	0.671
	2	0.77864	0.950	0.820
0.9	4	0.77903	0.950	0.820
	.	.	.	.
	50	0.77918	0.950	0.820

The $\bar{A}_{45}$'s are identically zero in all cases.

$$\delta\int\left(\frac{1}{2}\int_z(\rho^{(k)}(\dot{u}^2+\dot{v}^2)-Q_{55}^{(k)}u_{,z}^2-2Q_{45}^{(k)}u_{,z}v_{,z}-Q_{44}^{(k)}v_{,z}^2)dz\right)dt=0. \quad (12)$$

One-dimensional finite element modeling is employed using quadratic interpolations in the thickness direction with nodes of a given element at its top, mid, and bottom surfaces. The resulting algebraic eigenvalue problem incorporating time harmonic motion is of usual form, i.e., $[K]\{U\}=\omega^2[M]\{U\}$. Only the lowest two antisymmetric or antisymmetric-like motions are of interest. Finite element analysis of waves with finite wavelengths in laminated anisotropic plates, of which the present application is a special case, was given by Dong and Pauley (1978).

Determination of Generalized Principal Planes

Let $y=mx$ and $y=-x/m$ be equations of two mutually orthogonal lines in a plate contained within the generalized principal shear planes and let $\mathbf{i}^*$ and $\mathbf{j}^*$ be unit vectors along these lines. These unit vectors can be expressed in terms of the unit vectors $\mathbf{i}$ and $\mathbf{j}$ of the rectangular cartesian coordinate system through the direction cosines. Let $(u_1(z), v_1(z))$ and $(u_2(z), v_2(z))$ denote the cartesian displacement components of the lowest two antisymmetric modal patterns, normalized such that the maximum amplitude of each is equal to unity. The out-of-plane displacements v_1^*, v_2^* normal to the two principal planes can be expressed in terms of $(u_1(z), v_1(z))$ and $u_2(z), v_2(z))$ and the direction cosines involving the slope m:

$$v_1^*(z)=(u_1\mathbf{i}+v_1\mathbf{j})\cdot\mathbf{j}^*=\frac{m}{\sqrt{m^2+1}}u_1-\frac{1}{\sqrt{m^2+1}}v_1$$

$$v_2^*(z)=(u_2\mathbf{i}+v_2\mathbf{j})\cdot\mathbf{i}^*=\frac{1}{\sqrt{m^2+1}}u_2+\frac{m}{\sqrt{m^2+1}}v_2 \quad (13)$$

Thus, the integral of the squares of all out-of-plane displacements over the thickness profile can be viewed as the *polarization error* ϵ^2:

$$\epsilon^2=\int_h\left[(v_1^*)^2+(v_2^*)^2\right]dz$$

$$=\frac{1}{m^2+1}\left[(A_1+B_2)m^2+2(C_2-C_1)m+(B_1+A_2)\right] \quad (14)$$

where

$$A_i=\int_h(u_i)^2dz \quad ; \quad B_i=\int_h(v_i)^2dz \quad ;$$

$$C_i=\int_h(u_i)(v_i)dz;\ (i=1,2). \quad (15)$$

Minimization of ϵ^2, i.e., $\partial\epsilon^2/\partial m=0$, gives the following quad-

Table 3 Regular symmetric (±30 deg) angle-ply profile

λ	plies	$\bar{\Gamma}_{44}$	$\bar{\Gamma}_{55}$	Pr. Angle	$\bar{A}_{44}$	$\bar{A}_{55}$	$\bar{A}_{45}$	$\bar{k}^2_{22}$	$\bar{k}^2_{11}$
	3	0.10200	0.23172	-12.13	0.39824	0.70176	0.21088	0.256	0.330
	5	0.10511	0.23980	- 1.67	0.32991	0.77009	0.09089	0.319	0.311
	7	0.10564	0.24660	- 0.53	0.32607	0.77393	0.05984	0.324	0.319
	9	0.10584	0.24924	- 0.24	0.32537	0.77463	0.04517	0.325	0.322
0.1	11	0.10594	0.25053	- 0.13	0.32516	0.77484	0.03642	0.326	0.323
	13	0.10599	0.25127	- 0.08	0.32508	0.77492	0.03057	0.326	0.324
	15	0.10603	0.25172	- 0.05	0.32504	0.77496	0.02637	0.326	0.325
	.	.	.	.	.	.	.	.	.
	51	0.10612	0.25295	0.00	0.32500	0.77500	0.00765	0.327	0.326
	3	0.37943	0.59652	-10.70	0.59195	0.80805	0.13537	0.641	0.738
	5	0.38560	0.59322	- 1.57	0.55307	0.84693	0.06010	0.697	0.700
	7	0.38638	0.59575	- 0.52	0.55070	0.84930	0.03983	0.702	0.701
0.4	9	0.38666	0.59674	- 0.24	0.55024	0.84976	0.03010	0.703	0.702
	11	0.38679	0.59722	- 0.13	0.55011	0.84989	0.02428	0.703	0.703
	13	0.38686	0.59749	- 0.08	0.55005	0.84995	0.02038	0.703	0.703
	.	.	.	.	.	.	.	.	.
	51	0.38703	0.59812	0.00	0.55000	0.85000	0.00510	0.704	0.704
	3	0.75773	0.80157	-10.35	0.93171	0.96829	0.02234	0.813	0.828
	5	0.75912	0.80020	- 1.55	0.92550	0.97450	0.01000	0.820	0.821
	7	0.75917	0.80021	- 0.52	0.92512	0.97488	0.00664	0.821	0.821
0.9	9	0.75918	0.80022	- 0.24	0.92504	0.97496	0.00502	0.821	0.821
	11	0.75919	0.80023	- 0.13	0.92502	0.97498	0.00405	0.821	0.821
	.	.	.	.	.	.	.	.	.
	51	0.75920	0.80024	0.00	0.92500	0.97500	0.00085	0.821	0.821

Table 4 Regular antisymmetric (±30 deg) angle-ply profile

λ	plies	$\bar{\Gamma}_{44}$	$\bar{\Gamma}_{55}$	Pr. Angle	$\bar{A}_{44}$	$\bar{A}_{55}$	$\bar{k}^2_{22}$	$\bar{k}^2_{11}$
	2	0.10102	0.18673	0.00	0.32500	0.77500	0.311	0.241
	4	0.10448	0.22780	0.00	0.32500	0.77500	0.321	0.294
	6	0.10546	0.24384	0.00	0.32500	0.77500	0.324	0.315
0.1	8	0.10576	0.24814	0.00	0.32500	0.77500	0.325	0.320
	10	0.10590	0.24998	0.00	0.32500	0.77500	0.326	0.323
	12	0.10597	0.25094	0.00	0.32500	0.77500	0.326	0.324
	.	.	.	.	.	.	.	.
	50	0.10612	0.25295	0.00	0.32500	0.77500	0.327	0.326
	2	0.37927	0.56337	0.00	0.55000	0.85000	0.690	0.663
	4	0.38472	0.58855	0.00	0.55000	0.85000	0.699	0.692
	6	0.38613	0.59469	0.00	0.55000	0.85000	0.702	0.700
0.4	8	0.38655	0.59632	0.00	0.55000	0.85000	0.703	0.702
	10	0.38674	0.59701	0.00	0.55000	0.85000	0.703	0.702
	.	.	.	.	.	.	.	.
	50	0.38703	0.59811	0.00	0.55000	0.85000	0.704	0.704
	2	0.75883	0.79979	0.00	0.92500	0.97500	0.820	0.820
	4	0.75910	0.80012	0.00	0.92500	0.97500	0.821	0.821
0.9	6	0.75916	0.80019	0.00	0.92500	0.97500	0.821	0.821
	.	.	.	.	.	.	.	.
	50	0.75920	0.80024	0.00	0.92500	0.97500	0.821	0.821

The $\bar{A}_{45}$'s are identically zero in all cases.

ratic equation for the two values of m defining the two generalized principal planes:

$$m^2 + \frac{B_1 - B_2 + A_2 - A_1}{C_2 - C_1} m - 1 = 0. \tag{16}$$

Shear Rigidities for Some Regular Composite Laminates

A class of laminate profiles of considerable importance is that composed of plies or ply groups of the same orthotropic (or transversely isotropic) material and thickness. This class includes regular cross-ply and angle-ply profiles among others. Shear rigidities for several such profiles are presented here to reveal their inherent nature. The ratio of the two shear stiffnesses Q_{55} and Q_{44}, $\lambda = Q_{44}/Q_{55}$, is an obvious parameter of interest.

Both ply angle of a material and orientation of the generalized principal plane for $\bar{\Gamma}_{55}$ are angular measures of importance and their sign convention should be emphasized. As shown in Fig. 2, both angles are considered positive if they are measured in a counterclockwise sense from the x-axis. Note that this convention may be opposite to others (for example, Tsai and Hahn (1980)), where the angle is considered positive when measured from the fiber direction to the coordinate axis in a counterclockwise sense.

Because only one material is involved, all profiles are inertially homogeneous so that $\rho_2 = 0$ and Eq. (10) reduces to $\bar{\Gamma}_{55} = \rho_3 \omega_2^2$ and $\bar{\Gamma}_{44} = \rho_3 \omega_1^2$. The values for $\bar{\Gamma}_{55}$ and $\bar{\Gamma}_{44}$ quoted herein are nondimensionalized by $Q_{55}\,H$, where H is the total thickness and Q_{55} is the major shear stiffness, i.e., the larger of the two stiffnesses so that $\lambda \leq 1$. Thus, the shear rigidities for an actual plate can be found by scaling the pertinent data by $Q_{55}\,H$ for the profile under consideration.

While the transverse shear stiffnesses $\bar{\Gamma}_{55}$ and $\bar{\Gamma}_{44}$ are of primary interest, the tables include calculations for $\bar{A}_{55}$, $\bar{A}_{44}$, and $\bar{A}_{45}$, which are based on the ply properties with respect to the principal shear directions, i.e.,

Table 5 $\pi/4(0/90/+45/-45)$ **profile (four plies per group)**

λ	groups	$\bar{\Gamma}_{44}$	$\bar{\Gamma}_{55}$	Pr. Angle	$\bar{A}_{55}=\bar{A}_{44}$	$\bar{k}^2_{22}$	$\bar{k}^2_{11}$
	1	0.10710	0.21478	67.50	0.550	0.195	0.391
	2	0.14565	0.14565	NA	0.550	0.265	0.265
	3	0.14799	0.14799	NA	0.550	0.269	0.269
0.1	4	0.14870	0.14870	NA	0.550	0.270	0.270
	5	0.14901	0.14901	NA	0.550	0.271	0.271
	.	.	.	.	.	.	.
	10	0.14941	0.14941	NA	0.550	0.272	0.272
	1	0.39100	0.57221	67.50	0.700	0.559	0.817
	2	0.46650	0.46650	NA	0.700	0.666	0.666
0.4	3	0.46863	0.46863	NA	0.700	0.669	0.669
	4	0.46925	0.46925	NA	0.700	0.670	0.670
	.	.	.	.	.	.	.
	10	0.46987	0.46987	NA	0.700	0.671	0.671
	1	0.76102	0.79795	67.50	0.950	0.801	0.840
	2	0.77909	0.77909	NA	0.950	0.820	0.820
0.9	3	0.77915	0.77915	NA	0.950	0.820	0.820
	.	.	.	.	.	.	.
	10	0.77918	0.77918	NA	0.950	0.820	0.820

The $\bar{A}_{45}$'s are identically zero in all cases.

NA - not applicable, fully balanced profile, all planes are principal planes.

Table 6 $\pi/4(0/90/+45/-45)_s$ **symmetric profile (four plies per group)**

λ	groups	$\bar{\Gamma}_{44}$	$\bar{\Gamma}_{55}$	Pr. Angle	$\bar{A}_{55}=\bar{A}_{44}$	$\bar{k}^2_{22}$	$\bar{k}^2_{11}$
	2	0.12684	0.16901	-66.67	0.550	0.231	0.307
	4	0.13850	0.16008	-67.43	0.550	0.252	0.291
0.1	6	0.14223	0.15664	-67.48	0.550	0.259	0.285
	8	0.14408	0.15489	-67.49	0.550	0.262	0.282
	10	0.14518	0.15383	-67.50	0.550	0.264	0.280
	2	0.43202	0.50553	-67.27	0.700	0.617	0.722
	4	0.45182	0.48773	-67.48	0.700	0.645	0.697
0.4	6	0.45798	0.48181	-67.49	0.700	0.654	0.688
	8	0.46101	0.47885	-67.50	0.700	0.659	0.684
	10	0.46282	0.47708	-67.50	0.700	0.661	0.682
	2	0.77151	0.78680	-67.50	0.950	0.812	0.828
	4	0.77550	0.78285	-67.50	0.950	0.816	0.824
0.9	6	0.77675	0.78161	-67.50	0.950	0.818	0.823
	8	0.77736	0.78100	-67.50	0.950	0.818	0.822
	10	0.77773	0.78063	-67.50	0.950	0.819	0.822

The $\bar{A}_{45}$'s are identically zero in all cases.

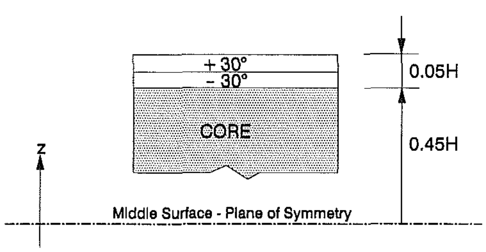

Fig. 3 Symmetrical sandwich profiles

$$\left[\bar{A}_{55}, \bar{A}_{44}, \bar{A}_{45}\right] = \sum_{k=1}^{N} \left[\bar{Q}_{55}^{(k)}, \bar{Q}_{44}^{(k)}, \bar{Q}_{45}^{(k)}\right](h_k - h_{k-1}). \quad (17)$$

From $\bar{\Gamma}_{55}$, $\bar{\Gamma}_{44}$ and $\bar{A}_{55}$, $\bar{A}_{44}$, the shear correction factors, $\bar{k}_{11}^2$ and $\bar{k}_{22}^2$ can be computed, i.e., $\bar{k}_{11}^2=\bar{\Gamma}_{55}/\bar{A}_{55}$ and $\bar{k}_{22}^2=\bar{\Gamma}_{44}/\bar{A}_{44}$. These shear correction factors should be of interest when comparing present values with those from previous studies on first-order shear deformation theory for laminated composite plates and shells. Note that $\bar{A}_{45}$ has no role even though it may be nonzero for certain profiles. This observation underlies an obvious inconsistency that is obviated by the introduction of generalized principal planes.

Tables 1 and 2 contain data on regular symmetric and antisymmetric (± 45 deg) angle-ply profiles. These are special cases of a cross-ply profile rotated by 45 deg. Therefore, the motions are polarized in two orthogonal planes at ± 45 deg, their principal shear plane orientations. Since the total thickness is held constant in all cases, the data illustrate the variation of shear stiffness with the number of plies. For the antisymmetric profile, a balanced design exist as evinced by $\bar{\Gamma}_{55}=\bar{\Gamma}_{44}$, i.e., isotropy in the transverse shear stiffnesses. In this case, the principal angle is not meaningful because $\Gamma_{45}=0$ for all coordinate systems. From Table 1, it is observed that as the number of plies increase, both shear stiffnesses, $\bar{\Gamma}_{55}$ and $\bar{\Gamma}_{44}$, converge onto the same value, which is that for the corresponding regular antisymmetric profile in Table 2.

Tables 3 and 4 contain data on symmetric and antisymmetric (± 30 deg) angle-ply profiles. The principal angles for a three-ply symmetric profile show the largest departure from the x-coordinate direction, i.e., for $\lambda=0.1$, 0.4, 0.9, the principal angles are -12.13 deg, -10.70 deg, and -10.35 deg, respectively. As the number of plies increases the principal angle

Table 7 Sandwich plate with (+30/−30/core/−30/+30) profile

λ	G_c/G	$\bar{\Gamma}_{44}$	$\bar{\Gamma}_{55}$	Pr. Angle	$\bar{A}_{44}$	$\bar{A}_{55}$	$\bar{A}_{45}$	$\bar{k}^2_{22}$	$\bar{k}^2_{11}$
	0.01	0.00824	0.00824	-26.2	0.05027	0.07773	0.01783	0.164	0.106
0.1	0.05	0.04116	0.04118	-26.2	0.08627	0.11373	0.01783	0.477	0.362
	0.10	0.08226	0.08236	-26.2	0.13127	0.15873	0.01782	0.627	0.519
	0.01	0.00824	0.00824	-26.2	0.06985	0.08815	0.01189	0.118	0.093
0.4	0.05	0.04118	0.04119	-26.2	0.10585	0.12415	0.01189	0.389	0.332
	0.10	0.08235	0.08237	-26.2	0.15085	0.16915	0.01189	0.546	0.487
	0.01	0.00824	0.00824	-26.2	0.10248	0.10552	0.00198	0.080	0.078
0.9	0.05	0.04119	0.04119	-26.2	0.13847	0.14153	0.00198	0.297	0.291
	0.10	0.08237	0.08237	-26.2	0.18347	0.18653	0.00198	0.449	0.442

tends toward zero. The departure from polarized motions for an eleven-layer profile is considerably less than a three-layer profile as seen upon comparison of Figs. 1(*b*) and 1(*c*). In the case of the antisymmetric profile, the coordinate directions are in fact the principal directions because of the balance of shear stiffness with respect to the coordinate directions. For four plies or less in this class of profiles there is a noticeable difference in shear stiffness in the two principal directions, which becomes less distinct as $\lambda \rightarrow 1$.

Tables 5 and 6 are concerned with profiles composed of $\pi/4$ ply groups. A $\pi/4$ ply group consists of a (0/90/+45/−45) lay-up or what is called a quasi-isotropic construction. The tabular data are given for groups of four plies rather than the total number of plies. In Table 5, it is seen that except for a one group profile, some sort of balance with respect to the middle surface exists as revealed by $\bar{\Gamma}_{55}=\bar{\Gamma}_{44}$. Note that $\bar{A}_{55}=\bar{A}_{44}$ for all groups; however, $\bar{\Gamma}_{55}$ is not equal to $\bar{\Gamma}_{44}$ for the profile of one group of four plies. For the case of symmetric layups of $\pi/4$ ply groups, which involves even number of groups for midplane symmetry, there is a noticable difference in the values of $\bar{\Gamma}_{55}$ and $\bar{\Gamma}_{44}$, even though $\bar{A}_{55}=\bar{A}_{44}$. The principal direction tends to −67.5 deg as the number of $\pi/4$ ply groups increase.

Shear Rigidities for a Sandwich Profile

A symmetric sandwich profile, as shown in Fig. 3, was considered. The total thickness is denoted by H and the profile consists of face sheets, each with two orthotropic (±30 deg) plies of thickness $h_{\text{face}}=0.05\text{H}$, and an isotropic core of thickness $h_{\text{core}}=0.90\text{H}$. Let the orthotropic ply shear stiffness, $Q_{55}=G$, the normalization factor in the two relevant parameters: (1) $\lambda=Q_{44}/Q_{55}$, ratio of ply shear stiffnesses and (2) G_c/G, ratio of core to ply stiffness.

Table 7 contains data for $\bar{\Gamma}_{44}$, $\bar{\Gamma}_{55}$, (all values are normalized by $Q_{55}H$) and $\bar{k}^2_{11}$, $\bar{k}^2_{22}$. It shows that the shear rigidities are quite low, reflecting the core's low shear modulus. The corresponding shear correction factors also differ significantly from $\pi^2/12=0.822$, the value associated with a homogeneous isotropic profile. However, for all cases λ, the shear rigidities $\bar{\Gamma}_{55}$ and $\bar{\Gamma}_{44}$, when based on (G_cH), are seen to be nearly equal to $(\pi_2/12)(G_cH)$. This observation shows that the shear rigidity is essentially that based on core shear stiffness with the face shear stiffnesses essentially playing no role.

Concluding Remarks

A procedure has been presented for constructing rational transverse shear constitutive relations for a first-order shear deformation theory suitable for laminated anisotropic shells and plates. The basic concept is analogous to that used by Mindlin (1951) and Dong and Tso (1972). For general laminated anisotropic profiles, it is necessary to hypothesize generalized principal shear planes because of nonpolarized motions. These principal planes were determined by a least-squares minimization of the out-of-plane motions. Data generated for a variety of regular laminated composite profiles showed that when $\lambda=Q_{44}/Q_{55}$ is low, the shear correction factors exhibit a large departure from that for a homogeneous, isotropic profile (where $\bar{k}^2_{11}=\bar{k}^2_{22}=\pi^2/12=0.822$). For highly anisotropic shear stiffnesses, it is essential that appropriate shear rigidities (rather than ad hoc values) be used in structural analysis in order to obtain reliable response data. The tables in this paper have been abbreviated. More complete data may be found in Chun (1991), where data for other profiles, such as $\pi/6$ ply groups and other regular angle-ply and sandwich profiles, are also given.

The accuracy and extent to which this shear constitutive relations capture the behavior in laminated anisotropic shells and plates involving shear are addressed in a companion paper (Chun and Dong, 1991). Note also that the shear rigidities are predicated on flat-plate results and assumed to apply to both plates and shells. The efficacy of this premise needs to be explored.

Finally, it is noted while a macro constitutive relation has been constructed in terms of shear resultants and the generalized shear angles, there is a drawback in terms of an inability to predict local transverse shear stresses from a stress-strain relation. Thus, recourse to equilibrium considerations, using essentially the same procedure as in classical theory, is necessary.

References

Bert, C. W., 1979, "Recent Research in Composite and Sandwich Plate Dynamics, "*Shock and Vibr. Dig.*, Vol. 11, No. 10, pp. 13–23.

Bert, C. W., 1984, "A Critical Evaluation of New Plate Theories Applied to Laminated Composites," *Compos. Struct.*, Vol. 2, pp. 329–347.

Bert, C. W., 1985, "Recent Research in Composite and Sandwich Plate Dynamics-IV," *Shock and Vibr. Dig.*, Vol. 17, No. 11, pp. 3–15.

Chatterjee, S. N., and Kulkarni, S. V., 1979, "Shear Correction Factors for Laminated Plates," *AIAA J.*, Vol. 17, No. 5, pp. 498–499.

Chun, C. K., 1991, "On a First-Order Shear Deformation Theory for Laminated Anisotropic Shells and Plates," PhD Dissertation, Civil Engineering Department University of California, Los Angeles, Calif.

Chun, C. K., and Dong, S. B., 1992, "Shear Constitutive Relations for Laminated Anisotropic Shells and Plates, Part II—Application to Vibration Analysis," ASME Journal of Applied Mechanics, Vol. 59, pp. 380–389.

Dong, S. B., and Tso, F. K. W., 1972, "On Laminated Orthotropic Shell Theory Including Transverse Shear Deformation," ASME Journal of Applied Mechanics, Vol. 39, No. 4, pp. 1091–1097.

Dong, S. B., 1972, "Structural Dynamic Behavior of Laminated Plates and Shells," *Proc. AIAA/ASME/SAE 13th Structs. Struc. Dyn. and Mat. Conf.*, AIAA Paper 72-406.

Dong, S. B., and Pauley, K. E., 1978, "Plane Waves in Anisotropic Plates," *J. Engr. Mech. Div.*, ASCE, 104-EM4, pp. 801–817.

Kapania, R. K., and Raciti, S., 1989, "Recent Advances in Analysis of Laminated Beams and Plates, Part I: Shear Effects and Buckling," *AIAA Journal*, Vol. 27, No. 7, pp. 923–934.

Kapania, R. K., and Raciti, S., 1989, "Recent Advances in Analysis of Laminated Beams and Plates, Part II: Vibrations and Wave Propagation," *AIAA Journal*, Vol. 27, No. 7, pp. 935–946.

Lessia, A. W., 1981, "Plate Vibration Research, 1976–1980: Complicating Effects," *Shock and Vibr. Dig.*, Vol. 13, No. 10, pp. 19–36.

Lessia, A. W., 1987, "A Review of Laminated Composite Plate Buckling," ASME *Appl. Mech. Rev.*, Vol. 40, No. 5, pp. 575–596.

Mindlin, R. D., 1951, "Influence of Rotatory Inertia and Shear on Flexural Motion of Isotropic, Elastic Plates," ASME Journal of Applied Mechanics, Vol. 18, pp. 31-38.

Noor, A. K., and Burton, W. S., 1989, "Assessment of Shear Deformation Theories for Multilayer Composite Plates," ASME Appl. Mech. Rev., Vol. 42, No. 1, pp. 1-13.

Reddy, J. N., 1981, "Finite Element Modeling of Layered, Anisotropic Composite Plates and Shells: A Review of Recent Research," *Sock and Vibr. Dig.*, Vol. 13, No. 12, pp. 3-12.

Reddy, J. N., 1982, "Survey of Recent Research in the Analysis of Composite Plates," *Compos. Tech. Rev.*, Vol. 4, pp. 101-104.

Reddy, J. N., 1985, "A Review of the Literature on Finite-Element Modeling of Laminated Composite Plates," *Shock and Vibr. Dig.*, Vol. 17, No. 4, pp. 3-8.

Reissner, E., 1945, "The Effect of Transverse Shear Deformation on Bending of Elastic Plates," ASME Journal of Applied Mechanics, Vol. 67, pp. A69-A77.

Reissner, E., 1947, "On Bending of Elastic Plates," *Quart. Appl. Math.*, Vol. 5, pp. 55-68.

Reissner, E., 1972, "A Consistent Treatment of Transverse Shear Deformations in Laminated Anisotropic Plates," *AIAA J.*, Vol. 10, No. 5, pp. 716-718.

Reissner, E., 1979, "Note on the Effect of Transverse Shear Deformations in Laminated Anisotropic Plates," *Comp. Meth. Appl. Mech, Engr.*, Vol. 20, No. 3, pp. 203-209.

Tsai, S. W., and Hahn, H. T., 1980, *Introduction to Composite Materials*, Technomic Publishing, Westport, Conn.

Whitney, J. M., and Pagano, N. J., 1970, "Shear Deformation in Heterogeneous, Anisotropic Plates," ASME Journal of Applied Mechanics, Vol. 37, pp. 1031-1036.

Whitney, J. M., 1972, "Stress Analysis of Thick Laminated Composite and Sandwich Plates," *J. Comp. Mat.*, Vol. 6, pp. 426-440.

Yang, P. C., Norris, C. H., and Stavsky, Y., 1966, "Elastic Wave Propagation in Heterogeneous Plates," *Int. J. Solids and Struct.*, Vol. 2, pp. 665-683.

Shear Constitutive Relations for Laminated Anisotropic Shells and Plates: Part II—Vibrations of Composite Cylinders

C. K. Chun

S. B. Dong
Mem. ASME.

Civil Engineering Department,
University of California,
Los Angeles, CA 90024

In Part I of this paper, a system of shear constitutive relations was proposed for a first-order shear deformation theory of laminated anisotropic plates and shells. For laminated anisotropic structures, these shear constitutive equations involved the concept of generalized shear planes. Herein, an extensive parametric study is presented to assess the modeling capability of these shear constitutive relations in a class of laminated composite and sandwich cylinders. Classical theory results are also given in order to fully understand the influence of anisotropy on the accuracy and ranges of validity of both first-order shear deformation theory and classical theory. It is seen that the proposed system of shear constitutive relations provides highly accurate frequency results over the range of anisotropy considered.

Introduction

The low shear moduli in laminated fiber composite plates and shells dispose such structures to greater shear deformation in comparison to their homogeneous isotropic counterparts. Consequently, the range of validity of classical theory is narrowed and a refined theory that accounts for shear deformation is needed. While a plethora of refined theories have appeared, no first-order shear deformation theory is available which is valid for laminated anisotropic shells and plates with arbitrary thickness profiles. In Part I, Dong and Chun (1992) proposed a system of shear constitutive equations for a first-order shear deformation theory. Herein, a study is presented to evaluate the efficacy of these constitutive relations in modeling vibrational behavior of a class of laminated composite structures over a range of material properties of practical interest.

The shear constitutive equations in a first-order shear deformation theory relate shear resultants (Q_1,Q_2) to their corresponding generalized shear angles $(\gamma_{1z},\gamma_{2z})$ in the form:

$$\begin{bmatrix} Q_1 \\ Q_2 \end{bmatrix} = \begin{bmatrix} \Gamma_{55} & \Gamma_{45} \\ \Gamma_{45} & \Gamma_{44} \end{bmatrix} \begin{bmatrix} \gamma_{1z} \\ \gamma_{2z} \end{bmatrix} \tag{1}$$

where $(\Gamma_{55},\Gamma_{44},\Gamma_{45})$ are shear rigidities. Dong and Chun (1992) proposed a method for assigning appropriate values to these shear rigidities. Their procedure may be considered as a generalization of the methodology of Mindlin (1951) and Dong and Tso (1972) for homogeneous isotropic plates and laminated orthotropic profiles, respectively. In order to quantify $(\Gamma_{55},\Gamma_{44},\Gamma_{45})$ for general laminated anisotropic plates and shells, a concept called *generalized principal shear planes* is needed because of the absence of polarized thickness-shear motions. Even though polarization in two mutually orthogonal planes may not exist, Eq. (1) admits a transformation to diagonal form. The hypothesis of generalized principal shear planes overcomes this inconsistency. These principal planes are established by a least-squares minimization of the out-of-plane motions of three-dimensional elasticity results. Upon establishing principal shear rigidities $(\bar{\Gamma}_{55},\bar{\Gamma}_{44})$, values in other coordinates follow via transformation. As an illustration of the procedure, Dong and Chun (1992) presented shear rigidities for some regular symmetric and antisymmetric composite laminates and a sandwich construction.

Herein, an assessment of the accuracy of the response data using these shear constitutive relations is undertaken by comparing the natural frequencies for circular cylindrical shells by 1st SDT with those of three-dimensional elasticity, the latter by finite element analysis due Huang and Dong (1984). In these comparisons, classical theory data are included in order to provide a complete perspective on shear deformation effects. Only the general class of regularly symmetric and antisymmetric composite profiles is studied. However, it represents an important class where many applications have been witnessed.

In the next section the relevant first-order shear deformation theory equations for a cylindrical shell and their specialization to classical theory are summarized. It is recalled that $\bar{\Gamma}_{55}$ and $\bar{\Gamma}_{44}$ are based on infinitely long thickness-shear motions in a

Contributed by the Applied Mechanics Division of The American Society of Mechanical Engineers for presentation at the 1992 ASME Summer Mechanics and Materials Meeting, Tempe, AZ, Apr. 28–May 1, 1992.

Discussion on this paper should be addressed to the Technical Editor, Prof. Leon M. Keer, The Technological Institute, Northwestern University, Evanston, IL 60208, and will be accepted until four months after final publication of the paper itself in the Journal of Applied Mechanics. Manuscript received by the ASME Applied Mechanics Division, Dec. 12, 1990; final revision, May 20, 1991.

Paper No. 92-APM-11.

flat plate. These rigidity values are to be directly incorporated into the analysis of shell structures where curvatures are present. It is tacitly assumed that the curvatures do not affect the shear rigidities so that no modification of their values is made. Also, the shear rigidities, $\overline{\Gamma}_{55}$ and $\overline{\Gamma}_{44}$, were determined independently of any information regarding E_L and E_T. Thus, a parametric study appears to be the only means to gain an appreciation of the role that these parameters on the accuracy and range of validity of this system of first-order shear deformation theory shear constitutive relations.

Natural Oscillations of Cylindrical Shells

Thin shell approximations are invoked, where the shell's radius/thickness (a/H) ratio is assumed small and neglected in comparison to unity. Establish right-handed cylindrical coordinates (x,θ,z) with (x,θ) as the reference surface axial and hoop coordinates and z as the normal or radial measure. In a first-order shear deformation theory the kinematic hypothesis asserts linearity of the shell displacements (U_x,U_θ,W) over the thickness in terms of three reference surface displacements (u_x,u_θ,w) and two bending rotations (β_x,β_θ), i.e.,

$$U_i(x,\theta,z,t)=u_i(x,\theta,t)+z\beta_i(x,\theta,t),\ (i=x,\theta);$$
$$W(x,\theta,z,t)=w(x,\theta,t). \quad (2)$$

The other dependent variables are the eight deformation measures and their corresponding force and moment resultants, which are grouped as follows: $\{\epsilon\}^T=[\epsilon_{xx},\epsilon_{\theta\theta},\gamma_{x\theta}]$, $\{\kappa\}^T=[\kappa_{xx},\kappa_{\theta\theta},\kappa_{x\theta}]$, $\{\gamma\}^T=[\gamma_{xz},\gamma_{\theta z}]$ and $\{N\}^T=[N_{xx},N_{\theta\theta},N_{x\theta}]$, $\{M\}^T=[M_{xx},M_{\theta\theta},M_{x\theta}]$, $\{Q\}^T=[Q_x,Q_\theta]$. The deformation measures in terms of the reference surface displacements and rotations are given by:

$$\epsilon_{xx}=u_{x,x};\quad \epsilon_{\theta\theta}=\frac{1}{a}\,(u_{\theta,\theta}+w);\quad \gamma_{x\theta}=u_{\theta,x}+\frac{1}{a}\,u_{x,\theta} \quad (3)$$

$$\kappa_{xx}=\beta_{x,x};\quad \kappa_{\theta\theta}=\frac{1}{a}\,\beta_{\theta,\theta};\quad \kappa_{x\theta}=\beta_{\theta,x}+\frac{1}{a}\,\beta_{x,\theta} \quad (4)$$

$$\gamma_{xz}=w_{,x}+\beta_x;\quad \gamma_{\theta z}=\frac{1}{a}(w_{,\theta}-u_\theta)+\beta_\theta. \quad (5)$$

In addition to shear constitutive relations of Eq. (1)[1], the constitutive equations relating the force and couple resultants to their corresponding deformations measures are involved:

$$\begin{bmatrix} N \\ M \end{bmatrix}=\begin{bmatrix} A & B \\ B & D \end{bmatrix}\begin{bmatrix} \epsilon \\ \kappa \end{bmatrix} \quad (6)$$

where $[A]$, $[B]$, and $[D]$ contain the extensional, coupling, and flexural rigidities. The five equations of motion are

$$\begin{gathered} aN_{xx,x}+N_{x\theta,\theta}=a(\rho_1\ddot{u}_x+\rho_2\ddot{\beta}_x) \\ aN_{x\theta,x}+N_{\theta\theta,\theta}+Q_\theta=a(\rho_1\ddot{u}_\theta+\rho_2\ddot{\beta}_\theta) \\ aQ_{x,x}+Q_{\theta,\theta}-N_{\theta\theta}=a\rho_1\ddot{w} \\ aM_{xx,x}+M_{x\theta,\theta}-aQ_x=a(\rho_2\ddot{u}_x+\rho_3\ddot{\beta}_x) \\ aM_{x\theta,x}+M_{\theta\theta,\theta}-aQ_\theta=a(\rho_2\ddot{u}_\theta+\rho_3\ddot{\beta}_\theta) \end{gathered} \quad (7)$$

where ρ_1, ρ_2, ρ_3 are inertial integrals of the mass density $\rho(z)$ over the thickness

$$(\rho_1,\rho_2,\rho_3)=\int_h \rho(z)(1,z,z^2)dz. \quad (8)$$

Substituting the force and moment resultants in terms of their corresponding deformation measures, as given by Eqs. (1), (3)–(6), into Eq. (7) leads to five displacement equations of motion, $L_i(u_x,u_\theta,w,\beta_x,\beta_\theta)=0$ $(i=1,2,\ldots,5)$. For sake of brevity, these equations are not given here but they may be found in Chun (1991, pg. 46). Five boundary conditions are involved in first-order shear deformation theory, which along the edge $x=$const. have the following form where the barred quantities refer to prescribed values.

$$\begin{gathered} N_{xx}=\overline{N}_{xx} \text{ or } u_x=\overline{u}_x; \\ N_{x\theta}+\frac{M_{x\theta}}{a}=\overline{N}_{x\theta}+\frac{\overline{M}_{x\theta}}{a} \text{ or } u_\theta=\overline{u}_\theta; \\ Q_x=\overline{Q}_x \text{ or } w=\overline{w}; \\ M_{xx}=\overline{M}_{xx} \text{ or } \beta_x=\overline{\beta}_x; \\ M_{x\theta}=\overline{M}_{x\theta} \text{ or } \beta_\theta=\overline{\beta}_\theta. \end{gathered} \quad (9)$$

For free vibrations with periodic spatial wave forms, the solution is simple harmonic motion in time and space, i.e.,

$$\begin{bmatrix} u_x(x,\theta,t) \\ u_\theta(x,\theta,t) \\ w(x,\theta,t) \\ \beta_x(x,\theta,t) \\ \beta_x(x,\theta,t) \end{bmatrix}=\begin{bmatrix} U_{xn} \\ U_{\theta n} \\ W_n \\ B_{xn} \\ B_{\theta n} \end{bmatrix} e^{i(\pi x/L+n\theta+\omega t)}=\{U\}e^{i(\pi x/L+n\theta+\omega t)} \quad (10)$$

where U_{xn}, $U_{\theta n}$, W_n, B_{xn}, $B_{\theta n}$ are modal amplitudes, n the circumferential wave number, L the half wavelength in the axial direction, and ω the circular frequency. Solution (10) represents an infinite harmonic wave train with periodic conditions every half wavelength L apart. Substitution of Eq. (10) into the five displacement equations of motion yields the standard matrix structural vibration problem

$$[K]\{U\}=\omega^2[M]\{U\} \quad (11)$$

where $[K]$ and $[M]$ are (5×5) hermitian and real positive symmetric matrices whose elements may be found in Chun (1991, pp. 49–50). The solution to Eq. (11) relates ω^2 to a given pair of wave numbers, $1/L$ and n. By systematically varying these wave numbers, the complete frequency spectrum can be covered.

Classical theory equations are obtained by ignoring shear deformation $(\gamma_{xz}=\gamma_{yz}=0)$ and rotatory and coupling inertia $(\rho_2=\rho_3=0)$. Thus, the last two equations of motion in (7) revert to equilibrium equations and β_θ, in terms of the reference surface displacements, takes the form:

$$\beta_x=-w_{,x};\quad \beta_\theta=-\frac{1}{a}(w_{,\theta}-u_\theta). \quad (12)$$

Three equations of motion are involved in classical theory, $L_i(u_x,u_\theta,w)=0$ $(i=1,2,3)$. At the edge $x=$const., four boundary conditions rather than five are accommodated in classical theory. More specifically, the first two and fourth conditions in Eq. (9) remain as given, but the third are fifth combine to become:

$$V_x=\overline{Q}_x+\frac{1}{a}\,\overline{M}_{x\theta,\theta} \text{ or } w=\overline{w}. \quad (13)$$

The solution to the classical theory equations is obtained in the same way, but in terms of the three reference surface displacements, i.e.,

$$\begin{bmatrix} u_x(x,\theta,t) \\ u_\theta(x,\theta,t) \\ w(x,\theta,t) \end{bmatrix}=\begin{bmatrix} U_{xn} \\ U_{\theta n} \\ W_n \end{bmatrix} e^{i(\pi x/L+n\theta+\omega t)}=\{U\}e^{i(\pi x/L+n\theta+\omega t)}. \quad (14)$$

Upon substitution of Eq. (14) into the equations of motion, the same algebraic eigenvalue problem form as that given by Eq. (11) arises, except that the matrix sizes are (3×3). The displacement equations of motion and the components of the

[1]Subscripts 1,2 in Eq. (1) refer to the x and θ directions in cylindrical coordinates.

(3×3) matrices are also contained in Chun (1991, pp. 51–53).

Equations for a plate in rectangular cartesian coordinates may be obtained from the shell equations by first substituting $y=a\theta$ and then taking the limit of $a\rightarrow\infty$ in all pertinent expressions.

Parametric Study of Shear Deformation

The range of validity of classical and first-order shear deformation theory theories is explored herein for the class of regularly symmetric and antisymmetric laminated composite and sandwich cylinders. This class refers to profiles composed of equal thickness laminas of the same unidirectional fiber-reinforced composite material. The bases of comparison are the finite element results predicated on linear three-dimensional elasticity by Huang and Dong (1984).

The amount of shear deformation is influenced by many factors. In a homogeneous isotropic cylinder, the parameters of importance are the radius a, total thickness H, axial wave length L, and circumferential wave number n. Three of these four parameters can be cast into two relevant ratios. They are the radius/thickness (a/H) ratio and the thickness/wave length of vibration (H/L) ratio. While these parameters obviously remain important in laminated composite structures, other factors share equally prominent roles. In this study, the ratio of the transverse shear moduli in the two principal material directions of the composite, $\lambda=G_2/G_1$, the orthotropic extensional moduli ratio, E_L/E_T, the ratio of G_1/E_T, and the number of layers comprising the laminate composite profile are parameters of importance. In all examples involving composites, the transverse shear modulus G_1 is assumed to be along the E_L direction. Moreover, the ratio for G_1/E_T was taken to the 0.5 for all cases with the anticipation that this is representative for typical composites. To also vary this ratio would enlarge the manuscript beyond a reasonable limit. All other parameters are varied by varying the ratios $\lambda=G_2/G_1$ and E_L/E_T.

Previous studies by Whitney and Leissa (1969), using classical theory, established that the extensional/flexural coupling inherent in laminated composite structures diminishes rapidly as the number of layers is increased. In other words, regularly antisymmetric profiles with more than two layers behave essentially as a profile of equal thickness composed of an infinite number of layers, or alternatively, a homogeneous profile. This is also seen to be valid here. Thus, the most critical cases in the present study are those of three (symmetric) or two (antisymmetric) layers and these constructions will occupy the bulk of our attention. Profiles with more than three layers will yield more accurate results in comparison with profiles of two and three layers.

Homogeneous Isotropic Cylinder. Frequency results for a homogeneous isotropic cylinder provide a baseline for assessing changes in the ranges of validity of first-order shear deformation theory and classical theories as a function of the (inherently low) shear rigidity in the class of laminated composite materials under consideration. A radius/thickness ratio a/H of 10 was selected with the view that it represents a reasonable nominal limit on thinness. For bodies with a smaller a/H ratio, analyses using three-dimensional elasticity rather than shell theory would be more appropriate. All frequencies are nondimensionalized by the factor $\sqrt{E/\rho H^2}$, where (E,ρ,H) are Young's modulus, density, and thickness, respectively. Poisson's ratio ν was assumed to be 0.25 in this example. In terms of the pertinent parameters in the present study, $\gamma=G_2/G_1=1$, $E_L/E_T=1$ and $G/E=0.4$. In Fig. 1, the frequency spectra, Ω versus H/L (where $\Omega=\omega/\sqrt{E/\rho H^2}$), for the lowest two branches are plotted for three circumferential wave numbers $(n=0,2,10)$. In these graphs, the percentage differences between results of first-order shear deformation theory and classical theories with the elasticity data are indicated.

It can be seen that both first-order shear deformation theory

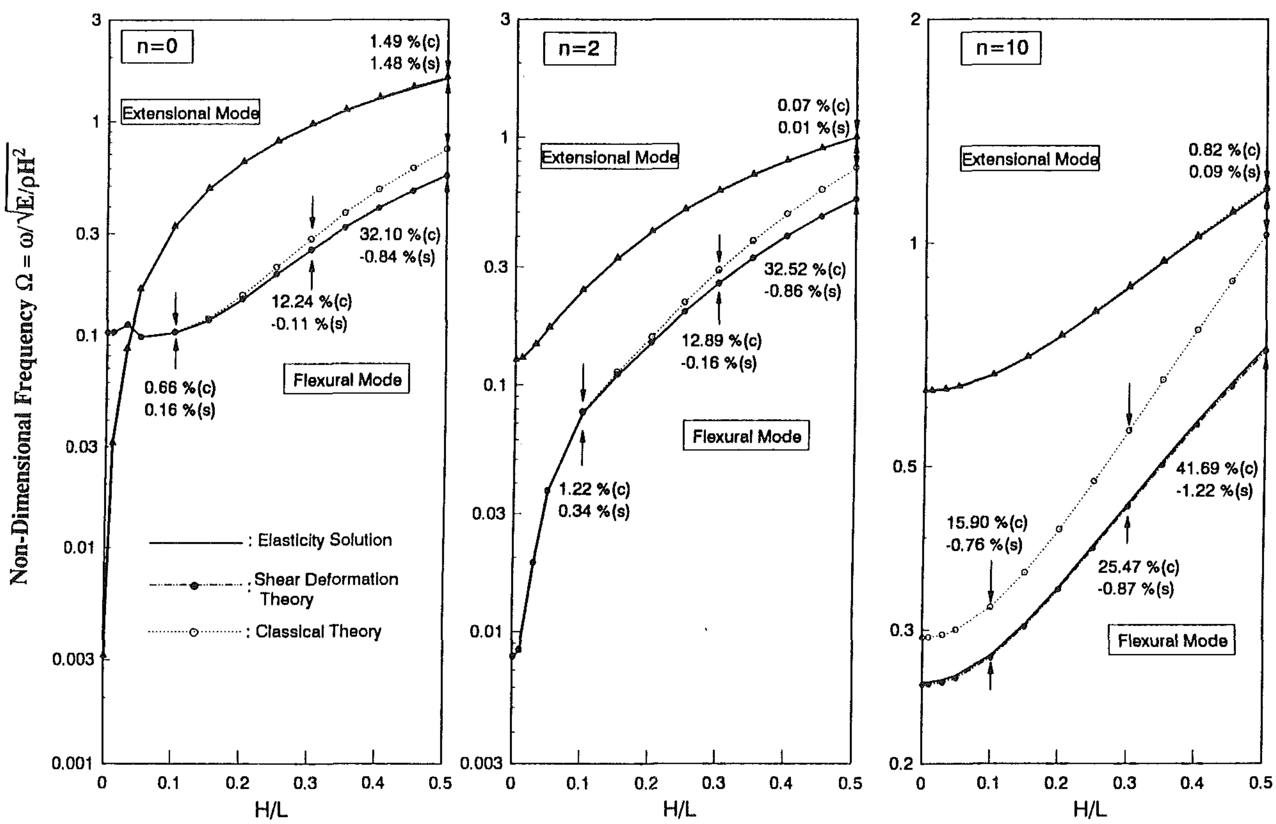

Fig. 1 Frequency spectra for isotropic cylinder-$\nu=0.25$, $a/H=10$

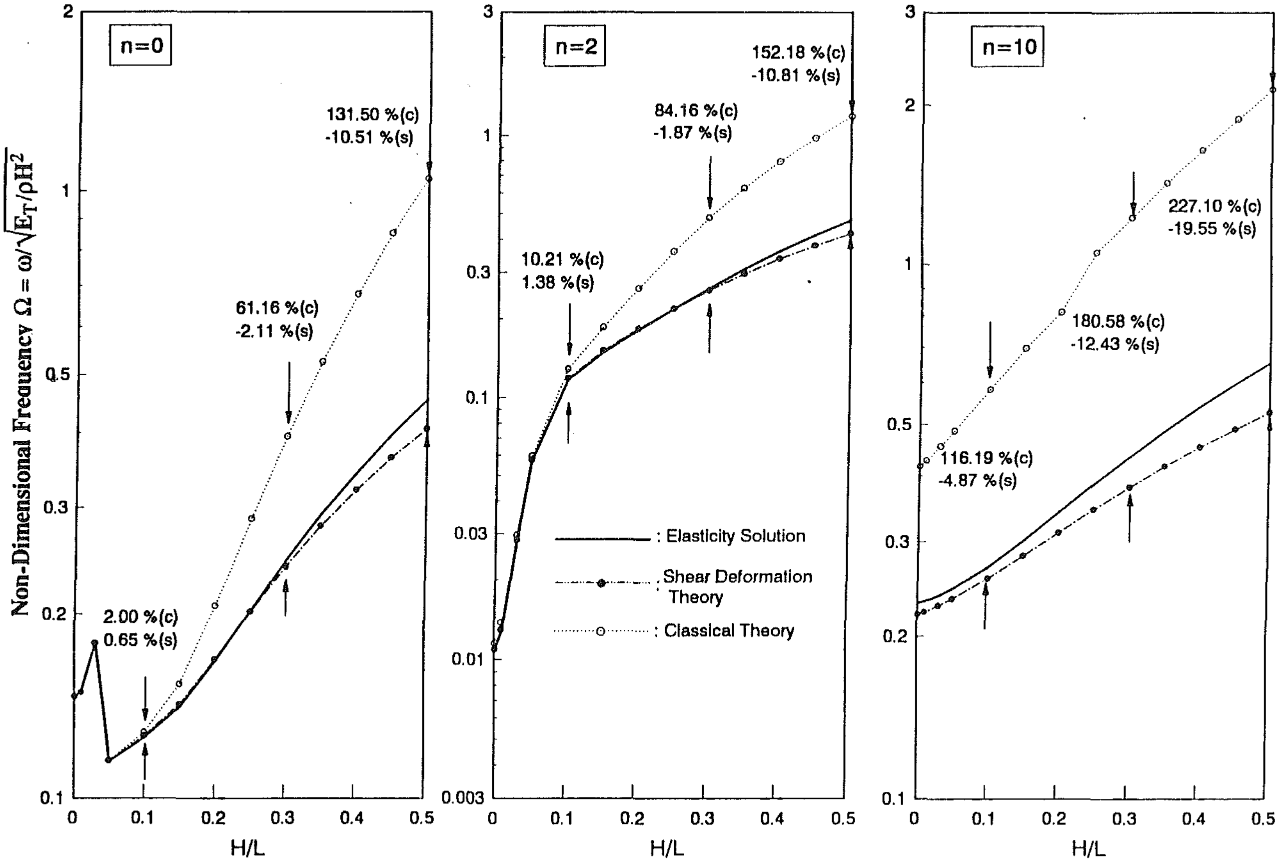

Fig. 2 Frequency spectra for first flexural mode in three-layer ±45 deg angle-ply cylinder-$\lambda = 0.1$, $E_L/E_T = 5$, $a/H = 10$

and classical theory data evince good agreement with three-dimensional elasticity over a wide H/L range for all three circumferential mode numbers. In this case of classical theory, the results are predictably less accurate with decreasing axial wave length and increasing circumferential wave number when shear deformation becomes important.

±45 Degree Angle-Ply Cylinder. This is a special case of a cross-ply (0 deg/90 deg) construction with material axes rotated by 45 deg with the coordinate axes. The thickness shear motions are polarized in two orthogonal planes in this case so that the concept of generalized shear planes is not tested here. Nevertheless, the results provide a benchmark for comparison of profiles with the absence of polarized motions. Again, the radius/thickness ratio $a/H = 10$ and the nondimensional frequency in this case is $\Omega = \omega/\sqrt{E_T/\rho H^2}$, where E_T, ρ, H are respectively, the transverse extensional modulus, mass density, and total thickness of all plies comprising the laminate. The shear rigidities for these two cases are given by Tables 1 and 2 of Part I of the paper.

Frequency spectra for the lowest two modes of vibration for a three-layer cylinder are shown in Figs. 2 and 3 for $E_L/E_T = 5$ and 50, respectively, $\lambda = 0.1$ and circumferential mode numbers $n = 0,2,10$. These figures illustrate the degradation of accuracy of classical theory data with increasing E_L/E_T ratio. It is seen that first-order shear deformation theory retains its accuracy in all cases with the exception of $n = 10$ and $E_L/E_T = 50$. In Fig. 4, the percentage error in the frequencies (percent error $= [(\omega - \omega_{\text{elast}}) \cdot 100/\omega_{\text{elast}}]$) for the specific value of $H/L = 0.1$ are plotted against E_L/E_T for a family of λ values, showing the loss in accuracy with decreasing λ. The modeling capability of first-order shear deformation theory appears to be much more reliable than classical theory over the ranges of E_L/E_T and circumferential mode numbers.

Data for the two-layer ±45 deg cylinder for $E_L/E_T = 5$ and 50 and $\lambda = 0.1$ and $n = 0,2,10$ are plotted in Figs. 5 and 6, respectively. The results show that both first-order shear deformation theory and classical theory for the two-layer ±45 deg lay-up are somewhat more accurate than the three-layer regular symmetric profile. The accuracy of the frequency data for $H/L = 0.1$ as a function of λ is shown in Fig. 7. It can be seen that the results for the two-layer case are less sensitive to λ as the maximum errors for the $E_L/E_T = 50$ are less than four percent for classical theory and 1.5 percent for first-order shear deformation theory.

±30 Degree Angle-Ply Cylinder. For profiles with a ±30 deg angle-ply lay-up, nonpolarized thickness-shear motions exist. The material properties, geometric parameters used here are the same as those of the ±45 deg angle-ply case and the shear rigidities are given in Tables 3 and 4 of Part I of this paper. Spectral curves for a three-layer cylinder with $E_L/E_T = 5$ and 50, $\lambda = 0.1$, and $n = 0,2,10$ are shown in Figs. 8 and 9, respectively. Some dramatic results can be seen in these figures. For example, for $n = 0$ and $H/L = 0.1$, the classical theory result shows a difference of 3.04 percent for $E_L/E_T = 5$ but suffers a considerable loss of accuracy for $E_L/E_T = 50$ where a difference of 40.79 percent is observed. This large disparity due to the higher orthotropy is also seen in circumferential wave numbers $n = 2,10$. The first-order shear deformation theory results are in excellent agreement, with the exception of the case $E_L/E_T = 50$ and $n = 10$. In Fig. 4, the percentage error of the lowest frequency is plotted against E_L/E_T with λ as a parameter. This plot indicates the various influences of these two parameters on the accuracy of first-order shear defor-

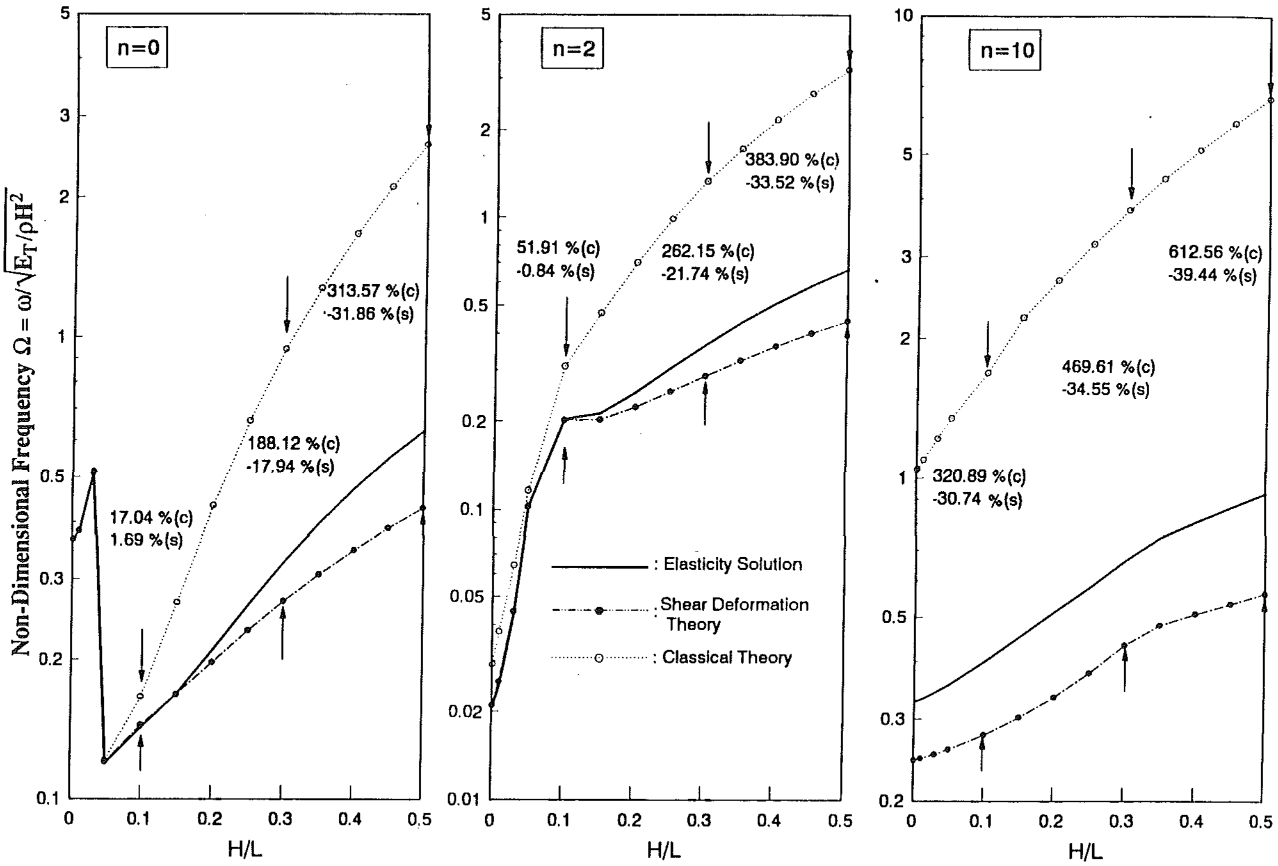

Fig. 3 Frequency spectra for first flexural mode in three-layer ±45 deg angle-ply cylinder-$\lambda = 0.1$, $E_L/E_T = 50$, $a/H = 10$

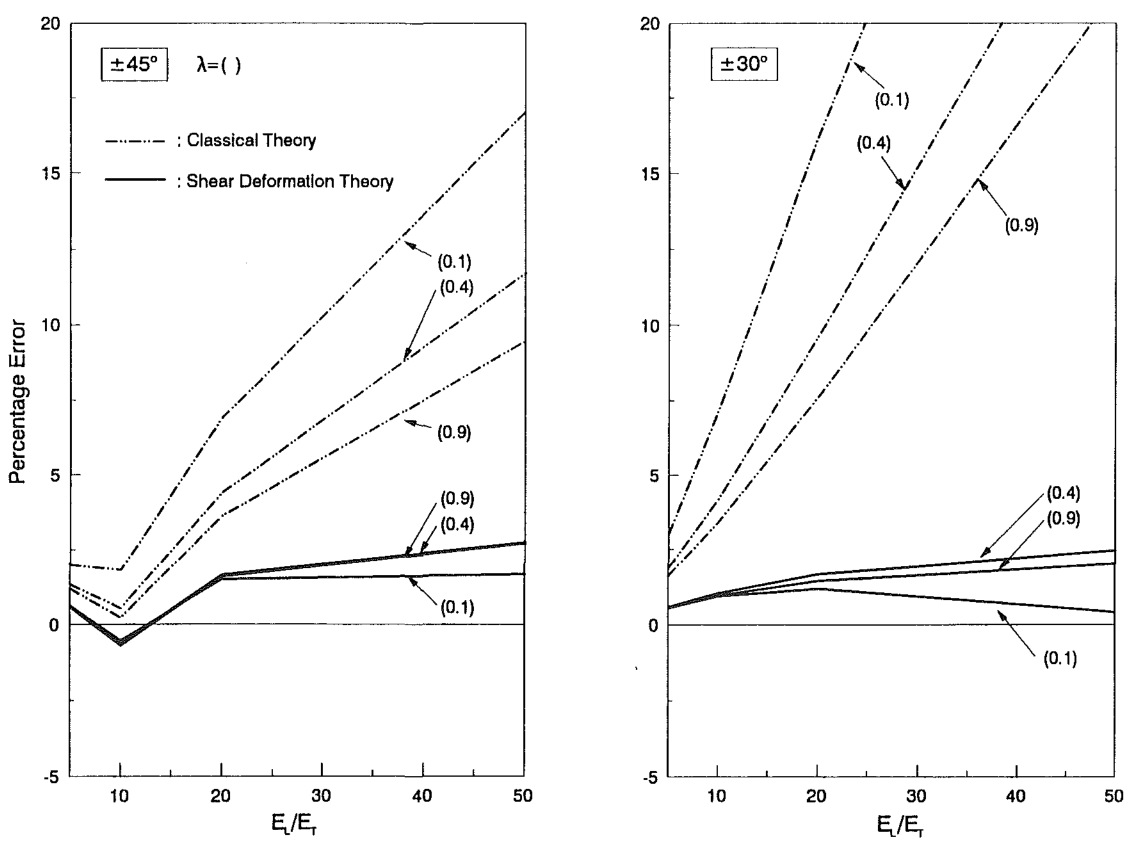

Fig. 4 Percentage difference for three-layer ±45 deg and ±30 deg angle-ply cylinders-$a/H = 10$, $n = 0$, $H/L = 0.1$

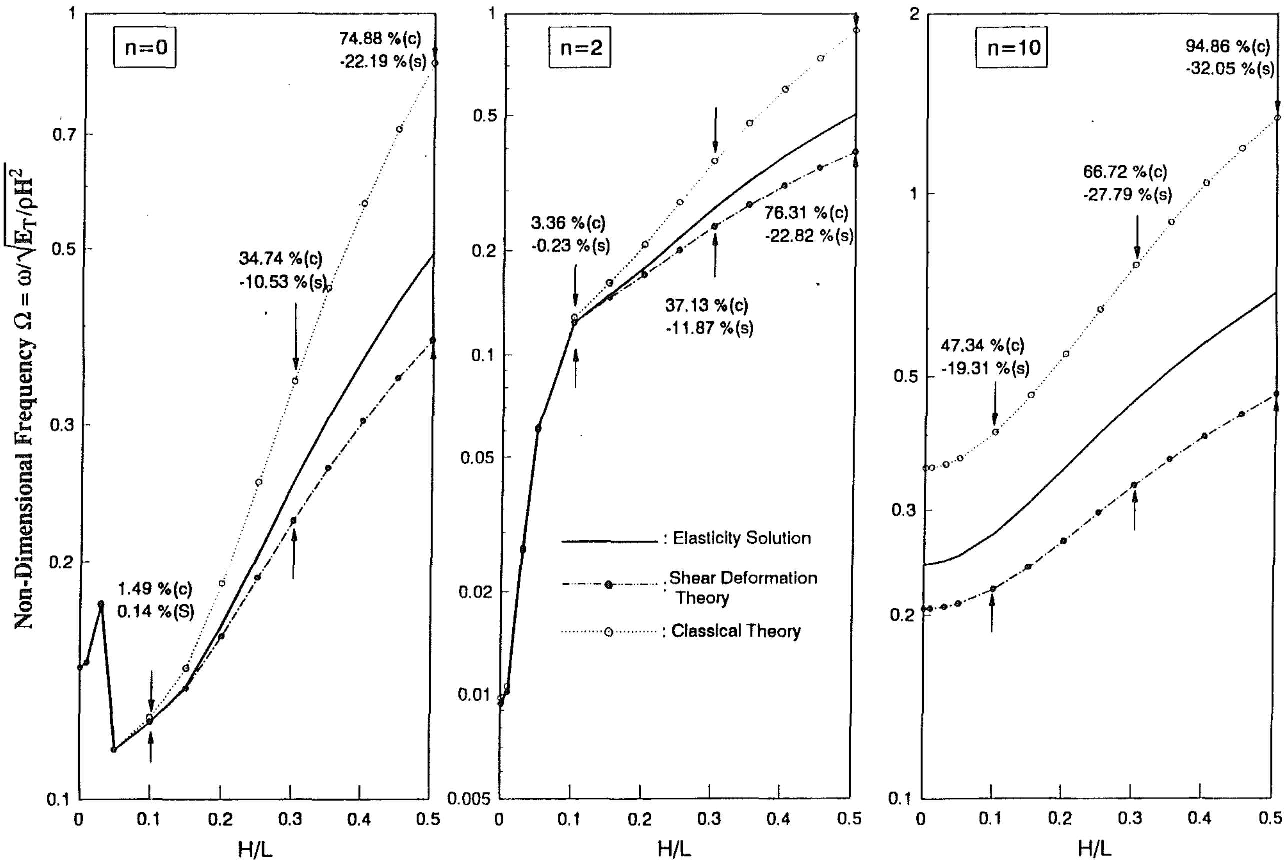

Fig. 5 Frequency spectra for first flexural mode in two-layer ±45 deg angle-ply cylinder-$\lambda = 0.1$, $E_L/E_T = 5$, $a/H = 10$

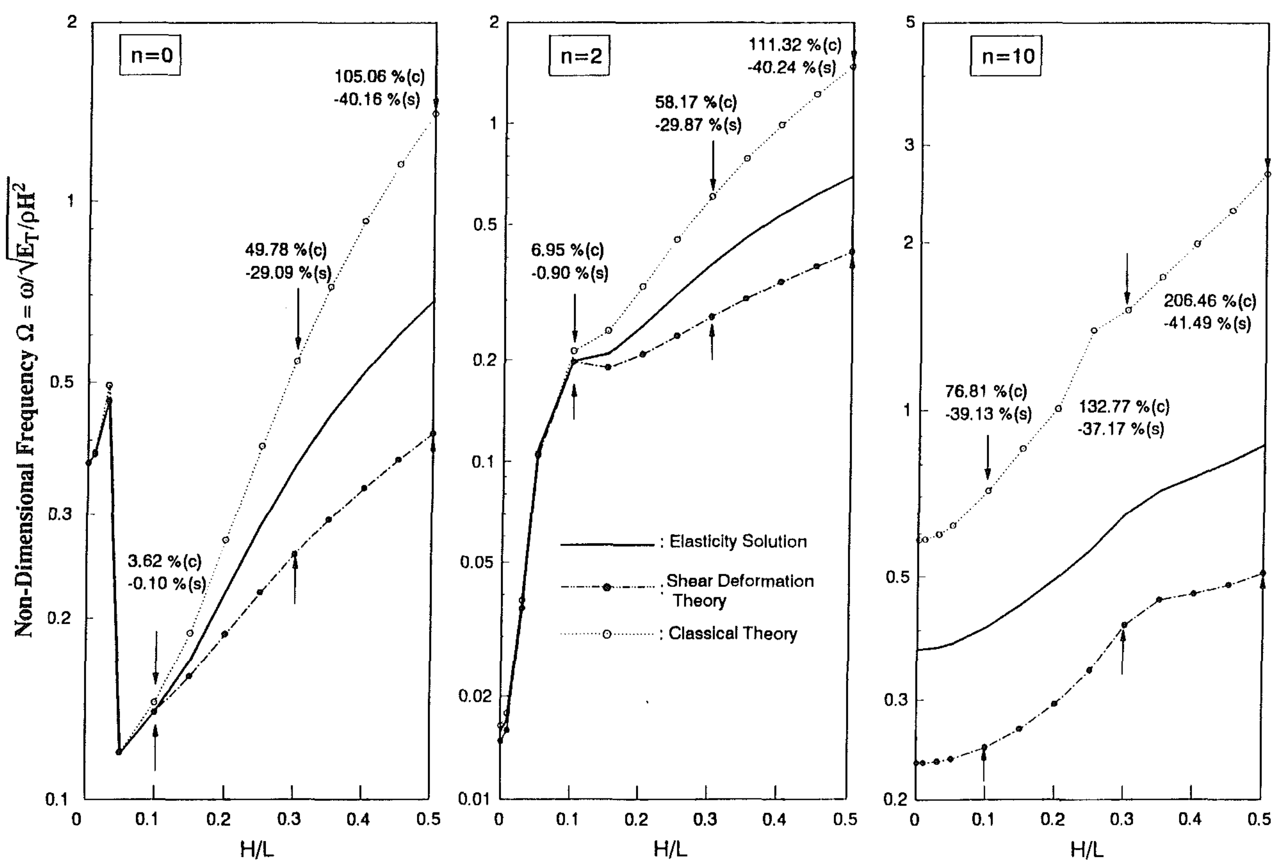

Fig. 6 Frequency spectra for first flexural mode in two-layer ±45 deg angle-ply cylinder-$\lambda = 0.1$, $E_L/E_T = 50$, $a/H = 10$

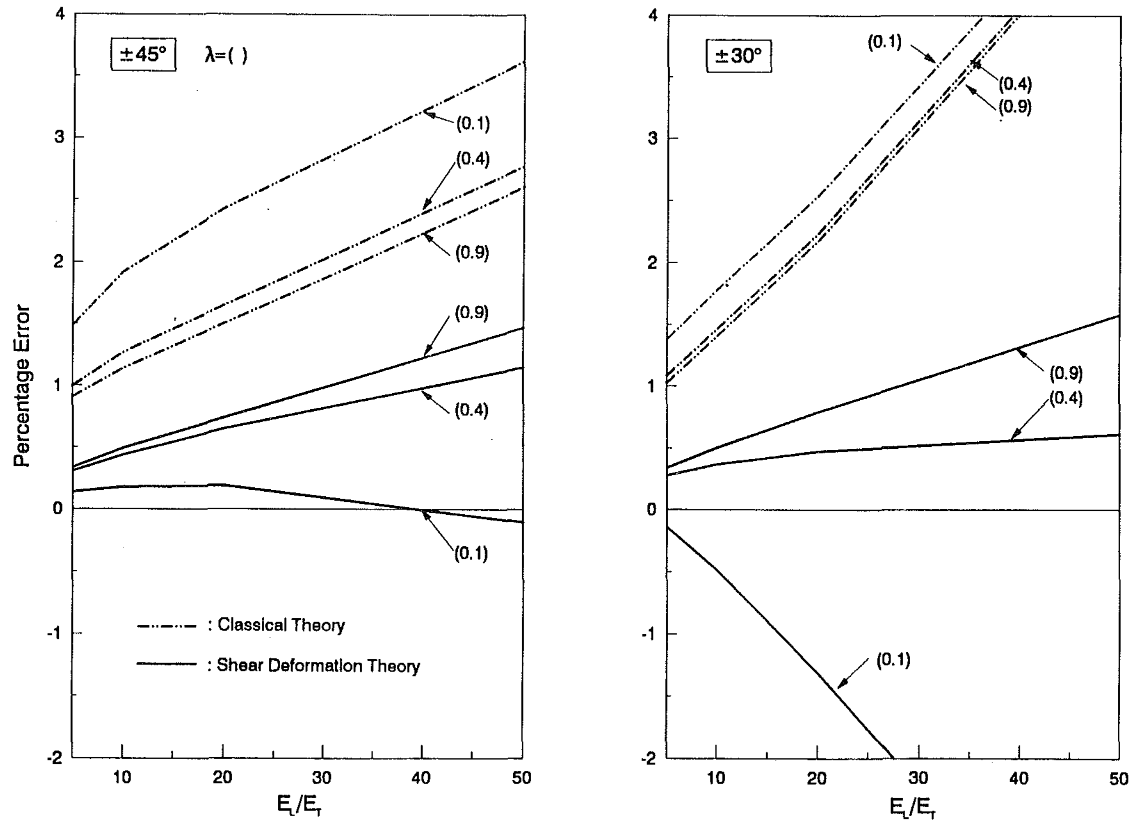

Fig. 7 Percentage difference for two-layer ±45 deg and ±30 deg angle-ply cylinders-$a/H = 10$, $n = 0$, $H/L = 0.1$

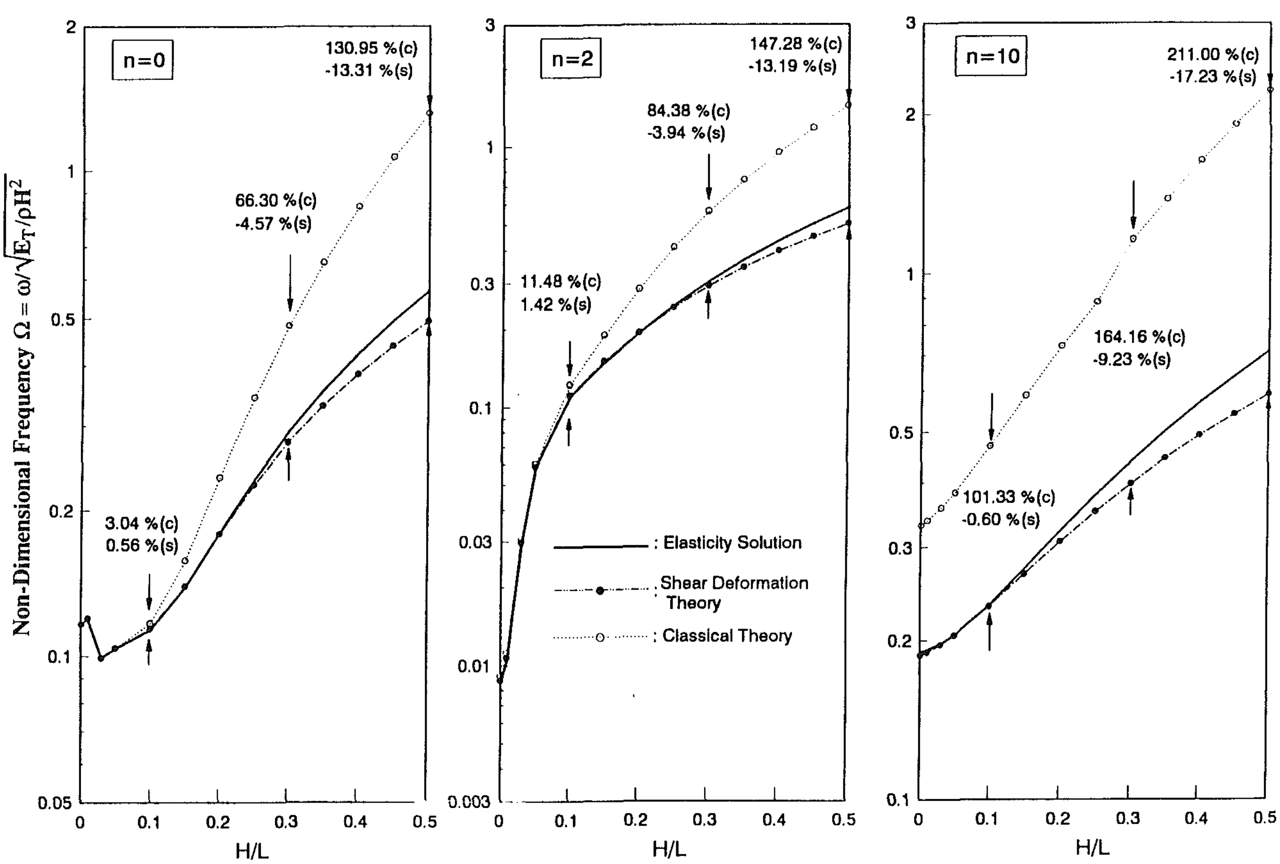

Fig. 8 Frequency spectra for first flexural mode in three-layer ±30 deg angle-ply cylinder-$\lambda = 0.1$, $E_L/E_T = 5$, $a/H = 10$

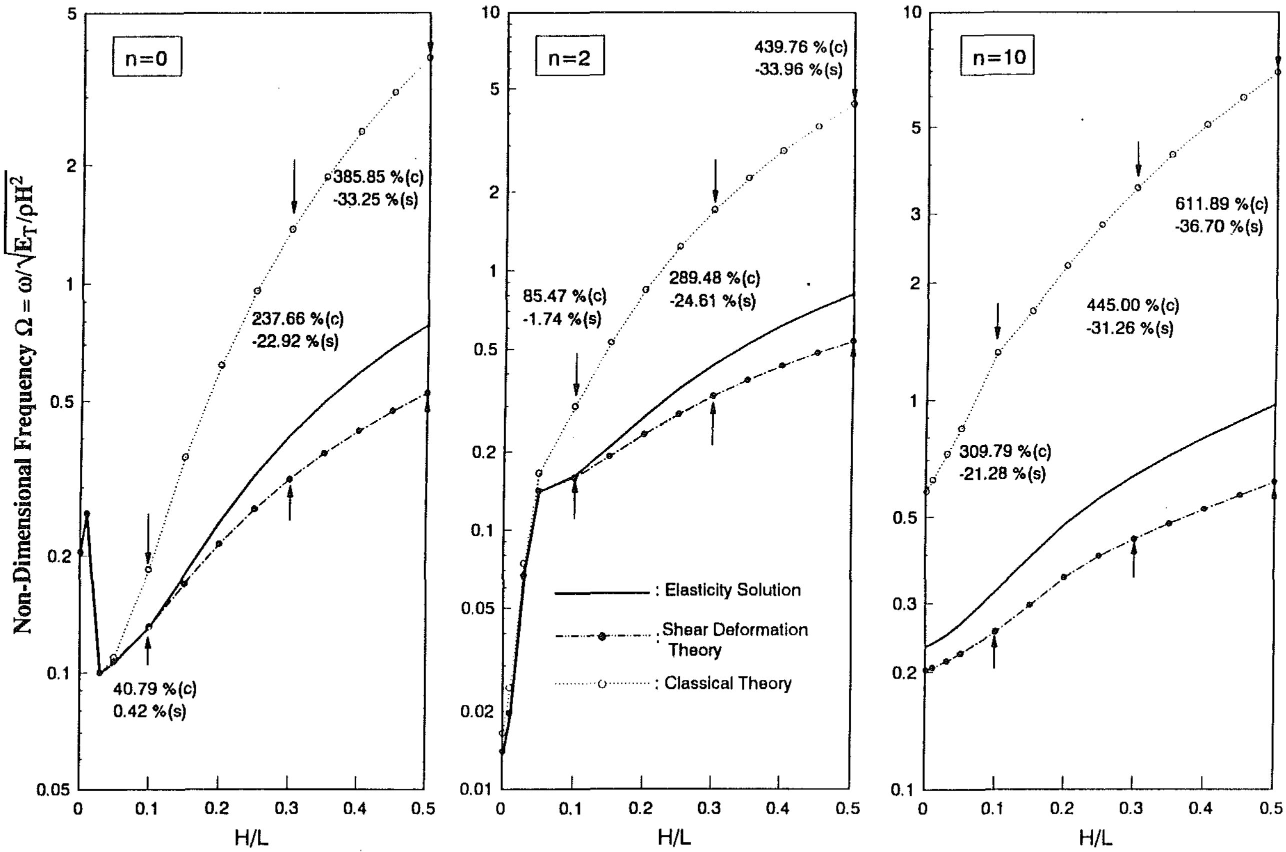

Fig. 9 Frequency spectra for first flexural mode in three-layer ±30 deg angle-ply cylinder-$\lambda = 0.1$, $E_L/E_T = 50$, $a/H = 10$

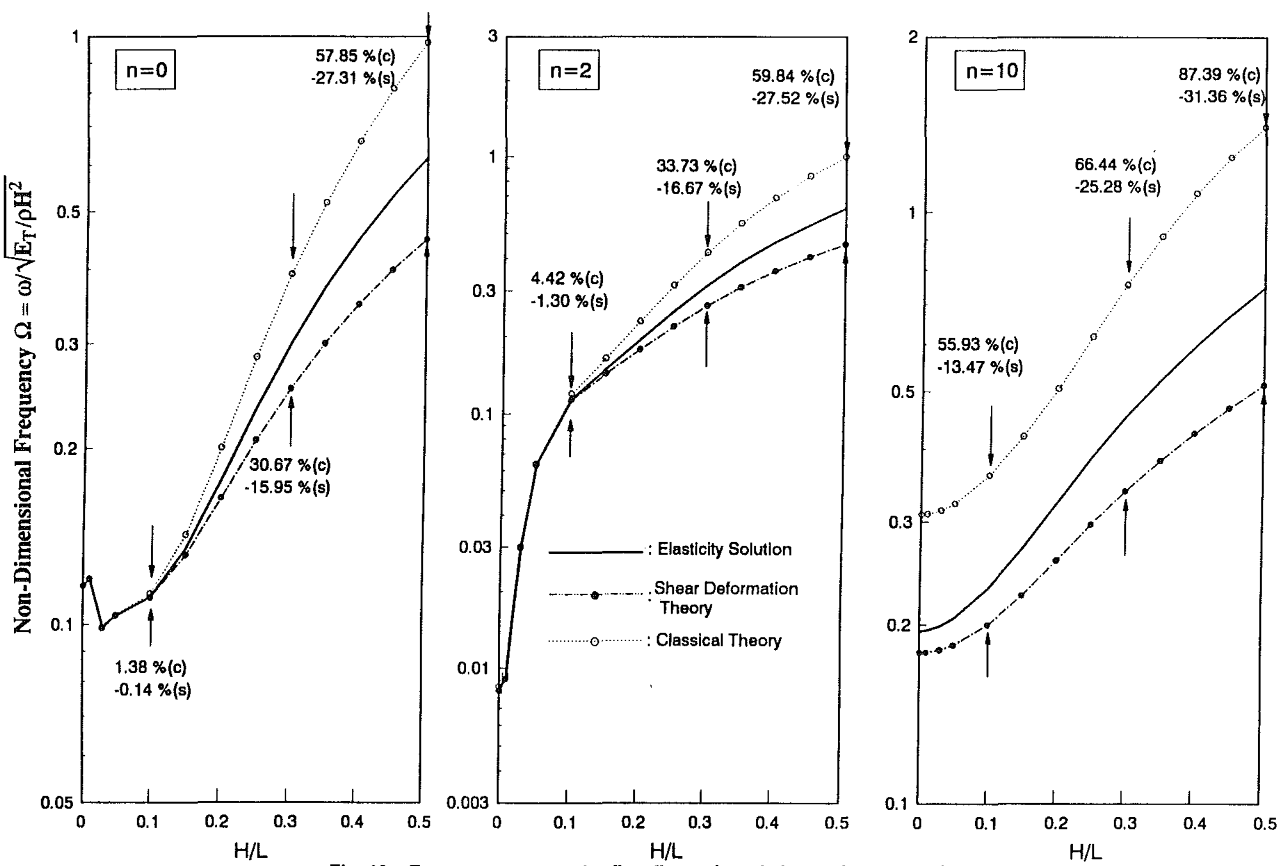

Fig. 10 Frequency spectra for first flexural mode in two-layer ±30 deg angle-ply cylinder-$\lambda = 0.1$, $E_L/E_T = 5$, $a/H = 10$

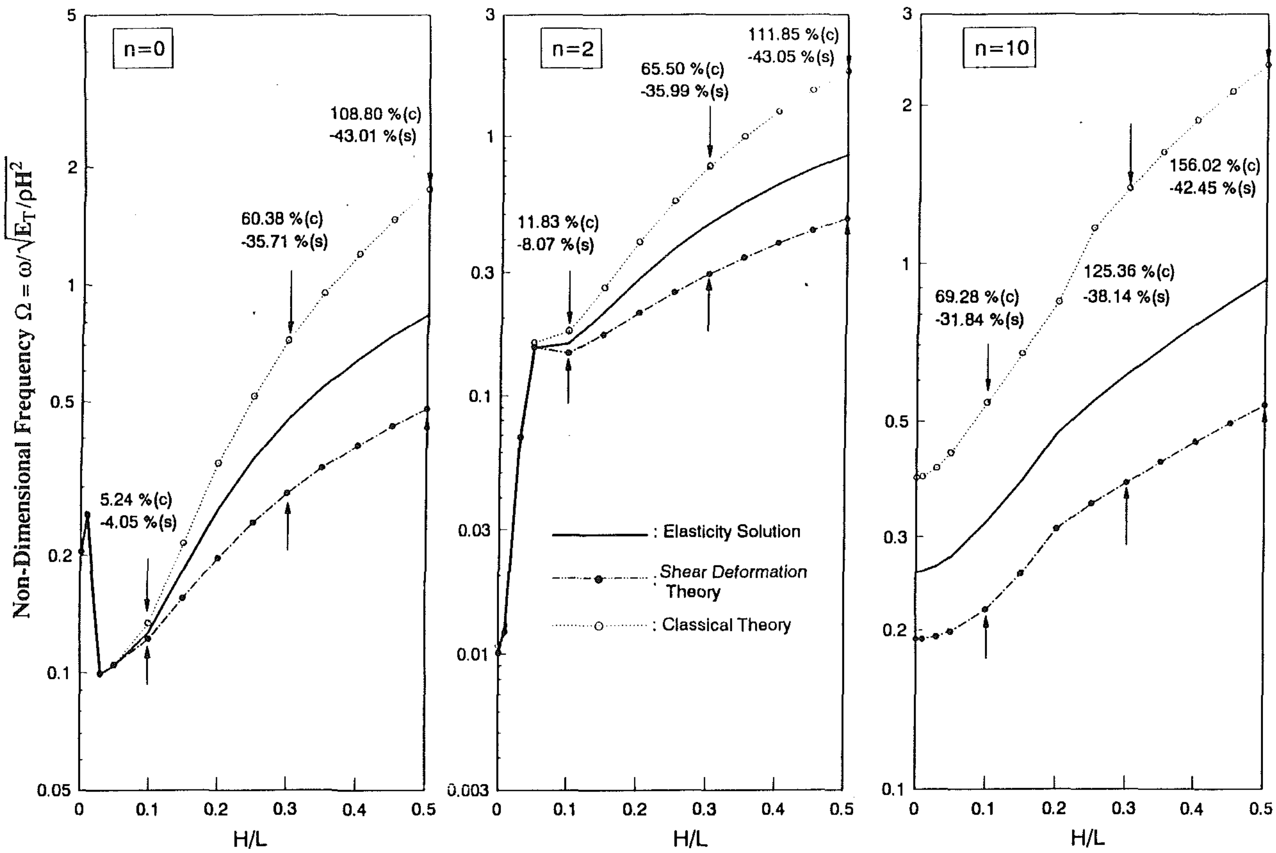

Fig. 11 Frequency spectra for first flexural mode in two-layer ±30 deg angle-ply cylinder-$\lambda = 0.1$, $E_L/E_T = 50$, $a/H = 10$

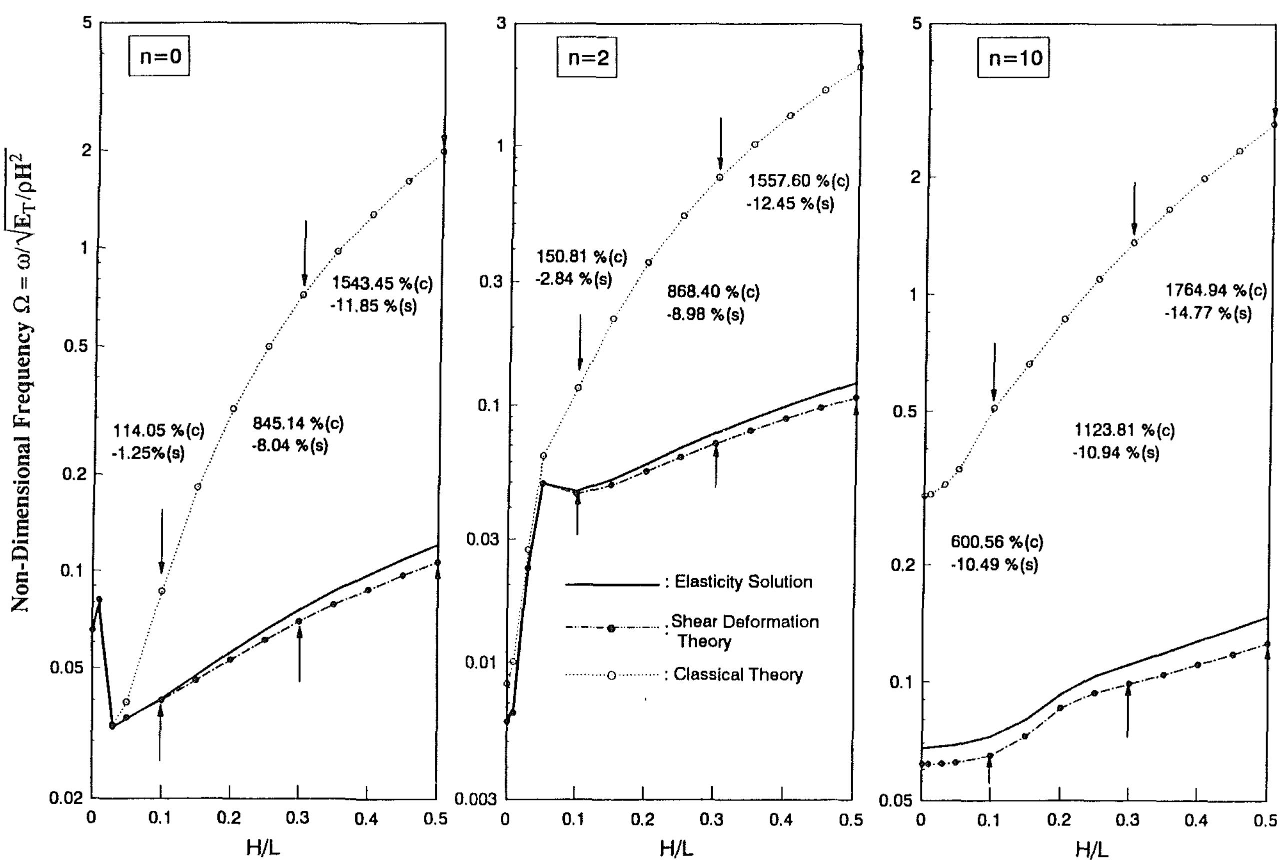

Fig. 12 Frequency spectra for first flexural mode in ±30 deg angle-ply sandwich cylinder-$\lambda = 0.1$, $E_L/E_T = 50$, $G_cG = 0.01$, $a/H = 10$

mation theory and classical theories. As these results are plotted side by side with the ± 45 deg angle-ply case, the error due to nonpolarized motions can also be seen.

Results for a two-layer ± 30 deg angle-ply lay-up are shown in Figs. 10, 11, and 7. The higher accuracy and lower sensitivity to λ for this antisymmetric lay-up are analogous to that seen in the ± 45 deg case.

Sandwich Construction. A sandwich cylinder with ± 30 deg face sheets was considered whose profile is shown in Fig. 3 of Part I. Each face is composed of two plies with a subtotal thickness of 0.05H and an isotropic core of 0.9H thickness. In this class of problems, there is one obvious additional parameter, expressed herein as the ratio G_c/G (ratio of the core shear stiffness to that of the composite). The shear rigidities for this profile are given in Table 7 of Part I. Frequencies are again nondimensionalized by $\sqrt{E_T/\rho H^2}$. In Fig. 12, frequency spectra are plotted for $E_L/E_T = 50$, $G_c/G = 0.01$, $\lambda = 0.1$, and $n = 0,2,10$. This plot shows the first-order shear deformation theory results to be very near the elasticity results but that classical theory results can degenerate quite rapidly with increasing axial and circumferential wave numbers. For parameters evincing less anisotropy, i.e., lower E_L/E_T ratios and higher G_c/G ratios, the differences between classical theory and elasticity are less dramatic. Plots showing these results may be found in Chun (1991).

Conclusions

The main purpose was evaluation of the proposed first-order shear deformation theory shear constitutive relations for the laminated anisotropic plates and shells. An extensive parametric study of the vibration frequencies of cylinders allowed an assessment of the range of validity of these relations. Also, classical theory results were given to provide a clearer understanding of the role of shear deformation in limiting the range of applications.

The numerical vibration results for the class of laminated composite and sandwich cylinders were believed to be a good representation of realistic applications. This parametric study helped delineate the range of validity of both first-order shear deformation theory and classical theory as influenced by the ratios E_L/E_T and $\lambda = G_2/G_1$. The degradation in the accuracy of classical theory results with increasing ratio of E_L/E_T was more evident in the three-layer (symmetric) profiles, and was substantially less in two-layer antisymmetric profiles. In comparison with a homogeneous, isotropic cylinder, the high E_L/E_T ratios and low λ values in laminated composite cylinders can strongly abbreviate the range of application of classical theory. More data on other profiles and on the influence of other parameters may be found in Chun (1991).

These shear constitutive relations based on the concept of generalized shear planes have been shown to possess good modeling capabilities over the application range intended for laminated composite plates and shells. Using the transverse shear stiffness values as reckoned by the proposed method should obviate any need for subsequent refinement of the results such as the a posteriori estimates of Noor and Peters (1989).

References

Chun, C. K., 1991, "On a First-Order Shear Deformation Theory for Laminated Anisotropic Shells and Plates," Ph.D. Dissertation, Civil Engineering Department, University of California, Los Angeles, California.

Dong, S. B., and Chun, C. K., 1992, "Shear Constitutive Relations for Laminated Anisotropic Shells and Plates: Part I—Methodology," ASME Journal of Applied Mechanics, Vol. 59, pp. 372–379.

Dong, S. B., and Tso, F. K. W., 1972, "On a Laminated Orthotropic Shell Theory Including Transverse Shear Deformation," ASME Journal of Applied Mechanics, Vol. 39, pp. 1091–1097.

Huang, K. H., and Dong, S. B., 1984, "Propagating Waves and Standing Vibrations in a Composite Cylinder," *J. Sound and Vibration*, Vol. 96, No. 3, pp. 363–379.

Mindlin, R. D., 1951, "Influence of Rotary Inertia and Shear on Flexural Motions of Isotropic Elastic Plates," ASME Journal of Applied Mechanics, Vol. 18, pp. 31–38.

Noor, A. K., and Peters J. M., 1989, "*A Posteriori* Estimates for Shear Correction Factors in Multilayered Composite Cylinders," *J. Engr. Mech. Div., ASCE*, Vol. 115, No. 6, pp. 1225–1244.

Whitney, J. M., 1969, "Bending-Extension Coupling in Laminated Plates Under Transverse Loading," *J. Comp. Mat.*, Vol. 3, pp. 20–28.

Whitney, J. M., and Leissa, A. W., 1969, "Analysis of Heterogeneous, Anisotropic Plates," ASME Journal of Applied Mechanics, Vol. 36, No. 2, pp. 261–266.

Mathematical Structure of Modal Interactions in a Spinning Disk-Stationary Load System

Jen-San Chen
Graduate Student.

D. B. Bogy
Professor,
Mem. ASME.

Department of Mechanical Engineering,
Computer Mechanics Laboratory,
University of California,
Berkeley, CA 94720

In a previous paper (Chen and Bogy, 1992) we studied the effects of various load parameters, such as friction force, transverse mass, damping, stiffness and the analogous pitching parameters, of a stationary load system in contact with the spinning disk on the natural frequencies and stability of the system when the original eigenvalues of interest are well separated. This paper is a follow-up investigation to deal with the situations in which two eigenvalues of the freely spinning disk are almost equal (degenerate) and strong modal interactions occur when the load parameters are introduced. After comparing an eigenfunction expansion with the finite element numerical results, we find that for each of the transverse and pitching load parameters, a properly chosen two-mode approximation can exhibit all the important features of the eigenvalue changes. Based on this two-mode approximation we study the mathematical structure of the eigenvalues in the neighborhood of degenerate points in the natural frequency-rotation speed plane. In the case of friction force, however, it is found that at least a four-mode approximation is required to reproduce the eigenvalue structure. The observations and analyses presented provide physical insight into the modal interactions induced by various load parameters in a spinning disk-stationary load system.

Introduction

The dynamics of a spinning disk in contact with a stationary load system has attracted much attention because of its applications in such fields as computer disk memory units and circular saws. Iwan and Moeller's (1976) work appears to be the first publication on this subject in which they calculated the natural frequencies of vibration and discussed the instabilities caused by the addition of translational mass, damping, and stiffness in the load system. Ono et al. (1991) extended Iwan and Moeller's work to include the corresponding rotational (pitching) parameters in the load system as well as the friction force between the spinning disk and the stationary load system (see Fig. 1). They concluded that pitching parameters have similar effects as their transverse counterparts and friction force tends to destabilize the forward travelling wave but stabilizes the reflected and backward travelling waves. In an attempt to give an explanation of these phenomena observed from calculations, Chen and Bogy (1992) derived expressions for the derivatives of the eigenvalues with respect to various parameters in the load system. However, this formulation is useful only when the eigenvalues of interest are well separated and interactions between the neighboring modes are negligible. However, it is not uncommon that some eigenvalues (which are purely imaginary in the case of a freely spinning disk) are

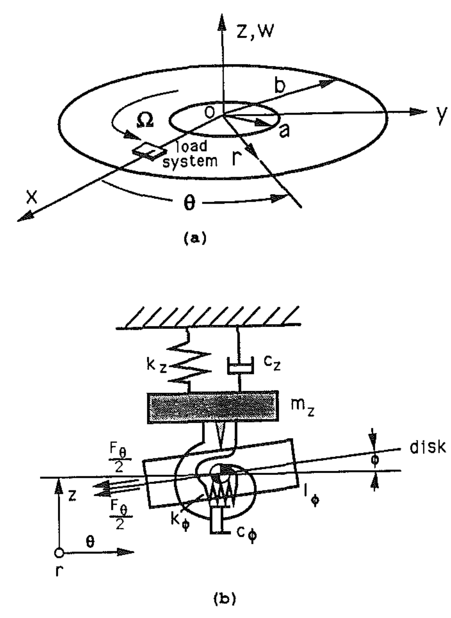

Fig. 1(*a*) Global picture of the spinning disk and the stationary load system, (*b*) parameters in the load system

Contributed by the Applied Mechanics Division of The American Society of Mechanical Engineers for presentation at the 1992 ASME Summer Mechanics and Materials Meeting, Tempe, AZ, Apr. 28–May 1, 1992.

Discussion on this paper should be addressed to the Technical Editor, Professor Leon M. Keer, The Technological Institute, Northwestern University, Evanston, IL 60208, and will be accepted until four months after final publication of the paper itself in the Journal of Applied Mechanics. Manuscript received by the ASME Applied Mechanics Division, Apr. 10, 1991; final revision, July 11, 1991.

Paper No. 92-APM-20.

very close to each other, or even identical. In such cases, the strong interactions between the neighboring modes have to be taken into account when the load parameters are applied. Although modal interactions in a spinning disk-stationary load system have been recognized for some time, the mathematical structure of these phenomena was not well understood.

While perturbation theory is a useful approach for dealing with this problem (Perkins and Mote, 1986), it encounters the difficulty that the radius of convergence of the perturbation series may approach zero as the unperturbed eigenvalues in question get closer to each other. In particular, when two eigenvalues coincide, the radius of convergence may vanish and the perturbation problem becomes singular (Bender and Orszag, 1978).

In the present paper we study the mathematical structure of this eigenvalue problem when two eigenvalues are identical or very close to each other in the frequency-rotation speed parameter space. By using the orthogonality relations developed in Chen and Bogy (1992) and the eigenfunction expansion method, we replace the original partial differential equation by a system of infinite linear homogeneous algebraic equations. Through a sequence of approximations obtained by truncating an infinite dimensional matrix, we establish that the sequence converges very fast to the exact solution in the presence of both the transverse and pitching parameters. Furthermore, it is found that a simple two-mode approximation displays the general features of the eigenvalue changes with the load parameters. Based on the two-mode approximation, we examine analytically the properties of the perturbed eigenvalues as functions of the load parameters when two modes are almost degenerate.

Equation of Motion

Consider a circular, elastic disk rotating in contact with a stationary load system containing transverse mass m_z, spring k_z, dashpot c_z, and the analogous pitching elements I_ϕ, k_ϕ, c_ϕ, as shown in Fig. 1. In addition, the load system applies a constant friction force F_θ to the disk in the circumferential direction at the coupling point between the load system and the spinning disk. The equation of motion of this coupled system, in terms of transverse displacement w and with respect to the stationary coordinate system (r, θ), can be written as

$$\rho h(w_{,tt}+2\Omega w_{,t\theta}+\Omega^2 w_{,\theta\theta})+D\nabla^4 w-\frac{h}{r}(\sigma_r r w_{,r})_{,r}-\frac{h\sigma_\theta}{r^2}w_{,\theta\theta}$$
$$=-\frac{1}{r}\delta(r-\xi)\delta(\theta)\left(m_z w_{,tt}+c_z w_{,t}+k_z w+\frac{F_\theta}{r}w_{,\theta}\right)$$
$$+\frac{1}{r^3}\delta(r-\xi)[(I_\phi w_{,tt\theta}+c_\phi w_{,t\theta}+k_\phi w_{,\theta})\delta(\theta)]_{,\theta} \quad (1)$$

where

$$D=\frac{Eh^3}{12(1-\nu^2)},\quad \nabla^4=\left(\frac{\partial^2}{\partial r^2}+\frac{1}{r}\frac{\partial}{\partial r}+\frac{1}{r^2}\frac{\partial^2}{\partial\theta^2}\right)^2.$$

The parameters Ω, ρ, h, E, and ν are the rotation speed, density, thickness, Young's modulus, and Poisson's ratio of the disk. $\delta(:)$ is the Dirac delta function. The coupling position between the load system and disk is assumed to be $r=\xi$ and $\theta=0$. The spinning disk is clamped at the inner radius $r=a$ and free at the outer radius $r=b$. The generalized plane stresses σ_r and σ_θ are due to the centrifugal effect. We neglect the effect of the friction force on these in-plane stresses because the coefficients of friction in the systems of interest are usually relatively low. Equation (1) can be rewritten in the operator form

$$(M+\hat{M})w_{,tt}+(G+\hat{G})w_{,t}+(K+\hat{K})w=0 \quad (2)$$

where

$$M=\rho h$$
$$\hat{M}=\delta(r-\xi)\delta(\theta)\left(\frac{m_z}{r}-\frac{I_\phi}{r^3}\frac{\partial^2}{\partial\theta^2}\right)-\frac{I_\phi}{r^3}\delta(r-\xi)\delta'(\theta)\frac{\partial}{\partial\theta}$$
$$G=2\rho h\Omega\frac{\partial}{\partial\theta}$$
$$\hat{G}=\delta(r-\xi)\delta(\theta)\left(\frac{c_z}{r}-\frac{c_\phi}{r^3}\frac{\partial^2}{\partial\theta^2}\right)-\frac{c_\phi}{r^3}\delta(r-\xi)\delta'(\theta)\frac{\partial}{\partial\theta}$$
$$K=D\nabla^4+\rho h\left[\Omega^2\frac{\partial^2}{\partial\theta^2}-\frac{1}{\rho r}\frac{\partial}{\partial r}\left(\sigma_r r\frac{\partial}{\partial r}\right)-\frac{\sigma_\theta}{\rho r^2}\frac{\partial^2}{\partial\theta^2}\right]$$
$$\hat{K}=\delta(r-\xi)\delta(\theta)\left(\frac{k_z}{r}-\frac{k_\phi}{r^3}\frac{\partial^2}{\partial\theta^2}+\frac{F_\theta}{r^2}\frac{\partial}{\partial\theta}\right)$$
$$-\frac{k_\phi}{r^3}\delta(r-\xi)\delta'(\theta)\frac{\partial}{\partial\theta}.$$

$\delta'(:)$ is the derivative of the Dirac delta function.

Equation (2) can also be cast in the first-order operator form

$$(\mathbf{A}+\hat{\mathbf{A}})\mathbf{x}_{,t}-(\mathbf{B}+\hat{\mathbf{B}})\mathbf{x}=\mathbf{0} \quad (3)$$

by defining the state vector

$$\mathbf{x}\equiv\begin{Bmatrix} w_{,t} \\ w \end{Bmatrix}$$

and the matrix differential operators

$$\mathbf{A}\equiv\begin{bmatrix} M & 0 \\ 0 & K \end{bmatrix},\quad \hat{\mathbf{A}}\equiv\begin{bmatrix} \hat{M} & 0 \\ 0 & \hat{K} \end{bmatrix},$$
$$\mathbf{B}\equiv\begin{bmatrix} -G & -K \\ K & 0 \end{bmatrix},\quad \hat{\mathbf{B}}\equiv\begin{bmatrix} -\hat{G} & -\hat{K} \\ \hat{K} & 0 \end{bmatrix}.$$

For a freely spinning disk (i.e., in the absence of the load system), Eq. (2) can be reduced to

$$Mw_{,tt}+Gw_{,t}+Kw=0. \quad (4)$$

Since M and K are symmetric and G is skew, Eq. (4) is a standard gyroscopic equation. The eigenvalues of the $e^{\lambda t}$ time-reduced form of Eq. (4), together with the associated homogeneous boundary conditions, are purely imaginary and occur in complex conjugate pairs, i.e., $\lambda_{mn}^0=i\omega_{mn}$, where ω_{mn} is real. The eigenfunction corresponding to λ_{mn}^0 is in general complex and assumes the form

$$w_{mn}^0=R_{mn}(r)e^{\pm in\theta}. \quad (5)$$

R_{mn} is a real-valued function of r. The eigenfunction corresponding to $\overline{\lambda}_{mn}^0$ is $\overline{w}_{mn}^0$, where overbar means complex conjugate. If we consider only the positive ω_{mn}, then w_{mn}^0 in Eq. (5) with $+in\theta$ is a backward travelling wave with n nodal diameters and m nodal circles, which is also denoted by $(m, n)_b$. Similarly, w_{mn}^0 with $-in\theta$ is a forward travelling wave $(m, n)_f$. Of interest is the dependence of the natural frequencies on the rotation speed Ω. The critical speed Ω_c for the mode (m, n) is defined as the rotation speed at which ω_{mn} of the backward travelling wave $(m, n)_b$ is zero. For Ω greater than Ω_c, this mode is a forward travelling wave, and is called a "reflected wave," denoted by $(m, n)_r$. Figure 2 shows the natural frequencies, both positive and negative, for a 5.25-in. computer floppy disk as functions of rotation speed. This result is obtained from a finite element computation presented in Ono et al. (1991). The material properties of the disk used in the calculation are $\rho=1.3\times10^3$ kg/m^3, $E=4.9\times10^9$ N/m^2, $\nu=0.3$, $h=0.078$ mm, $a=17.5$ mm, $b=65.0$ mm, and $\xi/b=0.75$.

It is noted from Fig. 2 that there are four different situations in which two eigenvalues become degenerate, that is, the natural frequency loci intersect.

Case A: A reflected wave meets a backward wave, for example, point A is the intersection of modes $(0,2)_r$ and $(0,1)_b$.

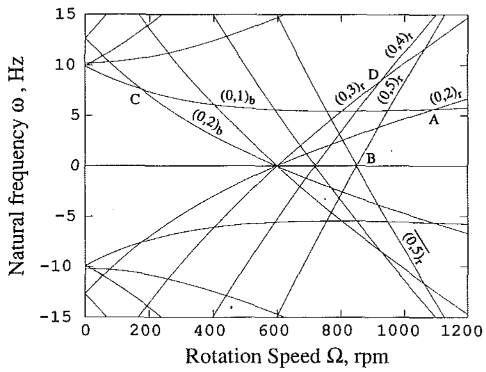

Fig. 2 Natural frequency versus rotation speed for a freely spinning disk

Case B: A backward wave meets its complex conjugate at its critical speed, for example, point B is the intersection of mode (0,5) and its complex conjugate, $\overline{(0,5)}$.

Case C: A forward or backward wave meets another forward or backward wave, for example, point C is the intersection of modes $(0,2)_b$ and $(0,1)_b$.

Case D: A reflected wave meets another reflected wave, for example, point D is the intersection of modes $(0,3)_r$ and $(0,4)_r$.

In the following, we shall study the behavior of eigenvalue changes in the neighborhood of these intersection points resulting from the addition of various load parameters.

Orthogonality Relations and Eigenfunction Expansion Theorem

It has been shown in Chen and Bogy (1992) that for a freely spinning disk, the orthogonality relations among the eigenfunctions can be written as follows:

$$\langle \mathbf{x}^0_{mn}, \mathbf{A}\mathbf{x}^0_{pq}\rangle = 0,\ \langle \mathbf{x}^0_{mn}, \mathbf{B}\mathbf{x}^0_{pq}\rangle = 0 \quad \text{if } \lambda^0_{mn} \neq \lambda^0_{pq} \tag{6}$$

where the inner product between two vectors $\mathbf{x}_{mn}$ and $\mathbf{x}_{pq}$ is defined as

$$\langle \mathbf{x}_{mn}, \mathbf{x}_{pq}\rangle = \int_0^{2\pi}\int_a^b \overline{\mathbf{x}}^T_{mn}\mathbf{x}_{pq} r\,dr\,d\theta$$

into Eq. (4) we get, for each n, an ordinary differential equation for $R_{mn}(r)$,

$$Q_n R_{mn}(r) = (\omega_{mn} \pm n\Omega)^2 R_{mn}(r)$$

where

$$Q_n = \frac{D}{\rho h}\left(\frac{\partial^2}{\partial r^2} + \frac{\partial}{r\partial r} - \frac{n^2}{r^2}\right)^2 - \left[\frac{\partial}{\rho r \partial r}\left(\sigma_r\, r\frac{\partial}{\partial r}\right) - \frac{n^2\sigma_\theta}{\rho r^2}\right].$$

Since Q_n is a self-adjoint linear differential operator in the domain $a \le r \le b$, the system of eigenfunctions $R_{mn}(r)$ is complete (Stakgold, 1979), in the L_2 sense, and the expansion theorem holds for $R_{mn}(r)$. Through a standard procedure for constructing a complete system of functions of two variables (Courant and Hilbert, 1962), it is established that the functions $\{R_{mn}(r)e^{\pm in\theta}\}$ form a complete system of functions in r and θ in the domain $0 < \theta \le 2\pi$, $a \le r \le b$.

After establishing the completeness of the eigenfunctions for a freely spinning disk, we can expand the eigenfunction solution $\mathbf{x}$ of Eq. (3) as the infinite linear combination

$$\mathbf{x} = \sum_{p=0}^{\infty}\sum_{q=-\infty}^{\infty} c_{pq}\mathbf{x}^0_{pq} \tag{8}$$

Substituting Eq. (8) into (3) and taking the inner product between $\mathbf{x}^0_{mn}$ and both sides of Eq. (3), with use of the orthogonality properties (6) and Eq. (7) we get

$$c_{mn}(\lambda - \lambda^0_{mn})\mathbf{A}^{mn}_{mn} + \sum_{p=0}^{\infty}\sum_{q=-\infty}^{\infty} c_{pq}(\lambda\hat{\mathbf{A}}^{mn}_{pq} - \hat{\mathbf{B}}^{mn}_{pq}) = 0$$

where

$$\mathbf{A}^{mn}_{pq} = \langle \mathbf{x}^0_{mn}, \mathbf{A}\mathbf{x}^0_{pq}\rangle$$
$$\hat{\mathbf{A}}^{mn}_{pq} = \langle \mathbf{x}^0_{mn}, \hat{\mathbf{A}}\mathbf{x}^0_{pq}\rangle$$
$$\hat{\mathbf{B}}^{mn}_{pq} = \langle \mathbf{x}^0_{mn}, \hat{\mathbf{B}}\mathbf{x}^0_{pq}\rangle.$$

Continuing this procedure through all the eigenfunctions we obtain an infinite matrix equation satisfied by the coefficients c_{mn}:

$$\mathbf{H}\mathbf{c} = \mathbf{0}$$

where

$$\mathbf{H} = \begin{bmatrix} (\lambda - \lambda^0_{00})\mathbf{A}^{00}_{00} + \lambda\hat{\mathbf{A}}^{00}_{00} - \hat{\mathbf{B}}^{00}_{00} & \lambda\hat{\mathbf{A}}^{00}_{01} - \hat{\mathbf{B}}^{00}_{01} & \ldots\lambda\hat{\mathbf{A}}^{00}_{10} - \hat{\mathbf{B}}^{00}_{10} & \ldots \\ \lambda\hat{\mathbf{A}}^{01}_{00} - \hat{\mathbf{B}}^{01}_{00} & (\lambda - \lambda^0_{01})\mathbf{A}^{01}_{01} + \lambda\hat{\mathbf{A}}^{01}_{01} - \hat{\mathbf{B}}^{01}_{01} & \ldots\lambda\hat{\mathbf{A}}^{01}_{10} - \hat{\mathbf{B}}^{01}_{10} & \ldots \\ \vdots & \vdots & & \\ \lambda\hat{\mathbf{A}}^{10}_{00} - \hat{\mathbf{B}}^{10}_{00} & \lambda\hat{\mathbf{A}}^{10}_{01} - \hat{\mathbf{B}}^{10}_{01} & & \vdots \\ \vdots & \vdots & & \end{bmatrix}$$

and $\mathbf{x}^T_{mn}$ is the transpose of the state vector $\mathbf{x}_{mn}$. In addition,

$$\lambda^0_{mn} = \frac{\langle \mathbf{x}^0_{mn}, \mathbf{B}\mathbf{x}^0_{mn}\rangle}{\langle \mathbf{x}^0_{mn}, \mathbf{A}\mathbf{x}^0_{mn}\rangle}. \tag{7}$$

To obtain the eigenvalues of Eq. (2) or (3) for the disk-load system, we represent its eigenfunction solution as an expansion in terms of the eigenfunctions of the freely spinning disk. Before proceeding further, it is desirable to argue that the eigenfunction expansion theorem holds in this case, i.e., every continuous complex function $f(r,\theta)$ satisfying the prescribed boundary conditions can be expanded in a uniformly convergent series in the eigenfunctions of the unloaded system

$$f(r,\theta) = \sum_{m=0}^{\infty}\sum_{n=-\infty}^{\infty} c_{mn} w^0_{mn}(r,\theta).$$

First we observe that the complex functions $\{e^{\pm in\theta}\}$ are complete, in the L_2 sense, in the domain $(0, 2\pi)$. By substituting the separable solution

$$w_{mn}(r,\theta,t) = R_{mn}(r)e^{i(\omega_{mn}t \pm n\theta)}$$

and

$$\mathbf{c} = (c_{00}, c_{01}, \cdots, c_{10}, c_{11}, \cdots)^T.$$

While in practice we are unable to deal with this infinite matrix $\mathbf{H}$, we can always devise an approximation sequence in which we expand $\mathbf{x}$ in terms of N modes with natural frequencies closest to the frequency range of interest. By doing so we can approximate Eq. (1) by a sequence of matrix equations

$$\mathbf{H}_N\mathbf{c}_N = \mathbf{0} \tag{9}$$

where the N by N matrix $\mathbf{H}_N$ is a truncation of matrix $\mathbf{H}$ by retaining only N rows and N columns. The existence of nontrivial solutions $\mathbf{c}_N$ satisfying Eq. (9) requires

$$\det\mathbf{H}_N = 0. \tag{10}$$

Equation (10) defines an Nth order polynomial in λ, which is a function of the various load parameters. In the following we will verify numerically the convergence of this approximation as N increases. It is noted that the off-diagonal terms in $\mathbf{H}_N$ are responsible for the modal interactions between these modes. In the special case in which only the diagonal terms are retained, Eq. (10) is equivalent to a system of N uncoupled linear equations in λ, and the results can be reduced to those presented in Chen and Bogy (1992), where modal interactions were not considered.

Effects of Transverse Mass m_z

It has been shown in Chen and Bogy (1992) that the presence of m_z in the load system tends to decrease the natural frequencies of the forward and backward waves, but increases the natural frequencies of the reflected waves as long as the natural frequency of interest is well separated from the others. However, if two modes are almost degenerate, the modal interactions are so strong that these rules are no longer applicable. The dashed lines in Fig. 3(*a*) are the natural frequency loci of modes $(0, 2)_r$ and $(0, 1)_b$ for a freely spinning disk. These two modes are degenerate when the rotation speed, denoted by Ω_d, is 1092.1 rpm, which corresponds to point A in Fig. 2. The solid lines in Fig. 3(*a*) are the corresponding results for the case $m_z = 0.1$ *g*. Both the solid and dashed lines are obtained by the finite element method. As m_z increases from zero and the rotation speed is lower than Ω_d, the natural frequencies tend to approach each other and eventually merge, while the real parts of λ_{mn} $(=\alpha_{mn} + i\omega_{mn})$ become nonzero and therefore instability is induced. On the other hand, no merging occurs when the rotation speed is higher than Ω_d. Moreover, when $\Omega = \Omega_d$ the natural frequencies separate, with one remaining unchanged and the other decreasing, as shown by the solid lines in Fig. 3(*a*). In Fig. 3(*b*) the rotation speed is fixed at 1090 rpm, just below Ω_d, while m_z ranges from 0 to 3g. The dashed lines, which are obtained by the finite element method show how the eigenvalues change as m_z increases. It is seen that these two natural frequency loci approach each other and merge for m_z greater than m_{z1}, and split again after m_z is greater than m_{z2}.

In order to reproduce the dashed lines in Fig. 3(*b*) by using the eigenfunction expansion method, we followed the procedure described in the preceding section. The solid lines in Fig. 3(*b*) show the progress of convergence as the number of eigenfunctions in the approximation increases. The eigenfunctions used in the expansion method are chosen in such a way

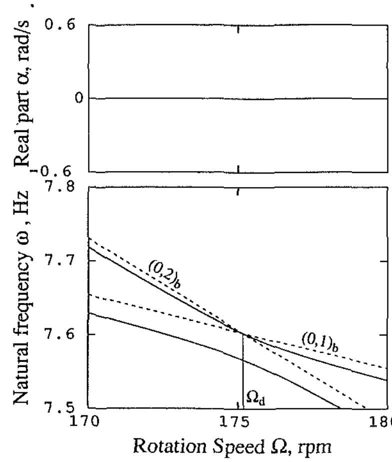

Fig. 4 Effects of transverse mass $m_z = 0.01$g in case C. $\Omega_d = 175.5$ rpm.

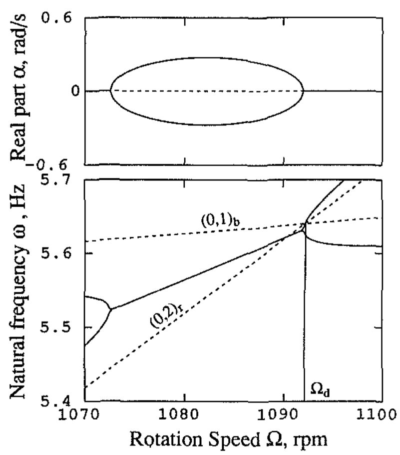

(*a*)

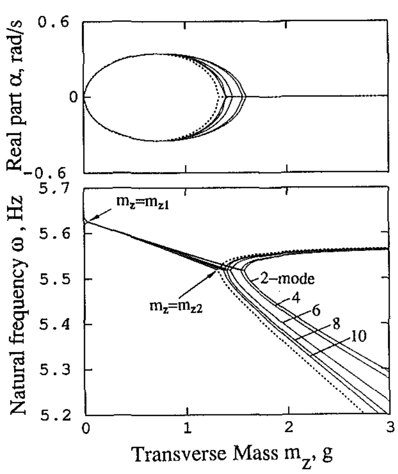

(*b*)

Fig. 3(*a*) Effects of transverse mass $m_z = 0.1$g in case A. $\Omega_d = 1092.1$ rpm. (*b*) Eigenfunction expansion approximations at $\Omega = 1090$ rpm.

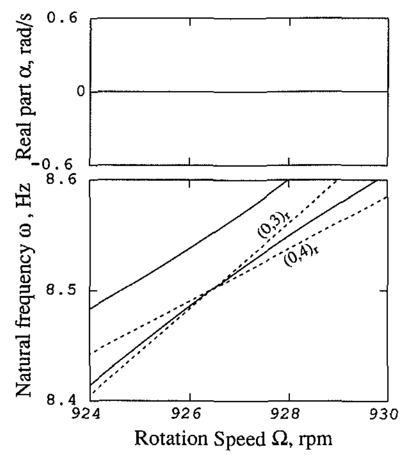

Fig. 5 Effects of transverse mass $m_z = 0.05$g in case D

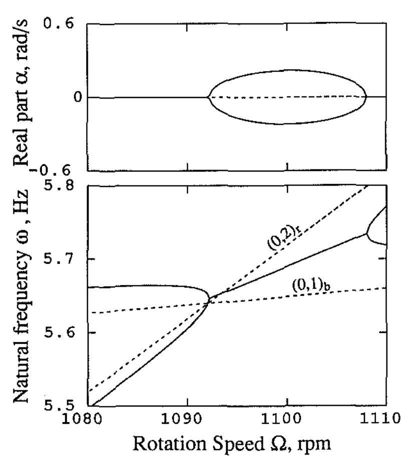

Fig. 6 Effects of transverse stiffness $k_z = 0.1$N/m in case A

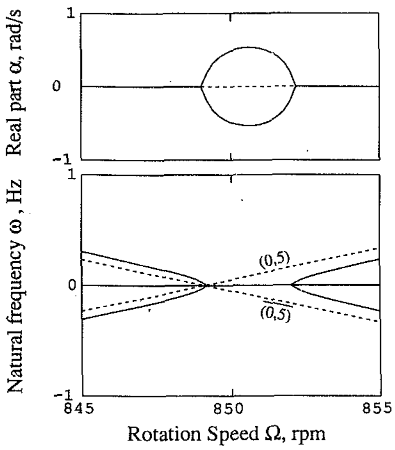

(a)

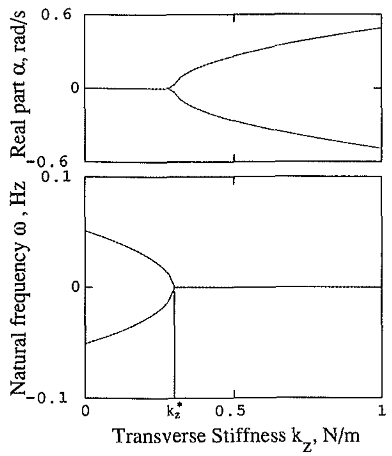

(b)

Fig. 7(*a*) Effects of transverse stiffness k_z = 1N/m in case B. Ω_c = 849.1 rpm. (*b*) Ω = 850 rpm.

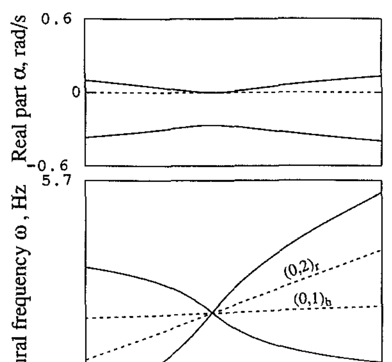

Fig. 8 Effects of transverse damping c_z = 0.01Ns/m in case A

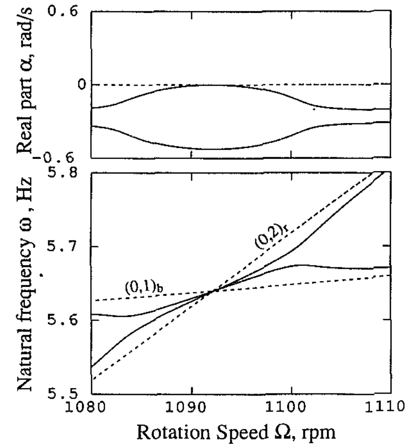

Fig. 9 Effects of friction force F_θ = 0.004N in case A

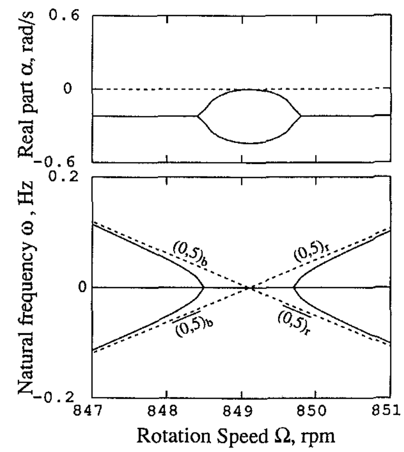

(a)

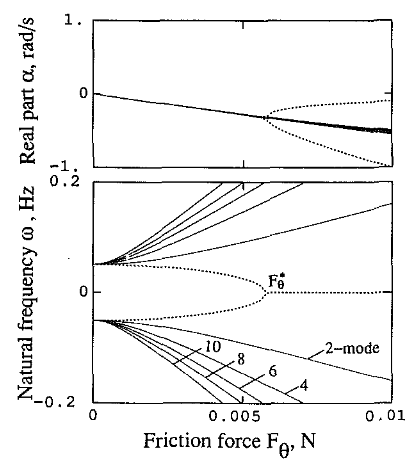

(b)

Fig. 10(*a*) Effects of friction force F_θ = 0.004N in case B. Ω_c = 849.1 rpm. (*b*) Eigenfunction expansion approximations at Ω = 850 rpm.

that their natural frequencies are closest to the frequency range of interest. It is found that the sequence of approximations converges monotonically to the finite element solution, the dashed lines. Furthermore, it is noted that even a simple two-mode approximation displays the important characteristics of the eigenvalue changes, i.e., the existence of a region between m_{z1} and m_{z2} in which two neighboring natural frequency loci merge and one of the modes becomes unstable.

The results presented in Fig. 4 through Figs. 10 are obtained by the finite element method, except those in Figs. 7(*b*) and 10(*b*). The dashed lines in Fig. 4 are the natural frequency loci of modes $(0,2)_b$ and $(0,1)_b$ for the freely spinning disk. These two modes are degenerate at Ω_d = 175.5 rpm, corresponding to point C in Fig. 2. The solid lines correspond to the case of m_z = 0.01 g. It is seen that these two loci veer away from each other in the ω–Ω plane and the degenerate natural frequencies separate with one remaining unchanged at point C and the other decreasing. No instability occurs in this case, since the real part of λ_{mn} remains zero.

Figure 5 shows the effect of m_z on the natural frequencies in the neighborhood of the intersection of two reflected waves $(0,3)_r$ and $(0,4)_r$, corresponding to point D in Fig. 2. The solid lines correspond to the case of $m_z = 0.05$ g, and it is seen that mass causes these two loci to veer away from each other, as in the case of two backward waves, point C.

In the neighborhood of the intersection of a backward wave and its complex conjugate pair, as for point B in Fig. 2, it is found that m_z has very little effect on the natural frequencies, and no instability is induced.

In order to understand the mathematical structure of these phenomena, we look into the details of the two-mode approximation. Assume for the freely spinning disk that the two neighboring modes of interests are w_{mn}^0 and w_{pq}^0 with natural frequencies ω_{mn} and ω_{pq}, respectively,

$$w_{mn}^0 = R_{mn}(r)e^{in\theta}$$
$$w_{pq}^0 = R_{pq}(r)e^{iq\theta}.$$

For convenience, we define some constants

$$R_{mn}^* = \int_a^b R_{mn}^2(r)rdr, \qquad R_{pq}^* = \int_a^b R_{pq}^2(r)rdr$$

$$S_{mn} = R_{mn}^*(\omega_{mn} + n\Omega)R_{pq}^2(\xi), \qquad S_{pq} = R_{pq}^*(\omega_{pq} + q\Omega)R_{mn}^2(\xi)$$

which will be used throughout. For this two-mode approximation, Eq. (10) now becomes a quadratic equation in the eigenvalue λ,

$$(\alpha_0 + \alpha_1\epsilon)\lambda^2 + (\beta_0 + \beta_1\epsilon)\lambda + \gamma_0 = 0 \tag{11}$$

where

$$\left.\begin{aligned}
\alpha_0 &= 16\pi^2\omega_{mn}\omega_{pq}(\omega_{mn} + n\Omega)(\omega_{pq} + q\Omega)R_{mn}^*R_{pq}^* \\
\alpha_1 &= 4\pi\omega_{mn}\omega_{pq}\xi(\omega_{mn}S_{pq} + \omega_{pq}S_{mn}) \\
\beta_0 &= -i(\omega_{mn} + \omega_{pq})\alpha_0 \\
\beta_1 &= -4\pi i\omega_{mn}^2\omega_{pq}^2\xi(S_{mn} + S_{pq}) \\
\gamma_0 &= -\omega_{mn}\omega_{pq}\alpha_0 \\
\epsilon &= \frac{m_z}{\rho h\xi}
\end{aligned}\right\} \tag{12}$$

α_0, α_1, γ_0 are real and β_0 and β_1 are purely imaginary. The solution of (11) can be written in terms of the parameter ϵ as

$$\lambda_{\pm} = \frac{-(\beta_0 + \beta_1\epsilon) \pm [(\beta_0 + \beta_1\epsilon)^2 - 4\gamma_0(\alpha_0 + \alpha_1\epsilon)]^{1/2}}{2(\alpha_0 + \alpha_1\epsilon)} \tag{13}$$

This defines $\lambda_{\pm}(\epsilon)$, where ϵ must be real and positive. In order to understand the mathematical structure of λ, it is convenient to allow ϵ to be complex and consider $\lambda_{\pm}$ as functions of the complex variable ϵ, which are analytic except at the zeros of the square root term. The square root branch points of $\lambda_{\pm}(\epsilon)$ are

$$\epsilon_{\pm} = S_{\pm}(\omega_{pq} - \omega_{mn}) \tag{14}$$

where

$$S_{\pm} = \frac{4\pi S_{mn}S_{pq}}{(\sqrt{S_{mn}} \pm i\sqrt{S_{pq}})^2 R_{mn}^2(\xi)R_{pq}^2(\xi)\omega_{mn}\omega_{pq}\xi}.$$

In case A where w_{mn}^0 is a backward wave and w_{pq}^0 is a reflected wave, we have $n > 0$ and $q < 0$. According to Chen and Bogy (1992), it is found that $S_{mn} > 0$ and $S_{pq} < 0$. Therefore, $S_{\pm}$ are real and negative. When $\Omega < \Omega_d$, it follows that $\omega_{pq} < \omega_{mn}$, and consequently, the branch points $\epsilon_{\pm}$ are real and positive. We choose $|\epsilon_-| < |\epsilon_+|$. When ϵ is real and in the region (ϵ_-, ϵ_+), which corresponds to (m_{z1}, m_{z2}) in Fig. 3(*b*), the imaginary parts of the eigenvalues λ_- and λ_+ are identical and their real parts have opposite signs. When ϵ is real and outside the region (ϵ_-, ϵ_+), the real parts vanish and the imaginary parts are different. On the other hand, when $\Omega > \Omega_d$ the branch points are real and negative, and consequently no merging occurs. In the special case that $\Omega = \Omega_d$ and $\omega_{mn} = \omega_{pq} = \omega$, it is easy to verify that $\lambda = i\omega$ is a root of Eq. (11), and the other root is $\dfrac{i\alpha_0\omega}{\alpha_0 + \alpha_1\epsilon}$. This verifies the observation that one of the degenerate eigenvalues remains unchanged and the other changes. If the perturbed eigenvalue is written in the form of a power series in ϵ, as is the usual procedure in perturbation theory, it is obvious that the radius of convergence of the perturbation series is equal to $|\epsilon_-|$. From Eq. (14) it can be seen that this radius of convergence approaches zero as $\omega_{pq} - \omega_{mn}$ approaches zero. In particular, when $\omega_{mn} = \omega_{pq}$ the radius of convergence vanishes and the perturbation problem becomes singular.

In case C both w_{mn}^0 and w_{pq}^0 are backward waves, and $n > 0$, $q > 0$, $S_{mn} > 0$, $S_{pq} > 0$. As a result $S_{\pm}$ are complex conjugate pairs and so are $\epsilon_{\pm}$. Since the ϵ associated with the physical mass m_z is changed along the positive real line in the complex ϵ-plane and the branch points $\epsilon_{\pm}$ are complex, the square root term in Eq. (13) is always nonzero and purely imaginary. Consequently, λ_+ and λ_- remain purely imaginary and distinct and no frequency merging occurs. Again, at $\Omega = \Omega_d$ and $\omega_{mn} = \omega_{pq} = \omega$, the two eigenvalues are $i\omega$ and $\dfrac{i\alpha_0\omega}{\alpha_0 + \alpha_1\epsilon}$.

In case D, both w_{mn}^0 and w_{pq}^0 are reflected waves, and $n < 0$, $q < 0$, $S_{mn} < 0$, $S_{pq} < 0$. Again, $S_{\pm}$ are complex conjugate pairs and so are $\epsilon_{\pm}$. Therefore the conclusion in the preceding paragraph applies equally well to this case.

In the final case B, w_{mn} is a backward wave and w_{pq} is its complex conjugate, $w_{pq}^0 = \overline{w}_{mn}^0$, and $\omega_{mn} = -\omega_{pq}$. β_0 and β_1 vanish and the eigenvalues are then readily obtained as

$$\lambda_{\pm} = \pm i\left[\frac{2\pi\omega_{mn}^2 S_{mn}}{2\pi S_{mn} + \epsilon\omega_{mn}R_{mn}^4(\xi)\xi}\right]^{1/2}$$

where S_{mn} is positive. Apparently, $\lambda_{\pm}$ are purely imaginary and no instability is induced. Both of the degenerate eigenvalues with $\omega = 0$ remain zero, and the critical speed is not changed by m_z.

Effects of Transverse Stiffness k_z

In cases when the eigenvalue of interest is well separated from the others, k_z tends to increase the natural frequencies of the forward and backward waves but decrease the natural frequency of the reflected wave, just opposite to the effect of m_z. Similar to the case of m_z, these rules are not applicable when the eigenvalues are almost degenerate. Figure 6 shows the effect of $k_z = 0.1$N/m in the neighborhood where modes $(0,1)_b$ and $(0,2)_r$ are degenerate. When the rotation speed is higher than $\Omega_d = 1092.1$ rpm, these two natural frequency loci merge. On the other hand, no merging occurs when $\Omega < \Omega_d$. At Ω_d the degenerate eigenvalues separate, with one remaining unchanged and the other increasing. These phenomena are very similar to those for m_z, except that merging occurs on the opposite side of Ω_d. If we fix the rotation speed a little higher than Ω_d, say at 1094 rpm, and change k_z, we observe a region of k_z between k_{z1} and k_{z2}, in which two natural frequency loci merge and one of these two modes becomes unstable. This characteristic is very similar to that described in Fig. 3(*b*), in which m_z is present and the rotation speed is lower than Ω_d.

The effects of k_z in cases C and D are the same as those of m_z. Veering occurs in the ω-Ω diagram and no instability is induced, which is similar to the behaviors described in Figs. 4 and 5. These observations suggest that the mathematical structure for the effects of k_z and m_z are very similar in cases A, C, and D.

Around point B, which is the intersection of a backward wave and its complex conjugate pair, k_z changes the eigenvalues in a unique way. Figure 7(a) shows that the natural frequency loci of modes (0,5) and $(\overline{0,5})$ merge and one of the modes becomes unstable when Ω is higher than the critical speed $\Omega_c = 849.1$ rpm. When $\Omega < \Omega_c$ these loci tend to diverge away from each other and no instability is induced. In Fig. 7(b) the rotation speed is fixed at 850 rpm, a little higher than Ω_c, and k_z is changed from 0 to 1 N/m. The dashed and solid lines, obtained by finite element method and two-mode approximation, respectively, are almost indistinguishable. It is found that when k_z is increased to k_z^*, the natural frequency loci merge to the value zero. As k_z increases beyond k_z^*, the magnitude of the real part becomes larger. It is also confirmed, through additional calculations not shown here, that a two-mode expansion is a very good approximation to the finite element solution in the cases A, C, and D.

Analogous to the procedure used to study the effects of m_z, we next look into the details of the two-mode approximation for k_z. The eigenvalues $\lambda_\pm$ can be obtained by solving the following quadratic equation:

$$(\alpha_0+\alpha_1\epsilon)\lambda^2+(\beta_0+\beta_1\epsilon)\lambda+(\gamma_0+\gamma_1\epsilon+\gamma_2\epsilon^2)=0 \qquad (15)$$

where α_0, β_0, and γ_0 are the same as those defined in Eq. (12), but α_1, β_1, γ_1, γ_2, and ϵ are changed to

$$\alpha_1=4\pi\xi(S_{pq}\omega_{pq}+S_{mn}\omega_{mn})$$

$$\beta_1=-4\pi\xi i[S_{mn}\omega_{mn}(\omega_{mn}+2\omega_{pq})+S_{pq}\omega_{pq}(\omega_{pq}+2\omega_{mn})]$$

$$\gamma_1=-2\omega_{mn}\omega_{pq}\alpha_1$$

$$\gamma_2=(\omega_{mn}-\omega_{pq})^2R_{mn}^2(\xi)R_{pq}^2(\xi)\xi^2$$

$$\epsilon=\frac{k_z}{\rho h\xi}.$$

The square root branch points of the function $\lambda(\epsilon)$ are the roots of a cubic equation

$$-4\gamma_2\alpha_1\epsilon^3+(\beta_1^2-4\gamma_1\alpha_1-4\gamma_2\alpha_0)\epsilon^2+2(\beta_0\beta_1-2\gamma_0\alpha_1-2\gamma_1\alpha_0)\epsilon+\beta_0^2-4\alpha_0\gamma_0=0 \qquad (16)$$

Since in cases A, C, and D we are interested in the situations where ω_{mn} is almost equal to ω_{pq}, or $|\omega_{mn}-\omega_{pq}| \ll |\omega_{mn}|$, it follows that γ_2 is very small. For the purpose of estimating the roots of Eq. (16), which are closest to the origin, γ_2 may be neglected so that Eq. (16) is reduced to a quadratic equation. In this way the square root branch points of $\lambda(\epsilon)$ can be found at

$$\epsilon_\pm=T_\pm(\omega_{mn}-\omega_{pq})$$

where

$$T_\pm=\frac{4\pi\alpha_0\xi[2\omega_{mn}\omega_{pq}(S_{mn}-S_{pq})-(\omega_{mn}\sqrt{S_{mn}}\pm i\omega_{pq}\sqrt{S_{pq}})^2]}{[\omega_{mn}(\omega_{mn}-2\omega_{pq})S_{mn}+\omega_{pq}(\omega_{pq}-2\omega_{mn})S_{pq}]^2+8\omega_{mn}\omega_{pq}(\omega_{mn}-\omega_{pq})^2S_{mn}S_{pq}}.$$

It is noted that the second term in the denominator is very small compared to the first term because $(\omega_{mn}-\omega_{pq})^2$ is negligible. In case A, where w_{mn} is a backward wave and w_{pq} is a reflected wave, $S_{mn}>0$ and $S_{pq}<0$. In general, the absolute values of S_{mn} and S_{pq} differ significantly because they are determined by different modeshapes. Consequently, the bracket term in the numerator is real and positive. Now since α_0 is negative in case A, both T_+ and T_- are real and negative. When $\Omega > \Omega_d$ we have $\omega_{mn} < \omega_{pq}$ and the branch points $\epsilon_\pm$ are real and positive. When ϵ is real and in the range (ϵ_-, ϵ_+), the imaginary parts of $\lambda_\pm$ coincide and merging occurs, similar to the case of m_z with $\Omega < \Omega_d$. On the other hand, when $\Omega < \Omega_d$, $T_\pm$ are real and negative and no merging occurs. In both cases C and D, $T_\pm$ are complex conjugates and so are $\epsilon_\pm$. The analyses and conclusions are then the same as those in the case of m_z.

In the final case B, for which a backward wave $(m, n)_b$ meets its complex conjugate at the critical speed, β_0 and β_1 vanish. In this case $|\omega_{mn}-\omega_{pq}| \approx 2|\omega_{mn}|$ and γ_2 is no longer negligible. Equation (16) can then be reduced to

$$\lambda^2=-\omega_{mn}\left[\omega_{mn}+\frac{R_{mn}^2(\xi)\xi\epsilon}{2\pi(\omega_{mn}+n\Omega)R_{mn}^*}\right]. \qquad (17)$$

For Ω higher than the critical speed, $\omega_{mn}<0$ and $\lambda(\epsilon)$ has a positive branch point

$$\epsilon^*=\frac{-2\pi\omega_{mn}(\omega_{mn}+n\Omega)R_{mn}^*}{R_{mn}^2(\xi)\xi}$$

which corresponds to k_z^* in Fig. 7(b). For $\epsilon < \epsilon^*$, the bracket in Eq. (17) is negative and $\lambda_\pm$ are purely imaginary. On the other hand, for $\epsilon > \epsilon^*$, $\lambda_\pm$ are real numbers. When Ω is lower than the critical speed, ϵ^* is real and negative and $\lambda_\pm$ are always purely imaginary for $\epsilon > 0$. These analyses verify the results shown in Figs. 7(a) and 7(b).

Effects of Transverse Damping c_z

Figure 8 shows the effect of $c_z = 0.01$Ns/m on the eigenvalues in case A. It is noted that the imaginary parts of the degenerate eigenvalues for modes $(0,1)_b$ and $(0,2)_r$ at Ω_d remain degenerate, while their real parts separate with one remaining zero and the other decreasing. No merging occurs in either the real or imaginary parts. Similarly, for cases B, C, and D we observe that the imaginary parts of the degenerate eigenvalues remain degenerate and unchanged, while the real parts separate with one remaining zero, and the other decreasing, increasing, or remaining unchanged, for cases C, D, and B, respectively. Again, it is verified through additional calculations that a two-mode approximation is satisfactory in the case of c_z.

Based on the two-mode approximation, it is found that for $\Omega = \Omega_d$ and $\omega_{mn}=\omega_{pq}=\omega$, the perturbed eigenvalues are $i\omega$ and $-\frac{\beta_1}{\alpha_0}\epsilon + i\omega$, where α_0 is defined in Eq. (12) and β_1 is changed to

$$\beta_1=4\pi\omega_{mn}\omega_{pq}\xi(S_{mn}\omega_{pq}+S_{pq}\omega_{mn}).$$

It is obvious that the imaginary parts of the eigenvalues remain unchanged at $i\omega$, one of the real parts vanishes and the other real part changes to $-\frac{\beta_1}{\alpha_0}\epsilon$. In case A, α_0 is negative and β_1 can be negative or positive, depending on the absolute values of S_{mn} and S_{pq}. Consequently, the other real part may decrease or increase, depending on the mode shapes of modes (m, n) and (p, q). In case C, both α_0 and β_1 are positive and the other real part becomes negative. In case D, $\alpha_0 > 0$ and $\beta_1 < 0$ and the other real part becomes positive. In case B, β_1 vanishes and both real parts remain zero. These analyses agree with our numerical observations.

Effects of Pitching Parameters

Numerical results show that the effects of pitching parameters are almost the same as their transverse counterparts, except that there is no interaction between two modes when one of them has no nodal diameter, i.e., $n = 0$. This is not a surprise if we examine the two-mode approximation. It can be shown easily that the procedure we have gone through for the transverse parameters applies almost in the same manner for the pitching parameters, except that we now replace $R_{mn}(\xi)$ and $R_{pq}(\xi)$ by $nR_{mn}(\xi)$ and $qR_{pq}(\xi)$, respectively. Moreover, when one of the two modes has no nodal diameter, the off-diagonal terms of $\mathbf{H}_2$ in Eq. (10) vanish and no modal interaction is induced.

Effects of Friction Force F_θ

Figure 9 shows the effects of $F_\theta = 0.004$N on the eigenvalues in case A. It is noted that the imaginary parts of the degenerate eigenvalues for modes $(0,1)_b$ and $(0,2)_r$ at Ω_d remain degenerate and unchanged, while their real parts separate with one remaining zero and the other decreasing. No merging occurs in either the real or imaginary parts. Similarly, as long as F_θ is small enough, we observe the same phenomena for cases C and D. In case B, however, friction force exhibits some unique effects on the behavior of eigenvalue changes. Figure 10(*a*) shows that for $F_\theta = 0.004$N, there exists a range of rotation speed immediately around the critical speed $\Omega_c = 849.1$ rpm, in which the natural frequency loci of modes (0,5) and $\overline{(0,5)}$ merge and remain zero, while the real parts separate. When $\Omega = \Omega_c$, one of the real parts remains zero and the other becomes negative. In Fig. 10(*b*) the rotation speed is fixed at 850 rpm and F_θ has the range 0 to 0.01N. The dashed lines, which are the finite element solutions, show that the natural frequency loci start to merge as F_θ increases to F_θ^* and remain so as F_θ continues increasing. The real parts coincide and remain negative for $F_\theta < F_\theta^*$, but separate for $F_\theta > F_\theta^*$. As F_θ increases to a very large value, it is found that the upper branch of the real part loci approaches zero. When we try to use eigenfunction expansion to reproduce the dashed lines by choosing the eigenfunctions with the smallest eigenvalues, we observe that the approximation deteriorates as the number of modes used in the expansion increases, as shown by the solid lines in Fig. 10(*b*). However, if we choose only the four modes $(0,5)_r$, $\overline{(0,5)}_r$, $(0.5)_f$, and $\overline{(0,5)}_f$ in the expansion, the result of this four-mode approximation agrees very well with the dashed lines, although the natural frequency of $(0,5)_f$, 110.7 Hz, is very large compared to the frequency range of our current interest. This phenomenon is also observed in cases A, C, and D. Consequently, a two-mode approximation can no longer exhibit all the important features of the eigenvalue changes in the case of friction force, but a properly chosen four-mode approximation is very good.

Conclusions

Modal interactions in a spinning disk-stationary load system are studied by use of a numerical finite element method and by an eigenfunction expansion method. Their mathematical structures are analyzed in detail by considering a two-mode approximation. The results can be summarized as follows:

(1) In the cases of A, C, and D, as shown in Fig. 2, for a transverse mass m_z there are two branch points $\epsilon_\pm$ associated with the eigenvalues as functions of $\epsilon = \dfrac{m_z}{\rho h \xi}$ on the complex ϵ-plane. In case A, $\epsilon_\pm$ are real and positive when $\Omega < \Omega_d$. Frequency merging occurs and instability is induced when ϵ lies between ϵ_+ and ϵ_- along the real line. If $\Omega > \Omega_d$, $\epsilon_\pm$ are real and negative and no merging occurs. In cases C and D, $\epsilon_\pm$ are complex conjugate pairs, no merging occurs but there is frequency veering.

(2) In the case of a transverse stiffness k_z, there also exist two branch points $\epsilon_\pm$ for cases A, C and D. In case A, $\epsilon_\pm$ are real and positive when $\Omega > \Omega_d$, but negative for $\Omega < \Omega_d$, just opposite to the effect of m_z. In cases C and D, $\epsilon_\pm$ are complex conjugate pairs. In case B, there exists a single real branch point ϵ^*. For Ω higher than the critical speed and $\epsilon > \epsilon^*$, merging occurs and instability is induced.

(3) In all the cases of A, B, C, and D, for a transverse damping c_z the imaginary parts of the degenerate eigenvalues remain degenerate and unchanged, while the real parts separate with one remaining zero and the other changing, except for case B, in which both real parts remain zero. No merging occurs in either the real or imaginary parts of the eigenvalues.

(4) The effects of the pitching parameters are almost the same as their transverse counterparts, except that there is no modal interaction if one of the modes has no nodal diameter.

(5) In cases A, C, and D, for friction force F_θ the imaginary parts of the degenerate eigenvalues remain degenerate and unchanged, while the real parts separate with one remaining zero and the other changing. No merging occurs in either the real or imaginary parts of the eigenvalues. In case B, however, there exists a range of rotation speeds immediately around the critical speed in which the natural frequency loci merge and remain zero, while the real parts separate. Unlike the transverse and pitching parameters, at least four modes are required in the eigenfunction expansion to reproduce the characteristics of the eigenvalue changes due to friction force.

Acknowledgment

This work was supported by the Computer Mechanics Laboratory at the University of California at Berkeley.

References

Bender, C. M., and Orszag, S. A., 1978, *Advanced Mathematical Methods for Scientists and Engineers*, McGraw-Hill, New York.

Chen, J.-S., and Bogy, D. B., 1991, "Effects of Load Parameters on the Natural Frequencies and Stability of a Flexible Spinning Disk with a Stationary Load System," ASME JOURNAL OF APPLIED MECHANICS, to appear.

Courant, R., Hilbert, D., 1962, *Methods of Mathematical Physics*, John Wiley and Sons, New York.

Iwan, W. D., and Moeller, T. L., 1976, "The Stability of a Spinning Elastic Disk With a Transverse Load System," ASME JOURNAL OF APPLIED MECHANICS, Vol. 43, pp. 485-490.

Ono, K., Chen, J.-S., and Bogy, D. B., 1991, "Stability Analysis of the Head-Disk Interface in a Flexible Disk Drive," ASME JOURNAL OF APPLIED MECHANICS, Vol. 58, pp. 1005-1014.

Perkins, N. C., and Mote, C. D., Jr., 1986, "Comments on Curve Veering in Eigenvalue Problems," *Journal of Sound and Vibration*, Vol. 106, No. 3, pp. 451-463.

Stakgold, Ivar, 1979, *Green's Functions and Boundary Value Problems*, John Wiley and Sons, New York.

M. D. Bird
Graduate Student.

C. R. Steele
Professor,
Fellow ASME.

Division of Applied Mechanics,
Stanford University,
Stanford, CA 94305

A Solution Procedure for Laplace's Equation on Multiply Connected Circular Domains

A solution procedure is presented for the two-dimensional Laplace's equation on circular domains with circular holes and arbitrary boundary conditions. The shape functions use the traditional trigonometric Fourier series on the boundaries with a power series decay into the domain thereby satisfying the governing equation exactly. The interaction of the boundaries is expressed simply and exactly resulting in quick processing time. The only simplification made is the use of a finite number of terms in the boundary conditions. The results are compared with a Green's function method due to Naghdi (1991) and a Möbius transformation method due to Honein et al. (1991).

1 Introduction

One of the more challenging problems in the field of solid mechanics is the determination of stresses in thin-walled shell structures. These problems are particularly nettlesome in the traditional framework of finite elements because the thinness of the shell acts as a constraint and the presence of boundary layers requires extremely fine meshing as shown by Mansouri (1991) resulting in considerable setup and run time. Another approach is that of Simos and Sadegh (1989) who suggest using a boundary integral method for these problems. However, the Green's functions for anything other than a spherical or cylindrical shell would be difficult to find and implement. Alternatively, asymptotic-Fourier series methods have been successfully used for shell intersection problems by Steele and Steele (1983). These procedures work well and avoid the problems of other methods. The main restriction of the asymptotic procedures is that they have been restricted to problems of no more than one intersection. In order to handle a more general class of problems it is necessary to deal with multiple intersections. Before delving into the complexities of shell theory, though, it is good to develop the basic principles for a simpler problem, i.e., Laplace's equation in two dimensions. The following is an analysis of steady-state heat conduction on a multiply connected domain using a Fourier series procedure. Numerical results are compared with those of Naghdi (1991) and Honein et al. (1991) for Saint-Venant flexure of bars and antiplane elasticity, respectively.

Contributed by the Applied Mechanics Division of THE AMERICAN SOCIETY OF MECHANICAL ENGINEERS for presentation at the 1992 ASME Summer Mechanics and Materials Meeting, Tempe, AZ, Apr. 28–May 1, 1992.

Discussion on this paper should be addressed to the Technical Editor, Prof. Leon M. Keer, The Technological Institute, Northwestern University, Evanston, IL 60208, and will be accepted until four months after final publication of the paper itself in the JOURNAL OF APPLIED MECHANICS. Manuscript received by the ASME Applied Mechanics Division, Mar. 7, 1991; final revision, Aug. 5, 1991.

Paper No. 92-APM-27.

The basic concept is that prescribing a given harmonic of the temperature function on one boundary has an effect on all other boundaries which can be computed *explicitly*. The interactions between the holes presented here for Laplace's equation are analogous to Graf's addition theorem of cylindrical functions for Bessel's equation (see Abramowitz and Stegun, 1965). It is also analogous to the "self-consistent" procedure of multiple scattering set forth by Twersky (1953, 1962). However, Twersky solves the reduced wave equation and retains only the first two terms while considering a few boundary conditions whereas the following analysis is of Laplace's equation with all the terms retained for arbitrary boundary conditions. The method is also in some ways similar to a boundary integral method, or it could be called a Trefftz-type finite element procedure where the discussion is for a single element (see Jirousek, 1978).

2 Analysis

Consider a circular domain with an arbitrary number of circular holes as shown in Fig. 1. The boundaries and radii are numbered from zero to the number of holes *NH* beginning with the outermost. The steady-state heat equation on this domain subject to prescribed temperature distributions on the boundaries is written

$$\nabla^2 T = 0 \tag{1}$$

and the temperature T at boundary number j will be denoted $T^{(j)}(R_j, \theta_j)$.

Finite Plate With no Holes. Consider first a circular plate without holes of (dimensionless) radius R_0 and a prescribed temperature at the boundary equal to $A^0(R_0, \theta_0)$. (A is used for a plate with a single boundary, T for one with multiple boundaries). Since the temperature must be periodic about the boundary, the boundary condition can be written as a Fourier series:

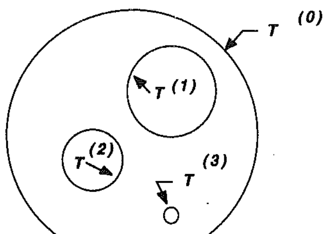

Fig. 1 Circular plate with circular holes; temperature prescribed on boundaries

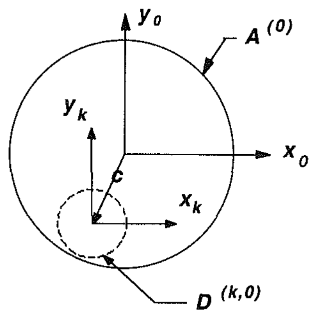

Fig. 2 Finite plate with boundary temperature $A^{(0)}$. Expand temperature on circle k.

$$A^{(0)}(R_0,\theta_0)=A_0^{(0)}+a_1^{(0)}\sin\theta_0+A_1^{(0)}\cos\theta_0+a_2^{(0)}\sin2\theta_0+\ldots \tag{2}$$

which is assumed to converge uniformly. The temperature everywhere in the plate, requiring regularity at the center, is

$$A^{(0)}(r_0,\theta_0)=A_0^{(0)}+\sum_{n=1}^{\infty}\left(\frac{1}{R_0}\right)^n[a_n^{(0)}r_0^n\sin n\theta_0+A_n^{(0)}r_0^n\cos n\theta_0] \tag{3}$$

where

R_0 = radius of the plate/L
r_0 = distance of a point from the center of the plate/L
L = a reference length.

A transformation of coordinates is now performed from the (r_0, θ_0) coordinate system to the (r_k, θ_k) coordinate system as shown in Fig. 2 to give

$$A^{(0)}(r_0,\theta_0)=D^{(k,0)}(r_k,\theta_k) \tag{4}$$

where

$$D^{(k,0)}(r_k,\theta_k)=\sum_{n=0}^{\infty}\left\{D_{0,n}^{(k,0)}+\sum_{m=1}^{n}[d_{m,n}^{(k,0)}r_k^m\sin m\theta_k+D_{m,n}^{(k,0)}r_k^m\cos m\theta_k]\right\}. \tag{5}$$

To determine the exact relationship between the coefficients of the two series, the transformation is carried out explicitly as follows considering the nth term of the series $A^{(0)}(r_0, \theta_0)$:

$$r_0^n\cos n\theta_0=\mathrm{Re}[z_0^n] \tag{6}$$

$$r_0^n\sin n\theta_0=\mathrm{Im}[z_0^n] \tag{7}$$

$$z_0^n=(c+z_k)^n \tag{8}$$

$$z_0^n=c^n+c^n\sum_{m=1}^{n}f(m,n)\left(\frac{z_k}{c}\right)^m \tag{9}$$

where

$$z_k=r_k(\cos\theta_k+i\sin\theta_k) \tag{10}$$

$$f(m,n)=\frac{n(n-1)\ldots(n-m+1)}{m!} \tag{11}$$

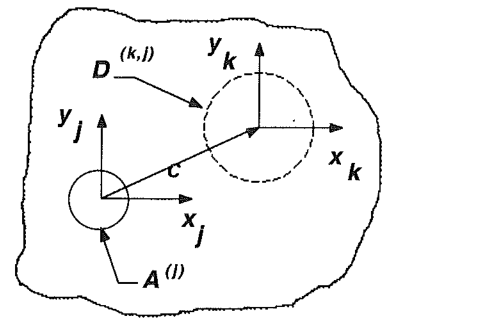

Fig. 3 Infinite plate with boundary temperature $A^{(j)}$. Expand temperature on circle k.

and c = complex vector from the center of the plate to the center of coordinate system k divided by the reference length L. It is seen, after taking real and imaginary parts of Eq. (9), that the coefficients of the two series are related

$$D_{0,n}^{(k,0)}=\frac{1}{R_0^n}[a_n^{(0)}\mathrm{Im}(c^n)+A_n^{(0)}\mathrm{Re}(c^n)] \tag{12}$$

$$d_{m,n}^{(k,0)}=\frac{f(m,n)}{R_0^n}[a_n^{(0)}\mathrm{Re}(c^{n-m})-A_n^{(0)}\mathrm{Im}(c^{n-m})] \tag{13}$$

$$D_{m,n}^{(k,0)}=\frac{f(m,n)}{R_0^n}[a_n^{(0)}\mathrm{Im}(c^{n-m})+A_n^{(0)}\mathrm{Re}(c^{n-m})] \tag{14}$$

for $m, n\neq0$. The constant term $(n=0)$ simply gives $D_{(0,0)}^{(k,0)}=A_0^{(0)}$.

Single Hole in an Infinite Plate. The next step is to consider a hole in an infinite plate with a temperature distribution prescribed at the edge of the hole $A^{(j)}(R_j, \theta_j)$. The boundary condition is written as a Fourier series

$$A^{(j)}(R_j,\theta_j)=A_0^{(j)}+a_1^{(j)}\sin\theta_j+A_1^{(j)}\cos\theta_j+a_2^{(j)}\sin2\theta_j+\ldots \tag{15}$$

and the temperature everywhere in the plate is written

$$A^{(j)}(r_j,\theta_j)=A_0^{(j)}\frac{\log r_j}{\log R_j}+\sum_{n=1}^{\infty}R_j^n[a_n^{(j)}r_j^{-n}\sin n\theta_j+A_n^{(j)}r_j^{-n}\cos n\theta_j] \tag{16}$$

where log denotes the natural logarithm. Again, a change of coordinates is performed—this time from the (r_j, θ_j) system to the (r_k, θ_k) system assuming $r_k<|c|$ as shown in Fig. 3 to give

$$A^{(j)}(r_j,\theta_j)=D^{(k,j)}(r_k,\theta_k) \tag{17}$$

where

$$D^{(k,j)}(r_k,\theta_k)=\sum_{n=0}^{\infty}\left\{D_{0,n}^{(k,j)}+\sum_{m=1}^{\infty}[d_{m,n}^{(k,j)}r_k^m\sin m\theta_k+D_{m,n}^{(k,j)}r_k^m\cos m\theta_k]\right\}. \tag{18}$$

The transformation is carried out in the Appendix which gives the relationship between the two sets of coefficients

$$D_{0,n}^{(k,j)}=R_j^n[a_n^{(j)}\mathrm{Im}(c^{-n})+A_n^{(j)}\mathrm{Re}(c^{-n})] \tag{19}$$

$$d_{m,n}^{(k,j)}=R_j^n g(m,n)[-a_n^{(j)}\mathrm{Re}(c^{-(n+m)})-A_n^{(j)}\mathrm{Im}(c^{-(n+m)})] \tag{20}$$

$$D_{m,n}^{(k,j)}=R_j^n g(m,n)[-a_n^{(j)}\mathrm{Im}(c^{-(n+m)})+A_n^{(j)}\mathrm{Re}(c^{-(n+m)})] \tag{21}$$

where

$$g(m,n)=(-1)^m\frac{n(n+1)\ldots(n+m-1)}{m!} \tag{22}$$

for $n\neq0$. The logarithmic term $(n=0)$ is also expanded in the Appendix giving

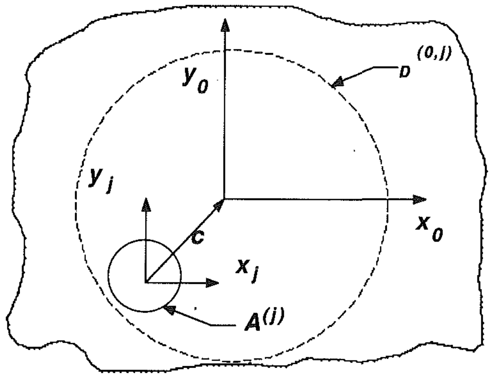

Fig. 4 Infinite plate with boundary temperature $A^{(j)}$. Expand temperature on circle 0.

$$D_0^{(k,j)}(r_k,\theta_k)=D_{0,0}^{(k,j)}+\sum_{m=1}^{\infty}[d_{m,0}^{(k,j)}r_k^m\sin m\theta_k + D_{m,0}^{(k,j)}r_k^m\cos m\theta_k] \quad (23)$$

where

$$D_{0,0}^{(k,j)}=\frac{A_0^{(j)}}{\log R_j}\log|c| \quad (24)$$

$$d_{m,0}^{(k,j)}=\frac{a_0^{(j)}}{\log R_j}\frac{(-1)^m}{m}\mathrm{Im}(c^{-m}) \quad (25)$$

$$D_{m,0}^{(k,j)}=\frac{A_0^{(j)}}{\log R_j}\frac{(-1)^m}{m}\mathrm{Re}(c^{-m}) \quad (26)$$

There is now one more set of expressions to be found. Given an infinite plate with a single hole j at which the temperature is prescribed $A^{(j)}(R_j, \theta_j)$, the boundary condition and solution can be written as in Eqs. (15)–(16); but this time the transformation is from the (r_j, θ_j) system to the (r_0, θ_0) system where $|c|<r_0$. The result (see Fig. 4 and the Appendix) is written

$$D^{(0,j)}(r_0,\theta_0)=\sum_{n=0}^{\infty}\left\{\sum_{m=n}^{\infty}[d_{m,n}^{(0,j)}r_0^{-m}\sin m\theta_0 + D_{m,n}^{(0,j)}r_0^{-m}\cos m\theta_0]\right\} \quad (27)$$

where

$$d_{n,n}^{(0,j)}=a_n^{(j)}R_j^n \quad (28)$$

$$D_{n,n}^{(0,j)}=A_n^{(j)}R_j^n \quad (29)$$

$$d_{m,n}^{(0,j)}=R_j^n g(m-n,n)[a_n^{(j)}\mathrm{Re}(c^{m-n})+A_n^{(j)}\mathrm{Im}(c^{m-n})] \quad (30)$$

$$D_{m,n}^{(0,j)}=R_j^n g(m-n,n)[-a_n^{(j)}\mathrm{Im}(c^{m-n})+A_n^{(j)}\mathrm{Re}(c^{m-n})] \quad (31)$$

for $n\neq 0$ and finally, for the logarithmic term,

$$D_0^{(0,j)}=D_{0,0}^{(0,j)}+\sum_{m=1}^{\infty}[d_{m,0}^{(0,j)}r_0^{-m}\sin m\theta_0 + D_{m,0}^{(0,j)}r_0^{-m}\cos m\theta_0] \quad (32)$$

where

$$D_{0,0}^{(0,j)}=A_0^{(j)}\frac{\log R_0}{\log R_j} \quad (33)$$

$$d_{m,0}^{(0,j)}=-\frac{a_0^{(j)}}{\log R_j}\frac{(-1)^m}{m}\mathrm{Im}(c^m) \quad (34)$$

$$D_{m,0}^{(0,j)}=-\frac{A_0^{(j)}}{\log R_j}\frac{(-1)^m}{m}\mathrm{Re}(c^m) \quad (35)$$

(see the Appendix).

Superposition. The original problem of a circular plate with various circular holes can now be thought of as being imbedded in an infinite plate with the boundary temperatures $T^{(j)}(R_j, \theta_j)$ prescribed on circular paths of radius R_j where $j=0, \ldots, NH$. The solution is then the sum of the above expansions

$$T^{(k)}(R_k,\theta_k)=A^{(k)}(R_k,\theta_k)+\sum_{\substack{j=0\\ j\neq k}}^{NH}D^{(k,j)}(R_k,\theta_k) \quad (36)$$

but since the $D^{(k,j)}(R_k, \theta_k)$ are simply linear functions of the $A_n^{(k)}$, $k\neq j$, it is possible to write the $T^{(j)}(\theta_j)$ as a linear combination of the $A_n^{(k)}$ as shown in Eq. (37) (provided we include only a finite number of coefficients, NC, which need not be the same on all boundaries in the various Fourier series):

$$\{\mathbf{T}\}=[\mathbf{TM}]\{\mathbf{A}\} \quad (37)$$

where

T = prescribed temperature on the boundaries,
TM = the temperature matrix, the entries of which are essentially the terms of the various sums above, and
A = the infinite domain vector defined above.

In a similar manner, the normal derivative of the temperature field can be computed along a circular path in a finite plate, or in an infinite plate with a single hole. A set of equations is obtained which can be written in matrix form

$$\{\mathbf{F}\}=[\mathbf{FM}]\{\mathbf{A}\} \quad (38)$$

where

F = the flux across the boundaries,
FM = the flux matrix, the entries of which are essentially derivatives with respect to r_k of those of **[TM]** multiplied by the thermal conductivity and plate thickness, and
A = the same infinite domain vector as before.

In a Dirichlet-type problem, **T** is specified, **TM** and **FM** are computed from the relative sizes and positions of the holes, and **A** is found to satisfy **T** and substituted into Eq. (38) to compute the fluxes at each boundary. Having **A**, it is straightforward to compute the temperature and flux at an arbitrary point in the domain by summing the effects of the $A_n^{(j)}$ at that point. This field point method is similar to that used in boundary integral methods. For a Neumann-type of problem, **F** is specified and **TM** and **FM** are computed from the geometry. However, $\{\mathbf{F}\}=[\mathbf{FM}]\{\mathbf{A}\}$ cannot be simply solved for **A** because **FM** is singular. This difficulty can be overcome by eliminating the row and column of the matrix which correspond to uniform heating (rigid body motion in solid mechanics). The remaining system of equations can be solved and substituted into Eq. (37). Using this procedure two things are accomplished:

1 The Neumann condition is satisfied exactly.
2 The column of zeroes in the flux matrix is eliminated.

For a problem of mixed type, where some of the boundaries have temperature prescribed and others have flux prescribed, the two equations can be combined to get:

$$\{\mathbf{F}\}=[\mathbf{FM}][\mathbf{TM}]^{-1}\{\mathbf{T}\}$$

or

$$\{\mathbf{F}\}=[\mathbf{K}]\{\mathbf{T}\} \quad (39)$$

where **K** is the conductivity matrix (the analog of the stiffness matrix of solid mechanics). This system can be partitioned and solved using various methods common in finite element analysis.

3 Convergence

It is of interest at this point to verify that the various sequences of terms generated are convergent. That is, in order to solve a problem, a finite number of terms in each expansion is used and it must be possible to make the error due to truncation arbitrarily small. From Eq. (14) we see

$$D_{m,n}^{(k,0)}R_k^m \sim A_n^{(0)}\,\frac{n(n-1)\ldots(n-m+1)}{m!}\left(\frac{R_k}{c}\right)^m\left(\frac{c}{R_0}\right)^n,\quad 0\le m\le n,\ k\neq 0 \qquad (40)$$

$$D_{m,n}^{(k,0)}R_k^m \sim A_n^{(0)}\left(\frac{R_k}{R_0}\right)^n,\quad n \text{ fixed},\ m\to n \qquad (41)$$

$$D_{m,n}^{(k,0)}R_k^m \sim A_n^{(0)}n^m\left(\frac{c}{R_0}\right)^n,\quad m \text{ fixed},\ n\to\infty \qquad (42)$$

which converges in both limits given that the $A_n^{(0)}$ represent the coefficients of a uniformly convergent Fourier series since the distance between the center of a plate and the center of a hole in the plate is always smaller than the radius of the plate. Similarly, from Eq. (21) we see

$$D_{m,n}^{(k,j)}R_k^m \sim A_n^{(j)}\,(-1)^m\,\frac{n(n+1)\ldots(n+m-1)}{m!}\left(\frac{R_k}{c}\right)^m\left(\frac{R_j}{c}\right)^n,\quad 0\le m,\ n\le\infty,\ j\neq 0 \qquad (43)$$

$$D_{m,n}^{(k,j)}R_k^m \sim A_n^{(j)}(-1)^m\left(\frac{R_k}{c}\right)^m,\quad n \text{ fixed},\ m\to\infty,\ j\neq 0 \qquad (44)$$

$$D_{m,n}^{(k,j)}R_k^m \sim A_n^{(j)}(-1)^m n^m\left(\frac{R_j}{c}\right)^n,\quad m \text{ fixed},\ n\to\infty,\ j\neq 0 \qquad (45)$$

$$D_{m,0}^{(k,j)}R_k^m = \frac{A_n^{(j)}}{(-m)^m\log R_j}\left(\frac{R_k}{c}\right)^m,\quad 1\le m\le\infty,\ j\neq 0,\ k \qquad (46)$$

all of which are convergent since, for unencircled holes, the distance between the hole centers is greater than either of the hole radii. Looking at the last set, i.e., Eq. (31), we see

$$D_{m,n}^{(0,j)}R_0^{-m} \sim A_n^{(j)}\,(-1)^m\,\frac{n(n+1)\ldots(n+m-1)}{m!}\left(\frac{c}{R_0}\right)^m\left(\frac{R_j}{c}\right)^n,\quad 1\le n\le\infty,\ n<m\le\infty \qquad (47)$$

$$D_{m,n}^{(0,j)}R_k^{-m} \sim A_n^{(j)}(-1)^m\left(\frac{c}{R_0}\right)^m,\quad n \text{ fixed},\ m\to\infty \qquad (48)$$

$$D_{m,n}^{(0,j)}R_k^{-m} \sim A_n^{(j)}(-1)^m\left(\frac{R_j}{R_0}\right)^m,\quad m \text{ fixed},\ n\to m \qquad (49)$$

$$D_{m,0}^{(0,j)}R_k^{-m} = \frac{A_0^{(j)}}{(-m)^m\log R_j}\left(\frac{c}{R_0}\right)^m,\quad 0\le m\le\infty \qquad (50)$$

and, again, these converge because the radius of the plate is always greater than the radius of a hole in the plate, as well as the separation between a hole and the center of the plate.

It was previously noted that one might wish to retain different numbers of terms on the different boundaries. For example, to maintain uniform accuracy everywhere, more terms need to be retained on the boundaries which are closer to one another than on those which are greatly separated. The preceding expressions can be used to estimate, in advance, how many terms need to be retained.

It is also clear that the reference length L must be chosen such that $R_j\neq 1$ for all j. Otherwise, $\log R_j = 0$ and the expressions would become meaningless. Jaswon (1963) has shown that this condition is generally required for multiply connected domains.

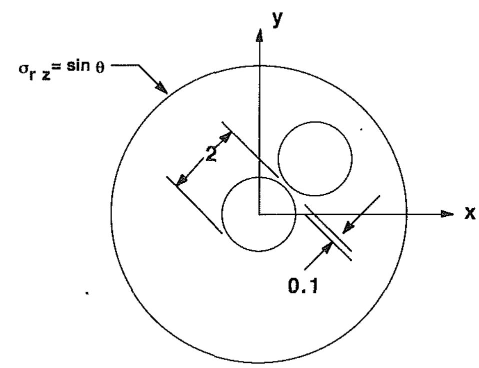

Fig. 5 Antiplane deformation of a large plate with traction-free holes and out of plane stress applied on the outer boundary

4 Error Estimation

The Fourier series procedure satisfies the governing equation exactly. The only errors introduced by the method are the truncation error due to using only a finite number of terms in the boundary conditions and the roundoff error due to the finite floating point precision of a digital computer. Since each of the terms in the Fourier series expansions decays moving from the boundary into the domain, the truncation error due to ignoring some of their contributions decays as well (Saint-Venant's principle). This produces an interior region in which the solution is orders of magnitude more accurate than it is on the boundary (see Jirousek, 1989). Since the maximum error is on the boundary, the error can be estimated, for a Dirichlet-type problem, by computing the temperature and flux on the boundary using the field point method and comparing with the prescribed temperature and the flux computed from the flux matrix. The maximum discrepancy for each is then an upper bound on the error of the calculation. If the error for either is too large, the problem can be run again retaining more terms on the boundaries for which greater resolution is desired.

5 Results

For the case of a single hole in the center of a circular plate, exact solutions can be found. Compared with these, the results using this procedure, encoded in single precision FORTRAN for either Dirichlet or Neumann conditions, are accurate to seven or eight decimal places when the ratio of outer to inner radius ranges between 1.01 and 1000. For a ratio of 1.0001, only a five place accuracy is attained.

For the less trivial case of nonaxisymmetric geometry we compare, with the results of Honein et al. (1991), for the case of antiplane strain of an infinite domain with two circular holes near one another as shown in Fig. 5. To approximate Honein's infinite plane with a uniform antiplane stress σ_{zy} at infinity, a plate of finite radius with a shear at the outer boundary $\sigma_{zr} = \sin\theta$ is used and the results are examined as the outer radius gets large. It is observed that the hoop stress on the hole at the center of the plate approaches that for the infinite domain as the radius of the plate gets large as shown in Fig. 6. Notice that the results for $R_0 = 15$ and those for the infinite domain agree to three figures so the difference cannot be discerned in the plot. This behavior is typical for the geometries considered by Honein.

It should be noted that Honein's procedure, while entirely analytical in nature, is restricted to the special case of two holes in an infinite domain. To extend the procedure to include additional holes or an outer boundary would be challenging.

In addition, our results have been compared with Naghdi's (1991) for Saint-Venant flexure of beams (see Sokolnikoff, 1956) as shown in Figs. 7–9. Naghdi defines the stress concentration S_c as

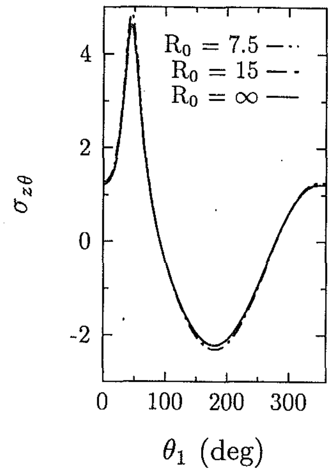

Fig. 6 As R_0 increases, $\sigma_{z\theta}$ at $r_1 = 1$ as computed by the Fourier series method converges to that found by Honein for the infinite plate

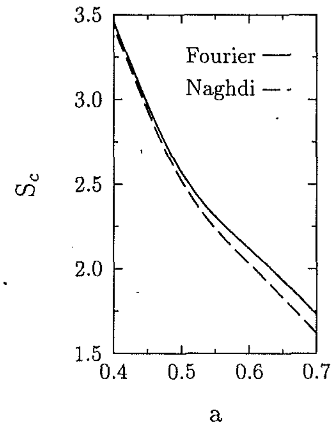

Fig. 9 Comparison of stress concentration at point B due to Naghdi and the Fourier series procedure for $\bar{\theta} = 3\pi/8$

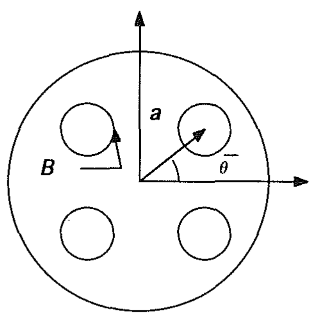

Fig. 7 Saint-Venant flexure of circular beam with four symmetrically located circular holes. Compute stress concentration at B.

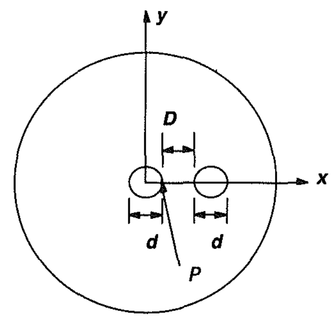

Fig. 10 Saint-Venant flexure of a circular beam with two circular holes. Maximum stress concentration is at point P.

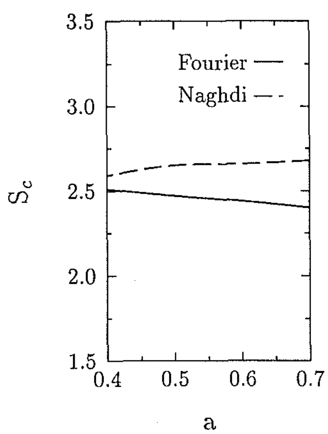

Fig. 8 Comparison of stress concentration at point B due to Naghdi and the Fourier series procedure for $\bar{\theta} = \pi/8$

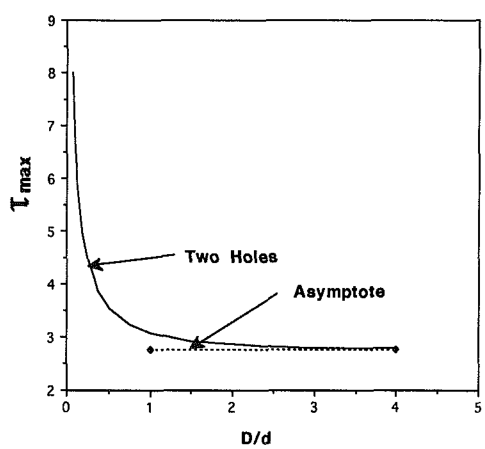

Fig. 11 Maximum shear stress in the geometry of Fig. 10 as a function of the spacing between the holes compared to the asymptotic value obtained when there is only one hole located at the center of the beam

$$S_c = \frac{\sigma_{zy} A}{W_y} \tag{51}$$

where A is the area of the beam cross-section and W_y is the weight acting in the y-direction. It can be shown that the stresses are subharmonic implying that their maxima are on the boundary. Naghdi considers geometries symmetric about both the x- and y-axes and concludes the maximum stress concentration to be at point B of Fig. 5. He then computes the stress concentration at point B for various geometries. Figures 8 and 9 compare values of S_c computed using the Fourier series approach with those reported by Naghdi for $R_0 = 10$, $R_i = 1.2$, Poisson's ratio $= 0.3$ and various values of a. It is seen that the two approaches disagree by as much as 11 percent. The grounds for this discrepancy have not yet been identified.

The examples using the Fourier series approach ran in an average of 1.51 seconds CPU time and 51.0 seconds user time including setting up all the input files on a Systems Concepts SC30M digital computer. For most examples, six terms in each of the sine and cosine series on each boundary were sufficient to yield an estimated error of less than 0.05 percent. For several geometries, 64 terms were retained on each boundary to give an estimated error of 1.0 e-11 percent.

An advantage of the Fourier series approach over that of Naghdi's is that it permits arbitrary hole location and size. The case of two holes located near the center of the beam, as shown

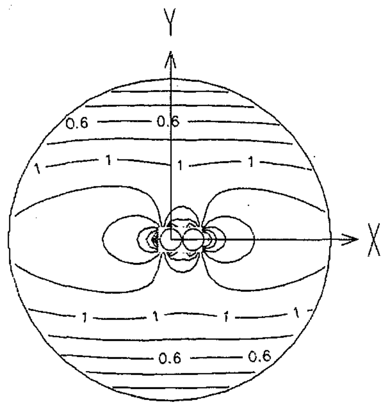

Fig. 12 Contour plot of S_c for geometry of Fig. 10 for $D/d = 0.0625$

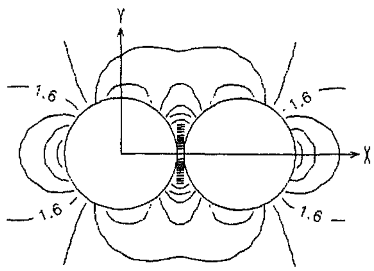

Fig. 13 Detail of Fig. 12

in Fig. (10), is considered. As the distance between the holes grows, the stress concentration approaches that for the case of a single hole in the beam as shown in Fig. (11). Contour plots of S_c for the case of closest approach ($D/d = 0.062$) are presented in Figs. (12) and (13). It is observed, for this hole arrangement, that when the distance between the holes is greater than twice the diameter of the holes, the coupling of the holes is negligible. Dozens of examples have been run using between two and five holes located and sized arbitrarily and it appears that the critical ratio of separation to diameter from Fig. (11) can be applied to general problems.

6 Conclusions

The method presented is shown to agree very well with the alternative analytic method of Honein while providing greater generality in that circular holes of arbitrary size, position, and number can be handled in a single, consistent framework. The Fourier series procedure requires no mesh generation and the stiffness matrix is assembled directly which implies it would be faster than purely numerical procedures such as finite differences or finite elements. It is not clear that there is a significant advantage over boundary integral methods in either ease of operation or run time. However, boundary element methods frequently give very high condition numbers for the system of equations to be solved. The method presented here produces systems of equations with condition numbers which appear to depend primarily on the number of holes and are nearly independent of the number of terms used and the spacing of the holes. For the Saint-Venant flexure examples with four holes, the condition number ranged from 17 to 22. In addition, the Fourier series procedure shows tremendous promise for thin shell intersection problems (see Steele and Steele, 1983).

The method can be extended to handle plate bending (see Bird and Steele, 1991) and problems involving circular material inclusions. In addition it should be fairly straightforward to extend it to plane elasticity and deformation of thin, shallow shells.

7 Acknowledgment

This material is based upon work supported under a National Science Foundation Graduate Fellowship.

References

Abramowitz, M., and Stegun, I., 1965, Handbook of Mathematical Functions, Dover Publications, New York.

Bird, M. D., and Steele, C. R., 1991, "A Separated Solution Procedure for Bending of Circular Plates with Circular Holes," *Applied Mechanics Review*, Vol. 44, Part 2, No. 10.

Honein, E., Honein, T., and Herrmann, G., 1991, "On Two Circular Inclusions in Harmonic Problems," *J. Quarterly of Applied Mechanics*, to appear.

Jaswon, M. A., 1963, "Integral Equation Methods in Potential Theory," *Proceedings of the Royal Society*, Vol. A275, pp. 23–34.

Jirousek, J., 1978, "Basis for Development of Large Finite Elements Locally Satisfying all Field Equations," *Computer Methods in Applied Mechanics and Engineering*, Vol. 14, pp. 65–92.

Jirousek, K., and Venkatesh, A., 1989, "A Simple Stress Error Estimator for Hybrid-Treffz p-Version Elements," *International Journal for Numerical Methods in Engineering*, Vol. 28, pp. 221–236.

Mansouri, S. A., 1991, "Elasto-Plastic Nonlinear Analysis of Nozzle-Cylinder Intersections Subjected to Internal and External Loads," Ph.D. Thesis, University of Illinois, Urbana-Champaign, Illinois.

Naghdi, A. K., 1991, "Bending of a Perforated Circular Cylindrical Cantilever," to appear in *International Journal of Solids and Structures*.

Simos, N., and Sadegh, A. M., 1989, "Self-Equilibrated Singular Solutions of a Complete Spherical Shell: Classical Theory Approach," ASME JOURNAL OF APPLIED MECHANICS, Vol. 56, pp. 105–112.

Sokolnikoff, S., 1956, *Mathematical Theory of Elasticity*, McGraw-Hill, New York.

Steele, C. R., and Steele, M. L., 1983, "Stress Analysis of Nozzles in Cylindrical Vessels with External Load," ASME *Journal of Pressure Vessels and Piping*, Vol. 105, pp. 191–200.

Twersky, V., 1953, "Multiple Scattering of Waves by Planar Random Distributions of Cylinders and Bosses," Institute of Mathematical Sciences, NYU, Report EM58.

Twersky, V., 1962, "Multiple Scattering of Waves and Optical Phenomena," *Journal of the Optical Society of America*, Vol. 52, pp. 145–171.

APPENDIX

Expansions for a Single Hole in an Infinite Plate

To expand the series prescribed on the hole j onto the circular path k, (provided k does not enclose j), consider the following for the nth term in the expansion

$$z_j^{-n} = (c + z_k)^{-n}$$

$$z_j^{-n} = c^{-n}\left(1 + \frac{z_k}{c}\right)^{-n}$$

$$z_j^{-n} = c^{-n} + c^{-n}\sum_{m=1}^{\infty}\frac{n(n+1)\ldots(n+m-1)}{m!}\left(\frac{-z_k}{c}\right)^m$$

$$z_j^{-n} = c^{-n} + c^{-n}\sum_{m=1}^{\infty} g(m,n)\left(\frac{z_k}{c}\right)^m$$

$$z_j^{-n} = c^{-n} + \sum_{m=1}^{\infty} g(m,n)c^{-(m+n)}z_k^m.$$

Taking the real and imaginary parts yields Eqs. (19)–(22).

The expansion for the logarithm is a little different in that it requires an integration as follows:

$$\log(r_j) = \mathrm{Re}[\log(z_j)]$$

$$\log(z_j) = \int\frac{dz_j}{z_j}$$

$$\frac{1}{z_j} = \frac{1}{c + z_k}$$

$$\frac{1}{z_j}=\frac{1}{c}\sum_{m=0}^{\infty}(-1)^m\left(\frac{z_j-c}{c}\right)^m$$

$$\log(z_j)+c_1=\frac{z_j}{c}-\sum_{m=2}^{\infty}(-1)^m\frac{1}{m}\left(\frac{z_j-c}{c}\right)^m$$

where

$$c_1=\text{constant of integration.}$$

To evaluate c_1, set $z_j=c$ giving

$$\log(c)+c_1=1$$

so

$$\log(z_j)=\frac{z_j}{c}-\sum_{m=2}^{\infty}(-1)^m\frac{1}{m}\left(\frac{z_j-c}{c}\right)^m+\log(c)-1$$

$$\log(z_j)=\frac{z_k+c}{c}-\sum_{m=2}^{\infty}(-1)^m\frac{1}{m}\left(\frac{z_k}{c}\right)^m+\log(c)-1$$

$$\log(z_j)=-\sum_{m=1}^{\infty}(-1)^m\frac{1}{m}\left(\frac{z_k}{c}\right)^m+\log(c).$$

Taking the real part then gives Eqs. (24)–(26).

To expand the series prescribed on the hole j onto the circular path k, provided k does enclose j, consider the following for the nth term in the expansion

$$z_j^{-n}=(z_k+c)^{-n}$$

$$z_j^{-n}=z_k^{-n}+z_k^{-n}\sum_{l=1}^{\infty}g(l,n)\left(\frac{c}{z_k}\right)^l$$

$$z_j^{-n}=z_k^{-n}+\sum_{m=n+1}^{\infty}g(m-n,n)c^{m-n}z_k^{-m}.$$

Taking real and imaginary parts gives Eqs. (28)–(31).

The expansion of the logarithmic term again requires an integration as shown.

$$\frac{1}{z_j}=\frac{1}{z_0+c}=\frac{1}{z_0\left(1+\dfrac{c}{z_0}\right)}$$

$$\frac{1}{z_j}=\sum_{m=1}^{\infty}\frac{(-c)^{m-1}}{(z_j-c)^m}$$

$$\log(z_j)+c_2=\log(z_j-c)-\sum_{m=1}^{\infty}\frac{(-c)^m}{m(z_j-c)^m}$$

where

$$c_2=\text{constant of integration}$$

To evaluate the constant, let $c=0$ which gives $c_2=0$. Thus, we see

$$\log(z_j)=\log(z_0)-\sum_{m=1}^{\infty}\frac{1}{m}\left(\frac{-c}{z_0}\right)^m$$

and taking the real part gives Eqs. (33)–(35).

Q.-S. Zheng
Professor.
Department of Civil Engineering,
Jiangxi Polytechnic University,
Nanchang, Jiangxi, China

K. C. Hwang
Professor,
Department of Engineering Mechanics,
Tsinghua University,
Beijing, China

On Cauchy's Mean Rotation

In this paper, a new treatment of Cauchy's measure of mean rotation in continuum mechanics is given, a representation theorem is proved, and the connection between Cauchy's measure and the finite rotation tensor is established. Cauchy's and Novozhilov's measures of mean rotation are compared.

1 Introduction

The theory of finite rotation of deformable body dates from Cauchy (1841). From Section 36 of Truesdell and Toupin's book (1960), we can read a modern statement about Cauchy's measure of mean rotation. Let $\{X, Y, Z\}$ be a given Cartesian coordinate system and $\{\mathbf{i}, \mathbf{j}, \mathbf{k}\}$, the orthonormal basis associated with this Cartesian reference. Let $\mathbf{N}_X = \mathbf{j} \cos\phi + \mathbf{k} \sin\phi$ be a unit vector perpendicular to the X-axis, and $\mathbf{n}_X$, the deformation of $\mathbf{N}_X$. Then Cauchy's mean rotation angle, denoted by $\overline{\vartheta_X}$; about the X-axis is just taken as the mean value of ϑ_X—the angle between $\mathbf{N}_X$ and the projection of $\mathbf{n}_X$ upon the Y-Z plane.

However, despite the elegance of Cauchy's concept, the representation formula of Cauchy's mean rotation angle $\overline{\vartheta_X}$ has been unresolved for about one and a half centuries, since 1841. Novozhilov (1948) most happily modified Cauchy's definition by putting the mean value $\overline{\tan\vartheta_X}$ of $\tan\vartheta_X$ in place of $\overline{\vartheta_X}$. He succeeded in evaluating $\overline{\tan\vartheta_X}$, which has been widely used as the measure of mean rotation in the last 40 years. Recently, Marzano (1987) evaluated the mean value of $\cos\vartheta_X$.

The problem of measures of rotation of a deformable body is much more difficult than that of a rigid body, just as stated by Truesdell and Toupin (1960, p. 273): "The theory of finite rotation has always presented singular difficulty, although the essential idea is simple." The rotation of a rigid body can be completely described by a rotation tensor or three Euler-Rodrigues parameters (Beatty, 1977; Cheng and Gupta, 1989). It is a global concept. However, there are many different measures of rotation of a deformable body. Each of them is, in general, a local concept and is a mean rotation in a sense. The line elements radiating from the same material point of the deformable body have, in general, different rotations.

Perhaps the finite rotation tensor $\mathbf{Q}$ in the polar decomposition of the deformation gradient (see, for example, Truesdell and Toupin, 1960; Gurtin, 1981) is the most important one among the measures of rotation of a deformable body. $\mathbf{Q}$ represents the rotation of the principal axes of strain. Another property related to $\mathbf{Q}$ comes from Grioli's theorem (Grioli, 1940), which may be read from page 290 of Truesdell and Toupin's work (1960): "Let a given homogeneous strain be decomposed into a translation, rotation, and a pure strain; then the translation and the rotation are precisely those defining the rigid deformation whose deviation from the given strain is the least possible." Some analogous conclusions to Grioli's were obtained by Martins and Podio-Guidugli (1979, 1980), and some further geometrical meanings of the finite rotation tensor may be read from Zheng and Hwang's work (1987a, 1987b).

In this paper we succeed in evaluating $\overline{\vartheta_X}$ with quite a simple formula. Two approaches are given: One is geometrical and related to the rotation circle, another is algebraic. We also show that Cauchy's mean rotation angle, evaluated with respect to the eigenvector of $\mathbf{Q}$, is actually equal to the rotation angle Θ of $\mathbf{Q}$. Furthermore, Cauchy's mean rotation angle can be related to a so-called projection polar decomposition. In the end part of the present paper, Cauchy's and Novozhilov's measures of mean rotation are compared. When compared to Novozhilov's measure, Cauchy's measure has simpler representation and unrestricted applicability.

Abstracts of this paper have been published in Chinese (Zheng and Hwang, 1988), with English translation (1989). Some developments and applications of this paper have been done (see Zheng and Hwang, 1987a, 1987b; Xiong and Zheng, 1989; Zheng, 1989).

2 Mathematical Preliminaries

Tensor algebra is the most convenient tool to use in the present analysis, and for background, the readers may refer to the books of Bowen and Wang (1976), Chadwick (1976), Gurtin (1981), Ogden (1984), etc.

All vectors and tensors belong to a three-dimensional Euclidean space. Denote the inner product, vector product, and tensor product of two arbitrary vectors $\mathbf{a}$ and $\mathbf{b}$ by $\mathbf{a}\cdot\mathbf{b} = \mathbf{b}\cdot\mathbf{a}$, $\mathbf{a}\times\mathbf{b}$, and $\mathbf{a}\otimes\mathbf{b}$, respectively; the norm of $\mathbf{a}$, by $|\mathbf{a}| = \sqrt{\mathbf{a}\cdot\mathbf{a}}$. We write $\mathbf{B}^T$ for the transpose of second-order tensor $\mathbf{B}$; $\mathrm{tr}\mathbf{B}$, the trace of $\mathbf{B}$. We call $\mathbf{B}$ symmetric if $\mathbf{B}^T = \mathbf{B}$, skew if $\mathbf{B}^T = -\mathbf{B}$.

There is a one-to-one correspondence between vectors and skew tensors: Given any skew tensor $\mathbf{A}$, there exists a unique vector $\mathbf{a}$, the axial vector of $\mathbf{A}$, such that (Gurtin, 1981, p. 8)

$$\mathbf{A}\mathbf{v} = \mathbf{a}\times\mathbf{v}, \tag{1}$$

Contributed by the Applied Mechanics Division of THE AMERICAN SOCIETY OF MECHANICAL ENGINEERS for publication in the JOURNAL OF APPLIED MECHANICS.

Discussion on the paper should be addressed to the Technical Editor, Prof. Leon M. Keer, The Technological Institute, Northwestern University, Evanston, IL 60208, and will be accepted until two months after final publication of the paper itself in the JOURNAL OF APPLIED MECHANICS. Manuscript received by the ASME Applied Mechanics Division, June 27, 1988; final revision, Jan. 20, 1990.

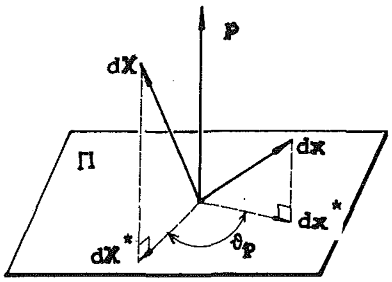

Fig. 1 Normal plane Π, projections dX^* and dx^*, and deformation rotation angle φ_p

for any vector $\mathbf{v}$, and conversely; indeed,

$$A_{21}=-A_{12}=a_3,\ A_{32}=-A_{23}=a_1,\ A_{13}=-A_{31}=a_2, \qquad (2)$$

where A_{ij} and a_k are the Cartesian components of $\mathbf{A}$ and $\mathbf{a}$, respectively. By the aid of the expansion theorem of triple vector product,

$$\mathbf{w}\times(\mathbf{u}\times\mathbf{v})=\mathbf{u}\,\mathbf{w}\cdot\mathbf{v}-\mathbf{v}\,\mathbf{w}\cdot\mathbf{u}, \qquad (3)$$

for any skew tensors $\mathbf{A}$, $\mathbf{B}$ and their axial vectors $\mathbf{a}$, $\mathbf{b}$, we have

$$\mathbf{ABv}=\mathbf{a}\times\mathbf{Bv}=\mathbf{a}\times(\mathbf{b}\times\mathbf{v})$$
$$=\mathbf{b}\,\mathbf{a}\cdot\mathbf{v}-\mathbf{v}\,\mathbf{a}\cdot\mathbf{b}=(\mathbf{b}\otimes\mathbf{a}-\mathbf{a}\cdot\mathbf{b}\,\mathbf{I})\mathbf{v}, \qquad (4)$$

in which $\mathbf{I}$ is the second-order identity tensor. This formula implies that

$$\mathbf{AB}=\mathbf{b}\otimes\mathbf{a}-\mathbf{b}\cdot\mathbf{a}\,\mathbf{I}. \qquad (5)$$

In particular, if a skew tensor $\mathbf{P}$ has the axial vector $\mathbf{p}$ with unit norm $|\mathbf{p}|=1$, then it follows from property (5) that

$$\mathbf{P}^2=\mathbf{p}\otimes\mathbf{p}-\mathbf{I}=(\mathbf{P}^2)^T,\ \mathbf{P}^3=-\mathbf{P},\ (\text{if } |\mathbf{p}|=1). \qquad (6)$$

For any second-order tensors $\mathbf{D}$, $\mathbf{G}$, symmetric tensor $\mathbf{S}$, and skew tensors $\mathbf{A}$, $\mathbf{B}$, the following properties can be easily proved (see, for example, Gurtin, 1981, Sect. 1)

$$\mathrm{tr}\mathbf{D}^T=\mathrm{tr}\mathbf{D},\ \mathrm{tr}(\mathbf{DG})=\mathrm{tr}(\mathbf{GD}),\ \mathrm{tr}\mathbf{A}=\mathrm{tr}(\mathbf{AS})=0. \qquad (7)$$

And from (5) and (6), we can obtain the useful identities:

$$\mathrm{tr}(\mathbf{AB})=-\mathrm{tr}(\mathbf{A}^T\mathbf{B})=-2\mathbf{a}\cdot\mathbf{b}; \qquad (8)$$

$$\mathrm{tr}(\mathbf{P}^4\mathbf{D})=\mathrm{tr}(-\mathbf{P}^2\mathbf{D})=\mathrm{tr}\mathbf{D}-\mathbf{p}\cdot\mathbf{Dp},\ (\text{if } |\mathbf{p}|=1). \qquad (9)$$

Hereafter, we shall always use the fixed triple $\{\mathbf{p}, \mathbf{P}, \Pi\}$ to express a skew tensor $\mathbf{P}$ with unit axial vector $\mathbf{p}$ and the normal plane Π of $\mathbf{p}$. For any vector $\mathbf{v}$, the projection $\mathbf{v}^*$ of $\mathbf{v}$ on Π should be

$$\mathbf{v}^*=\mathbf{v}-\mathbf{p}\,\mathbf{v}\cdot\mathbf{p}=(\mathbf{I}-\mathbf{p}\otimes\mathbf{p})\mathbf{v}=-\mathbf{P}^2\mathbf{v}, \qquad (10)$$

in which (6) has been used. The projection $\mathbf{D}^*$ on Π of any second-order tensor $\mathbf{D}$ is defined by $\mathbf{u}\cdot\mathbf{D}^*\mathbf{v}=\mathbf{u}^*\cdot\mathbf{D}\mathbf{v}^*$, where $\mathbf{u}$ and $\mathbf{v}$ are arbitrary vectors. From (10) it is obvious that

$$\mathbf{D}^*=\mathbf{P}^2\mathbf{D}\mathbf{P}^2. \qquad (11)$$

Because $(\mathbf{P}^2)^T=\mathbf{P}^2$, from (11) we know also $(\mathbf{D}^*)^T=(\mathbf{D}^T)^*$. It implies that the projections of any symmetric and skew tensors remain symmetric and skew, respectively. Finally, for any vector $\mathbf{c}$ of Π, since $\mathbf{c}\cdot\mathbf{p}=0$,

$$\mathbf{c}=\mathbf{c}-\mathbf{p}\,\mathbf{c}\cdot\mathbf{p}=-\mathbf{P}^2\mathbf{c}=\mathbf{c}^*. \qquad (12)$$

3 Cauchy's Measure of Mean Rotation

Consider a deformable body $\mathcal{B}$ moving in a three-dimensional Euclidean space. Let $\mathbf{X}$ and $\mathbf{x}$ be the position vectors of the typical material particle of $\mathcal{B}$ with respect to the reference configuration and the current configuration of $\mathcal{B}$, respectively. Thus, the deformation $d\mathbf{x}$ of the line element $d\mathbf{X}$ is given by $d\mathbf{x}=\mathbf{F}d\mathbf{X}$, where $\mathbf{F}=\partial\mathbf{x}/\partial\mathbf{X}$ is the deformation gradient.

Let $\{\mathbf{p}, \mathbf{P}, \Pi\}$ be the fixed triple defined in the last section, and $d\mathbf{X}^*$ and $d\mathbf{x}^*$, the projections on Π of $d\mathbf{X}$ and its deformation $d\mathbf{x}$. The angle ϑ_p, through which $d\mathbf{X}^*$ is right-handed turned to $d\mathbf{x}^*$, is called the *deformation rotation angle* with respect to $\mathbf{p}$ (see Fig. 1). Mathematically, we have

$$|d\mathbf{x}^*|\,|d\mathbf{X}^*|\cos\vartheta_\mathrm{p}=d\mathbf{X}^*\cdot d\mathbf{x}^*; \qquad (13a)$$

$$|d\mathbf{x}^*|\,|d\mathbf{X}^*|\sin\vartheta_\mathrm{p}=\mathbf{p}\cdot(d\mathbf{X}^*\times d\mathbf{x}^*)=(\mathbf{p}\times d\mathbf{X}^*)\cdot d\mathbf{x}^*. \qquad (13b)$$

Introduce the direction $\mathbf{N}=d\mathbf{X}/|d\mathbf{X}|$ of $d\mathbf{X}$, then

$$d\mathbf{X}^*/|d\mathbf{X}|=-\mathbf{P}^2d\mathbf{X}/|d\mathbf{X}|=-\mathbf{P}^2\mathbf{N}=\mathbf{N}^*,$$
$$d\mathbf{x}^*/|d\mathbf{X}|=(\mathbf{FN})^*; \qquad (14a)$$

$$\rho=|d\mathbf{x}^*|\,|d\mathbf{X}^*|/|d\mathbf{X}|^2=|(\mathbf{FN})^*|\,|\mathbf{N}^*|\geq 0. \qquad (14b)$$

Equations (13) and (14) yield

$$\rho\sin\vartheta_\mathrm{p}=(\mathbf{p}\times\mathbf{N}^*)\cdot(\mathbf{FN})^*=(\mathbf{PP}^2\mathbf{N})\cdot(\mathbf{P}^2\mathbf{FN})$$
$$=-\mathbf{N}\cdot\mathbf{P}^5\mathbf{FN}=-\mathbf{N}\cdot\mathbf{PFN},$$
$$\rho\cos\vartheta_\mathrm{p}=\mathbf{N}^*\cdot(\mathbf{FN})^*=(\mathbf{P}^2\mathbf{N})\cdot(\mathbf{P}^2\mathbf{FN})$$
$$=\mathbf{N}\cdot\mathbf{P}^4\mathbf{FN}=-\mathbf{N}\cdot\mathbf{P}^2\mathbf{FN}, \qquad (15)$$

in which the properties (1) and (6) have been used.

From (15) we also know that for a given deformation gradient $\mathbf{F}$ and direction $\mathbf{p}$, both ϑ_p and ρ are functions of $\mathbf{N}$; in particular, if $d\mathbf{X}$ or $\mathbf{N}$ belongs to Π, then from (12): $\mathbf{N}=\mathbf{N}^*=-\mathbf{P}^2\mathbf{N}$ and (15), the deformation rotation angle ϑ_p can be evaluated by

$$\rho\sin\vartheta_\mathrm{p}=-\mathbf{N}\cdot\mathbf{PF}^*\mathbf{N},\ \rho\cos\vartheta_\mathrm{p}=\mathbf{N}\cdot\mathbf{F}^*\mathbf{N}. \qquad (16)$$

Here, $\mathbf{F}^*=\mathbf{P}^2\mathbf{FP}^2$ is the projection of $\mathbf{F}$ on Π. As $\underline{\mathbf{N}}$ is taken all directions over Π, the mean value, denoted by $\bar{\vartheta}_\mathrm{p}$, of the deformation rotation angle $\vartheta_\mathrm{p}=\vartheta_\mathrm{p}(\mathbf{N})$ as a function of $\mathbf{N}$ is named the *Cauchy's mean rotation angle* with respect to $\mathbf{p}$; and the mean value, denoted by $\tan\tau_\mathrm{p}$, of $\tan\vartheta_\mathrm{p}(\mathbf{N})$ gives the *Novozhilov's mean rotation angle* τ_p with respect to $\mathbf{p}$.

Arbitrarily given a constant angle φ_0 and a direction $\mathbf{N}_0$ on plane Π, any direction $\mathbf{N}$ on Π can be expressed by

$$\mathbf{N}=\mathbf{N}(\varphi)=\mathbf{N}_0\cos(\varphi-\varphi_0)+\mathbf{p}\times\mathbf{N}_0\sin(\varphi-\varphi_0),$$
$$(-\pi<\varphi\leq\pi). \qquad (17)$$

Then, $\bar{\vartheta}_\mathrm{p}$ and τ_p can be represented by

$$\bar{\vartheta}_\mathrm{p}=\frac{1}{2\pi}\int_{-\pi}^{\pi}\vartheta_\mathrm{p}(\mathbf{N}(\varphi))\,d\varphi; \qquad (18)$$

$$\tan\tau_\mathrm{p}=\frac{1}{2\pi}\int_{-\pi}^{\pi}\tan\vartheta_\mathrm{p}(\mathbf{N}(\varphi))\,d\varphi. \qquad (19)$$

4 Representation Theorem of Cauchy's Mean Rotation

Introduce the additive decomposition of the deformation gradient $\mathbf{F}$ as follows:

$$\mathbf{F}=\mathbf{I}+\mathbf{E}+\mathbf{W}. \qquad (20)$$

Here, the symmetric tensor $\mathbf{E}$, the skew tensor $\mathbf{W}$, and the axial vector $\mathbf{w}$ of $\mathbf{W}$ satisfy

$$\mathbf{E}=\tfrac{1}{2}(\mathbf{F}+\mathbf{F}^T)-\mathbf{I},\ \mathbf{W}=\tfrac{1}{2}(\mathbf{F}-\mathbf{F}^T), \qquad (21a)$$

$$\mathbf{Wv}=\mathbf{w}\times\mathbf{v} \text{ for any vector } \mathbf{v}. \qquad (21b)$$

Let $\mathbf{N}$ be a direction on Π. Substituting the projection of (20) on Π

$$\mathbf{F}^*=\mathbf{I}^*+\mathbf{E}^*+\mathbf{W}^* \qquad (22)$$

into (16), we can write

$$\rho\sin\vartheta_\mathrm{p}=-\mathbf{N}\cdot\mathbf{P}(\mathbf{I}^*+\mathbf{E}^*+\mathbf{W}^*)\mathbf{N}$$
$$=-\mathbf{N}\cdot\mathbf{PE}^*\mathbf{N}-\mathbf{N}\cdot\mathbf{P}^3\mathbf{WP}^2\mathbf{N}$$
$$=\mathbf{PN}\cdot\mathbf{E}^*\mathbf{N}-\mathbf{N}\cdot\mathbf{PWN}=(\mathbf{p}\times\mathbf{N})\cdot(\mathbf{E}^*\mathbf{N})+\mathbf{w}\cdot\mathbf{p}, \qquad (23a)$$

$$\rho\cos\vartheta_\mathrm{p}=\mathbf{N}\cdot(\mathbf{I}^*+\mathbf{E}^*+\mathbf{W}^*)\mathbf{N}=1+\mathbf{N}\cdot\mathbf{E}^*\mathbf{N}. \qquad (23b)$$

In (23a), the properties $\mathbf{P}^3=-\mathbf{P}$, $-\mathbf{P}^2\mathbf{N}=\mathbf{N}$, and $\mathbf{PN}=\mathbf{p}\times\mathbf{N}$

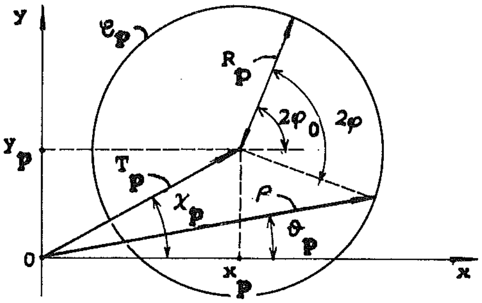

Fig. 2 Deformation rotation circle φ_p and deformation rotation angle Θ_p

have been used. Because $\mathbf{E}^*$ is symmetric, it follows from the spectral theorem (see, for example, Gurtin, 1981, Sect. 2) that

$$\mathbf{E}^* = \mathrm{E}_1^* \mathbf{n}_1 \otimes \mathbf{n}_1 + \mathrm{E}_2^* \mathbf{n}_2 \otimes \mathbf{n}_2, \tag{24}$$

with $\{\mathbf{n}_1, \mathbf{n}_2, \mathbf{p}\}$ orthonormal and $\mathrm{E}_1^* \geq \mathrm{E}_2^*$. Without loss of generality, we may require $\mathbf{n}_1 \times \mathbf{n}_2 = \mathbf{p}$, so that $\{\mathbf{n}_1, \mathbf{n}_2, \mathbf{p}\}$ is a right-handed orthonormal basis. Taking $\mathbf{n}_1$ as the direction $\mathbf{N}_0$ in (17) yields

$$\mathbf{N} = \mathbf{N}(\varphi) = \mathbf{n}_1 \cos(\varphi - \varphi_0) + \mathbf{n}_2 \sin(\varphi - \varphi_0), \; (-\pi < \varphi \leq \pi). \tag{25}$$

Substituting (25) into (23), one can obtain

$$\begin{aligned} \rho \sin\vartheta_\mathrm{p} &= \mathbf{w} \cdot \mathbf{p} - \frac{1}{2}(E_1^* - E_2^*) \sin[2(\varphi - \varphi_0)], \\ & \qquad\qquad\qquad\qquad (-\pi \leq \varphi \leq \pi). \\ \rho \cos\vartheta_\mathrm{p} &= 1 + \frac{1}{2}(E_1^* + E_2^*) + \frac{1}{2}(E_1^* - E_2^*) \cos[2(\varphi - \varphi_0)], \end{aligned} \tag{26}$$

To reveal the geometric meaning of formula (26), let $\{x, y\}$ be a plane Cartesian coordinate system and introduce a curve $\mathcal{C}_\mathrm{p}$ on x-y plane

$$\begin{aligned} x(\varphi) &= \rho \cos\vartheta_\mathrm{p} = x_\mathrm{p} + R_\mathrm{p} \cos[2(\varphi - \varphi_0)], \\ & \qquad\qquad\qquad (-\pi < \varphi \leq \pi), \\ y(\varphi) &= \rho \sin\vartheta_\mathrm{p} = y_\mathrm{p} - R_\mathrm{p} \sin[2(\varphi - \varphi_0)], \end{aligned} \tag{27}$$

in which

$$x_\mathrm{p} = 1 + \frac{1}{2}(E_1^* + E_2^*), \; y_\mathrm{p} = \mathbf{w} \cdot \mathbf{p}, \; R_\mathrm{p} = \frac{1}{2}(E_1^* - E_2^*). \tag{28}$$

It is obvious that this curve $\mathcal{C}_\mathrm{p}$ is two superimposed circles on x-y plane with center $(x_\mathrm{p}, y_\mathrm{p})$ and radius R_p (see Fig. 2), and $\mathcal{C}_\mathrm{p}$ resembles the well-known Mohr's circle (Timoshenko and Gere, 1972). We call $\mathcal{C}_\mathrm{p}$ the *rotation circle* corresponding to $\mathbf{p}$.

Use χ_p to denote the argument of the point $(x_\mathrm{p}, y_\mathrm{p})$ at x-y plane (see Fig. 2), that is[1]

$$T_\mathrm{p} \cos\chi_\mathrm{p} = x_\mathrm{p}, \; T_\mathrm{p} \sin\chi_\mathrm{p} = y_\mathrm{p}, \tag{29a}$$

$$T_\mathrm{p} = \sqrt{x^2{}_\mathrm{p} + y^2{}_\mathrm{p}}. \tag{29b}$$

In order to give some alternative forms of the coefficients x_p, y_p, T_p, and R_p, introduce a special orthonormal basis $\{\mathbf{e}_i\}$ with $\mathbf{e}_3 = \mathbf{p} = \mathbf{e}_1 \times \mathbf{e}_2$. Let F_{ij}, E_{ij}, W_{ij}, and w_k be the components of $\mathbf{F}$, $\mathbf{E}$, $\mathbf{W}$, and $\mathbf{w}$ in $\{\mathbf{e}_i\}$, respectively. By use of (22), and (7)–(9), from (28), we can easily obtain

$$\begin{aligned} x_\mathrm{p} &= 1 + \frac{1}{2}(E_1^* + E_2^*) = 1 + \frac{1}{2}(E_{11} + E_{22}) = \frac{1}{2}(F_{11} + F_{22}) \\ &= 1 + \frac{1}{2}\mathrm{tr}\mathbf{E}^* = 1 + \frac{1}{2}(\mathrm{tr}\mathbf{E} - \mathbf{p} \cdot \mathbf{E}\mathbf{p}) \\ &= \frac{1}{2}\mathrm{tr}\mathbf{F}^* = \frac{1}{2}(\mathrm{tr}\mathbf{F} - \mathbf{p} \cdot \mathbf{F}\mathbf{p}), \end{aligned} \tag{30a}$$

$$\begin{aligned} y_\mathrm{p} &= \mathbf{w} \cdot \mathbf{p} = w_3 = W_{21} = \frac{1}{2}(F_{21} - F_{12}) \\ &= -\frac{1}{2}\mathrm{tr}(\mathbf{PW}) = -\frac{1}{2}\mathrm{tr}(\mathbf{PF}); \end{aligned} \tag{30b}$$

$$T_\mathrm{p} = \sqrt{x_\mathrm{p}^2 + y_\mathrm{p}^2} = \frac{1}{2}\sqrt{(F_{11} + F_{22})^2 + (F_{21} - F_{12})^2}; \tag{30c}$$

$$\begin{aligned} R_\mathrm{p} &= \frac{1}{2}(E_1^* - E_2^*) = \frac{1}{2}\sqrt{(F_{11} - F_{22})^2 + (F_{21} + F_{12})^2} \\ &= \frac{1}{2}\sqrt{2\mathrm{tr}(\mathbf{E}^{*2}) - (\mathrm{tr}\mathbf{E}^*)^2} = \sqrt{(E_{11} - E_{22})^2/4 + E_{12}^2}. \end{aligned} \tag{30d}$$

Combining (29) and (30), we can obtain the invariance representation formulae

$$T_\mathrm{p} \cos\chi_\mathrm{p} = 1 + (\mathrm{tr}\mathbf{E} - \mathbf{p} \cdot \mathbf{E}\mathbf{p})/2, \; T_\mathrm{p} \sin\chi_\mathrm{p} = \mathbf{w} \cdot \mathbf{p}, \tag{31a}$$

$$T_\mathrm{p} = \sqrt{(\mathbf{w} \cdot \mathbf{p})^2 + [1 + (\mathrm{tr}\mathbf{E} - \mathbf{p} \cdot \mathbf{E}\mathbf{p})/2]^2}. \tag{31b}$$

According to the definition (18) and Fig. 2, the following theorem is quite evident.

Theorem 1. If the angular region of the deformation rotation angle ϑ_p is stipulated as

$$\mathcal{A}(\vartheta_\mathrm{p}; \chi_\mathrm{p}) = \{\vartheta_\mathrm{p}: -\pi + \chi_\mathrm{p} < \vartheta_\mathrm{p} \leq \pi + \chi_\mathrm{p}\}, \tag{32}$$

then the mean value $\overline{\vartheta_\mathrm{p}}$ of ϑ_p is equal to χ_p:

$$\overline{\vartheta}_\mathrm{p} = \chi_\mathrm{p}. \tag{33}$$

We can give an alternative proof of Theorem 1 as follows. Set $2\varphi_0 = \chi_\mathrm{p}$ and arrange (26) into the new form:

$$\begin{aligned} \rho \cos(\vartheta_\mathrm{p} - \chi_\mathrm{p}) &= T_\mathrm{p} + R_\mathrm{p} \cos(2\varphi), \\ & \qquad\qquad (-\pi < \varphi \leq \pi). \\ \rho \sin(\vartheta_\mathrm{p} - \chi_\mathrm{p}) &= -R_\mathrm{p} \sin(2\varphi), \end{aligned} \tag{34}$$

If we restrict $\vartheta_\mathrm{p} - \chi_\mathrm{p}$ to be evaluated in the domain (32), that is, $\vartheta_\mathrm{p} - \chi_\mathrm{p}$ as a function of φ maps the angular region $(-\pi, \pi]$ into itself, then (34) shows that $\vartheta_\mathrm{p} - \chi_\mathrm{p}$ is an odd function of φ. Therefore, the integration of this function on the symmetric angular region $(-\pi, \pi)$ of φ is exactly equal to zero:

$$0 = \frac{1}{2\pi}\int_{-\pi}^{\pi} (\vartheta_\mathrm{p} - \chi_\mathrm{p}) d\varphi = \frac{1}{2\pi}\int_{-\pi}^{\pi} \vartheta_\mathrm{p} d\varphi - \chi_\mathrm{p} = \overline{\vartheta_\mathrm{p}} - \chi_\mathrm{p}. \tag{35}$$

The algebraic proof of Theorem 1 is hereby completed.

5 Some Further Comments on the Cauchy's Measure of Mean Rotation Angle

We have to make a few comments upon the definition of Cauchy's measure of mean rotation and Theorem 1. In definition (18) there is an essential defect that the angular range of ϑ_p is ambiguously understood. However, this defect doesn't appear in the definition of *generalized local mean rotation* (Zheng and Hwang, 1987). As is well known, a most natural angular region of ϑ_p might be taken as $(-\pi, \pi]$. And in this case we call the mean value of ϑ_p the *original Cauchy's mean rotation angle* with respect to $\mathbf{p}$. $\overline{\vartheta_\mathrm{p}}$ evaluated by (33) of Theorem 1 is a generalized Cauchy's mean rotation angle rather than the original one, because the angular region of the deformation rotation angle ϑ_p in Theorem 1 is stipulated as $(-\pi + \chi_\mathrm{p}, \pi + \chi_\mathrm{p}]$.

It is clear from Fig. 2 that if and only if

$$T_\mathrm{p} > R_\mathrm{p}, \tag{36a}$$

i.e., by use of (30c,d),

$$D = F_{11}F_{22} - F_{12}F_{21} > 0, \tag{36b}$$

the deformation rotation angle ϑ_p can be evaluated as a continuous function on the deformation rotation circle. Otherwise, if $T_\mathrm{p} \leq R_\mathrm{p}$, different choice of fixed angular range of ϑ_p will

[1] In the exceptional case $T_\mathrm{p} = 0$ at a material point X, χ_p at X can be determined by considering the continuity of χ_p at X.

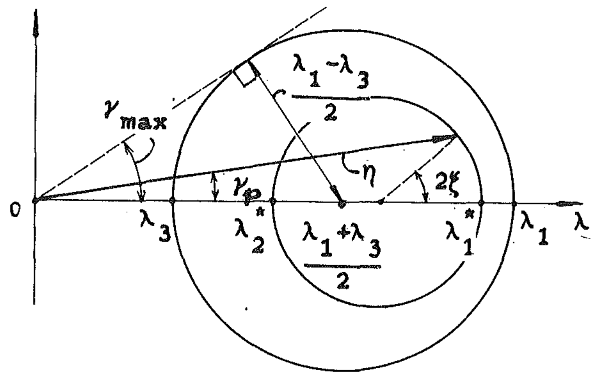

Fig. 3 Maximum pure deformation rotation angles γ_{max}

result in different mean value of ϑ_p^2. From Fig. 2 we can see that if the rotation circle is never crossed by a negative x-axis, then ϑ_p is certainly continuous on the rotation circle provided the range of ϑ_p is stipulated as $(-\pi, \pi]$. In this case, $\overline{\vartheta_p}=\chi_p$ is the original Cauchy's mean rotation angle.

Let $\mathbf{F}=\mathbf{QU}$ be the polar decomposition of the deformation gradient $\mathbf{F}$, in which the finite rotation tensor $\mathbf{Q}$ is proper orthogonal and the right stretch tensor $\mathbf{U}$ is positive definite symmetric. According to the spectral theorem, we can give the spectral form of $\mathbf{U}$ as follows:

$$\mathbf{U}=\lambda_1\mathbf{N}_1\otimes\mathbf{N}_1+\lambda_2\mathbf{N}_2\otimes\mathbf{N}_2+\lambda_3\mathbf{N}_3\otimes\mathbf{N}_3, \quad (\lambda_1\geq\lambda_2\geq\lambda_3>0). \tag{37}$$

Here, λ_1, λ_2, and λ_3 are the three principal values of $\mathbf{U}$; the three unit orthogonal vectors $\mathbf{N}_1$, $\mathbf{N}_2$, and $\mathbf{N}_3$ are the principal directions of $\mathbf{U}$ with $\mathbf{UN}_i=\lambda_i\mathbf{N}_i$, $i=1, 2, 3$. As is well known, the stretch tensor $\mathbf{U}$ stands for the local pure deformation, and $\mathbf{Q}$, the local rigid rotation. Let $\{\mathbf{p}, \mathbf{P}, \Pi\}$ be the fixed triple defined in Sect. 2, $\{\mathbf{e}_1, \mathbf{e}_2, \mathbf{p}\}$ be a right-handed orthonormal basis with $\mathbf{p}=\mathbf{e}_1\times\mathbf{e}_2$. Referring to (26) and (14b), it follows that the pure deformation rotation angle γ_p of the direction $\mathbf{N}(\xi)=\mathbf{e}_1\cos\xi+\mathbf{e}_2\sin\xi$ satisfies

$$2\eta\cos\gamma_p=(\lambda_1^*+\lambda_2^*)+(\lambda_1^*-\lambda_2^*)\cos(2\xi),$$
$$2\eta\sin\gamma_p=-(\lambda_1^*-\lambda_2^*)\sin(2\xi), \tag{38a}$$

and

$$\lambda_1^*=\max\{\mathbf{N}(\xi)\cdot\mathbf{UN}(\xi):\ -\pi<\xi\leq\pi\}, \tag{38b}$$
$$\lambda_2^*=\min\{\mathbf{N}(\xi)\cdot\mathbf{UN}(\xi):\ -\pi<\xi\leq\pi\}, \tag{38c}$$
$$\eta=\sqrt{(\lambda^*\cos\xi)^2+(\lambda_2^*\sin\xi)^2}\geq\lambda_2^*>0. \tag{38d}$$

In (38d) we have considered that the positive definiteness of $\mathbf{U}$ implies $\mathbf{e}\cdot\mathbf{Ue}>0$ for any direction $\mathbf{e}$. Since $\lambda_3\leq\lambda_2^*\leq\lambda_1^*\leq\lambda_1$, from (38) or Fig. 3, we can easily find that the maximum value γ_{max} of γ_p as the function of direction $\mathbf{p}$ and ξ is

$$\gamma_{max}=\arcsin\left(\frac{\lambda_1-\lambda_3}{\lambda_1+\lambda_3}\right)=\arctan\left(\frac{\lambda_1-\lambda_3}{\sqrt{4\lambda_1\lambda_3}}\right). \tag{39}$$

Denote the rotation angle of the finite rotation tensor $\mathbf{Q}$ by Θ. Because the absolute value of any deformation rotation angle is smaller than $|\Theta|+\gamma_{max}$, now we are in a position to state the following theorem.

Theorem 2. If the deformation obeys

$$|\Theta|+\gamma_{max}<\pi, \tag{40}$$

then the original Cauchy's mean rotation angle, with respect to any direction $\mathbf{p}$, certainly uniquely exists, and is equal to $\overline{\vartheta_p}=\chi_p$.

Since $\gamma_{max}<\pi/2$, a sufficient condition for (40) being valid may be given by $|\Theta|\leq\pi/2$.

6 Projection Polar Decomposition and Cauchy's Mean Rotation

Let $\{\mathbf{p}, \mathbf{P}, \Pi\}$ be the fixed triple defined in Sect. 2. For ease of statement, if a second-order tensor $\mathbf{D}$ is equal to its projection $\mathbf{D}^*$ upon the plane Π, we will call $\mathbf{D}$ to be projection invariant. From (11) and (6) we can easily prove that the projection $\mathbf{D}^*$ of any second order tensor $\mathbf{D}$ is projection invariant; both $\mathbf{P}$ and $\mathbf{P}^2$ are projection invariant, etc. Let T_p be given by (31b). We shall prove the following theorem.

Theorem 3. If $T_p>0$, then the projection $\mathbf{F}^*$ on Π of the deformation gradient $\mathbf{F}$ has unique right and left projection polar decompositions:

$$\mathbf{F}^*=\mathbf{R}_p\,\hat{\mathbf{U}}=\hat{\mathbf{V}}\,\mathbf{R}_p. \tag{41}$$

Here, $\mathbf{R}_p$ is the Cauchy's mean rotation tensor with respect to $\mathbf{p}$, that is, $\mathbf{R}_p$ is a proper orthogonal tensor with axis $\mathbf{p}$ and rotation angle $\overline{\vartheta_p}$ given in Theorem 1. The symmetric tensors $\hat{\mathbf{U}}$ and $\hat{\mathbf{V}}$, which are projection invariant, satisfy the inequalities:

$$\mathrm{tr}\hat{\mathbf{U}}>0, \text{ and } \mathrm{tr}\hat{\mathbf{V}}>0. \tag{42}$$

Only the right projection polar decomposition $(41)_1$ will be proved in detail. Let the canonical representation of some proper orthogonal tensor $\mathbf{R}$ with axis $\mathbf{p}$ and rotation angle ψ be (see, for example Guo (1980) or Xiong and Zheng (1989))

$$\mathbf{R}=\mathbf{I}+\mathbf{P}\sin\psi+\mathbf{P}^2(1-\cos\psi). \tag{43}$$

Because $\mathbf{P}^T=-\mathbf{P}$, $(\mathbf{P}^2)^T=\mathbf{P}^2$, for each $\mathbf{R}$ we may introduce a new projection invariant tensor:

$$\begin{aligned}\mathbf{G}(\psi)=\mathbf{R}^T\mathbf{F}^*&=[\mathbf{I}-\mathbf{P}\sin\psi+\mathbf{P}^2(1-\cos\psi)]\mathbf{F}^*\\&=\mathbf{F}^*-\mathbf{PF}^*\sin\psi+\mathbf{P}^2\mathbf{F}^*(1-\cos\psi)\\&=\mathbf{F}^*\cos\psi-\mathbf{PF}^*\sin\psi.\end{aligned} \tag{44}$$

In the derivation of (44), the property

$$\mathbf{P}^2\mathbf{F}^*=\mathbf{P}^2\mathbf{P}^2\mathbf{FP}^2=\mathbf{P}^4\mathbf{FP}^2=-\mathbf{P}^2\mathbf{FP}^2=-\mathbf{F}^* \tag{45}$$

has been used.

Introduce an orthonormal basis $\{\mathbf{e}_i\}$ with $e_3=\mathbf{p}=\mathbf{e}_1\times\mathbf{e}_2$. Suppose all the components are given in $\{\mathbf{e}_i\}$. Then the component matrices of $\mathbf{F}^*$ and $\mathbf{PF}^*$ should be

$$[\mathbf{F}^*]=\begin{bmatrix}F_{11}&F_{12}&0\\F_{21}&F_{22}&0\\0&0&0\end{bmatrix},\ [\mathbf{PF}^*]=\begin{bmatrix}-F_{21}&-F_{22}&0\\F_{11}&F_{12}&0\\0&0&0\end{bmatrix}. \tag{46}$$

From (44) and (46) it follows that

$$[\mathbf{G}(\psi)]=\begin{bmatrix}F_{11}\cos\psi+F_{21}\sin\psi&F_{12}\cos\psi+F_{22}\sin\psi&0\\F_{21}\cos\psi-F_{11}\sin\psi&F_{22}\cos\psi-F_{12}\sin\psi&0\\0&0&0\end{bmatrix}. \tag{47}$$

Noting that $\mathbf{G}(\psi)$ will be symmetric if and only if $G_{12}(\psi)=G_{21}(\psi)$, from (47) we can change the condition $G_{12}(\psi)=G_{21}(\psi)$ into the new form:

$$(F_{21}-F_{12})\cos\psi=(F_{11}+F_{22})\sin\psi. \tag{48}$$

However, from (30), (31), and (33) of Theorem 1, we know

$$T_p\sin\overline{\vartheta_p}=(F_{21}-F_{12})/2,\ T_p\cos\overline{\vartheta_p}=(F_{11}+F_{22})/2. \tag{49}$$

Hence, the condition (48) is equivalent to

[2] In fact (see Zheng and Hwang, 1987), through a complicated discussion based on complex analysis, we have proved the theorem: If the angular range of the deformation rotation angle ϑ_p is stipulated as

$$\mathfrak{a}(\vartheta_p;\beta)=\{\vartheta_p:\ -\pi+\beta<\vartheta_p\leq\pi+\beta\},$$

then the necessary and sufficient condition about β to ensure that the mean value of ϑ_p is equal to χ_p is

$$|\beta-\chi_p|\leq\pi-\arcsin(R_p/T_p), \text{ if } T_p\geq R_p; \text{ or}$$
$$\beta=\chi_p, \text{ if } T_p<R_p.$$

$$2\,T_p \sin(\psi - \overline{\vartheta_p}) = 0. \tag{50}$$

Recalling the assumption $T_p > 0$ in Theorem 3, we know that $\mathbf{G}(\psi)$ will be symmetric if and only if the parameter ψ is taken as

$$\psi_k = \overline{\vartheta_p} + k\pi,\ (k=0,\ \pm 1,\ \pm 2,\ \ldots). \tag{51}$$

Finally, substituting (51) and (49) into (47) will result in

$$\begin{aligned}\mathrm{tr}\mathbf{G}(\psi_k) &= (F_{11}+F_{22})\cos\psi_k + (F_{21}-F_{12})\sin\psi_k = 2T_p\cos(\psi_k - \overline{\vartheta_p})\\ &= 2T_p(-1)^k,\ (k=0,\ \pm 1,\ \pm 2,\ \ldots).\end{aligned} \tag{52}$$

It implies that in order to ensure $\mathrm{tr}\mathbf{G}(\psi_k) > 0$ the parameter ψ ought to be taken as

$$\psi_m = \overline{\vartheta_p} + 2m\pi,\ (m=0,\ \pm 1,\ \pm 2,\ \ldots). \tag{53}$$

However, substituting every ψ_m in (53) into (44), (47), and (52) will lead to the unique $\mathbf{R}_p$ and $\hat{\mathbf{U}} = \mathbf{G}(\psi_m)$ as well as the trace $\mathrm{tr}\hat{\mathbf{U}}$:

$$\mathbf{R}_p = \mathbf{R}(\psi_m) = \mathbf{I} + \mathbf{P}\sin\overline{\vartheta_p} + \mathbf{P}^2(1-\cos\vartheta_p); \tag{54}$$

$$[\hat{\mathbf{U}}] = [\mathbf{G}(\psi_m)] = \frac{1}{2T_p}\begin{bmatrix} F_{11}^2+F_{21}^2+D & F_{11}F_{12}+F_{22}F_{21} & 0\\ F_{11}F_{12}+F_{22}F_{22} & F_{22}^2+F_{12}^2+D & 0\\ 0 & 0 & 0\end{bmatrix}; \tag{55}$$

$$\mathrm{tr}\hat{\mathbf{U}} = \mathbf{2}\boldsymbol{T}_p. \tag{56}$$

Here, $D = F_{11}F_{22} - F_{21}F_{12}$. A similar discussion on $\mathbf{F}^* = \mathbf{V}^*\mathbf{R}_p$ will result in

$$[\hat{\mathbf{V}}] = \frac{1}{2T_p}\begin{bmatrix} F_{11}^2+F_{12}^2+D & F_{11}F_{22}+F_{21}F_{12} & 0\\ F_{11}F_{21}+F_{22}F_{12} & F_{22}^2+F_{21}^2+D & 0\\ 0 & 0 & 0\end{bmatrix}; \tag{57}$$

$$\mathrm{tr}\hat{\mathbf{V}} = 2T_p. \tag{58}$$

The proof of Theorem 3 is completed.

7 Finite Rotation Tensor and Cauchy's Mean Rotation

As an application of Theorem 1 and a development of Theorem 3, we can prove:

Theorem 4. The finite rotation tensor $\mathbf{Q}$ in the polar decomposition of the deformation gradient $\mathbf{F}$ can be interpreted as the Cauchy's mean rotation tensor with respect to the rotation axis of $\mathbf{Q}$.

Let $\mathbf{q}$ be the rotation axis of $\mathbf{Q}$ (i.e., the unit eigenvector of $\mathbf{Q}$: $\mathbf{Qq} = \mathbf{q}$, $|\mathbf{q}| = 1$); Θ, the rotation angle of $\mathbf{Q}$; and $\mathbf{U}$, the right stretch tensor. Then the component matrix of the polar decomposition $\mathbf{F} = \mathbf{QU}$, in an orthonormal basis $\{\mathbf{e}_i\}$ with $\mathbf{e}_3 = \mathbf{q} = \mathbf{e}_1 \times \mathbf{e}_2$, ought to be

$$[\mathbf{F}] = \begin{bmatrix}\cos\Theta & -\sin\Theta & 0\\ \sin\Theta & \cos\Theta & 0\\ 0 & 0 & 1\end{bmatrix}\begin{bmatrix}U_{11} & U_{12} & U_{13}\\ U_{21} & U_{22} & U_{23}\\ U_{31} & U_{32} & U_{33}\end{bmatrix}. \tag{59}$$

From (59) we obtain

$$\begin{aligned}F_{11}+F_{22} &= (U_{11}+U_{22})\cos\Theta,\\ F_{21}-F_{12} &= (U_{11}+U_{22})\sin\Theta.\end{aligned} \tag{60}$$

Because $\mathbf{U}$ is positive definite symmetric, it implies $U_{11} = \mathbf{e}_1.\ \mathbf{Ue}_1 > 0$ and $U_{22} = \mathbf{e}_2.\ \mathbf{Ue}_2 > 0$. Comparing Eq. (60) with (49) yields

$$\begin{aligned}\Theta &= \overline{\vartheta_p} + 2m\pi,\ (m=0,\ \pm 1,\ \pm 2,\ \ldots);\\ T_p &= \frac{1}{2}(U_{11}+U_{22}).\end{aligned} \tag{61}$$

This completes the proof of Theorem 4.

8 Comparison Between Cauchy's and Novozhilov's Measures of Mean Rotation

Suppose all the components in the present section are given in an arbitrary right-handed orthonormal basis $\{\mathbf{e}_i\}$. The formula of Novozhilov's mean rotation angle with respect to $\mathbf{e}_3$ is (see Novozhilov (1948) or Truesdell and Toupin (1960), Sect. 36)

$$\tan\tau_{e_3} = \frac{W_{21}}{\sqrt{(1+E_{11})(1+E_{22}) - E_{12}^2}}. \tag{62}$$

Noting that (see (30), etc.)

$$y_{e_3} = \mathbf{w}\cdot\mathbf{e}_3 = w_3 = W_{21},$$

$$x_{e_3} = 1 + \frac{1}{2}(\mathrm{tr}\mathbf{E} - \mathbf{e}_3\,\mathbf{E}\mathbf{e}_3) = 1 + \frac{1}{2}(E_{11}+E_{22}), \tag{63}$$

we can evaluate the tangent of Cauchy's mean rotation angle by

$$\tan\overline{\vartheta}_{e_3} = \frac{y_{e_3}}{x_{e_3}} = \frac{W_{21}}{1+\frac{1}{2}(E_{11}+E_{22})}. \tag{64}$$

This formula is obviously much simpler than (62).

Since the term under the radical sign of (62) may be rewritten as

$$\begin{aligned}(1+E_{11})(1+E_{22}) - E_{12}^2 &= \frac{1}{4}[(F_{11}+F_{22})^2\\ &\quad - (F_{11}-F_{22})^2 - (F_{21}+F_{12})^2] = x_{e_3}^2 - R_{e_3}^2,\end{aligned} \tag{65}$$

in which (30) has been utilized, from (62) we have[3]

$$\tan\tau_{e_3} = \frac{y_{e_3}}{\sqrt{x_{e_3}^2 - R_{e_3}^2}}. \tag{66}$$

Therefore, the Novozhilov's measure of mean rotation with respect to $\mathbf{e}_3$ has meaning if and only if

$$x_{e_3} > R_{e_3}. \tag{67}$$

(67) means that the rotation circle in Fig. 2 lies either in the first and forth quadrants, or in the second and third quadrants of the x-y plane. On the other hand, Cauchy's measure of mean rotation is always meaningful.

From (62)–(65), it follows that

$$|\tan\tau_{e_3}| \geq |\tan\vartheta_{e_3}|. \tag{68}$$

And if and only if the deformation rotation circle in Fig. 2 degenerates into a point, that is, $R_{e_2} = 0$, or

$$E_{11} = E_{22},\ \text{and}\ E_{12} = 0, \tag{69}$$

the relation (68) becomes equality.

Acknowledgments

The authors gratefully acknowledge the financial support rendered by the National Natural Science Foundation of China and the State Commission of the Education of China. The authors would also like to acknowledge the helpful suggestions of Prof. L. T. Wheeler, University of Houston.

[3] The exact formula of Novozhilov's measure of mean rotation should be

$$\tan\tau_{e_3} = \frac{\mathrm{sgn}(x_{e_3})y_{e_3}}{\sqrt{x_{e_3}^2 - R_{e_3}^2}}$$

in which $\mathrm{sgn}(x_{e_3}) = \pm 1$ is the sign of real number x_{e_3}.

References

Beatty, M. F., 1977, "Vector Analysis of Finite Rigid Rotations," ASME Journal of Applied Mechanics, Vol. 44, pp. 501–502.

Bowen, R. M., and Wang, C.-C., 1976, "Introduction to Vectors and Tensors," Plenum, New York.

Casey, J., 1983, "A Treatment of Rigid Body Dynamics," ASME Journal of Applied Mechanics, Vol. 50, pp. 905–907; Vol. 51, p. 227.

Cauchy, A.-L., 1841, "Memoire sur les dilatations, les condensations et les rotations produits par un changement de forme dans un systeme de points materiels," *Ex. d'an. Phys. Math.*, Vol. 2, pp. 302–330 = Oeuvres (2) Vol. 12, pp. 343–377.

Chadwick, P., 1976, *Continuum Mechanics*, George Allen and Unwin.

Cheng, H., and Gupta, K. C., 1989, "An Historical Note on Finite Rotations," ASME Journal of Applied Mechanics, Vol. 56, pp. 139–145.

Grioli, G., 1940, "Una Proprieta de Minimo Nella Cinematica Delle Deformazioni Finite," *Boll. Un. Mat. Ital.*, Vol. 2, No. 2, pp. 452–455.

Guo, Z.-H., 1981, "Representations of Orthogonal Tensors," *SM Archive*, Vol. 4, pp. 451–466.

Gurtin, M. E., 1981, *An Introduction to Continuum Mechanics*, Academic Press, New York.

Martins, L. C., and Podio-Guidugli, P., 1979, "A Variational Approach to the Polar Decomposition Theorem," *Rend. Accad. Naz. Lincei*, Vol. 66, pp. 487–493.

Martins, L. C., and Podio-Guidugli, P., 1980, "An Elementary Proof of the Polar Decomposition Theorem," *Amer. Math. Month.*, Vol. 87, pp. 288–290.

Martins, L. C., and Podio-Guidugli, P., 1989, "On the Local Measures of Mean Rotation in Continuum Mechanics," AMS (MOS) Subject Classification: 73B15.

Marzano, S., 1987, "On Mean Rotations in Finite Deformations," *Meccanica*, Vol. 22, pp. 223–226.

Novozhilov, V. V., 1948, "Foundations of the Nonlinear Theory of Elasticity," (in Russian; English Translation, 1953, Graylock Press, Rochester, N.Y.).

Ogden, R. W., 1984, *Nonlinear Elastic Deformations*, John Wiley, New York.

Timoshenko, S. P., and Gere, J. M., 1972, *Mechanics of Materials*, Van Nostrand Reinhold Company, New York.

Truesdell, C., and Toupin, R. A., 1960, "The Classical Field Theories," Encyclopedia of Physics, Vol. III/1, S. Flugge, ed., Springer-Verlag, Berlin, pp. 226–902.

Xiong, Z.-H., and Zheng, Q.-S., 1989a, "Moderate Strain Accompanied by Large Rotation," *Proc. 3rd Modern Math. Mech.*, by. W. Z. Chien and Z.-H. Guo, eds. Science Press, Beijing, pp. 498–503 (in Chinese).

Xiong, Z.-H., and Zheng, Q. S., 1989b, "Canonical Representations and Degree of Freedom Formulae of Orthogonal Tensors in *n*-Dimensional Euclidean Space," *Appl. Math. Mech.*, Vol. 10, pp. 93–101 (English Edition).

Zheng, Q.-S., and Hwang, K.-C., 1987, "Generalized Local Mean Rotation: Part I, Part II, *Proc. 2nd Modern Math. Mech.*, pp. 76–79 (in Chinese).

Zheng, Q.-S., and Hwang, K.-C., 1988, "Cauchy's Mean Rotation," *Chinese Science Bulletin*, Vol. 33, pp. 1705–1707 (in Chinese; English translation, 1989, Vol. 34, pp. 897–901).

The Geometry of Virtual Work Dynamics in Screw Space

Steven Peterson
Mechanical Engineering,
Department of Mechanical Engineering,
Vanderbilt University,
Nashville, TN 37235
Assoc. Mem. ASME

In this paper, screw theory is employed to develop a method for generating the dynamic equations of a system of rigid bodies. Exterior algebra is used to derive the structure of screw space from projective three space (homogeneous coordinate space). The dynamic equation formulation method is derived from the parametric form of the principle of least action, and it is shown that a set of screws exist which serves as a basis for the tangent space of the configuration manifold. Equations generated using this technique are analogs of Hamilton's dynamical equations. The freedom screws defining the manifold's tangent space are determined from the contact geometry of the joint using the virtual coefficient, which is developed from the principle of virtual work. This results in a method that eliminates all differentiation operations required by other virtual work techniques, producing a formulation method based solely on the geometry of the system of rigid bodies. The procedure is applied to the derivation of the dynamic equations for the first three links of the Stanford manipulator.

Introduction

Over the past two centuries, many methods of formulating the dynamic equations of rigid bodies have been developed. These methods can be classified as either Newton-Euler or energy methods. The Newton-Euler method is the most fundamental procedure for formulating dynamic equations. In this technique, all forces applied to the rigid body are identified, often with the aid of free-body diagrams, and set equal to the inertial forces (Pars, 1965, and Wittenburg, 1977). Visualization brought about by the use of the free-body diagram is often an aid in the derivation process. The technique's main drawback is the identification of constraint forces, which, especially in three-dimensional problems, becomes a tedious task (Wittenburg, 1977).

Energy methods eliminate the need to identify the constraint forces. In the most popular energy methods, those of Lagrange and Hamilton, kinetic energy and potential energy, or work functions, are specified, and variational calculus is used to determine the dynamic equations of motion (Lanczos, 1970). Since these methods are based on the minimization of a definite integral, the geometry of the resulting space serves as an important analytical tool. The drawback of these methods is their abstract nature. A picture analogous to the free-body diagram is not available to aid in the generation of the system equations. Furthermore, the methods are primarily designed to handle conservative systems. Frictional terms, an important factor in many rigid-body systems, can be included in Hamilton's method; however, the process involves minimizing the action integral using Lagrange multipliers (Whittaker, 1937), and is not physically intuitive.

Methods based on the principle of virtual work have been developed to alleviate problems encountered with the variational approach (Wittenburg, 1977, Kane and Levinson, 1985, and Roberson and Schwertassek, 1988). These procedures provide the ability to visualize externally applied forces, but also require the differentiation of constraint functions, which are not given any geometric significance. The virtual work methods also lack the manifold interpretations of the variational methods brought about by the minimization process. As a result, the analytical advantages of the variational techniques are lost.

The elliptic geometry of screw space can serve to enhance the visualization of virtual work methods. The initial applications of screw geometry to problems of rigid body mechanics were introduced by Ball (1990) and others in the late 1800's. Modern technology has driven a resurgence in the application of line geometry. Most of the applications have been in the field of kinematics. Some authors have applied line geometry to the formulation of dynamic equations employing Newton-Euler (Yang, 1969, and Pennock and Yang, 1983), Lagrange (Luh and Gu, 1987) and virtual work (Woo and Freudenstein, 1971, and Agrawal, 1988) formalisms. None of these methods have utilized the full power of line geometry to develop relationships between the dynamic equations and the geometry of the constraints.

In this paper, geometrical interpretations of virtual work methods applied to rigid-body dynamic analysis will be described in some detail. Exterior algebra is used to develop screw space from its underlying homogeneous coordinate space. Tensor methods are used to geometrically interpret the formulation method. The result is a relationship between the constraint

Contributed by the Applied Mechanics Division of The American Society of Mechanical Engineers for presentation at the 1992 ASME Summer Mechanics and Materials Meeting, Tempe, AZ, Apr. 28–May 1, 1992.

Discussion on this paper should be addressed to the Technical Editor, Prof. Leon M. Keer, The Technological Institute, Northwestern University, Evanston, IL 60028, and will be accepted until four months after final publication of the paper itself in the Journal of Applied Mechanics. Manuscript received by the ASME Applied Mechanics Division, Aug. 16, 1990; final revision, July 29, 1991.

Paper No. 92-APM-19.

geometry and the geometry of the dynamic system's configuration space.

The Mathematics of Differential Forms

The mathematical structure of homogeneous line space can be defined using the mathematics of differential forms (Bishop and Goldberg, 1968; Flanders, 1963). Exterior algebra, an extension of linear algebra, defines the underlying algebraic structure of differential calculus. Given the ordered set of basis $\mathbf{e}_1, \mathbf{e}_2, \ldots, \mathbf{e}_d$, which span the vector space V, the rules of exterior algebra are given as

$$\mathbf{e}_i \wedge \mathbf{e}_i = 0 \text{ for all } i \tag{1a}$$

$$\mathbf{e}_i \wedge \mathbf{e}_j = -\mathbf{e}_i \wedge \mathbf{e}_j \text{ for } i<j \tag{1b}$$

where $\wedge$ is the wedge product operator. A general form of the first order, called a 1-form, can be expressed as

$$\beta = b^j \mathbf{e}_j \tag{2}$$

where the coefficients b^j can be functions of other variables. (The indicial summation convention has been used throughout this paper. Unless noted otherwise, the index i sums over the number of bodies, N; j, and k sum over the dimension of the system's freedom space, n; and all other indices sum from 1 to 6. Superscripted variables represent contravariant indices, while subscripted variables represent covariant indices (Bishop and Goldberg, 1968, and Flanders, 1963).)

New linear spaces can be generated from V using the wedge product operator (Bishop and Goldberg, 1968). These new spaces are designated as $\wedge^p V$, and represent the space of pth order forms, p-forms, on V. These higher order forms are generated by forming the wedge product between lower order forms. The algebraic properties of $\wedge$ are shown below:

$$\lambda \wedge (\mu + \gamma) = \lambda \wedge \mu + \lambda \wedge \gamma \tag{3a}$$

$$\lambda \wedge (\mu \wedge \gamma) = (\lambda \wedge \mu) \wedge \gamma \tag{3b}$$

$$\mu \wedge \lambda = (-1)^{lm} \lambda \wedge \mu \tag{3c}$$

where μ is an lth order form and λ is a mth-order form. The wedge product is zero if the order of the result is larger than the order of the basis, d.

A space conjugate to $\wedge^p V$ is developed using the Hodge star operator. Given the wedge product

$$\mathbf{e}_{i_1} \wedge \ldots \wedge \mathbf{e}_{i_p}, \tag{4}$$

a set of indices $(j_1, \ldots, j_{d\text{-}p})$ is chosen such that $(i_1, \ldots, i_p, j_1, \ldots, j_{d\text{-}p})$ is an even permutation of $(1, \ldots, d)$; then the Hodge star operator is defined as

$$^*(\mathbf{e}_{i_1} \wedge \ldots \wedge \mathbf{e}_{i_p}) = (\mathbf{e}_{j_1} \wedge \ldots \wedge \mathbf{e}_{j_{d\text{-}p}}). \tag{5}$$

This space is designated by $\wedge^p V^*$. $\wedge^p V$ and $\wedge^p V^*$ are dual spaces.

The exterior derivative of a differential form is an operation which takes a pth-order form to a $(p+1)$th-order form. Its properties are summarized as:

$$d(\lambda + \mu) = d\lambda + d\mu \tag{6a}$$

$$d(\lambda \wedge \mu) = d\lambda \wedge \mu + (-1)^m \lambda \wedge d\mu \tag{6b}$$

$$d(d\omega) = 0 \tag{6c}$$

$$df = \frac{\partial f}{\partial x^j} dx^j \tag{6d}$$

where ω is a differential form and f is a function (a zeroth-order form).

Tensor Notation Applied to Screw Theory

Buchheim (1884) used exterior algebra to develop a theory of screws in elliptic space. Homogeneous point space, or projective space, is the linear space which serves as a basis for the rest of the theory. In this space, a point is represented by the expression

$$\mathbf{x} = x^h \mathbf{e}_h \tag{7}$$

where h sums from 1 to 4. The four independent coordinates are reduced to three by stating that point coordinates are equal if there exists a scalar, a, such that

$$\mathbf{x}' = a\mathbf{x}. \tag{8}$$

The resulting space includes Euclidean three space and the plane at infinity (Penna and Patterson, 1986). The addition of infinity to ordinary three-dimensional space has important theoretical consequences.

The dual space, specified by the Hodge star operator (Buchheim called this the conjugation operator), is the space of planes through three points. Table 1 shows the relationship between the basis of homogeneous point space and the basis of its dual space, homogeneous plane space.

Line space is generated by forming the wedge product between pairs of points (Buchheim, 1884)

$$\alpha = \mathbf{x} \wedge \mathbf{y} \tag{9}$$

where α is a 1×6 vector representing the line and $\mathbf{x}$ and $\mathbf{y}$ are homogeneous points on the line. These coordinates are called the ray coordinates of the line, and form the covariant screw space. The dual space, defined by the Hodge star operator, is represented by the axis coordinates of a line. These coordinates are determined by finding the meet between two planes (i.e., the wedge product of two planes), and form the contravariant screw space. Table 1 also shows the relationship between the ray and axis coordinates of a line.

The distinctions drawn above are important because they generate the mathematical framework which aids in the physical interpretation of mathematical operations. For example, if wrenches are expressed in axis coordinates, f_m, and twists are expressed in ray coordinates, $d\theta^m$, then virtual work, w, becomes

$$w = d\theta^m f_m \tag{10}$$

which is a natural pairing (Bishop and Goldberg, 1986) between the wrench and twist spaces. These interrelationships are summarized as

wrench space $\Leftrightarrow$ contravariant space $\Leftrightarrow$ functions on twist space

twist space $\Leftrightarrow$ covariant space $\Leftrightarrow$ functions on wrench-space

Traditionally, ray coordinates are used to express both the twist and wrench spaces (e.g., see Dimentburg, 1968). To accommodate this notation, the correlation $\tilde{\Delta}$ is introduced (Lipkin and Duffy, 1985) to perform the Hodge star operation

$$\tilde{\Delta} = \begin{bmatrix} 0 & I_3 \\ I_3 & 0 \end{bmatrix} \tag{11}$$

where I_3 represents the three-by-three identity matrix. This operation transforms covariant line vectors into contravariant space

$$^*(\alpha) = \tilde{\Delta}\alpha. \tag{12}$$

Table 1 The relationships between the homogeneous point coordinate bases and the plane, ray, and axis coordinate bases. The Hodge star operator transforms between dual bases.

Point Bases	$\overset{*}{\Leftrightarrow}$	Plane Bases	Ray Bases	$\overset{*}{\Leftrightarrow}$	Axis Bases
$\mathbf{e}_1$		$\mathbf{e}_2\wedge\mathbf{e}_4\wedge\mathbf{e}_3$	$\mathbf{e}_4\wedge\mathbf{e}_1$		$\mathbf{e}_3\wedge\mathbf{e}_2$
$\mathbf{e}_2$		$\mathbf{e}_3\wedge\mathbf{e}_4\wedge\mathbf{e}_1$	$\mathbf{e}_4\wedge\mathbf{e}_2$		$\mathbf{e}_1\wedge\mathbf{e}_3$
$\mathbf{e}_3$		$\mathbf{e}_1\wedge\mathbf{e}_4\wedge\mathbf{e}_2$	$\mathbf{e}_4\wedge\mathbf{e}_3$		$\mathbf{e}_2\wedge\mathbf{e}_1$
$\mathbf{e}_4$		$\mathbf{e}_1\wedge\mathbf{e}_2\wedge\mathbf{e}_3$	$\mathbf{e}_2\wedge\mathbf{e}_3$		$\mathbf{e}_1\wedge\mathbf{e}_4$
			$\mathbf{e}_3\wedge\mathbf{e}_1$		$\mathbf{e}_2\wedge\mathbf{e}_4$
			$\mathbf{e}_1\wedge\mathbf{e}_2$		$\mathbf{e}_3\wedge\mathbf{e}_4$

In this paper, the ray coordinates will be used to represent both twist and wrench axes, and the correlation will be used to transform wrenches into the contravariant space.

The applications of line geometry to rigid body mechanics was first described by Ball (1990). Ball's theory was based on two basic theorems of rigid-body mechanics. The first, due to Chasles, proved that a general rigid body displacement can be uniquely defined in terms of a rotation about a line fixed in space combined with a simultaneous translation parallel to the line. The second theorem, proved by Poinsot, states that any force-torque pair can be uniquely decomposed into a force along a line fixed in space and a torque in a plane normal to the line. A line fixed in space is the unifying geometric element in both definitions, making line geometry an ideal means of representing these quantities. Ball introduced the concept of a twist to represent an infinitesimal rigid body displacement and a wrench to represent the force-torque pair. The space formed by the set of all possible twists is called the twist space, while the set of all wrenches is called the wrench space. These spaces are dual line spaces, analogous to the ray and axis spaces, and the transformation between the two is described by $\tilde{\Delta}$. Lipkin and Duffy (1985) present a detailed discussion of the properties of elliptic geometry and its application to rigid-body mechanics.

Rigid-Body Transformation in Line Space

Rigid-body transformations in line space can be easily established using exterior algebra and standard homogeneous transformations. In homogeneous space, rigid-body transformations have the general form

$$x^l \epsilon_l = b^l_h x^h \mathbf{e}_h \tag{13}$$

where $\mathbf{e}_h$ and ϵ_l represent the fixed and moving frames, respectfully, and b^l_h represent the elements of the homogeneous transformation matrix B (h and 1 sum from 1 to 4). Using column vectors to represent the points, the matrix B has the form

$$B = \begin{bmatrix} b^1_1 & b^1_2 & b^1_3 & b^1_4 \\ b^2_1 & b^2_2 & b^2_3 & b^2_4 \\ b^3_1 & b^3_2 & b^3_3 & b^3_4 \\ 0 & 0 & 0 & 1 \end{bmatrix} \tag{14}$$

where the upper left three-by-three submatrix represents the rotation and the upper right three-by-one submatrix represents the translation of the rigid body. Computing the wedge product between two points in the rigid body, the following matrix represents the transformation of the ray coordinates of a line

$$B = \begin{bmatrix} b^4_4b^1_1 - b^1_4b^4_1 & b^4_4b^1_2 - b^1_4b^4_2 & b^4_4b^1_3 - b^1_4b^4_3 & b^4_2b^1_3 - b^1_2b^4_3 & b^4_3b^1_1 - b^1_3b^4_1 & b^4_1b^1_2 - b^1_1b^4_2 \\ b^4_4b^2_1 - b^2_4b^4_1 & b^4_4b^2_2 - b^2_4b^4_2 & b^4_4b^2_3 - b^2_4b^4_3 & b^4_2b^2_3 - b^2_2b^4_3 & b^4_3b^2_1 - b^2_3b^4_1 & b^4_1b^2_2 - b^2_1b^4_2 \\ b^4_4b^3_1 - b^3_4b^4_1 & b^4_4b^3_2 - b^3_4b^4_2 & b^4_4b^3_3 - b^3_4b^4_3 & b^4_2b^3_3 - b^3_2b^4_3 & b^4_3b^3_1 - b^3_3b^4_1 & b^4_1b^3_2 - b^3_1b^4_2 \\ b^2_4b^3_1 - b^3_4b^2_1 & b^2_4b^3_2 - b^3_4b^2_2 & b^2_4b^3_3 - b^3_4b^2_3 & b^2_2b^3_3 - b^3_2b^2_3 & b^2_3b^3_1 - b^3_3b^2_1 & b^2_1b^3_2 - b^3_1b^2_2 \\ b^3_4b^1_1 - b^1_4b^3_1 & b^3_4b^1_2 - b^1_4b^3_2 & b^3_4b^1_3 - b^1_4b^3_3 & b^3_2b^1_3 - b^1_2b^3_3 & b^3_3b^1_1 - b^1_3b^3_1 & b^3_1b^1_2 - b^1_1b^3_2 \\ b^1_4b^2_1 - b^2_4b^1_1 & b^1_4b^2_2 - b^2_4b^1_2 & b^1_4b^2_3 - b^2_4b^1_3 & b^1_2b^2_3 - b^2_2b^1_3 & b^1_3b^2_1 - b^2_3b^1_1 & b^1_1b^2_2 - b^2_1b^1_2 \end{bmatrix}. \tag{15}$$

Substituting Eq. (14) into this expression generates the general form of a rigid-body transformation in line space

$$B = \begin{bmatrix} b^1_1 & b^1_2 & b^1_3 & 0 & 0 & 0 \\ b^2_1 & b^2_2 & b^2_3 & 0 & 0 & 0 \\ b^3_1 & b^3_2 & b^3_3 & 0 & 0 & 0 \\ b^2_4b^3_1 - b^3_4b^2_1 & b^2_4b^3_2 - b^3_4b^2_2 & b^2_4b^3_3 - b^3_4b^2_3 & b^1_1 & b^1_2 & b^1_3 \\ b^3_4b^1_1 - b^1_4b^3_1 & b^3_4b^1_2 - b^1_4b^3_2 & b^3_4b^1_3 - b^1_4b^3_3 & b^2_1 & b^2_2 & b^2_3 \\ b^1_4b^2_1 - b^2_4b^1_1 & b^1_4b^2_2 - b^2_4b^1_2 & b^1_4b^2_3 - b^2_4b^1_3 & b^3_1 & b^3_2 & b^3_3 \end{bmatrix}. \tag{16}$$

This is the screw affinor described by Dimentburg (1968).

The justification for assigning the coefficients of the twist space to the axis space can be shown by computing the velocity of the rigid body in either the fixed or moving space. The velocity relationship can be determined by differentiating Eq. (13)

$$v^h \mathbf{e}_h = \frac{d}{dt}\,(b^h_l x^l)\mathbf{e}_h = \left(\frac{d}{dt}\,b^h_l\right) x^l \mathbf{e}_h. \tag{17}$$

Expressing the velocity in the moving system (remember, the coordinates x^l were originally specified in the moving system), this equation becomes

$$v^h b^{-1}{}^i_h \epsilon_i = \left(\frac{d}{dt}\,b^h_l\right) b^{-1}{}^i_h x^l \epsilon_i \tag{18}$$

where i sums from 1 to 4. The coefficients $(d/dt\ b^h_l) b^{-1}{}^i_h$ are the components of the angular velocity matrix, which in projective three space is given by

$$\Omega = \begin{bmatrix} 0 & \omega^1_2 & \omega^1_3 & \omega^1_4 \\ \omega^2_1 & 0 & \omega^2_3 & \omega^2_4 \\ \omega^3_1 & \omega^3_2 & 0 & \omega^3_4 \\ 0 & 0 & 0 & 0 \end{bmatrix} \tag{19}$$

where the upper left three-by-three submatrix is skew symmetric. In analogy to three-dimensional vector mechanics, Buchheim (1884) suggested the following formula for the velocity of a homogeneous point:

$$\dot{\mathbf{x}} = {}^*(\omega \wedge \mathbf{x}) \tag{20}$$

where ω is the angular velocity expressed in ray coordinates

$$\omega = (\omega^1, \omega^2, \omega^3, \omega^4, \omega^5, \omega^6) \tag{21}$$

(the superscripts correspond to rows in Table 1). This formula is accurate for all but the homogeneous coordinate of $\dot{\mathbf{x}}$. Assigning corresponding values to the angular velocity matrix gives

$$\Omega = \begin{bmatrix} 0 & -\omega^3 & \omega^2 & \omega^4 \\ \omega^3 & 0 & -\omega^1 & \omega^5 \\ -\omega^2 & \omega^1 & 0 & \omega^6 \\ 0 & 0 & 0 & 0 \end{bmatrix} \tag{22}$$

This shows that using ray coordinates for the twist space, the first three components correspond to the angular velocity vector and the second three components represent the linear velocity.

Virtual Work in Line Space

The work performed by a twist on a wrench is determined by the equation

$$w = d\theta \wedge {}^*(\mathbf{f}) = d\theta^l \tilde{\Delta}_{lh} f^h \tag{23}$$

where $d\theta$ and $\mathbf{f}$ are vectors representing the ray coordinates of the twist and wrench, respectively. The operation $\tilde{\Delta}_{lh} f^h$ transforms the wrench into axis space. A purely geometric quantity, called the virtual coefficient, is generated by normalizing this quantity with respect to the twist and wrench magnitudes. Since

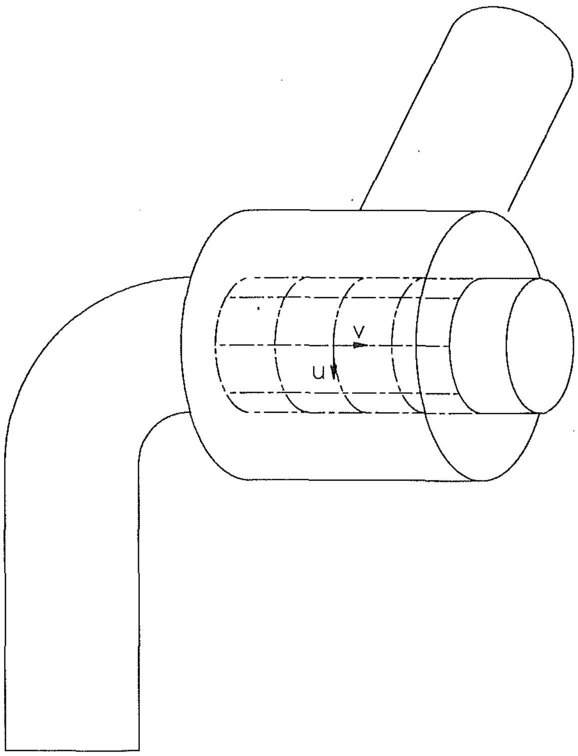

Fig. 1 A cylindrical joint showing the contact surface (dashed lines)

the twist and wrench spaces are duals of one another, the virtual coefficient can be calculated in either space.

The virtual coefficient plays an pre-eminent role in the theory of screws. If the virtual coefficient is zero, the twist and wrench are said to be reciprocal to one another. This means that the force can do no work against the displacement, or stated differently, the force cannot influence motions occuring about the twist's axis. The virtual coefficient is invariant with respect to coordinate system transformations.

By determining the set of screws reciprocal to a given set of screws, Ball (1900) used the virtual coefficient to geometrically define the freedom spaces of a rigid body subject to constraints. The freedom screw space is the set of lines reciprocal to the forces of constraint. If the geometry of contact between two surfaces is known, the constraint forces are assumed to be normal to the joint surface at these points of contact, the motions allowed by a joint can be computed using the virtual coefficient (Hunt, 1978; Waldron, 1972). This space is spanned by a set of reciprocal screws. Another set of reciprocal screws span the constraint space. Motion is allowed on the screws of freedom and disallowed on the screws of constraint.

The coordinates of an arbitrary twist in the freedom space of a joint is given by the equations

$$d\theta = \alpha_1 dq^1 + \ldots + \alpha_n dq^n \tag{24}$$

where α_i are the lines serving as a basis for the freedom space, and the ratio of the coefficients dq_i/dq_n; $i = 1 \ldots n-1$; uniquely specifies any twist axis in the space. Since the α_i are computed directly from the joint contact geometry, they depend only on the position and shape of the joint.

Using Eq. (24), the velocity of the rigid body can be expressed as

$$\omega = \alpha_1 \dot{q}^1 + \ldots + \alpha_n \dot{q}^n \tag{25}$$

where ω is the line vector associated with the angular velocity matrix, also known as the instantaneous screw axis. If the joint is moving, additional screws are included which represent joints between the current joint and the inertial reference frame. These expressions will be used later to generate the dynamic equations of a system of rigid bodies.

An Example of the Freedom Space Calculation

To illustrate the calculation of the freedom space of a joint, consider the cylindrical joint shown in Fig. 1. The region of contact between the rigid bodies in this joint is described by the equation of a cylinder, given below in parametric form

$$\mathbf{x}(\phi,\chi) = \begin{bmatrix} r\cos\phi + c_x \\ r\sin\phi + c_y \\ \chi \\ 1 \end{bmatrix} \tag{26}$$

where $0 \le \phi \le 2\pi$ and $-1 \le \chi \le 1$. The normal vector of the surface is given by the equation

$$\mathbf{n}(\phi,\chi) = \begin{bmatrix} -\cos\phi \\ -\sin\phi \\ 0 \\ 0 \end{bmatrix} \tag{27}$$

The set of line vectors representing the constraint wrenches is given by

$$\eta(\phi,\chi) = \mathbf{x}\wedge\mathbf{n} = \begin{bmatrix} -\cos\phi \\ -\sin\phi \\ 0 \\ \chi\sin\phi \\ -\chi\cos\phi \\ -c_x\sin\phi + c_y\cos\phi \end{bmatrix} \tag{28}$$

If the virtual coefficient between these constraint wrenches and an arbitrary twist vector is set equal to zero, the following equation is generated

$$d\theta^l \tilde{\Delta}_{lh}\eta^h = d\theta^1\chi\sin\phi - d\theta^2\chi\cos\phi + d\theta^3(c_y\cos\phi - c_x\sin\phi) - d\theta^4\cos\phi - d\theta^5\sin\phi = 0. \tag{29}$$

This equation must be true for all values of ϕ and χ. The following conditions on the coordinates of the twist are generated

$$d\theta^4 = d\theta^3 c_y$$
$$d\theta^5 = -d\theta^3 c_x \tag{30}$$

where $d\theta^3$ and $d\theta^6$ are arbitrary quantities.

Two reciprocal line vectors can be generated which span this freedom space

$$\alpha_1 = (0,0,1,c_y,-c_x,1) \tag{31}$$

$$\alpha_2 = (0,0,1,c_y,-c_x,-1). \tag{32}$$

This shows that the joint will only allow rotations about and translations along the line (0, 0, 1, c_x, c_y, 0). Notice that these vectors are not unique; three arbitrary choices were made in their specification. A similar calculation can be performed on an arbitrary joint shape. Only the geometry of the contact region is required to determine the freedom space of the joint.

Inertial Properties of a Rigid Body in Screw Space

The kinetic energy of a mass element in a general shape can be written as

$$dT = <\mathbf{v},\mathbf{v}> dm = \mathbf{v}\wedge{}^*(\mathbf{v})dm \tag{33}$$

where $\mathbf{v}$ is the velocity of a point in the space, dm is the mass at the point, and $<\bullet,\bullet>$ is the symbol of a natural pairing in the space. Since screw space is built upon projective three space, the expression for the velocity used in this equation is

$$v^l\mathbf{e}_l = \omega^l_h x^h \mathbf{e}_l. \tag{34}$$

Substituting the velocity into Eq. (33) generates the following expression

$$dT = \{\omega^l_h x^h \mathbf{e}_l \wedge{}^*(\omega^l_m x^m \mathbf{e}_l)\}dm = \{\omega^l_h x^h \omega^l_m x^m \mathbf{e}_l \wedge{}^*(\mathbf{e}_l)\}dm. \tag{35}$$

Integrating over the volume of the rigid body, the total kinetic energy of the body is determined. Using homogeneous transformations, this equation can be expressed as (Paul, 1981)

$$T = \mathrm{tr}(\Omega J \Omega^t) \tag{36}$$

where tr(•) is the trace operation, and the matrix J has the form

$$J = \begin{bmatrix} \frac{1}{2}(I_{yy}+I_{zz}-I_{xx}) & I_{xy} & I_{xz} & s_x \\ I_{xy} & \frac{1}{2}(I_{xx}+I_{zz}-I_{yy}) & I_{yz} & s_y \\ I_{xz} & I_{yz} & \frac{1}{2}(I_{xx}+I_{yy}-I_{zz}) & s_z \\ s_x & s_y & s_z & m \end{bmatrix} \tag{37}$$

where m is the total mass of the rigid body, s_i are the first mass moments of the rigid body, and I_{ij} are the mass moments of inertia. Using the line geometric representation of the angular velocity matrix, the following matrix can be written which represents the inertial properties of the mass in screw space

$$M = \begin{bmatrix} I_{xx} & I_{xy} & I_{xz} & 0 & -s_z & s_y \\ I_{xy} & I_{yy} & I_{yz} & s_z & 0 & -s_x \\ I_{xz} & I_{yz} & I_{zz} & -s_y & s_x & 0 \\ 0 & s_z & -s_y & m & 0 & 0 \\ -s_z & 0 & s_x & 0 & m & 0 \\ s_y & -s_x & 0 & 0 & 0 & m \end{bmatrix} \tag{38}$$

and the kinetic energy can be expressed as

$$T = \omega^l m_{lh} \omega^h. \tag{39}$$

Dimentberg (1968) called the matrix M the inertia binor.

The Parametric Form of the Principle of Least Action

Virtual work methods can be related to variational approaches using the parametric form of the principle of least action. In this form, action is defined as twice the definite integral of kinetic energy, using time as a dependent variable (Lanczos, 1970)

$$A = 2\int_a^b T t' \, d\tau \tag{40}$$

where T is the kinetic energy of the system, τ is an arbitrary independent parameter, and t' is the derivative of time with respect to τ. All energy methods of formulating dynamic equations for mechanical systems can be found by minimizing this functional. Differences between each of the methods are obtained by placing different constraints on the minimization process.

Using Eqs. (25) and (39), the kinetic energy of the system can be expressed as

$$T = \frac{1}{2}\,\omega_i^l m_{ilh} \omega_i^h = \frac{1}{2}\left(\frac{q'^k}{t'}\right) s_{ik}\alpha_{ik}^l m_{ilh} s_{ij} \alpha_{ij}^h \left(\frac{q'^j}{t'}\right) \tag{41}$$

where q'^i are derivatives of the position variables with respect to τ, α_{ij} is the jth screw spanning the motion space of the ith rigid body, and s_{ik} are the elements of a matrix S, which are defined as follows:

$$s_{ik} = \begin{cases} 1 \text{ if } \alpha_{ik} \text{ lies between the } i\text{th body and the inertial frame} \\ 0 \text{ if not.} \end{cases} \tag{42}$$

The matrix S can be computed from a graph of the system's topology. This form is made possible by the fact that the $\boldsymbol{\alpha}_{ij}$ are functions of the system's configuration exclusively. Time-dependent kinetic energy, caused by gyroscopic elements or prescribed motions, can also be expressed by representing their motion axes in the form of Eq. (25). Since the virtual work calculation is invariant with respect to coordinate system transformations, coordinate systems can be chosen such that the equations of each rigid body are expressed in their simplest form. This is a great advantage when formulating the equations of a complex system.

An extremely simple representation of the system can be obtained by rewriting Eq. (41) in terms of the system momentum. The momentum of the system associated with the kth velocity can be written as

$$p_k = s_{ik}\alpha_{ik}^l m_{ilh} s_{ij} \alpha_{ij}^h q^j \tag{43}$$

and the momentum associated with time is equal to the total energy of the system. Substituting this expression into Eq. (41) and determining its unconstrained minimum by setting the variation of Eq. (40) to zero generates the following simple equation:

$$\frac{dp_k}{d\tau} = 0. \tag{44}$$

Manifold Interpretations

Equation (44) can be interpreted as a generalization of the law of inertia, which states that a particle under its own inertia moves in a straight line with constant velocity (Lanczos, 1970). In this case, the straight line is a geodesic in the system's configuration space.

Upon closer examination, Eq. (43) can be seen to have two components. The first consists of the terms $s_{ik}\ \boldsymbol{\alpha}_{ik}$, which are the screw spanning the freedom space of the ith body. The line vectors generating this space are covariant vectors. The remaining terms in the momentum equation is a contravariant vector representing the momentum of the ith body. Thus, Eq. (43) represents a natural pairing between the freedom space and the system's momentum, meaning that the momentum is a function on the freedom space of the joint.

Following this logic, Newton's second law can be generalized by projecting the system's force vectors onto the tangent space of the configuration manifold

$$\frac{dp_k}{d\tau} = s_{ik}\alpha_{ik}^l \tilde{\Delta}_{lh} f_i^h \tag{45}$$

where $\mathbf{f}_i$ is the sum of the wrenches applied to the ith body. This expression, along with the definition of the momentum (Eq. (43)), are analogous to Hamilton's canonical equations of motion for rigid bodies. In this development no restrictions have been placed on the form of the system forces. Therefore, frictional forces can easily be incorporated into the equations of motion. Reparameterizing these equations with respect to time is done by dividing the rigid body momenta and velocities by t'.

The Integrability of Screw Spaces

The validity of the manifold representation requires the tangent space of the manifold to be integrable. The mathematics of differential forms provides the most convenient means of studying the integrability of the tangent space. The Frobenius integration theorem (Flanders, 1963) states that a set of differential one forms, w^i, is integrable if there exists a matrix of one forms, θ_j^i, such that

$$dw^i = \theta_j^i \wedge w^j. \tag{46}$$

In the case of kinematic manifolds, the integrability conditions are given by (Peterson, to appear)

$$d(\alpha_{ik}^l dq^k) = \frac{\omega_{ih}^l}{2} \wedge (\alpha_{ik}^h dq^k) \tag{47}$$

where ω_{ih}^l is an element of the angular velocity matrix describing the instantaneous motion of the ith coordinate system in line space.

It can be shown that if the screws spanning the freedom space of a joint are integrable, then tangent spaces composed of chains of these joints will also be integrable. It is a trivial exercise to show that the velocities of single-degree-of-freedom joints are always integrable to position coordinates. If the axes are independent (i.e., the derivatives on the left-hand side of Eq. (24) are zero), transformations represented by the motion axes must be order independent. This is true if the joint is purely translational, or if a rotation and translation occur about the same axis (as in the example described earlier). All other transformations are order dependent.

In higher degree-of-freedom joints, new generalized coordinates must be introduced so the dynamic equations can be integrated. One possible set of generalized coordinates are the dual Euler parameters (Rooney, 1978). In this case, simple equations exist which relate the derivatives of the dual Euler parameters to the angular velocity vector. Another solution is generated by spanning the freedom space of the joint with a chain of single-degree-of-freedom joints. This commonly used procedure almost always introduces singularities into the joint motion space.

Example: Stanford Manipulator

To show that the algorithm presented above generates the correct dynamic equations of a system of rigid bodies, the equations for the first three links of the Stanford manipulator arm (see Fig. 2) will be derived. These equations are given in symbolic form by Paul (1981). The system is a special type since its topological structure can be represented as a tree (Roberson and Schwertassek, 1988), thereby giving the matrix S the following triangular form

$$S=\begin{bmatrix}1&0&0\\1&1&0\\1&1&1\end{bmatrix}. \tag{48}$$

The tree structure simplifies the derivation of the dynamic equations.

There are two types of joints in the Stanford manipulator, revolute and prismatic. Following traditional approaches, the coordinate system for each part will be placed at the intersection of joint axes with the z-axis aligned with the motion axis (Hartenberg and Denavit, 1964). The local freedom spaces calculated from the contact geometry are

$$\alpha_{\text{revolute}}=(0,0,1,0,0,0) \tag{49}$$

$$\alpha_{\text{prismatic}}=(0,0,0,0,0,1). \tag{50}$$

These local joint freedom spaces must be transformed into the coordinate systems of each link. These transformation matrices are specified using the standard Hartenburg and Denavit parameters. The Hartenberg and Denavit parameters of the Stanford robot are given in Table 2. The tree topology of the machine indicates that recursion can be utilized to make this calculation extremely efficient.

The mass properties for the Stanford arm are given in Table 3. Notice that the joint coordinate systems are parallel to the principle inertia axes. This simplifies the resulting mass matrices. The mass properties can be simplified further by placing the body coordinate systems at the center of mass of each link.

Expressions for the generalized momenta can now be written. The momenta have the form

$$p_k=d_{kj}\dot{q}_j \tag{51}$$

where d_{kj} are elements of a generalized inertia matrix D and can be computed using the expression

$$d_{kj}=s_{ik}\alpha^{l}_{ik}m_{ihl}s_{ij}\alpha^{h}_{ij}. \tag{52}$$

Since M_i is a symmetric matrix, the generalized inertia matrix is symmetric. The elements of the generalized inertia matrix for this problem are given in the Appendix.

Finally, the effects of actuator and gravitational forces must be modeled. These forces are identified by drawing free-body diagrams of each link. The direction of the gravitational forces are determined by rotating the z-axis into each body's coordinate system. The total applied wrench, obtained by summing the gravitational and actuator forces for each body, are projected onto the tangent space of the configuration manifold using virtual work (see Eq. (45)). The equations describing the dynamic behavior of the system of rigid bodies are provided in the Appendix. These equations agree with those obtained by Paul (1981).

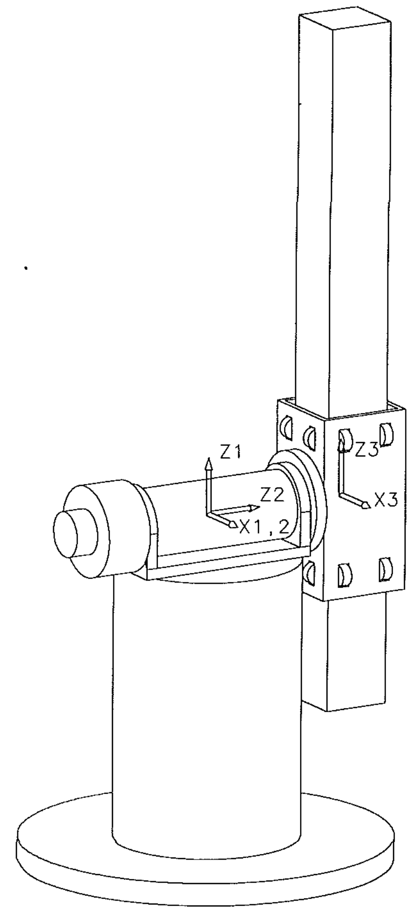

Fig. 2 The Stanford arm showing the orientation of each joint coordinate system

Table 2 Hartenberg and Denavit parameters of the Stanford manipulator (these values were obtained from Paul (1981))

Joint	θ	h	a	α
1	θ_1	0	0	−90 deg
2	θ_2	h_2	0	90 deg
3	0	h_3	0	0

Table 3 Inertia properties of the Stanford manipulator (these values were obtained from Paul (1981))

Link	x_c	y_c	z_c	m	I_{xx}	I_{yy}	I_{zz}
1	0.00	1.75	−11.05	9.25	0.276	0.255	0.071
2	0.00	−10.54	0.00	5.01	0.108	0.018	0.100
3	0.00	0.00	−64.47	4.25	2.510	2.510	0.006

Summary

This paper has presented a method of formulating the dynamic equations of a system of rigid bodies based on virtual work. The method utilizes the geometry of screw space to describe the freedom space of each body, and as a result provides a purely geometric representation of the rigid body constraints. By minimizing the integral of the parametric form of the kinetic energy (treating time as a dependent variable), the method was related to other variational principles. In this procedure, the screws of the system's freedom space form the basis of the tangent space of the configuration manifold. Forces are projected onto the configuration manifold using virtual work. The resulting equations are analogous to Hamilton's equations.

The advantages of the new approach are threefold. First, the development of the system equations can be performed without any differentiation operations. The tangent space is determined using the geometry of contact between bodies on either side of the joint. Since the method is based primarily on geometry, visual tools, such as free-body diagrams, can be used as an aid in the derivation process.

The second advantage is the simplicity of the resulting equations. Hamilton's equations are the simplest representation of a mechanical system's dynamic behavior. As a result, when applying this method extremely efficient simulation codes can be developed.

Finally, many analytical tools are available for investigating the characteristics of dynamic equations expressed in variational form. These methods are primarily aimed at understanding the system's motion in configuration space. Since this method generates similar geometry, all the tools of analytical mechanics can be brought to bear on the problem.

The method presented in this paper is not yet complete. Further research is required to develop methods of modeling closed loop chains. Also, efficient methods of computing constraint reactions are required to transform this technique into a useful design tool. With these additional algorithms, the new method provides a powerful new tool for studying the dynamics of multi-rigid body systems.

References

Agrawal, S. K., 1988, "Multi-Rigid-Body Dynamics: A d'Alembert's Method Using Dual Vectors," *Trends and Developments in Mechanisms, Machines and Robotics—1988*, ASME DE-Vol. 15-3, pp. 1–6.

Ball, R. S., 1900, *A Treatise on the Theory of Screws*, Cambridge University Press, Cambridge, U.K.

Bishop, R. L., and Goldberg, S. I., 1968, *Tensor Analysis on Manifolds*, Macmillan, New York.

Buchheim, A., 1884, "On the Theory of Screws in Elliptic Space," *Proceedings of the London Mathematical Society*, Vol. 15, pp. 83–98.

Dimentberg, F. M., 1968, *The Screw Calculus and its Applications in Mechanics* (English translation), National Technical Information Service, Publication number AD 680 993.

Flanders, H., 1963, *Differential Forms with Applications to the Physical Sciences*, Academic Press, New York.

Hartenberg, R. S., and Denavit, J., 1964, *Kinematic Synthesis of Linkages*, McGraw-Hill, New York.

Hunt, K. H., 1978, *Kinematic Geometry of Mechanisms*, Clarendon Press, Oxford, U.K.

Kane, T. R., and Levinson, D. A., 1985, *Dynamics: Theory and Applications*, McGraw-Hill, New York.

Lanczos, C., 1970, *The Variational Principles of Mechanics*, 4th ed., University of Toronto Press, Toronto.

Lipkin, H., and Duffy, J., 1985, "The Elliptic Polarity of Screws," ASME *Journal of Mechanisms, Transmissions and Automation in Design*, Vol. 107, pp. 377–87.

Luh, J. Y. S., and Gu, Y. L., 1987, "Lagrangian Formulation of Robot Dynamics with Dual-Number Transformation for Computational Simplification," personal communication.

Pars, L. A., 1965, *A Treatise on Analytical Dynamics*, John Wiley and Sons, New York.

Paul, R., 1981, *Robot Manipulators: Mathematics, Programming and Control*, M.I.T. Press, Cambridge, MA.

Penna, M. A., and Patterson, R. R., 1986, *Projective Geometry and Its Applications to Computer Graphics*, Prentice-Hall, Englewood Cliffs, NJ.

Pennock, G. R., and Yang, A. T., 1983, "Dynamic Analysis of a Multi-Rigid-Body Open-Chain System," ASME *Journal of Mechanisms, Transmissions and Automation in Design*, Vol. 105, pp. 28–34.

Peterson, S. W., to appear, "On the Integrability of Screw Spaces," ASME *Journal of Mechanical Design*.

Roberson, R. E., and Schwertassek, R., 1988, *Dynamics of Multibody Systems*, Springer-Verlag, Heidelberg, Germany.

Rooney, J., 1978, "A Comparison of Representations of General Screw Displacements," *Environment and Planning, B*, Vol. 5, pp. 45–88.

Waldron, K. J., 1972, "A Method of Studying Joint Geometry," *Mechanism and Machine Theory*, Vol. 7, pp. 347–53.

Whittaker, E. T., 1937, *A Treatise on the Analytical Dynamics of Particles and Rigid Bodies with an Introduction to the Problem of Three Bodies*, 4th ed., Cambridge University Press, London, U.K.

Wittenburg, V., 1977, *Dynamics of Systems of Rigid Bodies*, B. G. Teubner, Stuttgart, Germany.

Woo, L. S., and Freudenstein, F., 1971, "Dynamic Analysis of Mechanisms Using Screw Coordinates," ASME *Journal of Engineering for Industry*, Vol. 93, pp. 273–76.

Yang, A. T., 1969, "Analysis of an Offset Unsymmetric Gyroscope with Oblique Rotor Using (3 × 3) Matrices with Dual-Number Elements," ASME *Journal of Engineering for Industry*, Vol. 91, pp. 535–42.

APPENDIX

The dynamics equations describing the behavior of the Stanford manipulator are given below.

$$\dot{\mathbf{q}} = D^{-1}\mathbf{p}$$

where

$$\dot{\mathbf{q}} = \begin{bmatrix} \dot{\theta}_1 \\ \dot{\theta}_2 \\ \dot{h}_3 \end{bmatrix},$$

$\mathbf{p}$ is a vector containing the generalized momenta, and the elements of D are

$$d_{11} = I_{1yy} + m_2(h_2 + y_{c2})^2 + m_1 z_{c2}^2 + (I_{2xx} + I_{3xx} + m_3(h_3 + z_{c3})^2)\sin^2\theta_2 + (I_{2zz} + I_{3zz} + m_3 h_2^2)\cos^2\theta_2$$

$$d_{12} = d_{21} = -m_3 h_2 (h_3 + z_{c3})\cos\theta_2$$

$$d_{13} = d_{31} = -m_3 h_2 \sin\theta_2$$

$$d_{22} = I_{2yy} + I_{3yy} + m_3(h_3 + z_{c3})^2$$

$$d_{23} = d_{32} = 0$$

$$d_{33} = m_3.$$

The rate of change of the momenta are given by the equations

$$\dot{p}_1 = \tau_1$$

$$\dot{p}_2 = \tau_2 + m_3 g (h_3 + z_{c3})\sin\theta_2$$

$$\dot{p}_3 = f_3 - m_3 g \cos\theta_2$$

where τ_i and f_3 represent the actuator forces.

A Theorem on the Exact Nonsimilar Steady-State Motions of a Nonlinear Oscillator

A. F. Vakakis
Asst. Professor,
Department of Mechanical and Industrial Engineering,
University of Illinois,
Urbana, IL 61801
Assoc. Mem. ASME

T. K. Caughey
Professor,
Department of Applied Mechanics,
California Institute of Technology,
Pasadena, CA 91125

In this work the steady-state motions of a nonlinear, discrete, undamped oscillator are examined. This is achieved by using the notion of exact steady state, i.e., a motion where all coordinates of the system oscillate equiperiodically, with a period equal to that of the excitation. Special forcing functions that are periodic but not necessarily harmonic are applied to the system, and its steady response is approximately computed by an asymptotic methodology. For a system with cubic nonlinearity, a general theorem is given on the necessary and sufficient conditions that a excitation should satisfy in order to lead to an exact steady motion. As a result of this theorem, a whole class of admissible periodic functions capable of producing steady motions is identified (in contrast to the linear case, where the only excitation leading to a steady-state motion is the harmonic one). An analytic expression for the modal curve describing the steady motion of the system in the configuration space is derived and numerical simulations of the steady-state motions of a strongly nonlinear oscillator excited by two different forcing functions are presented.

1 Introduction

In many engineering applications, such as modal analysis and vibration isolation, there is a need to determine the steady-state responses of periodically forced mechanical structures. Moreover, information about the steady dynamical motion of a forced structural component is essential in order to design against large-amplitude resonant motions which may result in its early failure. Approximate analytic techniques for computating the steady dynamic response of simple nonlinear mechanical components already exist in the literature. However, the majority of these methods applies only to weakly nonlinear systems and assumes that the structural responses are approximately harmonic.

In this work, the notion of the exact steady state is used in order to study the forced response of a nonlinear discrete oscillator. The concept of nonlinear exact steady state was first introduced in Rosenberg (1966a,b) and implemented in the study of strongly nonlinear discrete oscillators.

By Rosenberg's definition, an n degree-of-freedom oscillator excited by a periodic forcing is in an exact steady state if it vibrates in unison, having as least period that of the excitation. A vibration in unison was defined as a motion where all the coordinates of the system vary equiperiodically reaching their extremum values at the same instant of time. Rosenberg showed that in an exact steady state, the motion of the system can be represented by a single line in the configuration space (modal line). Depending on the form of the corresponding modal line, the steady state was termed either similar (straight modal line), or nonsimilar (curved modal line). In addition, it was shown that these nonlinear resonances always occur in the neighborhoods of the nonlinear normal modes of the unforced systems (Rosenberg, 1966a; Yang et al., 1968).

The general problem of the existence of similar steady states was addressed in Kinney (1965) and Kinney et al. (1966), where special cam-functions were used as exciting forces. Subsequently, geometrical methods were used in the configuration space to detect and compute the modal lines of the forced motion. In the same references, a homogeneous two-degree-of-freedom system with cubic nonlinearity was examined (a system with stiffness proportional to the same power of the displacement). Elliptic forcing functions were used and it was shown that as many as five steady states may exist for a specific value of the frequency of the external excitation. The extension of these results to the nonhomogeneous system was presented in Caughey et al. (1991), where it was found that the topological portrait of the resonance curves representing similar steady-state motions changed when a bifurcation of the normal modes of the unforced system occurred. In such cases, a variation of a certain structural parameter leads to an increase of the resonance branches that describe the similar steady-state motion.

The only works that the authors were able to find on the problem of nonsimilar steady state were those by Kinney (1965) and Mikhlin (1974); in these works a set of functional equations for the derivation of the curved modal line that described the exact steady state was given. These equations became singular

Contributed by the Applied Mechanics Division of The American Society of Mechanical Engineers for presentation at the 1992 ASME Summer Mechanics and Materials Meeting, Tempe, AZ, Apr. 28–May 1, 1992.

Discussion on this paper should be addressed to the Technical Editor, Prof. Leon M. Keer, The Technological Institute, Northwestern University, Evanston, IL 60208, and will be accepted until four months after final publication of the paper itself in the Journal of Applied Mechanics. Manuscript received by the ASME Applied Mechanics Division, Sept. 24, 1990; final revision, July 1, 1991.
Paper No. 92-APM-21.

at the end points of the modal lines, and an asymptotic methodology for approximating the modal curve at low amplitudes was needed. In the same references, specific applications of the theory were given for a two-degree-of-freedom system with cubic nonlinearity, excited by elliptic-cosine functions.

In all of the aforementioned references, special forcing functions were considered for analyzing exact steady states. A basic feature, however, of nonlinear undamped discrete systems is that, depending on the form of the excitation, they may possess multiple steady-state solutions. A basic, general question therefore arises: *Suppose that a nonlinear discrete oscillator is acted by a periodic excitation. Under what conditions will this force produce an exact steady-state motion?* Evidently, the required conditions must depend on the degree of the nonlinearity as well as on the structural parameters of the system. In addition, steady-state motion for the class of undamped oscillators under investigation can be materialized only for a specific set of initial conditions. This is because in undamped systems, initial transients do not decay with time (as in systems with damping). As a result, one has to initiate the motion with specific initial conditions in order to obtain a periodic steady-state response. Thus, two specific subproblems result from the aforementioned general question: The first concerns the derivation of the necessary and sufficient conditions that a periodic force must satisfy in order to lead to an exact steady state. Then, given such an admissible periodic excitation, one has to compute the specific set of initial conditions of the oscillator that lead to an elimination of the initial transients of the response and give rise to a periodic steady-state motion.

In the following sections a general methodology for addressing the above problems is outlined. Then, an application of the theory is given for a two-degree-of-freedom oscillator with cubic nonlinearity.

2 General Formulation of the Problem

Consider the general n-degree-of-freedom undamped nonlinear system, excited by n forces $\epsilon p_i(t)$

$$\ddot{x}_i = f_i(x_1, \ldots, x_n) + \epsilon p_i(t), \; i=1, \ldots, n \tag{1}$$

subject to the set of initial conditions

$$x_i(0) = X_i, \; \dot{x}_i(0) = 0, \; i=1, 2, \ldots, n. \tag{2}$$

The forces $\epsilon p_i(t)$ are assumed to be weak since their amplitude is proportional to the parameter ϵ which is assumed to be of perturbation order (i.e., $|\epsilon| \ll 1$) and periodic with least common period T. Thus, the nonconservative system (1) can be regarded as resulting from the perturbation of a conservative one, corresponding to $\epsilon=0$. In what follows, it is assumed that the unperturbed (unforced) system has a potential function which is positive definite and symmetric with respect to the origin of the configuration space. This condition is satisfied when the stiffnesses of the system are odd functions of the displacements. Under these assumptions, it can be shown that the unperturbed system can possess normal modes of free oscillation which are symmetric with respect to the origin of the configuration space. Then, the steady-state motions of the perturbed (forced) system can be regarded as resulting from the perturbations of the normal modes of the unforced oscillator.

Initially, the formulation of Mikhlin (1974) will be followed in order to derive the functional equations describing the modal lines at the steady state. To this end, suppose that system (1) oscillates in an exact steady state. Then, the response $x_1(t)$ is periodic with minimum period T (equal to that of the excitation); therefore, at the steady state, one can express the time variable t as a single-valued function of the displacement x_r, for $t \in [0, T/2)$. Symbolically, this inversion can be written as

$$t = t(x_1), \; t \in [0, T/2). \tag{3}$$

Using (3) one can (in principle) eliminate the variable t from expression (1), and obtain the following equivalent autonomous system

$$\begin{aligned} \ddot{x}_i &= f_i(x_1, \ldots, x_n) + \epsilon p_i(t(x_1)) \\ &= f_i(x_1, \ldots, x_n) + \epsilon \hat{p}_i(x_1), \; i=1, \ldots, n \end{aligned} \tag{4}$$

where $\epsilon p_i(t(x_1)) \equiv \epsilon \hat{p}_i(x_1)$. *Note, however, that the equivalence between systems (1) and (4) only holds at the steady state.* The exact nonsimilar steady states of the original system (1) correspond to nonsimilar normal modes of the equivalent autonomous system (4), and as a result, the problem of the forced nonsimilar steady motion is converted to the problem of computing the nonsimilar modes of the equivalent autonomous system. This later problem has been investigated by several authors (Rand, 1971, 1974; Rosenberg et al., 1964; Atkinson et al., 1965) and a variety of techniques exist for its solution.

The nonsimilar normal modes of the equivalent system (4) (corresponding to nonsimilar steady states of the original problem (1)) are expressed as:

$$x_i = \hat{x}_i(x_r), \; i=1, \ldots, n, \; i \neq r. \tag{5}$$

Note that only one of the variables, namely x_r, is needed to parametrize the motion. The nonlinear functions $\hat{x}_i(\bullet)$ satisfy $(n-1)$ functional relations of the form (Mikhlin, 1974):

$$\begin{aligned} &2[h - V(\hat{x}_1(x_r), \ldots, \hat{x}_n(x_r))]\left[1 + \sum_{k=1, k\neq r}^{n} \left(\frac{d\hat{x}_k}{dx_r}\right)^2\right]^{-1} \frac{d^2\hat{x}_i}{dx_r^2} \\ &\quad + [f_r(\hat{x}_1(x_r), \ldots, \hat{x}_n(x_r)) + \epsilon \hat{p}_r(\hat{x}_1(x_r))] \frac{d\hat{x}_i}{dx_r} \\ &\quad = f_i(\hat{x}_1(x_r), \ldots, \hat{x}_n(x_r)) + \epsilon \hat{p}_i(\hat{x}_1(x_r)) \\ &\qquad i=1, 2, \ldots, n, \; i \neq r. \end{aligned} \tag{6}$$

The quantity h is the total (fixed) energy of the equivalent autonomous system and V is its potential energy. Observe that the functional equations (6) become singular at the maximum equipotential surface $V=h$ of the equivalent system, since the coefficients of the second derivatives of the displacements vanish here. Hence, it is necessary to develop an asymptotic scheme for computing the modal lines.

Complementing the aforementioned functional equations, there exist $(n-1)$ boundary orthogonality conditions that guarantee that the modal lines intersect orthogonally the maximum equi-potential surface of the equivalent system (Mikhlin, 1974):

$$\begin{aligned} &[f_r(\hat{x}_1(X_r), \ldots, \hat{x}_n(X_r)) + \epsilon \hat{p}_r(\hat{x}_1(X_r))] \left\{\frac{d\hat{x}_i}{dx_r}\right\}_{x_r = X_r} \\ &\quad = f_i(\hat{x}_i(X_r), \ldots, \hat{x}_n(X_r)) + \epsilon \hat{p}_i(\hat{x}_1(X_r)). \end{aligned} \tag{7}$$

A detailed asymptotic analysis will be carried out in the following section where a forced two-degree-of-system oscillator with cubic nonlinearity will be examined. The nonlinear relations (5) describing the modal lines of the nonsimilar modes of the equivalent system will be approximated by series expressions containing powers of the displacements:

$$\hat{x}_i(x_r) = \sum_{k=0}^{\infty} \epsilon^k \hat{x}_i^{(k)}(x_r), \; i=1, \ldots, n, \; i \neq r. \tag{8}$$

The kth-order approximations $\epsilon^k \hat{x}_i^{(k)}(x_r)$ will be also expressed in series representations as:

$$\hat{x}_i^{(k)}(x_r) = \sum_{j=1,3,5,\ldots}^{\infty} a_{ij}^{(k)} x_r^j, \; i=1, \ldots, n, \; i \neq r. \tag{9}$$

Note that only odd terms are included in the series (this is due to the required symmetries of the modal lines in the configuration space). The coefficients $a_{ij}^{(k)}$ in (9) will be determined by substituting the series representations in the functional relations (6)–(7) and matching coefficients of respective powers of x_r. Moreover, successive approximations for the amplitude X_r will be obtained by requiring that at each level of approximation, the period of the steady-state motion be equal to the period of the external excitation T. It can be shown that the asymptotic solution converges in any open subinterval of $[-X_r, X_r]$, but not at the limiting values $\pm X_r$ (a rigorous mathematical proof of the convergence can be found in Manevitch et al. (1972).

3 System With Cubic Nonlinearity: Basic Theorem

In this section, the general methodology of the previous section will be applied to the analysis of the forced motion of a specific oscillator. For the sake of simplicity, a two-degree-of-freedom system with cubic nonlinearity will be considered with an external force acting on one of the masses. However, later it will be shown how the results of this section can be generalized to the case of systems with more degrees-of-freedom and higher degree of nonlinearity.

The equations of motion of the system are given by

$$\begin{aligned}\ddot{x}_1+x_1+x_1^3+K_1(x_1-x_2)+K_3(x_1-x_2)^3&=\epsilon p(t)\\ \ddot{x}_2+x_2+x_2^3+K_1(x_2-x_1)+K_3(x_2-x_1)^3&=0\end{aligned}\qquad(10)$$

where $\epsilon p(t)$ is a small periodic force of period T. The scalars K_1 and K_3 are positive quantities of O(1), and represent the coefficients of the linear and nonlinear parts of the coupling stiffness. The initial conditions of the system are assumed to be of the form

$$x_i(0)=X_i,\ \dot{x}_i(0)=0,\ i=1,\ 2\qquad(11)$$

When $\epsilon=0$ (no excitation), the unforced system has two similar modes of free oscillation (Vakakis et al., 1988):

- A symmetric mode, where $x_2=x_1$ for all times.
- An antisymmetric mode, where $x_2=-x_1$ for all times.

When $\epsilon\neq 0$, the normal modes are perturbed, and the system becomes (weakly) *nonconservative*. At the steady state the time variable can be expressed as a function of the variable x_1: $t=t(x_1)$. Thus, in principle one can eliminate the time dependence in the expression of the forcing function and symbolically write

$$\epsilon p(t(x_1))\equiv\epsilon\hat{p}(x_1),\ t\in[0,T/2).\qquad(12)$$

As a result, at the steady state the forced problem (10) becomes equivalent to an autonomous one, described by the following set of equations:

$$\begin{aligned}\ddot{x}_1+x_1+x_1^3+K_1(x_1-x_2)+K_3(x_1-x_2)^3&=\epsilon\hat{p}(x_1)\\ \ddot{x}_2+x_2+x_2^3+K_1(x_2-x_1)+K_3(x_2-x_1)^3&=0\end{aligned}\qquad(13)$$

for $t\in[0,T/2)$. As mentioned earlier, a nonsimilar normal mode of the equivalent system (13) corresponds to a nonsimilar steady state for the forced problem (10). Such a motion is represented in the configuration plane by the modal line $x_2=\hat{x}_2(x_1)$.

This modal relation must hold at every value of time; therefore, the time derivatives of the coordinate x_2 during a nonsimilar normal mode motion can be expressed by the chain rule as $\dot{x}_2=\hat{x}_2'\dot{x}_1$, $\ddot{x}_2=\hat{x}_2''(\dot{x}_1)^2+\hat{x}_2'\ddot{x}_1$, where $(\bullet)'\equiv d/dx_1$ and $(\dot{\bullet})=d/dt$. Substituting for x_2, $\dot{x}_2$, and $\ddot{x}_2$ into the equations of motion (13) and eliminating the velocity $\dot{x}_1$ by integrating the first of the above equations by quadratures one obtains the following functional equation for the (unknown) modal function $\hat{x}_2(\bullet)$:

$$\begin{aligned}-2\hat{x}_2''\Bigg\{&\frac{(x_1^2-X_1^2)}{2}(1+K_1)+\frac{(x_1^4-X_1^4)}{4}\\&+\int_{X_1}^{x_1}[K_3(\xi-\hat{x}_2(\xi))^3-K_1\hat{x}_2(\xi)-\epsilon\hat{p}(\xi)]d\xi\Bigg\}\\&-\hat{x}_2'\{x_1+x_1^3+K_1x_1-\hat{x}_2K_1+K_3(x_1-\hat{x}_2)^3-\epsilon\hat{p}(x_1)\}\\&+\hat{x}_2+\hat{x}_2^3+K_1\hat{x}_2-K_1x_1+K_3(\hat{x}_2-x_1)^3=0.\end{aligned}\qquad(14)$$

This functional equation is analogous to the general expression (6) that was derived earlier for the general n-degree-of-freedom oscillator. Note that the coefficient of the second derivative of $\hat{x}_2$ becomes zero at $x_1=\pm X_1$. As a result, the asymptotic approximation to the solution will be valid only in open intervals contained in $[-X_1, X_1]$. To guarantee that the series solution intersects the maximum equi-potential surface at the points $(x_1, x_2)=(\pm X_1, \pm X_2)$, one imposes the additional boundary condition:

$$\begin{aligned}-\hat{x}_2'(X_1)\{&X_1+X_1^3+K_1X_1-\hat{x}_2(X_1)K_1\\&+K_3(X_1-\hat{x}_2(X_1))^3-\epsilon\hat{p}(X_1)\}\\&+\hat{x}_2(X_1)+\hat{x}_2(X_1)^3+K_1\hat{x}_2(X_1)\\&-K_1X_1+K_3(\hat{x}_2(X_1)-X_1)^3=0.\end{aligned}\qquad(15)$$

This equation is equivalent to the boundary orthogonality conditions (7) that were derived in the general formulation of the problem. The modal line of the equivalent autonomous system is asymptotically approximated as follows:

$$\hat{x}_2(x_1)=\hat{x}_2^{(0)}(x_1)+\epsilon\hat{x}_2^{(1)}(x_1)+O(\epsilon^2).\qquad(16)$$

The various orders of approximation will now be evaluated separately.

Zeroth Order Approximation. The zeroth order approximation $\hat{x}_2^{(0)}(x_1)$ is found by substituting (16) into the functional relations (14)–(15) and considering only terms of $O(1)$. The resulting responses correspond to the similar normal modes (straight modal lines) of the unperturbed system (with $\epsilon=0$):

$$\hat{x}_2^{(0)}(x_1)=cx_1,\ c=\pm 1.\qquad(17)$$

Moreover, the time response $x_1=x_1(t)$ is given in terms of an elliptic function

$$x_1(t)=X_{10}cn(qt,k)\qquad(18)$$

where

$$q^2=\lambda^2+\mu^2X_{10}^2,\ k^2=\mu^2X_{10}^2/2q^2,\ \lambda^2=1+K_1(1-c),\ \mu^2=1+K_3(1-c)^3.$$

The quantity X_{10} denotes the first-order approximation to the amplitude of oscillation X_1 and is a yet unknown quantity. To compute X_{10} one has to impose an additional condition, namely, that the oscillation (18) is of period T. This is because, at the steady state, the forced oscillation must be of the same period with that of the excitation. Thus, one requires that

$$\omega=\pi q/2K(k)=2\pi/T\qquad(19)$$

where ω is the frequency of oscillation in (rad/sec) and $K(\bullet)$ is the complete elliptic integral of the first kind. From (19), the amplitude X_{10} can be determined by a numerical root-finding technique.

First-Order Approximation. Considering $O(\epsilon)$ terms in (14)–(15), the following functional equations for the first-order approximation, $\hat{x}_2^{(1)}(x_1)$, result in

$$\begin{aligned}-2\hat{x}_2^{(1)\prime\prime}\Bigg\{&\frac{(x_1^2-X_{10}^2)}{2}[1+K_1(1-c)]\\&+\frac{(x_1^4-X_{10}^4)}{4}[1+K_3(1-c)^3]\Bigg\}\\&-\hat{x}_2^{(1)\prime}\{[1+K_1(1-c)]x_1+[1+K_3(1-c)^3x_1^3\}\\&+\hat{x}_2^{(1)}\{[1+K_1(1+c)]+3c^2x_1^2\}+\hat{p}_0(x_1)=0\end{aligned}\qquad(20)$$

and

$$\begin{aligned}-\hat{x}_2^{(1)\prime}(X_{10})\{&[1+K_1(1-c)]X_{10}+[1+K_3(1-c)^3]X_{10}^3\}\\&+\hat{x}_2^{(1)}(X_{10})\{[1+K_1(1+c)]+3c^2X_{10}^2\}+\hat{p}_0(X_{10})=0.\end{aligned}\qquad(21)$$

The term $\hat{p}_0$, which appears in the above equations, represents the first-order approximation to the function $p(t)$ when the time t is expressed as a function of x_1. Inverting the zeroth order solution (18) one obtains (Byrd et al., 1954)

$$x_1/X_{10}=cn(qt,k)\Rightarrow t=t(x_1)$$
$$=F(\sin^{-1}[1-(x_1/X_{10})^2]^{1/2},k)/q \quad (22)$$

and

$$\hat{p}_0(x_1)=p(F(\sin^{-1}[1-(x_1/X_{10})^2]^{1/2},k)/q). \quad (23)$$

In the above expressions, $F(\bullet,\bullet)$ is the incomplete elliptic integral of the first kind.

Thus, an explicit analytic expression is obtained for $\hat{p}_0(x_1)$, which in turn can be substituted into (20)–(21) to obtain the first-order approximation $\hat{x}_2^{(1)}(x_1)$. Note, however, that the above expression is very complicated and thus of little practical use. In order to obtain a simplified expression for $\hat{p}_0(x_1)$, a change of variables is now introduced. This involves the amplitude function, $am(\bullet,\bullet)$, defined as (Byrd et al., 1954):

$$cn(u,k)=\cos\phi\Rightarrow\phi=am(u,k). \quad (24)$$

Then from Eq. (22) one can write

$$cn(qt,k)=\cos\phi\Rightarrow\phi=am(qt,k) \quad (25)$$

and solve for the variable t

$$t=am^{-1}(\phi,k)/q\Rightarrow t=F(\phi,k)/q. \quad (26)$$

Using (26), one can eliminate the time variable from the expression of the forcing function as follows:

$$\hat{p}_0(x_1)\equiv\mathring{p}_0(\phi)\equiv p(F(\phi,k)/q). \quad (27)$$

Expression (27) replaces the complicated formula (23), and represents the first-order approximation to the forcing function. The displacement x_1 is also expressed in terms of the new variable ϕ, as

$$x_1\equiv\mathring{x}_1(\phi)=X_{10}\cos\phi. \quad (28)$$

Thus, the newly introduced variable ϕ replaces completely the displacement x_1 in the functional equations (20)–(21) and it can be regarded as the new time-like independent variable. Equations (27)–(28) provide a means for computing an alternative, simplified expression for the required forcing function $\hat{p}_0$. To achieve this, one has to expand the expression (27) of $\mathring{p}_0(\phi)$ in generalized Fourier series with respect to the variable ϕ (Bejarano and Sanchez, 1988, 1989; Margallo et al., 1988).

Referring to Eq. (26) and taking into account certain properties of the incomplete elliptic integral of the first kind, it can be shown that the following correspondence between the variables t and ϕ exists:

$$t\in[0,+T/2)\Rightarrow\phi\in[0,+\pi) \text{ and } t\in[-T/2,0)\rightarrow\phi\in[-\pi,0). \quad (29)$$

Clearly, in each of the above time intervals, the representation $t=t(x_1)$ has meaning (i.e., is a single-valued function). Moreover, the above relations, coupled with the assumption that the forcing function $\epsilon p(t)$ is periodic with period T, lead to the conclusion that the function $\mathring{p}_0(\phi)$ is also periodic in ϕ, with a period equal to 2π. It can be therefore, expanded in generalized Fourier series as follows:

$$\mathring{p}_0(\phi)=\sum_{n=0}^{\infty}A_n\cos n\phi+\sum_{m=1}^{\infty}B_m\sin m\phi \quad (30)$$

where the coefficients A_n and B_n are computed by the well-known Fourier series formulas

$$A_0=(1/2\pi)\int_{-\pi}^{\pi}\mathring{p}_0(\phi)d\phi,\ A_n=(1/\pi)\int_{-\pi}^{\pi}\mathring{p}_0(\phi)\cos n\phi\, d\phi$$

$$B_m=(1/\pi)\int_{-\pi}^{\pi}\mathring{p}_0(\phi)\sin m\phi\, d\phi. \quad (31)$$

Consider now the first-order approximation for the displacement, $\hat{x}_2^{(1)}(x_1)$, and express it in the following series form:

$$\hat{x}_2^{(1)}(x_1)=a_{21}^{(1)}x_1+a_{23}^{(1)}x_1^3+a_{25}^{(1)}x_1^5+\cdots. \quad (32)$$

Transforming into the new variable ϕ, one obtains

$$\hat{x}_2^{(1)}(x_1)\equiv\mathring{x}_2^{(1)}(\phi)=a_{21}^{(1)}X_{10}\cos\phi$$
$$+a_{23}^{(1)}X_{10}^3\cos^3\phi+a_{25}^{(1)}X_{10}^5\cos^5\phi+\cdots \quad (33)$$

Substituting now for $x_1=\mathring{x}_1(\phi)$, $\hat{p}_0(x_1)=\mathring{p}_0(\phi)$ and $\hat{x}_2^{(1)}(x_1)\equiv\mathring{x}_2^{(1)}(\phi)$ into the functional equations of the first approximation (20)–(21), one obtains the following final set of equations containing only trigonometric terms of the variable ϕ:

$$(-6a_{23}^{(1)}X_{10}\cos\phi-20a_{25}^{(1)}X_{10}^3\cos^3\phi)\left\{T_1^{(1)}X_{10}^2(\cos^2\phi-1)+T_2^{(1)}X_{10}^4(\cos^4\phi-1)/2\right\}$$
$$+(-a_{21}^{(1)}-3a_{23}^{(1)}X_{10}^2\cos^2\phi-5a_{25}^{(1)}X_{10}^4\cos^4\phi)\left\{T_1^{(1)}X_{10}\cos\phi+T_2^{(1)}X_{10}^3\cos^3\phi\right\}$$
$$+(a_{21}^{(1)}X_{10}\cos\phi+a_{23}^{(1)}X_{10}^3\cos^3\phi+a_{25}^{(1)}X_{10}^5\cos^5\phi)\left\{T_3^{(1)}+T_4^{(1)}X_{10}^2\cos^2\phi\right\}$$
$$+c\left\{\sum_{n=0}^{\infty}A_n\cos n\phi+\sum_{m=1}^{\infty}B_m\sin m\phi\right\}=0 \quad (34)$$

and

$$(-a_2^{(1)}-3a_{23}^{(1)}X_{10}^2-5a_{25}^{(1)}X_{10}^4)\left\{T_1^{(1)}X_{10}+T_2^{(1)}X_{10}^3\right\}$$
$$+(a_{21}^{(1)}X_{10}+a_{23}^{(1)}X_{10}^3+a_{25}^{(1)}X_{10}^5)\left\{T_3^{(1)}+T_4^{(1)}X_{10}^2\right\}+c\sum_{n=0}^{\infty}A_n=0 \quad (35)$$

where terms of $O(x_1^7)=O(\cos^7\phi)$ or higher were omitted and

$$T_1^{(1)}=1+K_1(1-c),\ T_2^{(1)}=1+K_3(1-c)^3,\ T_3^{(1)}=1+K_1(1+c),$$
$$T_4^{(1)}=3c^2. \quad (36)$$

An exact steady-state motion can only occur, provided that the above expressions lead to real solutions for the (as yet unknown) coefficients $a_{2j}^{(1)}$; in what follows, these coefficients will be obtained by suitably matching coefficients of respective powers of $\cos\phi$ and $\sin\phi$. Before doing this, however, there is a need to expand the terms $\cos n\phi$ and $\sin n\phi$ in powers of $\cos\phi$ and $\sin\phi$.

Considering the transformed functional relations (34)–(35), the following can be concluded as far as the generalized series of the forcing function is concerned:

(1) The coefficients of the sine terms of the generalized series (30) must be zero:

$$B_m=0,\ m=1,\ 2,\ 3,\ \ldots. \quad (37a)$$

This is because, the functional Eq. (34), terms containing powers of $\sin\phi$ cannot be balanced for any values of the coefficients $a_{2j}^{(1)}$. In fact, condition (37*a*) can be shown to be equivalent to the statement that the steady-state response of the undamped oscillator is either in phase or out of phase with the excitation, in the absence of damping (Vakakis, 1990).

(2) A second restriction on the coefficients of the Fourier series (30) results from the fact that there exist only odd powers of $\cos\phi$ in the functional equations (34)–(35). Hence, it is necessary that the Fourier series of $\mathring{p}_0(\phi)$ do not contain any even cosine terms

$$A_{2j}=0,\ j=0,\ 1,\ 2,\ \ldots. \quad (37b)$$

This condition is an immediate result of the fact that the nonlinearities of the oscillator under investigation are of odd degrees: there exist no even powers of $\cos\phi$ to balance the odd cosine terms of the generalized Fourier series of the excitation. In particular, for $j=0$, the above condition gives

$$\int_{-\pi}^{\pi}\mathring{p}_0(\phi)d\phi=\int_{-\pi}^{\pi}p(F(\phi,k)/q)d\phi=0. \quad (38)$$

The above equation is the equivalent for the system with cubic nonlinearity, of the analogous (trivial) condition satisfied by periodic forces in linear steady-state motions, namely that

$$\int_{-T/2}^{T/2} p(t)dt = 0 \quad \text{(linear theory).} \tag{39}$$

In fact, one can easily show that when the coefficients of the nonlinear terms in the equations of motion vanish, Eq. (38) degenerates to the expression (39). Note, however, that condition (38) does not imply (39).

Summarizing, it was found that in order for a steady state to exist, certain restrictions on the form of the periodic excitations must be posed. These are *necessary conditions* for a steady-state motion and are given by (37*a*)–(37*b*).

It can be also shown that once these conditions are met, one can always compute numerical values for the coefficients $a_{2j}^{(1)}$. To this end, suppose that the system is acted by a periodic excitation which satisfies conditions (37*a*)–(37*b*). Then it will be shown that, sufficiently close to a similar normal mode of the unforced system, an exact steady-state motion results. Note that, because of the nonlinearities a variety of responses are possible, such as aperiodic motions or sub and ultraharmonic ones; however, in this work only exact steady states are considered. Thus, sufficiently close to a normal mode of the unforced system the relations (37*a*)–(37*b*) can also be proven to be *sufficient* for the realization of an exact steady state.

For weak excitations that are sufficiently close to the normal mode, $x_2 = cx_1$, an exact steady state motion is described by the relation

$$\hat{x}_2(x_1) = (c + \epsilon a_{21}^{(1)})x_1 + \epsilon a_{23}^{(1)}x_1^3 + \epsilon a_{25}^{(1)}x_1^5 + O(\epsilon x_1^7, \epsilon^2). \tag{40}$$

The coefficients $a_{2j}^{(1)}$ can then be evaluated by matching the coefficients of the various powers of $\cos\phi$ in expressions (34)–(35). Details of this computation can be found in (Vakakis, 1990), and a synopsis of the analytic results is in the Appendix.

Since c can take either the value $+1$, or -1 (zeroth-order approximation), two possible exact nonsimilar steady-state motions exist, each one occurring in the neighborhood of a normal mode of the unforced system. Moreover, the time responses of the system can be evaluated by substituting the modal relation (40) into the first of the equations of motion (10), and integrating by quadratures. To achieve this, one must eliminate the trigonometric terms in the expression of $\hat{p}_0(\phi)$ by expanding them in powers of $\cos\phi$ and subsequently use the formula (28). Then the following asymptotic approximation for the forcing function results in

$$\epsilon\hat{p}(x_1) = \epsilon S_1^{(1)}(x_1/X_{10}) + \epsilon S_3^{(1)}(x_1/X_{10})^3 + \epsilon S_5^{(1)}(x_1/X_{10})^5 + O(\epsilon x_1^7, \epsilon^2) \tag{41}$$

where expressions for $S_j^{(1)}$ can be found in the Appendix.

Finally, an improved approximation for the amplitude of steady-state oscillation, X_1, can be derived by imposing the requirement that the period of steady motion is equal to T (equal to that of the force). Details for that computation can be found in (Vakakis, 1990). The stability of the steady-state motion can be examined by numerically computing its Floquet multipliers (Vakakis, 1990).

The results of this section can be summarized in the form of a theorem as follows:

Theorem. Consider a two-degree-of-freedom oscillator with cubic nonlinearity, excited by a periodic excitation $\epsilon p(t)$, and having equations of motion given by (10). Provided that the excitation is sufficiently small, and that the initial conditions are given by (11), a necessary and sufficient condition for the occurrence of exact steady-state motions in the neighborhoods of normal modes of the unforced system is that the generalized Fourier series of the excitation is of the form:

$$\hat{p}_0(\phi) = \sum_{j=0}^{\infty} A_{2j+1}\cos(2j+1)\phi$$

where

$$A_{2j+1} = (1/\pi)\int_{-\pi}^{\pi} \hat{p}_0(\phi)\cos(2j+1)\phi\, d\phi$$

and the function $\hat{p}_0(\phi)$ is evaluated by the expression

$$\hat{p}_0(\phi) \equiv p(F(\phi,k)/q).$$

In the above equations, $F(\bullet,\bullet)$ is the incomplete elliptic integral of the first kind, and the quantities q and k depend on the structural parameters of the oscillator and the period of the external force.

Moreover, at the steady state, the system generally oscillates as in a nonsimilar normal mode.

The following remarks are appropriate at this point.

- Although the theorem is stated for a specific set of initial conditions, this does not restrict its validity. For different initial conditions, the analysis can be carried out in exactly the same way, with different restrictions, however, to the forcing functions.
- The theorem can be generalized easily to systems with more than two-degrees-of-freedom. In that case more than one functional equation and boundary orthogonality condition are involved, but the basic steps of the analysis remain unaltered.
- Finally, the theorem can be extended to systems with a degree of nonlinearity higher than three. In that case, the incomplete elliptic integral of the first kind in the argument of the forcing function $\epsilon p(t)$ should be replaced by an (untabulated) incomplete integral.

4 Numerical Applications

Applications of the theorem were made by considering two specific forms for the forcing function

$\epsilon p_1(t) = \epsilon P_1\cos\psi t$ and

$$\epsilon p_2(t) = \epsilon(P_2/2)\tan^{-1}\{2\alpha\cos\omega t/(1-\alpha^2)\}. \tag{42}$$

Both of these functions satisfy the conditions of the theorem and therefore lead to exact steady-state motions. Details about the numerical computations can be found in (Vakakis, 1990), and the resulting steady-state motions are shown at Figs. 1(*a*-*b*). Both these motions are proven to be orbitally stable. It must be noted, however, that in each case, there exists an additional branch of steady solutions near the symmetric mode that is orbitally unstable. These motions will not be presented here.

It can be seen that at the steady state the displacement has the period of the excitation. Note also, that although the force is restricted to small values, the displacements are of $O(1)$.

5 Discussion

In this work, a detailed analysis of a two-degree-of-freedom system with cubic nonlinearity was carried out, and it was shown that close to each of its normal modes, an exact nonsimilar steady-state response exists. To prove this, the forced problem was transformed, at the steady state, to an equivalent unforced one; an asymptotic analysis was then implemented to find the nonsimilar normal modes of the transformed system. These oscillations were then shown to correspond to nonsimilar steady states of the original forced problem.

Using this methodology a general theorem was stated, and the general class of periodic functions that can produce exact steady-state motions in the system with cubic nonlinearity was identified. Moreover, extensions of the theorem can be made for systems with many degree-of-freedom and arbitrary odd nonlinearities.

The theorem assumes that the unforced system has nonlinear normal modes and its results are only valid for weak excitations. The resulting asymptotic expansions are valid in the neighborhoods of the unperturbed normal modes and their

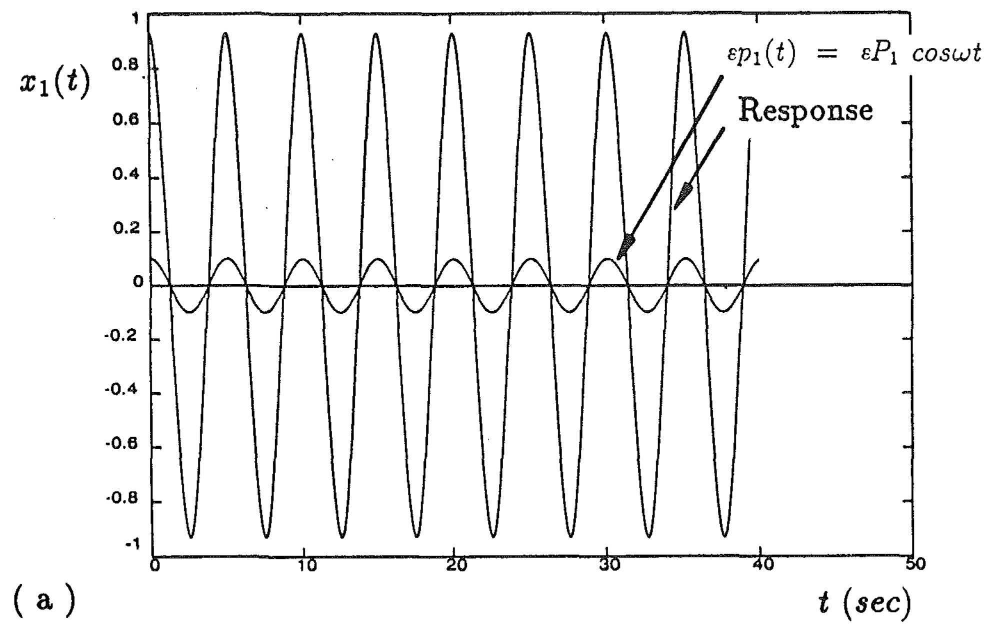

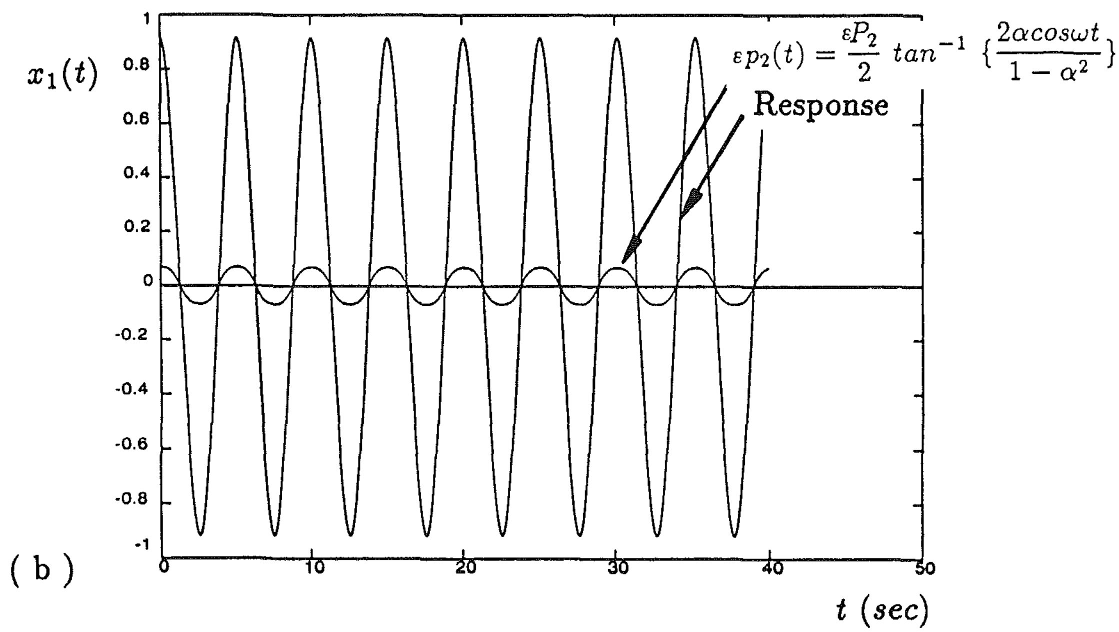

Fig. 1 Displacement x_1 during a nonsimilar steady-state oscillation in the neighborhood of the normal mode $c = +1$. Numerical values of the parameters: $K_1 = 1.3$, $K_3 = 0.7$. (*a*) Forcing function $\epsilon p_1(t)$, $\epsilon P_1 = 0.10$, $\omega = 1.25$, (*b*) Forcing function $\epsilon p_2(t)$, $\epsilon P_2 = 0.15$, $\omega = 1.25$, $\alpha = 0.5$.

accuracy is improved when one computes higher order terms (that were omitted in the present analysis).

A general conclusion of this work is that the concept of nonlinear normal mode can be successfully used for studying the forced response of nonlinear discrete oscillators. This is because steady-state motions result as perturbations of normal modes, *provided that the system is excited by a suitable admissible periodic forcing function*. Although harmonic functions are included in the general class of admissible excitations, this work showed that these are not the only forcing functions leading to exact steady states: In fact, a whole class of periodic functions was identified capable of producing steady motions. This outlines a limitation of the majority of conventional methods, since they only consider harmonic excitations and assume only predominantly harmonic responses. No such assumptions were made here, since the general nonsimilar steady-state responses were expressed in asymptotic series whose dominant terms consisted of the normal mode motions. Hence, for weak excitations, and close to the corresponding normal modes, the steady solutions derived here are expected to be more accurate than those obtained by conventional methodologies.

Finally, the mathematical formulation developed in this work has direct application in practical engineering problems involving periodically forced mechanical components. By modelling these components by discrete linear and nonlinear elements one is able to use the outline formulation in order to compute forced dynamical responses. The advantage of the present method over existing ones lies on the use of elliptic functions (instead of harmonic ones) as zeroth order approximations of the steady motions; *thus, the nonlinearities of the system are taken into account in the zeroth-order approximation* and this leads to more accurate results compared to averaging or asymptotic methods which assume harmonic zeroth-order approximations. Current work by the authors is focused on applying the presented methodology for predicting the dynamic response of realistic models of practical nonlinear structures such as bladed-disk assemblies and large periodic truss members.

References

Atkinson, C., and Taskett, B., 1965, "A Study of the Nonlinearly Related Model Solutions of Coupled Nonlinear Systems by Superposition Techniques," ASME JOURNAL OF APPLIED MECHANICS, Vol. 32, pp. 359–364.

Bejarano, D., and Sanchez, M., 1988, "Generalized Exponential, Circular and Hyperbolic Functions for Nonlinear Wave Equations," *Journal of Mathematical Physics*, Vol. 29, No. 8, pp. 1847–1853.

Bejarano, D., and Sanchez, M., 1989, "Generalized Fourier Series for Nonlinear Systems," *Journal of Sound and Vibration*, Vol. 134, No. 2, pp. 333–341.

Byrd, P., and Friedman, D., 1954, *Handbook of Elliptic Integrals for Engineers and Physicists*, Springer-Verlag, New York.

Caughey, T., and Vakakis, A., 1991, "A Method for Examining Steady State Solutions of Forced Discrete Systems with Strong Nonlinearities," *International Journal of Nonlinear Mechanics*, Vol. 26, No. 1, pp. 89–103.

Kinney, W., 1965, "On the Geometrization of the Forced Oscillations of Nonlinear Systems Having Many Degrees of Freedom," Ph.D. Thesis, University of California, Berkeley, CA.

Kinney, W., and Rosenberg, R., 1966, "On the Steady State Vibrations of Nonlinear Systems with Many Degrees of Freedom," ASME JOURNAL OF APPLIED MECHANICS, Vol. 33, No. 2, pp. 406–412.

Manevich, L., and Mikhlin, I., 1972, "On Periodic Solutions Close to Rectilinear Normal Vibration Modes," *PMM*, Vol. 36, No. 6, pp. 1051–1058.

Margallo, G., Bejarano, D., and Yuste, B., 1988, "Generalized Fourier Series for the Study of Limit Cycles," *Journal of Sound and Vibration*, Vol. 125, No. 1, pp. 13–21.

Mikhlin, I., 1974, "Resonance Modes of Near-Conservative Nonlinear Systems," *PMM*, Vol. 38, No. 3, pp. 459–464.

Rand, R., 1971, "A Higher Order Approximation for Nonlinear Normal Modes in Two Degree of Freedom Systems," *International Journal of Nonlinear Mechanics*, Vol. 6, pp. 545–547.

Rand, R., 1974, "A Direct Method for Nonlinear Normal Modes," *International Journal of Nonlinear Mechanics*, Vol. 9, pp. 363–368.

Rosenberg, R., and Kuo, J., 1964, "Nonsimilar Normal Mode Vibrations of Nonlinear Systems Having Two Degrees of Freedom," ASME JOURNAL OF APPLIED MECHANICS, Vol. 31, pp. 283–290.

Rosenberg, R., 1966a, "On Nonlinear Vibrations of Systems with Many Degrees of Freedom," *Advances in Applied Mechanics*, Vol. 9, pp. 155–242.

Rosenberg, R., 1966b, "Steady State Forced Vibrations," *International Journal of Nonlinear Mechanics*, Vol. 1, p. 95.

Vakakis, A., and Caughey, T., 1988, "Free and Forced Vibration of Certain Strongly Nonlinear Systems," Dynamics Laboratory Report DYNL-88-1, Caltech, Pasadena, CA.

Vakakis, A., 1990, "Analysis and Identification of Linear and Nonlinear Normal Modes in Vibrating Systems," Ph.D. Thesis, California Institute of Technology, Pasadena, CA.

Yang, T. L., and Rosenberg, R., 1968, "On Forced Vibrations of a Particle in the Plane," *International Journal of Nonlinear Mechanics*, Vol. 3, pp. 47–63.

APPENDIX

The coefficients $a_{2j}^{(1)}$ of the modal relation (40) are given by the following analytic expressions (Vakakis, 1991):

$$a_{23}^{(1)} = \frac{(T_1^{(1)} - T_3^{(1)})a_{21}^{(1)}}{6T_1^{(1)}X_{10}^2 + 3T_2^{(1)}X_{10}^4} - \frac{cS_1^{(1)}/X_{10}}{6T_1^{(1)}X_{10}^2 + 3T_2^{(1)}X_{10}^4}$$

$$\equiv L_1^{(1)}a_{21}^{(1)} + L_2^{(1)}$$

$$a_{25}^{(1)} = \frac{(L_1^{(1)}(9T_1^{(1)} - T_3^{(1)}) + T_2^{(1)} - T_4^{(1)})a_{21}^{(1)}}{20T_1^{(1)}X_{10}^2 + 10T_2^{(1)}X_{10}^4} + \frac{-(cS_3^{(1)}/X_{10}^3) + L_2^{(1)}(9T_1^{(1)} - T_3^{(1)})}{20T_1^{(1)}X_{10}^2 + 10T_2^{(1)}X_{10}^4}$$

$$\equiv L_3^{(1)}a_{21}^{(1)} + L_4^{(1)}$$

$$a_{21}^{(1)} = L_5^{(1)}/L_6^{(1)}$$

where

$$L_5^{(1)} = (3L_2^{(1)}X_{10}^2 + 5L_4^{(1)}X_{10}^4(T_1^{(1)}X_{10} + T_2^{(1)}X_{10}^3) - (L_2^{(1)}X_{10}^3 + L_4^{(1)}X_{10}^5)(T_3^{(1)} + T_4^{(1)}X_{10}^2) - c(S_1^{(1)} + S_3^{(1)} + S_5^{(1)})$$

and

$$L_6^{(1)} = X_{10}(1 + L_1^{(1)}X_{10}^2 + L_3^{(1)}X_{10}^4)(T_3^{(1)} + T_4^{(1)}X_{10}^2) - X_{10}(1 + 3L_1^{(1)}X_{10}^2 + 5L_3^{(1)}X_{10}^4)(T_1^{(1)} + T_2^{(1)}X_{10}^2)$$

where the quantities $T_j^{(1)}$ are given by expressions (36), and

$$S_1^{(1)} = A_1 - 3A_3 + 5A_5 + \cdots$$

$$S_3^{(1)} = 4A_3 - 20A_5 + \cdots$$

$$S_5^{(1)} = 16A_5 + \cdots$$

where A_j are the coefficients of the odd cosine terms in the generalized Fourier series (30) (their values are given by the second of expressions (31)).

On the Dynamics of a Conservative Elastic Pendulum

Roger F. Gans
Department of Mechanical Engineering,
University of Rochester,
Rochester, NY 14627
Mem. ASME

This paper presents a finite element model of the elastica, without dissipation, in a form realizable in the laboratory: a set of rigid links connected by torsion springs. The model is shown to reproduce the linear elastic behavior of beams. The linear beam, and most nonlinear beams are not periodic. (The linear eigenfrequencies are incommensurate.) They do exhibit a basic cyclic behavior, the beam waving back and forth with a measurable period. Extensive exploration of the behavior of a four-link model reveals windows of periodicity—isolated points in parameter space where the motion is nearly periodic. (The basic phase plane diagrams are asymmetric, and the time evolution of the motion distributes this asymmetry symmetrically in time.) The first such window shows a period twice the basic cycle time, the next, less well observed one, four times the basic cycle time.

1 Introduction

Many flexible objects and structures undergo large deformations without suffering large strains. Think of rolling up a sheet of paper, or bending a metal tape measure. The equilibrium shapes of these bent objects are calculated using the theory of the *elastica*. The static theory of the elastica has been exhaustively treated in the monograph by Frisch-Fay (1962). The dynamic problem is more difficult. It has been seriously attacked only during the last decade or two, partly in response to interest in the behavior and control of flexible structures, both in the robotics community (e.g., Cannon and Schmitz, 1984; Singh and Schy, 1986; Daniel et al., 1988) and in the space structures community (e.g., Balas, 1982; Meirovitch et al., 1984; Schaechter, 1981, 1982). Both communities share a common interest in making their structures as light as possible while retaining the ability to control them precisely. The state of the art appears to be the careful control of a cantilever beam undergoing small deflections, so that linear beam theory can be applied. This paper addresses the dynamics of flexible beams for large deflections, where linear beam theory must be replaced by the theory of the elastica.

The general dynamical equations have been given by Antman and Kenney (1981). Caflisch and Maddocks (1984, hereafter referred to as CM) provide a specialization to a two-dimensional system, which they use to establish the stability of the classical buckling solutions in a full dynamic setting. Antman and Liu (1979) discuss time-dependent solutions for beams with general constitutive laws under the two restrictions that the bar be infinitely long, and that the deflections be in the form of traveling waves. These two restrictions combine to reduce the partial differential system to an ordinary differential system. The work most closely related to that presented here is that of Snyder and Wilson (1990, hereafter referred to as SW). SW present a fascinating application of their work, modeling the behavior of bellows mechanisms with a view toward eventual control of such systems. Similar work has been done by Simo and Vu-Quoc (1986a,b, hereafter referred to as SV). Note that control is still a long way off. Both this work and SW are too computationally intensive for real-time applications.

The simplest dynamical problem is that of the free oscillation of a simple beam, one with a rectangular cross-section, obeying Hooke's law, fixed at one end and free at the other. Two extreme cases that leap to mind are the beam by itself and the beam with a massive "bob" at a free end. I call the latter an *elastica pendulum*. SV deal with the former case (and with damping, which I omit.) SW deal with the latter, sans damping and inertia.

I constructed a model of this elastica pendulum (Gans, 1989) valid under the assumption that the beam inertia is negligible compared to that of the bob. This is the same assumption as that of SW, and the analysis was similar, although I looked only at the free oscillations of the system. My model predicted that the period of the gravest oscillation is hardly different from that predicted by simple small deflection linear theory. The beam's behavior, however, is not simple. As the bob moves through its arc, it is subject to violent short-term accelerations apparently related to incipient "snap through"—the appearance of inflection points in the beam profile as bending waves propagate up and down the length of the beam. The relaxation scheme I used apparently obscured the details of the violent behavior, which were detectable only in the tip accelerations. SW specifically avoided this situation; "the sequence of loading and the range of motion are specified so that the elastica has single curvature ..." (SW, p. 205), and they did not look in detail at the dynamic behavior of the tip mass. In this paper I introduce a better model, and use that model to discuss the behavior of the system. The model includes both translational and rotational inertia of the beam. One can add damping and

Contributed by the Applied Mechanics Division of The American Society of Mechanical Engineers for publication in the ASME Journal of Applied Mechanics.

Discussion on this paper should be addressed to the Technical Editor, Prof. Leon M. Keer, The Technological Institute, Northwestern University, Evanston, IL 60208, and will be accepted until four months after final publication of the paper itself in the Journal of Applied Mechanics. Manuscript received by the ASME Applied Mechanics Division, Sept. 17, 1990; final revision, Aug. 20, 1990.

locally applied external forces and loadings. I omit these in the interest of clarity. The simple model's behavior has a rich dynamical structure, and this paper focuses on that behavior.

Let me remark that the current study is different from and complementary to the work over the past decade of Moon and his co-workers, summarized in his recent monograph (Moon, 1987). Moon deals with forced motion in weakly dissipative systems. The "Moon beam" is an elastic system that is a physical realization of Duffing's equation: the forced oscillation of a beam appropriately modeled by inclusion of the first nonlinear term in the deformation, not by the full *elastica* model used here. I am dealing with unconstrained motion in conservative systems.

I will show that the Lagrangian of a mass spring system made up of rigid links joined by linear torsion springs is equivalent to the Lagrangian of the elastica pendulum in the limit that the number of links goes to infinity. The only requirement is to choose the spring constant proportional to the number of links. Once this relationship has been established, it becomes possible to study the behavior of the continuous system using quite crude segmented systems, for which massive amounts of dynamical data can be obtained. It is also possible to examine the behavior of the segmented systems experimentally, although I have not done this yet. Note also that the continuous system cannot be solved analytically, so that the continuous solutions are themselves discrete, finite dimensional results. Nothing is lost in practice by this new program.

The plan of this paper is to begin by establishing the connection between the continuous and segmented beam models. Once this has been done, in Section 2, I will discuss some of the segmented models in detail and finally offer some conjectures as to the applicability of these systems to the continuous system. A rich structure of possible behavior is uncovered, and this paper cannot examine all the modes. The major feature I have been able to identify is isolated windows (in parameter space) of near-periodic behavior in a nonlinear dynamic system that is not periodic in its linear limit. This near-periodic behavior has aspects of period doubling strongly reminiscent of the classical period doubling route to chaos.

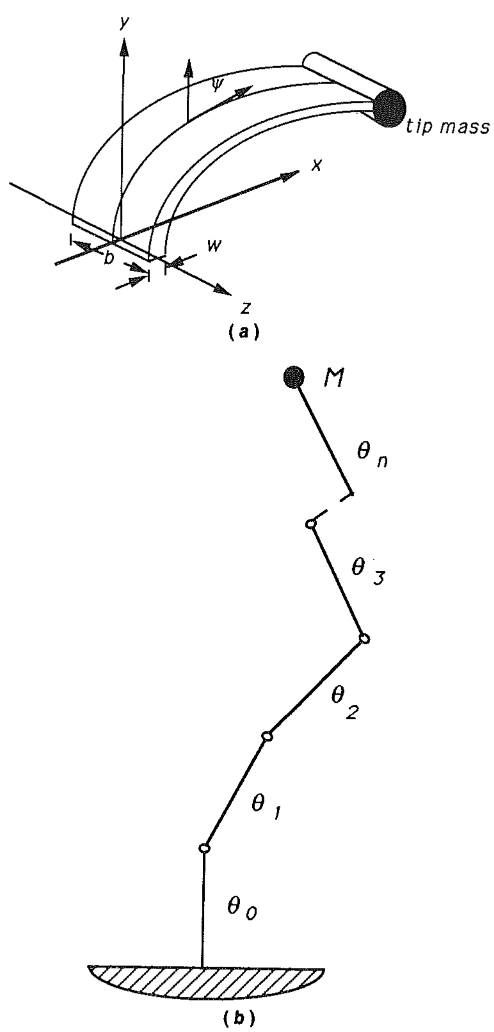

Fig. 1 The large deflection elastica; (a) sketch of the beam, (b) the two-dimensional segmented model

2 Formulation

Consider an inextensible beam with a rectangular cross-section, thickness w, width b, and length L. Let ρ and E denote the density and Young's modulus of the beam material. The mass of the beam $m = \rho bwL$. Let a point mass Mm be fixed at one end, and let the other end be fixed. Assume that $b \gg w$ so that it is reasonable to suppose that motion will be confined to a plane and twist can be neglected. Let the beam be oriented as in Fig. 1(a). Define θ as the angle between the tangent to the beam at any point and the x-axis. The angle ψ shown in the figure is the complement of θ, and it is useful in discussing the linear case, for which its absolute value is small. Let s denote the arclength along the beam, $0 \leq s \leq L$.

The kinetic energy of this beam-mass system can be written

$$T=\frac{1}{2}\int_0^L\left\{J\dot{\theta}^2+\mu\left\{\left[\int_0^s\dot{\theta}\cos\theta du\right]^2+\left[\int_0^s\dot{\theta}\sin\theta du\right]^2\right\}\right\}ds$$
$$+mM\left\{\left[\int_0^L\dot{\theta}\cos\theta du\right]^2+\left[\int_0^L\dot{\theta}\sin\theta du\right]^2\right\} \quad (1)$$

where J is the mass moment of inertia per unit length, μ the mass per unit length, and I use a dot to denote differentiation with respect to time. The first term on the right-hand side represents the kinetic energy of the beam itself, both rotational and translational, and the second term the (translational) kinetic energy of the point mass at the tip. The potential (elastic) energy V is given by

$$V=\frac{1}{2}\int_0^L EI\left\{\frac{\partial\theta}{\partial s}\right\}^2 ds. \quad (2)$$

These expressions are the unconstrained versions of the same expressions given by CM, who showed how to derive an integro-differential system from this by Hamilton's principle. They do not solve that system. Any solution must be found using numerical methods, which means that some discretization is a consequence of seeking a solution. Consider that introduced by discretizing the expression for the Lagrangian

$$L=T-V=\frac{1}{2}\int_0^L\left\{J\dot{\theta}^2+\mu\left\{\left[\int_0^s\dot{\theta}\cos\theta du\right]^2\right.\right.$$
$$\left.\left.+\left[\int_0^s\dot{\theta}\sin\theta du\right]^2\right\}-EI\left\{\frac{\partial\theta}{\partial s}\right\}^2\right\}ds$$
$$+\frac{1}{2}mM\left\{\left[\int_0^L\dot{\theta}\cos\theta du\right]^2+\left[\int_0^L\dot{\theta}\sin\theta du\right]^2\right\}. \quad (3)$$

Let the beam be divided into $n+1$ equal segments, labeled $0, 1, \ldots, n$. Let $N = n + 1$. Let the beam have a uniform cross-section, so that the jth segment has mass m/N, length L/N and mass moment of inertia

$$J=m[(L/N)^2+w^2]/12 \quad (4)$$

for $j = 0, 1, 2, \ldots n$. Figure 1(b) shows the segmented model in two dimensions.

I approximate the inner integral using the trapezoidal rule:

$$N\int_0^L f ds = \frac{1}{2}f_0 + \frac{1}{2}f_n + \sum_{k=1}^{n-1} f_k \tag{5}$$

and the outer integral as simple boxes

$$N\int_0^L f ds = \sum_{k=0}^{n} f_k. \tag{6}$$

This leads to an approximate Lagrangian

$$L \cong \frac{1}{2}\sum \Bigg\{ (m/N)[(L/N)^2 + w^2]/12\dot{\theta}_j^2 - EI(N/L)(\theta_2 - \theta_{j-1})^2 + \frac{mL^2}{N^3}\Bigg[\left(\dot{\theta}_j\cos\theta_j/2 + \sum_1^j \dot{\theta}_k\cos\theta_k\right)^2 + \left(\dot{\theta}_j\sin\theta_j/2 + \sum_1^j \dot{\theta}_k\sin\theta_k\right)^2\Bigg]\Bigg\} + \frac{MmL^2}{N^2}\Bigg[\left(\sum_1^j \dot{\theta}_k\cos\theta_k\right)^2 + \left(\sum_1^j \dot{\theta}_k\sin\theta_k\right)^2\Bigg] \tag{7}$$

where again the dot denotes differentiation with respect to time. This expression is recognizable as the Lagrangian of a set of segments of mass m/N, carrying an end load, connected by torsional springs with a linear spring constant $EI(N/L)$, where $EI = Ebw^3/12$ is the bending stiffness of the beam. In the limit that $N \to \infty$, Eq. (7) becomes Eq. (3).

It is convenient to nondimensionalize the problem. Let lengths (x, y, s) be scaled by L, mass by m, energy by EI/L, the elastic energy scale, and time by $(L/w)^2(\rho ws2/E)^{1/2}$, where ρ denotes the density of the beam material. The time scale is long compared to the time required for an elastic wave to propagate either across or along the beam. The dimensionless spring constant is $N/12$. The governing equations for the discrete dynamical system can now be obtained in the form of a second-order system:

$$[\dot{\theta}] = [\phi]$$
$$\{A\}[\dot{\phi}] = [b] \tag{8}$$

where $[\theta]$, $[\phi]$, and $[b]$ are column vectors and $\{A\}$ is a square matrix. The elements of $\{A\}$ are denoted by A_{jk} and are given by

$$A_{jk} = \begin{cases} [(n+1/3-k)h + M]h^2 & \text{if } k = j \\ [(n+1/2-k)h + M]h^2\cos(\theta_k - \theta_j) & \text{otherwise} \end{cases} \tag{9}$$

and the right-hand side vector $[b]$ has elements given by

$$b_j = (h+2M)h^2\sin(\theta_n - \theta_j)\theta_n^2/2 + (N/12)\delta\theta_j + \Sigma[(a_{jkn} + 1/2)h + M]h^2\sin(\theta_k - \theta_j)\theta_k^2 \tag{10}$$

where $h = 1/N$ is the interval of integration, and the dimensionless mass of a link,

$$a_{jkn} = \begin{cases} n-k \text{ if } k \le j \\ n-j \text{ if } k > j \end{cases} \tag{11}$$

and

$$\delta\theta_j = \begin{cases} \theta_{n-1} - \theta_n & \text{if } j = n \\ \theta_{j+1} - 2\theta_j + \theta_{j-1} & \text{otherwise.} \end{cases} \tag{12}$$

The linear problem for the model is of some interest. The details are straightforward, and will be omitted here. The hypothesis of simple harmonic motion at a frequency ω leads to an eigenvalue problem. The problem can be solved exactly for $N = 2$ or 3, as the eigenvalue equation is linear or quadratic in ω^2, respectively. For $N > 3$ numerical methods are appropriate.

3 Results

3.1 Model Verification and Linear Results. The system (8) is nonlinear. Only numerical solutions are possible for the full system, but the eigenfunction solution to the linearized problem is available to assess the problem qualitatively. I solve the nonlinear system (8) using a variable step Runge-Kutta scheme adapted from that in Press et al. (1986). The code conserves energy to the accuracy imposed on the step-size monitoring, typically one part in 10^4. Three simple initial conditions are used: (1) that resulting from a force applied to the free end at right angles to the beam, (2) that resulting from a pure moment applied to the free end, and (3) that resulting from a buckling load, a compressive load parallel to the beam. Different initial conditions lead to different behavior, but certain universal behavior persists for all loading situations.

Global oscillatory behavior is most easily seen in the elastic energy as a function of time. (This is not good enough to explore some of the more subtle and important behaviors.) I have examined this for beams of 3, 4, 8, and 10 segments, all with the same initial force loading condition ($f_H = 0.01$—the offset varies with the number of links, from 0.01 to 0.03—and spring constants 1/4, 1/3, 2/3, and 10/12.) The computed frequency is linear in $1/N$. The asymptotic frequency for $1/N = 0$ is 0.1556.

There are two simple analytic limits available for comparison. The first is the two-segment beam (a simple mass-spring system). The second is a continuous beam with $M \gg 1$ in the small displacement limit. The latter is a beam bending model obtained by neglecting the mass of the beam and assuming an inertial load at the tip. Linear beam theory gives $\omega = 0.1581$ for this case. The code reproduces the two-segment result, and its predictions tend to the linear limit as $N \to \infty$. The two percent difference between the asymptotic frequency and the analytic frequency is easily accounted for by the neglect of beam inertia in the analytic result.

It is interesting to ask what happens in the absence of the end mass. The calculated system behavior is less smooth. The energy plots show some asymmetry, and the period is less easily determined. All the results conserve energy (to at least 4 parts in 10^5); the problem is not numerical stability. As the number of segments increases the system becomes smoother and smoother, and the oscillations more and more sinusoidal. Moreover, the period has the same sort of asymptotic behavior as the heavy ended beam. I have calculated the frequency for $N = 3, 4, 5, 6, 8, 10$, and 20 link beams, and they are linearly related to $1/N$. The $N \to \infty$ dimensionless frequency of oscillation is bounded by $0.99 < \omega < 1.02$. The exact linear result for a fixed-free beam in these same units is 1.01499 ... (cf., Tse et al., 1978, pp. 262 ff.)

The linear problem sheds considerable light on the model. The frequencies of individual modes are apparently not commensurate. If the frequencies are incommensurate, even the behavior of the linear beam will not be periodic. In any case, periodic behavior with periods near the cycle time is not to be expected. Although the elastic energy is observed to be (apparently) periodic, the detailed motion cannot be periodic, and the elastic energy cannot be used as the sole diagnostic of the motion. A more useful representation is in a phase plane—θ versus $\dot{\theta}$. For a restricted number of segments (I will concentrate on a four-segment model), phase planes of one or more segments can be examined for evidence of periodicity. A circle represents purely sinusoidal motion, and a retraced figure represents periodic motion.

3.2 Nonlinear Behavior.

3.2.1 The twenty segment beam of Gans (1989). This paper has been motivated in part by the special case I presented earlier (Gans, 1989). The initial tip position was $x = 0.8$ and $y = 0.2$. The free end of the beam was moment-free. The tip force was compressive, ten degrees from the vertical, a buckling-type load. The computations used a 20-segment model and calculated the time evolution through one cycle of the

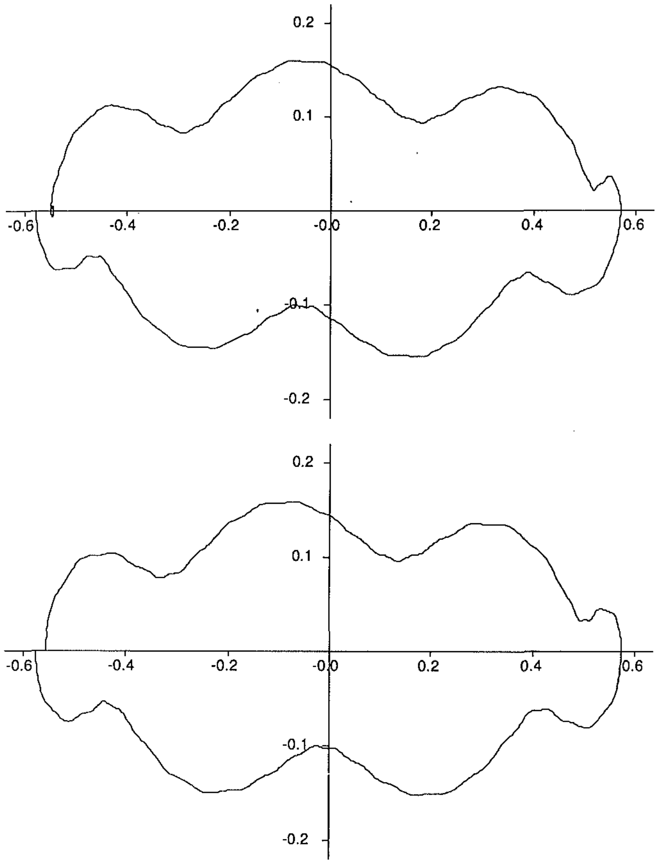

Fig. 2(*a*)

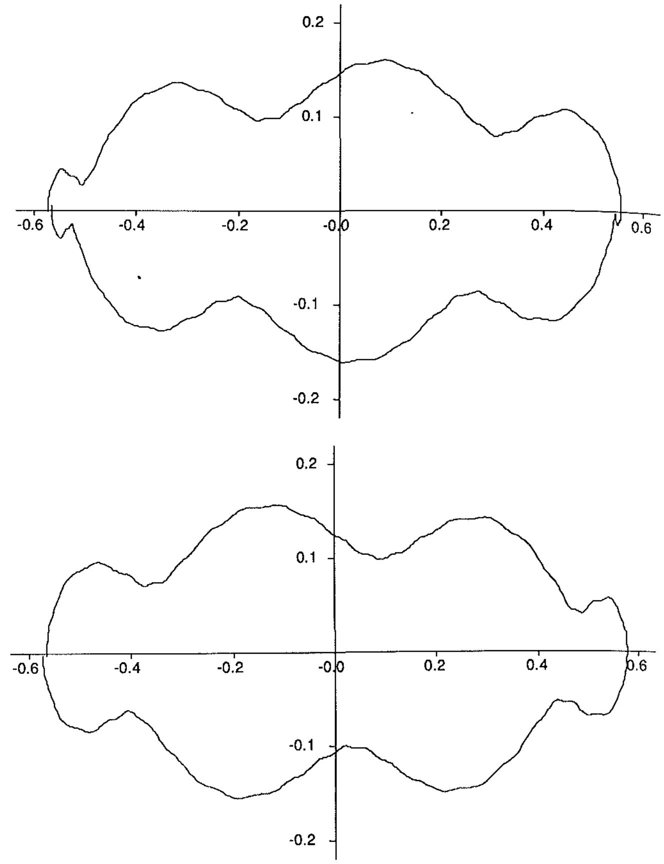

Fig. 2(*c*)

Fig. 2 Phase planes for the first window of periodicity for force loading f_H = 0.147; (*a*) shows time steps 1-603 and 604-1242, (*b*) shows time steps 31052-31696 and 31697-32303, (*c*) shows time steps 63777-64427 and 64428-65041

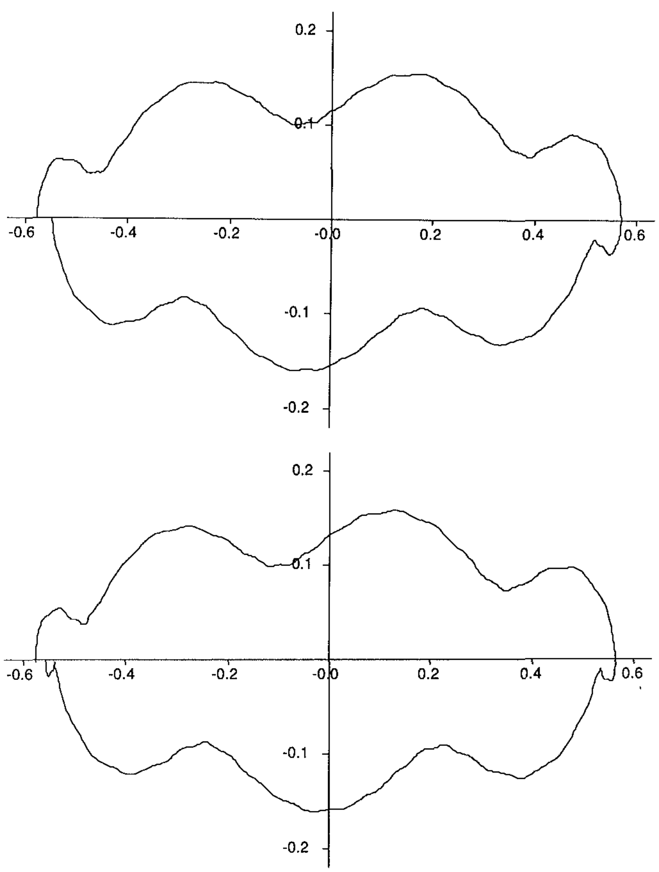

Fig. 2(*b*)

beam. The motion of the tip of the beam is apparently periodic but not sinusoidal, and the fundamental frequency of the motion is 0.1629. This can be compared to 0.1581 calculated from the simple linear theory and 0.1620 from the (linear) frequency versus $1/N$ relation discussed previously.

While energy and tip motion appear smooth, the tip *acceleration* shows dramatic spikes near the neutral position $x = 0$, $y = 1$. These were associated with the appearance, or near appearance, of inflection points in the beam profile, what one might call incipient snap through. I repeated these calculations using the method described in this paper with a view to understanding the behavior near the neutral position and determining the reflection, if any, of the spikes in the elastic energy versus time plots. Even the fundamental frequency of the energy is less easily determined here than in the work cited. (This is because the present method resolves the behavior near the neutral position, which was apparently unintentionally swept under the rug in the previous work.) The observed energy frequency lies between 0.1659 and 0.1689. Of interest is the dramatically violent behavior occurring near the minimum of elastic energy—near the neutral position $x = 0$, $y = 1$. The most dramatic of these correspond to the spikes in the acceleration of the mass cited previously.

The 20-segment beam is not ideal for exploring the qualitative behavior of these systems. It requires the integration of a 38th degree nonlinear first-order system with a fairly dense interaction matrix. Numerical experiment shows that time steps need to be of the order of 0.0004 for the code to run, so that a single period in the energy requires of the order of 47,000 time steps, a full cycle twice that. 65,536 even time steps took

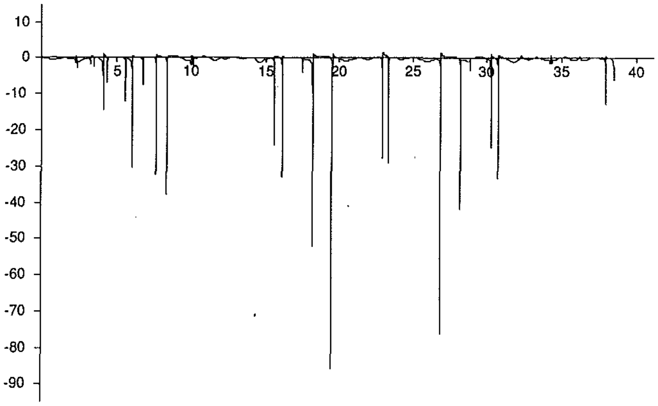

Fig. 3 Radial tip acceleration for the case of a beam initially bent double

about six days on a Sun 3/50 workstation (albeit running in a network over which I have no control). A considerably simpler model will serve to explore the qualitative behavior of these systems, and I have chosen to use the four-segment beam. This reduces the system to sixth order, making it possible to explore longer time behavior. Not only is the effort per time step reduced, the size of the time steps can be increased.

3.2.2 The Four-Segment Beam With M = *10.* The main purpose of this section is to introduce the reader to some of the behavior displayed by the simple four segment beam. The beam behavior is certainly sensitive to initial conditions; however, I am reluctant to introduce the word *chaos* at this time. Most of the standard tools of chaos analysis have been developed for the understanding of forced dissipative systems, and are not applicable to the present system. (I have looked at some constant time interval Poincaré maps; these do not seem helpful, as the beam behavior is never exactly periodic.) In future, forcing and dissipation will be added; at this time I explore only the free oscillations already mentioned.

Choosing initial conditions by locating the tip of the beam is not particularly satisfactory. I have looked at all three equilibrium initial conditions mentioned previously: (1) a given force perpendicular to the beam (beam bending), characterized by the force magnitude f_H, (2) a pure moment applied at the end of the beam, characterized by the elastic energy e, and (3) and a compressive (buckling) force parallel to the beam, characterized by the force magnitude f_B. The first two of these have a linear region. Buckling is inherently nonlinear. One would expect quantitatively different behavior for these three conditions.

The existence of linear solutions provides another static check of the code, as does a comparison with buckling stability. With the scaling introduced in this paper, linear continuous beam bending predicts a displacement of $4f_H$, and the continuous moment model predicts a deflection of $2\sqrt{(3e/2)}$. At sufficiently small values of f_H and e, these are verified even for the four-segment beam. The critical buckling load for the fixed-free beam is $\pi^2 EI/L^2$, which translates to 0.20562 ... ($= \pi^2/48$) in the present nondimensional system. The critical buckling load for the four-segment beam, which is stiffer, is observed (computationally) to be between 0.2640 and 0.2641. The tip position at 0.2641 is $x = 0.01$, $y = 1.00$, with an initial elastic energy of 0.00003.

I have examined beam bending for f_H from 0.035 up to 1.0. The most interesting observation is the existence of windows of almost periodic motion at $f_H = 0.147$ and in the vicinity of $f_H = 0.704$. The $f = 0.147$ case is clearly distinguishable from cases as close as 0.1465 and 0.1475. The latter is less well defined. The former period is twice the fundamental cycle time (four times the period of the elastic energy); the latter period is four times the fundamental cycle time. This almost periodicity is detectable by examining the phase plane diagram of the outer (fourth) link. Over a short period of time, every other complete cycle is the same within the resolution available from graphic representation. (This behavior is observed in the phase plane diagrams for the other two mobile links as well.) There is a slow drift, however, so that cycles separated by longer times are not identical.

I have calculated the behavior of this case for 65,536 time steps, corresponding to a dimensionless time of 2791. Figures 2(*a*)-(*c*) show the phase plane diagrams for link four for the first two cycles, the middle two cycles, and the last two complete cycles. Family resemblances are obvious. There is evidence for a very long period oscillation converting the left-right asymmetry in the first pair of figures to its mirror image. This is to be expected from symmetry.

The period in the second window is four times the basic cycle time. Overlapping successive cycles show duplication at every fourth cycle. As in the doubled period case, there is a gradual shift of the overall asymmetry, presumably resulting in a very long period modulation or oscillation. The modulation period is shorter and the base period longer than those of the first window. This makes it more difficult to locate the window precisely. I've examined the range of f_H from 0.7 to 0.72. The neighborhood of 0.704 is clearly correct, but carefully examination of phase plane diagrams from 0.7030 to 0.7047 at intervals of 0.0001 does not allow a clear choice to be made. This is in distinct contrast to the first window, where overlapping cycles are clear. I've taken $f_h = 0.7043$ as typical. (Considerations of space prevent my illustrating this part of the discussion.)

I have found the first window of periodicity for both other types of initial loading. For the moment loading, it appears at $e = 0.0138$. The moment start-up case shows the difference between examining the phase plane and the bulk energy. The curves of elastic energy versus time are not smooth, although they appear periodic. There is an asymmetry between left going and right going half cycles, but there is no indication of period doubling. The beam bending case (fixed f_H) has a very smooth, apparently periodic, elastic energy versus time plot. The detailed phase planes for moment start-up are very different from the beam bending case, but the period doubling behavior is identical. There is an asymmetry that shifts on a long time scale. I have not looked for the next period doubling in this case, in part because the phase planes are sufficiently complex that the search, conducting using human pattern recognition, is quite difficult. Period doubling for the buckling load appears in a window at $f_B = 0.2742$. The plot of elastic energy versus time is neither as smooth as the beam bending case nor as rough as the moment case, although it does exhibit the left-right asymmetry characteristic of the latter. Again I have not looked for the second window.

4 Discussion

The most dramatic behavior of the four-segment beam, and probably of the continuous beam as well, is the appearance of windows of near periodicity. The existence of windows is independent of the *nature* of the initial condition, although extremely sensitive to its *magnitude* in each case explored. There does not seem to be any unifying parameter for the different types of loading—neither energy nor tip offset. The initial energies for the three different cases are 0.0220, 0.0138, and 0.0211. That for the second window is much higher: 0.1229. The zero offsets for the three cases are $x = 0.33$, 0.24, and 0.32, respectively.

It is tempting to identify the windows of periodicity with windows of periodicity in the case of classical chaotic behavior, and the apparent repeated doubling of the period with respect to the fundamental cycle time with the period doubling route to chaos. I mention these analogies here only because they leap to the eye. Further work is needed.

The windows of periodicity have occupied most of the attention in this paper. There is no room for detailed discussion of the spikes and their correlation with snap through. I have looked at this question in a preliminary way. The four-segment beam shows less contrast than the 20-segment beam for comparable energy levels. There is a gradual concentration of radial force as the magnitude of the initial condition increases. Figure 3 shows a distinctive case. The initial condition is a constant moment sufficient to bend the beam over on itself, so that the tip starts at the origin. The energy associated with this is $e = 1.2337$, and the resulting radial force contrast is immense. This work will be pursued in a later paper.

References

Antman, S. S., and Kenney, C. S., 1981, "Large, Buckled States on Nonlinearity Elastic Rods Under Torsion, Thrust and Gravity," *Arch. Rat. Mech. Anal.*, Vol. 76, pp. 289–338.

Antman, S. S., and Liu, T. P., 1979, "Travelling Waves in Hyperelastic Rods," *Q. Appl. Math.*, Vol. 36, No. 4, pp. 377–399.

Balas, M. J., 1982, "Trends in Large Space Structure Control: Fondness Hopes, Wildest Dreams," *IEEE Trans. Auto. Control*, Vol. AC-27, No. 3, pp. 522–535.

Caflisch, R. E., and Maddocks, J. H., 1984, "Nonlinear Dynamical Theory of the Elastica," *Proc. Royal Soc. Edinburgh*, Vol. 99A, pp. 1–23.

Cannon, R. H., Jr., and Schmitz, E., 1984, "Initial Experiments on the End-Point Control of a Flexible One-Link Robot," *Intl. J. Robotics Res.*, Vol. 3, No. 3, pp. 62–75.

Daniel, R. W., Irving, M. A., Fraser, A. R., and Lambert, M., 1988, "The Control of Compliant Manipulator Arms," *Robotics Research: The 4th Intl. Symposium*, R. C. Boles and R. Roth, eds., M.I.T. Press, pp. 119–125.

Frisch-Fay, R., 1962, *Flexible Bars*, Butterworths, London.

Gans, R. F., 1989, "On Large Oscillations of an Elastica Pendulum," *Developments in Mechanics: Proceedings of the 21st Midwest Mech. Conf.*, Vol. 15, pp. 221–222.

Meirovich, L., Baruh, H., Montgomery, R. C., and Williams, J. P., 1984, "Nonlinear Natural Control of an Experimental Beam," *J. Guidance Control Dynamics*, Vol. 7, No. 4, pp. 437–442.

Moon, F. C., 1987, *Chaotic Vibrations: An Introduction for Applied Scientists and Engineers*, John Wiley and Sons, New York.

Press, W. H., Flannery, B. P., Teukolsky, S. A., and Vetterling, W. T., 1986, *Numerical Recipes: The Art of Scientific Computing*, Cambridge Univ. Press, Sec. 15.2, 16.3.

Schaechter, D. B., 1981, "Optimal Local Control of Flexible Structures," *J. Guidance Control*, Vol. 4, No. 1, pp. 22–26.

Schaechter, D. B., 1982, "Hardware Demonstration of Flexible Beam Control," *J. Guidance Control Dynamics*, Vol. 5, No. 1, pp. 48–53.

Simo, J. C., and Vu-Quoc, L., 1986a, "On the Dynamics of Flexible Beams Under Large Overall Motions: Part 1—The Plane Case," ASME Journal of Applied Mechanics, Vol. 53, pp. 849–854.

Simo, J. C., and Vu-Quoc, L., 1986b, "On the Dynamics of Flexible Beams Under Large Overall Motions: Part 2—The Plane Case," ASME Journal of Applied Mechanics, Vol. 53, pp. 855–863.

Singh, S. N., and Schy, A. A., 1986, "Elastic Robot Control: Nonlinear Inversion and Linear Stabilization," *IEEE Trans. Aerospace Electronic Sys.*, Vol. AES-22, No. 4, pp. 340–347.

Snyder, J. M., and Wilson, J. F., 1990, "Dynamics of the Elastica With End Mass and Follower Loading," ASME Journal of Applied Mechanics, Vol. 57, No. 1, pp. 203–208.

Tse, F. S., Morse, I. E., and Hinkle, R. T., *Mechanical Vibrations: Theory and Applications*, Allyn and Bacon, Boston, pp. 262 ff.

M. G. Satish
Associate Professor.

J. Zhu
Research Associate.

Department of Civil Engineering,
Technical University of Nova Scotia,
Halifax, Nova Scotia B3J 2X4, Canada

Flow Resistance and Mass Transfer in Slow Non-Newtonian Flow Through Multiparticle Systems

Finite difference solutions for a power-law fluid flow through an assemblage of solid particles at low Reynolds numbers are obtained using both the free-surface cell model and the zero-vorticity cell model. It is shown that, unlike in the case of power-law fluid flow past a single solid sphere, the flow drag decreases with decrease of flow behavior index, and that the degree of this reduction is more significant at low voidage. The results from this study are found to be in good agreement with the approximate solutions at slight pseudoplastic anomaly and the available experimental data. The results are presented in closed form and compare favorably with the variational bounds and the modified Blake-Kozeny equations. Numerical results show that a decrease in the flow behavior index leads to a slight increase in the mass transfer rate for an assemblage of solid spheres, but this increase is found to be small compared with that for a single solid sphere.

1 Introduction

Slow non-Newtonian flow past an assemblage of solid spheres represents an idealization of many industrially important processes. Examples of such flows include the flow of crude oil through porous rock, the flow of polymer solutions through sand and sandstone in tertiary oil recovery, the filtration of polymer solutions and flow of polymer solutions and melts through granular beds in catalytic polymerization processes.

Several attempts have been made for modeling flow past an assemblage of spherical particles. The first approach is the classical capillary model to study the porous structure and is used to develop a modified Blake-Kozeny equation. Experimental data on pressure drop in fixed and fluidized beds have been correlated using the capillary model by a number of investigators (Christopher and Middleman, 1965; Gaitonde and Middleman, 1967; Gregory and Griskey, 1967; Marshall and Metzner, 1967; Yu et al., 1968; Siskovic et al., 1971; Kemblowski and Mertl, 1974; Mishra et al., 1975; Brea et al., 1976, Park et al., 1976; Kemblowski and Michniewicz, 1979). Only a few theoretical studies of non-Newtonian fluid flow through multiparticle systems have been attempted so far. There is a definite need for studies related to obtaining precise information on the local velocity distributions around solid spheres in an assembly, in order to predict mass transfer in fixed and fluidized beds.

The second approach to modeling flow through multiparticle systems is by the use of the cell model. According to this model, each particle, assumed to be uniformly spaced in the assemblage, is enveloped by a spherical fluid cell which represents the interparticle interactions. The radius of this hypothetical surface is related to the voidage of the assemblage considered. In the free-surface cell model of Happel (1958), the shear stress vanishes on the cell surface. Kuwabara (1959) has proposed a zero-vorticity cell model in which a zero vorticity is imposed on the hypothetical surface. For Newtonian fluids, the cell model has been proved to be a simple and excellent model for the multiparticle system, especially in the case of packed beds. Cell model theory provides theoretical support for the validity of Darcy's law. It not only demonstrates the simple linear relationship between the flow rate and the pressure drop observed first by Darcy, but also gives numerical values for the proportionality coefficient which is very close to the experimental value.

The free-surface cell model has been extended to power-law fluids and to Ellis fluid model by Mohan and Raghuraman (1976a, 1976b) and to Carreau fluid model by Chhabra and Raman (1984). They obtained upper and lower bounds on the flow resistance for an assemblage of solid spheres by using a combination of Happel's free-surface cell model and the variational principles. Kawase and Ulbrecht (1981) have obtained an approximate solution to the equations of motion for power-law flow through an assemblage of solid spheres under the assumption that deviation from Newtonian flow behavior was very small. The cell models have been used to investigate the weakly elastic effects on the flow resistance of viscoelastic fluids through packed beds (Zhu, 1990; Zhu and Satish, 1991a).

Contributed by the Applied Mechanics Division of The American Society of Mechanical Engineers for presentation at the 1992 Applied Mechanics and Materials Meeting, Tempe, AZ, Apr. 28–May 1, 1992.

Discussion on this paper should be addressed to the Technical Editor, Prof. Leon M. Keer, The Technological Institute, Northwestern University, Evanston, IL 60208, and will be accepted until four months after publication of the paper itself in the Journal of Applied Mechanics. Manuscript received by the ASME Applied Mechanics Division, May 14, 1991; final revision, Dec. 11, 1991. Associate Editor: R. M. Bowen.

Paper No.92-APM-34.

In the present study, the equations of motion are solved using finite difference method by applying Happel's free surface cell model and/or Kuwabara's zero-vorticity cell model. In this work, the numerical solutions for the pressure drop and mass-transfer coefficient are obtained and then compared with the solutions based on the variational principles, approximate analytical solutions, semi-empirical model obtained by extending the Blake-Kozeny equation and with the available experimental findings.

2 Statement of the Problem and Numerical Implementation

It is assumed that the rheological behavior of the fluids can be represented by a power-law model:

$$\tau_{ij}=2K(2\Pi)^{(n-1)/2}D_{ij} \tag{1}$$

where τ_{ij} is the deviatotic stress tensor, D_{ij} is the rate of deformation tensor, K is power-law fluid consistency index, n is power-law fluid behavior index, and the second invariant of the rate of deformation tensor, Π, is given by:

$$\Pi=D_{rr}^2+D_{\theta\theta}^2+D_{\phi\phi}^2+2D_{r\theta}^2. \tag{2}$$

The power-law model provides the simplest representation of shear thinning behavior but its inability to predict a constant viscosity in the limit of low deformation rate raises doubts about its suitability for describing creeping flow. The power-law model is physically correct at high shear rates. The shear rates in cell model are usually high enough, especially in the case of low voidage, so that this model could be used to characterize the shear thinning behavior of the fluids (Satish and Zhu, 1991).

The following nondimensional variables are introduced such that:

$$D_{ij}^*=\frac{D_{ij}}{(V_0/R)}, \qquad \Pi^*=\frac{\Pi}{(V_0/R)^2}$$

$$\tau_{ij}^*=\frac{\tau_{ij}}{\mathrm{K}(\mathrm{V}_0/\mathrm{R})^n}, \qquad p^*=\frac{p-p_0}{K(V_0/R)^n}$$

$$v_i^*=\frac{v_i}{V_0}, \qquad \xi=\frac{r}{R}, \qquad \Psi^*=\frac{\Psi}{V_0R^2} \tag{3}$$

where V_0 is the superficial velocity and R is the radius of sphere particle.

The stream function Ψ^* is defined such that:

$$v_\xi^*=-\frac{1}{\xi^2\sin\theta}\frac{\partial\Psi^*}{\partial\theta}, \quad v_\theta^*=\frac{1}{\xi\sin\theta}\frac{\partial\Psi^*}{\partial\xi} \tag{4}$$

where v_ξ^* and v_θ^* are dimensionless radial and azimuthal velocity components, respectively. Eliminating the pressure terms in the equations of motion and introducing the vorticity ω^* in the equations, we obtain the following governing equations:

$$E^{*2}\Psi^*=\omega^*\xi\sin\theta \tag{5}$$

$$(2\Pi^*)^{(n-1)/2}E^{*2}(\omega^*\xi\sin\theta) + (n-1)(2\Pi^*)^{(n-3)/2}\left[\frac{\partial\Pi^*}{\partial\xi}\frac{\partial}{\partial\xi}(\omega^*\xi\sin\theta) + \frac{\partial\Pi^*}{\partial\theta}\frac{1}{\xi^2}\frac{\partial}{\partial\theta}(\omega^*\xi\sin\theta)\right]=2(1-n)F(\xi,\theta)\sin\theta \tag{6}$$

where

$$E^{*2}=\frac{\partial^2}{\partial\xi^2}+\frac{\sin\theta}{\xi^2}\frac{\partial}{\partial\theta}\left(\frac{1}{\sin\theta}\frac{\partial}{\partial\theta}\right) \tag{7}$$

$$F(\xi,\theta)=\frac{\partial}{\partial\xi}\left[\xi D_{\xi\theta}^*(2\Pi^*)^{(n-3)/2}\frac{\partial\Pi^*}{\partial\xi}+D_{\theta\theta}^*(2\Pi^*)^{(n-3)/2}\frac{\partial\Pi^*}{\partial\theta}\right] - \frac{\partial}{\partial\theta}\left[D_{\xi\xi}^*(2\Pi^*)^{(n-3)/2}\frac{\partial\Pi^*}{\partial\xi}+\frac{D_{\xi\theta}^*}{\xi}(2\Pi^*)^{(n-3)/2}\frac{\partial\Pi^*}{\partial\theta}\right]. \tag{8}$$

The boundary conditions on the solid sphere surface are specified as follows:

$$\text{at } \xi=1, \qquad v_\xi^*=v_\theta^*=0 \tag{9a}$$

and on the outer sphere surface, at $\xi=s$:

$$v_\xi^*=\cos\theta \tag{9b}$$

$$D_{\xi\theta}^*=0. \tag{9c}$$

Kuwabara's zero-vorticity cell model (Kuwabara 1959) assumes that the vorticity is equal to zero on the imaginary spherical surface. In this model, the following boundary condition is used instead of Eq. (9c).

$$\omega^*=0 \qquad \text{at } \xi=s \tag{9d}$$

where s is the dimensionless radius of the cell related to the voidage of the multiparticle assemblage by the expression:

$$s=\frac{R_1}{R}=(1-\epsilon)^{1/3}. \tag{10}$$

In Eq. (10), R_1 is the radius of the hypothetical fluid envelope and ϵ is the bed voidage.

When solving Eqs. (5) and (6), boundary conditions are required that specify Ψ^* and ω^*.

Along the axis of symmetry,

$$\theta=0^\circ \text{ and } \theta=180^\circ, \quad \Psi^*=0, \quad \omega^*=0. \tag{11}$$

On the sphere surface,

$$\xi=1, \quad \Psi^*=0, \quad \omega^*=\frac{E^{*2}\Psi^*}{\sin\theta}. \tag{12}$$

On the outer sphere surface,

$$\xi=s, \quad \Psi^*=-\frac{1}{2}\xi^2\sin^2\theta \tag{13}$$

$$\omega^*=2(v_\theta^*+\sin\theta)/s \quad \text{(for free-surface cell model)} \tag{14a}$$

$$\omega^*=0 \quad \text{(for zero-vorticity cell model).} \tag{14b}$$

To obtain numerical solutions of the governing Eqs. (5) and (6), the finite difference technique was used. A small step size was used near the sphere since the stream function and vorticity vary very rapidly and a relatively large step size was found to be adequate far from the surface. This was achieved by using equal intervals in $z(\xi=e^Z)$ in Eqs. (5) and (6). The solution consists of the stream function and the vorticity fields. Central space differences were used and resulting finite difference equations were solved using the successive over-relaxation method (SOR). In order to verify the validity of the present numerical study, the numerical results were compared with the analytical solutions of their Newtonian flow counterpart for all the voidages considered. It was found that the stream function was in agreement with analytical solution within 0.01 percent and vorticity was within 0.1 percent and drag coefficient was satisfied within 1–2 percent.

3 Results and Discussion

3.1 Flow Drag. The surface pressure is calculated using the following relation:

$$p_s^*(\theta)=p_1^*+\int_0^\theta(2\Pi^*)^{(n-1)/2}\left[\frac{\partial\omega^*}{\partial z}+\omega^*\left(1+\frac{n-1}{2\Pi^*}\frac{\partial\Pi^*}{\partial z}\right)\right]\Bigg|_{z=0}d\theta \tag{15}$$

where

$$p_1^*=2\int_0^{1ns}(2\Pi^*)^{(n-1)/2}\left[\frac{\partial\omega^*}{\partial\theta}-\frac{(n-1)D_{\xi\xi}^*}{2\Pi^*}\frac{\partial\Pi^*}{\partial z}\right]\Bigg|_{\theta=0}dz. \tag{16}$$

The flow drag on the solid sphere is given as:

$$F_D=2\pi R^2\left[\int_0^\pi(-p)_{r=R}\cos\theta\sin\theta\,d\theta-\int_0^\pi(\tau_{r\theta})_{r=R}=\sin^2\theta d\theta\right] =2\pi R^2K(V_0/R)^nD_0 \tag{17}$$

Table 1 Y_D as function of ϵ and n

ϵ \ Y_D \ n	n = 0.5		n = 0.6		n = 0.7		n = 0.8		n = 0.9		n = 1.0	
	Free Surface	Zero Vorticity	Free Surface	Zero Vorticity	Free Surface	Zero Vorticity	Free Surface	Zero Vorticity	Free Surface	Zero Vorticity	Free Surface	Zero Vorticity
0.4	10.40	14.45	15.82	21.06	24.07	31.08	36.65	46.01	55.75	68.28	84.92	101.65
0.5	6.26	8.65	9.00	12.15	12.91	16.97	18.48	23.80	26.45	33.34	37.89	46.77
0.6	4.12	5.77	5.61	7.67	7.63	10.18	10.34	13.53	13.89	18.00	18.92	23.91
0.7	2.87	4.04	3.72	5.07	4.81	6.42	6.18	8.13	7.93	10.28	10.15	12.97
0.8	2.09	2.87	2.57	3.44	3.16	4.15	3.85	4.99	4.68	6.00	5.66	7.18
0.9	1.59	2.04	1.84	2.32	2.11	2.65	2.42	3.00	2.76	3.40	3.11	3.78
0.99	1.32	1.45	1.38	1.50	1.42	1.55	1.46	1.59	1.48	1.60	1.48	1.60

where

$$D_0 = -\int_0^{\pi} p_s^*(\theta)\cos\theta\sin\theta d\theta - \int_0^{\pi} (\tau_{r\theta}^*)_{z=0}\sin^2\theta d\theta. \quad (18)$$

The drag coefficient for non-Newtonian fluid behavior is therefore

$$Y_D = \frac{C_D}{24/\mathrm{Re}'} = \frac{2^n}{6} D_0 \quad (19)$$

where C_D is given as

$$C_D = \frac{F_D}{\frac{1}{2}\rho V_0^2 \pi R^2} \quad (20)$$

and Re′ is Reynolds number for power-law fluid defined as

$$\mathrm{Re}' = \frac{\rho V_0^{2-n}(2R)^n}{K}. \quad (21)$$

In (20) and (21) ρ is the density of fluids.

From the force equilibrium on the cell, we can obtain the pressure drop as

$$\frac{\Delta p}{L} = \frac{F_D}{\frac{4}{3}\pi R_1^3} = \frac{3KV_0^n D_0(1-\epsilon)}{2R^{1+n}}. \quad (22)$$

The computed results for Y_D based both on the free-surface cell model and on the zero-vorticity cell model are given in Table 1 for various values of the bed voidage ϵ and the flow behavior index n. It can be seen that the zero-vorticity cell model predicts slightly higher drag coefficient than the analysis based on the free-surface cell model. This occurs because the zero-vorticity cell model yields a large energy dissipation in the envelope than that due to the particle alone, owing to the additional work done by the stresses at the outer boundary. The work is done on the surroundings, which induces extra dissipation of energy. Figure 1 shows Y_D as a function of n for various values of ϵ for free-surface cell model simulation. As may be expected, the shear thinning behavior results in a decrease in drag coefficient. The reason is mainly because smaller porosity causes stronger shear and hence stronger reduction in the flow drag. The degree of reduction becomes weaker as the voidage becomes larger.

The theoretical predictions based on the variational principle presented by Mohan and Raghuraman (1976a) and the approximate solutions of Kawase and Ulbrecht (1981) are also shown plotted in Fig. 1. Mohan and Raghuraman (1976a) have obtained bounds on the flow drag by the use of variational principles and the arithmetic averages of their predictions are shown in Fig. 1. It can be seen that the results from the present analysis fall within the variational bounds of Mohan and Raghuraman's (1976a) predictions. As may be expected, when the flow behavior index n is far from 1, (i.e., $|n - 1| = O(1)$), discrepancy between the present predictions and the approximate solutions of Kawase and Ulbrecht (1981) is evident. It may be noted that Kawase and Ulbrecht (1981) have assumed that the deviation from Newtonian flow behavior is slight (i.e., $|n - 1| \ll 1$). The bigger the value of $|n - 1|$, the larger will be the discrepancy between the two solutions. Further, we may infer that the approximate solutions of Kawase and Ulbrecht (1981) are accurate for predicting the flow drag of non-Newtonian fluids when the shear thinning behavior of fluids is slight and overestimate the flow drag coefficient as $|n - 1|$ increases. It can also be seen that the plot of log (Y_D) is almost linear with the flow behavior index n. This result implies that non-Newtonian flow behavior has little influence on the flow field inside the cell and the drag reduction is mainly caused by the reduction in viscosity due to the shear thinning behavior. A similar phenomenon has been found in the case of swarm of bubbles (Zhu and Satish, 1991b).

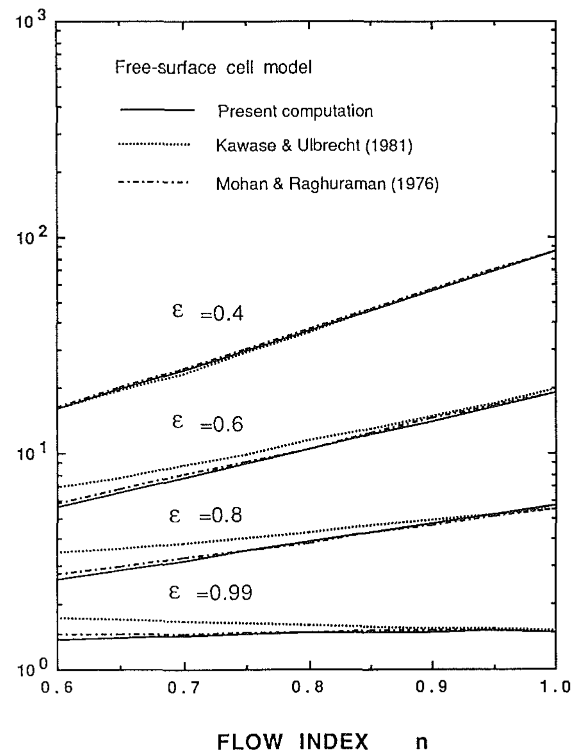

Fig. 1 Effect of non-Newtonian flow behavior index on the drag coefficient

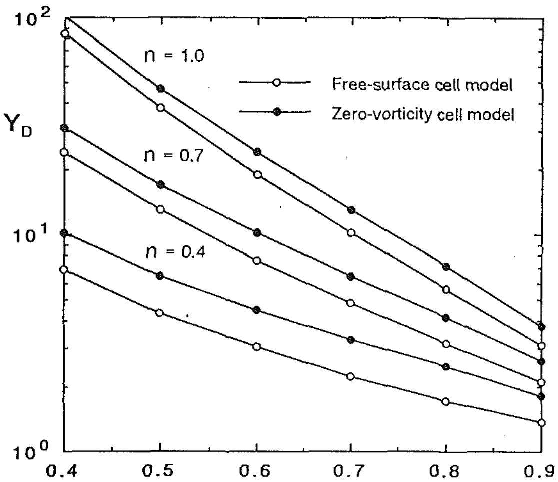

Fig. 2 Effect of bed voidage on the drag coefficient

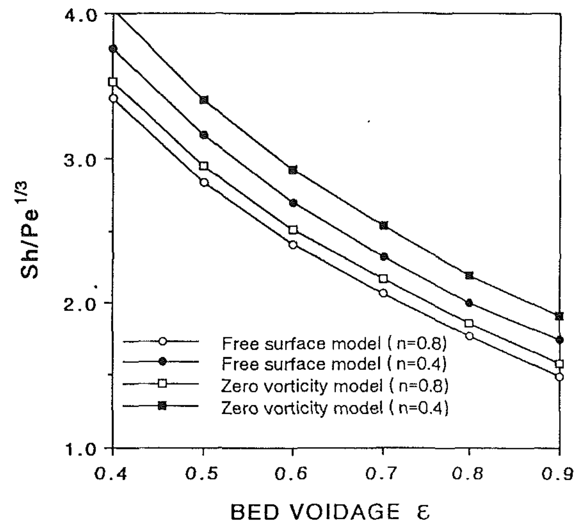

Fig. 4 Effect of bed voidage on the mass transfer rate

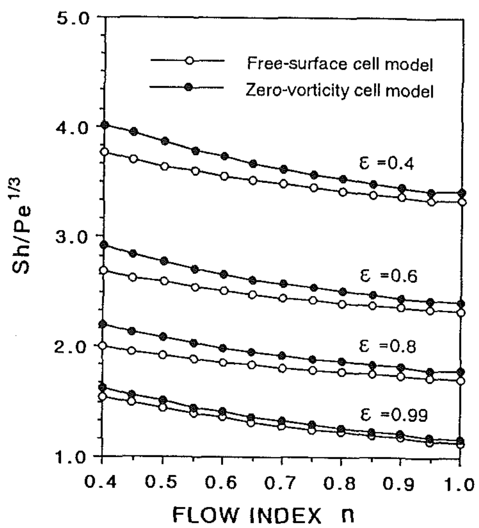

Fig. 3 Effect of non-Newtonian flow behavior index on the mass transfer rate

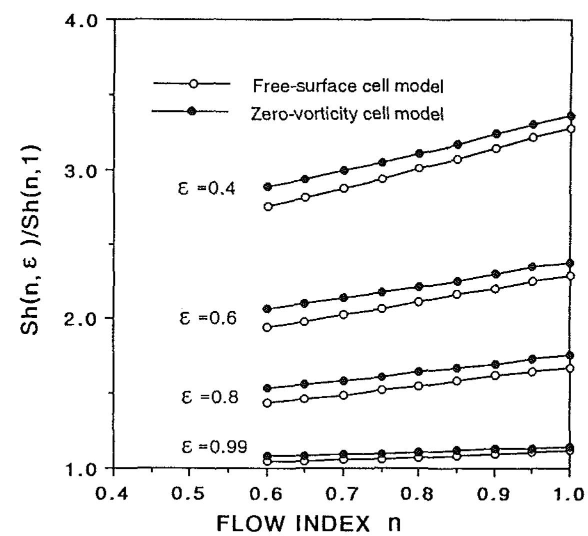

Fig. 5 Effect of non-Newtonian flow behavior index on the normalized mass transfer rate

Figure 2 shows Y_D as a function of voidage ϵ at different values of flow behavior index n. It can be seen that the drag coefficient decreases as the bed voidage increases and the degree of this reduction becomes less significant as the pseudoplastic anomaly of fluids becomes stronger. This result indicates that the shear thinning behavior of fluids results in a reduction of the voidage effect on the drag coefficient.

3.2 Mass Transfer. The present study provides the precise information on the local velocity distributions around the solid sphere, which could be used to predict the mass transfer rate. A theoretical prediction of the mass-transfer coefficient around a solid sphere can be obtained by using the thin concentration boundary layer approximation of Lochiel and Calderbank (1964)

$$Sh/Pe^{1/3} = 0.641 \left\{ \int_0^\pi (-v_\theta^{*\prime})_{\xi=1} \sin^{3/2}\theta d\theta \right\}^{2/3} \tag{23}$$

where Sh denotes Sherwood number defined as $k(2R)/D$ and Pe is the Peclet number defined as $V_0(2R)/D$. In these definitions, k is the mass transfer rate and D is the molecular diffusivity. $(v_\theta^{*\prime})_{\xi=1}$ is the gradient of azimuthal velocity component on the sphere surface and can be evaluated as follows:

$$(v_\theta^{*\prime})_{\xi=1} = \frac{\partial v_\theta^*}{\partial \xi}\bigg|_{\xi=1} = \omega^*|_{z=0}. \tag{24}$$

Equation (23) together with (24) gives the relationship between the rate of mass transfer and the flow behavior index n as well as the bed voidage ϵ. The use of this equation is restricted to the regime of high Peclet number and low Reynolds number.

Numerical predictions of the Sherwood number, Sh, calculated from Eq. (23) are plotted in Fig. 3 as functions of flow behavior index n at different values of bed voidage ϵ and in Fig. 4 as functions of bed voidage ϵ at different values of the flow behavior index n. It is found that the zero-vorticity cell model predicts slightly higher mass transfer rate than the free-surface cell model. It can be seen that the value of the Sherwood number for multiparticle systems increases slightly with the decrease in the value of the flow behavior index. However, this increase is small compared with that for a single solid sphere and thus the ratio $Sh(n, \epsilon)/Sh(n, \epsilon = 1)$ decreases with

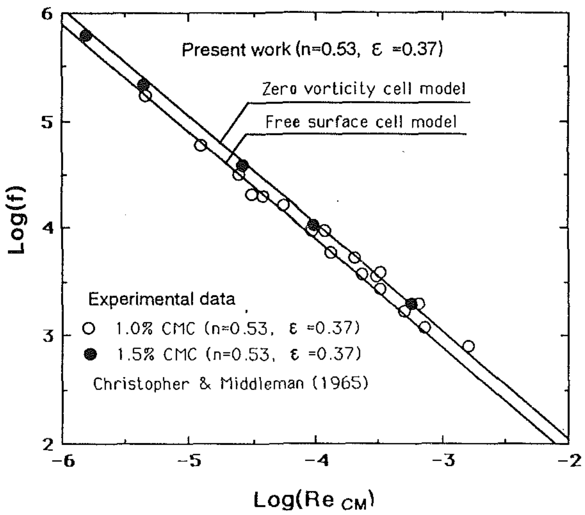

Fig. 6(a) $n = 0.53, \epsilon = 0.37$

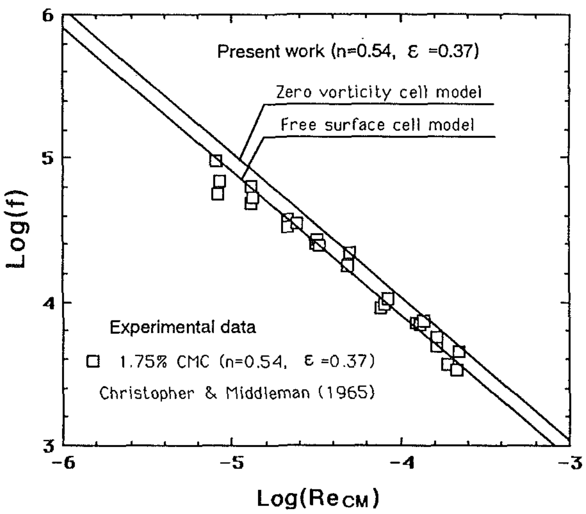

Fig. 6(b) $n = 0.54, \epsilon = 0.37$

Fig. 6 Comparison between present predictions and experimental data of Christopher and Middleman (1965)

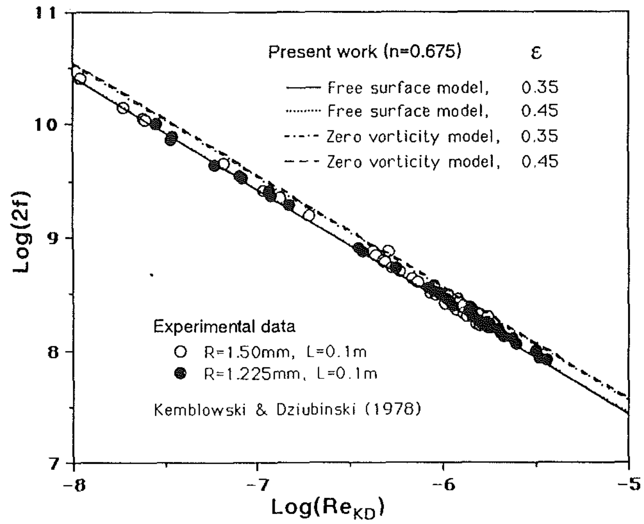

Fig. 7 Comparison between present predictions and experimental data of Kemblowski and Dziubinski (1978)

the decrease of n, as shown in Fig. 5. It can also be seen that an increase in the bed voidage causes a decrease in the mass transfer rate.

4 Comparison with Experimental Results

It is convenient to express the drag coefficient in terms of more familiar quantities, namely friction factor f and Reynolds number Re′. The friction factor f is defined as

$$f=\frac{\Delta p}{L}\,\frac{2R\epsilon^3}{\rho V_0^2(1-\epsilon)}\,. \tag{25}$$

Combining Eq. (25) with Eq. (22), we can obtain

$$f\,\mathrm{Re}'=18\epsilon^3 Y_D. \tag{26}$$

Christopher and Middleman (1965) have defined the modified Reynolds number Re_{CM} in developing the modified Blake-Kozeny equation as follows:

$$\mathrm{Re}_{CM}=\frac{2R\rho V_0^{2-n}}{150H(1-\epsilon)} \tag{27}$$

where H is a factor which accounts for the non-Newtonian behavior, given as

$$H=\frac{K}{12}\left(9+\frac{3}{n}\right)^n\left(\frac{2R\epsilon^2}{1-\epsilon}\right)^{(1-n)} \tag{28}$$

After simplification, it follows that

$$f\,\mathrm{Re}_{CM}=\frac{36}{25\left(9+\dfrac{3}{n}\right)^n}\,\frac{\epsilon^{1+2n}}{(1-\epsilon)^n}\,Y_D. \tag{29}$$

Substituting Y_D from Eq. (19) into Eq. (29), the relationships between f and Re_{CM} may be easily established. These relationships are compared in Figs. 6(a) and 6(b) with the experimental data obtained by Christopher and Middleman (1965) using a fixed bed of voidage $\epsilon = 0.37$ and an aqueous solution of carboxymethylcellulose (CMC).

Kemblowski and Dziubinski (1978) have defined the Reynolds number as follows:

$$\mathrm{Re}_{KD}=\frac{2R\rho V_0^{2-n}}{H(1-\epsilon)}=150\ \mathrm{Re}_{CM}. \tag{30}$$

The experimental results of Kemblowski and Dziubinski (1978), for the flow of molten polypropylene through packed beds of steel spheres of diameter 2.45 mm and 3.0 mm, are compared with the present model in Fig. 7. The bed voidages were not given in their paper. For randomly packed bed of uniform spheres, the voidage was estimated to be around 0.4. In Fig. 7, both free-surface cell model and zero-vorticity cell model predictions for $\epsilon = 0.35$ and $\epsilon = 0.45$ are plotted. It can be seen that cell model predictions show little voidage dependence on the friction factor-Reynolds number relationship. From Figs. 6 and 7, it can be seen that the cell model successfully predicts the friction factor for the flow of power-law fluids through multiparticle systems at low Reynolds numbers.

Now, one can compare the present computational results with several modified Blake-Kozeny equations which are semi-empirical and successfully used in predicting the flow drag in experimental data correlation. The modified Blake-Kozeny equation using the "capillary model" was given by Christopher and Middleman (1965)

$$f\,\mathrm{Re}'/(1-\epsilon)=G_1(n,\epsilon) \tag{31}$$

where

$$G_1(n,\epsilon)=12.5\left(9+\frac{3}{n}\right)^n(1-\epsilon)^{n-1}\epsilon^{2(1-n)}. \tag{32}$$

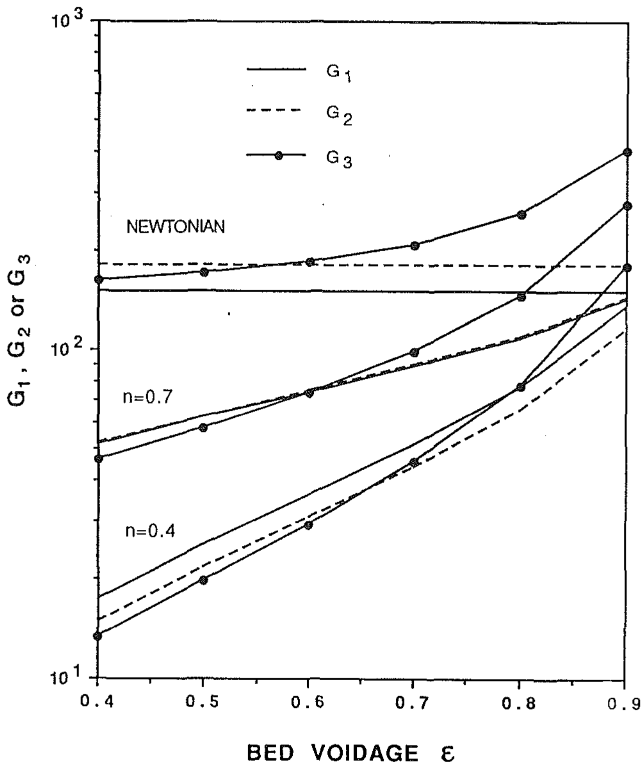

Fig. 8 Correlations for the pressure drop of power-law fluid flowing through multiparticle systems

The value of Eq. (31) in correlating the experimental data, has already been established by several authors (Christopher and Middleman, 1965; Gaitonde and Middleman, 1967; Marshall and Metzner, 1967; Siskovic et al., 1971; Yu et al., 1968, Kemblowski and Mertl, 1974; Mishra et al., 1975).

Kemblowski and Michniewicz (1979) have proposed an improved relation, which was shown to be more rigorous in correlating with the experimental data. It can be written as:

$$f\,\mathrm{Re}'/(1-\epsilon)=G_2(n,\epsilon) \tag{33}$$

where

$$G_2(n,\epsilon)=180(15\sqrt{2})^{n-1}\left(\frac{3n+1}{4n}\right)^n(1-\epsilon)^{n-1}\epsilon^{2(1-n)}. \tag{34}$$

Equation (26) from the present analysis may be written as

$$f\,\mathrm{Re}'/(1-\epsilon)=G_3(n,\epsilon) \tag{35}$$

where

$$G_3(n,\epsilon)=\frac{18\epsilon^3}{(1-\epsilon)}\,Y_D. \tag{36}$$

In Fig. 8, comparisons of G_1, G_2, and G_3 as functions of bed voidage ϵ are shown. When the bed voidage is less than 0.7, it may be seen that the cell model's prediction shows a fair agreement with Christopher and Middleman's equation and a closer agreement with Kemblowski and Michniewicz's relationship. This is consistent with the fact that the cell model predicts flow drag with reasonable success in the case of $\epsilon<0.7$ for Newtonian fluids. The cell model's prediction overestimates the flow drag in fluidized beds whose porosities are higher than 0.7. This perhaps corresponds to the special condition which minimizes the particle-agglomeration effects since agglomeration effects result in reduced values for the flow drag. Hence, it is observed that the cell model can be applied to predict the flow resistance of both the Newtonian fluids and the power-law fluids with equal success.

5 Conclusions

Flow problems of power-law fluid through multiparticle systems under the creeping flow conditions are solved by finite difference method. The results of the present study indicate that the cell model is an excellent alternative approach to the capillary model in analyzing the creeping flow of non-Newtonian fluids in a particle assemblage. A definite advantage of the cell model is that it can predict the precise local velocity information around solid spheres in the assemblage which can be used to obtain mass transfer in packed beds.

The present analysis indicates that the zero-vorticity cell model predicts slightly higher drag coefficient and mass transfer rate than the free-surface cell model. It is also predicted that the reduction in the drag coefficient due to the pseudoplasticity of the fluids is more significant for lower voidage assemblages and that the shear thinning behavior of fluids results in a reduction of the voidage effect on the drag coefficient. The predicted reduction of the friction factor due to the shear thinning behavior of the fluids is in fair agreement with (a) the experimental findings, (b) the available theoretical solutions based on the variational principle, (c) the approximate analytical solutions in slight non-Newtonian condition, and (d) the most reliable semi-empirical correlations for the flow resistance in fixed and fluidized beds.

In the present study, the mass transfer rate for multiparticle systems have also been computed. It is shown that the mass transfer rate for the multiparticle systems increases due to the pseudoplastic anomaly of the fluids, but the enhancement in mass transfer rate is small compared with the case of a single solid sphere.

Acknowledgment

The authors are grateful to the referees for their reviews and invaluable comments which have contributed to the improvement of this paper. The financial support from NSERC Grant No. OGP0036340 is kindly acknowledged.

References

Brea, F. M., Edwards, M. F., and Wilkinson, W. L., 1976, "The Flow of Non-Newtonian Slurries Through Fixed and Fluidized Beds," *Chem. Eng. Sci.*, Vol. 31, pp. 329–336.

Chhabra, R. P., and Raghuraman, J., 1984, "Slow Non-Newtonian Flow Past an Assemblage of Rigid Spheres," *Chem. Eng. Commun.*, Vol. 27, pp. 23–46.

Christopher, R. H., and Middleman, S., 1965, "Power-law Flow Through a Packed Tube," *I&EC. Fundls.*, Vol. 4, pp. 422–426.

Gaitonde, N. Y., and Middleman, S., 1967, "Flow of Viscoelastic Fluids Through Porous Media," *I&EC. Fundls.*, Vol. 6, pp. 145–147.

Gregory, D. R., and Griskey, R. G., 1967, "Flow of Molten Polymers Through Porous Media," *AIChE. J.*, Vol. 13, pp. 122–125.

Happel, J., 1958, "Viscous Flow in Multiparticle System: Slow Motion of Fluids Relative to Beds of Spherical Particles," *AIChE. J.*, Vol. 4, pp. 197–201.

Kawase, Y., and Ulbrecht, J. J., 1981, "Drag and Mass Transfer in Non-Newtonian Flows Through Multiparticle Systems at Low Reynolds Number," *Chem. Eng. Sci.*, Vol. 36, pp. 1193–1202.

Kemblowski, Z., and Dziubinski, M., 1978, "Resistance to Flow of Molten Polymers Through Granular Beds," *Rheol. Acta*, Vol. 17, pp. 176–187.

Kemblowski, Z., and Mertl, J., 1974, "Pressure Drop During the Flow of Stokesian Fluids Through Granular Beds," *Chem. Eng. Sci.*, Vol. 29, pp. 213–223.

Kemblowski, Z., and Michniewicz, M., 1979, "A New Look at the Laminar Flow of Power Law Fluids Through Granular Beds," *Rheol. Acta*, Vol. 18, pp. 730–739.

Kuwabara, S., 1959, "The Forces Experienced by Randomly Distributed Parallel Circular Cylinders or Spheres in a Viscous Flow at Small Reynolds Numbers," *J. Phys. Soc. Japan*, Vol. 14, pp. 527–532.

Lochiel, A. C., and Calderbank, P. H., 1964, "Mass Transfer in the Continuous Phase Around Axisymmetric Bodies of Revolution," *Chem. Eng. Sci.*, Vol. 19, pp. 471–484.

Marshall, R. J., and Metzner, A. B., 1967, "Flow of Viscoelastic Fluids Through Porous Media," *I&EC. Fundls.*, Vol. 6, pp. 393–400.

Mishra, P., Singh, D., and Mishra, I. M., 1975, "Momentum Transfer to

Newtonian and Non-Newtonian Fluids Flowing Through Packed and Fluidized Beds," *Chem. Eng. Sci.*, Vol. 30, pp. 397-405.

Mohan, V., and Raghuraman, J., 1976a, "A Theoretical Study of Pressure Drop for Non-Newtonian Creeping Flow Past an Assemblage of Spheres," *AIChE. J.*, Vol. 22, pp. 259-264.

Mohan, V., and Raghuraman, J., 1976b, "Bounds on the Drag for Creeping Flow of an Ellis Fluid Past an Assemblage of Spheres," *Int. J. Multiphase Flow*, Vol. 2, pp. 581-589.

Park, H. C., Hawley, M. C., and Blanks, R. F., 1975, "The Flow of Non-Newtonian Solutions Through Packed Beds," *Polym. Eng. Sci.*, Vol. 15, pp. 761-773.

Satish, M. G., and Zhu, J., 1991, "Numerical and Analytical Solutions for Flows of Non-Newtonian Fluids Through Packed Beds," Internal Report CE 91-04, Technical University of Nova Scotia.

Siskovic, N., Gregory, D. R., and Griskey, R. G., 1971, "Viscoelastic Behavior of Molten Polymers in Porous Media," *AIChE. J.*, Vol. 17, pp. 281-285.

Yu, Y. H., Wen, C. Y., and Bailie, R. C., 1968, "Power-Law Fluids Through Multiparticle System," *Can. J. Chem. Eng.*, Vol. 46, pp. 149-154.

Zhu, J., 1990, "On the Flow Resistance of Viscoelastic Fluids Through Packed Beds," *Rheol. Acta*, Vol. 29, pp. 409-415.

Zhu, J., and Satish, M. G., 1991a, "A Theoretical Study of Viscoelastic Creeping Flow Past an Assemblage of Rigid Spheres," submitted for publication.

Zhu, J., and Satish, M. G., 1991b, "Slow Non-Newtonian Flow Past a Swarm of Bubbles," submitted for publication.

Free-Surface Oscillations in a Slowly Draining Tank

Qiao-Nian Zhou[1]
Assoc. Mem. ASME.

W. P. Graebel
Mem. ASME.

Department of Mechanical Engineering
and Applied Mechanics,
The University of Michigan,
Ann Arbor, MI 48109

The initial behavior of a free surface in a draining (filling) circular tank is analyzed using a linearized model. The withdrawal (injection) of fluid damps (enhances) oscillations which either exist before the withdrawal (filling) or are induced by the withdrawal (injection). The initial growth rate of the drainage-initiated free-surface oscillations strongly depends on the initial behavior of the drain rate function. If the drain is turned on gradually, the drainage-initiated free-surface oscillation is weaker compared to the forced one, so there are no drainage-initiated oscillations. However, if the drain is turned on suddenly, the induced oscillatory motion dominates the forced motion. For periodic drainage, the results show that the strongest resonant oscillation occurs when the drainage frequency ω coincides with the first natural frequency of the flow system. All of the nonresonant modes of the oscillations are stable regardless of the initial behavior of the drain rate. If $q(t) = \sin\omega t$, all of the resonant oscillations are stable. In the case when $q(t) = \cos\omega t$, the initial jump in the drainage means that the resonance modes can be either unconditionally unstable, unconditionally stable, or conditionally unstable, depending on the various parameters.

1 Introduction

Recent numerical results (Zhou and Graebel, 1990) show that a jet forms in the center of a free surface in a cylindrical tank when it is slowly drained with a constant drain rate. The strength of the jet appears to depend on the initial height of the free surface. Small initial height h_0 results in a strong jet. For example, the tip of the jet rises for $h_0 = 0.35$, while it moves down with the mean free surface for $h_0 = 1$.

Miles (1962) investigated the effect of the drainage on the free-surface oscillations, and concluded that withdrawal of fluid from a cylindrical tank damps the oscillations on the free surface. His conclusion does not distinguish oscillations which may exist initially from those induced by the drainage. Saad and Oliver (1964) used a linearized model, with inertial terms completely neglected, to study the motion of the free surface in both a circular and a rectangular tank under constant drain rates. Effects of surface tension were included. For zero surface tension, their results concluded that both withdrawal and injection of fluid cause the free surface to oscillate if the drain rate is less than a critical value. The induced free-surface oscillations grow exponentially if fluid flows out of the tank, and are exponentially damped if fluid flows into the tank. If there is no surface tension, their results also concluded that higher-order modes with large wave numbers are nonoscillatory. Their results are thus opposite to that of Miles.

In this paper, a model which includes a linearized inertial term is used to study the unsteady motion of the free surface in a circular draining or filling tank. The modal amplitude functions are obtained using perturbation techniques valid for predicting the long-time behavior of the free-surface motion. Emphasis is on the influence of draining or filling on free-surface oscillations which may exist initially or are initiated by the draining or filling, as well as on the effect of the initial behavior of the drain rate on the oscillation amplitude. The resonant responses of the free surface to a simple-harmonic drainage with various resonant frequencies and their stability are also examined.

The paper begins with the fundamental equations and boundary conditions described in Section 2. In Section 3, two special cases are studied. A summary of the results is presented in Section 4.

2 Basic Equations and the General Solution

We consider an inviscid, incompressible fluid contained in a circular tank of radius R. The top surface of the fluid is open and is stress-free. Surface tension is assumed negligible. A sink of finite radius a is located at the center of the tank bottom. The sink is taken to have a strength $Qq(t)$, where Q is the absolute value of the maximum strength, and $q(t)$ represents the time variation of the sink strength with unity maximum absolute value. If $q(t)$ is negative, fluid is withdrawn from the tank. If $q(t)$ is positive, fluid enters the tank.

Since the fluid is inviscid and incompressible, and the initial

[1]Currently at the Department of Mechanical Engineering, University of Toronto, Toronto, Ontario M5S 1A4, Canada.

Contributed by the Applied Mechanics Division of The American Society of Mechanical Engineers for presentation at the 1992 ASME Summer Mechanics and Materials Meeting, Tempe, AZ, Apr. 28–May 1, 1992.

Discussion on this paper should be addressed to the Technical Editor, Professor Leon M. Keer, The Technological Institute, Northwestern University, Evanston, IL 60208, and will be accepted until four months after final publication of the paper itself in the Journal of Applied Mechanics. Manuscript received by the ASME Applied Mechanics Division, June 13, 1990; final revision, Nov. 12, 1991.

Paper No. 92-APM-24.

state of the flow is assumed free of vorticity, a velocity potential exists. Moreover, we assume that the flow is axisymmetric. We choose the radius R of the tank as the characteristic length, $T = \sqrt{R/g}$ as the characteristic time, and $U = \sqrt{gR}$ as the characteristic velocity. The potential is scaled by RU. In the dimensionless units, the radius of the tank is unity, the sink radius is denoted by a, and $h(t)$ is the mean elevation of the free surface. By continuity, the mean height is given by

$$h(t) = h_0 + \frac{F}{\pi}\int_0^t q(\tau)d\tau, \tag{1}$$

where h_0 is the initial height of the free surface, and F is the Froude number defined by

$$F = \frac{Q}{\sqrt{gR^5}}. \tag{2}$$

The total velocity potential is

$$\phi_{\text{total}}(r,z,t) = \phi(r,z,t) + \dot{h}(t)z \tag{3}$$

where ϕ is the perturbed potential which satisfies the axisymmetric Laplace's equation.

The free-surface elevation is of the form

$$z_f(r,t) = h(t) + \eta(r,t) \tag{4}$$

where η is the perturbed free-surface elevation. In order for the linear assumption to be valid, it is assumed that $|\eta(r,t)|$, $|\nabla\eta|$, and $|\nabla\phi(r,h(t),t)|$ are all small.

The boundary conditions on the tank side wall and the bottom are

$$\frac{\partial\phi}{\partial r}(1,z,t) = \frac{\partial\phi}{\partial r}(0,z,t) = 0 \tag{5}$$

and

$$\frac{\partial\phi}{\partial z}(r,0,t) = \begin{cases} Fq(t)v_o(r) - \dot{h}(t) & 0\le r\le a \\ -\dot{h}(t) & a<r\le 1 \end{cases} \tag{6}$$

where $v_o(r)$ is the dimensionless normal velocity distribution in the sink area which, according to (3), is constrained by

$$\int_0^a rv_o(r)dr = \frac{1}{2\pi}. \tag{7}$$

The linearized free-surface kinematic and dynamic boundary conditions are

$$\frac{\partial\phi}{\partial z} = \frac{\partial\eta}{\partial t} \text{ on } z = h(t), \tag{8}$$

and

$$\frac{\partial\phi}{\partial t} + \dot{h}(t)\frac{\partial\phi}{\partial z} + \eta(r,t) = 0 \text{ on } z = h(t). \tag{9}$$

The initial conditions are taken as expansions of the form

$$\phi(r,h_0,0) = \sum_{m=1}^{\infty}\alpha_m J_0(k_m r), \text{ and } \eta(r,0) = \sum_{m=1}^{\infty}\beta_m J_0(k_m r) \tag{10}$$

where α_m and β_m are known constants once $\phi(r,h_0,0)$ and $\eta(r,0)$ are specified. If the flow starts from rest, then $\alpha_m = \beta_m = 0$.

The potential satisfying (5)–(6) is

$$\phi(r,z,t) = \sum_{m=1}^{\infty} J_0(k_m r)\{FR_m q(t)\sinh(k_m z) + D_m(t)\cosh(k_m z)\}, \tag{11}$$

where k_m is the mth root of the first-order Bessel function, and the R_m are constants given by

$$R_m = 2\int_0^a rv_o(r)J_0(k_m r)dr/[k_m J_0^2(k_m)]. \tag{12}$$

If we define

$$y_m(t) = FR_m q(t)\sinh(k_m h(t)) + D_m(t)\cosh(k_m h(t)), \tag{13}$$

then the perturbed free-surface elevation is, from (9),

$$\eta(r,t) = -\sum_{m=1}^{\infty}\frac{dy_m(t)}{dt}J_0(k_m r), \tag{14}$$

and the perturbed surface potential is

$$\phi(r,h(t),t) = \sum_{m=1}^{\infty} y_m(t)J_0(k_m r). \tag{15}$$

From (8), (9), (11), and (14), we obtain

$$\frac{d^2y_m}{dt^2} + k_m\tanh(k_m h(t))y_m = -F\frac{R_m k_m q(t)}{\cosh(k_m h(t))}. \tag{16a}$$

From (10), (11), (13), and (14), it follows that

$$y_m(0) = \alpha_m, \ \frac{dy_m(0)}{dt} = -\beta_m. \tag{16b}$$

3 The Amplitude Functions for Small Froude Number

The frequency of any oscillation governed by Eq. (16*a*) will not be constant. A general solution of (16*a*) is difficult to obtain even when $q(t)$ is a constant. In the following, we seek perturbation solutions of (16*a*,*b*) based on expansions in F.

Free-surface oscillations can be caused either by initial conditions, or by the draining or filling of the tank. In this section, we study these mechanisms under the assumption of small Froude number F. We examine the dynamic response of the free surface to a power-law withdrawal rate, and also to periodic excitations (e.g., $q(t) = \cos\omega t$ or $\sin\omega t$), including the resonance case when the excitation frequency ω is a multiple of the system's natural frequency.

3.1 Case 1: Power-Law Drainage. We consider first the case where $q(t)$ is of the form

$$q(t) = \pm\left(\frac{t}{t_0}\right)^l, \tag{17}$$

where t_0 is the time duration of interest and l is a non-negative integer. Thus,

$$h(t) = h_0 \pm (\epsilon t)^{l+1}, \text{ where } \epsilon = \left[\frac{F}{\pi(l+1)t_0^l}\right]^{\frac{1}{l+1}}. \tag{18}$$

The plus sign is chosen if the tank is being filled, and the negative sign if the tank is being emptied. Since $\epsilon \ll 1$, it is necessary that $F \ll t_0^l$. This condition can be easily satisfied if, for example, $t_0 \ge 1$.

Equation (16*a*,*b*) can be solved by a multivariable expansion technique. We define two disparate times by

$$t_1 = \int_0^t \sqrt{k_m\tanh(k_m h(\tau))}d\tau, \text{ and } t_2 = \epsilon t. \tag{19}$$

Here, t_1 is the fast time (of the same order as t) and t_2 is the slow time scale. We take the solution in the form

$$y_m(t) = \sum_{n=0}^{\infty}\epsilon^n G_n(t_1,t_2). \tag{20}$$

Substituting (20) into (16*a*,*b*), and using the two-variable perturbation technique, we have

$$\frac{\partial^2 G_k}{\partial t_1^2} + G_k = -\frac{2}{\sqrt{k_m\tanh(k_m h)}}\left[\pm\frac{k_m(l+1)t_2^l}{2\sinh(2k_m h)}\frac{\partial G_{k-1}}{\partial t_1} + \frac{\partial^2 G_{k-1}}{\partial t_1\partial t_2}\right] - (\pm)\frac{(l+1)\pi R_m t_2^l}{\sinh(k_m h)}\delta_{k,1} - \frac{1}{k_m\tanh(k_m h)}\frac{\partial^2 G_{k-2}}{\partial t_2^2} \tag{21a}$$

with

$$G_k(0,0) = \alpha_m \delta_{k,0}, \tag{21b}$$

and

$$\frac{\partial G_k(0,0)}{\partial t_1} = -\frac{1}{\sqrt{k_m \tanh(k_m h_0)}}\left[\frac{\partial G_{k-1}(0,0)}{\partial t_2} + \beta_m \delta_{k,0}\right]. \tag{21c}$$

The solutions of (21a) are then of the form

$$G_n(t_1,t_2) = A_n(t_2)\cos t_1 + B_n(t_2)\sin t_1 + \gamma_n(t_2) \tag{22}$$

where $\gamma_n(t_2)$ are given by the recursion equation

$$\gamma_{n+2}(t_2) = -\frac{1}{k_m \tanh(k_m h)}\frac{d^2\gamma_n(t_2)}{dt_2^2}, \tag{23a}$$

with the starting values

$$\gamma_0(t_2) = 0,\ \gamma_1(t_2) = -(\pm)\frac{(l+1)\pi R_m t_2^l}{\sinh(k_m h)}. \tag{23b}$$

Equations (23a,b) indicate that $\gamma_{2n}(t_2) = 0$ for any integer n. In (22) $A_n(t_2)$, $B_n(t_2)$ are given as

$$A_0(t_2) = \alpha_m C(t_2),\ B_0(t_2) = -\frac{\beta_m C(t_2)}{\sqrt{k_m \tanh(k_m h_0)}}, \tag{24a}$$

$$A_n(t_2) = C(t_2)\left[A_n(0) + \int_0^{t_2}\frac{\ddot{B}_{n-1}(\tau)C(\tau)}{2\sqrt{k_m \tanh(k_m h_0)}}d\tau\right], \tag{24b}$$

$$B_n(t_2) = C(t_2)\left[B_n(0) - \int_0^{t_2}\frac{\ddot{A}_{n-1}(\tau)C(\tau)}{2\sqrt{k_m \tanh(k_m h_0)}}d\tau\right], \tag{24c}$$

where

$$A_n(0) = -\gamma_n(0),\ B_n(0) = -\frac{\dot{A}_{n-1}(0) + \dot{\gamma}_{n-1}(0)}{\sqrt{k_m \tanh(k_m h_0)}},\ n \ge 1, \tag{24d}$$

and

$$C(t_2) = \left[\frac{\tanh(k_m h_0)}{\tanh(k_m h)}\right]^{1/4}. \tag{25}$$

For high order modes ($m \to \infty$), k_m approaches ∞, hence $C(t_2)$ will approach 1. All of the $A_n(t_2)$, $B_n(t_2)$ will approach 0 except A_0, which is constant, and t_1 will approach $\sqrt{k_m \tanh(k_m h_0)}\,t$, with $\gamma_n(t_2)$ approaching 0. Thus, high order modes do not feel the influence of the sink, and are equal to the natural modes of standing cylindrical free surface waves of constant depth h_0. This is because the high order modes have wave lengths which are small compared to the depth, and so the influence of the sink decreases. This conclusion is in disagreement with Saad et al. (1964), who concluded that higher order modes were non-oscillatory. Similarly, for large depths, variation in the depth is not important, and the oscillation is similar to a constant depth case.

The leading order solution $G_0(t_1,t_2)$ depends on the initial disturbances in the flow. If $q(t) = 0$, $h(t)$ would equal its initial value h_0, and $C(t_2) = 1$. Consequently, $G_n(t_1,t_2) = 0$, $n = 1, 2, \cdots$. This solution is precisely that of the natural oscillations of a free surface in a circular tank without drainage. If the flow starts from rest, then $G_0(t_1,t_2) = 0$ since $\alpha_m = \beta_m = 0$. The oscillations in this case are initiated solely by the drainage, and will hereafter be called drainage-initiated oscillations.

Free surface oscillations responding to the initial disturbances are given by

$$\eta(r,t) = \sum_{m=0}^{\infty}\left\{\alpha_m[k_m^2 \tanh(k_m h_0)\tanh(k_m h)]^{1/4}\sin t_1 + \beta_m\left[\frac{\tanh(k_m h)}{\tanh(k_m h_0)}\right]\cos t_1\right\}J_0(k_m r) + O(\epsilon) \tag{26}$$

Equation (26) shows that the amplitudes of the oscillation due to the initial disturbance decay (amplify) if $h(t)$ decreases (increases). Therefore, withdrawal of fluid from the tank damps any free surface oscillations which exist initially. This conclusion is consistent with the result of Miles (1962). Equation (26) also shows that the faster $h(t)$ decreases (increases), the faster the initial disturbance decays (magnifies). Since $h(t)$ decreases at the fastest rate if $l = 0$, the sudden withdrawal of fluid with a constant rate has the maximum damping effect on the initial free surface oscillation, provided that F is kept the same. Moreover, a larger drain rate (which results in a larger F) produces larger damping. Generally speaking, for a drain rate $q(t)$ with the behavior $q(t) \sim t^l$ for small t, the initial behavior of the free surface motion will be characterized by (26). Therefore, for the initial moment the above conclusion is valid for any drain rate $q(t)$.

Although withdrawal of fluid damps any oscillations initially present, it generates new forced oscillations on the free surface (i.e., drainage-initiated oscillations). Drainage-initiated free surface oscillations can be examined by taking $\alpha_m = \beta_m = 0$, $m = 1, 2, \ldots$ It is clear from (23a) and (23b) that $\gamma_n(t_2) = 0$, $n = 0, 1, \ldots, l$, and that

$$\gamma_{l+1}(0) = -(\pm)\frac{(-1)^{\frac{l}{2}}\pi R_m (l+1)!}{[k_m \tanh(k_m h_0)]^{1/2}\sinh(k_m h_0)}, \quad \text{if } l = 0, 2, 4, \ldots \tag{27a}$$

$$\dot{\gamma}_l(0) = -(\pm)\frac{(-1)^{\frac{l-1}{2}}\pi R_m (l+1)!}{[k_m \tanh(k_m h_0)]^{\frac{l-1}{2}}\sinh(k_m h_0)}, \quad \text{if } l = 1, 3, 5, \ldots \tag{27b}$$

From (24a–d), we have that $A_n(t_2) = B_n(t_2) = 0$, $n = 1, 2, \ldots, l$, and

$$A_{l+1}(0) = -\gamma_{l+1}(0),\ B_{l+1}(0) = 0, \text{ if } l = 0, 2, 4, \ldots \tag{28a}$$

$$B_{l+1}(0) = -\frac{\dot{\gamma}_l(0)}{\sqrt{k_m \tanh(k_m h_0)}},\ A_{l+1}(0) = 0, \quad \text{if } l = 1, 3, 5, \ldots \tag{28b}$$

The drainage-initiated free surface oscillation is

$$\eta(r,t) = \frac{F}{2\pi(l+1)t_0^l}\sum_{m=0}^{\infty} J_0(k_m r)[k_m^2 \tanh(k_m h_0)\tanh(k_m h)]^{1/4} \times \{[1 + (-1)^l]A_{l+1}(0)\sin t_1 - [1 - (-1)^l]B_{l+1}(0)\cos t_1\} - \sum_{m=0}^{\infty} J_0(k_m r)\sum_{n=0}^{L}\epsilon^{2n+2}\dot{\gamma}_{2n+1}(t_2) + O(F\epsilon) \tag{29}$$

in which $L = (l-1)/2$ if l = odd, $L = l/2 - 1$ if l is a positive even integer, and $L = 0$ if $l = 0$.

The double summation terms in (29) represent the forced solution. The drainage-initiated oscillations which are described by the single summation are of order F regardless of the value l. The amplitude of the drainage-initiated oscillation again damps for an emptying tank. From Eqs. (27a)–(28b) the amplitudes of high order modes are seen to be negligible due to large k_m. Thus the contribution of high order modes towards the drainage-initiated free surface oscillation are not important, and the lower modes are sufficient to describe the free surface shape.

The complete response of the free surface to the initial disturbances and the drainage is the sum of (26) and (29). Unless h_0 is very small, i.e., the tank is either very shallow, or else the tank is rapidly drained, the initial disturbance-induced oscillations given by (26) will dominate overwhelmingly. Hence, in the presence of initial disturbances, the drainage-initiated oscillations can be neglected.

In the absence of initial disturbances, the visibility of the drainage-initiated free-surface oscillations depends on the relative importance of the forced solution terms and the oscillatory terms. Equation (29) shows that the drainage-initiated oscillations are proportional to F, and are independent of l. The forced solution is

$$\sum_{n=0}^{L} \epsilon^{2n+2}\dot{\gamma}_{2n+1}(t_2)=(\pm)\frac{F^2}{\pi}\frac{R_m k_m \cosh(k_m h)}{\sinh^2(k_m h)}+O(F^4), \quad \text{when } l=0, \tag{30a}$$

$$\sum_{n=0}^{L} \epsilon^{2n+2}\dot{\gamma}_{2n+1}(t_2)= -(\pm)\frac{FR_m}{t_0^l}\sum_{n=0}^{L}\frac{(-1)^n l\cdot\cdot\cdot(l-2n)t^{l-2n-1}}{[k_m\tanh(k_m h)]^n\sinh(k_m h)}+O(F\epsilon), \quad \text{when } l\le 1. \tag{30b}$$

The free-surface elevation (29) then becomes

$$\eta(r,t)=F\sum_{m=1}^{\infty} J_0(k_m r)\frac{(\pm)R_m}{\sinh(k_m h_0)} \times [k_m^2\tanh(k_m h_0)\tanh(k_m h)]^{1/4}\sin t_1+O(F^2),\ l=0, \tag{31a}$$

$$\begin{aligned}\eta(r,t)=(\pm)\frac{(-1)^{\frac{l-1}{2}}Fl!}{t_0^l}\sum_{m=1}^{\infty}R_m J_0(k_m r) &\times\left\{\frac{1}{[k_m\tanh(k_m h)]^{\frac{l-1}{2}}\sinh(k_m h)} - \frac{C^{-1}(t_2)\cos t_1}{[k_m\tanh(k_m h_0)]^{\frac{l-1}{2}}\sinh(k_m h_0)}\right\}\\ &+\frac{(\pm)F}{t_0^l}\sum_{m=1}^{\infty}R_m J_0(k_m r)\sum_{n=0}^{l-3/2}\frac{(-1)^n l\cdot\cdot\cdot(l-2n)t^{l-2n-1}}{[k_m\tanh(k_m h)]^n\sinh(k_m h)}\\ &+O(F\epsilon),\ l=1,3,\cdot\cdot\cdot,\end{aligned} \tag{31b}$$

$$\begin{aligned}\eta(r,t)=-(\pm)\frac{(-1)^{\frac{1}{2}}Fl!}{t_0^l}\sum_{m=1}^{\infty}R_m J_0(k_m r) &\times\left\{\frac{t}{[k_m\tanh(k_m h)]^{l/2-1}\sinh(k_m h)} - \frac{C^{-1}(t_2)\sin t_1}{[k_m\tanh(k_m h_0)]^{l/2-1}\sinh(k_m h_0)}\right\}\\ &+\frac{(\pm)F}{t_0^l}\sum_{m=1}^{\infty}R_m J_0(k_m r)\sum_{n=0}^{l/2-2}\frac{(-1)^n l\cdot\cdot\cdot(l-2n)t^{l-2n-1}}{[k_m\tanh(k_m h)]^n\sinh(k_m h)}\\ &+O(F\epsilon),\ l=2,4,\cdot\cdot\cdot.\end{aligned} \tag{31c}$$

Equations (31a–c) show that drainage-initiated free-surface oscillations dominate the main character of the flow only if the sink is turned on suddenly (i.e., $l = 0$). If the flow is started in a gradual manner in a draining tank (i.e., $l \geq 1$), the drainage-initiated oscillations are overshadowed by the forced motion. Because in a draining tank $h(t)$ decreases, the oscillatory part of the motion decays while the forced free-surface motion magnifies. Initially, these two effects balance each other. Oscillations can be appreciable only in a filling tank where $h(t)$ is an increasing function of t, where oscillations are magnified while the forced motion decays, resulting in the eventual dominance of the oscillations. The asymptotic free-surface motion in a filling tank is the combination of a mean surface motion, which elevates the mean surface, plus oscillations. Equations (31a–c) clearly show that the asymptotic oscillations in a filling tank are standing waves.

Furthermore, (31b) and (31c) show that a large l magnifies the difference between the forced motion and the oscillations so that it produces greater dominance of the forced motion over the oscillations, thus making the oscillatory motion less visible. Therefore, turning on the sink gradually can reduce the drainage-initiated free-surface oscillations.

Equation (31a) shows that the drainage-initiated free-surface oscillations decay in an emptying tank and grow in a filling tank. Therefore, the present analysis does not support the conclusion obtained by Saad et al. (1964) that drainage-initiated oscillations amplify (decay) in an emptying (filling) tank. The disagreement is caused by two factors: (a) neglect or inclusion of the linearized inertial term; (b) the method of finding the amplitude function. In the present study, the linearized inertial term is retained and the amplitude function is valid for predicting long-time behavior. Saad and Oliver's solution was obtained by complete neglect of the inertial terms and by replacing the variable coefficient by a constant in Eq. (4.1) of their paper, which is seen to be inappropriate for the present problem.

Equation (31a) also indicates that for small initial height, the drainage-induced oscillations are strong. In the nonlinear numerical simulation (Zhou and Graebel, 1990) it was found that for $F = 0.1$, $h_0 = 0.35$ results in a jet stronger than that when $h_0 = 1$. Although the phenomenon of the jet formation is highly nonlinear, (31a) may suggest that the strength of the jet, which occurs only when F is small, depends on the amplitudes of the drainage-initiated oscillations and is closely related to the free-surface oscillations. The kinematic mechanism of the formation of the jet is that more fluid flows towards the central region than the rate of withdrawal, hence part of the fluid flowing towards the center must move up relative to the mean surface to form a jet. When the oscillation is strong, more fluid will flow towards the center and results in a strong jet.

3.2 Case 2: Periodic Drainage.

We study next the case when the drain rate function is a simple harmonic function. Two cases will be solved, i.e., the drain rate is a sine or a cosine function. In both cases the flow is started from rest.

Assuming that

$$q(t)=\cos\omega t,\ h(t)=h_0+\epsilon\sin\omega t,\ \text{where } \epsilon=\frac{F}{\pi\omega}, \tag{32}$$

in which ω is a constant, it is expected that if for some m, $\omega = \sqrt{\tanh(k_m h_0)} + O(\epsilon)$, resonant behavior will appear resulting in large oscillations.

In the following, we expand

$$k_m\tanh(k_m h(t))=\omega_m^2+\sum_{n=1}^{\infty}\epsilon^n a_n\sin^n\omega t, \quad \omega_m=\sqrt{k_m\tanh(k_m h_0)}, \tag{33a}$$

$$\frac{\pi\omega k_m R_m}{\cosh(k_m h)}=\sum_{n=0}^{\infty}\epsilon^n b_n\sin^n\omega t. \tag{33b}$$

The values that we will use are

$$a_1=k_m^2-\omega_m^4,\ a_2=-\omega_m^2 a_1,\ b_0=\pi\omega R_m\sqrt{a_1},\ b_1=-\omega_m^2 b_0. \tag{34}$$

Note that a_1 is always positive and a_2 is always negative. ω_m is the mth natural frequency of the free-surface oscillation.

By virtue of (33a,b), Eq. (16a) can be transformed into

$$\frac{d^2y_m}{dt^2}+\omega_m^2 y_m=-y_m\sum_{n=1}^{\infty}\epsilon^n a_n \sin^n\omega t - \sum_{n=0}^{\infty}\epsilon^{n+1}b_n\sin^n\omega t\cos\omega t. \quad (35)$$

If $\omega \neq \omega_m$ and $\omega \neq 2\omega_m$, we may assume that the solution to (35) is of the form

$$y_m(t)=G_0(t,\tilde{t})+\epsilon G_1(t,\tilde{t})+\epsilon^2 G_2(t,\tilde{t})+\cdots, \quad (36)$$

where $\tilde{t}=\epsilon^2 t$. Inserting (36) into (35) and letting the coefficients of like powers of ϵ be zero gives

$$\frac{\partial^2 G_0}{\partial t^2}+\omega_m^2 G_0=0, \quad (37a)$$

$$\frac{\partial^2 G_1}{\partial t^2}+\omega_m^2 G_1=-a_1 G_0\sin\omega t - b_0\cos\omega t, \quad (37b)$$

$$\frac{\partial^2 G_2}{\partial t^2}+\omega_m^2 G_2=-a_2 G_0\sin^2\omega t - a_1 G_1\sin\omega t - 2\frac{\partial^2 G_0}{\partial t\partial\tilde{t}}-\frac{b_1}{2}\sin 2\omega t, \quad (37c)$$

with

$$G_n(0)=\alpha_m\delta_{n,0}, \text{ and } \frac{\partial G_n(0,0)}{\partial t}+\frac{\partial G_{n-2}(0,0)}{\partial\tilde{t}}=-\beta_m\delta_{n,0}, \quad n=0,\ 1,\ 2. \quad (37d)$$

This set of equations yields the solutions

$$G_0(t,\tilde{t})=A_0(\tilde{t})\cos\omega_m t+B_0(\tilde{t})\sin\omega_m t. \quad (38)$$

If $\omega_m \neq 2\omega$, we have

$$A_0(\tilde{t})=\alpha_m\cos\Theta\tilde{t}-\frac{\beta_m}{\omega_m}\sin\Theta\tilde{t},$$

$$B_0(\tilde{t})=-\frac{\beta_m}{\omega_m}\cos\Theta\tilde{t}-\alpha_m\sin\Theta\tilde{t}. \quad (39a)$$

If $\omega_m = 2\omega$, $A_0(\tilde{t})$ and $B_0(\tilde{t})$ are given by

$$A_0(\tilde{t})=\alpha_m\cos\Theta\tilde{t}+\left(\frac{c}{\Theta}-\frac{2\beta_m}{\omega}\right)\sin\Theta\tilde{t},$$

$$B_0(\tilde{t})=\left(\frac{c}{\Theta}-\frac{2\beta_m}{\omega}\right)\cos\Theta\tilde{t}-\alpha_m\sin\Theta\tilde{t}-\frac{c}{\Theta}. \quad (39b)$$

In Eqs. (39a,b)

$$\Theta=\frac{a_1}{4\omega_m}\left(\frac{a_1}{\omega^2-4\omega_m^2}-\omega_m^2\right), \text{ and } c=-\frac{b_0}{8\omega}\left(\frac{a_1}{15\omega^2}-4\omega^2\right).$$

Equations (39a,b) show that the response of the free surface to a periodic excitation is harmonic with amplitude modulation. If $\omega \neq \omega_m/2,\ 2\omega_m$, the drainage-initiated oscillations are proportional to F and are always stable on the $\tilde{t}$ scale. The stability is marginal, i.e., the amplitudes are bounded. When $\omega_m = 2\omega$, the drainage-initiated oscillations are comparable to the initial disturbance-induced motion.

The drain rate function $q(t)$ used here is equivalent for small times to the case $l = 0$ in the previous section. The drainage-initiated oscillation is $O(F)$. It can be shown without difficulty that if $q(t) = \sin\omega t$ (equivalent to $l = 1$ for small time), the drainage-initiated oscillation is proportional to $O(F^2)$. These results are consistent with that of the previous section.

Applying the multiple scales method to the resonant free-surface motion corresponding to $\omega = \omega_m$, we let $t_1 = \omega t$, $t_2 = \epsilon^2 t_1$, and seek the solution of (35) in the form

$$y_m(t)=\frac{1}{\epsilon}G_{-1}(t_1,t_2)+G_0(t_1,t_2)+\epsilon G_1(t_1,t_2)+\cdots. \quad (40)$$

In terms of the new variables t_1 and t_2, we can write

$$\frac{\partial^2 G_{-1}}{\partial t_1^2}+G_{-1}=0, \quad (41a)$$

$$\frac{\partial^2 G_0}{\partial t_1^2}+G_0=-\frac{a_1}{\omega^2}G_{-1}\sin t_1, \quad (41b)$$

$$\frac{\partial^2 G_1}{\partial t_1^2}+G_1=-\frac{a_2}{\omega^2}G_{-1}\sin^2 t_1-\frac{a_1}{\omega^2}G_0\sin t - 2\frac{\partial^2 G_{-1}}{\partial t_1\partial t_2}-\frac{b_0}{\omega^2}\cos t, \quad (41c)$$

and

$$G_n(0,0)=\alpha_m\delta_{n,0},\ \frac{\partial G_n(0,0)}{\partial t_1}+\frac{\partial G_{n-2}(0,0)}{\partial t_2}=-\frac{\beta_m\delta_{n,0}}{\omega}, \quad n=-1,\ 0,\ 1. \quad (41d)$$

Solving (41a–d) for the first two terms gives

$$G_{-1}(t_1,t_2)=A_{-1}(t_2)\cos t_1+B_{-1}(t_2)\sin t_1, \quad (42a)$$

$$G_0(t_1,t_2)=A_0(t_2)\cos t_1+B_0(t_2)\sin t_1-\frac{a_1}{2\omega^2}B_{-1}(t_2)+\frac{a_1}{6\omega^2}[A_{-1}(t_2)\sin 2t_1-B_{-1}(t_2)\cos 2t_1]. \quad (42b)$$

Letting

$$\alpha=\frac{5a_1^2}{24\omega^4}-\frac{3a_2}{8\omega^2},\ \gamma=\frac{a_1^2}{24\omega^4}+\frac{a_2}{8\omega^2},$$

since a_1 is positive and a_2 is negative, α is positive. The sign of γ depends on k_m and h_0. If $\gamma < 0$,

$$A_{-1}(t_2)=-\frac{b_0}{2\omega^2\gamma}(1-\cos\sqrt{-\alpha\gamma}t_2),$$

$$B_{-1}(t_2)=-\frac{b_0}{2\omega^2\sqrt{-\alpha\gamma}}\sin\sqrt{-\alpha\gamma}t_2,$$

$$A_0(t_2)=\alpha_m\cos\sqrt{-\alpha\gamma}t_2-\frac{\beta_m}{\omega}\sqrt{-\frac{\alpha}{\gamma}}\sin\sqrt{-\alpha\gamma}t_2,$$

$$B_0(t_2)=-\frac{\beta_m}{\omega}\cos\sqrt{-\alpha\gamma}t_2+\alpha_m\sqrt{-\frac{\gamma}{\alpha}}\sin\sqrt{-\alpha\gamma}t_2. \quad (43a)$$

If $\gamma = 0$,

$$A_{-1}(t_2)=\frac{\alpha b_0}{4\omega^2}t_2^2,\ B_{-1}(t_2)=-\frac{b_0}{2\omega^2}t_2,$$

$$A_0(t_2)=\frac{\alpha\beta_m}{\omega}t_2+\alpha_m,\ B_0(t_2)=-\frac{\beta_m}{\omega}. \quad (43b)$$

If $\gamma > 0$,

$$A_{-1}(t_2)=-\frac{b_0}{2\omega^2\gamma}[1-\cosh(\sqrt{\alpha\gamma}t_2)],$$

$$B_{-1}(t_2)=-\frac{b_0}{2\omega^2\sqrt{\alpha\gamma}}\sinh(\sqrt{\alpha\gamma}t_2),$$

$$A_0(t_2)=\alpha_m\cosh(\sqrt{\alpha\gamma}t_2)+\frac{\beta_m}{\omega}\sqrt{\frac{\alpha}{\gamma}}\sinh(\sqrt{\alpha\gamma}t_2),$$

$$B_0(t_2)=-\frac{\beta_m}{\omega}\cosh(\sqrt{\alpha\gamma}t_2)-\alpha_m\sqrt{\frac{\gamma}{\alpha}}\sinh(\sqrt{\alpha\gamma}t_2). \quad (43c)$$

From this we see that the strongest resonant oscillation occurs when the forcing frequency ω coincides with one of the natural frequencies. In this case, the drainage-initiated motion is far stronger than the initial disturbance-induced motion.

When γ is positive, the amplitude of the mth mode of the resonant oscillation grows exponentially and the induced free-surface motion is unstable. The necessary and sufficient condition for a positive γ is

$$k_m - 2\omega^2 > 0, \text{ or } h_0 < h_{mc} = \tanh^{-1}\left(\frac{1}{2}\right)/k_m, \tag{44}$$

where $\tanh^{-1}$ is the arc-hyperbolic tangent function, and h_{mc} is the critical depth for the stability of the mth resonant mode. The largest possible h_{mc} for an exponentially growing resonant motion is $h_{1c} = \tanh^{-1}(0.5)/k_1 = 0.143$. If $h_0 > h_{1c}$, the resonance is stable. If $h_0 \mp h_{mc}$, secular instability occurs. The exponentially decaying resonant motion occurs if $h_0 > h_{mc}$. Thus, a large initial depth h_0 induces exponentially decaying resonant oscillations.

If the forcing frequency ω is fixed, different h_0 will give different orders of resonant modes. Higher-order resonance is more unstable. Suppose h_n and h_m with $n > m$ are two initial depths which correspond to nth and mth resonant modes. According to (33a) they are

$$h_n = \frac{1}{k_n}\tanh^{-1}\left(\frac{\omega^2}{k_n}\right), \text{ and } h_m = \frac{1}{k_m}\tanh^{-1}\left(\frac{\omega^2}{k_m}\right). \tag{45}$$

If the nth resonant mode is stable, i.e., $h_m > h_{hc} = \tanh(0.5)/k_n$, we can immediately see that $\omega^2 > k_n/2$. Since $n > m$ which leads to $k_n > k_m$, with the help of (45) and $\omega^2/k_m > 0.5$ we obtain

$$h_m = \frac{1}{k_m}\tanh^{-1}\left(\frac{\omega^2}{k_m}\right) > \frac{1}{k_m}\tanh^{-1}(0.5) = h_{mc}.$$

Hence, the mth resonant mode is exponentially decaying and thus is stable. This result is not obvious because $h_{nc} < h_{mc}$ if $n > m$.

The situation is reversed if we consider the case in which h_0 is fixed and ω is varying. Since higher-order resonant modes have smaller critical initial depths, higher-order resonant modes are more stable for constant h_0. Therefore, a large forcing frequency ω will induce stable resonance.

The nondimensional time scale over which the amplitude of the resonant oscillation has appreciable variation is

$$T_s = \frac{1}{\omega\sqrt{\alpha|\gamma|}\epsilon^2} = \frac{24\pi^2\omega^5}{(k_m^2 - \omega^4)\sqrt{(5k_m^2 + 4\omega^4)|k_m^2 - 4\omega^4|}F^2}. \tag{46}$$

If h_0 and ω are fixed, which may induce both stable and unstable oscillations, a decreasing F results in an increasing T_s. Since the amplitude of the resonant oscillation is inversely proportional to F, the resulting oscillation is stronger, but takes a longer time to be seen. Figure 1 shows $F^2T_s/24\pi^2$ versus the initial depth h_0 according to (46) and (33a) for the first four modes. In the figure the k_m ($m = 1, 2, 3, 4$) are the parameters. The negative values represent the unstable situation where $h_0 < h_{mc}$. T_s has two poles located at $h_0 = h_{mc}$ and $h_0 = \infty$, and a zero at $h_0 = 0$. For a deep tank, h_0 is greater than the critical value h_{mc} so resonant oscillations are stable. Since h_0 is large, ω^2 is close to k_m, hence T_s is large. As a consequence, resonance takes a long time to be visible. As h_0 decreases towards h_{mc}, T_s has a minimum value at which the stable resonance has the fastest rate of amplitude modulation. When $h_0 < h_{mc}$, the resulting unstable motion is unbounded. Since T_s decreases monotonically with decreasing h_0, small initial depth gives fast growth rate.

For the case when $\omega = 2\omega_m$, we define $t_1 = \omega t/2$ and $t_2 = \epsilon t_1$. The solution of (35) is again given by (40) with now $G_{-1}(t_1,t_2) = 0$. Since in this case t_2 is proportional to ϵ, rather than ϵ^2, the perturbation equations governing $G_n(t_1,t_2)$ are

$$\frac{\partial^2 G_0}{\partial t_1^2} + G_0 = 0, \tag{47a}$$

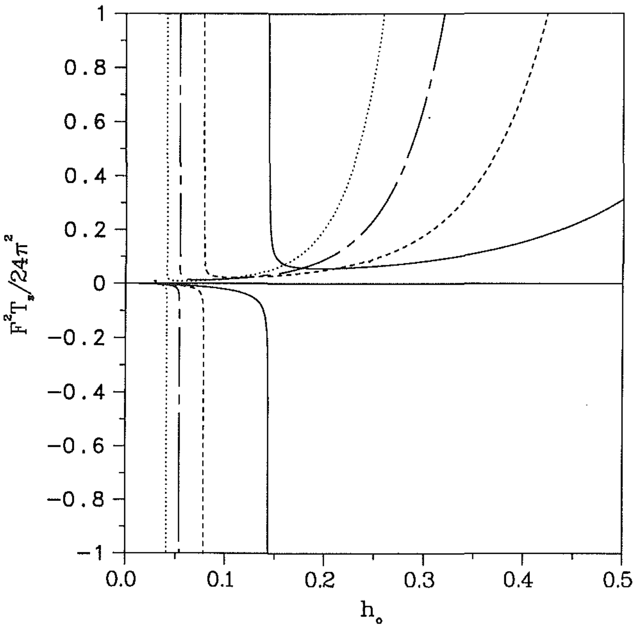

Fig. 1 $F^2T_s/24\pi^2$ **as a function of** h_0**. The negative values denote the unstable modes.** ——— $m = 1$, $\cdots$ $m = 2$, — · — $m = 3$, · · · · · $m = 4$.

$$\frac{\partial^2 G_1}{\partial t_1^2} + G_1 = -4\frac{a_1}{\omega^2}G_0\sin 2t_1 - 2\frac{\partial^2 G_0}{\partial t_1 \partial t_2} - 4\frac{b_0}{\omega^2}\cos 2t_1, \tag{47b}$$

with the initial conditions

$$G_m(0,0) = \alpha_m\delta_{n,0}, \quad \frac{\partial G_n(0,0)}{\partial t_1} + \frac{\partial G_{n-1}(0,0)}{\partial t_2} = -\frac{2\beta_m\delta_{n,0}}{\omega}, \quad n = 0, 1. \tag{47c}$$

The leading terms of the initial condition-induced oscillations are given by

$$G_0(t_1,t_2) = \alpha_m \exp\left(\frac{a_1}{\omega^2}t_2\right)\cos t_1 - \frac{2\beta_m}{\omega}\exp\left(-\frac{a_1}{\omega^2}t_2\right)\sin t_1. \tag{48a}$$

The leading drainage-initiated resonant oscillations are

$$G_1(t_1,t_2) = -\frac{4b_0}{3\omega^2}\exp\left(\frac{a_1}{\omega^2}t_2\right)\cos t_1 + \frac{4b_0}{3\omega^2}\cos 2t_1. \tag{48b}$$

Solutions (48a,b) imply the unconditional instability of the resonant responses to $\omega = 2\omega_m$. The rate of growth is given by

$$\mu = \frac{a_1 t_2}{\omega^2 t} = \frac{Fk_m}{4\pi\sinh(2k_m h_0)}. \tag{49}$$

μ is a decreasing function of the initial depth h_0 as well as of k_m. Hence, the resonant free-surface oscillations grow faster for a smaller h_0, a lower mode or a larger F.

It is interesting that the stability behavior is totally reversed if $q(t) = \sin\omega t$. In this case,

$$h(t) = h_0 + \epsilon(1 - \cos\omega t), \text{ where } \epsilon = \frac{F}{\pi\omega}. \tag{50}$$

Equations (33a,b) are now

$$k_m\tanh(k_m h(t)) = \omega_m^2 + \sum_{n=1}^{\infty}\epsilon^n a_n(1 - \cos\omega t)^n, \quad \omega_m = \sqrt{k_m\tanh(k_m h_0)}, \tag{51a}$$

$$\frac{\pi\omega k_m R_m}{\cosh(k_m h)} = \sum_{n=0}^{\infty}\epsilon^n b_n(1 - \cos\omega t)^n, \tag{51b}$$

in which a_n, b_n are defined by (34).

Using the same methods with $a_n \sin^n \omega t$ in (33a,b) being replaced by $a_n(1-\cos\omega t)^n$ and $b_n \sin^n \omega t$ by $b_n(1-\cos\omega t)^n$, we obtain the following results:

If $\omega = 2\omega_m$, defining $t_1 = \omega_m t$ and $t_2 = \epsilon t_1$ and assuming the solution of (16a,b) to be (40) with $G_{-1}(t_1,t_2) = 0$, we obtain

$$G_0(t_1,t_2) = \left[\alpha_m \cos\frac{\sqrt{3}a_1}{\omega^2} t_2 - \frac{2\sqrt{3}\beta_m}{\omega} \sin\frac{\sqrt{3}a_1}{\omega^2} t_2\right] \cos t_1 - \left[\frac{\alpha_m}{\sqrt{3}} \sin\frac{\sqrt{3}a_1}{\omega^2} t_2 + \frac{2\beta_m}{\omega} \cos\frac{\sqrt{3}a_1}{\omega^2} t_2\right] \sin t_1. \quad (52a)$$

For the drainage-initiated oscillations, $G_0(t_1,t_2) = 0$. The leading terms are

$$G_1(t_1,t_2) = -\frac{8b_0}{\sqrt{3}\omega^2} \sin\frac{\sqrt{3}a_1}{\omega^2} t_2 \cos t_1 - \frac{8b_0}{3\omega^2} \cos\frac{\sqrt{3}a_1}{\omega^2} t_2 \sin t_1 + \frac{4b_0}{3\omega^2} \sin 2t_1. \quad (52b)$$

If $\omega = \omega_m$, the proper variables are $t_1 = \omega t$ and $t_2 = \epsilon t_1$. The solution is still of the form given by (40). The first two terms are

$$G_0(t_1,t_2) = \alpha_m \cos\left(t_1 + \frac{a_1}{2\omega^2} t_2\right) + \left(\frac{b_0}{a_1} - \frac{\beta_m}{\omega}\right) \sin\left(t_1 + \frac{a_1}{2\omega^2} t_2\right) - \frac{b_0}{a_1} \sin t_1, \quad (53a)$$

$$G_1(t_1,t_2) = \left(\frac{8a_2b_0}{a_1^2} - \frac{b_0}{3}\right) \cos\left(t_1 - \frac{a_1}{2\omega^2} t_2\right) + \left(\frac{2b_1}{a_1} + \frac{b_0}{3}\right) \sin\left(t_1 + \frac{a_1}{2\omega^2} t_2\right) - \left(\frac{8a_2b_0}{a_1^2} - \frac{b_0}{3}\right) \cos t_1 - \left(\frac{2b_1}{a_1} + \frac{b_0}{3}\right) \sin t_1. \quad (53b)$$

If $\omega_m = 2\omega$, setting $t_1 = \omega t$ and $t_2 = \epsilon t_1$, and taking the solution the form of (40) with $G_{-1}(t_1,t_2) = 0$, we have

$$G_0(t_1,t_2) = \alpha_m \cos\left(2t_1 + \frac{a_1}{2\omega^2} t_2\right) - \frac{\beta_m}{\omega} \sin\left(2t_1 + \frac{a_1}{2\omega^2} t_2\right). \quad (54a)$$

The leading drainage-initiated oscillations are given by

$$G_1(t_1,t_2) = \left(\frac{b_0}{6\omega^2} - \frac{b_1}{2a_1}\right) \sin\left(2t_1 + \frac{a_1}{\omega^2} t_2\right) + \frac{b_1}{2a_1} \sin 2t_1 - \frac{b_0}{3\omega^2} \sin t_1. \quad (54b)$$

It is seen that the free-surface oscillations corresponding to a sinusoidal drain rate are one order weaker than that corresponding to the cosine drain rate, due to the more gradual turning on of the sink. The free-surface oscillations, whether they are resonant or not, are unconditionally stable. Comparing the cosine drain rate with the sine drain rate, we conclude that if the flow starts from rest in a gradual manner, the possible resonance is unconditionally stable.

4 Concluding Remarks

Free-surface oscillations that may be initiated either by the combination of the initial disturbances and the drainage or solely by the drainage have been investigated through a model which contains the linearized inertial term. The amplitude functions are then found in an asymptotic expansion based on small Froude number.

For small Froude numbers, the present results show that draining or filling generates oscillations on the free surface. The present results support Miles' conclusion (1962) that draining (filling) damps (amplifies) the oscillations regardless of the cause of initiation, but is in disagreement with that of Saad and Oliver's (1964).

Our solution shows a strong influence of the initial behavior of the drain rate function on the visibility of drainage-initiated free-surface oscillations. If $q(t) \sim t^l$ where $l \geq 1$ for small t, the drainage-initiated oscillations are very weak, and may be almost invisible, since the drainage-initiated oscillatory motion decays while the forced motion (nonoscillatory) grows and both balance each other initially. When the drain rate function has an initial discontinuity, such as an impulsive start of the flow, the drainage-initiated oscillations are one order (in F) stronger than the forced one, hence the free-surface motion is oscillatory. In a filling tank the asymptotic motion is identical to that in a circular tank with constant depth h_0.

It is suggested that a small h_0 induces strong drainage-initiated oscillations may be the reason why a small h_0 results in a strong jet (Zhou and Graebel, 1990).

We also studied the resonant behavior of the free surface motion excited by periodic drainage. It was found that if the initial drain rate is zero, i.e., $q(t) = \sin\omega t$, all of the oscillatory modes, resonant and nonresonant alike, are bounded, and thus are stable. When the drain rate has an initial discontinuity, i.e., $q(t) = \cos\omega t$, the nonresonant and the higher-order resonant modes are stable. The primary resonant mode ($\omega = \omega_m$) is conditionally stable. The secondary resonant mode ($\omega = 2\omega_m$) is unconditionally unstable.

Acknowledgments

This work was partially supported under the Program in Ship Hydrodynamics (PSH) at the University of Michigan, funded by the University Research Initiative of the Office of Naval Research, (contract No. N000184-86-K0684) and by NSF grant MSM-8707646.

References

Miles, J. W., 1962, "Note On The Damping of Free Surface Oscillations Due To Drainage," *J. Fluid Mech.*, Vol. 12, p. 438.

Saad, Michel A., and Oliver, David A., 1964, "Linearized Time Dependent Free Surface Flow in Rectangular and Cylindrical Tanks," *Proc. Heat Transfer And Fluid Mech. Inst.*, Stanford Univ. Press, Stanford, CA, p. 81.

Zhou, Q. N., and Graebel, W. P., 1990, "Axisymmetric Draining of a Cylindrical Tank with Free Surfaces," *J. Fluid Mech.*, Vol. 221, pp. 511-532.

Nonaxisymmetric Waves of a Stratified Vertical Vortex

Y. T. Fung

Center for Advance Space Sensing,
Naval Research Laboratory,
Washington, DC 20375

The interfacial conditions for a cylindrical and an axial vortex sheet or thin fluid layer are obtained for a general class of vortex flows in a radius and gravity-stratified environment. The flow is assumed to be inviscid and incompressible. No Boussinesq approximation is required. In addition to the kinematic and dynamic conditions that the flow has to satisfy in the centrifugal and gravitational directions, a third condition, which restrains the interaction of the centrifugal and gravitational force fields, has to be imposed on those vortex sheets. This is consistent with the previous derived criteria for this type of vortex motions, in which a third condition based on pressure and force balance must be satisfied. Nonaxisymmetric instability for a special flow profile is examined and the stability boundary is obtained to show the behavior of this type of stratified vertical vortex. The results provide us with some information on the instability mechanism for the generation of the horizontal vortices in the ocean and for the spiral type of vortex breakdown in tornadoes and waterspouts in the atmosphere.

1 Introduction

Coherent vortex motions widely exist in the atmosphere and in the ocean. Vortex trails generated in the lee of certain islands (Pao and Kao, 1976) and horizontal vortices evolving in the late wakes of a towed axisymmetric body (Pao and Kao, 1977; Lin and Pao, 1979) are a few of the examples we encounter. The latter is particularly interesting because they exist only in a stratified fluid but not in a homogeneous environment.

Vortex motions in the atmosphere and in the ocean are subject to strong influence of density inhomogeneity due to the temperature or salinity fluctuations. Even though it is very small as in the ocean and in the atmosphere, such density inhomogeneity, once interacting with the gravity, plays a very subtle role in generating the organized flow structures.

Many researchers have investigate the role that density inhomogeneities play in flow behaviors, especially under the influence of gravity and other force fields. Stability analyses have been performed for two-dimensional shear flows in a gravity-stratified environment (Miles, 1961; Howard, 1961) and for swirling flows in a radius-stratified environment (Fung Kurzweg, 1975). In those analyses, only one force field, gravitational or centrifugal, is present within the flow field, and the stability criteria so derived only respond to that particular force field in its respective direction.

Contributed by the Applied Mechanics Division of THE AMERICAN SOCIETY OF MECHANICAL ENGINEERS for presentation at the 1992 ASME Winter Annual Meeting, Anaheim, CA, Nov. 8–13, 1992.

Discussion on this paper should be addressed to the Technical Editor, Prof. Leon M. Keer, The Technical Institute, Northwestern University, Evanston IL 60208, and will be accepted until four months after final publication of the paper itself in the JOURNAL OF APPLIED MECHANICS. Manuscript received by the ASME Applied Mechanics Division, Aug. 23, 1990; final revision, Nov. 1, 1991. Associate Editor: J. T. C. Liu.

92-WA/APM-14.

For vortex motions in the atmosphere and in the ocean, both the gravity and the self-induced centrifugal force field are present. Our freedom of analysis is limited not only by the presence of the two force fields, but also by the requirement of pressure balance between the interaction of the two. Also, because of this pressure balance requirement, the radius-dependent density component may appear in an originally gravity-stratified fluid, and further complicates the analysis.

To understand the behavior of vertical vortices in a stratified fluid is of great importance as it may lead to the physical mechanism which triggers the development of the coherent structures in stratified fluids. For that reason, Fung (1985, 1986) analysed a general class of vortex flows in a both radius and gravity-stratified environment. Necessary and sufficient conditions were obtained for the stability or instability of the flows. To maintain the stability of certain types of vortex motions, the flow has to satisfy the requirements in the centrifugal direction, the gravitational direction, and the pressure balance that restrains the interaction of the two force fields.

Even thought stability criteria have been derived for this general class of vortex flows to provide us with some upper-bound information on stability or instability, they do not yield sufficient knowledge of instability for a given flow profile. Solutions to the governing equations must be obtained before the detailed instability characteristics for the particular flow profile can be observed. Unfortunately, analytical solutions in terms of well-known functions for general vortex flows are very difficult to find except for a few broken-line profiles. Analyses of vortex sheet-type flows have therefore become a tool to look at the behavior of this type of stratified vortex motions.

Following the analysis of vortex motions for a general class of radius-dependent vortex sheets (Fung, 1983), we will analyse the interfacial conditions for both the cylindrical and axial vortex sheet (or thin fluid layer) in a radius and gravity-stratified environment. Nonaxisymmetric instability will be examined for a special gravity-stratified profile. The stability boundary will be obtained to determine the flow condition in a nonaxisymmetric configuration. This type of nonaxisymmetric instability may be responsible for the generation mechanism of the horizontal vortices in the ocean, and for the spiral type of vortex breakdown of a straight vortex column in tornadoes and waterspouts in the atmosphere (Lugt, 1989).

2 Governing Equations

The stratified column vortex to be considered is confined within a cylindrical coordinates (r,θ,z) with the z-axis pointing at the opposite direction of gravity. The fluid with density ρ is assumed to be inviscid, incompressible, and nonheat conducting. No Boussinesq approximation is made. The equations of motion for the velocities u_r, u_θ, and u_z in the respective r, θ, and z-directions are

$$\rho\left(\frac{\partial u_r}{\partial t}+u_r\frac{\partial u_r}{\partial r}+\frac{u_\theta}{r}\frac{\partial u_r}{\partial \theta}-\frac{u_\theta^2}{r}+u_z\frac{\partial u_r}{\partial z}\right)=-\frac{\partial P}{\partial r} \quad (1)$$

$$\rho\left(\frac{\partial u_\theta}{\partial t}+u_r\frac{\partial u_\theta}{\partial r}+\frac{u_\theta}{r}\frac{\partial u_\theta}{\partial \theta}+\frac{u_r u_\theta}{r}+u_z\frac{\partial u_\theta}{\partial z}\right)=-\frac{1}{r}\frac{\partial P}{\partial \theta} \quad (2)$$

$$\rho\left(\frac{\partial u_z}{\partial t}+u_r\frac{\partial u_z}{\partial r}+\frac{u_\theta}{r}\frac{\partial u_z}{\partial \theta}+u_z\frac{\partial u_z}{\partial z}\right)=-\frac{\partial P}{\partial z}. \quad (3)$$

The continuity equation is

$$\frac{\partial u_r}{\partial r}+\frac{u_r}{r}+\frac{1}{r}\frac{\partial u_\theta}{\partial \theta}+\frac{\partial u_z}{\partial_z}=0 \quad (4)$$

and the incompressible condition is

$$\frac{\partial \rho}{\partial t}+u_r\frac{\partial \rho}{\partial r}+\frac{u_\theta}{r}\frac{\partial \rho}{\partial \theta}+u_z\frac{\partial \rho}{\partial z}=0. \quad (5)$$

Let the vortex have a steady-state angular velocity $\Omega(r,z)$ and be embedded in a fluid with density $\rho_o(r,z)$. The corresponding governing equations of motions for the steady-state are

$$\frac{\partial P_o}{\partial r}=\rho_o r\Omega^2 \quad (6)$$

$$\frac{\partial P_o}{\partial \theta}=0 \quad (7)$$

$$\frac{\partial P_o}{\partial z}=-\rho_o g, \quad (8)$$

Let the flow be perturbed as follows:

$$u_r=\hat{u}$$
$$u_\theta=r\Omega(r,z)+\hat{v}$$
$$u_z=\hat{\omega}$$
$$P=P_o(r,z)+\hat{P}$$
$$\rho=\rho_o\ (r,z)+\hat{\rho} \quad (9)$$

where the quantities with a hat stand for small perturbations from their steady-state profiles. Equations. (1) to (5) admit the following normal modes solutions for the perturbation quantities

$$\hat{\phi}(r,\theta,z)=\phi(r,z)\ \exp\ [i(m\theta-\omega t)]. \quad (10)$$

Here, m is the azimuthal wave number, an integer, and $\omega = \omega_r + \omega_i$ is the complex eigenfrequency. We further introduce the Lagrangian displacements such that

$$\eta(r,z)=-i\frac{u}{m\Omega-\omega} \quad (11a)$$

$$\zeta(r,z)=-i\frac{w}{m\Omega-\omega}. \quad (11b)$$

Within the framework of the normal mode analysis, we obtain the following set of linearized equations governing the stability of the flow:

$$\rho_o\{(N^2-\Phi_r)\eta-\Phi_z\zeta\}=\frac{\partial p}{\partial r}+\frac{2m\Omega}{rN}p \quad (12)$$

$$\rho_o\{\Psi_r\eta+(N^2+\Psi_z)\zeta\}=\frac{\partial p}{\partial z} \quad (13)$$

$$\frac{\partial \eta}{\partial r}+\left(1-\frac{2m\Omega}{N}\right)\frac{\eta}{r}+\frac{\partial \zeta}{\partial z}=\frac{1}{\rho_o N^2}\frac{m^2}{r^2}p. \quad (14)$$

Here, $N = m\Omega - \omega$, the Doppler-shifted frequency, and

$$\Phi_r=\frac{1}{\rho_o r^3}\frac{\partial}{\partial r}[\rho_o(r^2\Omega)^2],$$

$$\Phi_z=\frac{1}{\rho_o}\frac{\partial}{\partial z}(\rho_o r\Omega^2),$$

$$\Psi_r=\frac{g}{\rho_o}\frac{\partial \rho_o}{\partial r},$$

$$\Psi_z=\frac{g}{\rho_o}\frac{\partial \rho_o}{\partial z}.$$

The boundary conditions for eqs. (12) to (14) are

$$\eta=0 \quad \text{at} \quad r=R_1,R_2 \quad (15a)$$

$$\zeta=0 \quad \text{at} \quad z=Z_1,Z_2 \quad (15b)$$

where R_1,R_2,Z_1, and Z_2 are locations of rigid boundaries. For unbounded flows as in the atmosphere and ocean, the boundaries will be extended to infinity to represent that perturbations of the flow can not propagate to infinity.

3 Interfacial Conditions

The interfacial conditions for a cylindrical vortex sheet or a cylindrical fluid layer have been investigated in detail for a general class of radius-dependent stratified vortices (Fung, 1983). The presence of gravity in a stratified environment, however, creates much more complicated issues as in most of the situations we encounter. As demonstrated in the studies for compressible and incompressible vortex motions under gravity (Fung 1985, 1986), the interaction of the centrifugal and gravitational force fields plays an important role in flow stability. In addition to the conditions that the flow has to satisfy in the centrifugal and gravitational directions, a third condition based on the interaction of force fields and on the resultant pressure constraint is imposed on the flow to influence the development of organized flow structures in a gravity-stratified environment. For this reason, the validity of those interfacial conditions originally derived only for radius-stratified vortex motions is at best uncertain.

To resolve this uncertainty, we will examine the interfacial conditions for this general class of vortex motions in a both centrifugally and gravitationally stratified environment. We assume a cylindrical and an axial vortex sheet (or thin fluid layer) to exist within the flow field. Both vortex sheets or fluid layers may possess possible discontinuities in all components of the density and velocity fields.

The cylindrical vortex sheet or fluid layer to be considered has its steady-state location at $r = R$. Integrating eqs. (12) to (14) across the cylindrical interface in the radial direction and assuming that all the quantities across the interface are bounded, we obtain the following conditions:

$$\langle\eta\rangle_R=0 \quad (16a)$$

$$\langle p\rangle_R+\langle\rho_o r\Omega^2\rangle_R\eta(R)=0 \quad (16b)$$

$$\langle\rho_o\rangle_R=0 \quad (16c)$$

where $\langle\phi\rangle_R = \phi(R_{+0}) - \phi(R_{-0})$ represents a possible jump condition at $r = R$. The physical arguments for eqs. (16a) and

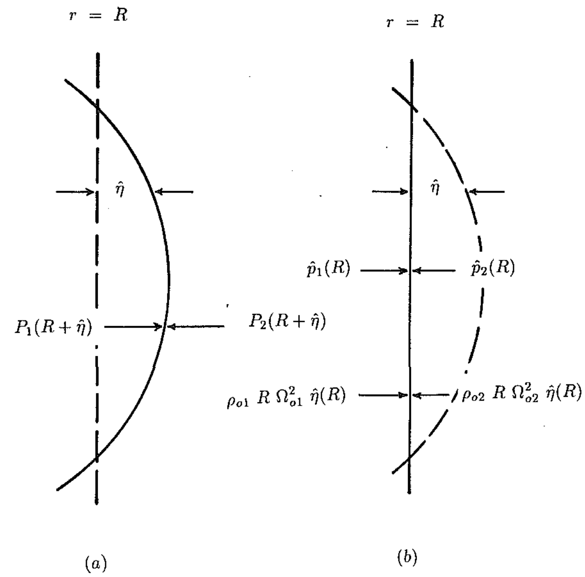

Fig. 1 Decomposition of the total pressure into the force components at the cylindrical interface

(16*b*) can be viewed from the steady equation of motion in the radial direction. By integrating eq. (6) in the radial direction, we obtain the steady-state pressure for the inner and outer regions as follows:

$$P_{01}(r,z) = -\int_{R_o}^{r} \rho_{01}(r',z)r'\Omega^2(r',z)dr' \quad (R_o \le r < R) \qquad (17a)$$

$$P_{02}(r,z) = -\int_{R_o}^{R} \rho_{01}(r',z)r'\Omega^2(r',z)dr' - \int_{R}^{r} \rho_{02}(r',z)r'\Omega^2(r',z)dr' \quad (R \le r < \infty) \qquad (17b)$$

where the subscripts 1 and 2 respectively represent the quantities in the inner the outer regions divided by the vortex sheet, and R_o is an arbitrary reference location within the inner region: Assume the cylindrical vortex sheet is disturbed such that the deformed surface is prescribed by

$$r = R + \hat{\eta}(r,\theta,z;t). \qquad (18)$$

Take the total derivative of (18) and assume a solution with a form described in (10). The kinematic interfacial condition in eqs. (16*a*) immediately follows the argument that the displacement should be continuous across the cylindrical interface. The dynamic condition can also be revealed by examining the pressure condition at the interface. Such a condition requires that the total pressure be continuous across the deformed interface, i.e.,

$$P_1(R+\hat{\eta}) = P_2(R+\hat{\eta}). \qquad (19)$$

Subtracting eqs. (17*a*) and (17*b*) from (19) and assuming that all the quantities in the mean flow are bounded and continuous within the interval $[R, R+\hat{\eta}]$, we obtain, within the framework of normal mode analysis, the linearized perturbation condition for the dynamic interfacial balance condition in the radial direction as given in eq. (16*b*).

The procedure to obtain eq. (16*b*) from eq. (19) represents a dissolution of the total pressure force acting at the *perturbed* cylindrical surface of the vortex sheet (Fig. 1(*a*)) into the pressure and centrifugal force components acting at the *steady-state* interface (Fig. 1(*b*)). This procedure of force decomposition clearly demonstrates that the deformation of a cylindrical vortex sheet perturbs both the pressure field and the centrifugal force field created by the rotation of fluids. Equation (16*a*) and (16*b*) are similar to those for radius-dependent rotating flows (Fung, 1983) except the quantities now depend on both the radial and axial coordinates.

It is also interesting to point out that even though the quanities in conditions (16) are values across the cylindrical vortex sheet, the condition in (16*a*) and (16*b*) are quantities interacting with perturbations while the condition in (16*c*) is a result of the pressure balance condition and is independent of the perturbation condition.

For an axial vortex sheet with its steady-state located at $z = Z$, similar conditions can be obtained by integrating eqs. (12) to (14) across the axial vortex sheet in the axial direction. Assuming that all the quantities across the axial interface are bounded and continuous, we obtain

$$\langle \zeta \rangle_z = 0 \qquad (20a)$$

$$\langle p \rangle_z - \langle \rho_o \rangle_z \zeta(Z) = 0 \qquad (20b)$$

$$\langle \rho_o \Omega^2 \rangle_z = 0 \qquad (20c)$$

where $\langle \psi \rangle_z = \psi(Z_{+0}) - \psi(Z_{-0})$ represents a possible jump condition at $z = Z$. Equations (20*a*) and (20*b*) are, respectively, the kinematic and dynamic interfacial conditions for the axial vortex sheet with their physical meaning to be given as follows.

Assume that the axial vortex sheet originally located at the axial location Z is perturbed such that the perturbation surface is described by

$$z = Z + \hat{\zeta}(r,\theta,z;t). \qquad (21)$$

Taking the derivate of eq. (21) with the solution prescribed in eq. (10), one obtains eq. (20*a*) with the argument that no gap is allowed to exist at the perturbed vortex sheet.

The dynamic interfacial condition in Eq. (20*b*) can be obtained by examining the equation of motion in the z-direction. The steady-state total pressure below and above the vortex sheet are, respectively,

$$P_{03}(r,z) = -\int_{Z_o}^{z} \rho_{03}(r,z')g\,dz' \quad (Z_0 \le z < Z) \qquad (22a)$$

$$P_{04}(r,z) = -\int_{Z_o}^{Z} \rho_{04}(r,z')g\,dz' - \int_{Z}^{z} \rho_{04}(r,z')g\,dz' \quad (Z \le z < \infty) \qquad (22b)$$

where the subscripts 3 and 4 represent the quantities in the lower and upper regions divided by the axial vortex sheet, and Z_0 is an arbitrary reference location anywhere within the lower region. If the vortex sheet is perturbed according to eq. (21), the total pressure should be balanced at the perturbed interface such that

$$P_3(Z+\hat{\zeta}) = P_4(Z+\hat{\zeta}). \qquad (23)$$

Assuming all the mean flow quantities are bounded and continuous within the interval $[R, R+\hat{\zeta}]$, we obtain, by subtracting eqs. (22) from eq.(23), the perturbation condition for the dynamic pressure balance at the perturbed interface as the one given in eq. (20*b*). The procedure to obtain eq.(20*b*) from eq.(23) represents another dissolution of the total pressure force acting at the *perturbed* surface of the vortex sheet (Fig. 2(*a*)) into the individual force components acting at the *steady-state* interface (Fig. 2(*b*)). As also shown earlier in the case for the cylindrical vortex sheet, this procedure of force decomposition clearly demonstrates that the perturbation of an axial vortex sheet perturbs not only the pressure field, but also the gravitational force field that interacts with density variations should gravity-stratified fluids be considered. Also similar to the conditions in eqs. (16), both eqs. (20*a*) and (20*b*) depend on perturbation quantities, while eq. (20*c*) does not.

In addition to the kinematic and dynamical conditions that the flow with a cylindrical or an axial vortex sheet has to satisfy, two more conditions as described by eqs. (16*c*) and (20*c*) are

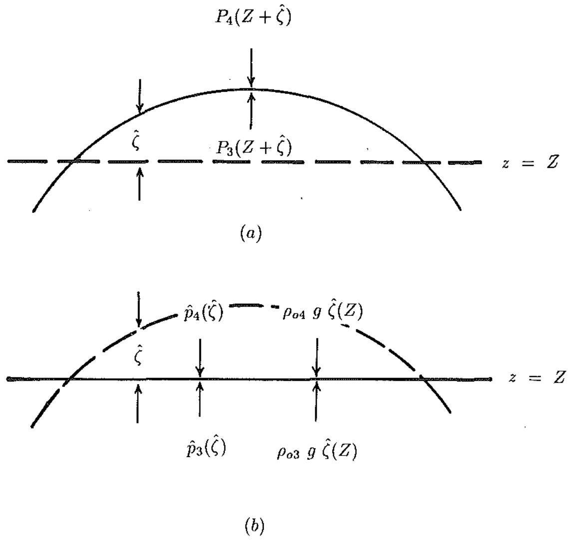

Fig. 2 Decomposition of the total pressure into the force components at the axial interface

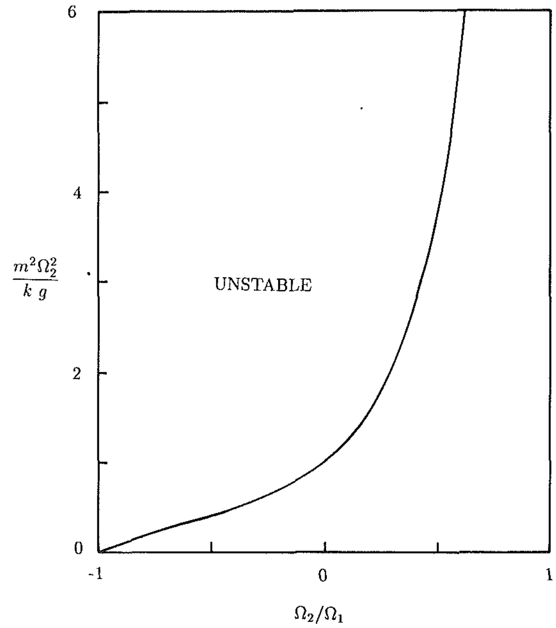

Fig. 3 Stability boundary of the stratified vertical vortex

imposed for vortex motions in a stratified environment. These two conditions are the result of the pressure constraint that dominates the variation of the velocity and density in the flow field. The way such pressure constraint affects the flow characteristics have been examined in the stability analysis of compressible and incompressible vortex motions in stratified fluids (Fung, 1985, 1986). In addition to the stability criteria, the flow has to satisfy in the radial and axial directions and a third criterion has to be imposed as a result of the pressure balance contraint. Contrast to the kinematic and dynamic conditions (16*a*), (16*b*), (20*a*), and (20*b*) that interact with the perturbation displacement and perturbation pressure, neither condition (16*c*) nor condition (20*c*) involves any perturbation quantity in the flow field.

It should be pointed out that eqs. (16) and (20) are kinematic, dynamic, and pressure balance conditions, and are valid for both compressible and incompressible flows.

4 An Analytical Solution

While the stability or instability criteria provide us with some upper-bound information on the flow, they don't yield sufficient information on flow instability, if any, for a particular flow profile until solutions are obtained. Numerical solutions are possible, but sometimes they have difficulty revealing the underlining mechanism. Unfortunately, analytical solutions in terms of well-known functions are difficult to obtain, especially for the flow under consideration. Solutions, if they exist, will have to satisfy the equations in the radial and gravitational directions, and the pressure balance condition that restrains the interaction of the flow quantities in both directions.

To have an insight to the stability mechanism of stratified vortex motions, we select one of the few flow profiles in which analytical solutions exist. Consider a uniformly rotating column vortex to be superimposed on another one with different density and velocity, such that

$$\Omega(r,z)=\Omega_1 \;\; \rho_o(r,z)=\rho_1 \quad \text{for} \quad 0<z<\infty \tag{24}$$

$$\Omega(r,z)=\Omega_2 \;\; \rho_o(r,z)=\rho_2 \quad \text{for} \quad -\infty<z<0. \tag{25}$$

The statically stable density distribution requires that $\rho_1 \le \rho_2$. The solutions of Eqs. (12) to (14) for the flow profile described in Eq. (24) in the upper region are as follows:

$$\eta_1=\frac{1}{\rho_1(N_1^2-4\Omega_1^2)}\left\{A_1\left[\frac{2m\Omega_1}{N_1}+\frac{kq_1rJ_m'(kq_1r)}{J_m(kq_1r)}\right]J_m(kq_1r)\right.$$

$$\left.+B_1\left[\frac{2m\Omega_1}{N_1}+\frac{kq_1rY_m'(kq_1r)}{Y_m(kq_1r)}\right]Y_m(kq_1r)\right\}e^{-kz}, \tag{26a}$$

$$\zeta_1=-\frac{k}{\rho_1N_1^2}\,[A_1J_m(kq_1r)+B_1Y_m(kq_1r)]e^{-kz}, \tag{26b}$$

$$p_1=[A_1J_m(kq_1r)+B_1Y_m(kq_1r)]e^{-kz}. \tag{26c}$$

The solutions for the flow profile described in eq. (25) in the lower region are

$$\eta_2=\frac{1}{\rho_1(N_2^2-4\Omega_2^2)}\left\{A_2\left[\frac{2m\Omega_2}{N_2}+\frac{kq_2rJ_m'(kq^2r)}{J_m(kq_2r)}\right]J_m(kq_2r)\right.$$

$$\left.+B_2\left[\frac{2m\Omega_2}{N_2}+\frac{kq_2rY_m'(kq_2r)}{Y_m(kq_2r}\right]Y_m(kq_2r)\right\}e^{kz}, \tag{27a}$$

$$\zeta_2=\frac{k}{\rho_2N_2^2}\,[A_2J_m(kq_2r)+B_2Y_m(kq_2r)]\,e^{kz}, \tag{27b}$$

$$p_2=[A_2J_m(kq_2r)+B_2Y_m(kq_2r)]\,e^{kz}. \tag{27c}$$

Here, J_m and Y_m are, respectively, the Bessel functions of the first and second kinds of order m. The axial wave number k is assumed to be positive. The subscript 1 and 2 denotes the quantities in the corresponding upper and lower regions. The doppler shifted frequencies are $N_j = m\Omega_j - \omega t$ and $q_j = \sqrt{1-4\Omega_j^2/N_j^2}$ where the subscript $j = 1,2$. The constants A_1, B_1, A_2, and B_2 are to be determined by the interfacial and boundary conditions. The boundary conditions which require the solutions in both regions to be bounded at infinity have been imposed in eqs. (26) and (27). Utilizing the interfacial conditions (20) at $z = 0$ for both upper and lower regions, and requiring that the solutions in both regions to be bounded at the axis, one obtains, after some mathematical maneuvering, the following secular relation that governs the flow stability.

$$(\rho_1+\rho_2)\omega^2-2m(\rho_1\Omega_1+\rho_2\Omega_2)\omega+kg(\rho_1-\rho_2)+m^2(\rho_1\Omega_1^2+\rho_2\Omega_2^2)=0 \tag{28}$$

The vortex will be stable if

$$kg(\rho_2^2-\rho_1^2)-m^2\rho_1\rho_2(\Omega_2-\Omega_1)^2\ge 0. \tag{29}$$

The first term in eq. (29) is simply the gravity stratification effect on stability. It is obvious that the flow will always be unstable for all rotating configurations if $\rho_2 < \rho_1$, a statically unstable density distribution under gravity. For a statically stable density distribution $\rho_2 \geq \rho_1$ as in the present case being considered, positive density difference, reinforced by the axial wave number k, stabilizes the flow as one would normally expect. The angular velocity difference in the second term of eq. (29), however, interacts with the azimuthal wave number and generates rotating shear effects which always destabilize the flow. The flow is especically susceptible to shear instability for large azimuthal wave numbers as one would exect.

While eq. (29) shows that the stability condition is dominated by both the gravitational effect of the density gradient and by the shear effect of the angular velocity gradient, a constraint condition prescribed in eq. (20*c*) also plays a role in the final stability. Apply condition (20*c*) into Eq. (29). The stability condition for the vortex is now

$$1-\left(\frac{\Omega_2}{\Omega_1}\right)^2 \geq \frac{m^2\Omega_2^2}{kg}\left(1-\frac{\Omega_2}{\Omega_1}\right)^2. \qquad (30)$$

The stability boundaries are plotted in Fig. 3 to show how the ratio of the velocities and the wave numbers affect the stability of the flow. While large azimuthal wave numbers reinforcing angular shear tend to destabilize the flow, large axial wave numbers, reinforcing the gravity, stabilizes vortices with an originally stable density distribution. The final stability condition will be determined by the resultant direction of perturbations.

5 Discussion

The interfacial conditions for a cylindrical and an axial vortex sheet are derived for a general class of vortex motions in a radius and gravity-stratified environment. These conditions are valid for both compressible and incompressible flows. No Boussinesq approximation is required. All the flow quantities are allowed to vary in both the radial and axial directions. In addition to the earlier derived kinematic and dynamic conditions required in their respectively radial and axial directions, a third condition resulting from the pressure balance constraint must also be satisfied. Similar requirements were also shown in earlier analyses for the same type of vortex motions (Fung, 1985, 1986). Based on the requirements shown in this paper, fluids with light density can be embedded in an environment with heavier density if the lighter ones have a large angular velocity. This phenomenon is observed in a numerical study on the horizontal vortex in stratified fluids (Fung and Chang, 1991).

The analytical solution obtained for a special kind of flow profile reveals some of the stability characteristics for the stratified vertical vortex. While the centrifugal and gravitational forces have their independent influence on the motion of the vortex, they interact with the wave numbers in their corresponding directions. The azimuthal wave number reinforces the angular shear effect and the axial wave number reinforces the gravity stratification effect. The resultant flow condition will be determined by their final interaction.

References

Fung, Y. T., 1983, "Stability Characteristics for Flows of the Vortex-Sheet Type," *Journal of Fluid Mechanics*, Vol. 135, p. 201.

Fung, Y. T., 1985, "On the Stability of Vortex Motions in Compressible Stratified Fluids," ASME *Journal of Fluids Engineering*, Vol. 107, p. 73.

Fung, Y. T., 1986, "Richardson Criteria for Stratified Vortex Motions under Gravity," *The Physics of Fluids*, Vol. 29, p. 368.

Fung, Y. T., and Chang, S. W., 1991, "Surface and Internal Signatures of Organized Vortex Motions in stratified Fluid—Generation and Evolution of Horizontal Vortices," submitted for publication.

Fung, Y. T., and Kurzweg, U. H., 1975, "Stability of Swirling Flows with Radius-Dependent Density," *Journal of Fluid Mechanics*, Vol. 72, p. 243.

Howard, L. N., 1961, note on a paper of John Miles, *Journal of Fluid Mechanics*, Vol. 10, p. 509.

Lin, J. T., and Pao, Y. H., 1979, "Wakes in Stratified Fluids," *Annual Review of Fluid Mechanics*, Vol. 11, p. 317.

Lugt, H. J., 1989, "Vortex Breakdown in Atmospheric Columnar Vortices," *Bulletin of American Meteorological Society*, Vol. 70, p. 1526.

Miles, J. W., 1961, "On the Stability of Heterogenous Shear Flows," *Journal of Fluid Mechanics*, Vol. 10, p. 496.

Pao, H. P., and Kao, T. W., 1976, "On Vortex Trails over Ocean Islands," *Atmospheric Science* (Meterological Society of the Republic of China), Vol. 3, p. 28.

Pao, H. P., Kao, T. W., 1977, "Vortex structure in the Wake of a Sphere," *The Physics of Fluids*, Vol. 20, p. 187.

Journal of Applied Mechanics

Brief Notes

A Brief Note is a short paper that presents a specific solution of technical interest in mechanics but which does not necessarily contain new general methods or results. A Brief Note should not exceed 1500 words *or equivalent* (a typical one-column figure or table is equivalent to 250 words; a one line equation to 30 words). Brief Notes will be subject to the usual review procedures prior to publication. After approval such Notes will be published as soon as possible. The Notes should be submitted to the Technical Editor of the JOURNAL OF APPLIED MECHANICS. Discussions on the Brief Notes should be addressed to the Editorial Department, ASME, United Engineering Center, 345 East 47th Street, New York, N. Y. 10017, or to the Technical Editor of the JOURNAL OF APPLIED MECHANICS. Discussions on Brief Notes appearing in this issue will be accepted until two months after publication. Readers who need more time to prepare a Discussion should request an extension of the deadline from the Editorial Department.

A Note on the Use of High-Speed Infrared Detectors for the Measurement of Temperature Fields at the Vicinity of Dynamically Growing Cracks in 4340 Steel

Alan T. Zehnder[1,3] and Ares J. Rosakis[2,3]

Introduction

The dissipation of energy, due to plastic deformation, near the tip of a dynamically propagating crack may result in large temperature increases of the material near the crack tip. It is suspected that such temperature increases will strongly affect the nature of the near-tip deformation field and may result in changes of the dynamic fracture toughness of the material. To investigate these effects experimental measurements of the crack-tip temperature distribution were performed using a noncontact system of eight high-speed infrared (IR) detectors focused on eight discrete points perpendicular to the prospective crack path.

Experimental Arrangement

The experiments were performed on wedge loaded, double cantilever beam specimens of 4340 steel with heat treatment and material properties identical to those used by Zehnder and Rosakis (1983). The in-plane specimen dimensions were 15.14 cm × 6.09 cm, the thickness was 1 cm, and the specimen contained an initially blunted notch which was 3.81 cm long. The specimen geometry is shown in Fig. 1.

The temperature field near the tip of the dynamically propagating crack was recorded using a high-speed infrared detector system. This system is similar to the one used by Hartly, Duffy, and Hawley (1987), who studied heat generation during adiabatic shear band formation. This noncontact measurement uses an eight element, linear array of InSb IR detectors to record the time history of temperature increase at eight discrete points on the specimen surface. The points are aligned perpendicularly to the prospective crack path.

Using the system of spherical mirrors, shown in Fig. 2, radiation from the eight points on the specimen is focussed onto the eight IR detector elements with a magnification of one. As shown in Fig. 2, the areas of measurements, both on the specimen and on the IR detector, are eight squares (0.16 mm × 0.16 mm) and the spacing between them is 0.2 mm. The high spatial resolution of the system allows for the measurement of temperature well within the crack-tip plastic zone.

The voltage output of each of the infrared detector elements was separately amplified and recorded on high-speed digital oscilloscopes. The recorded signals were then converted into temperature increase through an experimentally obtained calibration. The rise time of the IR detectors and their amplifiers is $0.75\mu s$, which is safely below the minimum experimentally observed rise time of $2.5\mu s$.

The crack-tip velocity history was simultaneously recorded in the back of the specimen by means of a grid of conductive paint placed perpendicular to the crack path. As the crack runs, the conductive strips are broken and the resistance of the whole grid is increased, providing the time history of the crack motion.

Experimental Results

Figure 3 shows the time record of the temperature measured by each of the eight detector elements as the crack tip approaches and passes through the detection points. Time $t=0$ corresponds to the triggering of the oscilloscopes. For this

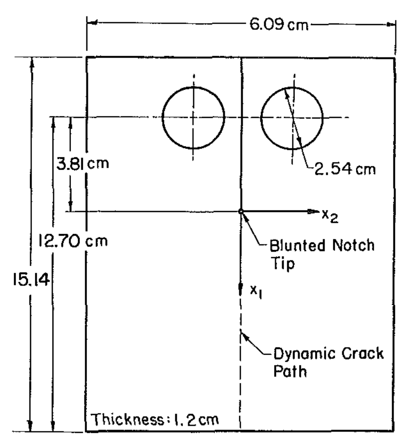

Fig. 1 Specimen geometry

[1]Graduate Aeronautical Laboratories, California Institute of Technology, Pasadena, CA 91125.

[2]Currently at the Department of Theoretical and Applied Mechanics, Cornell University, Ithaca, NY 14853-1503.

[3]Assoc. Mem. ASME.

Contributed by the Applied Mechanics Division of THE AMERICAN SOCIETY OF MECHANICAL ENGINEERS. Manuscript received by the ASME Applied Mechanics Division, Mar. 16, 1989; final revision, Jan. 22, 1990.

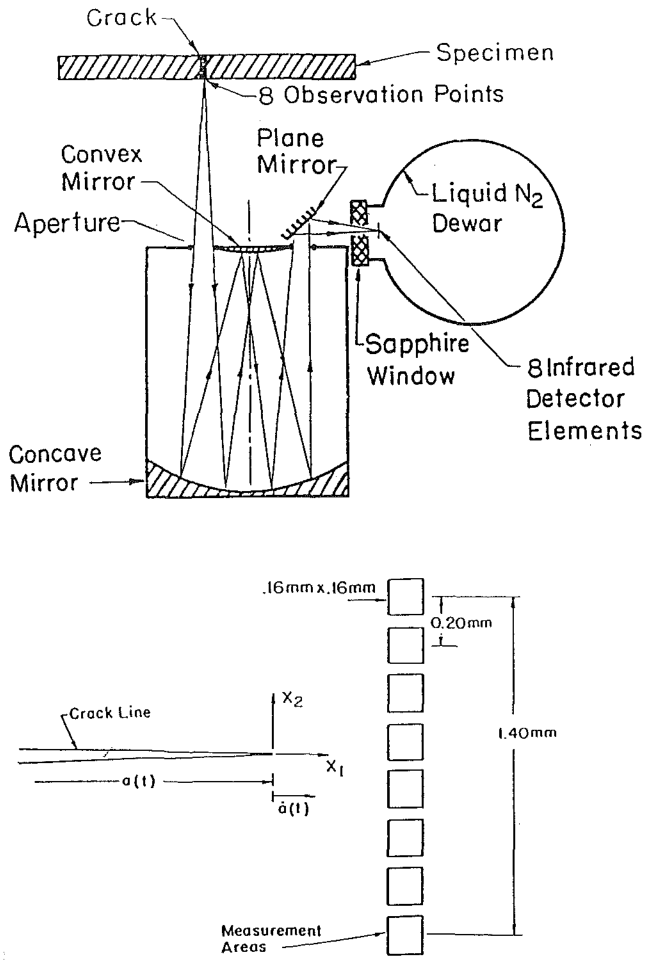

Fig. 2 Schematic of the experimental set-up. The top shows the focusing of radiation onto the infrared detectors. The bottom shows the location of measurement areas relative to crack line.

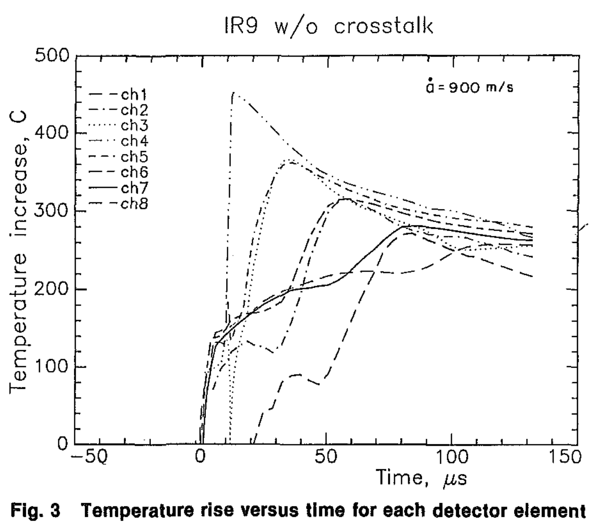

Fig. 3 Temperature rise versus time for each detector element

particular experiment, the crack propagation speed was constant through most of the specimen and equal to approximately 900 m/s. The maximum temperature increase of 450°C was recorded by element 4 (Ch4 in the figure). The minimum rise time of 2.5μs was also recorded by this element. In this experiment, the crack tip traversed the array of detection points slightly off center, but through the region focused on element

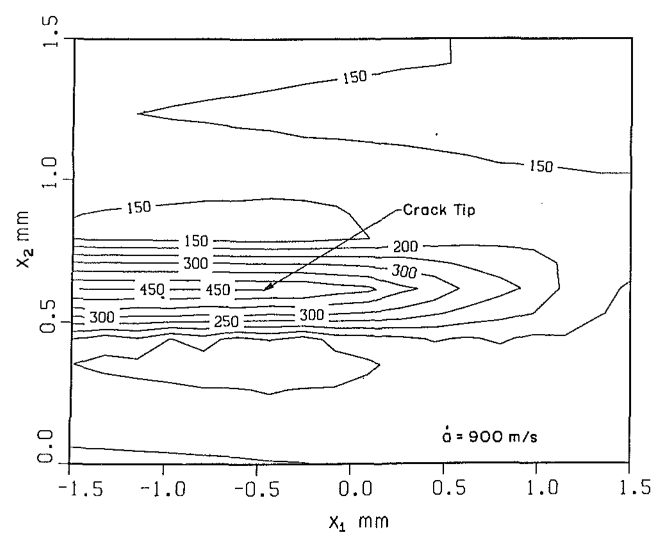

Fig. 4 Contours of equal temperature rise at the vicinity of the propagating crack. Temperature increase is in °C.

4. Thus, as may be expected by symmetry, the elements to the left and right of element 4 (channels 3 and 5) recorded temperatures very similar but not exactly equal to each other. These points also had markedly slower rise times than element 4.

An alternative means of viewing these results is shown in Fig. 4. This figure shows contours of equal temperature in the vicinity of the propagating crack. These were obtained from the temperature versus time results of Fig. 3, by converting the time axis into distance parallel to the direction of crack growth, using the measured crack-tip speed of 900 m/s. Each detector element corresponds to a fixed distance from the crack on a line perpendicular to the direction of crack growth. In this figure, the estimated crack-tip position is $x_1 = -0.5$ mm.

The isotherms of Fig. 4 clearly show that the region of intense heating (temperatures ranging from 450°C–150°C) extends approximately 0.5 mm ahead of the crack tip while the half-width of the resulting wake of temperatures is approximately 0.25 mm. It should be observed that the isotherms in the wake region behind the crack tip remain almost parallel to the crack line for at least 1.5 mm, suggesting that at least *locally*, the deformation remains essentially adiabatic.

An estimate of the size of the region of intense heating relative to the plastic zone size can be obtained by an elementary calculation. The maximum extent of the plane-stress plastic zone radius, is $r_p \approx 0.25\ (K_I^d/\sigma_o)^2$, where K_I^d is the dynamic stress intensity factor and σ_o is the yield stress in uniaxial tension. During crack growth, K_I^d is often assumed to be equal to the dynamic fracture toughness, K_{IC}^d, of the material. For this particular heat treatment of 4340 steel, K_{IC}^d can be inferred from the experimental results of Zehnder and Rosakis (1989) who give its dependence on crack-tip speed. For a speed of 900 m/s, $K_{IC}^d = 130$ MPa $\sqrt{\text{m}}$ which corresponds to $r_p \approx 2$ mm for $\sigma_o = 1450$ MPa. The results show that the region of intense heating is limited to distances roughly equal to $r_p/4$ from the crack tip.

The results presented in this technical note are preliminary. We are now conducting an extensive set of experiments covering a wide range of crack-tip velocities and materials including a variety of ductilities of 4340 steel as well as several titanium alloys.

Acknowledgments

Support of the ONR through contract N00014-85-K-0596 is gratefully acknowledged. The authors would also like to thank Mr. K. Wang for his valuable assistance in these experiments.

References

Hartley, K. A., Duffy, J., and Hawley, R. H., 1987, "Measurement of the Temperature Profile During Shear Band Formation in Steels Deforming at High Strain Rates," *Journal of the Mechanics and Physics of Solids*, Vol. 35, pp. 283–301.

Zehnder, A. T., and Rosakis, A. J., 1989, "Dynamic Fracture Initiation and Propagation in 4340 Steel Under Impact Loading," Caltech Internal Report SM86-6, to appear in *International Journal of Fracture*.

A Note on the Interface Crack Problem

H. Lu[4] and T. J. Lardner[4,5]

Introduction

The use of a complex dislocation density to formulate the governing equations for interface crack problems has provided a convenient encompassing method to obtain stress intensity factors and energy release rates (see Rice (1968), Thouless et al. (1987), Hutchinson et al. (1987), Suo and Hutchinson (1989a, 1989b, 1990), He and Hutchinson (1989), Suo (1989), and Hutchinson and Suo (1991)). The governing equation for the dislocation density is a singular integral equation of the second kind, the solution to which can be obtained numerically, e.g., see Gerasoulis and Vichnevetsky (1984). Jacobi polynomials can be used since they appear as the fundamental solution to the integral equations (Erdogan (1969), Erdogan and Gupta (1971, 1972), and Erdogan et al. (1972)). However, these polynomials are not convenient because the coefficients in the polynomials depend on the material constants; instead Chebyshev polynomials are more suited for numerical work as demonstrated in the works cited previously.

The purpose of this Brief Note is to consider the classical interface crack problem (England (1965) and Rice and Sih (1965))—a crack on a bimaterial interface—with a view to obtaining a number of interesting results for the stress intensity factor when the traction on the crack is expanded in a series of Chebyshev polynomials. We also obtain an interesting result for the stress intensity factor for a crack in a homogeneous material. The basic equations can be found in the references cited.

Formulation

The interface crack is modeled by a dislocation density function along the crack and the equation for the dislocation density following the formulations in the references cited above takes the form

$$\beta i A(u)+\frac{1}{\pi}\int_{-1}^{1}\frac{A(t)}{t-u}\,dt=\frac{\overline{p}(u)}{2\pi},\quad |u|<1 \tag{1}$$

$$\int_{-1}^{1}A(t)dt=0 \tag{2}$$

where $A(t)$ is the dislocation density. Equation (1) is of the second kind arising from the concentrated load in the expression for the traction induced by the dislocations on the interface (see, e.g., Dundurs and Markenscoff (1989) and Hui and Lagoudas (1990)).

The stress intensity factor is related to the dislocation density in the form

$$\overline{K}=(2\pi)^{3/2}\sqrt{1-\beta^2}\lim_{t\to 1^-}A(t)(1-t)^{1/2+i\epsilon}. \tag{3}$$

In the usual approach to the numerical solution of (1) and (2), we assume that the approximate solution can be written in a finite series of N Chebyshev polynomials of the first kind in the form

$$A(t)=\left(\frac{1+t}{1-t}\right)^{i\epsilon}\frac{1}{\sqrt{1-t^2}}\sum_{k=0}^{N}A_kT_k(t)=W(t)\sum_{k=0}^{N}A_kT_k(t). \tag{4}$$

Upon substitution of (4) into (1) and use of the result

$$\int_{-1}^{1}\frac{W(t)T_k(t)}{t-u}\,dt=-\pi\beta i W(u)T_k(u)+\frac{\pi}{\cosh\pi\epsilon}Q_k(u) \tag{5}$$

where $Q_k(t)$ is the principal part of $T_k(t)(t+1)^{-1/2+i\epsilon}(t-1)^{-1/2-i\epsilon}$ at infinity, we find

$$\sum_{k=0}^{N}A_kQ_k(u)=\frac{\cosh\pi\epsilon}{2\pi}\overline{p}(u). \tag{6}$$

The functions $Q_k(u)$ are expressible as linear combinations of Chebyshev polynomials of the second kind U_k and are given in the appendix.

Equation (2), upon integration and upon use of the expressions for Q_k together with a recurrence relation for U_k, leads to

$$A_0+\frac{1}{2}\left\{A_1(4i\epsilon)+A_2(-8\epsilon^2)+A_3\frac{4}{3}i\epsilon(1-8\epsilon^2)+\cdots\right\}=0. \tag{7}$$

The expression for $\overline{K}$ follows from (3) and (4):

$$\overline{K}=\pi^{3/2}2^{1+i\epsilon}\sqrt{1-\beta^2}\sum_{k=0}^{N}A_k. \tag{8}$$

We see that when $\epsilon=0$, $A_0=0$, and (6) becomes

$$\sum_{k=1}^{N}A_kU_{k-1}(u)=\frac{\overline{p}(u)}{2\pi}. \tag{9}$$

Orthogonality of the $U_k(u)$ then gives

$$A_k=\frac{1}{\pi^2}\int_{-1}^{1}\overline{p}(u)\sqrt{1-u^2}U_{k-1}(u)du,\quad k\geq 1 \tag{10}$$

for the coefficients in the solution (4). The expressions for A_k can also be written in the form

$$A_k=\frac{1}{2\pi^2}\int_{-1}^{1}\frac{\overline{p}(u)}{\sqrt{1-u^2}}[T_{k-1}(u)-T_{k+1}(u)]du,\quad k\geq 1 \tag{11}$$

upon use of relations between U_k and T_k.

If the load is expanded in a series of T_k,

$$\overline{p}(u)=\sum_{k=0}^{N-1}a_kT_k(u) \tag{12}$$

where

$$a_0=\frac{1}{\pi}\int_{-1}^{1}\frac{\overline{p}(t)dt}{\sqrt{1-t^2}};\ a_k=\frac{2}{\pi}\int_{-1}^{1}\frac{\overline{p}(t)T_k(t)dt}{\sqrt{1-t^2}},\quad k\geq 1 \tag{13}$$

then the coefficients A_k become

$$A_1=\frac{1}{4\pi}\{2a_0-a_2\}$$

$$A_k=\frac{1}{4\pi}\{a_{k-1}-a_{k+1}\},\quad k=2,\ldots N. \tag{14}$$

It follows therefore that

[4]Department of Civil Engineering, University of Massachusetts, Amherst, MA 01003.

[5]Fellow ASME.

Manuscript received by the ASME Applied Mechanics Division, May 1, 1990; final revision, Jan. 23, 1991.

References

Hartley, K. A., Duffy, J., and Hawley, R. H., 1987, "Measurement of the Temperature Profile During Shear Band Formation in Steels Deforming at High Strain Rates," *Journal of the Mechanics and Physics of Solids*, Vol. 35, pp. 283–301.

Zehnder, A. T., and Rosakis, A. J., 1989, "Dynamic Fracture Initiation and Propagation in 4340 Steel Under Impact Loading," Caltech Internal Report SM86-6, to appear in *International Journal of Fracture*.

A Note on the Interface Crack Problem

H. Lu[4] and T. J. Lardner[4,5]

Introduction

The use of a complex dislocation density to formulate the governing equations for interface crack problems has provided a convenient encompassing method to obtain stress intensity factors and energy release rates (see Rice (1968), Thouless et al. (1987), Hutchinson et al. (1987), Suo and Hutchinson (1989a, 1989b, 1990), He and Hutchinson (1989), Suo (1989), and Hutchinson and Suo (1991)). The governing equation for the dislocation density is a singular integral equation of the second kind, the solution to which can be obtained numerically, e.g., see Gerasoulis and Vichnevetsky (1984). Jacobi polynomials can be used since they appear as the fundamental solution to the integral equations (Erdogan (1969), Erdogan and Gupta (1971, 1972), and Erdogan et al. (1972)). However, these polynomials are not convenient because the coefficients in the polynomials depend on the material constants; instead Chebyshev polynomials are more suited for numerical work as demonstrated in the works cited previously.

The purpose of this Brief Note is to consider the classical interface crack problem (England (1965) and Rice and Sih (1965))—a crack on a bimaterial interface—with a view to obtaining a number of interesting results for the stress intensity factor when the traction on the crack is expanded in a series of Chebyshev polynomials. We also obtain an interesting result for the stress intensity factor for a crack in a homogeneous material. The basic equations can be found in the references cited.

Formulation

The interface crack is modeled by a dislocation density function along the crack and the equation for the dislocation density following the formulations in the references cited above takes the form

$$\beta i A(u)+\frac{1}{\pi}\int_{-1}^{1}\frac{A(t)}{t-u}\,dt=\frac{\overline{p}(u)}{2\pi},\quad |u|<1 \tag{1}$$

$$\int_{-1}^{1}A(t)dt=0 \tag{2}$$

where $A(t)$ is the dislocation density. Equation (1) is of the second kind arising from the concentrated load in the expression for the traction induced by the dislocations on the interface (see, e.g., Dundurs and Markenscoff (1989) and Hui and Lagoudas (1990)).

The stress intensity factor is related to the dislocation density in the form

$$\overline{K}=(2\pi)^{3/2}\sqrt{1-\beta^2}\lim_{t\to 1-}A(t)(1-t)^{1/2+i\epsilon}. \tag{3}$$

In the usual approach to the numerical solution of (1) and (2), we assume that the approximate solution can be written in a finite series of N Chebyshev polynomials of the first kind in the form

$$A(t)=\left(\frac{1+t}{1-t}\right)^{i\epsilon}\frac{1}{\sqrt{1-t^2}}\sum_{k=0}^{N}A_kT_k(t)=W(t)\sum_{k=0}^{N}A_kT_k(t). \tag{4}$$

Upon substitution of (4) into (1) and use of the result

$$\int_{-1}^{1}\frac{W(t)T_k(t)}{t-u}\,dt=-\pi\beta iW(u)T_k(u)+\frac{\pi}{\cosh\pi\epsilon}Q_k(u) \tag{5}$$

where $Q_k(t)$ is the principal part of $T_k(t)(t+1)^{-1/2+i\epsilon}(t-1)^{-1/2-i\epsilon}$ at infinity, we find

$$\sum_{k=0}^{N}A_kQ_k(u)=\frac{\cosh\pi\epsilon}{2\pi}\overline{p}(u). \tag{6}$$

The functions $Q_k(u)$ are expressible as linear combinations of Chebyshev polynomials of the second kind U_k and are given in the appendix.

Equation (2), upon integration and upon use of the expressions for Q_k together with a recurrence relation for U_k, leads to

$$A_0+\frac{1}{2}\left\{A_1(4i\epsilon)+A_2(-8\epsilon^2)+A_3\frac{4}{3}i\epsilon(1-8\epsilon^2)+\cdots\right\}=0. \tag{7}$$

The expression for $\overline{K}$ follows from (3) and (4):

$$\overline{K}=\pi^{3/2}2^{1+i\epsilon}\sqrt{1-\beta^2}\sum_{k=0}^{N}A_k. \tag{8}$$

We see that when $\epsilon=0$, $A_0=0$, and (6) becomes

$$\sum_{k=1}^{N}A_kU_{k-1}(u)=\frac{\overline{p}(u)}{2\pi}. \tag{9}$$

Orthogonality of the $U_k(u)$ then gives

$$A_k=\frac{1}{\pi^2}\int_{-1}^{1}\overline{p}(u)\sqrt{1-u^2}U_{k-1}(u)du,\quad k\geq 1 \tag{10}$$

for the coefficients in the solution (4). The expressions for A_k can also be written in the form

$$A_k=\frac{1}{2\pi^2}\int_{-1}^{1}\frac{\overline{p}(u)}{\sqrt{1-u^2}}[T_{k-1}(u)-T_{k+1}(u)]du,\quad k\geq 1 \tag{11}$$

upon use of relations between U_k and T_k.

If the load is expanded in a series of T_k,

$$\overline{p}(u)=\sum_{k=0}^{N-1}a_kT_k(u) \tag{12}$$

where

$$a_0=\frac{1}{\pi}\int_{-1}^{1}\frac{\overline{p}(t)dt}{\sqrt{1-t^2}};\ a_k=\frac{2}{\pi}\int_{-1}^{1}\frac{\overline{p}(t)T_k(t)dt}{\sqrt{1-t^2}},\quad k\geq 1 \tag{13}$$

then the coefficients A_k become

$$A_1=\frac{1}{4\pi}\{2a_0-a_2\}$$

$$A_k=\frac{1}{4\pi}\{a_{k-1}-a_{k+1}\},\quad k=2,\ldots N. \tag{14}$$

It follows therefore that

[4]Department of Civil Engineering, University of Massachusetts, Amherst, MA 01003.

[5]Fellow ASME.

Manuscript received by the ASME Applied Mechanics Division, May 1, 1990; final revision, Jan. 23, 1991.

$$\overline{K}=2\pi^{3/2}\sum_{k=0}^{N}A_k=\frac{\sqrt{\pi}}{2}\{(2a_0-a_2)+(a_1-a_3)+\cdots+a_{N-1}\}$$

$$=\sqrt{\pi}\left\{a_0+\frac{1}{2}a_1\right\}. \quad (15)$$

Equation (15) shows that the stress intensity factor for a finite crack in an infinite homogeneous medium depends only on the first two coefficients of the expansion of the loading $p(t)$ on the crack surface in Chebyshev polynomials—a result not immediately obvious. We will show how this result can be obtained from the exact solution of (1).

Returning to (6) in the case when $\epsilon \neq 0$, we see that if $\overline{p}(u)$ is expanded as in (12), then the coefficients A_k can be found again from orthogonality of the U_k in the expression for Q_k. The value of A_0 is then obtained from (7). The stress intensity factor then follows from (8) in a series of power of ϵ; we will show the explicit expression below.

It turns out that in this special case we can solve (1) exactly (Muskhelishvili, 1953) to find

$$A(t)=\frac{\overline{p}(t)}{2\pi}\frac{\beta i}{1-\beta^2}-\frac{1}{2\pi^2}\frac{W(t)}{1-\beta^2}\int_{-1}^{1}\frac{\overline{p}(\tau)d\tau}{W(\tau)(\tau-t)}+CW(t). \quad (16)$$

The constant C appearing in (16) is identically zero; this follows from the continuity condition (2) using direct integration.

It follows from (3) and (16) that the stress intensity factor is (in agreement with Rice and Sih (1965) and Suo (1989)),

$$\overline{K}=\frac{\cosh\pi\epsilon}{\sqrt{\pi}}2^{i\epsilon}\int_{-1}^{1}\left(\frac{1-t}{1+t}\right)^{i\epsilon}\frac{1+t}{\sqrt{1-t^2}}\overline{p}(t)dt. \quad (17)$$

The stress intensity factors for two classical interface problems are obtained directly from (17); i.e., (1) when the crack is loaded by a uniform pressure $p(t) = p_0$,

$$\overline{K}=p_0\sqrt{\pi}2^{i\epsilon}(1-2i\epsilon) \quad (18)$$

and (2) when the crack is loaded by a concentrated load $p(t) = p_0\delta(t-c)$,

$$\overline{K}=\frac{p_0}{\sqrt{\pi}}2^{i\epsilon}\cosh\pi\epsilon\left(\frac{1+c}{1-c}\right)^{i\epsilon}\left(\frac{1+c}{1-c}\right)^{1/2}. \quad (19)$$

In the general case, the loading $p(t)$ can be expanded in a series of Chebyshev polynomials of the first kind as in (12). When $\epsilon = 0$, Eq. (17) becomes

$$\overline{K}=\frac{1}{\sqrt{\pi}}\int_{-1}^{1}\frac{1+t}{\sqrt{1-t^2}}p(t)dt. \quad (20)$$

We note that $1/\sqrt{1-t^2}$ in (20) is the weight function of the Chebyshev polynomials of the first kind and $T_0(t) = 1$, $T_1(t) = t$. It follows that if the arbitrary loading is in the form (12), Eq. (20) becomes

$$\overline{K}=\frac{1}{\sqrt{\pi}}\sum_{k=0}^{N}a_k\int_{-1}^{1}\frac{T_0(t)+T_1(t)}{\sqrt{1-t^2}}T_k(t)dt \quad (21)$$

and by the orthogonality property of the Chebyshev polynomials we find, as before,

$$\overline{K}=\sqrt{\pi}\left(a_0+\frac{1}{2}a_1\right). \quad (22)$$

For the bimaterial case, $\epsilon \neq 0$, when we substitute (12) into (16) and carry out the integration, we find

$$A(t)=\frac{\cosh\pi\epsilon}{2\pi}W(t)\sum_{k=0}^{N-1}a_k\tilde{Q}_k(t) \quad (23)$$

where the $\tilde{Q}_k(t)$ is the principal part of $T_k(t)(t-1)^{1/2+i\epsilon}(t+1)^{1/2-i\epsilon}$ at infinity.

The stress intensity factor then becomes

$$\overline{K}=\sqrt{\pi}\,2^{i\epsilon}\sum_{k=0}^{N-1}a_k\tilde{Q}_k(1). \quad (24)$$

The expressions for the $\tilde{Q}_k(t)$ are given in the Appendix. We note that when $\epsilon = 0$, the $\tilde{Q}_k(t)$ reduce to simple linear combinations of the Chebyshev polynomials of the second kind $U_k(t)$, and that $\tilde{Q}_k(1) = 0$, $k \geq 2$.

It follows from (24) and the expressions for $\tilde{Q}_k(1)$ that the expression for the stress intensity factor when $\epsilon \neq 0$ can be expressed as follows:

$$\overline{K}=\sqrt{\pi}2_{i\epsilon}\left\{a_0+\frac{1}{2}a_1-2i\epsilon\left[a_0+a_1+\frac{2}{3}a_2+\frac{1}{3}a_4+\ldots\right]-2\epsilon^2\left[a_1+2a_2+\frac{5}{3}a_4+\ldots\right]+\ldots\right\} \quad (25)$$

where the additional terms can be easily obtained.

We rewrite (25) in the form

$$\overline{K}=2^{i\epsilon}\{\overline{K}_0+\sqrt{\pi}o(\epsilon)\}. \quad (26)$$

We see that the correction to the homogeneous stress intensity factor is of order ϵ, that the $2^{i\epsilon}$ appears naturally as a multiplicative factor, and that the explicit expression to any order in ϵ for the stress intensity factor can be written down once the coefficients a_k are found.

Acknowledgment

Part of this work has been supported by the Institute for Interface Science at the University of Massachusetts funded in part by IBM.

References

Dundurs, J., and Markenscoff, X., 1989, "A Green's Function Formulation of Anticracks and Their Interaction With Load-Induced Singularities," ASME Journal of Applied Mechanics, Vol. 56, pp. 550–555.

England, A. H., 1965, "A Crack Between Dissimilar Media," ASME Journal of Applied Mechanics, Vol. 32, pp. 400–402.

Erdogan, F., 1969, "Approximate Solution of Singular Integral Equations," *SIAM J. Appl. Math.*, Vol. 17, pp. 1041–1059.

Erdogan, F., and Gupta, G. D., 1971, "Layered Composites with an Interface Flaw," *Int. J. Solids Structures*, Vol. 7, pp. 1089–1107.

Erdogan, F., and Gupta, G. D., 1972, "On the Numerical Solution of Singular Integral Equations," *Quart. Appl. Math.*, Vol. 30, pp. 525–534.

Erdogan, F., Gupta, G. D., and Cook, T. S., 1972, "Numerical Solution of Singular Integral Equations," *Methods of Analysis and Solutions of Crack Problems*, G. C. Sih, ed., Vol. 1, Noordhoff Int. Pub., pp. 368–425.

Gerasoulis, A., and Vichnevetsky, R., 1984, "Numerical Solution of Singular Integral Equations," IMACS Symposium, Dept. of Computer Science, Rutgers University, New Jersey.

He, M. Y., and Hutchinson, J. W., 1989, "Kinking of a Crack out of an Interface," ASME Journal of Applied Mechanics, Vol. 56, pp. 270–278.

Hui, C.-Y., and Lagoudas, D. C., 1990, "Stress Fields of Interface Dislocations," ASME Journal of Applied Mechanics, Vol. 57, pp. 247–248.

Hutchinson, J. W., Mear, M. E., and Rice, J. R., 1987, "Crack Paralleling an Interface Between Dissimilar Materials," ASME Journal of Applied Mechanics, Vol. 54, pp. 828–832.

Hutchinson, J. W., and Suo, Z., 1991, "Mixed Mode Cracking in Layered Materials," *Advances in Applied Mechanics*, Vol. 28, J. W. Hutchinson and T. Y. Wu, eds.

Muskhelishvili, N. I., 1953, *Some Basic Problems of the Mathematical Theory of Elasticity*, Noordhoff, Holland.

Rice, J. R., and Sih, G. C., 1965, "Plane Problems of Cracks in Dissimilar Media," ASME Journal of Applied Mechanics, Vol. 32, 418–423.

Rice, J., 1968, "Mathematical Analysis in the Mechanics of Fracture," *Fracture: An Advanced Treatise*, Vol. 2, H. Liebowitz, ed., Academic Press, New York.

Suo, Z., 1989, "Singularities Interacting with Interfaces and Cracks—I. Isotropic Materials," *Int. J. Solids Structures*, Vol. 25, pp. 1133–1142.

Suo, Z., and Hutchinson, J. W., 1989a, "Steady-State Cracking in Brittle Substrates Beneath Adherent Films," *Int. J. Solids Structures*, Vol. 25, pp. 1337–1353.

Suo, Z., and Hutchinson, J. W., 1989b, "Sandwich Specimens For Measuring Interface Crack Toughness," *I. Mater. Sci. Eng.*, Vol. A107, pp. 135–143.

Suo, Z., and Hutchinson, J. W., 1990, "Interface Crack Between Two Elastic Layers," *Int. J. Fracture*, Vol. 43, pp. 1–18.
Thouless, M. D., Evans, A. G., Ashby, M. F., and Hutchinson, J. W., 1987, "The Edge Cracking and Spalling of Brittle Plates," *Acta Met.*, Vol. 35, pp. 1333–1341.

APPENDIX

The $Q_k(t)$ in (5) are the principal part of $T_k(t)(t-1)^{-1/2-i\epsilon}(t+1)^{-1/2+i\epsilon}$ at infinity. They are of the form

$$Q_0(t)=0;\ Q_k(t)=\sum_{n=0}^{k-1}\hat{A}_nU_{k-1-n};\quad k\geq 1$$

where the first ten coefficients are

$$\hat{A}_0=1$$
$$\hat{A}_1=4i\epsilon$$
$$\hat{A}_2=-8\epsilon^2$$
$$\hat{A}_3=-\frac{4}{3}i\epsilon(8\epsilon^2-1)$$
$$\hat{A}_4=\frac{16}{3}\epsilon^2(2\epsilon^2-1)$$
$$\hat{A}_5=\frac{4}{15}i\epsilon(32\epsilon^4-40\epsilon^2+3)$$
$$\hat{A}_6=-\frac{8}{45}\epsilon^2(32\epsilon^4-80\epsilon^2+23)$$
$$\hat{A}_7=-\frac{4}{315}i\epsilon(256\epsilon^6-1120\epsilon^4+784\epsilon^2-45)$$
$$\hat{A}_8=\frac{32}{315}\epsilon^2(16\epsilon^6-112\epsilon^4+154\epsilon^2-33)$$
$$\hat{A}_9=\frac{4}{2835}i\epsilon(512\epsilon^8-5376\epsilon^6+12768\epsilon^4-6544\epsilon^2+315).$$

The $\tilde{Q}_k(t)$ in (23) are the principal part of $T_k(t)(t-1)^{1/2+i\epsilon}(t+1)^{1/2-i\epsilon}$ at infinity. They are of the form

$$\tilde{Q}_0(t)=\frac{1}{2}U_1(t)-2i\epsilon$$
$$\tilde{Q}_1(t)=\frac{1}{4}U_2(t)-i\epsilon U_1(t)-\frac{1}{4}(8\epsilon^2+1)$$

and

$$\tilde{Q}_k(t)=\sum_{n=0}^{k+1}\tilde{A}_nU_{k+1-n};\quad k\geq 2$$

where the first ten coefficients are

$$\tilde{A}_0=\frac{1}{4}$$
$$\tilde{A}_1=-i\epsilon$$
$$\tilde{A}_2=-\frac{1}{2}(4\epsilon^2+1)$$
$$\tilde{A}_3=\frac{1}{3}i\epsilon(8\epsilon^2+5)$$
$$\tilde{A}_4=\frac{1}{12}(32\epsilon^4+32\epsilon^2+3)$$
$$\tilde{A}_5=-\frac{8}{15}i\epsilon(4\epsilon^4+5\epsilon^2+1)$$
$$\tilde{A}_6=-\frac{16}{45}\epsilon^2(4\epsilon^4+5\epsilon^2+1)$$
$$\tilde{A}_7=\frac{8}{315}i\epsilon(32\epsilon^6+28\epsilon^4-7\epsilon^2-3)$$
$$\tilde{A}_8=\frac{8}{315}\epsilon^2(16\epsilon^6-21\epsilon^2-5)$$
$$\tilde{A}_9=-\frac{8}{2835}i\epsilon(64\epsilon^8-96\epsilon^6-168\epsilon^4+\epsilon^2+9).$$

Symmetrizable Systems in Mechanics and Control Theory

W. R. Kliem[6]

Stability investigations of nonconservative systems $M\ddot{X}+B\dot{X}+CX=0$ *in mechanics and control theory become substantially easier if the coefficient matrices* B *and* C *are either both real symmetric or both complex symmetric. It is therefore of interest to give conditions under which, by means of a similarity transformation, a system may be converted into one of these forms. We discuss the following questions: Are such systems robust with respect to perturbations in the entries of the coefficient matrices? Do relevant applications exist?*

Introduction

Systems of linear differential equations of the form

$$M\ddot{X}+B\dot{X}+CX=0 \tag{1}$$

play an important role as mathematical models of mechanical systems. The vector X represents the generalized coordinates and the mass matrix M is assumed to be real symmetric and nonsingular. In the general *nonconservative* case, B and C are square matrices but otherwise arbitrary.

In the control of mechanical systems by position feedback, the matrix C can be written as $K+\gamma H$, where the stiffness matrix K is symmetric. H reflects the locations of sensors and actuators and is in general not symmetric. γ denotes a single gain variable.

Although, many papers deal with the *stability* of nonconservative systems, there is still a lack of practical stability results. A number of existing theorems only give sufficient conditions (e.g., Frik, 1972; Kliem and Pommer, 1986; Ahmadian and Inman, 1986) and often lead to poor stability limits. Another class of results like the classical algebraic and geometric criteria of Routh-Hurwitz and Liénard-Chipart are rather cumbersome.

This difficulty exists only for the most general nonconservative case. Stability investigations become substantially easier if the system matrices B and C are either both real symmetric or both complex symmetric, i.e., $a_{ij}=a_{ji}$ rather than $a_{ij}=\overline{a}_{ji}$ (Hermitian).

Especially the stability of the real symmetric case, which is the most important for applications, is well understood (see, e.g., Huseyin, 1978). A more general theory for both B and C being normal matrices includes this case (Pommer and Kleim, 1987), but shall not be dealt with here, since applications are fairly rare.

Consequently, it is of some interest to investigate whether, by means of a similarity transformation (which preserves the eigenvalues), a nonconservative system (1) can be brought into a form belonging to one of the two symmetric cases mentioned above. Then the system is called *real symmetrizable* or *complex symmetrizable*, respectively. In both cases it is a matter of a

[6]Mathematical Institute, The Technical University of Denmark, DK-2800 Lyngby, Denmark.

Manuscript received by the ASME Applied Mechanics Division, July 11, 1990; final revision, Dec. 18, 1990.

Suo, Z., and Hutchinson, J. W., 1990, "Interface Crack Between Two Elastic Layers," *Int. J. Fracture*, Vol. 43, pp. 1–18.
Thouless, M. D., Evans, A. G., Ashby, M. F., and Hutchinson, J. W., 1987, "The Edge Cracking and Spalling of Brittle Plates," *Acta Met.*, Vol. 35, pp. 1333–1341.

APPENDIX

The $Q_k(t)$ in (5) are the principal part of $T_k(t)(t-1)^{-1/2-i\epsilon}(t+1)^{-1/2+i\epsilon}$ at infinity. They are of the form

$$Q_0(t)=0;\ Q_k(t)=\sum_{n=0}^{k-1}\hat{A}_n U_{k-1-n};\quad k\geq 1$$

where the first ten coefficients are

$$\hat{A}_0=1$$

$$\hat{A}_1=4i\epsilon$$

$$\hat{A}_2=-8\epsilon^2$$

$$\hat{A}_3=-\frac{4}{3}\,i\epsilon(8\epsilon^2-1)$$

$$\hat{A}_4=\frac{16}{3}\,\epsilon^2(2\epsilon^2-1)$$

$$\hat{A}_5=\frac{4}{15}\,i\epsilon(32\epsilon^4-40\epsilon^2+3)$$

$$\hat{A}_6=-\frac{8}{45}\,\epsilon^2(32\epsilon^4-80\epsilon^2+23)$$

$$\hat{A}_7=-\frac{4}{315}\,i\epsilon(256\epsilon^6-1120\epsilon^4+784\epsilon^2-45)$$

$$\hat{A}_8=\frac{32}{315}\,\epsilon^2(16\epsilon^6-112\epsilon^4+154\epsilon^2-33)$$

$$\hat{A}_9=\frac{4}{2835}\,i\epsilon(512\epsilon^8-5376\epsilon^6+12768\epsilon^4-6544\epsilon^2+315).$$

The $\tilde{Q}_k(t)$ in (23) are the principal part of $T_k(t)(t-1)^{1/2+i\epsilon}(t+1)^{1/2-i\epsilon}$ at infinity. They are of the form

$$\tilde{Q}_0(t)=\frac{1}{2}\,U_1(t)-2i\epsilon$$

$$\tilde{Q}_1(t)=\frac{1}{4}\,U_2(t)-i\epsilon U_1(t)-\frac{1}{4}\,(8\epsilon^2+1)$$

and

$$\tilde{Q}_k(t)=\sum_{n=0}^{k+1}\tilde{A}_n U_{k+1-n};\quad k\geq 2$$

where the first ten coefficients are

$$\tilde{A}_0=\frac{1}{4}$$

$$\tilde{A}_1=-i\epsilon$$

$$\tilde{A}_2=-\frac{1}{2}\,(4\epsilon^2+1)$$

$$\tilde{A}_3=\frac{1}{3}\,i\epsilon(8\epsilon^2+5)$$

$$\tilde{A}_4=\frac{1}{12}\,(32\epsilon^4+32\epsilon^2+3)$$

$$\tilde{A}_5=-\frac{8}{15}\,i\epsilon(4\epsilon^4+5\epsilon^2+1)$$

$$\tilde{A}_6=-\frac{16}{45}\,\epsilon^2(4\epsilon^4+5\epsilon^2+1)$$

$$\tilde{A}_7=\frac{8}{315}\,i\epsilon(32\epsilon^6+28\epsilon^4-7\epsilon^2-3)$$

$$\tilde{A}_8=\frac{8}{315}\,\epsilon^2(16\epsilon^6-21\epsilon^2-5)$$

$$\tilde{A}_9=-\frac{8}{2835}\,i\epsilon(64\epsilon^8-96\epsilon^6-168\epsilon^4+\epsilon^2+9).$$

Symmetrizable Systems in Mechanics and Control Theory

W. R. Kliem[6]

Stability investigations of nonconservative systems $\mathrm{M}\ddot{\mathrm{X}}+\mathrm{B}\dot{\mathrm{X}}+\mathrm{CX}=0$ *in mechanics and control theory become substantially easier if the coefficient matrices* B *and* C *are either both real symmetric or both complex symmetric. It is therefore of interest to give conditions under which, by means of a similarity transformation, a system may be converted into one of these forms. We discuss the following questions: Are such systems robust with respect to perturbations in the entries of the coefficient matrices? Do relevant applications exist?*

Introduction

Systems of linear differential equations of the form

$$M\ddot{X}+B\dot{X}+CX=0 \tag{1}$$

play an important role as mathematical models of mechanical systems. The vector X represents the generalized coordinates and the mass matrix M is assumed to be real symmetric and nonsingular. In the general *nonconservative* case, B and C are square matrices but otherwise arbitrary.

In the control of mechanical systems by position feedback, the matrix C can be written as $K+\gamma H$, where the stiffness matrix K is symmetric. H reflects the locations of sensors and actuators and is in general not symmetric. γ denotes a single gain variable.

Although, many papers deal with the *stability* of nonconservative systems, there is still a lack of practical stability results. A number of existing theorems only give sufficient conditions (e.g., Frik, 1972; Kliem and Pommer, 1986; Ahmadian and Inman, 1986) and often lead to poor stability limits. Another class of results like the classical algebraic and geometric criteria of Routh-Hurwitz and Liénard-Chipart are rather cumbersome.

This difficulty exists only for the most general nonconservative case. Stability investigations become substantially easier if the system matrices B and C are either both real symmetric or both complex symmetric, i.e., $a_{ij}=a_{ji}$ rather than $a_{ij}=\bar{a}_{ji}$ (Hermitian).

Especially the stability of the real symmetric case, which is the most important for applications, is well understood (see, e.g., Huseyin, 1978). A more general theory for both B and C being normal matrices includes this case (Pommer and Kleim, 1987), but shall not be dealt with here, since applications are fairly rare.

Consequently, it is of some interest to investigate whether, by means of a similarity transformation (which preserves the eigenvalues), a nonconservative system (1) can be brought into a form belonging to one of the two symmetric cases mentioned above. Then the system is called *real symmetrizable* or *complex symmetrizable*, respectively. In both cases it is a matter of a

[6]Mathematical Institute, The Technical University of Denmark, DK-2800 Lyngby, Denmark.

Manuscript received by the ASME Applied Mechanics Division, July 11, 1990; final revision, Dec. 18, 1990.

simultaneous transformation $W^{-1}BW$ and $W^{-1}CW$. With only little loss of generality M is assumed to be a unit matrix I.

We want to discuss the following questions: What are the *conditions* for system (1) to be symmetrizable? How *robust* is this property with respect to perturbations in the entries of the coefficient matrices? Do relevant *applications* exist?

Results

Inman (1983) was the first to give a condition for a system to be real symmetrizable. But his condition is difficult to check and therefore new conditions were given by Pommer and Kliem (1987). Recently, Inman and Olsen (1988) extended the symmetrizable case to linear operators. The complex symmetrizable case has to our knowledge not been dealt with in the literature.

A main result is the following:

Theorem 1: *The real matrices* B *and* C *are simultaneously real symmetrizable if and only if there exist modal matrices* T_B *and* T_C *(consisting of full eigenvector sets of* B *and* C*), such that* $T_B^{-1}T_C$ *is orthogonal, or equivalently,* $T_BT_B^T = T_CT_C^T$.

The proof can be found in Pommer and Kliem (1987) and is based on the fact that all transformation matrices W can be written as product of a modal matrix and a unitary matrix. This fact is also useful when constructing a transformation matrix W, but this does not seem to be well known (see, e.g., Piché, 1990).

The condition (including proof) for B and C to be *simultaneously complex symmetrizable* is the same as in Theorem 1. Notice that all matrices might be complex in this case. Then $T_B^{-1}T_C$ "complex orthogonal" does not mean "unitary," but $(T_B^{-1}T_C)^{-1} = (T_B^{-1}T_C)^T$ as for real matrices.

The check of the condition in Theorem 1 is rather easy if we have a computer program to our disposal which can compute modal matrices (see Pommer and Kliem, 1987). For the matrix order $n = 2$, a geometric interpretation of Theorem 1 might be useful:

Theorem 2: B *and* C *are simultaneously real symmetrizable if and only if (1) we can choose* $T_B = T_C$ *or 2) the eigenvectors of* B *and* C *can be chosen interweaved in the plane such that an eigenvector of* B *alternate with an eigenvector of* C*, etc.,* ($b_1 = e^{i\theta_1}$, $c_1 = e^{i\varphi_1}$, $b_2 = e^{i\theta_2}$, $c_2 = e^{i\varphi_2}$ *with* $\theta_1 < \varphi_1 < \theta_2 < \varphi_2$).

So for $n = 2$, many matrix pairs (B, C) will be simultaneously real symmetrizable, and this property will in general be robust with respect to perturbations.

In the rest of this section we will confine ourselves to the *real* symmetrizable case; but practically all the statements made also hold for the complex case.

For matrix orders $n > 2$, a geometric interpretation of Theorem 1 is rather complicated. Then the condition imposes severe requirements on the modal matrices, which will be satisfied in few applications only. And if the condition is satisfied, small changes in the matrix entries will normally destroy this property: for $n > 2$, symmetrizable systems are *not* robust with respect to perturbations in the coefficient matrices.

This pessimistic statement is in force in regard to modeling when the matrices B and C do not have rather pathological forms. There is, though, one useful exception, namely if one of the matrices is structurally diagonal.

Theorem 3: *If* B *is any diagonal matrix and* C *is symmetrizable by a diagonal transformation matrix, then* B *and* C *are simultaneously symmetrizable.*

The proof is straightforward.

Theorem 4: *(Piché, 1990): If* B *is diagonal with nonzero and distinct entries in the diagonal,* C *is arbitrary, and* B *and* C *are simultaneously symmetrizable, then simultaneous symmetry can be achieved by a diagonal transformation matrix.*

Applications in Mechanics and Control

(1) A double pendulum is subjected to a follower force P, acting on the free end (Hermann and Jong, 1965). For certain choices of the parameters we get Eq. (1) with $M = I$ and

$$B=\begin{Bmatrix} 2 & -1 \\ -3 & 2 \end{Bmatrix}, C=\begin{Bmatrix} -P+3 & P-2 \\ P-5 & -P+4 \end{Bmatrix}. \tag{2}$$

Here, B and C are simultaneously real symmetrizable for the whole range $0 \le P \le 1.36$, according to Theorem 2, and the system can easily be shown to be stable.

For $P > 1.36$ the system is not symmetrizable any more and for some critical value of P, the system will become unstable by flutter.

(2) Pflüger's column is a simply supported undamped oscillating bar, affected by distributed tangential forces (e.g., Huseyin, 1978). To give an example of a real symmetrizable system in the case $n > 2$, we add a damping force proportional to the velocity. The governing differential equation can, by Galerkins method, be converted to an eigenvalue problem:

$$(\lambda^2 I + \lambda k I + C)u = 0 \tag{3}$$

where k is the coefficient of damping.

The matrix order n of I and C is equal to the number of chosen mode functions. C is nonsymmetric but real symmetrizable by a diagonal transformation matrix W. Since $B = kI$ is also symmetric, B and C are simultaneously symmetrizable according to Theorem 3. Thus, stability is lost by buckling when $\det C = 0$.

(3) Piché (1990) deals with the system

$$I\ddot{X} + B\dot{X} + CX = -\gamma HX, \tag{4}$$

occurring in active control by position feedback. If we assume modal coordinates X and modal damping, B and C are both diagonal. But the control input matrix H is in general not symmetric. However, it is advantageous if Eq. (4) is real symmetrizable; hence, it is natural to ask when this is the case. The answer is given by Piché (1990), here slightly improved:

Theorem 5: *System (4) with* $B = diag\,\{b_i\}$ *and* $C = diag\{\omega_i^2\}$ *is assumed to have either all* b_i*s distinct or all* ω_i^2*s distinct. Then system (4) is real symmetrizable if and only if* H *is symmetrizable by a diagonal transformation matrix.*

The proof is immediately established by Theorems 3 and 4.

(4) In the dynamics of symmetric rotor systems, the mathematical model for small vibrations is usually written as (Müller (1981)):

$$M\ddot{Z} + (D_1 + D_2 + i\Omega G)\dot{Z} + (K + i\Omega D_2)Z = 0 \tag{5}$$

with all system matrices M, D_1 (external damping), D_2 (internal damping), and G and K symmetric and positive semidefinite. Ω is the angular velocity. Then both $B = D_1 + D_2 + i\Omega G$ and $C = K + i\Omega D_2$ are already complex symmetric. But sometimes the system is not provided in this desirable form, as in the following example given by Pfützner (1972):

For a certain rotor, clamped in one end, the oscillations are modeled by

$$\begin{Bmatrix} 8 & 0 \\ 0 & 0.08 \end{Bmatrix} \begin{Bmatrix} \ddot{r} \\ \ddot{\varphi} \end{Bmatrix} + \begin{Bmatrix} 2 & 0 \\ 0 & 0.2 + i0.16\Omega \end{Bmatrix} \begin{Bmatrix} \dot{r} \\ \dot{\varphi} \end{Bmatrix} + \begin{Bmatrix} 12.54 \cdot 10^6 + i\Omega & i1.25 \cdot 10^6 \\ -i1.25 \cdot 10^6 & 0.17 \cdot 10^6 + i0.1\Omega \end{Bmatrix} \begin{Bmatrix} r \\ \varphi \end{Bmatrix} = \begin{Bmatrix} 0 \\ 0 \end{Bmatrix}. \tag{6}$$

Here, the matrix C is not complex symmetric. But the system is complex symmetrizable and can be transformed into

$$\begin{Bmatrix} 1 & 0 \\ 0 & 1 \end{Bmatrix} \ddot{q} + \begin{Bmatrix} 0.25 & 0 \\ 0 & 2.5 + i2\Omega \end{Bmatrix} \dot{q} + \begin{Bmatrix} 1.57 \cdot 10^6 + i0.125\Omega & 1.56 \cdot 10^6 \\ 1.56 \cdot 10^6 & 2.13 \cdot 10^6 + i1.25\Omega \end{Bmatrix} q = 0 \tag{7}$$

with the possibility to find a better stability limit for Ω using a criterion of Frik (1972).

Conclusions

Real and complex symmetrizable systems are not robust with respect to perturbations in the entries of the coefficient matrices. So, from a modeling point of view, such systems will only have limited practical importance.

Exceptions are real symmetrizable systems with matrix order $n = 2$ (Theorem 2) and real and complex symmetrizable systems with any matrix order n, if special diagonality conditions are fulfilled (Theorem 3 and 4).

References

Ahmadian, M., and Inman, D. J., 1986, "Some Stability Results for General Linear Lumped-Parameter Dynamic Systems," ASME Journal of Applied Mechanics, Vol. 53, pp. 10–14.

Frik, M., 1972, "Zur Stabilität nichtkonservativer linearer Systeme," *ZAMM* Vol. 52, pp. T47–T49.

Herrmann, G., and Jong, I.-C., 1965, "On the Destabilizing Effect of Damping in Nonconservative Elastic Systems," ASME Journal of Applied Mechanics, Vol. 32, pp. 592–597.

Huseyin, K., 1978, *Vibrations and Stability of Multiple Parameter Systems*, Sijthoff and Noordhoff, Alpen aan den Rijn, The Netherlands.

Inman, D. J., 1983, "Dynamics of Asymmetric Nonconservative Systems," ASME Journal of Applied Mechanics, Vol. 50, pp. 199–203.

Inman, D. J., and Olsen, C. L., 1988, "Dynamics of Symmetrizable Nonconservative Systems," ASME Journal of Applied Mechanics, Vol. 55, pp. 206–212.

Kliem, W., and Pommer, C., 1986, "On the Stability of Linear Nonconservative Systems," *Quart. Appl. Math.*, Vol. 43, No. 4, pp. 457–461.

Müller, P. C., 1981, "Allgemeine lineare Theorie für Rotorsysteme ohne oder mit kleinen Unsymmetrien," *Ingenieur-Archiv*, Vol. 51, pp. 61–74.

Pfützner, H., 1976, "Zur Stabilität der Laval-Welle mit innerer und äusserer Dämpfung unter Berücksichtigung der Kreiselwirkung der Rotormasse" *Forsch. Ing.-Wes.*, Vol. 42, No. 4, pp. 130–135.

Piché, R., 1990, "On the Symmetrizability of Structural Control Systems with Noncolocated Sensors and Actuators," ASME *Journal of Dynamic Systems, Measurement, and Control*, Vol. 112, pp. 249–252.

Pommer, C., and Kliem, W., 1987, "Simultaneously Normalizable Matrices," *Linear Algebra and its Applications*, Vol. 94, pp. 113–125.

Determination of the Angular Velocity Vector in Orthogonal Curvilinear Coordinate Systems

D. L. Richardson[7]

An efficient, general procedure is developed for assembling the components of the angular velocity vector of orthogonal curvilinear coordinate frames.

Introduction

Consider a reference frame $\mathfrak{F}$ and a relative motion frame $\mathfrak{R}$ whose orientation is defined relative to $\mathfrak{F}$. Let (q_1, q_2, q_3) be the coordinate triad associated with $\mathfrak{R}$, and let $\mathbf{r}$ be the position of any point P in $\mathfrak{F}$. Assume that $\mathbf{r}$ can be expressed unambiguously in terms of the q_i. We have

$$\mathbf{r} \equiv \mathbf{r}(q_1, q_2, q_3),$$

and consequently,

$$d\mathbf{r} = \frac{\partial \mathbf{r}}{\partial q_1} dq_1 + \frac{\partial \mathbf{r}}{\partial q_2} dq_2 + \frac{\partial \mathbf{r}}{\partial q_3} dq_3. \tag{1}$$

[7]Department of Aerospace Engineering and Engineering Mechanics, University of Cincinnati, Cincinnati, OH 45221-0070.

Manuscript received by the ASME Applied Mechanics Division, 10/16/90; final revision, Dec. 5, 1990.

From here, define the curvilinear unit-vector basis triad $(\mathbf{e}_1, \mathbf{e}_2, \mathbf{e}_3)$ through the relation

$$\frac{\partial \mathbf{r}}{\partial q_i} = h_i \mathbf{e}_i. \tag{2}$$

Require that these unit vectors be mutually orthogonal. As a consequence,

$$\frac{\partial \mathbf{r}}{\partial q_i} \cdot \frac{\partial \mathbf{r}}{\partial q_j} = \begin{cases} 0, & i \neq j \\ h_i^2, & i = j. \end{cases} \tag{3}$$

Defined in this way, the frame $\mathfrak{R}$ is known as an orthogonal curvilinear coordinate frame with orthogonal curvilinear coordinates q_i. The factors h_i are called the curvilinear scale factors of frame $\mathfrak{R}$.

The angular velocity of $\mathfrak{R}$ relative to $\mathfrak{F}$ is the vector $\boldsymbol{\omega}$ that satisfies the relation

$$\frac{d\mathbf{e}_i}{dt} = \boldsymbol{\omega} \times \mathbf{e}_i, \quad i = 1, 2, 3. \tag{4}$$

If ω is written

$$\boldsymbol{\omega} = \omega_1 \mathbf{e}_1 + \omega_2 \mathbf{e}_2 + \omega_3 \mathbf{e}_3, \tag{5}$$

it will be shown that the components of $\boldsymbol{\omega}$ are given by the compact expressions

$$\left.\begin{aligned} \omega_1 &= \frac{1}{h_2}\frac{\partial h_3}{\partial q_2}\dot{q}_3 - \frac{1}{h_3}\frac{\partial h_2}{\partial q_3}\dot{q}_2. \\ \omega_2 &= \frac{1}{h_3}\frac{\partial h_1}{\partial q_3}\dot{q}_1 - \frac{1}{h_1}\frac{\partial h_3}{\partial q_1}\dot{q}_3. \\ \omega_3 &= \frac{1}{h_1}\frac{\partial h_2}{\partial q_1}\dot{q}_2 - \frac{1}{h_2}\frac{\partial h_1}{\partial q_2}\dot{q}_1. \end{aligned}\right\} \tag{6}$$

Proof of the Main Result

Consider the unit vector $\mathbf{e}_i$ as a function of the three curvilinear coordinates,

$$\mathbf{e}_i \equiv \mathbf{e}_i(q_1, q_2, q_3).$$

Accordingly, its derivative is

$$\frac{d\mathbf{e}_i}{dt} = \frac{\partial \mathbf{e}_i}{\partial q_1}\dot{q}_1 + \frac{\partial \mathbf{e}_i}{\partial q_2}\dot{q}_2 + \frac{\partial \mathbf{e}_i}{\partial q_3}\dot{q}_3, \quad i = 1, 2, 3. \tag{7}$$

In the Appendix, it is shown that the partial derivatives of the curvilinear unit vectors with respect to the coordinates are given by

$$\frac{\partial \mathbf{e}_i}{\partial q_j} = \frac{1}{h_i}\frac{\partial h_j}{\partial q_i}\mathbf{e}_j, \quad i = 1, 2, 3, \quad i \neq j, \tag{8}$$

and

$$\frac{\partial \mathbf{e}_i}{\partial q_i} = -\frac{1}{h_j}\frac{\partial h_i}{\partial q_j}\mathbf{e}_j - \frac{1}{h_k}\frac{\partial h_i}{\partial q_k}\mathbf{e}_k, \; i = 1, 2, 3, \quad i \neq j \neq k. \tag{9}$$

Substituting into the right-hand sides of (7) produces

$$\left.\begin{aligned} \frac{d\mathbf{e}_1}{dt} &= \dot{q}_1\left(-\frac{1}{h_2}\frac{\partial h_1}{\partial q_2}\mathbf{e}_2 - \frac{1}{h_3}\frac{\partial h_1}{\partial q_3}\mathbf{e}_3\right) + \frac{\dot{q}_2}{h_1}\frac{\partial h_2}{\partial q_1}\mathbf{e}_2 + \frac{\dot{q}_3}{h_1}\frac{\partial h_3}{\partial q_1}\mathbf{e}_3, \\ \frac{d\mathbf{e}_2}{dt} &= \dot{q}_2\left(-\frac{1}{h_3}\frac{\partial h_2}{\partial q_3}\mathbf{e}_3 - \frac{1}{h_1}\frac{\partial h_2}{\partial q_1}\mathbf{e}_1\right) + \frac{\dot{q}_3}{h_2}\frac{\partial h_3}{\partial q_2}\mathbf{e}_3 + \frac{\dot{q}_1}{h_2}\frac{\partial h_1}{\partial q_2}\mathbf{e}_1, \\ \frac{d\mathbf{e}_3}{dt} &= \dot{q}_3\left(-\frac{1}{h_1}\frac{\partial h_3}{\partial q_1}\mathbf{e}_1 - \frac{1}{h_2}\frac{\partial h_3}{\partial q_2}\mathbf{e}_2\right) + \frac{\dot{q}_1}{h_3}\frac{\partial h_1}{\partial q_3}\mathbf{e}_1 + \frac{\dot{q}_2}{h_3}\frac{\partial h_2}{\partial q_3}\mathbf{e}_2. \end{aligned}\right\} \tag{10}$$

Returning to (4) and using (5) gives

with the possibility to find a better stability limit for Ω using a criterion of Frik (1972).

Conclusions

Real and complex symmetrizable systems are not robust with respect to perturbations in the entries of the coefficient matrices. So, from a modeling point of view, such systems will only have limited practical importance.

Exceptions are real symmetrizable systems with matrix order $n = 2$ (Theorem 2) and real and complex symmetrizable systems with any matrix order n, if special diagonality conditions are fulfilled (Theorem 3 and 4).

References

Ahmadian, M., and Inman, D. J., 1986, "Some Stability Results for General Linear Lumped-Parameter Dynamic Systems," ASME JOURNAL OF APPLIED MECHANICS, Vol. 53, pp. 10–14.

Frik, M., 1972, "Zur Stabilität nichtkonservativer linearer Systeme," *ZAMM* Vol. 52, pp. T47–T49.

Herrmann, G., and Jong, I.-C., 1965, "On the Destabilizing Effect of Damping in Nonconservative Elastic Systems," ASME JOURNAL OF APPLIED MECHANICS, Vol. 32, pp. 592–597.

Huseyin, K., 1978, *Vibrations and Stability of Multiple Parameter Systems*, Sijthoff and Noordhoff, Alpen aan den Rijn, The Netherlands.

Inman, D. J., 1983, "Dynamics of Asymmetric Nonconservative Systems," ASME JOURNAL OF APPLIED MECHANICS, Vol. 50, pp. 199–203.

Inman, D. J., and Olsen, C. L., 1988, "Dynamics of Symmetrizable Nonconservative Systems," ASME JOURNAL OF APPLIED MECHANICS, Vol. 55, pp. 206–212.

Kliem, W., and Pommer, C., 1986, "On the Stability of Linear Nonconservative Systems," *Quart. Appl. Math.*, Vol. 43, No. 4, pp. 457–461.

Müller, P. C., 1981, "Allgemeine lineare Theorie für Rotorsysteme ohne oder mit kleinen Unsymmetrien," *Ingenieur-Archiv*, Vol. 51, pp. 61–74.

Pfützner, H., 1976, "Zur Stabilität der Laval-Welle mit innerer und äusserer Dämpfung unter Berücksichtigung der Kreiselwirkung der Rotormasse" *Forsch. Ing.-Wes.*, Vol. 42, No. 4, pp. 130–135.

Piché, R., 1990, "On the Symmetrizability of Structural Control Systems with Noncolocated Sensors and Actuators," ASME *Journal of Dynamic Systems, Measurement, and Control*, Vol. 112, pp. 249–252.

Pommer, C., and Kliem, W., 1987, "Simultaneously Normalizable Matrices," *Linear Algebra and its Applications*, Vol. 94, pp. 113–125.

Determination of the Angular Velocity Vector in Orthogonal Curvilinear Coordinate Systems

D. L. Richardson[7]

An efficient, general procedure is developed for assembling the components of the angular velocity vector of orthogonal curvilinear coordinate frames.

Introduction

Consider a reference frame $\mathfrak{F}$ and a relative motion frame $\mathfrak{R}$ whose orientation is defined relative to $\mathfrak{F}$. Let (q_1, q_2, q_3) be the coordinate triad associated with $\mathfrak{R}$, and let $\mathbf{r}$ be the position of any point P in $\mathfrak{F}$. Assume that $\mathbf{r}$ can be expressed unambiguously in terms of the q_i. We have

$$\mathbf{r} \equiv \mathbf{r}(q_1, q_2, q_3),$$

and consequently,

$$d\mathbf{r} = \frac{\partial \mathbf{r}}{\partial q_1} dq_1 + \frac{\partial \mathbf{r}}{\partial q_2} dq_2 + \frac{\partial \mathbf{r}}{\partial q_3} dq_3. \tag{1}$$

[7]Department of Aerospace Engineering and Engineering Mechanics, University of Cincinnati, Cincinnati, OH 45221-0070.

Manuscript received by the ASME Applied Mechanics Division, 10/16/90; final revision, Dec. 5, 1990.

From here, define the curvilinear unit-vector basis triad $(\mathbf{e}_1, \mathbf{e}_2, \mathbf{e}_3)$ through the relation

$$\frac{\partial \mathbf{r}}{\partial q_i} = h_i \mathbf{e}_i. \tag{2}$$

Require that these unit vectors be mutually orthogonal. As a consequence,

$$\frac{\partial \mathbf{r}}{\partial q_i} \cdot \frac{\partial \mathbf{r}}{\partial q_j} = \begin{cases} 0, & i \neq j \\ h_i^2, & i = j. \end{cases} \tag{3}$$

Defined in this way, the frame $\mathfrak{R}$ is known as an orthogonal curvilinear coordinate frame with orthogonal curvilinear coordinates q_i. The factors h_i are called the curvilinear scale factors of frame $\mathfrak{R}$.

The angular velocity of $\mathfrak{R}$ relative to $\mathfrak{F}$ is the vector $\boldsymbol{\omega}$ that satisfies the relation

$$\frac{d\mathbf{e}_i}{dt} = \boldsymbol{\omega} \times \mathbf{e}_i, \quad i = 1, 2, 3. \tag{4}$$

If ω is written

$$\boldsymbol{\omega} = \omega_1 \mathbf{e}_1 + \omega_2 \mathbf{e}_2 + \omega_3 \mathbf{e}_3, \tag{5}$$

it will be shown that the components of $\boldsymbol{\omega}$ are given by the compact expressions

$$\left.\begin{aligned} \omega_1 &= \frac{1}{h_2}\frac{\partial h_3}{\partial q_2}\dot{q}_3 - \frac{1}{h_3}\frac{\partial h_2}{\partial q_3}\dot{q}_2. \\ \omega_2 &= \frac{1}{h_3}\frac{\partial h_1}{\partial q_3}\dot{q}_1 - \frac{1}{h_1}\frac{\partial h_3}{\partial q_1}\dot{q}_3. \\ \omega_3 &= \frac{1}{h_1}\frac{\partial h_2}{\partial q_1}\dot{q}_2 - \frac{1}{h_2}\frac{\partial h_1}{\partial q_2}\dot{q}_1. \end{aligned}\right\} \tag{6}$$

Proof of the Main Result

Consider the unit vector $\mathbf{e}_i$ as a function of the three curvilinear coordinates,

$$\mathbf{e}_i \equiv \mathbf{e}_i(q_1, q_2, q_3).$$

Accordingly, its derivative is

$$\frac{d\mathbf{e}_i}{dt} = \frac{\partial \mathbf{e}_i}{\partial q_1}\dot{q}_1 + \frac{\partial \mathbf{e}_i}{\partial q_2}\dot{q}_2 + \frac{\partial \mathbf{e}_i}{\partial q_3}\dot{q}_3, \quad i = 1, 2, 3. \tag{7}$$

In the Appendix, it is shown that the partial derivatives of the curvilinear unit vectors with respect to the coordinates are given by

$$\frac{\partial \mathbf{e}_i}{\partial q_j} = \frac{1}{h_i}\frac{\partial h_j}{\partial q_i}\mathbf{e}_j, \quad i = 1, 2, 3, \quad i \neq j, \tag{8}$$

and

$$\frac{\partial \mathbf{e}_i}{\partial q_i} = -\frac{1}{h_j}\frac{\partial h_i}{\partial q_j}\mathbf{e}_j - \frac{1}{h_k}\frac{\partial h_i}{\partial q_k}\mathbf{e}_k, \; i = 1, 2, 3, \quad i \neq j \neq k. \tag{9}$$

Substituting into the right-hand sides of (7) produces

$$\left.\begin{aligned} \frac{d\mathbf{e}_1}{dt} &= \dot{q}_1\left(-\frac{1}{h_2}\frac{\partial h_1}{\partial q_2}\mathbf{e}_2 - \frac{1}{h_3}\frac{\partial h_1}{\partial q_3}\mathbf{e}_3\right) + \frac{\dot{q}_2}{h_1}\frac{\partial h_2}{\partial q_1}\mathbf{e}_2 + \frac{\dot{q}_3}{h_1}\frac{\partial h_3}{\partial q_1}\mathbf{e}_3, \\ \frac{d\mathbf{e}_2}{dt} &= \dot{q}_2\left(-\frac{1}{h_3}\frac{\partial h_2}{\partial q_3}\mathbf{e}_3 - \frac{1}{h_1}\frac{\partial h_2}{\partial q_1}\mathbf{e}_1\right) + \frac{\dot{q}_3}{h_2}\frac{\partial h_3}{\partial q_2}\mathbf{e}_3 + \frac{\dot{q}_1}{h_2}\frac{\partial h_1}{\partial q_2}\mathbf{e}_1, \\ \frac{d\mathbf{e}_3}{dt} &= \dot{q}_3\left(-\frac{1}{h_1}\frac{\partial h_3}{\partial q_1}\mathbf{e}_1 - \frac{1}{h_2}\frac{\partial h_3}{\partial q_2}\mathbf{e}_2\right) + \frac{\dot{q}_1}{h_3}\frac{\partial h_1}{\partial q_3}\mathbf{e}_1 + \frac{\dot{q}_2}{h_3}\frac{\partial h_2}{\partial q_3}\mathbf{e}_2. \end{aligned}\right\} \tag{10}$$

Returning to (4) and using (5) gives

$$\left.\begin{aligned}\frac{d\mathbf{e}_1}{dt}&=-\omega_2\mathbf{e}_3+\omega_3\mathbf{e}_2,\\ \frac{d\mathbf{e}_2}{dt}&=\omega_1\mathbf{e}_3-\omega_3\mathbf{e}_1,\\ \frac{d\mathbf{e}_3}{dt}&=-\omega_1\mathbf{e}_2+\omega_2\mathbf{e}_1.\end{aligned}\right\} \tag{11}$$

Comparing coefficients of like unit vectors in the foregoing sets of equations produces six equations for the three unknowns ω_1, ω_2, ω_3. However, three of these equations are redundant. This leaves three independent expressions, one for each ω_i, which is the result displayed in Eqs. (6).

Example

Let $\mathfrak{F}$ be a Cartesian frame with rectangular components (x_1, x_2, x_3), and let $\mathfrak{R}$ be a reference frame of parabolic coordinates. The coordinate transformation is

$$x_1=q_1q_2\cos q_3,\ x_2=q_1q_2\sin q_3,\ x_3=(q_1^2-q_2^2)/2, \tag{12}$$

and the scale factors are

$$h_1=h_2=\sqrt{q_1^2+q_2^2},\quad h_3=q_1q_2. \tag{13}$$

Substituting into (6) gives

$$\omega_1=\frac{q_1\dot{q}_3}{\sqrt{q_1^2+q_2^2}},\ \omega_2=-\frac{q_2\dot{q}_3}{\sqrt{q_1^2+q_2^2}},\quad \omega_3=\frac{q_1\dot{q}_2-q_2\dot{q}_1}{q_1^2+q_2^2}. \tag{14}$$

This result checks with that of Kane and Levinson (1990) in their Table 1.

Comment

The recent paper of Kane and Levinson (1990) provides an alternative method for obtaining the same results that are produced by Equations (6). In the notations of this paper, their expressions for the components of the angular velocity vector are

$$\left.\begin{aligned}\omega_1&=\frac{1}{h_2h_3}\left(\frac{d}{dt}\frac{\partial\mathbf{r}}{\partial q_2}\right)\cdot\frac{\partial\mathbf{r}}{\partial q_3},\\ \omega_2&=\frac{1}{h_3h_1}\left(\frac{d}{dt}\frac{\partial\mathbf{r}}{\partial q_3}\right)\cdot\frac{\partial\mathbf{r}}{\partial q_1},\\ \omega_3&=\frac{1}{h_1h_2}\left(\frac{d}{dt}\frac{\partial\mathbf{r}}{\partial q_1}\right)\cdot\frac{\partial\mathbf{r}}{\partial q_2}.\end{aligned}\right\} \tag{15}$$

The position vector $\mathbf{r}$ is expressed in the $\mathfrak{F}$ frame as

$$\mathbf{r}=x_1\mathbf{a}_1+x_2\mathbf{a}_2+x_3\mathbf{a}_3, \tag{16}$$

where $(\mathbf{a}_1, \mathbf{a}_2, \mathbf{a}_3)$ is the Cartesian unit triad of $\mathfrak{F}$ with corresponding components (x_1, x_2, x_3). Whenever the x_i are expressed in terms of curvilinear coordinates, the components of the angular velocity vector can be determined from (15) in a straightforward manner.

From the point of view of computational efficiency, it would appear that Eqs. (6) of this paper require less labor than the expressions of Kane and Levinson.

Reference

Kane, T. R., and Levinson, D. A., 1990, "Orthogonal Curvilinear Coordinates and Angular Velocity," ASME Journal of Applied Mechanics, Vol. 57, pp. 468–470.

APPENDIX

Expressions for the partial derivatives of the unit basis vectors of a curvilinear system are obtained as follows. It is assumed throughout that $i \neq j \neq k$ unless indicated otherwise.

For Eq. (8), differentiate the defining relations

$$h_i\mathbf{e}_i=\frac{\partial\mathbf{r}}{\partial q_i},\ h_j\mathbf{e}_j=\frac{\partial\mathbf{r}}{\partial q_j}, \tag{17}$$

and assume continuity in the second partial derivatives so that

$$\frac{\partial^2\mathbf{r}}{\partial q_iq_j}=\frac{\partial^2\mathbf{r}}{\partial q_jq_i}. \tag{18}$$

Rearrange the results to produce

$$h_i\frac{\partial\mathbf{e}_i}{\partial q_j}=-\frac{\partial h_i}{\partial q_j}\mathbf{e}_i+\frac{\partial h_j}{\partial q_i}\mathbf{e}_j+h_j\frac{\partial\mathbf{e}_j}{\partial q_i}. \tag{19}$$

Now, differentiate the identity $\mathbf{e}_i\cdot\mathbf{e}_i = 1$ to get

$$\frac{\partial\mathbf{e}_i}{\partial q_j}\cdot\mathbf{e}_i=0, \tag{20}$$

which shows that $\dfrac{\partial\mathbf{e}_i}{\partial q_j}$ does not have an $\mathbf{e}_i$ component. In addition, this derivative does not have an $\mathbf{e}_k$ component which is established as follows: From Eq. (3), differentiate the identities

$$\frac{\partial\mathbf{r}}{\partial q_i}\cdot\frac{\partial\mathbf{r}}{\partial q_j}=\frac{\partial\mathbf{r}}{\partial q_i}\cdot\frac{\partial\mathbf{r}}{\partial q_k}=\frac{\partial\mathbf{r}}{\partial q_j}\cdot\frac{\partial\mathbf{r}}{\partial q_k}=0, \tag{21}$$

to obtain the equation sequence

$$\frac{\partial^2\mathbf{r}}{\partial q_i\partial q_k}\cdot\frac{\partial\mathbf{r}}{\partial q_j}=-\frac{\partial\mathbf{r}}{\partial q_i}\cdot\frac{\partial^2\mathbf{r}}{\partial q_j\partial q_k}=\frac{\partial^2\mathbf{r}}{\partial q_i\partial q_j}\cdot\frac{\partial\mathbf{r}}{\partial q_k}=-\frac{\partial\mathbf{r}}{\partial q_j}\cdot\frac{\partial^2\mathbf{r}}{\partial q_i\partial q_k}. \tag{22}$$

Thus,

$$\frac{\partial^2\mathbf{r}}{\partial q_i\partial q_k}\cdot\frac{\partial\mathbf{r}}{\partial q_j}=0, \tag{23}$$

and as a consequence,

$$\frac{\partial^2\mathbf{r}}{\partial q_i\partial q_j}\cdot\frac{\partial\mathbf{r}}{\partial q_k}=0. \tag{24}$$

After substituting from Eq. (2), the identity above becomes

$$h_k\mathbf{e}_k\cdot\frac{\partial}{\partial q_i}(h_j\mathbf{e}_j)=h_jh_k\mathbf{e}_k\cdot\frac{\partial\mathbf{e}_j}{\partial q_i}=0. \tag{25}$$

By applying the foregoing analysis to Eq. (19), it follows that $\dfrac{\partial\mathbf{e}_i}{\partial q_j}$ has only an $\mathbf{e}_j$ component, and because $\dfrac{\partial\mathbf{e}_j}{\partial q_i}\cdot\mathbf{e}_j = 0$, we have

$$\frac{\partial\mathbf{e}_i}{\partial q_j}=\frac{1}{h_i}\frac{\partial h_j}{\partial q_i}\mathbf{e}_j,\quad i=1,2,3,\quad i\neq j. \tag{26}$$

To establish Eq. (9), differentiate the following identities

$$\mathbf{e}_i\cdot\mathbf{e}_j=0,\quad \mathbf{e}_i\cdot\mathbf{e}_k=0 \tag{27}$$

to obtain

$$\left.\begin{aligned}\mathbf{e}_i\cdot\frac{\partial\mathbf{e}_j}{\partial q_i}+\mathbf{e}_j\cdot\frac{\partial\mathbf{e}_i}{\partial q_i}&=0,\\ \mathbf{e}_i\cdot\frac{\partial\mathbf{e}_k}{\partial q_i}+\mathbf{e}_k\cdot\frac{\partial\mathbf{e}_i}{\partial q_i}&=0.\end{aligned}\right\} \tag{28}$$

Substituting from Eq. (26) produces

$$\left.\begin{aligned}\mathbf{e}_i\cdot\left(\frac{1}{h_j}\frac{\partial h_i}{\partial q_j}\mathbf{e}_i\right)+\mathbf{e}_j\cdot\frac{\partial\mathbf{e}_i}{\partial q_i}&=0,\\ \mathbf{e}_i\cdot\left(\frac{1}{h_k}\frac{\partial h_i}{\partial q_k}\mathbf{e}_i\right)+\mathbf{e}_k\cdot\frac{\partial\mathbf{e}_i}{\partial q_i}&=0.\end{aligned}\right\} \tag{29}$$

The first of these equations provides the jth component of $\partial\mathbf{e}_i/\partial q_i$, and the second gives the kth component. In addition, the ith component is zero. Collecting results gives

$$\frac{\partial\mathbf{e}_i}{\partial q_i}=-\frac{1}{h_j}\frac{\partial h_i}{\partial q_j}\mathbf{e}_j-\frac{1}{h_k}\frac{\partial h_i}{\partial q_k}\mathbf{e}_k,\quad i=1,\ 2,\ 3,\quad i\neq j\neq k. \tag{30}$$

Eigenfrequencies of an Elastic Sphere With Fixed Boundary Conditions

P. J. Schafbuch[8,11], F. J. Rizzo[9,11], and R. B. Thompson[10,11]

Introduction

One basic problem of elastodynamics which has an analytical solution is the free vibration of a homogeneous, isotropic elastic sphere. Lamb (1882) first solved this problem, and classic texts on elasticity such as Love (1927) often cite or reproduce his solution. Eringen and Suhubi (1975) provide tables of eigenfrequencies for this traction-free boundary condition case. However, the equally fundamental case of fixed displacement boundary conditions has, to our knowledge, been largely ignored. Perhaps this is due to a lack of physical situations for which a true fixed boundary condition exists. The traction-free boundary condition case was motivated by geophysical considerations. Research into boundary integral equation formulations of elastic wave scattering has produced a need to know the characteristic frequencies of the fixed displacement or Dirichlet problem.

Some work has been done on this problem in a quantum mechanical context. In his fundamental work on the theory of specific heats, Peter Debye (1912) considered an elastic sphere with fixed boundary conditions and looked at asymptotic limits of the size and number of eigenfrequencies. To do this, he developed the general characteristic equations but left them unsolved. In this Brief Note, we provide solutions to these equations for selected cases.

Debye's Equations

Debye's approach parallels that of Lamb in that time-harmonic motion is assumed, but he introduces both scalar and vector potential functions. In more modern nomenclature we then write the displacement field as

$$\mathbf{u} = \nabla \Phi + \nabla \times \mathbf{\Pi} \tag{1}$$

with $\nabla \cdot \mathbf{\Pi} = 0$ to isolate the irrotational and incompressible field components. The problem can then be broken down into a set of three Helmholtz equations for Φ, Π_1, and Π_2. Each of the potential functions can be written as an infinite sum where the angular dependence is expressed in terms of spherical harmonics. For example,

$$r\Pi_1 = \sum_{n=0}^{\infty} A_n \psi_n(k_T r) S_n(\theta,\phi) \tag{2}$$

where (r, θ, ϕ) are spherical coordinates and k_T is the wave number for a transverse (shear) wave. For each spherical harmonic, S_n, there is a corresponding function ψ_n which defines the radial (r) dependency. These radial functions turn out to be Riccati-Bessel functions and are related to the spherical Bessel function of the first kind, j_n, by the expression $\psi_n(z) = zj_n(z)$. Note that our definition of ψ_n is consistent with that of Debye but differs by a factor of z from that in Lamb (1882) and Love (1927). The expansion coefficients, e.g., A_n, are determined via the Dirichlet boundary conditions to within a multiplicative constant for the eigenvalue problem.

For the sake of brevity, the derivation will not be reproduced but merely the results stated. Just as with the traction-free case, there are two classes of motion possible. Class I motions are based on shear distortions where the displacement field remains completely solenoidal. The characteristic equation for this motion is expressed as a simple function of the dimensionless frequency $k_T a$ where a is the sphere radius.

$$\psi_n(k_T a) = 0 \tag{3}$$

Class II motion involves coupled longitudinal and transverse internal wave fields which taken together satisfy the boundary conditions. The characteristic equation is hence also a function of $k_L a$, the longitudinal wave dimensionless frequency, and has the form

$$n(n+1)\psi_n(k_T a)\psi_n(k_L a) = (k_T a)(k_L a)^2 \frac{d\psi_n(k_T a)}{d(k_T a)} \times \frac{d}{d(k_L a)}\left[\frac{\psi_n(k_L a)}{k_L a}\right]. \tag{4}$$

The longitudinal and transverse wave numbers are expressed by and related through the material's Lamé constants (λ,μ) and density (ρ), as shown in Love. Characteristic Eqs. (3) and (4) have, in general, infinitely many roots (modes m) for each harmonic n.

Two similar classes of motion exist in a hollow sphere as discussed by Shah, Ramkrishnan, and Datta (1969). Our approaches and solution methods are akin, except for differences relating to boundary conditions.

Solution Method

The eigenfrequencies associated with Class I shear motions are simply related to the zeroes of spherical Bessel functions of order n. The zeroth spherical surface harmonic is a constant which precludes this kind of motion. Thus, beginning with the first harmonic, the eigenfrequencies are

$$\omega_{In}^{(m)} = \frac{z_n^{(m)}}{a}\sqrt{\frac{\mu}{\rho}} \tag{5}$$

where $z_n^{(m)}$ is the mth zero of the nth spherical Bessel function.

If harmonics or zeroes beyond available tabulated values are desired, the spherical Bessel functions can be built up from recursion relationships, as given by Abramowitz and Stegun (1965). These functions become cumbersome to generate explicitly for high harmonics even with symbolic manipulation programs. However, the functional form need not be generated. The functions' values can be generated point by point numerically with two-level recursion formulas. Roots of Eq. (3) are then found numerically in either case.

Solutions for Class II motion can be obtained by a similar procedure. If the functional forms are not generated explicitly, recursion formulas expressing the ψ_n derivatives in Eq. (4) can be derived from the aforementioned formulas for Bessel functions. The zeroth harmonic for this motion class is a special case. Equation (4) for n equal to zero reduces to

$$k_L a = \tan(k_L a) \tag{6}$$

which is independent of the transverse wave number, k_T, since the motion is purely dilatational.

Results

Equation (5) showed that the eigenfrequencies of Class I motion are related to spherical Bessel function zeroes. Since these zeroes are tabulated in mathematics handbooks such as Abramowitz and Stegun, they will not be reproduced here. The eigenfrequencies of the radial ($n = 0$) modes of Class II

[8]Research Specialist. Present address: Fisher Controls, Marshalltown, IA 50158. Assoc. Mem. ASME.
[9]Professor and Mem. ASME.
[10]Professor and Associate Director. Mem. ASME.
[11]Center for Nondestructive Evaluation and Department of Aerospace Engineering and Engineering Mechanics, Iowa State University, Ames, IA 50011.
Manuscript received by the ASME Applied Mechanics Division, June 29, 1990; final revision, Dec. 26, 1990.

Table 1 Transverse wave dimensionless eigenfrequencies of Class II motion

Harmonic	$\nu = 1/4$		$\nu = 1/3$	
1	3.98978	6.20296	4.31104	6.28319
	9.25856	10.32782	9.30867	11.80491
	12.49756	15.57714	12.56637	15.64226
	16.00854	18.79676	18.35945	18.84956
2	5.77510	7.73594	6.14067	8.00848
	10.67013	12.59144	10.75399	13.76003
	13.99104	17.06532	14.70966	17.12557
	18.40041			
3	7.29284	9.32252	7.60292	9.81182
	12.06687	14.61599	12.22253	15.22962
	15.57109	18.50656	17.12725	18.63066
4	8.65331	10.92254	8.90405	11.54633
	13.46630	16.30743	13.74763	16.65140
	17.37159	19.93332	19.29100	
5	9.92375	12.49147	10.13181	13.14327
	14.88209	17.77994	15.34071	18.07228
	19.29420			
6	11.14131	14.00203	11.32014	14.60584
	16.32227	19.17997	16.97116	19.51348
7	12.32560	15.44445	12.48389	15.96990
	17.78588		18.58437	
8	13.48730	16.82213	13.63065	17.26947
	19.26246			
9	14.63266	18.14550	14.76475	18.52695
10	15.76561	19.42638	15.88893	19.75568
11	16.88873		17.00505	
12	18.00383		18.11444	
13	19.11222		19.21809	

motion are also related to spherical Bessel function zeroes. As can be inferred from Eq. (6) and Bessel function relationships,

$$\omega_{II0}^{(m)} = \frac{z_1^{(m)}}{a}\sqrt{\frac{\lambda + 2\mu}{\rho}}. \tag{7}$$

In terms of $k_L a$, these are 4.49341, 7.72525, 10.90412, etc.

Table 1 gives values of $k_T a$ corresponding to Class II eigenfrequencies, $\omega_{IIn}^{(m)}$, for Poisson's ratios of 1/4 and 1/3 and $n > 0$. All the modes with $k_T a$ less than 20 are given. For a Poisson's ratio of 1/4, there are 52 Class II modes in this range. For ν equal to 1/3, there are only 47 modes. As Poisson's ratio increases, the material becomes less compressible, so an individual mode's frequency increases. The number of Class I modes is independent of Poisson's ratio and remains fixed at 38 for $k_T a < 20$. The eigenfrequencies of each harmonic and Class are interlaced, but there is an orderly increase in the eigenfrequency for the fundamental mode of each subsequent harmonic. The only exception is the Class II radial modes which have higher frequencies than their rotatory ($n = 1$) counterparts.

Verification

Our motivation for solving this problem also provides an independent means of checking the calculations. Integral equation representations of exterior domain elastodynamic problems are plagued by certain irregular frequencies at which the equation has infinitely many or no solutions. When these equations are solved numerically, this difficulty presents itself as an ill-conditioned matrix. Martin (1991) has shown that these irregular frequencies are the eigenfrequencies of the associated interior problem with Dirichlet boundary conditions. We have checked the eigenfrequencies (up through harmonic five) reported here by comparing the condition number of a boundary element method (BEM) generated matrix (Rezayat, Shippy, and Rizzo 1986) at the predicted frequency with the condition number of nearby frequency matrices. The results confirm these calculations.

Conclusions

These results are useful to BEM and other integral equation researchers who are attempting to understand and solve the irregular frequency problem in elastodynamics. In particular, precise knowledge of all these frequencies allows countermeasures such as the BIFILM algorithm (Rezayat, et al., 1986) to be tested. These results can also serve as a check on numerical methods for elastic continuum modal analysis.

Acknowledgments

This work was sponsored by the Center for NDE at Iowa State University and was performed at the USDOE Ames Laboratory which is operated by Iowa State under Contract No. W-7405-ENG-82. One author (Rizzo) was partially supported by the Office of Naval Research under Contract No. N00014-86-K-0551.

References

Abramowitz, M., and Stegun, I. A., 1965, *Handbook of Mathematical Functions*, Dover, New York.

Debye, P., 1912, "Zur Theorie der Spezifischen Wärmen," *Annalen der Physik*, Ser. 4, Vol. 39, pp. 789–839.

Eringen, A. C., and Suhubi, E. S., 1975, *Elastodynamics*, Vol. II, Academic Press, New York.

Lamb, H., 1882, "On the Vibrations of an Elastic Sphere," *London Math. Soc. Proc.*, Vol. 13, pp. 189–212.

Love, A. E. H., 1927, *A Treatise on the Mathematical Theory of Elasticity*, 4th ed., Dover, New York.

Martin, P. A., 1991, "Identification of Irregular Frequencies in Simple Direct Integral-Equation Methods for Scattering by Homogeneous Inclusions," *Wave Motion*, Vol. 13, pp. 185–192.

Rezayat, M., Shippy, D. J., and Rizzo, F. J., 1986, "On Time-Harmonic Elastic-Wave Analysis by the Boundary Element Method for Moderate to High Frequencies," *Comput. Method Appl. M.*, Vol. 55, pp. 349–367.

Shah, A. H., Ramkrishnan, C. V., and Datta, S. K., 1969, "Three-Dimensional and Shell-Theory Analysis of Elastic Waves in a Hollow Sphere," ASME Journal of Applied Mechanics, Vol. 36, pp. 431–444.

The Response Spectrum of a Nonlinear Oscillator

Huw G. Davies[12,13] and Qiang Liu[12,13]

The response of a nonlinear oscillator excited by white noise is considered. A truncated Hermite polynomial series is used as an approximation to the probability density function. While this approach has been used before by many authors to obtain statistics such as the time-dependent mean or mean-square values, it has not been noted before that the approach can be extended to obtain the correlation function and spectrum. This series when substituted into the Fokker-Planck equation yields a set of time-dependent moment equations, which can be solved numerically for the correlation functions, or, after a Fourier transform, a set of complex algebraic equations which can be solved for the spectrum. Examples of spectra for the Duffing and van der Pol oscillators are shown.

Introduction

The spectrum of the random response of a system provides useful information in many engineering applications. It can be fairly easily measured on an actual structure or machine, and gives an immediate picture that characterizes the system in terms of modal resonance frequencies. For a linear system, the spectrum can also be calculated easily if the input spectrum is known (see, for example, Lin, 1967).

For a nonlinear system, the situation is often much more complicated. Studies of the sinusoidal excitation of nonlinear

[12]Department of Mechanical Engineering, University of New Brunswick, Fredericton, New Brunswick, E3B 5A3, Canada.

[13]Mem. ASME.

Manuscript received by the ASME Applied Mechanical Division, Aug. 23, 1990; final revision, Jan. 24, 1991.

Table 1 Transverse wave dimensionless eigenfrequencies of Class II motion

Harmonic	ν = 1/4		ν = 1/3	
1	3.98978	6.20296	4.31104	6.28319
	9.25856	10.32782	9.30867	11.80491
	12.49756	15.57714	12.56637	15.64226
	16.00854	18.79676	18.35945	18.84956
2	5.77510	7.73594	6.14067	8.00848
	10.67013	12.59144	10.75399	13.76003
	13.99104	17.06532	14.70966	17.12557
	18.40041			
3	7.29284	9.32252	7.60292	9.81182
	12.06687	14.61599	12.22253	15.22962
	15.57109	18.50656	17.12725	18.63066
4	8.65331	10.92254	8.90405	11.54633
	13.46630	16.30743	13.74763	16.65140
	17.37159	19.93332	19.29100	
5	9.92375	12.49147	10.13181	13.14327
	14.88209	17.77994	15.34071	18.07228
	19.29420			
6	11.14131	14.00203	11.32014	14.60584
	16.32227	19.17997	16.97116	19.51348
7	12.32560	15.44445	12.48389	15.96990
	17.78588		18.58437	
8	13.48730	16.82213	13.63065	17.26947
	19.26246			
9	14.63266	18.14550	14.76475	18.52695
10	15.76561	19.42638	15.88893	19.75568
11	16.88873		17.00505	
12	18.00383		18.11444	
13	19.11222		19.21809	

motion are also related to spherical Bessel function zeroes. As can be inferred from Eq. (6) and Bessel function relationships,

$$\omega_{II0}^{(m)} = \frac{z_1^{(m)}}{a}\sqrt{\frac{\lambda + 2\mu}{\rho}}. \tag{7}$$

In terms of $k_L a$, these are 4.49341, 7.72525, 10.90412, etc.

Table 1 gives values of $k_T a$ corresponding to Class II eigenfrequencies, $\omega_{IIn}^{(m)}$, for Poisson's ratios of 1/4 and 1/3 and $n > 0$. All the modes with $k_T a$ less than 20 are given. For a Poisson's ratio of 1/4, there are 52 Class II modes in this range. For ν equal to 1/3, there are only 47 modes. As Poisson's ratio increases, the material becomes less compressible, so an individual mode's frequency increases. The number of Class I modes is independent of Poisson's ratio and remains fixed at 38 for $k_T a < 20$. The eigenfrequencies of each harmonic and Class are interlaced, but there is an orderly increase in the eigenfrequency for the fundamental mode of each subsequent harmonic. The only exception is the Class II radial modes which have higher frequencies than their rotatory ($n = 1$) counterparts.

Verification

Our motivation for solving this problem also provides an independent means of checking the calculations. Integral equation representations of exterior domain elastodynamic problems are plagued by certain irregular frequencies at which the equation has infinitely many or no solutions. When these equations are solved numerically, this difficulty presents itself as an ill-conditioned matrix. Martin (1991) has shown that these irregular frequencies are the eigenfrequencies of the associated interior problem with Dirichlet boundary conditions. We have checked the eigenfrequencies (up through harmonic five) reported here by comparing the condition number of a boundary element method (BEM) generated matrix (Rezayat, Shippy, and Rizzo 1986) at the predicted frequency with the condition number of nearby frequency matrices. The results confirm these calculations.

Conclusions

These results are useful to BEM and other integral equation researchers who are attempting to understand and solve the irregular frequency problem in elastodynamics. In particular, precise knowledge of all these frequencies allows countermeasures such as the BIFILM algorithm (Rezayat, et al., 1986) to be tested. These results can also serve as a check on numerical methods for elastic continuum modal analysis.

Acknowledgments

This work was sponsored by the Center for NDE at Iowa State University and was performed at the USDOE Ames Laboratory which is operated by Iowa State under Contract No. W-7405-ENG-82. One author (Rizzo) was partially supported by the Office of Naval Research under Contract No. N00014-86-K-0551.

References

Abramowitz, M., and Stegun, I. A., 1965, *Handbook of Mathematical Functions*, Dover, New York.

Debye, P., 1912, "Zur Theorie der Spezifischen Wärmen," *Annalen der Physik*, Ser. 4, Vol. 39, pp. 789–839.

Eringen, A. C., and Suhubi, E. S., 1975, *Elastodynamics*, Vol. II, Academic Press, New York.

Lamb, H., 1882, "On the Vibrations of an Elastic Sphere," *London Math. Soc. Proc.*, Vol. 13, pp. 189–212.

Love, A. E. H., 1927, *A Treatise on the Mathematical Theory of Elasticity*, 4th ed., Dover, New York.

Martin, P. A., 1991, "Identification of Irregular Frequencies in Simple Direct Integral-Equation Methods for Scattering by Homogeneous Inclusions," *Wave Motion*, Vol. 13, pp. 185–192.

Rezayat, M., Shippy, D. J., and Rizzo, F. J., 1986, "On Time-Harmonic Elastic-Wave Analysis by the Boundary Element Method for Moderate to High Frequencies," *Comput. Method Appl. M.*, Vol. 55, pp. 349–367.

Shah, A. H., Ramkrishnan, C. V., and Datta, S. K., 1969, "Three-Dimensional and Shell-Theory Analysis of Elastic Waves in a Hollow Sphere," ASME Journal of Applied Mechanics, Vol. 36, pp. 431–444.

The Response Spectrum of a Nonlinear Oscillator

Huw G. Davies[12,13] and Qiang Liu[12,13]

The response of a nonlinear oscillator excited by white noise is considered. A truncated Hermite polynomial series is used as an approximation to the probability density function. While this approach has been used before by many authors to obtain statistics such as the time-dependent mean or mean-square values, it has not been noted before that the approach can be extended to obtain the correlation function and spectrum. This series when substituted into the Fokker-Planck equation yields a set of time-dependent moment equations, which can be solved numerically for the correlation functions, or, after a Fourier transform, a set of complex algebraic equations which can be solved for the spectrum. Examples of spectra for the Duffing and van der Pol oscillators are shown.

Introduction

The spectrum of the random response of a system provides useful information in many engineering applications. It can be fairly easily measured on an actual structure or machine, and gives an immediate picture that characterizes the system in terms of modal resonance frequencies. For a linear system, the spectrum can also be calculated easily if the input spectrum is known (see, for example, Lin, 1967).

For a nonlinear system, the situation is often much more complicated. Studies of the sinusoidal excitation of nonlinear

[12]Department of Mechanical Engineering, University of New Brunswick, Fredericton, New Brunswick, E3B 5A3, Canada.

[13]Mem. ASME.

Manuscript received by the ASME Applied Mechanical Division, Aug. 23, 1990; final revision, Jan. 24, 1991.

oscillators show how complicated the response can be, including, for example, multiple valued response, subharmonics, limit cycles, and chaos (Guckenheimer and Holmes, 1983; Nayfeh and Mook, 1979). Even though present in the sinusoidal case, not all of these phenomena peculiar to nonlinear response may show up when the excitation is white noise. But the spectrum is still a useful description of the response, although one must expect now that the character of the spectrum may change as the excitation level of the white noise is changed.

It appears that the difficulties inherent in obtaining the spectrum for a nonlinear oscillator have resulted in very little work on the topic. Of course, one can use equivalent linearization for an oscillator with nonlinear stiffness (Lin, 1967), but this approach, while surprisingly accurate for the mean-square response, is far less accurate when estimating the spectrum. A fairly general approach has been given by Wen (1975, 1976). He estimated stationary and nonstationary mean-square values, probability density functions, and spectral densities based on numerical solutions for the eigenvalues and eigenfunctions associated with an appropriate Fokker-Planck equation. Wen was particularly interested in results for hysteretic restoring forces. An alternate, also numerical, approach to that of Wen is presented as follows. The advantages of the present approach are mainly that only *algebraic* equations have to be solved for the spectrum, and also that as these algebraic equations are generated by the computer program, the results can be estimated to high accuracy.

The spectrum of a Duffing oscillator excited by white noise has been discussed by Miles (1989). His approach is an adaption of equivalent linearization, which takes into account that the effective resonance frequency is amplitude dependent. Miles averages over an ensemble of equivalent linear systems, each with its own equivalent resonance frequency. Iteration is used to find an appropriate constant involved in the determination of higher order ensemble averages. His approach seems to estimate accurately both the increase of the effective resonance frequency and the broadening of the resonance peak as the excitation amplitude is increased. The approach can be extended to nonlinear oscillators with more complicated nonlinear stiffness, but cannot be used for oscillators with nonlinear damping.

Liu and Davies (1988, 1990a) have shown how nonstationary probability density functions describing the response of oscillators with nonlinear damping and stiffness can be obtained by using a truncated series of Hermite polynomials as an approximate solution of a Fokker Planck equation for the joint pdf $p(x, \dot{x}; t)$. In the stationary case, this approach has been discussed for example by Crandall (1980). In the nonstationary case the coefficients in the series are time-dependent expected values $E[H_m(x)H_n(\dot{x})]$ where H_m and H_n are Hermite polynomials.

The approach described in Liu and Davies (1988, 1990a) is extended here to find the correlation function $E[x(t_1)x(t_2)]$ of the response, and hence the spectrum $S(\omega, t_1)$. We note that the fourth-order joint pdf $p(x(t_1), \dot{x}(t_1); x(t_2), \dot{x}(t_2))$ satisfies the same Fokker Planck equation as before. A set of first-order differential equations for moments such as $E[x(t_1)H_m(x(t_2))H_n(\dot{x}(t_2))]$ can be obtained from the Fokker-Planck equation—the required correlation function being given, of course, by choosing $m = 1$ and $n = 0$. The initial conditions required to solve these differential equations are the (possibly time-dependent) moments obtained earlier (Liu and Davies, 1988, 1990a). We actually find it more convenient to take a single-sided Fourier transform of these differential equations and solve a set of complex algebraic equations directly for the spectrum.

Applications are shown below for the Duffing oscillator, showing the change in resonance frequency and broadening of the resonance peak as the excitation level increases (as shown by Miles (1989)), and for the van der Pol oscillator, showing a limit cycle-type response which is quenched as the excitation level increases.

Non-Gaussian Closure and Spectrum

Although the method to be described can be applied to a fairly general case, we consider here just the second-order system

$$\dot{x} = \nu \tag{1}$$

$$\dot{\nu} = -x - \beta\nu - g(x, \nu) + hW \tag{2}$$

where g is a nonlinear function of x and $\nu \equiv \dot{x}$, W is stationary Gaussian white noise with zero mean and correlation $R(\tau) = 2\delta(\tau)$, and h is a constant switched from zero at time $t = 0$. It will be assumed that g is a symmetric function so that $E[x] = 0$ and $E[\nu] = 0$, although as shown in Liu and Davies (1988, 1990a), a more general nonlinear function can be handled.

As shown in Liu and Davies (1988, 1990a), the response probability density function is approximated by the truncated series

$$p(x, \nu, t) = \frac{1}{2\pi\sigma_1(t)\sigma_2(t)} \exp\left\{-\frac{1}{2}(y_1^2 + u_1^2)\right\} \times \sum_{k+j=0}^{k+j=N} C_{kj}(t) H_k^1 H_j^2 \tag{3}$$

where

$$y_1 = x/\sigma_1(t),\ u_1 = \nu/\sigma_2(t),\ \sigma_1^2(t) = E[x^2],\ \sigma_2^2(t) = E[\nu^2],$$
$$H_k^1 = H_k(y_1),\ H_j^2 = H_j(u_1),\ C_{kj}(t) = E[H_k^1 H_j^2]/k!j!, \text{ and}$$
$$H_k(\cdot) \text{ and } H_j(\cdot) \text{ are Hermite polynomials.}$$

The pdf (3) satisfies the Fokker-Planck equation associated with Eqs. (1) and (2):

$$\mathcal{L} = \frac{\partial p}{\partial t} + \nu\frac{\partial p}{\partial x} - \frac{\partial}{\partial \nu}[(\beta\nu + x + g(x, \nu))p] - h^2\frac{\partial^2 p}{\partial \nu^2} = 0. \tag{4}$$

A set of equations for the unknown response statistics σ_1, σ_2, and C_{mn} can be obtained by substituting Eq. (3) into (4) and making use of the orthogonality properties of the Hermite polynomials:

$$\begin{aligned}
&\dot{C}_{mn} + \frac{\dot{\sigma}_1}{\sigma_1}[mC_{mn} + C_{m-2,\,n}] + \frac{\dot{\sigma}_2}{\sigma_2}[nC_{mn} + C_{m,n-2}] \\
&\quad - \frac{\sigma_2}{\sigma_1}[(n+1)C_{m-1,\,n+1} + C_{m-1,\,n-1}] \\
&\quad + \frac{\sigma_1}{\sigma_2}[(m+1)C_{m+1,\,n-1} + C_{m-1,\,n-1}] + \beta[nC_{mn} + C_{m,\,n-2}] \\
&\quad - \frac{h^2}{\sigma_2^2}C_{m,\,n-2} + \frac{n}{\sigma_2 m!n!}\int\int_{-\infty}^{+\infty} g(x, \nu)H_m^1 H_{n-1}^2 p\sigma_1\sigma_2 dy_1 du_1 = 0 \\
&\sigma_1(0) = \sigma_2(0) = 0,\ C_{mn}(0) = 0,\ (m+n \neq 0).
\end{aligned} \tag{5}$$

The solution of Eq. (5) gives all the time-dependent response statistics up to order N. One can substitute these statistics into expression (3) to approximate the nonstationary joint response probability density function. Some examples have been discussed in Liu and Davies (1988, 1990a).

We turn now to the correlation function. It is convenient to define $x_1 = x(t_1)$, $\nu_1 = \nu(t_1)$, $x_2 = x(t_2)$ and $\nu_2 = \nu(t_2)$, and to write $t_2 = t_1 + \tau$. The Fokker-Planck equation is rewritten with the notation $t \to \tau$, $x \to x_2$ and $\nu \to \nu_2$. The new Fokker-Planck equation is satisfied by the conditional probability $p(x_2, \nu_2, \tau | x_1, \nu_1)$ and hence also by the joint probability

$$p(x_1, \nu_1; x_2, \nu_2; \tau) = p(x_2, \nu_2, \tau | x_1, \nu_1)p(x_1, \nu_1) \tag{6}$$

where $p(x_1, \nu_1)$ is the stationary pdf.

We define

$$\phi_{mn} = \frac{x_1}{\sigma_1} H_m \left(\frac{x_2}{\sigma_1}\right) H_n \left(\frac{\nu_2}{\sigma_2}\right) = y_1 H_m(y_2) H_n(u_2) = y_1 H_m^1 H_n^2 \quad (7)$$

where we note now that σ_1 and σ_2 are the stationary values. A set of coupled differential equations for $B_{mn} = E[\phi_{mn}]/m!n!$ can then be obtained from the relationship

$$\int\int\int\int \mathcal{L}\phi_{mn} dx_1 dx_2 d\nu_1 d\nu_2 = 0 \quad (8)$$

and the recurrence relations of the Hermite polynomials. For example,

$$\int\int\int\int \frac{\partial p}{\partial t_2} \phi_{mn}\, dx_1 dx_2 d\nu_1 d\nu_2 = \frac{dB_{mn}}{d\tau} \quad (9)$$

and

$$\int\int\int\int \nu_2 \frac{\partial p}{\partial x_2} \phi_{mn}\, dx_1 dx_2 d\nu_1 d\nu_2 = -\frac{1}{\sigma_1}\int\int\int\int \nu_2 \frac{\partial \phi_{mn}}{\partial y_2} p\, dx_1 dx_2 d\nu_1 d\nu_2 = -\frac{\sigma_2}{\sigma_1}\int\int\int\int u_2 y_1 m\, H_{m-1}^1\, H_n^2\, p\, dx_1 dx_2 d\nu_1 d\nu_2.$$

The final equation is

$$= -\frac{\sigma_2}{\sigma_1} m!n!((n+1)B_{m-1,\, m+1} + B_{m-1,\, n-1}) \quad (10)$$

$$\frac{dB_{mn}}{d\tau} - \frac{\sigma_2}{\sigma_1}[(n+1)B_{m-1,\, n+1} + B_{m-1,\, n-1}] + \frac{\sigma_1}{\sigma_2}[(m+1)B_{m+1,\, n-1} + B_{m-1,\, n-1}] + \beta[nB_{mn} + B_{m,\, n-2}] - \frac{h^2}{\sigma_2^2} B_{m,\, n-2} + \frac{n}{\sigma_2 m!n!} E[g(x_2, \nu_2)\phi_{m,\, n-1}] = 0 \quad (11)$$

The initial conditions required to solve this set of coupled first-order differential equations for $B_{mn}(\tau)$ are given by

$$B_{mn}(0) = E[y_1 H_m(y_1) H_n(\nu_1)] = (m+1)C_{m+1,\, n} + C_{m-1,\, n} \quad (12)$$

where the C_{mn} here are the stationary values obtained from the previous analysis (Liu and Davies, 1988, 1990a). We then have, for example, that the autocorrelation of the response is

$$R(\tau) = E[x(\tau)x(t+\tau)] = \sigma_1^2 B_{10}(\tau). \quad (13)$$

The set of Eqs. (11) is linear, provided of course that the nonlinear function $g(x, \nu)\phi_{m,\, n-1}$ can be written as a sum of Hermite polynomials. This is obviously the case if g consists of polynomial terms; for example x^3 or $x^2\nu$. In this case, the spectrum can be obtained by taking the single-sided Fourier transform

$$S_{mn}(\omega) = \int_0^\infty B_{mn}(\tau) e^{i\omega\tau} d\tau. \quad (14)$$

The initial conditions enter the equations since

$$\int_0^\infty \frac{dB_{mn}}{d\tau} e^{i\omega\tau} d\tau = -B_{mn}(0) - i\omega\, S_{mn}. \quad (15)$$

Equation (11) is thus transformed to a set of coupled complex algebraic equations. The spectrum of the response (the Fourier transform of $R(\tau)$ in Eq. (13)) is given by

$$S(\omega) = \sigma_1^2 (S_{10} + S_{10}^*)/2\pi \quad (16)$$

where the asterisk denotes the complex conjugate.

Applications

In the stationary limit, the set of Eq. (5) for $C_{km}(t)$ as $t \to \infty$ becomes algebraic. As the Fourier transformed set (11) is also of course algebraic, in principle the spectrum can be found by solving two sets of only algebraic equations, the first nonlinear (in σ_1 and σ_2, although linear in C_{km}), and the second (for S_{mn}) linear. In practice it turns out to be more convenient to solve the full time-dependent equations for C_{km} then once the coefficients seem to be close to a stationary limit, to use these values as an initial guess for the solution of the time-independent algebraic version of Eq. (5). The solution for S_{mn} once the C_{km} are known requires only matrix inversion. It should be pointed out that the computer program itself generates the sets of equations; this enables very large numbers of equations to be used. In the van der Pol example below, we use $k + m = 20$, and thus involve 120 coefficients in the Hermite series approximation to the pdf. It has been found that the subsequent solution for the terms S_{mn} often requires a smaller value of N. We note also that the form of the equations shows that $S_{mn} = 0$ for $(m+n)$ even.

Details of the numerical procedures have been discussed more fully by Liu and Davies (1990b) for a more general second-order system. Liu (1990) has also extended the results to oscillators with hysteretic restoring forces, requiring a triple summation approximation to the pdf.

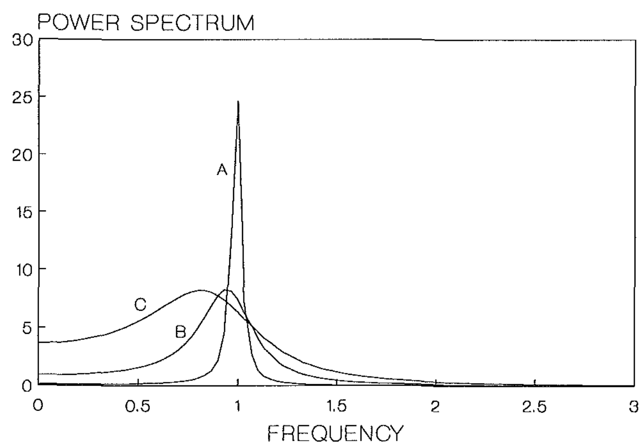

Fig. 1 The response spectra of a Duffing oscillator to different excitations. $\beta = 0.2$, $\alpha = 0.5$; A:$h = 0.1$, B:$h = 0.4$, C:$h = 0.8$ $m + n \leq 10$, **giving 35 equations.**

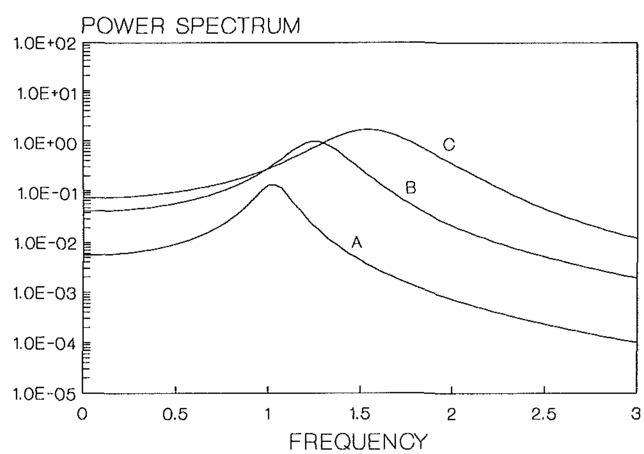

Fig. 2 The response spectra of a van der Pol oscillator to different excitations. $\beta = -0.2$, $\alpha = 0.2$; A:$h = 0.4$, B:$h = 1.2$, C:$h = 2.4$. $m + n \leq 20$, **giving 120 equation for pdf, but** $M = n \leq 16$, **giving 80 equations for** S_{mn}.

Figure 1 shows the spectrum for a Duffing oscillator with $g(x, \nu) = \alpha x^3$. As the excitation level increases the resonance frequency increases, and the width of the resonance peak also increases. This is in keeping with the result of Miles (1989). An increase in the response level causes an increase in the effective resonance frequency; a random response contains all amplitudes each with its effective resonance frequency and contributes to the broadening of the peak.

Figure 2 shows the spectrum for a van der Pol oscillator with $g(x, \nu) = \alpha x^3 \nu$ and $\beta = -\alpha$ in Eq. (2). In the case of sinusoidal excitation with a frequency close to one, at low excitation levels, the response has components at the excitation frequency and at the entrained free-oscillation frequency of one. As the excitation amplitude is increased beyond a critical value the free-oscillation decays. Fig. 2 shows for the random case a large peak at a frequency $\nu = 1$ for small excitation levels. The peak broadens considerably and flattens as the excitation level is increased suggesting that the free-oscillation component is also partly quenched in the random case.

Conclusion

Some results have been obtained for the spectrum of the response of nonlinear oscillators to white noise excitation. The results are obtained as an extension of previous work by the authors (Liu and Davies, 1988, 1990a) and complement earlier work by Miles (1989) and Wen (1975, 1976).

The work was supported by the Natural Sciences and Engineering Research Council of Canada.

References

Crandall, S. H., 1980, "Non-Gaussian Closure for Random Vibration of Nonlinear Oscillator," *International Journal of Nonlinear Mechanics*, Vol. 15, pp. 303–313.

Guckenheumer, J., and Holmes, P., 1983, *Nonlinear Oscillations, Dynamical Systems, and Bifurcations of Vector Fields*, Springer-Verlag, New York.

Liu, Q., and Davies, H. G., 1988, "Application of Non-Gaussian Closure to the Nonstationary Response of a Duffing Oscillator," *International Journal of Nonlinear Mechanics*, Vol. 23, pp. 241–250.

Liu, Q., and Davies, H. G., 1990a, "Nonstationary Response pdf of Nonlinearity Damped Oscillators Subjected to White Noise Excitation," *Journal of Sound and Vibration*, accepted for publication.

Liu, Q., and Davies, H., 1990b, "On a Type of Non-Gaussian Closure in Nonlinear Random Response Analysis: Theory and Computation," *International Journal of Computers and Structures*, submitted for publication.

Liu, Q., and Davies, H. G., 1991, "Response Analysis of a Hysteretic System Under Random Excitations," *Journal of Sound Vibration*, accepted for publication.

Miles, R. N., 1989, "An Approximate Solution for the Spectral Response of Duffing's Oscillator with Random Input," *Journal of Sound and Vibration*, Vol. 132, pp. 43–49.

Nayfeh, A. H., and Mook, D. T., 1979, *Nonlinear Oscillations*, John Wiley and Sons, New York.

Wen, Y. K., 1975, "Approximate Method for Nonlinear Random Vibration," *Journal of Engineering Mechanics*, ASCE, New York, Vol. 101, pp. 389–401.

Wen, Y. K., 1976, "Method for Random Vibration of Hysteretic Systems," *Journal of Engineering Mechanics*, ASCE New York, Vol. 102, pp. 249–263.

Extension of Vlasov's Semi-membrane Theory to Reinforced Composite Shells

V. Birman[14]

Governing equations for the statics and dynamics of reinforced composite shells are developed based on Vlasov's semi-membrane shell theory. These equations have closed-form solutions illustrated for buckling and free vibration problems. The buckling solution converges to the known result for unstiffened isotropic shells.

[14]Engineering Education Center, University of Missouri-Rolla, St. Louis, MO 63121. Mem. ASME.

Manuscript received by the ASME Applied Mechanics Division, Jan. 30, 1991; final revision, Feb. 25, 1991.

Introduction

Reinforced composite shells have been a subject of a number of analytical studies. Typically, these studies were based on Donnell-type theory of shells (Block, 1968; Bogdanovich, 1986; Birman, 1988, 1990a, 1990b; Birman and Bert 1990). Donnell's shell theory is usually acceptable, if the axial or circumferential size of deformation waves is small. A comparison of Donnell, Morley, Love, and Sanders shell theories applied to unstiffened composite shells was performed by Bert and Reddy (1982). It was shown that Donnell-type theory yields results, which are in a good agreement with other theories if the radius-to-thickness ratio exceeds 20. However, it is necessary to note that Donnell's shell theory is not appropriate for long shells. In addition, this theory has been used to develop closed-form solutions only for one type of boundary condition.

Vlasov (1944) developed a theory for long isotropic cylindrical shells where stress couples M_x and M_{xy} and the transverse shear stress resultant Q_x are negligible (here, x and y are axial and circumferential coordinates, respectively).

In addition, the middle surface of the shell was assumed inextensible in the circumferential direction, i.e., $\epsilon^y = 0$ and in-surface shearing deformations were neglected ($\gamma_{xy} = 0$).

The theory based on these assumptions is called Vlasov's semi-membrane shell theory. An example of application of this theory to stability problems of isotropic cylindrical shells subject to axial compression can be found in Vol'mir's monograph (1967). Note that Vlasov's semi-membrane theory is based on Love's first approximation shell theory whose particular case it represents.

In this Note, Vlasov's theory is extended to long, reinforced composite cylindrical shells. Obviously, reinforcements should be light and closely spaced to justify the assumptions of the theory.

Governing Equations

Consider a symmetrically laminated cylindrical shell reinforced by axial and circumferential stiffeners. The strain-displacement relationships used in Vlasov's semi-membrane theory are

$$
\begin{aligned}
&\epsilon_x = u_{,x} && \kappa_x = -w_{,xx} \\
&\epsilon_y = v_{,y} - \frac{w}{R} = 0 && \kappa_y = -w_{,yy} - \frac{w}{R^2} \\
&\gamma_{xy} = u_{,y} + v_{,x} = 0 && \kappa_{xy} = -w_{,xy} - \frac{v_{,x}}{2R}
\end{aligned} \tag{1}
$$

where all notations are standard and the radial deflection w is positive if directed to the center of curvature. The stresses in the shell and stiffeners can be calculated as functions of strains using Hookean relationships omitted for brevity. The axial stress resultant and the circumferential stress couple used in the analysis are

$$
\begin{aligned}
N_x &= A_{11}\epsilon_x + \sum_s \delta(y-y_s) E_s A_s (\epsilon_x + z_s \kappa_x) \\
M_y &= D_{12}\kappa_x + D_{22}\kappa_y + \sum_r \delta(x-x_r) E_r I_{or} \kappa_y
\end{aligned} \tag{2}
$$

where A_{11} is the axial extensional stiffness of the shell, D_{ij} are its bending stiffnesses, A_r and A_s are stiffener cross-sectional areas, x_r and y_s are coordinates of the stiffener centroids, E_s and E_r are the moduli of elasticity of the stiffeners, I_{or} is the moment of inertia of a ring stiffener about the shell middle

Figure 1 shows the spectrum for a Duffing oscillator with $g(x, \nu) = \alpha x^3$. As the excitation level increases the resonance frequency increases, and the width of the resonance peak also increases. This is in keeping with the result of Miles (1989). An increase in the response level causes an increase in the effective resonance frequency; a random response contains all amplitudes each with its effective resonance frequency and contributes to the broadening of the peak.

Figure 2 shows the spectrum for a van der Pol oscillator with $g(x, \nu) = \alpha x^3 \nu$ and $\beta = -\alpha$ in Eq. (2). In the case of sinusoidal excitation with a frequency close to one, at low excitation levels, the response has components at the excitation frequency and at the entrained free-oscillation frequency of one. As the excitation amplitude is increased beyond a critical value the free-oscillation decays. Fig. 2 shows for the random case a large peak at a frequency $\nu = 1$ for small excitation levels. The peak broadens considerably and flattens as the excitation level is increased suggesting that the free-oscillation component is also partly quenched in the random case.

Conclusion

Some results have been obtained for the spectrum of the response of nonlinear oscillators to white noise excitation. The results are obtained as an extension of previous work by the authors (Liu and Davies, 1988, 1990a) and complement earlier work by Miles (1989) and Wen (1975, 1976).

The work was supported by the Natural Sciences and Engineering Research Council of Canada.

References

Crandall, S. H., 1980, "Non-Gaussian Closure for Random Vibration of Nonlinear Oscillator," *International Journal of Nonlinear Mechanics*, Vol. 15, pp. 303–313.

Guckenheumer, J., and Holmes, P., 1983, *Nonlinear Oscillations, Dynamical Systems, and Bifurcations of Vector Fields*, Springer-Verlag, New York.

Liu, Q., and Davies, H. G., 1988, "Application of Non-Gaussian Closure to the Nonstationary Response of a Duffing Oscillator," *International Journal of Nonlinear Mechanics*, Vol. 23, pp. 241–250.

Liu, Q., and Davies, H. G., 1990a, "Nonstationary Response pdf of Nonlinearity Damped Oscillators Subjected to White Noise Excitation," *Journal of Sound and Vibration*, accepted for publication.

Liu, Q., and Davies, H., 1990b, "On a Type of Non-Gaussian Closure in Nonlinear Random Response Analysis: Theory and Computation," *International Journal of Computers and Structures*, submitted for publication.

Liu, Q., and Davies, H. G., 1991, "Response Analysis of a Hysteretic System Under Random Excitations," *Journal of Sound Vibration*, accepted for publication.

Miles, R. N., 1989, "An Approximate Solution for the Spectral Response of Duffing's Oscillator with Random Input," *Journal of Sound and Vibration*, Vol. 132, pp. 43–49.

Nayfeh, A. H., and Mook, D. T., 1979, *Nonlinear Oscillations*, John Wiley and Sons, New York.

Wen, Y. K., 1975, "Approximate Method for Nonlinear Random Vibration," *Journal of Engineering Mechanics*, ASCE, New York, Vol. 101, pp. 389–401.

Wen, Y. K., 1976, "Method for Random Vibration of Hysteretic Systems," *Journal of Engineering Mechanics*, ASCE New York, Vol. 102, pp. 249–263.

Extension of Vlasov's Semi-membrane Theory to Reinforced Composite Shells

V. Birman[14]

Governing equations for the statics and dynamics of reinforced composite shells are developed based on Vlasov's semi-membrane shell theory. These equations have closed-form solutions illustrated for buckling and free vibration problems. The buckling solution converges to the known result for unstiffened isotropic shells.

[14]Engineering Education Center, University of Missouri-Rolla, St. Louis, MO 63121. Mem. ASME.

Manuscript received by the ASME Applied Mechanics Division, Jan. 30, 1991; final revision, Feb. 25, 1991.

Introduction

Reinforced composite shells have been a subject of a number of analytical studies. Typically, these studies were based on Donnell-type theory of shells (Block, 1968; Bogdanovich, 1986; Birman, 1988, 1990a, 1990b; Birman and Bert 1990). Donnell's shell theory is usually acceptable, if the axial or circumferential size of deformation waves is small. A comparison of Donnell, Morley, Love, and Sanders shell theories applied to unstiffened composite shells was performed by Bert and Reddy (1982). It was shown that Donnell-type theory yields results, which are in a good agreement with other theories if the radius-to-thickness ratio exceeds 20. However, it is necessary to note that Donnell's shell theory is not appropriate for long shells. In addition, this theory has been used to develop closed-form solutions only for one type of boundary condition.

Vlasov (1944) developed a theory for long isotropic cylindrical shells where stress couples M_x and M_{xy} and the transverse shear stress resultant Q_x are negligible (here, x and y are axial and circumferential coordinates, respectively).

In addition, the middle surface of the shell was assumed inextensible in the circumferential direction, i.e., $\epsilon^y = 0$ and in-surface shearing deformations were neglected ($\gamma_{xy} = 0$).

The theory based on these assumptions is called Vlasov's semi-membrane shell theory. An example of application of this theory to stability problems of isotropic cylindrical shells subject to axial compression can be found in Vol'mir's monograph (1967). Note that Vlasov's semi-membrane theory is based on Love's first approximation shell theory whose particular case it represents.

In this Note, Vlasov's theory is extended to long, reinforced composite cylindrical shells. Obviously, reinforcements should be light and closely spaced to justify the assumptions of the theory.

Governing Equations

Consider a symmetrically laminated cylindrical shell reinforced by axial and circumferential stiffeners. The strain-displacement relationships used in Vlasov's semi-membrane theory are

$$\begin{aligned} &\epsilon_x = u_{,x} && \kappa_x = -w_{,xx} \\ &\epsilon_y = v_{,y} - \frac{w}{R} = 0 && \kappa_y = -w_{,yy} - \frac{w}{R^2} \\ &\gamma_{xy} = u_{,y} + v_{,x} = 0 && \kappa_{xy} = -w_{,xy} - \frac{v_{,x}}{2R} \end{aligned} \qquad (1)$$

where all notations are standard and the radial deflection w is positive if directed to the center of curvature. The stresses in the shell and stiffeners can be calculated as functions of strains using Hookean relationships omitted for brevity. The axial stress resultant and the circumferential stress couple used in the analysis are

$$N_x = A_{11}\epsilon_x + \sum_s \delta(y - y_s) E_s A_s (\epsilon_x + z_s \kappa_x)$$

$$M_y = D_{12}\kappa_x + D_{22}\kappa_y + \sum_r \delta(x - x_r) E_r I_{or} \kappa_y \qquad (2)$$

where A_{11} is the axial extensional stiffness of the shell, D_{ij} are its bending stiffnesses, A_r and A_s are stiffener cross-sectional areas, x_r and y_s are coordinates of the stiffener centroids, E_s and E_r are the moduli of elasticity of the stiffeners, I_{or} is the moment of inertia of a ring stiffener about the shell middle surface, and z_s is a distance between the middle surface and the centroid of an axial stiffener positive, if the stiffener is attached to the internal surface of the shell.

Equations of equilibrium or motion are obtained from Love's first-approximation shell theory:

$$N_{x,x}+N_{xy,y}=-q_x$$
$$N_{xy,x}+N_{y,y}-\frac{1}{R}M_{y,y}=-q_y$$
$$M_{y,yy}+\frac{N_y}{R}=-q \tag{3}$$

where q_x and q_y are in-surface distributed loads and q is an outside pressure.

The compatibility equation is

$$R\epsilon_{x,yyyy}+\frac{1}{R}\epsilon_{x,yy}=\kappa_{y,xx}. \tag{4}$$

Combining Eqs. (3) and (4) and using (2), one obtains the following differential equation:

$$-\frac{1}{R}\Omega\Omega M_y+\frac{\overline{E}_s}{R^2}\Omega w_{,xxxx}+\frac{\overline{A}_{11}}{R}\left(\frac{\partial^2}{\partial\beta^2}+1\right)w_{,\alpha\alpha\alpha\alpha}=-R\Omega Q \tag{5}$$

where

$$\Omega=\frac{\partial^4}{\partial\beta^4}+1$$
$$\alpha=\frac{x}{R}\quad\beta=\frac{y}{R}$$
$$\overline{A}_{11}=A_{11}+\sum_s\delta(y-y_s)E_sA_s$$
$$\overline{E}_s=\sum_s\delta(y-y_s)E_sA_sz_s$$
$$Q=-q_{,\beta\beta}-q_{x,\alpha\alpha}+q_{y,\beta}. \tag{6}$$

The substitution of M_y from (2) into (5) and the exclusion of the operator $(\partial^2/\partial\beta^2+1)$ yield

$$\overline{D}_{22}\Omega\Omega w+D_{12}\Omega w_{,\alpha\alpha\beta\beta}+\overline{E}_sRw_{,\alpha\alpha\alpha\alpha\beta\beta}+\overline{A}_{11}R^2w_{,\alpha\alpha\alpha\alpha}=-R^4Q_{,\beta\beta} \tag{7}$$

where

$$\overline{D}_{22}=D_{22}+\sum_r\delta(x-x_r)E_rI_{or}. \tag{8}$$

In a particular case of an isotropic shell, Eq. (7) reduces to that presented by Vol'mir (1967).

Note that the present theory is applicable in the case of light, closely spaced stiffeners. This justifies the application of the smeared stiffeners technique. Therefore,

$$\delta(y-y_s)=1/l_s$$
$$\delta(x-x_r)=1/l_r$$

where l_s and l_r are the spacings of the corresponding stiffeners.

Buckling Problem. If the shell is subject to an axial loading N_1, $q=-N_1w_{,xx}$, $q_y=-N_1v_{,xx}$, and $q_x=0$. Substituting these expressions into Q given by (6) and using (1), one obtains

$$Q=-\frac{N_1}{R^2}(w_{,\alpha\alpha}-w_{,\alpha\alpha\beta\beta}). \tag{9}$$

Suppose that

$$w=W\sin n\beta, \tag{10}$$

n being an integer. Then (7) yields an ordinary differential equation for W:

$$(\overline{A}_{11}R^2-\overline{E}_sRn^2)W_{,\alpha\alpha\alpha\alpha}+n^2[(1-n^2)n^2D_{12}+(n^2+1)N_1R^2]W_{,\alpha\alpha}+\overline{D}_{22}n^4(1-n^2)^2W=0. \tag{11}$$

The integral of (11) includes four constants of integration. If the ends of the shell are clamped, i.e., $w=w_{,\alpha}=0$, the substitution of the integral of (11) into the boundary conditions and the nonzero requirement for constants of integration yield the buckling equation. Another type of boundary condition can be formulated, if the shell is supported by equally spaced elastic bulkheads. Then for each span of the shell the boundary conditions are $w_{,\alpha}=0$, $w(L,0)=\pm gQ_x(L,0)$ where g is a bulkhead radial compliance and Q_x is the transverse shear stress resultant. Notably, although Q_x, M_x, and M_{xy} were neglected to develop the governing equation, in reality they exist, although negligible compared to Q_y and M_y. Therefore, Q_x can be expressed in terms of w using Eqs. (1) and

$$Q_x=M_{x,x}+M_{xy,y}$$
$$M_x=D_{11}\kappa_x+D_{12}\kappa_y+\sum_s\delta(y-y_s)E_s(A_sz_s\epsilon_x+I_{os}\kappa_x)$$
$$M_{xy}=D_{66}\kappa_{xy}$$
$$u=U\sin n\beta\quad U=-\frac{1}{n}V_{,x}$$
$$v=V\cos n\beta\quad V_{,x}=-2RnW_{,x}. \tag{12}$$

The expression for the twisting stress couple can be extended to include torsional stiffnesses of reinforcements without significant complication of the analysis.

If the ends are simply supported and unrestricted against axial movements ($N_x=0$),

$$W=f\sin\lambda\alpha\quad\lambda=\frac{m\pi R}{L} \tag{13}$$

where m is an integer satisfies the boundary conditions. Critical loads obtained from (11) are

$$N_{1cr}=\frac{(\overline{A}_{11}R^2-\overline{E}_sRn^2)\lambda^4+n^4(n^2-1)D_{12}\lambda^2+n^4(n^2-1)^2\overline{D}_{22}}{n^2(n^2+1)R^2\lambda^2}. \tag{14}$$

The buckling load corresponding to a chosen value of n is obtained from (14) where $\lambda=\overline{\lambda}$ obtained by minimization of N_{1cr} with respect to λ. If the shell is unstiffened and the material is isotropic, these results converge to the solution obtained by Vol'mir (1967).

Vibration Problem. In this problem, $q=-\rho w_{,tt}$, $q_x=-\rho u_{,tt}$, and $q_y=-\rho v_{,tt}$, ρ being the mass per unit area

$$\rho=\overline{\rho}+\sum_s\delta(y-y_s)\rho_sA_s+\sum_r\delta(x-x_r)\rho_rA_r. \tag{15}$$

In (15), $\overline{\rho}$ is the mass per unit area of the unstiffened shell and ρ_s, ρ_r are mass densities of stiffener materials. Using

$$w=We^{i\omega t}\sin n\beta, \tag{16}$$

and smeared stiffeners technique, one obtains a dynamic counterpart of (11):

$$(\overline{A}_{11}R^2-\overline{E}_sRn^2)W_{,\alpha\alpha\alpha\alpha}+[D_{12}n^4(1-n^2)+\rho R^4\omega^2]W_{,\alpha\alpha}+[\overline{D}_{22}n^4(1-n^2)^2-\rho R^4n^2(n^2+1)\omega^2]W=0. \tag{17}$$

If the shell is simply supported and (13) can be used, the corresponding squared frequency is

$$\omega^2=\frac{(\overline{A}_{11}R^2-\overline{E}_sRn^2)\lambda^4+n^4(n^2-1)D_{12}\lambda^2+n^4(n^2-1)^2\overline{D}_{22}}{\rho R^4[\lambda^2+n^2(n^2+1)]}. \tag{18}$$

The integral of (17) can also be subject to other boundary conditions discussed above yielding the frequency equation for these cases.

Concluding Remarks

Important conclusions can be obtained from (14) and (18). Ring stiffeners always increase buckling loads and natural frequencies of semi-membrane cylindrical shells. Axial stiffeners have the same effect in all practically important situations.

Limitations of the semi-membrane theory, i.e., shell and stiffener geometries and material characteristics appropriate for its application can be established by comparison of results (14), (18) with available solutions. It would be preferable to use Love's first-approximation theory for the comparison, since Vlasov's theory represents its particular case. An extensive parametric analysis necessary to formulate these limitation exceeds the scope of this Note.

Vlasov's semi-membrane theory of isotropic shells represents a particular case of the theory developed here. The advantage of the present theory is that it can be used to obtain closed-form solutions for various boundary condition which are not available using other theories of shells.

Acknowledgment

Discussions with Prof. C. W. Bert of the University of Oklahoma are warmly appreciated.

References

Bert, C. W., and Reddy, V. S., 1982, "Composite Shells of Bimodulus Composite Materials," *Journal of Engineering Mechanics*, ASCE, Vol. 108, No. EM5, pp. 675-688.

Birman, V., 1988, "Axisymmetric Divergence of Ring-Stiffened Composite Cylindrical Shells Subject to Axial Compression," ASME JOURNAL OF APPLIED MECHANICS, Vol. 55, pp. 984-985.

Birman, V., 1990a, "Divergence Instability of Reinforced Composite Circular Cylindrical Shells," *International Journal of Solids and Structures*, Vol. 26, pp. 571-580.

Birman, V., 1990b, "Thermal Dynamic Problems of Reinforced Composite Cylinders," ASME JOURNAL OF APPLIED MECHANICS, Vol. 57, pp. 941-947.

Birman, V., and Bert, C. W., 1990, "Dynamic Stability of Reinforced Composite Cylindrical Shells in Thermal Fields," *Journal of Sound and Vibrations*, Vol. 142, pp. 183-190.

Block, D. L., 1968, "Influence of Discrete Ring Stiffeners and Prebuckling Deformations on the Buckling of Eccentrically Stiffened Orthotropic Cylinders," NASA, TN D-4283.

Bogdanovich, A. E., 1986, "Nonlinear Problems of the Dynamic Buckling of Reinforced Laminar Cylindrical Shells," *Soviet Applied Mechanics*, Vol. 22, pp. 745-753.

Vlasov, V. Z., 1944, "Governing Differential Equations of a General Theory of Elastic Shells," *Applied Mathematics and Mechanics*, Vol. 8, No. 2 (in Russian).

Vol'mir, A. S., 1967, *Stability of Deformable Systems*, Nauka Publishers, Moscow, pp. 511-521 (in Russian).

Stability of Flow Between Two Rotating Cylinders in the Presence of a Constant Heat Flux at the Outer Cylinder and Radial Temperature Gradient: Narrow Gap Problem

M. A. Ali[15], H. S. Takhar[16], and V. M. Soundalgekar[17]

Introduction

The study of the effects of constant heat flux at the inner cylinder on the stability of flow of a viscous incompressible fluid between two rotating concentric cylinders was presented by Takhar et al. (1988) in the case of a narrow gap. Instead of constant heat flux at the inner cylinder, if there is a constant heat flux at the outer cylinder, how is the stability of flow affected? This question is studied in this paper. All the earlier references on this topic are referred in Takhar et al. (1988).

[15]Department of Mathematics, Bahrain University, Bahrain.

[16]Department of Engineering, Manchester University, Manchester M13 9P1, UK.

[17]Brindavan Society, Thane 400601, India. Mem. ASME.

Manuscript received by the ASME Applied Mechanics Division, Mar. 10, 1989; final revision, March 7, 1991.

Mathematical Analysis For a three-dimensional, axisymmetric, and incompressible viscous flow, and neglecting viscous dissipative heat, the steady state solutions can be shown to be

$$u=w=0,\ V=Ar+\frac{B}{r}$$

$$A=\frac{\Omega_2R_2^2-\Omega_1R_1^2}{R_2^2-R_1^2},\ B=\frac{R_1^2R_2^2\,(\Omega_1-\Omega_2)}{R_2^2-R_1^2}$$

$$\bar{\theta}=T-T_1=\frac{qR_2}{K}\ln\frac{r}{R_1} \quad (1)$$

where R_1, R_2 are the radii of the inner and the outer cylinders, respectively. For the velocity field, the usual no-slip boundary conditions are assumed and for the temperature field. For constant heat flux at the outer cylinder and the inner cylinder at temperature T_1, the boundary conditions are assumed as follows:

$$T=T_1 \text{ at } r=R_1 \text{ and } \frac{dT}{dr}=\frac{q}{K} \text{ at } r=R_2. \quad (2)$$

Here, (u, v, w) are the velocity components in the (r, θ, z) directions, K is the thermal conductivity, and q is the constant heat flux at the outer cylinder.

Following the usual procedure for deriving the differential equations for the marginal state of stability, we can show that these differential equations are as follows for a narrow gap:

$$(D^2-a^2)^2u=-a^2\mathrm{Ta}[g(x)v+N\cdot(g(x))^2\theta] \quad (3)$$

$$(D^2-a^2)v=u \quad (4)$$

$$(D^2-a^2)\theta=u \quad (5)$$

with following boundary conditions:

$$u=Du=V=\theta=0 \text{ at } x=0$$

$$u=Du=V=D\theta=0 \text{ at } x=1. \quad (6)$$

The nondimensional quantities are defined as follows:

$$d=R_2-R_1,\ x=\frac{r-R_1}{d},\ D=\frac{d}{dX}$$

$$a=\lambda d,\ \mu=\Omega_2/\Omega_1,\ g(x)=1-(1-\mu)x$$

$$\mathrm{Pr}=\nu/K,\ u=\frac{\nu}{2Ad^2}\bar{u},\ \theta=\frac{2A}{\Omega_1}\frac{1}{\mathrm{Pr}}\left(\frac{K}{qR_2}\right)T$$

$$\mathrm{Ta}=-\frac{4A\Omega_1d^4}{\nu^2},\ \mathrm{Ra}=\frac{\mathrm{Pr}\Omega_1^2d^4\left(\frac{qR_2}{K}\right)\alpha}{\nu_2}$$

$$N=-\frac{\mathrm{Pr}\alpha(qR_2/K)\Omega_2}{4A}=\frac{\mathrm{Ra}}{\mathrm{Ta}}. \quad (7)$$

Here, Ra is the Rayleigh number, Ta is the Taylor number, Pr is the Prandtl number, and N is the ratio of Ra and Ta. The only difference between the present set of Eqs. (3)-(6) and those of Eqs. (12)-(15) of Takhar et al. (1988) is that the sign of N in Eq. (3) is positive in the present case and here the boundary conditions on θ are interchanged. Thus, we have a two-point boundary value problem defined by Eqs. (3)-(5) with boundary conditions (6) for determining the eigenvalues a_c, Ta_c for given values of μ and N. Here, a_c, Ta_c are the critical values of the wave number a and the Taylor number Ta. Ta_c helps us determine the speeds of the two cylinders in relative motion at which the transition in the fluid-flow takes place from its initial state to its final unstable state with the corresponding a_c which then determines the spacing of the vortices in the axial direction.

Results and Discussion These values of a_c and Ta_c are listed in Table 1 and in order to get the physical insight into the problem, we show the variation of Ta_c in Figs. 1-2. To compare the effect of constant heat flux at the outer cylinder, CHF_0, quencies of semi-membrane cylindrical shells. Axial stiffeners have the same effect in all practically important situations.

Limitations of the semi-membrane theory, i.e., shell and stiffener geometries and material characteristics appropriate for its application can be established by comparison of results (14), (18) with available solutions. It would be preferable to use Love's first-approximation theory for the comparison, since Vlasov's theory represents its particular case. An extensive parametric analysis necessary to formulate these limitation exceeds the scope of this Note.

Vlasov's semi-membrane theory of isotropic shells represents a particular case of the theory developed here. The advantage of the present theory is that it can be used to obtain closed-form solutions for various boundary condition which are not available using other theories of shells.

Acknowledgment

Discussions with Prof. C. W. Bert of the University of Oklahoma are warmly appreciated.

References

Bert, C. W., and Reddy, V. S., 1982, "Composite Shells of Bimodulus Composite Materials," *Journal of Engineering Mechanics*, ASCE, Vol. 108, No. EM5, pp. 675-688.

Birman, V., 1988, "Axisymmetric Divergence of Ring-Stiffened Composite Cylindrical Shells Subject to Axial Compression," ASME JOURNAL OF APPLIED MECHANICS, Vol. 55, pp. 984-985.

Birman, V., 1990a, "Divergence Instability of Reinforced Composite Circular Cylindrical Shells," *International Journal of Solids and Structures*, Vol. 26, pp. 571-580.

Birman, V., 1990b, "Thermal Dynamic Problems of Reinforced Composite Cylinders," ASME JOURNAL OF APPLIED MECHANICS, Vol. 57, pp. 941-947.

Birman, V., and Bert, C. W., 1990, "Dynamic Stability of Reinforced Composite Cylindrical Shells in Thermal Fields," *Journal of Sound and Vibrations*, Vol. 142, pp. 183-190.

Block, D. L., 1968, "Influence of Discrete Ring Stiffeners and Prebuckling Deformations on the Buckling of Eccentrically Stiffened Orthotropic Cylinders," NASA, TN D-4283.

Bogdanovich, A. E., 1986, "Nonlinear Problems of the Dynamic Buckling of Reinforced Laminar Cylindrical Shells," *Soviet Applied Mechanics*, Vol. 22, pp. 745-753.

Vlasov, V. Z., 1944, "Governing Differential Equations of a General Theory of Elastic Shells," *Applied Mathematics and Mechanics*, Vol. 8, No. 2 (in Russian).

Vol'mir, A. S., 1967, *Stability of Deformable Systems*, Nauka Publishers, Moscow, pp. 511-521 (in Russian).

Stability of Flow Between Two Rotating Cylinders in the Presence of a Constant Heat Flux at the Outer Cylinder and Radial Temperature Gradient: Narrow Gap Problem

M. A. Ali[15], H. S. Takhar[16], and V. M. Soundalgekar[17]

Introduction

The study of the effects of constant heat flux at the inner cylinder on the stability of flow of a viscous incompressible fluid between two rotating concentric cylinders was presented by Takhar et al. (1988) in the case of a narrow gap. Instead of constant heat flux at the inner cylinder, if there is a constant heat flux at the outer cylinder, how is the stability of flow affected? This question is studied in this paper. All the earlier references on this topic are referred in Takhar et al. (1988).

[15]Department of Mathematics, Bahrain University, Bahrain.

[16]Department of Engineering, Manchester University, Manchester M13 9P1, UK.

[17]Brindavan Society, Thane 400601, India. Mem. ASME.

Manuscript received by the ASME Applied Mechanics Division, Mar. 10, 1989; final revision, March 7, 1991.

Mathematical Analysis For a three-dimensional, axisymmetric, and incompressible viscous flow, and neglecting viscous dissipative heat, the steady state solutions can be shown to be

$$u=w=0,\ V=Ar+\frac{B}{r}$$

$$A=\frac{\Omega_2R_2^2-\Omega_1R_1^2}{R_2^2-R_1^2},\ B=\frac{R_1^2R_2^2\,(\Omega_1-\Omega_2)}{R_2^2-R_1^2}$$

$$\bar{\theta}=T-T_1=\frac{qR_2}{K}\ln\frac{r}{R_1} \qquad (1)$$

where R_1, R_2 are the radii of the inner and the outer cylinders, respectively. For the velocity field, the usual no-slip boundary conditions are assumed and for the temperature field. For constant heat flux at the outer cylinder and the inner cylinder at temperature T_1, the boundary conditions are assumed as follows:

$$T=T_1 \text{ at } r=R_1 \text{ and } \frac{dT}{dr}=\frac{q}{K} \text{ at } r=R_2. \qquad (2)$$

Here, (u, v, w) are the velocity components in the (r, θ, z) directions, K is the thermal conductivity, and q is the constant heat flux at the outer cylinder.

Following the usual procedure for deriving the differential equations for the marginal state of stability, we can show that these differential equations are as follows for a narrow gap:

$$(D^2-a^2)^2u=-a^2\mathrm{Ta}[g(x)v+N\cdot(g(x))^2\theta] \qquad (3)$$

$$(D^2-a^2)v=u \qquad (4)$$

$$(D^2-a^2)\theta=u \qquad (5)$$

with following boundary conditions:

$$u=Du=V=\theta=0 \text{ at } x=0$$

$$u=Du=V=D\theta=0 \text{ at } x=1. \qquad (6)$$

The nondimensional quantities are defined as follows:

$$d=R_2-R_1,\ x=\frac{r-R_1}{d},\ D=\frac{d}{dX}$$

$$a=\lambda d,\ \mu=\Omega_2/\Omega_1,\ g(x)=1-(1-\mu)x$$

$$\mathrm{Pr}=\nu/K,\ u=\frac{\nu}{2Ad^2}\bar{u},\ \theta=\frac{2A}{\Omega_1}\frac{1}{\mathrm{Pr}}\left(\frac{K}{qR_2}\right)T$$

$$\mathrm{Ta}=-\frac{4A\Omega_1d^4}{\nu^2},\ \mathrm{Ra}=\frac{\mathrm{Pr}\Omega_1^2d^4\left(\frac{qR_2}{K}\right)\alpha}{\nu_2}$$

$$N=-\frac{\mathrm{Pr}\alpha(qR_2/K)\Omega_2}{4A}=\frac{\mathrm{Ra}}{\mathrm{Ta}}. \qquad (7)$$

Here, Ra is the Rayleigh number, Ta is the Taylor number, Pr is the Prandtl number, and N is the ratio of Ra and Ta. The only difference between the present set of Eqs. (3)-(6) and those of Eqs. (12)-(15) of Takhar et al. (1988) is that the sign of N in Eq. (3) is positive in the present case and here the boundary conditions on θ are interchanged. Thus, we have a two-point boundary value problem defined by Eqs. (3)-(5) with boundary conditions (6) for determining the eigenvalues a_c, Ta_c for given values of μ and N. Here, a_c, Ta_c are the critical values of the wave number a and the Taylor number Ta. Ta_c helps us determine the speeds of the two cylinders in relative motion at which the transition in the fluid-flow takes place from its initial state to its final unstable state with the corresponding a_c which then determines the spacing of the vortices in the axial direction.

Results and Discussion These values of a_c and Ta_c are listed in Table 1 and in order to get the physical insight into the problem, we show the variation of Ta_c in Figs. 1-2. To compare the effect of constant heat flux at the outer cylinder, CHF_0,

Table 1 Values of the critical Taylor number Ta_c and the critical wave number c

μ	N	a_c	Ta_c	μ	N	a_c	Ta_c
0.0	1.0	2.977	2057.5	−0.25	1.0	3.030	2866.4
	0.75	3.005	2282.8		0.75	3.050	3148.6
	0.50	3.037	2562.7		0.50	3.076	3491.9
	0.25	3.077	2919.6		0.25	3.107	3918.2
	0.0	3.127	3390.0		0.0	3.145	4461.4
0.25	1.0	2.929	1530.9	−0.5	1.0	3.080	4151.0
	0.75	2.962	1720.5		0.75	3.103	4554.3
	0.50	3.003	1962.8		0.5	3.129	5043.2
	0.25	3.053	2283.1		0.25	3.161	5647.8
	0.0	3.120	2725.3		0.0	3.199	6413.8
0.5	1.0	2.887	1175.2	−.75	1.0	3.108	6231.1
	0.75	2.925	1338.2		0.75	3.169	6967.
	0.50	2.972	1552.8		0.5	3.236	7880.5
	0.25	3.035	1847.3		0.25	3.312	9032.5
	0.0	3.118	2275.4		0.0	3.407	11361.8
0.75	1.0	2.851	926.3	−.1.0	1.0	2.989	9507.0
	0.75	2.892	1067.9		0.75	3.276	11297.3
	0.50	2.944	1259.5		0.50	3.567	13380.5
	0.25	3.016	1532.7		0.25	3.808	15794.5
	0.0	3.118	1951.5		0.0	3.999	18662.9
1.0	1.0	2.820	746.7				
	0.75	2.861	870.5				
	0.50	2.918	1042.5				
	0.25	2.998	1296.7				
	0.0	3.119	1707.8				

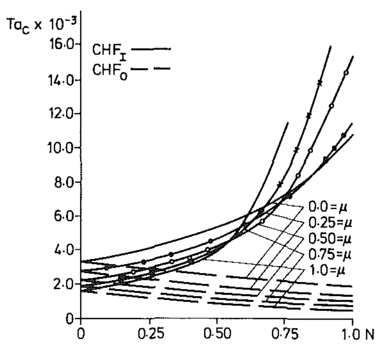

Fig. 1 Variation of Ta_c for $\{+\mu\}$

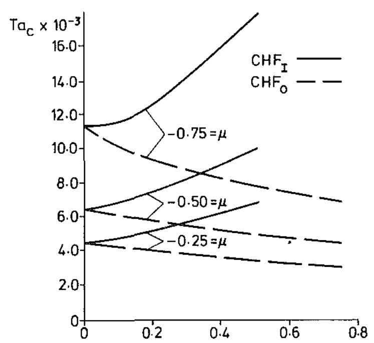

Fig. 2 Variation of Ta_c for $\{-\mu\}$

with that at the inner cylinder, CHF_1, we have plotted the values of Ta_c taken from Takhar, Ali, and Soundalgekar (1988) on the same graphs for the same values of μ and N. It is interesting to note from these two figures that for both $\pm\mu$, the flow is more stable in both the cases of co-rotating and counterrotating cylinders when there is a constant heat flux at the inner rotating cylinder, because Ta_c is found to increase with increasing N and μ in the presence of CHF at the inner rotating cylinder. But in the presence of constant heat flux at the outer cylinder, the values of Ta_c are found to decrease with increasing N, i.e., the fluid flow gets destabilized owing to increasing values of N where μ is constant. However, the trend for instability is different in the case of co-rotating and counterrotating cylinders. In the presence of co-rotating cylinders, Fig. 1, when μ increases due to increasing the rotational speed of the outer cylinder, Ta_c decreases, which can be physically interpreted as the flow getting destablizied early as the angular speed of the outer cylinder goes on increasing as compared to that of the inner cylinder in the presence of CHF at the outer cylinder. But in the presence of counterrotating cylinders, Fig. 2, as the angular speed of the outer cylinder increases, as compared to that of the inner cylinder, the flow getsmore and more stable, because the value of Ta_c is observed to increase with increasing $\{-\mu\}$.

It is interesting to note that an increase in N leads to a decrease in the value of a_c in the presence of constant heat flux at the outer cylinder, whereas in the presence of constant heat flux at the inner cylinder, a_c is observed to increase with increasing the value of N. Thus, due to constant heat flux at the inner cylinder, the spacing between the vortices increases in the axial direction where N increases. But an increase in N leads to an increase in spacings between the vortices in the axial direction in the presence of constant heat flux at the outer cylinder.

Conclusions

(1) The fluid flow is more stable when the two cylinders are counterrotating with CHF at the outer cylinder.

(2) In the presence of CHF at the outer cylinder, the fluid flow gets destablizied owing to increasing N for all μ. The destabliziation is greater when the angular speed of the outer cylinder ($\mu > 0$) steadily increases. But the flow gets stable more and more when the angular speed of the outer cylinder ($\mu < 0$) increases more and more when N is constant.

References

Takhar, H. S., Ali, M. A., and Soundalgekar, V. M., 1988, "Effects of Radial Temperature Gradient on the Stability of Flow In a Narrow-Gap Annulus With Constant Heat Flux at the Inner Rotating Cylinder," *Wärme und Stöffuber-tragnung*, Vol. 22, pp. 22–28.

On the Validity of Bilinear Restoring Characteristics for Elastoplastic Beam Vibrations

H. Schmieg[18,20] and P. Vielsack[19,20]

We consider elastoplastic vibrations of an initially horizontal cantilever beam subject to vertical movements

$$y = A\sin\Omega t \tag{1}$$

of the support. An elastic-viscous-plastic one-degree-of-freedom model is shown in Fig. 1. Its equation of motion

$$m\ell^2\left(\ddot{\varphi}+\frac{\ddot{y}}{\ell}\cos\varphi\right)+M(\varphi,\,\dot{\varphi})=mg\ell\cos\varphi \tag{2}$$

contains the history-dependent restoring characteristic $M(\varphi, \dot{\varphi})$ of the three element unit. Plastic states are associated with irreversible angle increments. Denoting $\varphi_I^{(n)}$ as sum of all increments up to the nth, the plastic state the restoring characteristic reads

$$M(\varphi,\,\dot{\varphi}) = \begin{cases} k(\varphi-\varphi_I^{(n)})+d\dot{\varphi}; & |\varphi-\varphi_I^{(n)}|\le M_p/k; \quad \dot{\varphi}\gtrless 0 \\ M_p\mathrm{sgn}\dot{\varphi}+d\dot{\varphi}; & \varphi\mathrm{sgn}\dot{\varphi}>\varphi_I^{(n)}\mathrm{sgn}\dot{\varphi}+M_p/k; \quad \dot{\varphi}\neq 0. \end{cases} \tag{3}$$

All data are taken from an actual beam made of mild steel with length $\ell = 200$ mm, rectangular cross-section $b/h = 20$ mm/2 mm, $E = 2\cdot 10^5$ N/mm^2, yield stress $\sigma_o = 300$ N/mm^2. This gives the spring constant $k = 3EI/\ell = 37$ Nm and the plastic moment $M_p = \sigma_o bh^2/4 = 5.95$ Nm. The single mass is $m = 1.5$ kg. Excitation is determined by the amplitude $A = 3$ mm and a frequency ratio $\Omega/\omega = 0.98$, where $\omega = (k/m\ell^2)^{1/2}$.

To discuss the influence of the viscous part in the three-element unit, we investigate two values of the dimensionless damping parameter $D = (d/2)/(m\ell^2\omega)$. A small number $D = 0.0015$ is measured for pure elastic motion. In the case of multiple plastic states, the viscous damping characteristic must capture the pointed loops of the restoring characteristic. Experimental results indicate a value $D = 0.03$ which is fairly constant for the problem under consideration. A procedure to solve the Eqs. (2) and (3) was described by Vielsack (1986). Results are shown in Fig. 2. Corresponding axes have identical scales.

Qualitatively, both cases of damping lead to a similar angle-time behavior $\varphi(t)$. The corresponding characteristics exhibit quantitative differences. The bilinear relation in the case of small damping is frequently found in literature to describe elastoplastic structural vibrations. In contrast only large damping creates realistic loops. Distances between two neighboring loops correspond to plastic increments. They decrease in both cases while increasing the number of plastic states. In addition the final deformed positions differ extremely with the maximum number of plastic states. We get $\varphi_I^{(26)} = 50$ deg for $D = 0.0015$ and $\varphi_I^{(40)} = 35$ deg for $D = 0.03$. The validity of a three-element unit for elastoplastic beam vibrations depends highly on the accurate choice of the viscous part.

Experimental investigations are based on the same data as given above. A beam is clamped at a thin-walled tube with special arrangement and connection of strain gauges to measure the moment $M(t)$. The tube is fixed on a shaker with absolute displacement $y(t)$. An opto-electronical device measures the vertical and horizontal absolute displacement of the moving mass. Combining these three signals by a simple geometrical relation yields $\varphi(t)$. Eliminating time t from the parametric representation $M = M(t)$ and $\varphi = \varphi(t)$ leads to the experimental results $M = M(\varphi)$ shown in Fig. 3.

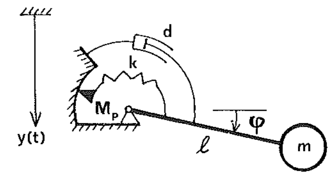

Fig. 1 Rigid-body model

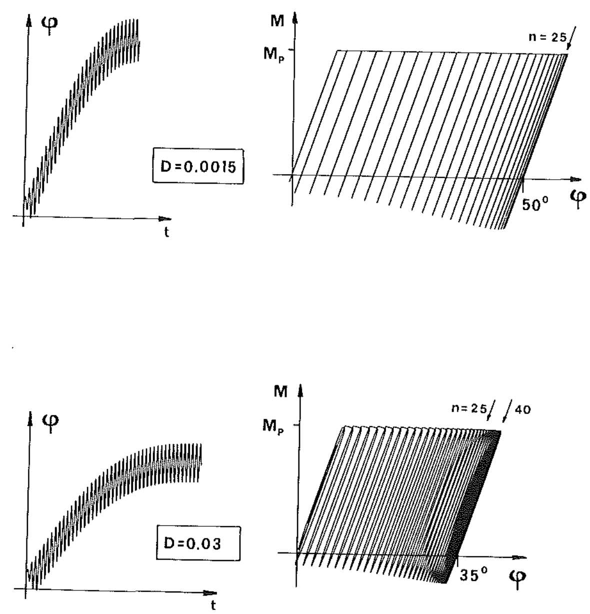

Fig. 2 Theoretical results

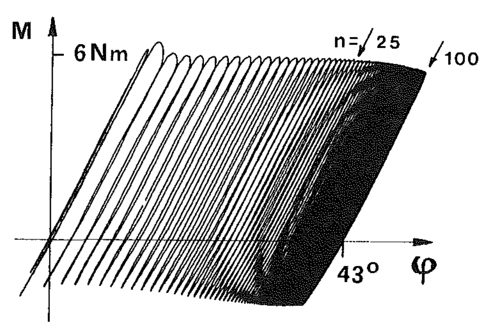

Fig. 3 Experimental result

Correspondence to the theoretical predictions for $D = 0.03$ is evident. Both constants k and M_p agree with their calculated values. If we compare the sum $\varphi_I^{(n)}$ of all plastic increments up to $n = 25$ we get $\varphi_I^{(25)} = 29$ deg from theory and $\varphi_I^{(25)} = 30$ deg from experiment. In contradiction to theory the loops do not converge for $n > 25$. Instead of a limiting angle we observe a small but permanent drift.

References

Vielsack, P., 1986, "Totale Stabilität in der Plastokinetik," *Zeitschrift für Angewandte Mathematik und Mechanik*, Vol. 66, pp. 321–329.

[18]Dr. -Ing.

[19]Professor.

[20]Institut fur Mechanik, Universitat Karlsruhe, 7500 Karlsruhe, Postfach 6980, Germany.

Manuscript received by the ASME Applied Mechanics Division, June 14, 1988; final revision, Jan. 18, 1989.

Thin Elastic Cylindrical Sheet Pressured Onto a Convex Corner

C. Y. Wang[21]

Pressure molding is an important process in the formation of thin-walled products. However, the final shape may not conform exactly to the mold due to resistance of the material. A previous paper (Wang 1985) studied the pressing of a two-dimensional thin sheet into a concave corner, which models the initial phase of pressure molding. The present Note complements that source by considering the convex corner. As we shall see later, there are some significant differences.

Figure 1 shows the cross-section of a sheet being pressed by pressure p onto a rigid corner with angle $\beta < \pi$. Assuming the regions of contact are well lubricated, only normal forces act on the sheet. Let the coordinate axes x', y' be located at one of the points of separation. A local moment balance gives

$$dm = -py'ds'\sin\theta + (G' - px')ds'\cos\theta \qquad (1)$$

where s' is the arc length $m = EI\,d\theta/ds'$ is the local moment per width and EI is the flexural rigidity (= (Young's modulus)(width)(thickness)^3/12(1 − (Poisson ratio)^2)). We normalize all lengths by $(EI)^{1/3}p^{-1/3}$ and all forces by $(EI)^{1/3}p^{2/3}$ and drop primes. The large deformation elastica equations are

$$\frac{d^2\theta}{ds^2} = -y\sin\theta + (G - x)\cos\theta \qquad (2)$$

$$\frac{dx}{ds} = \cos\theta,\ \frac{dy}{ds} = \sin\theta. \qquad (3)$$

The boundary conditions at origin are

$$x(0) = y(0) = \theta(0) = \frac{d\theta}{ds}(0) = 0. \qquad (4)$$

The last boundary condition is due to the fact that the sheet is pressed flat against the mold for $x' < 0$. The situation is similar to a flat-lying sheet of paper bent by an edge moment (gravity is equivalent to pressure when θ is small).

At the corner $s = l$ we need

$$y(l) = 0,\ \theta(l) = \frac{1}{2}(\beta - \pi). \qquad (5)$$

Equations (2)–(4) are integrated numerically with the fifth-order Runge-Kutta-Fehlberg algorithm. The point force G is adjusted to satisfy Eq. (5) at the same point. A step size of $\Delta s = 0.05$ is found to be sufficient for five figure accuracy. After the solution is found, the point force at the corner is

$$F = 2(c - G)\sin(\beta/2), \qquad (6)$$

$$c = x(l). \qquad (7)$$

The maximum moment or curvature (normalized by $(EI)^{2/3}p^{1/3}$) occurs at the corner

$$M = \frac{1}{2}c^2 - Gc = -\frac{d\theta}{ds}(l). \qquad (8)$$

Numerical solutions, however, become inaccurate for $\beta \approx 180$ deg or the almost flat corner. For these cases a perturbation method is used. We set $\epsilon \equiv (\tau - \beta)^{1/3}2^{-1/3}$ and

$$s = \epsilon t,\ \theta = \epsilon^3\phi,\ x = \epsilon\xi,\ y = \epsilon^4\eta,\ G = \epsilon g,\ l = \epsilon\lambda. \qquad (9)$$

[21]Department of Mathematics, Michigan State University, East Lansing, MI 48824-1027. Mem. ASME.

Manuscript received by the ASME Applied Mechanics Division, Nov. 1, 1989; final revision, Feb. 13, 1990.

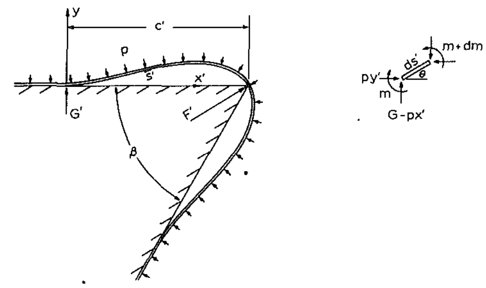

Fig. 1 The coordinate system

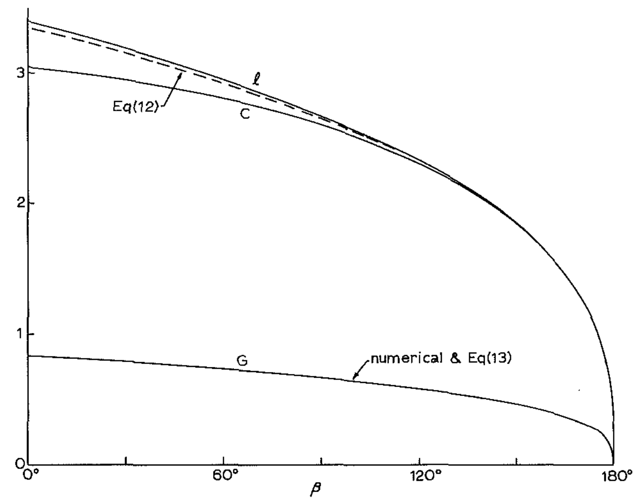

Fig. 2 The reactive force *G*, distance to corner *c*, and free length *ℓ*

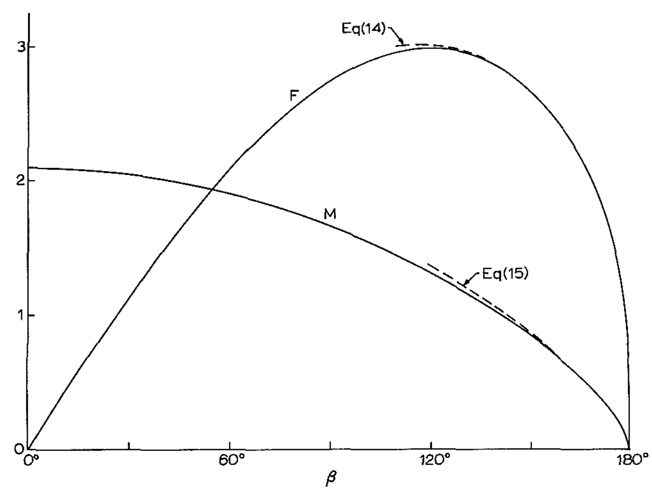

Fig. 3 The reactive force *F* and the maximum moment *M* at the corner

The governing equations are linearized to

$$\phi''(t) = g - \xi,\ \xi'(t) = 1,\ \eta'(t) = \phi \qquad (10)$$

with the boundary conditions

$$\phi(0) = \phi'(0) = \xi(0) = \eta(0) = 0,\ \eta(\lambda) = 0,\ \phi(\lambda) = -1. \qquad (11)$$

Without going into the details the approximate solutions are

$$c = l = \epsilon\lambda = [12(\pi - \beta)]^{1/3} \qquad (12)$$

$$G = \epsilon g = \frac{1}{4}[12(\pi - \beta)]^{1/3} \qquad (13)$$

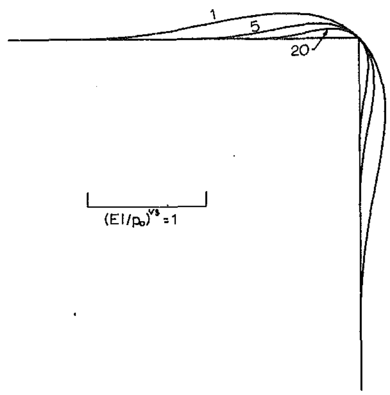

Fig. 4 Pressing onto a right corner. Values are for (p/p_0).

$$F=\frac{3}{2}\,[12(\pi-\beta)]^{1/3}\sin\frac{\beta}{2} \tag{14}$$

$$M=\left[\frac{3}{2}\,(\pi-\beta)\right]^{2/3}. \tag{15}$$

The results are shown in Figs. 2 and 3. Our approximate solutions are fairly accurate for 120 deg $<\beta\leq 180$ deg. Notice that the corner force F reaches a maximum near $\beta = 119.75$ deg. When $\beta = 0$, the sheet is pressed into a hairpin loop. We find $G = 0.8377$, $M = 2.1054$, $c = 3.0541$, $l = 3.4217$. This loop was studied by Fleherty, Keller, and Rubinow (1972) who obtained a value of 3.422 for l.

Although the governing equations are the same, the boundary conditions for the convex corner differ from those of the concave corner of Wang (1985). This is due to the corner reactive force on the sheet making the higher derivatives of θ discontinuous there. The results also show marked differences. All the parameters of the convex corner case are bounded while forces, and moments become infinite for the acute concave corner.

Similarity exists for given β. If flexural rigidity EI is constant, the lengths change as $p^{-1/3}$ and forces change as $p^{2/3}$. Figure 4 shows the effect of increasing pressure on a sheet enveloping a rigid right corner. It takes increasing pressure to force the elastic sheet to conform. In reality, the maximum moment M at the corner becomes large enough that a plastic hinge appears. Even so, it still takes infinite pressure albeit at a faster rate to force the sheet into a right angle. Therefore, in the design of pressure molds, convex corners should be rounded with a curvature determined by the results of this Note using the maximum pressure available.

References

Flaherty, J. E., Keller, J. B., and Rubinow, S. I., 1972, "Post Buckling Behavior of Elastic Tubes and Rings with Opposite Sides in Contact," *SIAM Journal of Applied Mathematics*, Vol. 23, pp. 446–455.

Wang, C. Y., 1985, "Deformation of a Wedged Elastic Sheet due to Pressure," ASME Journal of Applied Mechanics, Vol. 52, pp. 485–487.

Journal of Applied Mechanics

Book Reviews

Mechanical Vibration Analysis and Computation, by D. E. Newland. John Wiley and Sons, New York, 1989. 583 pages. Price: $59.95.

REVIEWED BY ANDRES SOOM[1]

This book is a fine addition to currently available vibration texts. It covers linear vibrations in considerable detail and makes appropriate use of matrix methods and computational techniques.

The first chapter is devoted to describing the relation between the impulse and frequency response of a single-degree-of-freedom oscillator. The next two chapters emphasize frequency response characteristics of multi-degree-of-freedom systems and include a section on damping measures.

Matrix methods are introduced in the fourth chapter and are related to natural frequencies and mode shapes in Chapter 5, which includes a good discussion of complex modes. Singular and defective matrices are covered in Chapter 6. The next four chapters combine numerical methods and general response functions for response calculations. Chapter 11, which deals with systems with symmetric matrices, also introduces Lagrange's equations.

Two chapters are devoted to continuous systems. The first chapter emphasizes longitudinal vibrations of elastic rods and the second transverse vibrations of beams and plates. The book concludes with a chapter on parametric and nonlinear vibrations which includes solutions of the Mathieu equations and the Duffing equations, along with discussion of stability, jump phenomena internal resonances, a brief mention of chaotic vibration, and approximate methods for finding periodic responses.

The book is very well written and is rich with examples that illustrate fundamental concepts, computational issues, and applications of the material to both simple and sophisticated practical vibration problems.

Although the material presented is self-contained, the book would be most suitable for advanced undergraduate or beginning graduate students with some previous background in mechanical vibrations, linear algebra, and dynamic systems analysis.

[1]Professor, Department of Mechanical and Aerospace Engineering, State University of New York, Buffalo, NY 14260.

Theory of Wire Rope, by G. A. Costello. Springer-Verlag, New York, 1990. 106 pages. Price: $59.00.

REVIEWED BY C. W. BERT[2]

For a very long time, there has been a great need for a monograph such as this. This is especially true since wire rope has been used since the days of Babylon (700 BC). Although there have been some users manuals and numerous technical papers on the subject, to the best of the reviewer's knowledge, this is the first monograph devoted solely to wire rope.

In a brief introductory chapter, the reader is introduced to the components and construction of wire rope. This is followed by a chapter on the equilibrium of a single curved wire, as presented in A. E. H. Love's treatise on elasticity. Chapter 3 discusses the static response of a strand consisting of a straight center wire and multiple helical wires. This includes the geometry involved and the response to axial and bending loads, multilayered strands, and detailed calculation of bending and contact stresses.

In Chapter 4 ropes of complicated cross-sections are analyzed for static response. Chapter 5 covers frictional effects and the effective length of broken wires. Chapter 6 is devoted to testing, including axial testing, size effects, and fatigue life. Chapter 7 discusses and analyzes the failure phenomenon known as "birdcaging," which is peculiar to wire rope. Rope rotation is treated in Chapter 8. The monograph is concluded with an extensive list of references and bibliography as well as an ample subject index.

In summary, the book fills very ably a need for a concise treatment of the mechanics of wire rope under static and fatigue loading. This monograph should be in the libraries of every mechanical engineering and manufacturing concern having any use for wire rope. It also should be of great interest to applied mechanicians in general.

[2]School of Aerospace and Mechanical Engineering, University of Oklahoma, Norman, OK 73019-0601.